

A FUNDAMENTAL STUDY OF NO REDUCTION
WITH HYDROGEN OVER IR(110)

Thesis by
Dale Edward Ibbotson

In Partial Fulfillment of the Requirements
for the Degree of
Doctor of Philosophy

California Institute of Technology
Pasadena, California

1981

(Submitted January 13, 1981)

To my loving wife, Elizabeth

It is a capital mistake to theorize before one has data.
Insensibly one begins to twist facts to suit theories,
instead of theories to suit facts.

-Sir Arthur Conan Doyle

ACKNOWLEDGMENTS

Jim Taylor helped me during the early years of my experimental work at Caltech. He gave me much insight into how problem-solving should be approached. Although we had our difficulties, we coauthored four papers that are presented in the appendix.

Steve Wittrig helped obtain much of the data presented in this thesis. We complemented each other in many ways which allowed us to accomplish a great deal in a comparatively short time. I appreciated his friendship as well.

My advisor, W. Henry Weinberg, allowed me much freedom in choosing my research. As the work developed, I looked to him as one to try ideas on and as a source of encouragement. I am grateful to him for these qualities and for his financial support through a grant by the National Science Foundation (No. CHE77-14976).

Others that aided me were-- secretary Kathy Lewis--machinists George Griffith, Chic Nakawatase and Ray Reed--and electronics fellows Mike Nagy and John Yehle. They deserve recognition for their very essential work.

The support, understanding and patience of my wife, Elizabeth, to whom this thesis is dedicated, has been worth more than can be estimated. She helped in many of the boring mechanics in putting together the manuscripts. When I needed a boost, she was there. I am indebted also to my parents, John and Laura, for their encouragement and support.

ABSTRACT

The heterogeneously catalyzed reduction of NO with hydrogen over Ir(110), as well as the chemisorption of the individual reactants and some of the products, has been studied at low pressures ($< 10^{-5}$ torr). The experiments were performed with several surface sensitive probes: thermal desorption mass spectrometry (TDS), contact potential difference (CPD) measurements, LEED, X-ray and UV photoelectron spectroscopies and Auger electron spectroscopy.

CHAPTER 2 describes the chemisorption of hydrogen on Ir(110). The Ir(110)-(1x2) reconstructed surface is stable in hydrogen at pressures from 10^{-9} to 10^{-5} torr and surface temperatures from 130 to 1000 K, the conditions investigated. Absolute coverage measurements indicate the saturation density at 130 K on Ir(110) is $(2.2 \pm 0.2) \times 10^{15}$ atoms cm^{-2} . Thermal desorption measurements indicate hydrogen obeys second order desorption kinetics and exhibits two features, β_1 and β_2 states, with intensities 2:1, respectively, which exchange isotopically with one another. However, β_2 hydrogen obeys first order adsorption kinetics with an initial probability of adsorption S_0 equal to unity, while β_1 hydrogen has an S_0 equal to 7×10^{-3} and obeys second order kinetics. Rate parameters for hydrogen desorption from Ir(110) show a sympathetic increase up to at least half of saturation for the β_2 state where E_d and ν_d assume values of 23 kcal-mole $^{-1}$ and $1.5 \times 10^{-2} \text{cm}^2\text{-s}^{-1}$, respectively. For the β_1 state, $E_d = 17 - 10\theta$ kcal-mole $^{-1}$ from θ equal to 0.4 - 0.7 and ν_d maintains an average value of $10^{-7} \text{cm}^2\text{-s}^{-1}$. The CPD and UPS measurements are used to infer probable binding sites for the β_1 and β_2 states of hydrogen which are consistent with the absolute coverage determined from TDS.

CHAPTER 3 discusses the interaction of hydrogen and CO on Ir(110). The co-adsorption of hydrogen and CO was undertaken to understand the effects of a model poison, CO, for hydrogen chemisorption. The adsorption of hydrogen on preadsorbed CO, or vice versa, causes less hydrogen to occupy the β_2 state and shifts the occupancy to the β_1 state preferentially. An apparent increase in the probability of adsorption of hydrogen in the β_1 state occurs for small CO

coverages. At high CO coverages, the Ir(110) surface is poisoned to hydrogen adsorption. Exposing CO to preadsorbed hydrogen causes the binding energy of hydrogen to decrease with increasing CO exposure. Eventually, hydrogen is displaced from the surface for sufficient CO exposures. The induced dipole of hydrogen is unaffected by CO compared to the clean surface, as measured by the CPD. The results indicate CO poisons β_2 sites for hydrogen by a simple site blocking mechanism and may exclude β_1 sites at high CO coverages by a hydrogen-CO repulsive interaction.

CHAPTER 4 presents the results for the molecular chemisorption of N_2 and the co-adsorption of N_2 with hydrogen on Ir(110) at low temperatures. Photoelectron spectroscopy shows molecular levels of N_2 at 8.0 ($5\sigma + 1\pi$) and 11.8 (4σ) eV in the valence band and at 399.2 eV with a satellite at 404.2 eV in the N(1s) region. The kinetics of adsorption and desorption of N_2 show that both precursor kinetics and interadsorbate interactions are important for this chemisorption system. Adsorption occurs with S_0 equal to unity up to saturation coverage ($4.8 \times 10^{14} \text{ cm}^{-2}$) and thermal desorption gives rise to two peaks. The activation energy for desorption varies between 8.5 and 6.0 kcal-mole $^{-1}$ at low and high coverages, respectively. Results of the co-adsorption of N_2 and hydrogen indicate that adsorbed N_2 resides in the missing row troughs on Ir(110) -(1x2). Furthermore, N_2 is displaced by hydrogen, and the β_2 state of hydrogen blocks virtually all N_2 adsorption.

CHAPTER 5 considers the chemisorption of NO on Ir(110). Adsorption of NO on Ir(110) proceeds by precursor kinetics with S_0 equal to unity independent of surface temperature. Saturation of Ir(110) is achieved in molecular form at $9.6 \times 10^{14} \text{ cm}^{-2}$ below 300 K. Approximately 35 % of a saturated overlayer desorbs as NO in two peaks with equal intensities. The balance desorbs as N_2 and O_2 where N_2 begins to desorb after the first peak of NO is nearly completed. Estimates were made of the activation energies for the various surface reactions that occur as the surface is heated. At low coverages of NO, N_2 desorbs with E equal to 36 kcal-

mole⁻¹. The activation energy for the dissociation of NO is near 25 kcal-mole⁻¹ for a saturated overlayer, but varies for smaller coverages of NO. Desorption of NO at saturation is associated with energies of 23 and 33 kcal-mole⁻¹ for the two peaks. The first peak represents desorption of NO from an oxygen-free surface and the second peak represents, at least in part, the recombination of nitrogen and oxygen adatoms on a partially oxidized surface. Oxygen tends to stabilize NO to dissociation and desorption as N₂, as reflected in TDS. Moreover, UPS and CPD results indicate NO is stabilized on oxygen overlayers compared to the clean Ir(110) surface.

CHAPTER 6 discusses the reaction of NO and deuterium to form N₂, ND₃ and D₂O over Ir(110). In addition, the competitive co-adsorption of NO and deuterium and the thermal desorption of the resulting overlayer were performed to gain further insight into the observed steady state rates of reaction, via TDS and CPD measurements. Small precoverages of deuterium do not affect the adsorption kinetics of NO on Ir(110) but do cause more N₂ to desorb relative to NO at saturation on the clean surface. Deuterium will adsorb on a saturated overlayer of NO. However, deuterium is strongly blocked from adsorbing on an Ir(110) surface that has both NO and oxygen adsorbed, which is a condition that occurs for some steady state reaction conditions. Under steady state conditions, the reduction of NO shows a marked hysteresis as the surface temperature is cycled for a large enough value of R(P_{D₂} / P_{NO}). A plateau in the reduction rate appears at some T that persists as T decreases until at lower values of T the rate falls irreversibly. For larger values of R, ND₃ is produced between 470 - 630 K and competes strongly with N₂ production. Otherwise, N₂ and D₂O are the only products of the reduction reaction. Tentative explanations of the empirical rate models derived from the steady state rate data are discussed in light of XPS, UPS and LEED results that are presented as well.

TABLE OF CONTENTS

CHAPTER 1:	INTRODUCTION	1
CHAPTER 2:	THE CHEMISORPTION OF HYDROGEN ON THE (110) SURFACE OF IRIIDIUM	15
CHAPTER 3:	THE CO-ADSORPTION OF HYDROGEN AND CARBON MONOXIDE ON THE (110) SURFACE OF IRIIDIUM	60
CHAPTER 4:	THE CHEMISORPTION OF N ₂ ON THE (110) SURFACE OF IRIIDIUM	83
CHAPTER 5:	THE CHEMISORPTION OF NO ON THE (110) SURFACE OF IRIIDIUM	116
CHAPTER 6:	THE REDUCTION OF NO WITH D ₂ OVER IR(110)	161
CHAPTER 7:	SUMMARY	217
APPENDIX A:	THE ADSORPTION OF WATER ON THE RECONSTRUCTED IR(110)-(1x2) SURFACE	224
APPENDIX B:	A TRANSIENT STUDY OF THE CO-ADSORPTION AND REACTION OF DEUTERIUM AND OXYGEN ON IR(110)	248
APPENDIX C:	"ORDER PLOT" IN THERMAL DESORPTION MASS SPECTROMETRY	255
APPENDIX D:	THE CHEMISORPTION OF CO ON CLEAN AND OXIDIZED IR(110)	260
APPENDIX E:	THE CHEMISORPTION OF OXYGEN ON THE (110) SURFACE OF IRIIDIUM	317
APPENDIX F:	A TRANSIENT STUDY OF THE CO-ADSORPTION AND REACTION OF CO AND OXYGEN ON IR(110)	354
APPENDIX G:	THE OXIDATION OF CARBON MONOXIDE OVER THE (110) SURFACE OF IRIIDIUM	375
APPENDIX H:	ADDITIONS TO THE POL OPERATING SYSTEM	388

CHAPTER 1
INTRODUCTION

The motivation for this thesis was to gain a more thorough understanding of the various processes that may be important in heterogeneously catalyzed reactions. More specifically, this study deals with: (1) measuring the thermodynamic properties of an adsorbed phase, (2) determining the elementary chemical steps of a reaction on a catalyst surface, (3) developing expressions to describe these steps, (4) microscopically locating the binding sites for the adatoms and admolecules, and (5) identifying the chemical nature of the adsorbates.

The approach used in this thesis was to study the heterogeneously catalyzed reduction of NO with hydrogen over Ir(110), as well as the chemisorption of the reactants and some of the products. This system was studied through gas-solid interactions that could be measured using surface-sensitive techniques. These surface-sensitive techniques include thermal desorption mass spectrometry (TDS), contact potential difference (CPD) measurements, low-energy electron diffraction (LEED), UV and X-ray photoelectron spectroscopies, and Auger electron spectroscopy. The nature of these probes limits their use to total pressures below 10^{-5} torr whereas the surface temperature could be varied from 95 to 1700 K.

The reasons for choosing the reaction between NO and hydrogen over Ir(110) are the following. This reaction represents one class of reactions where both reactants must

dissociate on the catalyst surface in order to form products. In a general view, the data available via the surface-sensitive probes mentioned are difficult to interpret even for the simplest reactants that are studied. Insight into simple reactions that can be understood on a microscopic scale serves to modify our view of the role a catalyst plays. Moreover, the reduction of NO is important commercially to control automobile emissions. Fundamental studies of this reaction therefore are useful beyond strictly scientific interest. Although the reactants have received a great deal of attention individually chemisorbed on the transition metals, reactive co-adsorption studies under vacuum conditions are few. Additionally, atmospheric studies of NO reduction over supported transition metals reveal a trend in the selectivity of the metals to the formation of ammonia or nitrogen, which may be understood more clearly by fundamental studies under well characterized conditions. Finally, iridium has received little attention with regard to the chemisorption of gases and reactions of adsorbed species.

The Ir(110) surface, in particular, was chosen for this study for several reasons. An ordered array of surface atoms provided by using a single crystal surface simplifies defining the surface geometry and the type of adsites available for chemisorption and reaction. Moreover, measurements involving surface-sensitive probes, such as LEED, CPD measurements and TDS, are more reproducible with single crystals than with

polycrystalline foils. If a simple termination of the bulk is considered, Ir(110) has a surface consisting of a regular series of rows and troughs. However, the surface when free of impurities reconstructs from the bulk structure to form a surface with every other row of atoms dissolved into the bulk. The surface may be visualized as densely packed micro-facets inclined to one another which are separated by ridges. This open structure not only exposes second layer Ir atoms but third layer Ir atoms as well. Thus, Ir(110) in its reconstructed form provides a wide variety of adsites and also represents a good model for surface defects. Under the influence of adsorbed species the surface may relax back to the bulk structure, which certainly would affect the elementary steps of reactions that depend upon certain types of active sites.

The presentation of this thesis is as follows. The chemisorption of hydrogen and NO on Ir(110) are presented in Chapters 2 and 5, respectively. Chapter 3 deals with the co-adsorption of hydrogen and CO on Ir(110) which gives further insight into the chemisorption properties of hydrogen in the presence of a model poison, CO. The molecular chemisorption of N₂ on Ir(110), one of the products in the reduction of NO, is presented in Chapter 4. Chapter 6 presents the results for the heterogeneously catalyzed reduction of NO with hydrogen over Ir(110). Following the summary in

Chapter 7, seven appendices describe additional studies performed on Ir(110) and one appendix details changes introduced to the experimental system employed in this work. The chemisorption of water (another reduction product encountered) on Ir(110) is presented in Appendix A. Appendix B shows a brief study of hydrogen and oxygen co-adsorption and reaction on Ir(110). The use of order plots in analyzing thermal desorption mass spectra is discussed in Appendix C in conjunction with data from Chapter 2 concerning hydrogen desorption from Ir(110). Appendices D and E deal with CO and oxygen chemisorption on Ir(110), respectively. The co-adsorption of CO and oxygen and subsequent reaction to form CO₂ under transient and steady state conditions over Ir(110) are described in Appendices F and G, respectively. Additions to the POL operating system, which are a 16-bit digital-to-analog converter to improve the measurement of several mass peaks in TDS and a software command that facilitates data analysis, are presented in Appendix H.

The remaining portion of this introduction will describe the surface techniques used here in studying the reactions of molecules on surfaces at low pressures and will discuss briefly the information that is available through these techniques. It should be stressed here that no single measurement technique will characterize a chemical system fully. An experimenter can understand the chemisorption and reaction properties of molecules on surfaces only through the intel-

ligent use of several techniques in an integrated program of study.

One of the oldest and most universal techniques that has been used in chemisorption studies is thermal desorption mass spectrometry (TDS). The experiment involves heating a surface covered with adsorbed gases and monitoring one or more species that evolve from the surface. If the volume surrounding the sample is pumped rapidly the intensity of a particular mass is proportional to the rate of desorption. Integration of the intensity with respect to time gives a relative measure of the coverage at any point in time. This technique was first used to study desorption from polycrystalline filaments (1). General reviews of desorption may be found in the literature (2). The rate of desorption may be expressed in the simplest form as a preexponential factor multiplied by a coverage to an integral exponent and an exponential of the ratio of an activation energy to the surface temperature. In its general form, the preexponential factor and the activation energy may vary with surface coverage. From TDS, information concerning the preexponential factor, the activation energy, the kinetic order and absolute coverage are possible to extract in some cases. Also, multiple sites and/or interadsorbate interactions may be deduced from several features appearing with respect to time or surface temperature during desorption.

Although the relative coverage of a gas may be calculated directly by integration as mentioned previously, other parameters in the desorption expression must be calculated using some form of analysis. The exponential of the coverage factor is assumed usually to represent the order of the rate limiting step for desorption. Many methods require the assumption that the rate parameters do not vary with surface coverage and that they may be calculated from two spectral features(3). These methods stem generally from the work of Redhead(4) and require only one desorption spectrum for any particular analysis of the rate parameters. Other forms of analysis use several desorption spectra at any point in coverage where the initial coverage(5) or the heating schedule(6) is varied between each spectrum. Several features in a desorption spectrum may be due to multiple sites but these must be deduced from other data, if possible. Inter-adsorbate interactions(7) or precursor intermediates(8,9) may be incorporated also into a desorption expression in order to explain anomalous preexponential factors, orders of desorption and shapes of desorption spectra. However, none of these modifications can predict the behavior of an adsorbate a priori. The kinetics of adsorption and the appearance of ordered overlayer structures(LEED) often are needed to justify their use.

If a series of exposures (pressure-time product) of a

gas are performed on a surface and the resulting TDS are recorded, the integrated intensities (relative coverages) plotted as a function of exposure give the adsorption kinetics of the gas. The initial probability of adsorption is equal to the slope of this curve at zero coverage once the absolute coverage is known and is independent of surface temperature, if adsorption is unactivated. Several analytical models have been used to fit the shape of the coverage-exposure curves by incorporating the effects due to an intermediate to chemisorption (precursor) and interadsorbate interactions. The simplest form of adsorption kinetics is the first or second order Langmuir type for associative or dissociative adsorption, respectively. A precursor model for associative (10) or dissociative (11) adsorption often will explain the slow variation of the probability of adsorption as a function of coverage. Since interadsorbate interactions as well as precursor kinetics may be important, both of these effects have been incorporated into a model (12). Appropriate limits on these models must, however, give the Langmuir type in order to be consistent. These are the major models used to describe the adsorption process for a single adsorbate. Little work has been performed on co-adsorbed systems since each system presents its own unique conditions of order and interactions.

Another technique used to measure adsorption and desorption phenomena is contact potential difference (CPD) measure-

ments. Although the highest energy level occupied by electrons in a metal (Fermi level) does not change in energy upon chemisorption of gases, a change may occur in the effective energy barrier for an electron to enter or exit a metal surface. The change (CPD) is due to the formation of a dielectric layer as a result of charge transfer between the surface and the adsorbate. Information concerning the degree of charge transfer as a function of surface coverage can give the effective dipole and polarizability of the surface complex (13). Moreover, coverage and temperature dependences of CPD measurements can be used to infer binding sites (14,15). The coverage dependence of the CPD may be used also to infer a change in the type of binding site sampled as the coverage increases, as seen for oxygen on Ir(110) (16). Many techniques have been developed to continuously measure the CPD during gas adsorption, but they can be divided into two classes- the diode method (17,18) and the capacitive method (19,20). Typically, the magnitude of the CPD is less than one eV (plus or minus sign) and acceptable levels of noise are on the order of 10 meV. If the response of the measurement is sufficiently fast (100 ms), the coverage-CPD relation is independent of temperature and the surface can be heated as the CPD measurement is recorded, the time derivative of the CPD gives the rate of adsorption or desorption of a gas (20). This may be compared to the desorption as measured by a mass spectrometer (21). Using the CPD as a coverage indicator at a series of

temperatures and pressures allows the isosteric heat of adsorption to be calculated using the Clausius-Clapeyron expression (22). Thus, CPD measurements used in conjunction with TDS measurements provides a powerful tool to characterize adsorption and desorption behavior.

Insofar as identification of adsorbed species is concerned, TDS gives only indirect evidence on the question of whether small molecules are dissociated or intact by the reaction order in desorption or by isotopic exchange experiments. Also, an activated process (dissociation) may occur as the surface is heated. To circumvent these problems, Auger electron spectroscopy may be used to determine the identity of the adsorbed species. The Auger mechanism is a three-electron process involving a core hole (created by high energy electrons or photons) and two higher lying levels. The nature of this mechanism makes it a convenient "fingerprint" for identifying elemental compositions on surfaces and determining their relative coverages (23). Furthermore, AES line shape analysis may be used to determine the molecular or dissociative nature of adsorbed species (24), since a large redistribution of features is expected if it is part of a molecule that dissociates. Also, the oxidation of a metal forms a different compound, which was seen by AES for Al (25). Thus, chemical effects may be seen using AES as an analysis tool. However, chemical effects may concern all three levels which are involved in the Auger process and are difficult to in-

terpret in this manner.

A technique that involves a one-electron process is easier to use conceptually in order to study chemical effects. This is accomplished via UV and X-ray photoelectron spectroscopies-UPS and XPS, respectively. Ideally, the mechanism involves a monoenergetic photon which ionizes an electron that is bound in an atom or molecule. The kinetic energy imparted to the electron is approximately equal to the difference in the energy of the photon and the binding energy of the electron. Core and valence levels are sampled via XPS and valence levels are sampled via UPS by virtue of their photon energies. Information concerning the chemical state of an element is available through XPS(26). Also the integrated intensity of the transitions is a measure of the relative coverage(27). Although UPS cannot be used easily to measure coverages, it is a sensitive indicator of the chemical and bonding nature of adsorbates on surfaces. Often UPS represents a fingerprint technique for adsorbed molecules compared to the gas phase(28). Moreover, complex calculations are required to predict the observed emission behavior in the valence region (29).

The final technique that will be discussed is low-energy electron diffraction(LEED). At the very least LEED is an invaluable tool to monitor qualitatively two-dimensional ordering of overlayers or changes in the order of the substrate. Correlating the LEED superstructure of and ordered array of

adsorbates with the relative coverage can give straightforwardly the absolute coverage. Moreover, processes such as surface oxidation may be followed by LEED as seen for the formation of a surface oxide on Ir(110)(16) and the epitaxial growth of a bulk oxide on Ni(111)(30). Ordered structures of adsorbed species may affect the rates of reaction. For example, the desorption of CO from Ru(001) is affected strongly by the formation of a LEED superstructure(21). LEED may also indicate the condition of the surface, as seen for the steady state oxidation of CO over Ir(110)(31). Although LEED patterns are used to fix relative positions of adsorbates their absolute positions are accessible only through complex calculations(32). Calculations performed by others in the present context of Ir(110) are valuable since the clean surface structure is known now(33), which is different from the bulk structure.

In summary, the surface-sensitive techniques described here have been employed to characterize the various chemisorption properties of small molecules on the (110) surface of iridium. In particular, the goal of this thesis is to gain insight into the heterogeneously catalyzed reduction of NO with hydrogen over Ir(110).

References

1. G. Ehrlich, J. Phys. Chem. 60, 1388(1956).
2. L. D. Schmidt, Catalysis Rev. Sci. Eng. 9, 115(1974).
3. For a review see: C. M. Chan, R. Aris and W. H. Weinberg, Appl. Surface Sci. 1, 360(1978).
4. P. A. Redhead, Vacuum 12, 203(1962).
5. J. L. Falconer and R. J. Madix, J. Catalysis 48, 262(1977).
6. J. L. Taylor and W. H. Weinberg, Surface Sci. 78, 259(1978).
7. D. L. Adams, Surface Sci. 42, 12(1974).
8. D. A. King, Surface Sci. 64, 43(1977).
9. R. Gorte and L. D. Schmidt, Surface Sci. 76, 559(1978).
10. P. Kisliuk, J. Phys. Chem. Solids 3, 95(1957).
11. P. Kisliuk, J. Phys. Chem. Solids 5, 78(1958).
12. D. A. King and M. G. Wells, Proc. R. Soc.(London) Ser. A 339, 245(1974).
13. J. R. MacDonald and C. A. Barlow, J. Chem. Phys. 39, 412(1963).
14. K. Christmann and G. Ertl, Surface Sci. 60, 365(1976).
15. G. Ertl, M. Neumann and K. M. Streit, Surface Sci. 64, 393(1977).
16. J. L. Taylor, D. E. Ibbotson and W. H. Weinberg, Surface Sci., 79 349(1979).
17. K. Christmann and H. Herz, Rev. Sci. Instrum. 50, 988(1979).
18. For an AC method see: J. L. Taylor and W. H. Weinberg, J. Vacuum Sci. Technol. 15, 1811(1978).
19. R. W. Pasco and J. Ficalora, Rev. Sci. Instrum. 51, 246(1980).
20. H. A. Engelhardt, P. Feulner, H. Pfnur and D. Menzel, J. Phys. E. 10, 1133(1977).

References, continued

21. H. Pfnur, P. Feulner, H. A. Engelhardt and D. Menzel, Chem. Phys. Letters 59, 481(1978).
22. For example see: K. Christmann, O. Schober, G. Ertl and M. Neumann, J. Chem. Phys. 60, 4528(1974).
23. G. Ertl, Low Energy Electrons and Surface Chemistry, Verlag Chemie, Weinheim, 1974.
24. T. Kawai, K. Kunimori, T. Kondow, T. Onishi and K. Tamaru, Jap. J. Appl. Phys. Suppl. 2, Pt. 2, 513(1974).
25. L. A. Harris, J. Appl. Phys. 39, 1419(1968).
26. For example see: G. Pirug and H. P. Bonzel, J. Catalysis 50, 64 (1977).
27. For example see: E. Umbach, S. Kulkarni, P. Feulner and D. Menzel, Surface Sci. 88, 65(1979).
28. D. W. Turner, C. Baker, A. D. Baker and C. R. Brundle: Molecular Photoelectron Spectroscopy, Wiley, New York, 1970.
29. G. Doyen and G. Ertl, J. Chem. Phys. 68, 5417(1978).
30. P. H. Holloway and J. B. Hudson, Surface Sci. 43, 141(1974).
31. J. L. Taylor, D. E. Ibbotson and W. H. Weinberg, J. Catalysis 62, 1(1980).
32. P. J. Estrup and E. G. McRae, Surface Sci. 25, 1(1971).
33. C. M. Chan, M. A. Van Hove, W. H. Weinberg and E. D. Williams, Solid State Commun. 30, 47(1979); Surface Sci. 91, 400(1980).

CHAPTER 2

THE CHEMISORPTION OF HYDROGEN ON THE (110)

SURFACE OF IRIDIUM

(The text of Chapter 2 consists of an article coauthored with T. S. Wittrig and W. H. Weinberg that has been published in Journal of Chemical Physics 72, 4885(1980).)

Abstract

The chemisorption of hydrogen on Ir(110) was studied under ultra-high vacuum conditions with thermal desorption mass spectrometry, LEED, contact potential difference measurements and ultraviolet photoelectron spectroscopy. The Ir(110)-(1x2) reconstructed surface is stable in hydrogen at pressures from 10^{-9} to 10^{-5} torr and surface temperatures from 130 to 1000 K, the conditions investigated. No streaks or spots were observed in the LEED pattern due to the presence of hydrogen. Absolute coverage measurements indicate the saturation density at 130 K on Ir(110) is $2.2 \pm 0.2 \times 10^{15}$ atoms \cdot cm $^{-2}$. Thermal desorption measurements indicate that hydrogen obeys second order desorption kinetics and exhibits two features, β_1 and β_2 states, with intensities 2:1, respectively, which exchange isotopically with one another. However, β_2 hydrogen obeys first order adsorption kinetics with an initial sticking probability S_0 equal to unity, while β_1 hydrogen has an S_0 equal to 7×10^{-3} and obeys second order kinetics. Rate parameters for hydrogen desorption from Ir(110) were calculated as a function of fractional surface coverage. A sympathetic increase in the rate parameters up to at least half of saturation is observed for the β_2 state of hydrogen, where E_d and ν_d assume the values 23 kcal/mole and 1.5×10^{-2} cm 2 \cdot s $^{-1}$, respectively. The increase is attributed to adatom-adatom attractive interactions of hydrogen in the β_2 state. For the β_1 state, the energy of desorption, in kcal-mole $^{-1}$, is given by $E_d = 17 - 10\theta$ from θ equal to 0.4 - 0.7, and the preexponential factor, ν_d , varies weakly as a function of coverage with an average value of $2 \frac{1}{x} 2 \times 10^{-7}$ s $^{-1}$. The contact potential difference (CPD) increases

linearly with coverage up to 0.20 eV and reaches a maximum at 0.30 eV for the β_2 state of hydrogen for $T \leq 300$ K. A continuous decrease in the CPD occurs over the β_1 state up to saturation at 140 K and becomes lower than the clean surface contact potential for total fractional coverages above 0.9. Probable binding sites for the β_1 and β_2 states are inferred from the absolute coverage measurements and the CPD measurements. Ultraviolet (HeI, $h\nu = 21.2$ eV) photoelectron spectra of hydrogen show a broad H(1s) level centered approximately at 6.1 eV below the Fermi level. A strong decrease in the d-band emission occurs near the Fermi level after adsorption of the β_2 state, which suggests preferred binding locations for this state of hydrogen on the Ir(110)-(1x2) surface.

1. Introduction

The study of hydrogen chemisorption on Ir(110) was undertaken to give insight into several of the elementary reactions which are important in reduction catalysis. Thermal desorption mass spectrometry (TDS), LEED, contact potential difference (CPD) measurements and ultraviolet photoelectron spectroscopy (UPS) were used to investigate the properties of hydrogen chemisorption, e.g., desorption kinetics, adsorption kinetics, the structure of the overlayer-substrate system, charge transfer in the overlayer, and the electronic nature of the H-Ir bond.

Although hydrogen chemisorption has been investigated extensively on various surfaces of the platinum metals, including Ni (1,2), Rh (3,4), Pd (5,6), Pt (7-12) and Ir (3,13,14), little work has been performed on single crystals of Ir. The present comparative study on Ir(110) will complement the work done on other single crystal surfaces of the platinum metals. In general, many aspects of hydrogen chemisorption have common features among this class of metals. Nonactivated dissociative adsorption is observed with initial sticking probabilities ranging from 0.1 to 0.4 with the exception of Pt(100)-(5x20) which seems not to adsorb hydrogen (10). Generally, adsorption is described either by a dissociative Langmuir model or by a second order precursor model. However, first order adsorption kinetics are observed for hydrogen adsorption on Ni(111) and Ni(100) (2). Two to three features appear in the thermal desorption spectra depending upon the metal and surface orientation. Most of these features are described by second order desorption kinetics, but the low coverage feature for hydrogen desorption from Ni(110) (2) and oxidized Pt(110) (9) displays first order desorption characteristics. Reported values for the activation energy of desorption at low coverage range from 17 to 25 kcal/mole for the

platinum metals. Hydrogen forms few ordered overlayer structures on the platinum metals. A (2x2) structure is observed on Ni(111) (15-17), whereas a (1x1) overlayer structure forms on Pd(111) (5,6). Also, a (1x2) structure is formed on (110) surfaces of Pd (4) and Ni (1,2,18). Faint streaks appear in the LEED pattern for a saturated hydrogen overlayer on a stepped Pt(111) surface (12) which are attributed to ordering along the steps. Finally, the CPD increases for hydrogen on most platinum metal surfaces, typically between 0.1 and 0.6 eV depending on the metal and surface orientation, i.e., a net transfer of electrons to H atoms occurs from the metal if hydrogen lies above the surface plane. On Pt(111) (8) and stepped Pt(111) (12), a decrease in CPD occurs with increasing hydrogen coverage in addition to a small initial increase in the CPD which is more pronounced on the stepped surface. Further, an initial increase in the CPD of 0.1 eV and then a decrease to a final value of 0.03 eV is observed at 120 K on Ni(100) (19) and Ni(111) at low temperatures (17). Ultraviolet photoelectron spectra of hydrogen chemisorbed on (111) surfaces of Ni (20,21), Pd (20,21) and Pt (21) show H(1s) induced levels at 5.8, 6.4 and 7.3 eV below the Fermi level, respectively. For Pd (19,20) and Pt (20), a strong redistribution of d-band emission occurs near the Fermi edge, in contrast to Ni. The present work is in general agreement with these previous studies; however, new results are presented for hydrogen on Ir(110).

2. Experimental Procedures

The experiments were performed in an ion-pumped stainless steel bell jar with a base pressure below 2×10^{-10} torr. Several surface sensitive probes — a quadrupole mass spectrometer, LEED optics, a CPD apparatus, an

Auger electron, and X-ray and UV-photoelectron spectrometers — are contained in the experimental chamber. A double pass cylindrical mirror analyzer was used to perform the electron kinetic energy analysis. All probes were interfaced to a PDP 11/10 computer (22). Although all data reported here, except the LEED data, were obtained in digital form, the data are shown in analog form to facilitate the presentation. A detailed description of the experimental system is reported elsewhere (23), with the exception of the ultraviolet lamp. The HeI radiation was produced by a microwave discharge cavity at the end of a two-stage, differentially pumped stainless steel capillary array. When a HeI discharge at a pressure of 1 torr was used, the base pressure in the belljar rose by 1×10^{-9} torr. For HeI radiation, typical count rates near the Fermi edge were from 90,000 to 110,000 count-s⁻¹ for a constant pass energy of 25 eV.

The substrate was cut from a single crystal of Ir and was polished to within 1° of the (110) orientation using standard polishing techniques. Carbon was cleaned from the substrate through a series of oxidation and reduction cycles. Annealing above 1600 K removed O, Ca and K impurities. Details of the cleaning procedure are described elsewhere (23). The substrate was heated resistively by two 10 mil Ta support wires or cooled conductively by liquid nitrogen. Temperatures were measured with a W/5%Re-W/26%Re thermocouple spotwelded to a 1 mm^2 Ta foil sandwich on the back of the Ir crystal and were referenced to an icepoint junction. Temperatures are accurate within ± 5 K for all values reported here.

3. LEED Observations

If a simple termination of the bulk is considered, the Ir(110) surface is a series of rows and troughs. However, a clean surface is reconstructed to form a (1x2) LEED pattern (24), a situation which occurs also on Pt (110) (25). Very recently, the structure of reconstructed Ir(110) has been determined to be a surface with every other row of surface atoms missing in the [001] direction (26). Thus, not only are second layer Ir atoms exposed, but third layer atoms under the locations of the missing rows are exposed also. The surface may be thought of as (111) planes inclined to one another containing an equal number of two inequivalent types of three-fold sites and two inequivalent types of two-fold sites between the first and second layers. There are a total of four three-fold sites and four two-fold sites present in each reconstructed unit cell. Also, one additional high symmetry site is contained in each unit cell either on top of the rows of Ir atoms or directly above the third layer of Ir atoms. This knowledge, coupled with other data presented below, may be used to infer preferred binding sites for hydrogen on Ir(110).

Under all conditions examined, i.e., for surface temperatures from 130 to 1300 K and pressures from 10^{-9} to 10^{-5} torr hydrogen, the structure of the surface was stable and showed the (1x2) reconstruction. No additional spots or streaks occurred in the LEED pattern for any coverage of hydrogen on the surface, even at 130 K. As the hydrogen coverage increased, the substrate pattern remained a sharp (1x2) with the background increasing only slightly at high coverage. Annealing a hydrogen-covered substrate to the onset of hydrogen desorption and recooling to 130 K caused no observable changes at any hydrogen coverage.

4. Absolute Coverage Determination

Absolute coverage calibrations were performed for hydrogen on Ir(110) by two methods, both using TDS. The two methods, outlined below, employ known absolute coverages for CO and oxygen on Ir(110) from previous studies in the same experimental system (23,27). The basis for both techniques is to compare relative experimental parameters between hydrogen and another gas which has an accurate coverage calibration in atoms or molecules per unit area to determine the number of hydrogen atoms per unit surface area.

The first technique is a comparison of the integrated intensities of mass 2 and mass 28 in thermal desorption spectra of hydrogen and CO for saturation coverages. The relative mass spectrometric sensitivities for H₂ and CO were determined by calibration with respect to an ion gauge where the ionization efficiencies were known. A poppet valve contained in the system was closed sufficiently so that the ratio of the pumping speeds was equal to the ratio of the square root of the molecular weights of the desorbing molecules. The absolute sensitivity of the mass spectrometer to CO was determined from the CO spectrum for saturation coverage at 300 K, which is equal to 9.6×10^{14} molecules - cm⁻² (23). The thermal desorption spectrum for a saturation coverage of hydrogen at 130 K, the lowest temperature accessible during these experiments, was obtained by exposing the surface to 300 Langmuirs (L) of H₂ (1 L \equiv 10⁻⁶ torr-s). At greater exposure to H₂, adsorption becomes reversible at 130 K, although the spectrum is quite reproducible up to 300 L. Then, absolute coverages of hydrogen (atoms - cm⁻²) were determined from twice the product of the

absolute sensitivity of the mass spectrometer to CO, the ratio of the relative sensitivities for CO and H₂, the ratio of the pumping speeds for H₂ and CO, and the ratio of the pressure-time integrals for the saturation spectra of H₂ and CO.

The second technique used to determine absolute coverages of hydrogen employs oxygen and deuterium. As described below, deuterium and hydrogen have identical adsorption properties on Ir(110). Deuterium was used to minimize baseline drift in the mass spectrometer from adsorption of background H₂O on the sample manipulator. For certain coverage ranges of co-adsorbed deuterium and oxygen, all the oxygen reacts during thermal desorption to form D₂O (28). If one knows the absolute initial coverage of oxygen, then an absolute calibration for D₂O is known. Moreover, if a known relative coverage of deuterium is co-adsorbed with any coverage of oxygen below the temperature where any species desorb, and the surface is heated, the difference between the amount of deuterium that desorbs with no oxygen present and the amount that desorbs with oxygen present is equal to the coverage of deuterium that reacts to form D₂O. This difference can then be used to calculate absolute coverages of deuterium (or, equivalently, hydrogen) from the coverage calibration for D₂O. The experimental conditions that meet the above requirements are described briefly. A more detailed account will appear in a later publication (28).

When more than 100 L D₂ is exposed at 130 K to a surface oxide on Ir(110), and the surface is heated, all the oxide desorbs as D₂O (28). The surface oxide is formed by exposing an Ir(110) surface to more than 0.8 L O₂ followed by annealing to 1200 K. The coverage of the oxide is 2.4×10^{14} atoms - cm⁻² and has associated with it a (1x4) LEED pattern

(27). Any excess oxygen desorbs as O_2 . Since the oxygen coverage on the oxide surface is known, a calibration for D_2O may be obtained from the integrated intensities of the mass 20 signal in the thermal desorption spectrum. To obtain a known relative coverage of deuterium, the Ir(110) surface is exposed to D_2 at 130 K. In order to co-adsorb oxygen and not lose any deuterium during oxygen adsorption due to reaction or desorption, small exposures of O_2 (< 0.5 L) are applied to the deuterium overlayer (28). Any of the D_2 signal lost during a flash will be due to reaction to form D_2O , which is measured simultaneously. The method discussed above allows several measurements to be made quickly in order to minimize inaccuracies due to drift in system constants. This method presents a more accurate technique to determine absolute coverages for hydrogen (deuterium) than the first method described where relative pumping speeds must be known, and large exposures of both gases (H_2 and CO) must be used.

The results of the two independent methods to determine absolute coverages of hydrogen on Ir(110) are in excellent agreement. For saturation (300 L) exposure of H_2 at 130 K, the first method yields $N_{sat} = 2.3 \times 10^{15}$ atoms \cdot cm^{-2} ; whereas the second, more accurate, method yields $N_{sat} = 2.2 \pm 0.2 \times 10^{15}$ atoms \cdot cm^2 . This value for the saturation coverage of hydrogen on Ir(110) is very reasonable when compared to other platinum metal surfaces. Saturation coverages of hydrogen on the platinum metals are difficult to determine due to the general lack of order in overlayers. However, between 1 and 2×10^{15} atoms \cdot cm^{-2} of hydrogen adsorb on Pd(110) (29) and Ni(110) (1,2), in good agreement with the value determined here. As shown below, two distinct states are observed for hydrogen in thermal desorption spectra which have relative populations of

2:1 for low and high binding energy states, respectively. This corresponds to approximately 3 atoms and 1.5 atoms for each state of hydrogen in each unit cell for the reconstructed surface. Since more hydrogen could be adsorbed if surface temperatures below 130 K could be reached, the low binding energy state may reach a saturation of 4 hydrogen atoms in each unit cell — the number of three-fold sites or the number of two-fold sites available on the (1x2) surface. Although the saturation coverage determined at 130 K is only accurate to $\pm 10\%$, the agreement between the number of three-fold sites, or the number of two-fold sites, and the number of atoms in the low binding energy state is excellent. Three-fold sites are preferred as probable binding sites since hydrogen binds to both types of inequivalent three-fold sites on Ni(111) (17). Figure 1 presents a summary of the probable binding sites of hydrogen on Ir(110).

5. Desorption Kinetics

Several thermal desorption spectra of H₂ from Ir(110) were measured as a function of H₂ exposure at 130 K. These data are used for investigating both the desorption and the adsorption kinetics of hydrogen on Ir(110).

Figure 2 shows representative curves of 30 desorption spectra for hydrogen on Ir(110). The average heating rate (β) for each spectrum was 21 K/s. Two features appear with relative integrated intensities of 2:1 and are defined as β_1 and β_2 states, respectively. Although both features exhibit a decrease in peak temperature with increasing surface coverage, characteristic of second order desorption kinetics, their rate parameters

display markedly different behavior, as will be shown. The β_2 state fills to completion after 0.35 L and shows only a 15 K decrease in peak temperature. After the β_2 state is occupied fully, the β_1 state fills at a much slower rate and decreases in peak temperature by more than 100 K over the accessible coverage range. The β_2 state of hydrogen shown in Fig. 2 desorbs in the same temperature range as previously seen for hydrogen adsorption on Ir(110) (30) and Ir(111) (31) near 300 K.

Dissociative adsorption of hydrogen on the platinum metals is reported for all surface orientations investigated (1-15). However, first order desorption kinetics have been observed on Ni(110) (2) and oxidized Pt(110) (9) for the most tightly bound states. For the β_2 state of hydrogen on Ir(110), the slight decrease in peak temperature may imply first order desorption with a small decrease in the activation energy of desorption. Hydrogen and deuterium were adsorbed sequentially at 130 K to determine if both species (β_1 and β_2) are indeed adsorbed dissociatively and if isotopic exchange occurs between the states. As shown in Fig. 3, H_2 , HD and D_2 are desorbed during a thermal desorption experiment in which 0.45 L D_2 was adsorbed to fill the β_2 state, followed by 5.0 L H_2 . From the thermal desorption spectra, it is clear that dissociative adsorption and mixing between the β_1 and β_2 states do occur. Many other experiments were performed with various sequential exposures of H_2 and D_2 that are not shown. Regardless of the exposure sequence or the amount of each component adsorbed, the product distribution was similar to those in Fig. 3. Overall, statistical mixing of H and D is confirmed at each point in the desorption spectra: values of the isotope distribution coefficient

$K_{id} \left[\frac{[I_{HD}]^2}{I_{D_2} I_{H_2}} \right]$ range from 3 to 4.5. The terms I_{HD} , I_{D_2} and I_{H_2} are the

gas phase intensities of the products of the desorption reaction, corrected for differences among their respective experimental system constants. Within the errors of the experiment, the values of K_{id} agree very well with the calculated value of approximately four for complete mixing (3). Isotopic exchange experiments on polycrystalline Ir resulted in $K_{id} \sim 3$ for adsorption at 100 K (3).

The order plots in Fig. 4 were constructed from the thermal desorption data in Fig. 2 to determine whether the kinetics of desorption of hydrogen in the β_2 state are first order or second order. For low coverages, it is usually assumed that the slope of a plot of $\ln R_d$ as a function of $\ln \theta$ at constant temperature is equal to the desorption order, where R_d and θ are the rate of desorption and the fractional surface coverage of hydrogen, respectively. As calculated from Fig. 4, the slope for $T \geq 380$ K is equal to two, indicating second order desorption for the β_2 state. At lower temperatures, where the β_1 state desorbs, the slopes are much greater than two, indicating a change in the rate parameters with coverage. This is evidenced also by the broad, asymmetric desorption behavior seen in Fig. 2, although the desorption is expected to obey second order kinetics since it adsorbs dissociatively, and the adsorption kinetics (see sect. 6) show no evidence for the participation of a precursor (32).

However, the slope calculated from the order plots, even at low coverages, may not represent the true order of the desorption reaction.

For the β_2 state described here, the calculated order is, in fact, two; but this was shown to be the result of the cancellation of other terms that contribute to the slope of an order plot (33). Briefly, the derivation involves the following expression for the desorption rate,

$$R_d = v_d(\theta)\theta^n \exp[-E_d(\theta)/kT] . \quad (1)$$

The order n is assumed to be a constant integer representing the elementary desorption reaction. Logarithmic differentiation of Eq. (1) with respect to the fractional surface coverage at constant T yields

$$\left(\frac{\partial \ln R_d}{\partial \ln \theta}\right)_T = n + \left(\frac{\partial \ln v_d(\theta)}{\partial \ln \theta}\right)_T - \frac{1}{kT} \left(\frac{\partial E_d(\theta)}{\partial \ln \theta}\right)_T . \quad (2)$$

Usually, it is assumed that the last two terms of the right-hand side of Eq. (2) are zero, and n is the slope of an order plot. However, recent experimental evidence has shown that both rate parameters, E_d and v_d can vary strongly with coverage (23,34). This is also the case for hydrogen

on Ir(110) as will be shown below. If the terms $\left(\frac{\partial \ln v_d}{\partial \ln \theta}\right)_T$ and $\left(\frac{\partial E_d}{\partial \ln \theta}\right)_T$ are large, the slope of an order plot may not be equal to n . As an example, the slope of the experimental order plot in Fig. 4 for $T = 390$ K is equal to 2.0 ± 0.1 . The calculated slope [Eq. (2)], using the rate parameters presented below, is equal to 2.2 ± 1.5 . The large error limits are due to the uncertainty in measuring the derivatives $\left(\frac{\partial \ln v_d}{\partial \ln \theta}\right)_T$ and $\left(\frac{\partial E_d}{\partial \ln \theta}\right)_T$.

Although the experimental and calculated values of the slope of an order

plot are in excellent agreement, the terms $-\frac{1}{kT} \left(\frac{\partial E_d}{\partial \ln \theta} \right)_T$ and $\left(\frac{\partial \ln v_d}{\partial \ln \theta} \right)_T$ are equal to -4.6 and 4.8, respectively. It is evidently fortuitous that they cancel one another.

Since the system is pumped rapidly, the desorption rate is proportional to the intensity of the mass spectrometer (I). Thus,

$$\frac{-d\theta}{dt} = \eta I, \quad (3)$$

where η is a proportionality constant. The coverage at any point in a desorption spectrum is determined by integrating Eq. (3):

$$\theta^0 - \theta(t) = \eta \int_0^t I dt. \quad (4)$$

The heating schedule may be of any form so long as the intensity and temperature are monitored independently with time. If the initial coverage (θ^0) is known, the constant η may be calculated from an integration of Eq. (4) over the whole desorption spectrum. The desorption rate and temperature may be varied for any particular coverage either by changing the initial coverage or by changing the heating rate, while keeping the initial coverage constant. Then, Arrhenius plots may be constructed of $\ln R_d$ as a function of T^{-1} at constant coverage with slope $[-E_d(\theta)/k]_\theta$ and intercept $\ln[v_d(\theta)\theta^n/\eta]_\theta$. If the coverage is known in absolute units, $v_d(\theta)$ may be calculated in units of surface diffusivity, $\text{cm}^2 \text{ s}^{-1}$.

The rate parameters E_d and v_d were determined from an integral method using variable heating rates (35). Eleven desorption spectra of hydrogen from Ir(110) were measured by varying the nominal heating rate from 5 to 110 K/s. The initial fractional coverage was fixed at 0.82 ± 0.01 for

each measurement by exposing the surface to 100 L H₂ at 130 K. The high degree of accuracy for the relative initial coverage was obtained since background contaminants of CO and H₂O were low ($\leq 10^{-10}$ torr), and the poppet valve in the chamber was partially closed to reduce loading of the pumps during exposures. Arrhenius plots constructed from the data are shown in Fig. 5. Although the change in heating rate was smaller for the plots at higher coverages due to nonlinear heating at the beginning of each measurement, sufficient accuracy was available since the preexponential factor was small, as evidenced by the broad shape of the β_1 state in Fig. 2. This construction may not be valid if simultaneous desorption from multiple, distinct sites occurs at any particular coverage. The β_1 and β_2 states are separated in energy sufficiently that desorption from multiple sites at any instant will not be important except possibly near the depletion of β_1 and the beginning of desorption from β_2 . It is, however, probable that if two types of three-fold sites are participating in bonding for the β_1 state (based on the clean surface structure and the coverage determination for hydrogen), the broad desorption spectrum of the β_1 state may be a composite of these sites which cannot be resolved by thermal desorption spectra. However, they may be resolved by CPD measurements (see sect. 7).

In Fig. 6, the desorption energy and preexponential factor from the Arrhenius plots are shown as a function of surface coverage. An increase in E_d and ν_d is observed up to a fractional coverage of 0.20. It is well known that defects on the surface and edges of the crystal tend to broaden thermal desorption spectra, particularly at low coverage, and this would depress the calculated rate parameters. However, the magnitude of the

increase in E_d (5 kcal/mole) and ν_d (factor of 500) for the β_2 state is too large to be explained in this way. The rapid variation in the rate parameters between fractional coverages of 0.25 and 0.35 is associated with the completion of the β_2 state of hydrogen. At higher coverages, E_d decreases approximately linearly with coverage ($10 \text{ kcal-mole}^{-1} \text{- monolayer}^{-1}$), and ν_d varies only weakly with coverage. A similar decrease in E_d is observed for CO on Ir(110) (23). A continuous decrease in E_d for hydrogen adsorbed on Ni (2) and Pd (5) has been reported for their respective high coverage states. The dramatic change in the behavior of the rate parameters when the β_2 state is complete and the β_1 state begins to populate is further evidence for different binding sites between β_1 and β_2 states. Furthermore, the adsorption kinetics reflect a marked change in binding sites, as seen in the next section. The maximum value for the energy of desorption, 23 kcal/mole, is close to the isosteric heats of 22 and 24 kcal/mole measured on the (110) surfaces of Ni (2) and Pd (5). These values are comparable since hydrogen adsorption is believed to be unactivated. From the peak temperature for hydrogen desorption from oxidized Pt(110), an energy of desorption of 22 kcal/mole is estimated and 24 kcal/mole is calculated from TDS for polycrystalline Ir (3). Moreover, the maximum ν_d calculated is $1.5 \times 10^{-2} \text{ cm}^2 \text{- s}^{-1}$ for Ir(110) compared to $2.2 \times 10^{-2} \text{ cm}^2 \text{- s}^{-1}$ for polycrystalline Ir (3).

The compensation effect (36) occurs for hydrogen desorption from the β_2 state on Ir(110). In other words, the desorption energy and pre-exponential factor vary in sympathy. This effect was reported for CO on Ir(110) (23) and CO on Ru(001) (34). In the case of Ru(001), the rate parameters pass through a maximum associated with the completion of a

$(\sqrt{3} \times \sqrt{3})R30^\circ$ structure, after which a rapid decrease in the rate parameters was observed. Although the preexponential factor was not measured for hydrogen on Ni(110), an increase in the isosteric heat was seen due to two-dimensional condensation, as evidenced by isotherm data (2). Two-dimensional condensation may occur also for hydrogen on Ir(110). Another possibility is that one-dimensional condensation occurs if hydrogen atoms form chains in the direction of the Ir atoms rows, due to the attractive interactions inferred from the rate parameters. The absence of order in the hydrogen overlayer as observed by LEED (see sect. 3) in this coverage range may indicate that a substrate temperature of 130 K is too high to observe ordering over the coherence width of the electron beam. This is not surprising since exchange is rapid between β_1 and β_2 states at 130 K as evidenced by hydrogen and deuterium co-adsorption. Moreover, hydrogen is well known to be a weak scatterer in LEED.

6. Adsorption Kinetics

The adsorption kinetics of hydrogen on Ir(110) at 130 K have been calculated from the thermal desorption spectra in Fig. 2 making use of Eq. (4). Identical kinetics are observed for deuterium adsorption. An absolute coverage may be associated with each exposure since the saturation coverage is known, 2.2×10^{15} atoms - cm^{-2} . The surface coverage-gas exposure relations for the β_1 and β_2 states are shown in Fig. 7 where the completion of the β_2 state is indicated at a fractional coverage of 0.33. A smooth curve has been drawn through the data to aid in the presentation.

Since a sharp change in the adsorption characteristics is evident, the kinetics of hydrogen adsorption in the β_1 and β_2 states will be modeled separately.

Figure 8(a) presents the adsorption kinetics of the β_2 state of hydrogen. The fractional coverage has been normalized to the saturation value of the β_2 state. Although adsorption is dissociative, the kinetics fit a first order Langmuir model extremely well with a calculated initial sticking probability S_0 equal to 1.1 ± 0.05 from a least squares fit of the data. The 10% error from unity in S_0 in absolute terms is quite reasonable, considering errors in the measurement of the integrated intensities and absolute coverage. Deuterium follows the same kinetics with a calculated S_0 of 1.06 ± 0.05 . Since S_0 is equal to one and first order Langmuir kinetics are obeyed, the adsorption of hydrogen into the β_2 state on Ir(110) is limited only by the flux of molecules to the surface that impinge on an empty site. Simple first order adsorption kinetics have been observed also on the (111) and (100) surfaces of Ni (2).

In contrast, the adsorption kinetics of the β_1 state of hydrogen, or deuterium, on Ir(110) are quite different, as shown in Fig. 8(b). Again, the fractional coverage has been normalized to the saturation value (300 L H_2) of the β_1 state. Two models for describing dissociative adsorption were used to fit the kinetic data. The Langmuir model describes the data well with $S_0 = (7 \pm 0.3) \times 10^{-3}$. The model developed by Kisliuk is used for describing precursor kinetics (37). A parameter K is contained in the expression for the sticking probability as a function of coverage and is inversely proportional to the lifetime of a precursor species on the surface. The curve in Fig. 8(b) corresponds to $K = 1.0$ and

$S_0 = 7 \times 10^{-3}$. Notice that only at high coverage are the models shown in Fig. 8(b) not identical. The value of K calculated for the β_1 state indicates that if a precursor does exist, it has a very short lifetime. Since both models fit equally well, the contribution of a precursor is not important in this case. Moreover, the preexponential factor calculated for the β_1 state as a function of coverage is nearly constant by assuming a θ^2 dependence in the rate of desorption. These data and the idea of microscopic reversibility tend to rule out precursor kinetics since the calculated preexponential factor would not be constant if a precursor is involved in desorption (32).

7. Contact Potential Difference Measurements

If a clean, well ordered Ir(110) surface is exposed to hydrogen, the CPD ($\Delta\phi$) increases initially to a maximum value of 0.30 eV near the completion of the β_2 desorption state, as shown in Fig. 9(a). Upon further exposure to hydrogen the CPD decreases over the β_1 desorption state and nearly reaches the clean surface value of the contact potential at 250 L, as shown in Fig. 9(b). For hydrogen exposures greater than 250 L, at 140 K, the contact potential continuously drops below the clean surface value until the adsorption of hydrogen becomes reversible. A similar shape of the CPD as a function of hydrogen exposure was observed on Ni(100) (19) and Ni(111) (17) at low temperature and to a lesser extent on Pt(111) (8) and stepped Pt(111) (12), although the magnitude of the decrease on the two platinum surfaces is comparable to the observed decrease in Fig. 9(b) for Ir(110). An increase in the CPD was also observed on Ir

field emission tips (13,14), but no subsequent decrease was seen.

The maximum CPD obtained in Fig. 9(a) depended sensitively on both the cleanliness and the order on the surface. The presence of small amounts of CO markedly depressed the maximum CPD observed for hydrogen due to preferential blocking of β_2 sites (38). Further, for substrate temperatures above 300 K, the CPD decreases in Fig. 9(a) due to slow desorption of hydrogen from β_2 sites. However, if a background pressure of hydrogen is maintained to ensure sufficient hydrogen is present to fill β_2 sites, the CPD still reaches a maximum somewhat less than 0.30 eV. The maximum CPD decreases to 0.26 eV near 380 K, even at pressures of 10^{-5} torr of hydrogen. It is likely that this is due to a change in the equilibrium distribution of adsorbed hydrogen between β_1 and β_2 sites as the substrate temperature increases.

In order to examine more closely the adsorption properties of hydrogen on Ir(110), the CPD measurements were related to the fractional coverage (via the adsorption kinetics) at points of constant exposure, as shown in Fig. 10. A linear relation is observed between $\Delta\phi$ and θ for three coverage ranges: (1) 0 - 0.20, (2) 0.35 - 0.60 and (3) ≥ 0.85 . Region (1) corresponds to adsorption of hydrogen on β_2 sites, and regions (2) and (3) correspond to adsorption on β_1 sites. Between fractional coverages of 0.20 and 0.35, the CPD becomes nonlinear in its increase in coverage, reaches a maximum near $\theta = 0.33$ and begins to decrease at higher coverages. From both the adsorption kinetics and the desorption kinetics, it is apparent that this is due to the completion of the β_2 state and the simultaneous population of the β_1 state. However, it should be noted that the nonlinear behavior cannot be attributed solely to the superposition of sites being occupied that increase (β_2) and decrease (β_1)

the contact potential since this disagrees with other data presented earlier. The CPD and coverage are related simply in the three linear regions by

$$\Delta\phi = 4\pi C_s \mu_0 \theta, \quad (5)$$

where μ_0 is the surface dipole for the Ir-H system. The calculated values of μ_0 are +0.14, -0.016 and -0.22 Debye (1 Debye $\equiv 10^{-18}$ esu-cm) for coverage regions (1), (2) and (3), respectively, where a positive dipole points away from the surface. On Ni(100) $\mu_0 \sim +0.05$ Debye for low hydrogen coverage (19), and this appears to be the general order of magnitude for hydrogen on the platinum metals.

Since the CPD increases when β_2 adsorption sites are populated, either metal atoms donate electrons to H atoms if adsorption is above the surface plane (A in Fig. 1), or H atoms donate electrons to metal atoms if adsorption occurs below the surface plane (B in Fig. 1). The open surface structure of reconstructed Ir(110) and the covalent nature of the H-Ir bond makes either situation plausible a priori. However, the UPS results presented in the next section imply that the location associated with hydrogen in the β_2 state is, in fact, the site B in Fig. 1. For β_1 sites, the CPD decreases continuously indicating that these are truly different from β_1 sites, as suggested by the absolute coverage measurements, the desorption kinetics and the adsorption kinetics.

The fact that two different slopes ($\frac{d\Delta\phi}{d\theta}$) exist in the coverage range where β_1 sites are filled, as well as the broad desorption behavior, may support further the postulate of two inequivalent sites participating in adsorption for β_1 (C and D in Fig. 1). Assuming that two sites are occupied and that the change in slope of Fig. 10 represents the completion of one site and the population of the second site allows the calculation of the difference in the energy of adsorption between the two sites, the energy difference calculated is between 0.5 and 1.0 kcal/mole, which is quite reasonable for slightly different adsorption sites. For an equal population of these two sites, approximately 20% more hydrogen must be adsorbed at saturation as evidenced by Fig. 10 and Sect. 4. If Fig. 10 is extrapolated to $\theta = 1.20$, a saturation CPD of -0.50 eV would result, with respect to the clean surface. For a background pressure of hydrogen of 2×10^{-6} torr and a substrate temperature of 140 K, the equilibrium CPD is -0.20 eV. Therefore, to saturate the surface completely, lower substrate temperatures are needed since the saturation coverage used here has a CPD of -0.14 eV.

To summarize the CPD results for hydrogen on Ir(110), at least two types of sites may participate in hydrogen adsorption in the low temperature β_1 desorption feature which are different from the preferred sites that are occupied by the hydrogen that desorbs from the high temperature β_2 sites. The two different β_1 sites are energetically different by approximately 0.5 to 1.0 kcal/mole for adsorption of hydrogen. These data correlate well with the data presented in previous sections, demonstrating the difference in the properties of these sites for hydrogen on Ir(110).

8. Ultraviolet Photoelectron Spectra

If hydrogen is exposed to the Ir(110) surface in order to fill the β_2 state, the HeI UPS spectrum shows a strong change in the d-band near the Fermi level (E_F) as seen in curve (b) compared to curve (a) (clean surface) in Fig. 11. The difference spectrum (c) in Fig. 11 exhibits a large attenuation (19%) in the d-band peak centered at 1.6 eV below E_F on the clean surface, a small enhancement at 3.6 eV and the growth of a feature near 6.1 eV. This attenuation is continuous, but nonlinear, with coverage as shown for two smaller coverages of hydrogen in the β_2 state, curves (d) and (e) in Fig. 11. Somewhat similar changes in the d-band emission have been observed on Pt(111) (21) and Pd(111) (20,21), in contrast, however, to results for hydrogen on Ni(111) (20,21).

However, the attenuation observed here for hydrogen in the β_2 state on Ir(110) is quite large compared to Pt and Pd. This attenuation is probably not due to the destruction of a surface state of the reconstructed clean surface since CO adsorption on Ir(110) only causes a weaker, uniform decrease in the same region of the d-band (38). Further, the change in shape is not likely to be the formation of a surface state when hydrogen is adsorbed in the β_2 state since small amounts of CO co-adsorbed with hydrogen displace H atoms from β_2 sites to β_1 sites (via TDS), and the HeI UPS reflect only a continuous decrease in β_2 population (38). This marked attenuation may be a result of interference between the wavefunctions of the metal d-electrons and the hydrogen electron as suggested in a theoretical prediction of photoemission spectra of hydrogen on transition metals (39). It was predicted also in the theory (39) that,

for a strong attenuation, the H atom may be below the surface plane of the metal. Therefore, the UPS data for hydrogen on Ir(110) in the β_2 state imply that site B in Fig. 1, in the missing row trough, would be more likely than site A, on top of the existing rows. From the CPD measurements presented in the last section, site B would represent a net electron transfer from H atoms to the metal since the CPD increases over the β_2 state. Also, the data presented in previous sections suggest that the β_1 state corresponds to a net electron transfer to the metal if three-fold sites are populated, C and D in Fig. 1.

For an equal coverage of hydrogen in the β_1 state, the additional change in the region near E_F is much less as seen by comparing HeI difference spectra for saturated β_2 and equal coverages of β_1 and β_2 in curves (a) and (b) in Fig. 12, respectively. A comparison of curves (a) and (b) further shows the increase in the intensity of the H(1s) induced level at 6.1 eV below E_F . To accentuate this broad feature, (a) and (b) were subtracted from one another, and this is shown in curve (c) of Fig. 12. The full-width at half-maximum of the H(1s) level in (c) is approximately 2.3 eV, larger than observed for Pt(111) (21) and Pd(111) (20,21).

9. Summary

The chemisorption of hydrogen on Ir(110) has been studied under ultra-high vacuum conditions with thermal desorption mass spectrometry, LEED, contact potential difference measurements and ultraviolet photoelectron spectroscopy. The results of the present study were compared with other work performed previously on the platinum metals.

Although no ordered structures were observed with LEED to correlate exposures with absolute coverages for hydrogen, absolute coverages were determined by two methods using thermal desorption mass spectrometry. The maximum coverage of hydrogen on Ir(110) at 130 K is $2.2 \pm 0.2 \times 10^{15}$ atoms cm^{-2} . Two states, β_1 and β_2 , of hydrogen desorb with relative intensities of 2:1 and exhibit marked differences in their adsorption and desorption kinetics. The rate parameters for hydrogen desorption were measured as a function of surface coverage of hydrogen. Hydrogen in the β_2 state shows a sympathetic increase in the rate parameters up to at least half of its saturation coverage where E_d and ν_d assume values of 23 kcal/mole and $1.5 \times 10^{-2} \text{ cm}^2 \text{ s}^{-1}$, respectively. This increase may be due to a strong H-H interaction. The energy for hydrogen desorption from the β_1 state decreases linearly with increasing surface coverage and obeys the relation $E_d = 17 - 10\theta$ for total fractional coverages between 0.4 and 0.7. The preexponential factor for desorption varies only weakly with coverage for β_1 and is approximately equal to $2 \frac{1}{x} 2 \times 10^{-7} \text{ cm}^2 \text{ s}^{-1}$.

Both states are adsorbed dissociatively, and isotopic exchange occurs between them. Desorption for all surface coverages was modeled best as second order.

The adsorption kinetics of the β_2 state of hydrogen follows a first order Langmuir model with an initial sticking probability of unity. The initial sticking probability of the β_1 state of hydrogen is 7×10^{-3} and obeys second order Langmuir kinetics. The adsorption kinetics of both states are independent of substrate temperature up to desorption. Contact potential differences were measured as a function of hydrogen ex-

posure at 140 K and were related to the fractional coverage by the adsorption kinetics. For the β_2 state, the CPD increases to a maximum of 0.30 eV for $T \leq 300$ K and is linear with respect to coverage up to 0.20 eV. The CPD decreases continuously over the β_1 state and reaches values that are below the clean surface contact potential near the saturation coverage that is attainable at 140 K. Two linear regions were observed with very different slopes ($\frac{d\Delta\phi}{d\theta}$) for the β_1 state of hydrogen. This implies that more than one type of site is participating in this coverage region.

Probable sites for hydrogen adsorption on Ir(110) were postulated from the absolute coverage determination and the CPD measurements. Bonding either above the top rows of Ir atoms or between the rows of Ir atoms in the locations of the missing Ir rows are preferred for the β_2 state of hydrogen with trough sites between the rows more likely from the UPS results. The β_1 state of hydrogen may bind to two types of three-fold sites or to two types of two-fold sites exposed on the reconstructed surface [(111) microfacets on the terraces], with the former being preferred in analogy to results obtained on Ni.

The HeI UPS data show a marked change in the d-band emission near E_F for the β_2 state of hydrogen. A large attenuation and change in shape occurs which is continuous, but nonlinear, with fractional coverage. These phenomena may be due to destructive interference between metal d-electrons and the hydrogen electron. Furthermore, they suggest that β_2 hydrogen adsorbs below the surface plane of the metal. As the surface is increasingly covered with hydrogen, the H(1s) induced level grows in, centered at 6.1 eV below E_F , with a concomitant decrease in the emission near E_F . In the case of β_1 hydrogen, this effect is much less pronounced than in the case of β_2 hydrogen.

Acknowledgment

The authors are grateful for the financial support of the National Science Foundation under Grant Number DMR77-14976.

References

1. T. N. Taylor and P. J. Estrup, J. Vacuum Sci. Technol. 11, 244 (1974).
2. K. Christmann, O. Schober, G. Ertl and M. Neumann, J. Chem. Phys. 60, 4528 (1974).
3. V. J. Mimeault and R. S. Hansen, J. Chem. Phys. 45, 2240 (1966).
4. J. T. Yates, Jr., P. A. Thiel and W. H. Weinberg, Surface Sci. 84, 427 (1979).
5. H. Conrad, G. Ertl and E. E. Latta, Surface Sci. 41 235 (1974).
6. T. Engel and H. Küppers, Surface Sci. (to be published).
7. K. E. Lu and R. R. Rye, Surface Sci. 45, 677 (1974).
8. K. Christmann, G. Ertl and T. Pignet, Surface Sci. 54, 365 (1976).
9. R. W. McCabe and L. D. Schmidt, Surface Sci. 60, 85 (1976).
10. C. R. Helms, H. P. Bonzel and S. Kelemen, J. Chem. Phys. 65, 1773 (1976).
11. R. W. McCabe and L. D. Schmidt, Surface Sci, 65, 189 (1977).
12. K. Christmann and G. Ertl, Surface Sci. 60, 365 (1976).
13. J. R. Arthur and R. S. Hansen, J. Chem. Phys. 36, 2062 (1962).
14. H. F. Kempin, K. Klapper and G. Ertl, Nouveau J. Chim (Paris) 1, 295 (1977).
15. J. C. Bertolini and G. Dalmai-Imelik, Colloqu. Intern. CNRS, Paris 1969, p. 135.
16. J. Behm, K. Christmann and G. Ertl, Solid State Commun. 25, 763 (1978).
17. M. A. Van Hove, G. Ertl, K. Christmann, J. Behm and W. H. Weinberg, Solid State Commun. 28, 373 (1978); K. Christmann, J. Behm, G. Ertl, M.A. Van Hove and W. H. Weinberg, J. Chem. Phys. 70, 4168 (1979).

18. K. H. Reider and T. Engel, Phys. Rev. Letters 43, 373 (1979).
19. K. Christmann, Z. Naturforsch. 34a, 22 (1979).
20. H. Conrad, G. Ertl, J. Küppers and E. E. Latta, Surface Sci. 58, 578 (1976).
21. J. E. Demuth, Surface Sci. 65, 369 (1977).
22. J. L. Taylor, Ph.D. Thesis, California Institute of Technology, 1978.
23. J. L. Taylor, D. E. Ibbotson and W. H. Weinberg, J. Chem. Phys. 69, 4298 (1978).
24. K. Christmann and G. Ertl, Z. Naturforsch. 28a, 1144 (1973).
25. C. M. Comrie and R. M. Lambert, J. Chem. Soc. Faraday Trans. I. 72, 1659 (1976).
26. C. M. Chan, M. A. Van Hove, W. H. Weinberg and E. D. Williams, Solid State Commun. 30, 47 (1979); Surface Sci. 90, 000 (1979).
27. J. L. Taylor, D. E. Ibbotson and W. H. Weinberg, Surface Sci. 79, 349 (1979).
28. D. E. Ibbotson, Ph. D. Thesis, California Institute of Technology, 1981.
29. H. Conrad, G. Ertl and E. E. Latta, J. Catal. 35, 363 (1974).
30. B. E. Nieuwenhuys and G. A. Somorjai, Surface Sci. 72, 8 (1978).
31. B. E. Nieuwenhuys, D. I. Hagen, G. Rovida and G. A. Somorjai, Surface Sci. 59, 155 (1976).
32. R. Gorte and L. D. Schmidt, Surface Sci. 76, 559 (1978).
33. T. S. Wittrig, D. E. Ibbotson and W. H. Weinberg, Appl. Surface Sci. 4, 234 (1980).
34. H. Pfnür, P. Feulner, H. A. Engelhardt and D. Menzel, Chem. Phys. Letters 59, 481 (1978).
35. J. L. Taylor and W. H. Weinberg, Surface Sci. 78, 259 (1978).
36. G. C. Bond, Catalysis by Metals, Academic, New York, 1962.

References (continued)

37. P. Kisliuk, J. Phys. Chem. Solids 5, 78 (1958).
38. D. E. Ibbotson, T. S. Wittrig and W. H. Weinberg, Surface Sci. 97, 297(1980).
39. G. Doyen and G. Ertl, J. Chem. Phys. 68, 5417(1978).

Figure Captions

- Fig. 1: Probable locations of hydrogen on Ir(110)-(1 x 2). A and B represent two possible locations for the β_2 state of hydrogen. C and D denote the preferred binding sites for the β_1 state of hydrogen, which are inequivalent three-fold sites.
- Fig. 2: Thermal desorption spectra of hydrogen from Ir(110) as a function of gas exposure. The adsorption temperature is 130 K, and the heating rate is 21 K/s. The ratio of the β_1 and β_2 states is 2:1 at saturation coverage.
- Fig. 3: Representative thermal desorption spectra of H_2 , HD and D_2 from a co-adsorbed layer of hydrogen and deuterium. In this experiment, 0.45 L D_2 was exposed first, which approximately fills the β_2 state, and then, subsequently, 5.0 L H_2 was exposed.
- Fig. 4: Order plots for hydrogen desorption from Ir(110) using the data in Fig. 2.
- Fig. 5: Arrhenius plots obtained for hydrogen desorption by keeping the initial coverage constant and varying the heating rate (see text).
- Fig. 6: Activation energy (E_d) and preexponential factor (ν_d) for hydrogen desorption from Ir(110) as a function of fractional surface coverage.
- Fig. 7: The coverage-exposure relation for hydrogen on Ir(110). The β_2 state saturates after a 0.35 L exposure as noted in the figure. A smooth curve has been drawn through the data to facilitate the presentation.

Fig. 8: Analytic fits to the adsorption kinetics derived from the data in Fig. 2. (a) First order Langmuir fit to the β_2 state with S_0 calculated to be 1.1. The coverage is normalized to saturation of the β_2 state. (b) Second order fits to the β_1 state: — Langmuir with $S_0 = 7 \times 10^{-3}$; --- Kisliuk with $K = 1.0$ and $S_0 = 7 \times 10^{-3}$. The coverage is normalized to saturation of the β_1 state.

Fig. 9: The CPD of hydrogen on Ir(110) as a function of exposure at 140K. (a) Hydrogen adsorption on β_2 sites. (b) Hydrogen adsorption on β_1 sites.

Fig. 10: The CPD of hydrogen on Ir(110) as a function of fractional coverage at 140K. The data were calculated from Figs. 7 and 9.

Fig. 11: Hydrogen adsorbed into the β_2 state on Ir(110). HeI UP spectra are shown for the clean surface in (a) and for $\theta_H = 0.33$ in (b). Included are difference spectra for various fractional coverages of β_2 hydrogen: (c) 1.0, (d) 0.6 and (e) 0.4.

Fig. 12: HeI UP difference spectra for (a) β_2 hydrogen, (b) equal coverages of β_1 and β_2 hydrogen, and (c) β_1 hydrogen only.

PROBABLE LOCATIONS OF HYDROGEN ON Ir (110)-(1×2)

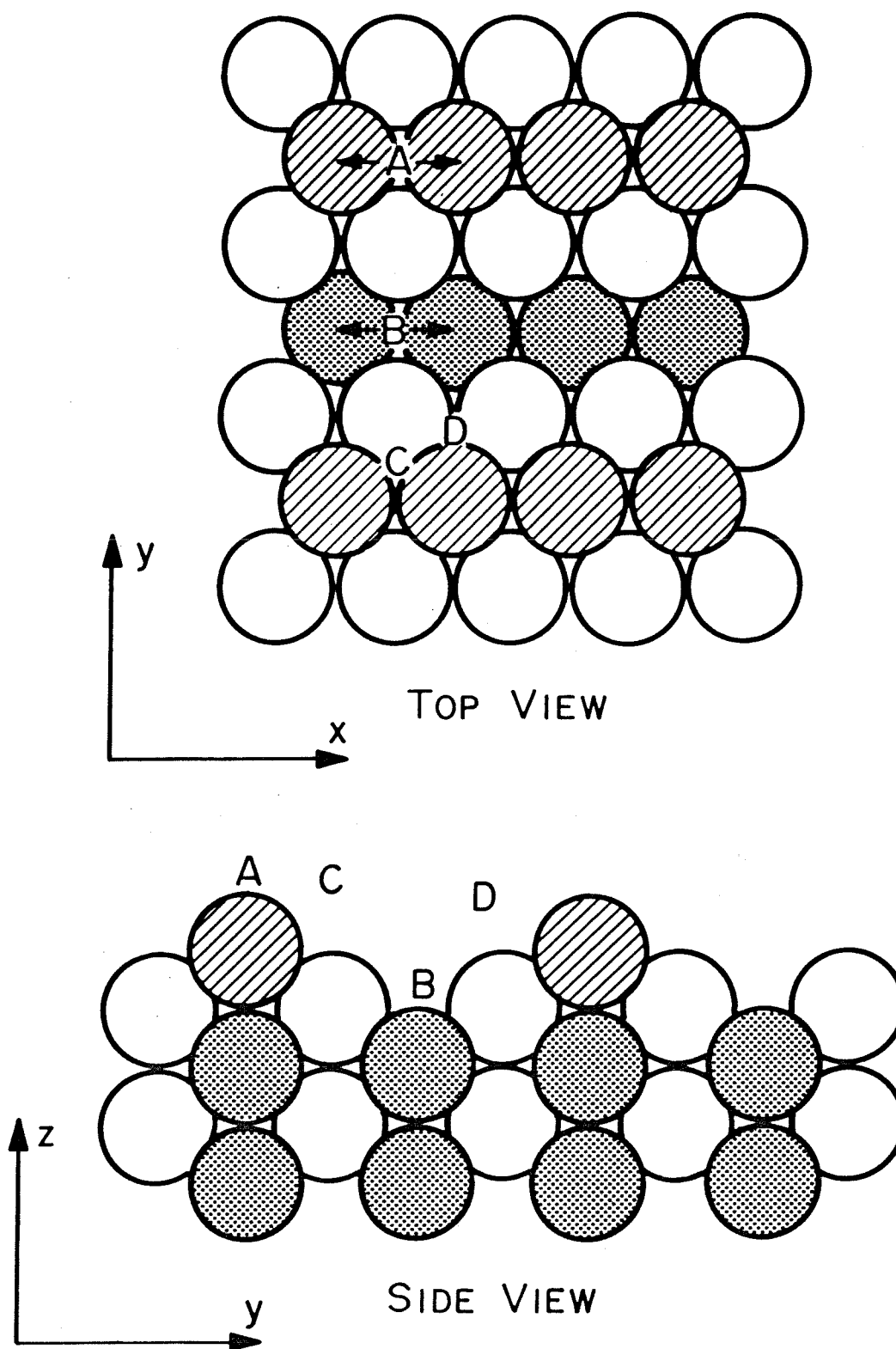


Fig. 1

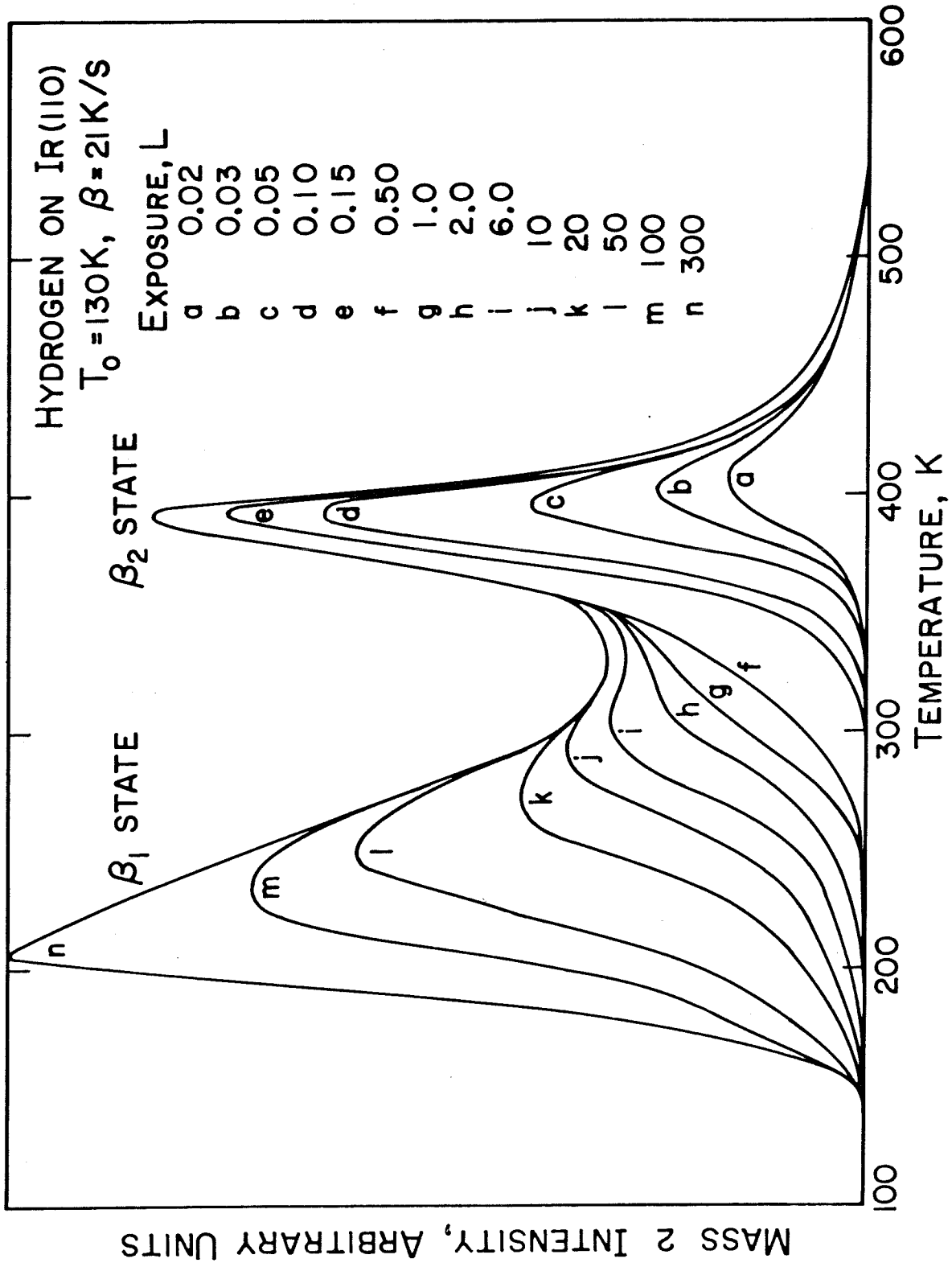


Fig. 2

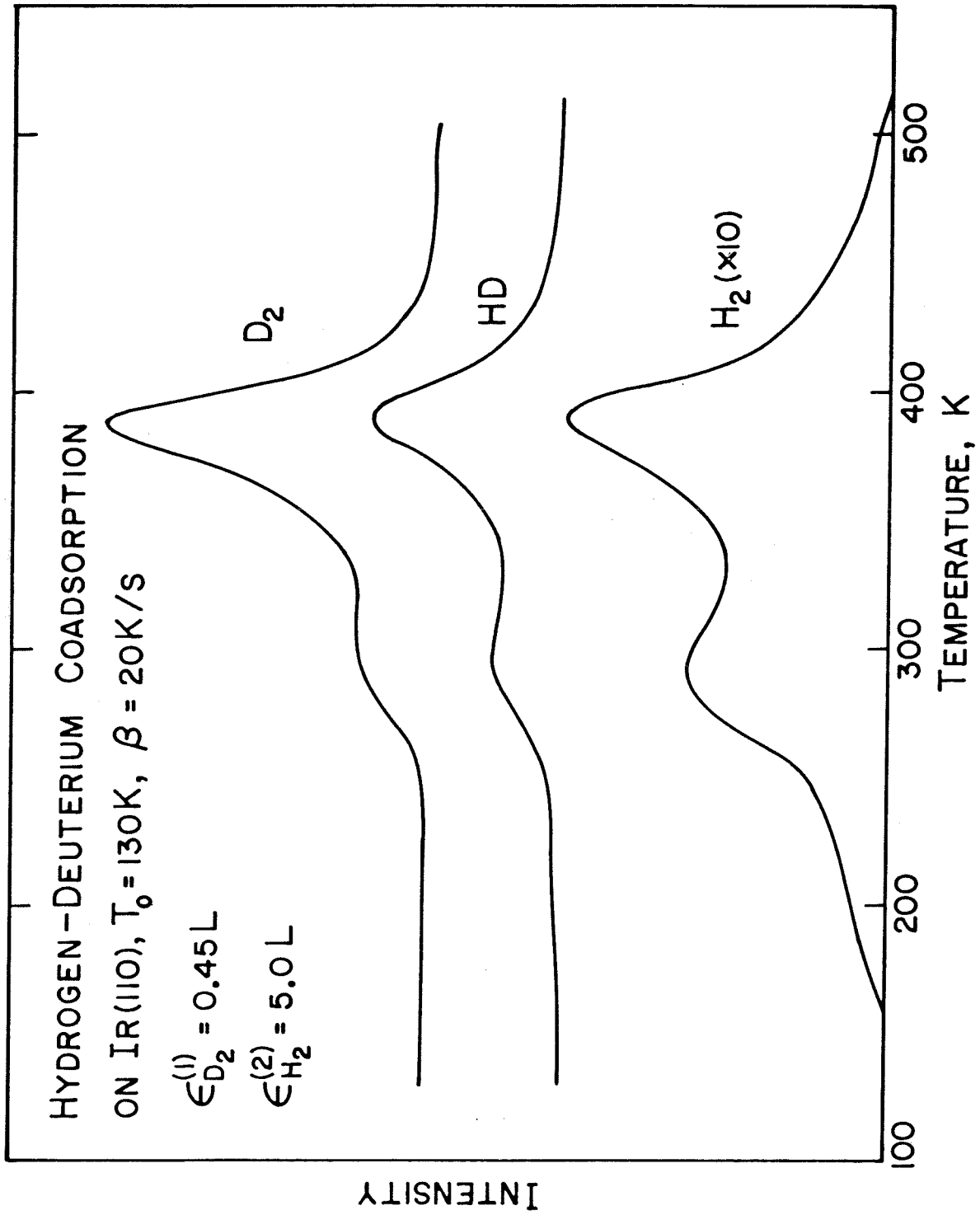


Fig. 3

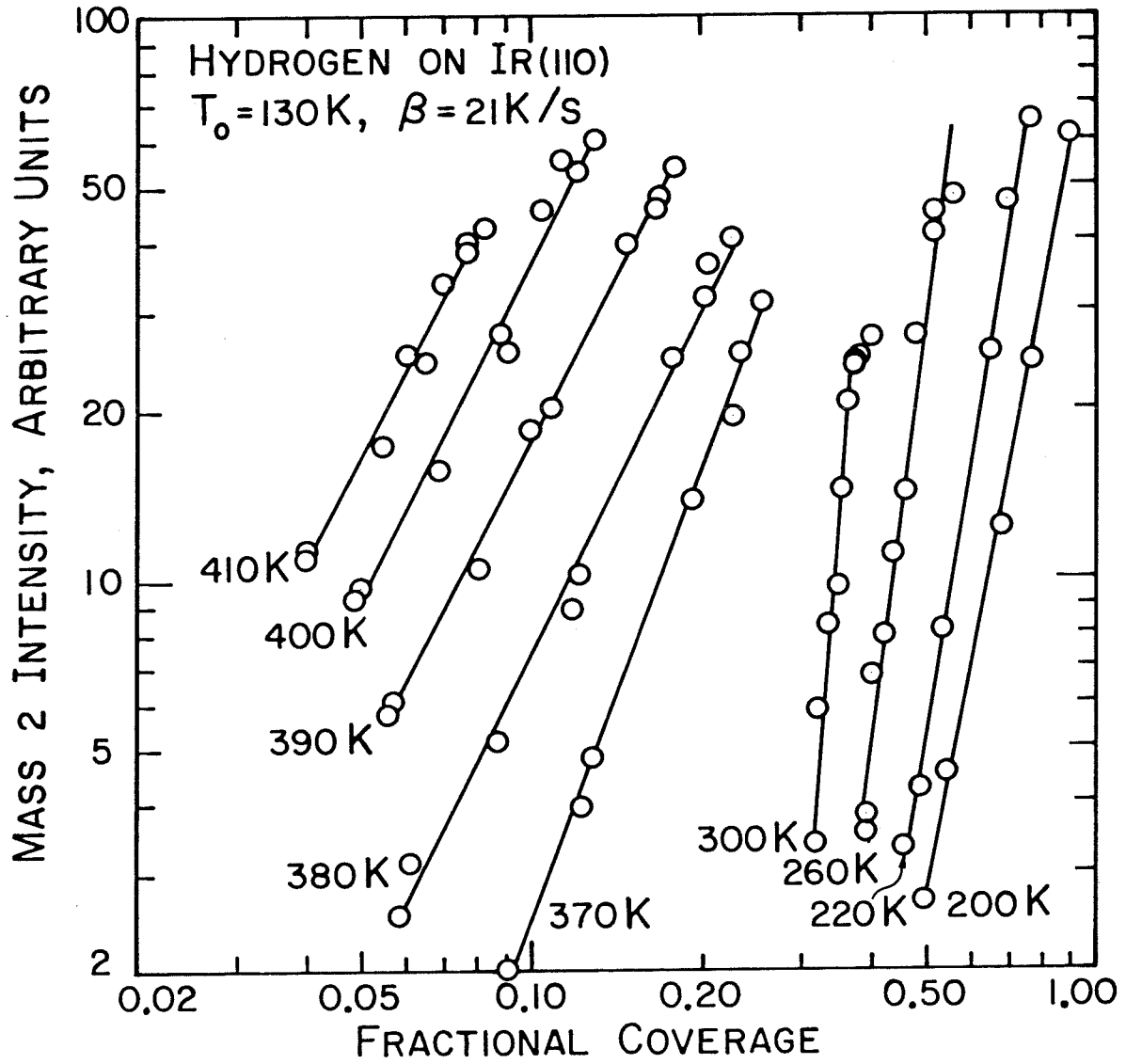


Fig. 4

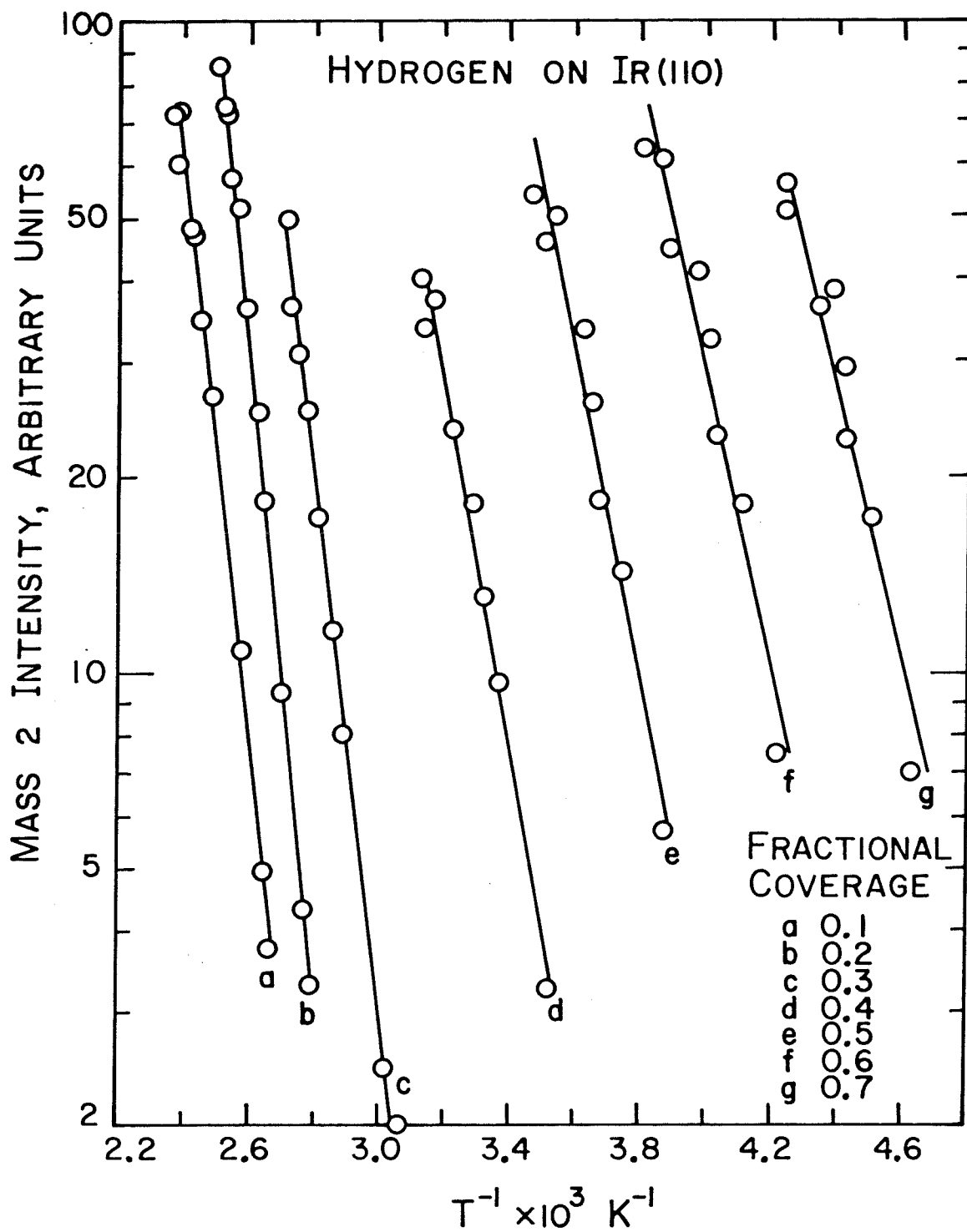


Fig. 5

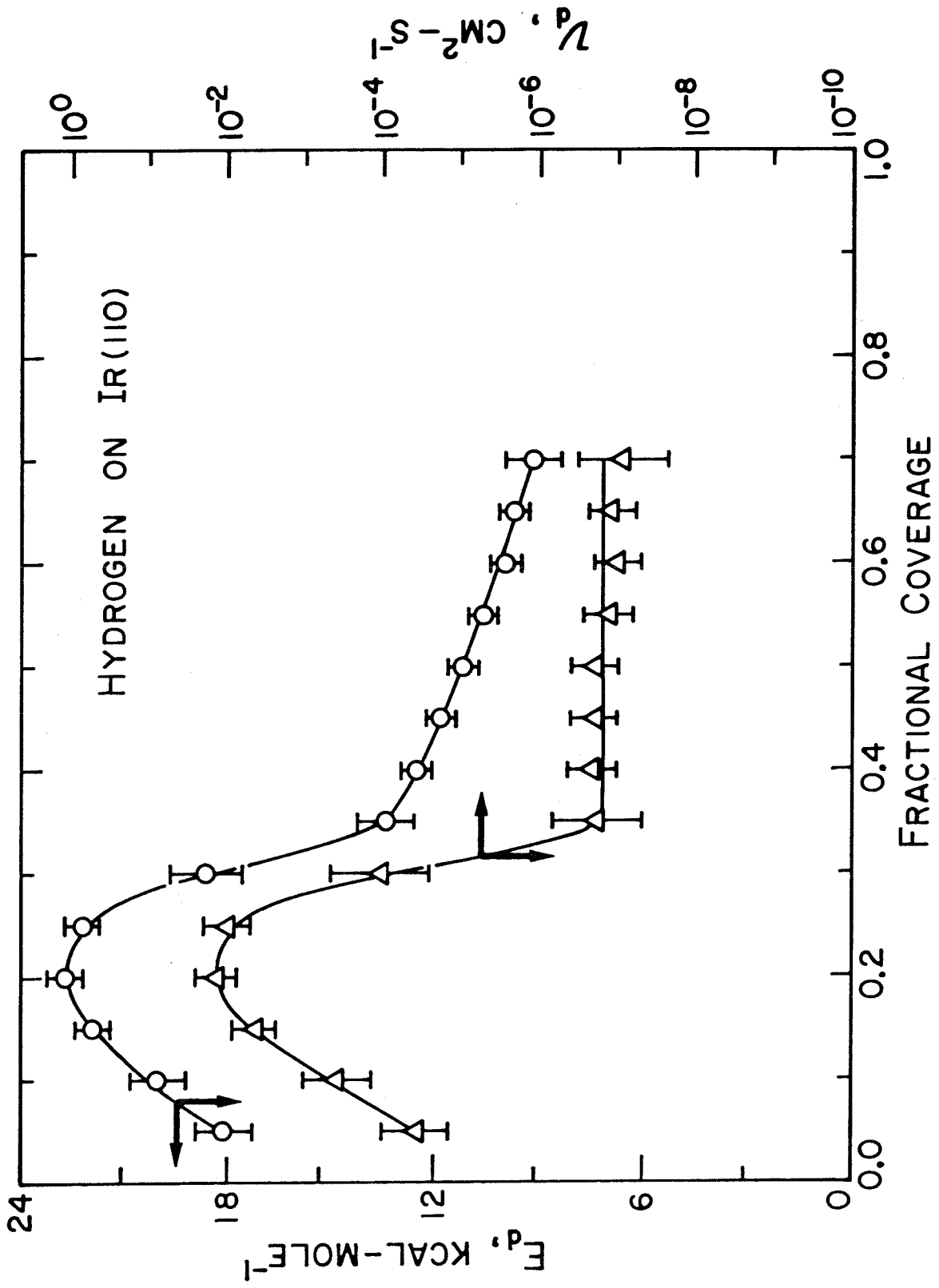


Fig. 6

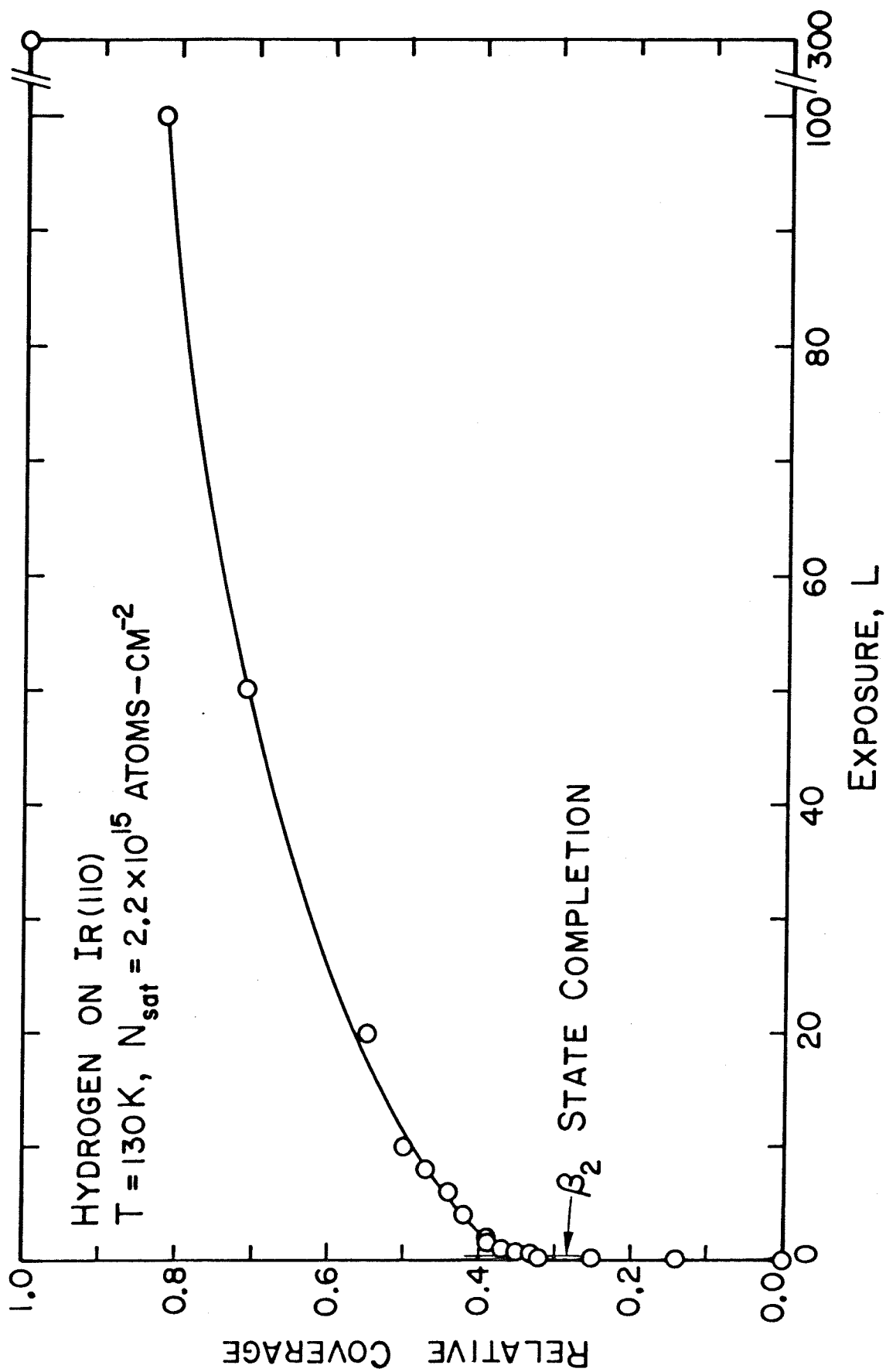


Fig. 7

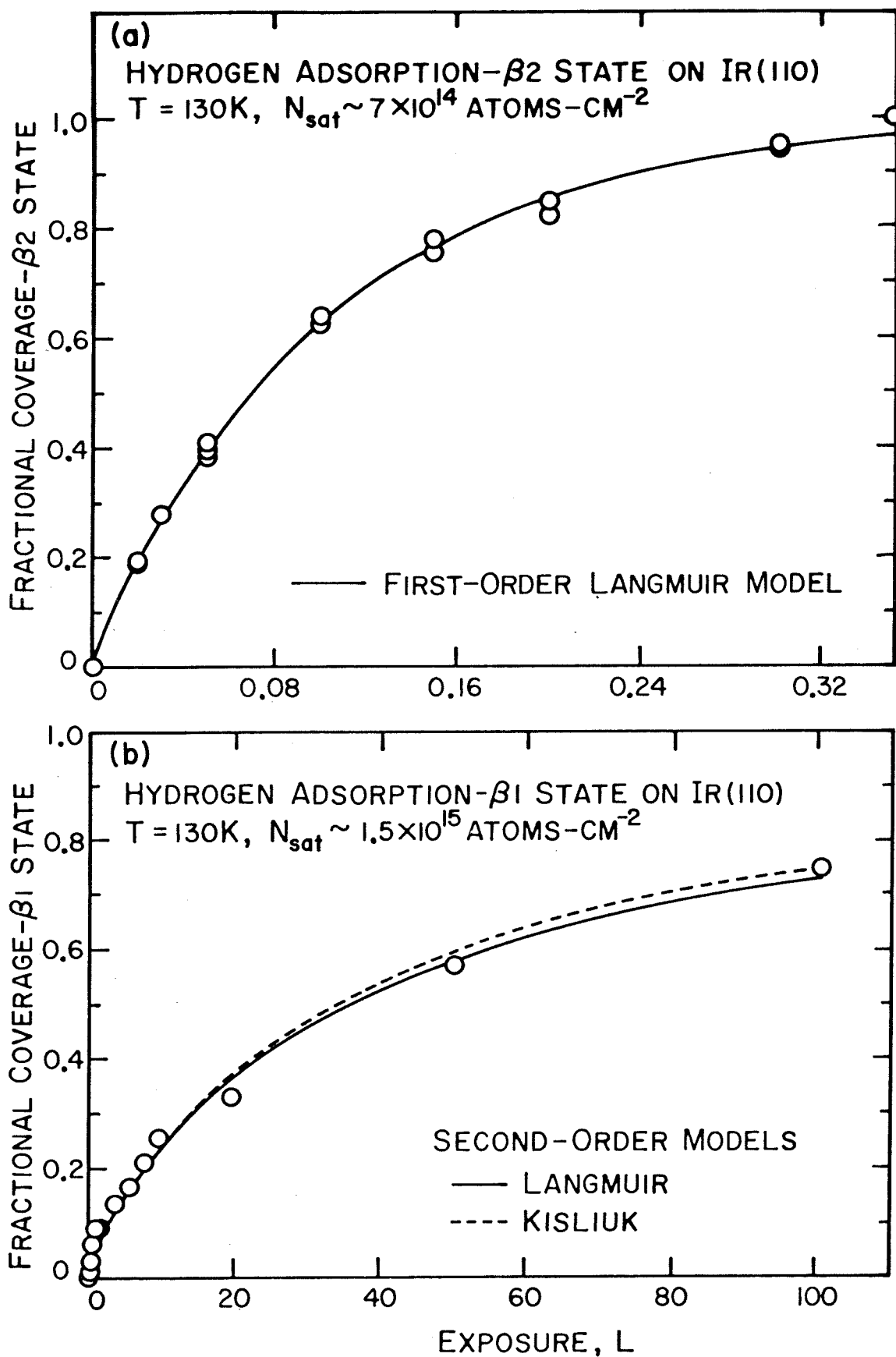


Fig. 8

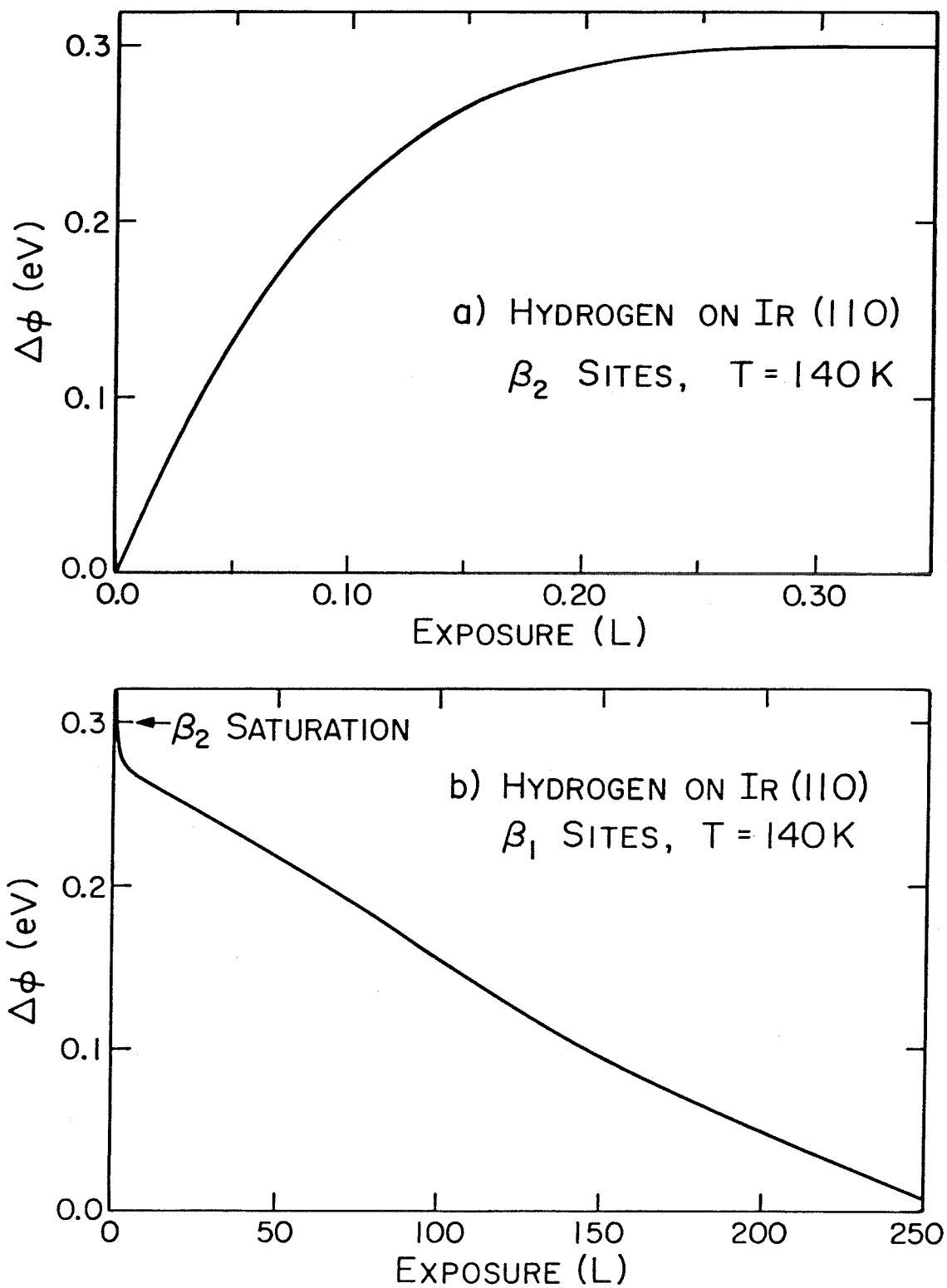


Fig. 9

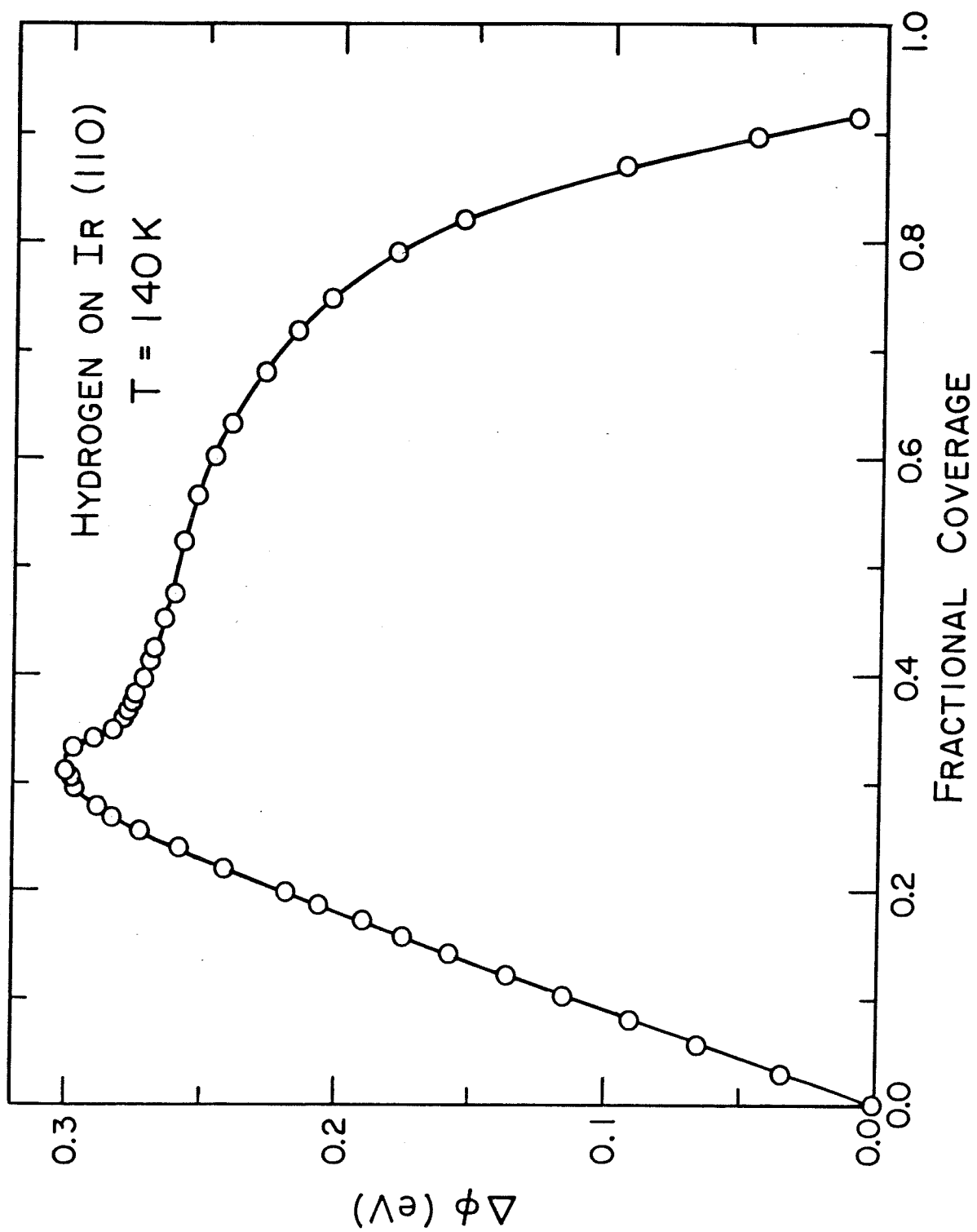


Fig. 10

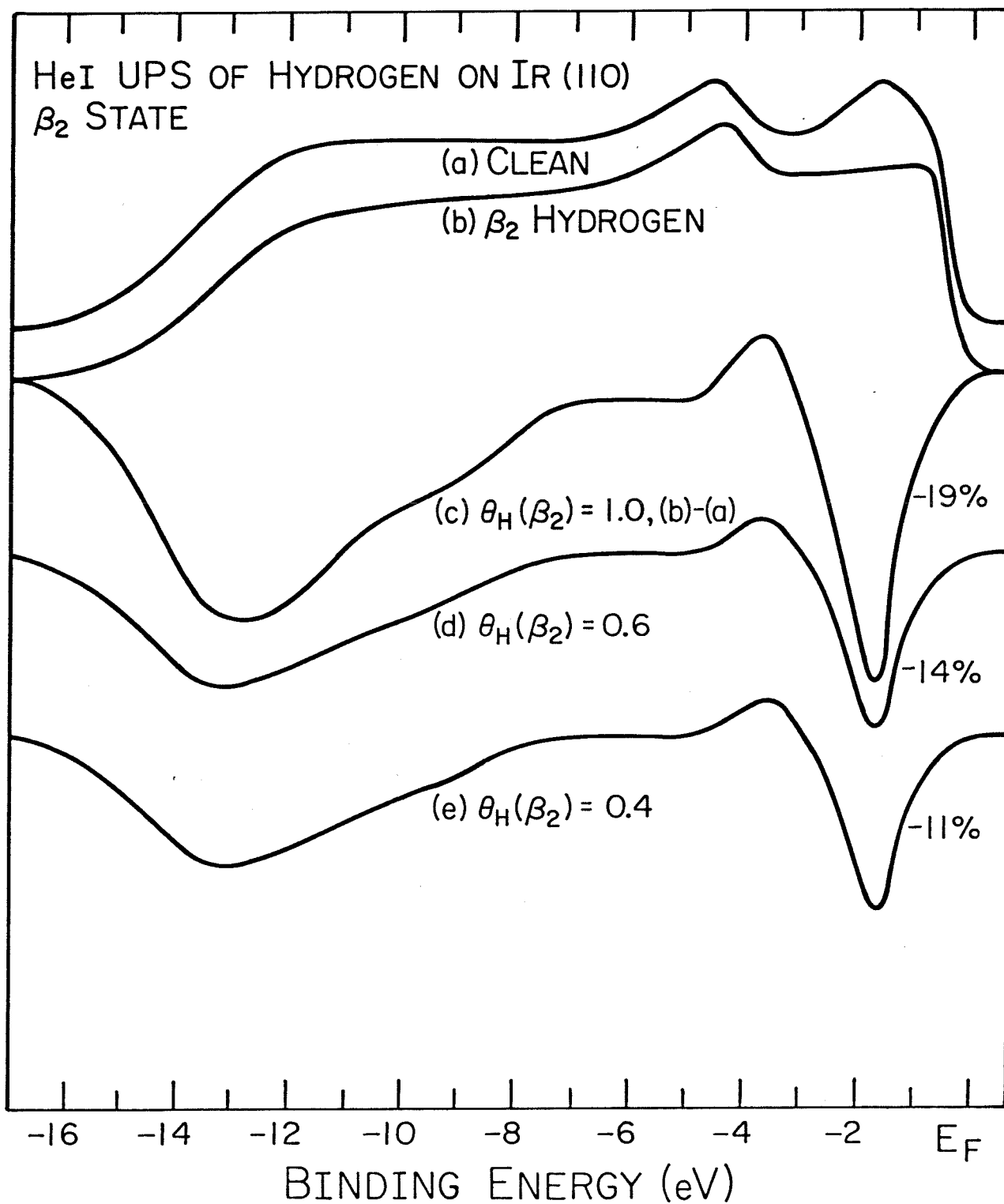


Fig. 11

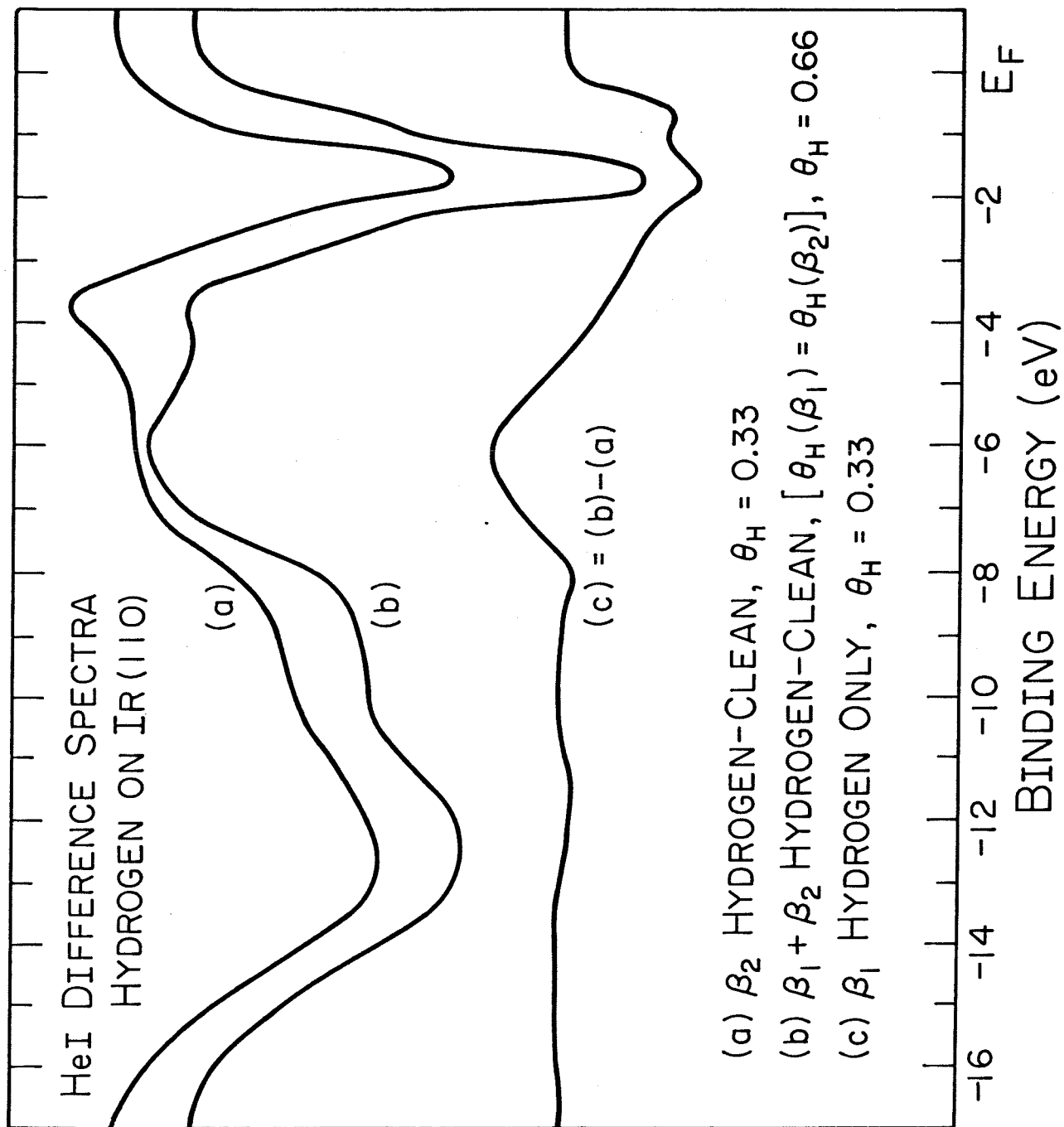


Fig. 12

CHAPTER 3

THE CO-ADSORPTION OF HYDROGEN AND CARBON
MONOXIDE ON THE (110) SURFACE OF IRIDIUM

(The text of Chapter 3 consists of an article coauthored with T. S. Wittrig and W. H. Weinberg that has been published in Surface Science 97, 297(1980).)

Abstract

The nonreactive co-adsorption of hydrogen and carbon monoxide on Ir(110) was studied under ultra-high vacuum conditions with thermal desorption mass spectrometry, LEED, contact potential difference measurements and UPS. No changes in the Ir(110) - (1x2) reconstructed surface structure or ordering of the adsorbed layers were observed with LEED due to the presence of hydrogen and CO co-adsorbed. The adsorption of hydrogen on pre-adsorbed CO, or vice versa, causes less hydrogen to occupy the high temperature β_2 state and shifts the occupancy to the low temperature β_1 state preferentially. An apparent increase in the sticking probability of hydrogen for adsorption in the β_1 state for small CO coverage is discussed. At high CO coverage, the Ir(110) surface is poisoned to hydrogen adsorption. Exposing CO to pre-adsorbed hydrogen causes the binding energy of hydrogen to decrease with increasing CO exposure. Eventual displacement of hydrogen from the surface occurs for large CO exposures. The contact potential difference (CPD) as a function of hydrogen exposure on pre-adsorbed CO complements the desorption data for both the β_1 and β_2 states of hydrogen. For low coverages of CO, relating the CPD to hydrogen coverage shows the induced dipole of hydrogen is unchanged from the clean surface. Furthermore, the HeI UP spectra of small coverages of hydrogen and CO indicate the valence orbitals of CO are not affected detectably by the presence of hydrogen. The results indicate CO poisons β_2 sites for hydrogen by a simple site blocking mechanism and may exclude β_1 sites at high CO coverages by a hydrogen-CO repulsive action.

1. Introduction

The co-adsorption of hydrogen and carbon monoxide on Ir(110) was undertaken to understand the effects of a model poison, CO, for hydrogen chemisorption. Thermal desorption mass spectrometry (TDS), LEED, contact potential difference (CPD) measurements and ultraviolet photoelectron spectroscopy (UPS) were used to investigate the influence of CO on the chemisorption properties of hydrogen on Ir(110).

Previous work concerned with the co-adsorption of hydrogen and carbon monoxide on the Group VIII transition metals included studies on Pt(111) (1), polycrystalline Pt(2) and Rh(3, 4), Rh(111) (5), Pd(110) (6) and an Ir field emission tip (7). Generally, it has been observed that CO displaces hydrogen from the surface when hydrogen is pre-adsorbed, and CO blocks sites for subsequent hydrogen adsorption, i.e., acts as a poison for hydrogen adsorption. Only one ordered LEED superstructure has been observed for hydrogen and CO co-adsorbed which is a (1 x 3) overlayer pattern on Pd(110) (6) when both adsorbates are in intimate contact with one another at a third their individual saturation concentrations. Weak mutual interactions are inferred since no variation in the desorption energy of H₂ was measured. However, anomalously high temperatures for hydrogen desorption have been reported for large exposures of a H₂/CO gas mixture to polycrystalline Pt(2) and Rh(3) surfaces. Moreover, H₂ desorption spectra from Pt(111) (1) and Rh films (4) change due to the presence of CO. Also, segregation of hydrogen and CO may occur on Rh(111) (5). The results

described here for the co-adsorption of hydrogen and CO on Ir(110) complement this previous work on the other Group VIII metals.

2. Experimental Procedures

The experiments were performed in an ion-pumped stainless steel bell jar with a base pressure below 2×10^{-10} torr. A detailed description of the experimental system is reported elsewhere (8), with the exception of the ultraviolet lamp. The HeI radiation was produced by a microwave discharge cavity at the end of a two stage, differentially pumped stainless steel capillary array. Operation of the HeI discharge at one torr caused the pressure in the bell jar to rise by 1×10^{-9} torr. For HeI radiation, typical count rates near the Fermi edge were from 90,000 to 110,000 counts⁻¹ using a double pass CMA at a constant pass energy of 25 eV. Details of the preparation of the Ir(110) crystal and the cleaning procedure are described elsewhere (8, 9).

3. Hydrogen TDS from Hydrogen/CO Overlayers and LEED Results

Three sets of thermal desorption spectra were collected as a function of exposure for hydrogen on Ir(110) with various precoverages of CO at 130K. The spectra are shown in Fig. 1 for CO fractional coverages of 0.10, 0.25 and 0.50, where $\theta_{CO} = 1.0$ corresponds to 9.6×10^{14} molecules -cm^{-2} (8). In addition, the spectra for hydrogen chemisorbed on a surface with no CO present are reproduced (9) for comparison. The thermal desorption spectra of CO are not presented since CO desorbs at temperatures where hydrogen desorption is complete (8). For each curve shown in Figs. 1(b), (c) and (d), the surface was exposed to a known flux of CO at 300K as noted in the figures. Then the surface was cooled to 130K and exposed to H₂ with a subsequent heating rate for desorption of 20K-s⁻¹. Small errors in the CO

exposure or variation of the CO background pressure cause noticeable fluctuation in the shape of the high temperature desorption state, which will be referred to as the β_2 state of hydrogen. A 10 L exposure of CO on Ir(110), followed by a saturation exposure of H₂, caused no hydrogen to adsorb.

The most striking observation about the influence of CO on hydrogen adsorption is that the β_2 state is affected more strongly than the β_1 state (low temperature state), particularly at low CO coverages. This is not due to a change in the surface structure since the reconstructed Ir(110) - (1 x 2) is stable upon CO adsorption (8) and hydrogen adsorption (9), but rather it is due to a direct hydrogen-CO interaction. Although an extensive search for an ordered overlayer superstructure was performed, no ordering over the coherence width of the LEED beam occurred for any coverage of hydrogen and CO co-adsorbed. Therefore, no long range order is established between hydrogen and CO, but a short range interaction must take place.

As the coverage of CO increases, the amount of hydrogen that desorbs in the β_2 state decreases, as seen in Fig. 1. Since the integrated intensities can be related to an absolute coverage of H atoms (9) that desorb from the β_2 state and the coverage of CO is known, the number of sites blocked by CO can be calculated. For clean Ir(110), the saturation coverage of the β_2 state is 7×10^{14} atoms-cm⁻², and it obeys first order adsorption kinetics with an initial sticking probability of unity (9). For every CO molecule adsorbed, approximately 1.5 sites for H atoms are blocked for the CO coverages presented in Fig. 1. At a coverage of 0.50, CO effectively blocks hydrogen from the β_2 sites. Interestingly,

the number of sites of hydrogen in the β_2 state blocked by each CO is nearly equal to the ratio of the saturation coverage of CO in molecule-cm⁻² and the saturation coverage of β_2 hydrogen in atoms-cm⁻². Moreover, if the number of blocked sites are accounted for when $\theta_{CO}^0 = 0.25$, the initial sticking probability for hydrogen is still equal to one. For $\theta_{CO}^0 = 0.10$ the calculated initial sticking probability is 0.8, a 20% decrease over simple site blocking. Still, the interaction of hydrogen with the β_2 sites is strong when low coverages of CO are present, and the rate of adsorption depends essentially on an impinging H₂ molecule finding an empty site as the controlling step. At least for the spectra shown in Fig. 1(b), where the β_2 feature is still resolved well, only a small decrease occurs in peak temperature at its saturation coverage compared to the results for the clean surface shown in Fig. 1(a). The presence of CO evidently does not affect strongly the desorption of the β_2 state of hydrogen other than blocking sites. The sites associated with the β_2 state have been deduced from the absolute coverage of hydrogen and UPS results to be above the third layer of Ir atoms exposed in the missing row locations on the reconstructed Ir(110) surface (9). Inferences drawn from contact potential difference measurements for CO on Ir(110) also place the binding sites of CO between the topmost row of Ir atoms (8), which would be reasonable if CO directly blocks β_2 sites for hydrogen as these data and data presented later suggests.

Whereas the β_2 state is attenuated even for low coverages of CO, the β_1 state of hydrogen is enhanced in coverage for equal exposures compared to the clean surface. Figure 2 reproduces the thermal desorption spectra of 10 L H₂ exposed to a surface containing fractional coverages of CO of 0, 0.10 and 0.25. An increase in the coverage of the β_1 state up to a CO coverage of 0.25 occurs, where for this CO coverage the β_1 state

contains as much hydrogen as would be present for 50 L H_2 on the clean surface, although the desorption occurs at lower temperature when CO is present for equal $\theta_H(\beta_1)$. At least up to $\theta_{CO} = 0.25$, the saturation coverage of the β_1 state is not affected. However, increasing the coverage of CO always decreases the total coverage of hydrogen for a constant exposure, particularly above $\theta_{CO} = 0.25$.

The enhancement of adsorption of hydrogen into the β_1 state in the presence of small amounts of CO may be explained in two ways. First, adsorbed CO molecules may tend to orient H_2 molecules as they impinge on the surface to favor β_1 sites, which are the two types of three-fold sites on the clean surface (9). At higher CO coverages, this effect becomes unimportant since CO is compressed on the surface blocking β_1 sites as well. Second, a channeling effect may occur from hydrogen originally adsorbed in β_2 sites to hydrogen adsorbed in β_1 sites leaving a β_2 site vacant for additional hydrogen adsorption during the exposure. This possibility cannot be ruled out since CO is still somewhat mobile even at 130K (8), and exchange does occur between the β_1 and β_2 sites (9). As adsorbed CO migrates, β_2 hydrogen may be pushed to β_1 sites. The reverse conversion from β_1 to β_2 may in turn be inhibited by CO, but more hydrogen may adsorb into β_2 from the gas phase. This would describe a channeling of hydrogen to enhance artificially the apparent sticking probability of hydrogen adsorption into the β_1 state on Ir(110). Either of the two mechanisms presented is equally plausible. A small effect that enhances β_1 adsorption will be reflected as a large effect in the amount of β_1 hydrogen adsorbed compared to the clean surface, since for this case second order Langmuir kinetics are obeyed with a small initial sticking probability of 7×10^{-3} .

The effect of CO adsorption on a constant amount of pre-adsorbed hydrogen is shown in Fig. 3. In this experiment, 0.8 L H₂ was exposed to the surface at 130K and subsequently to different amounts of CO, as noted in the figure, at the same temperature. The desorption spectra were then recorded at a heating rate of 20 K-s⁻¹. The integrated intensity of hydrogen for each spectrum is the same for these CO exposures; in other words no displacement of hydrogen from the surface by CO occurs. A continuous displacement is observed from the β_2 to the β_1 sites, however, with increasing CO exposures. For exposures greater than 10 L some hydrogen is desorbed from the surface. Comparisons of Figs. 1 and 3 show that for equivalent coverages of hydrogen and CO, the desorption spectra for hydrogen are the same. Regardless of the exposure sequence, CO tends to occupy its preferred sites rather than hydrogen. It should be noted that the sticking probability of CO is decreased somewhat from the clean surface when hydrogen is present, although this effect was not investigated in detail.

These results indicate that segregation of H atoms and CO molecules on the surface into separate islands does not occur since β_2 hydrogen should be observed to desorb from hydrogen islands. However, partial segregation of H atoms and CO molecules does occur on Rh(111) (5). Co-adsorption studies of hydrogen and CO on Pd(110) show no change in the desorption energy for hydrogen compared to the clean surface (6), different from the observations on Ir(110). Finally, no high temperature desorption states of hydrogen were observed under the conditions examined, although such states have been reported for large exposures of an H₂/CO gas mixture both on polycrystalline Pt (2) and Rh (3).

4. CPD and UPS Measurements

Contact potential differences measurements were performed to complement the TDS data presented in the previous section and to observe how the charge transfer of hydrogen is affected by the presence of CO. Also, UPS measurements were performed for low coverages of hydrogen and CO to determine if a strong mutual interaction is reflected in the valence orbitals of CO.

For various precoverages of CO, the CPD of hydrogen in the β_2 state on Ir(110) changes strongly with exposure, compared to the clean surface, as shown in Fig. 4. The CPD of hydrogen in the β_2 state was not plotted as a function of fractional coverage because the coverage-exposure of hydrogen in this state, for a given precoverage of CO, is quite sensitive to small errors in CO precoverage, particularly with such small exposures of hydrogen (Fig. 4). However, for the β_1 state of hydrogen, the coverage-exposure relation could be determined, since small errors in CO precoverage affected the β_1 coverage to a small extent only. The same precoverages of CO were used as for the TDS results presented in the previous section: 0, 0.10, 0.25 and 0.50 ML. It is apparent that small amounts of CO depress markedly the maximum CPD observed for hydrogen in β_2 sites. From the TDS results, it was seen that CO blocks β_2 sites for hydrogen; and for $\theta_{CO} = 0.50$ ML, β_2 desorption is almost totally suppressed. For this coverage of CO in Fig. 4, the CPD monotonically decreases in contrast to the other three curves shown in this figure. This indicates that β_2 sites are blocked effectively and β_1 sites are populated since the CPD of the latter decreases with the coverage of hydrogen, as will be shown. At least for a precoverage of CO of 0.10 ML, the calculated dipole for the hydrogen-metal complex over

the first half of β_2 adsorption is equal to the dipole calculated for the clean surface, 0.14 Debye (9), where the CPD is linear with the fractional coverage of hydrogen. Therefore, the charge transfer for hydrogen in β_2 sites in the presence of small amounts of CO is not affected to a measurable extent. Site blocking by CO is the dominant effect in this coverage regime.

Since the observed dipole of β_2 hydrogen does not change with small amounts of CO present, the HeI UP spectra of hydrogen and CO coadsorbed in this coverage regime were measured to determine whether the valence levels of these two species shift, indicative of a strong mutual interaction. Sufficient hydrogen was exposed to the surface to fill the β_2 state on surfaces with 0, 0.10 and 0.25 ML CO present. The corresponding HeI UP difference spectra are shown in Fig. 5. For the spectrum with no CO present, Fig. 5(a), the H(1s) level can be seen as a broad transition centered at 6.1 eV below the Fermi level, E_F . Also in Fig. 5(a), the large attenuation in the d-band centered at 1.6 eV below E_F and a small enhancement at 3.6 eV below E_F are observed due to hydrogen in β_2 sites (9). As the precoverage of CO increases, the valence levels of CO grow in as evidenced in Figs. 5(b) and (c) by peaks at 11.3, 8.7 and 7.6 eV below E_F which are not changed either in shape or energy from that measured for CO with no hydrogen present. Therefore, CO does not appear to be affected markedly by hydrogen in β_2 sites although they compete directly for these sites as shown previously. Also, as the coverage of CO increases, both the attenuation of the d-band of the metal as well as the enhancement at 3.6 eV decrease. Furthermore, the H(1s) level becomes indiscernible in Figs. 5(b)

and (c). These changes with the coverage of CO indicate the coverage of β_2 hydrogen is decreased since any hydrogen adsorbed in β_1 sites has a small effect on the d-band, and CO at, for example, 0.25 ML attenuates the d-band uniformly by less than 5%. It is concluded from these UPS data that the valence levels of CO are not strongly perturbed by hydrogen on Ir(110), and CO blocks β_2 sites for hydrogen, in agreement with the TDS and CPD results.

In contrast to the β_2 sites of hydrogen in the presence of CO on Ir(110), TDS data show an enhancement of the sticking probability of hydrogen into β_1 sites when small coverages of CO are present. This enhancement is reflected in the CPD measurements in Fig. 6 as well. Increasing the precoverage of CO causes the CPD of hydrogen adsorbing into β_1 sites to decrease more rapidly with exposure as compared to the clean surface. The data were obtained by exposing the surface to the various amounts of CO, exposing the surface to sufficient hydrogen to fill first β_2 sites, and then recording the CPD as a function of hydrogen exposure.

In order to examine more carefully how the adsorption of hydrogen into β_1 sites on Ir(110) is affected by CO, the coverage determination of hydrogen (9) was used to relate the CPD and the concentration of hydrogen in the β_1 sites as shown in Fig. 7. It is seen that for precoverages of CO of 0, 0.10 and 0.25 ML, the slopes of the CPD ($\Delta\phi$) as a function of coverage of β_1 hydrogen [$N_H(\beta_1)$] are very nearly the same for the range of $N_H(\beta_1)$ shown here which accounts for approximately one-third of the total β_1 concentration on the clean surface. For these coverages of CO and hydrogen, it may be concluded that the dipole of the hydrogen-metal complex is relatively unaffected. However, a cursory examination of the trend for β_1 hydrogen adsorbing on 0.50 ML CO seen in Fig. 7 would

point to a definite change in the induced dipole for hydrogen due to the presence of CO. But some of the initial β_1 sites are actually excluded by this coverage of CO as seen in Fig. 1(d). The higher coverage β_1 sites of hydrogen that must then be occupied exhibit a larger decrease in the CPD as a function of coverage (9). Therefore, the change in behavior of hydrogen for 0.50 ML of CO pre-adsorbed in Fig. 7 may be reflecting essentially this partial blockage of the first β_1 sites occupied by hydrogen and that even for this range of hydrogen and CO coverages the induced dipole of hydrogen is not affected greatly on a microscopic scale. The partial blockage of β_1 sites at higher CO coverage may be more due to an H-CO repulsive interaction than a direct competition for binding sites.

5. Summary

The co-adsorption of hydrogen and CO on Ir(110) has been studied under ultra-high vacuum conditions with thermal desorption mass spectrometry, LEED, contact potential difference measurements and UPS. The present results complement other work performed previously on the platinum metals.

Although no ordered structures were observed with LEED when hydrogen and CO were co-adsorbed under any of the conditions examined, the adsorption and desorption properties of hydrogen are affected strongly by the presence of small amounts of CO. For small coverages of pre-adsorbed CO, a continuous decrease in desorption from the low coverage β_2 state of hydrogen is observed with increasing CO coverages. A concomitant increase occurs for the high coverage β_1 state of hydrogen which is interpreted as either an orienting effect by CO for an impinging H_2 molecule or a continuous conversion of hydrogen from the β_2 to the β_1 state during the hydrogen exposure due to the partial mobility of CO which converts H

atoms from the β_2 to the β_1 state. At high CO coverages, the surface is poisoned to hydrogen adsorption. The adsorption of CO on pre-adsorbed hydrogen shows the same desorption trends for H_2 as for the reverse exposure sequence at equivalent coverages. The binding energy of hydrogen decreases as the CO coverage increases, and H_2 desorption occurs at the adsorption temperature (130K) for large CO exposures.

The CPD of hydrogen on pre-adsorbed CO also is affected strongly. However, the induced dipole of hydrogen in the β_2 state is the same as for the clean surface if the number of sites blocked by each CO molecule (1.5) is taken into account. Moreover, the HeI UP spectra of low coverages of CO and of hydrogen in the β_2 sites show no changes in the valence orbitals of CO and only reflect the blocking of β_2 sites by CO for hydrogen adsorption. For the β_1 state, the induced dipole of hydrogen in the presence of less than 0.25 ML of CO is the same as for clean Ir(110) as well. For 0.50 ML of CO pre-adsorbed, some of the first β_1 sites are excluded for hydrogen adsorption due to either a direct blocking or a hydrogen-CO repulsive interaction. The CPD in this case reflects a shift in the hydrogen to the second β_1 site that exhibits a larger decrease with coverage.

References

1. V. H. Baldwin, Jr. and J. B. Hudson, *J. Vacuum Sci. Technol.* 8, 49 (1971).
2. K. Kawasaki, T. Kodama, H. Miki and T. Kioka, *Surface Sci.* 64, 349 (1977).
3. K. Kawasaki, M. Shibata, H. Miki and T. Kioka, *Surface Sci.* 81, 370 (1979).
4. M. G. Wells, N. W. Cant and R. G. Greenler, *Surface Sci.* 67, 541 (1977).
5. E. D. Williams, P. A. Thiel, W. H. Weinberg, and J. T. Yates, Jr., *J. Chem. Phys.* 72, 3496 (1980).
6. H. Conrad, G. Ertl and E. E. Latta, *J. Catalysis* 35, 363 (1974).
7. H. F. Kempin, K. Klapper and G. Ertl, *Nouveau J. Chim. (Paris)* 1, 295 (1977).
8. J. L. Taylor, D. E. Ibbotson and W. H. Weinberg, *J. Chem. Phys.* 69 4298 (1978).
9. D. E. Ibbotson, T. S. Wittrig and W. H. Weinberg, *J. Chem Phys.* 72, 4885 (1980).

Figure Captions

- Fig. 1: Thermal desorption spectra from Ir(110) of hydrogen which was adsorbed at 130K on various fractional coverages of CO. The initial coverage of CO was accomplished by exposing the surface to CO at 300 K and cooling to 130K: (a) $\theta_{\text{CO}} = 0$, (b) $\theta_{\text{CO}} = 0.10$ (c) $\theta_{\text{CO}} = 0.25$, and (d) $\theta_{\text{CO}} = 0.50$.
- Fig. 2: Thermal desorption of 10 L H_2 exposed at 130K to 0, 0.10 and 0.25 fractional coverages of CO. Note the decrease in the area of the β_2 state and the increase in the area of the β_1 state as the precoverage of CO increases.
- Fig. 3. Thermal desorption of H_2 from pre-adsorbed hydrogen (0.8 L) exposed to varying amounts of CO: (a) 0 L, (b) 0.25 L, (c) 0.6 L, and (d) 1.5 L. All exposures were carried out at 130K.. The coverage of hydrogen is constant over these CO exposures.
- Fig. 4: The CPD of hydrogen as a function of exposure for the β_2 sites (low coverage) on Ir(110) for various precoverages of CO: (a) 0, (b) 0.10, and (c) 0.25, and (d) 0.50 ML.
- Fig. 5: HeI UP difference spectra for β_2 hydrogen on Ir(110) on pre-coverages of CO: (a) 0, (b) 0.10, and (c) 0.25 ML. For each spectrum, the surface was exposed to sufficient hydrogen to fill the β_2 sites as evidenced by TDS and CPD measurements.

Fig. 6: The CPD of hydrogen as a function of exposure for the β_1 sites (high coverage) on Ir(110) for precoverages of CO: (a) 0, (b) 0.10, (c) 0.25, and (d) 0.50 ML.

Fig. 7: The CPD of hydrogen as a function of the concentration in the β_1 sites for 0, 0.10, 0.25, and 0.50 ML of CO pre-adsorbed. The data were calculated from the integrated intensities in Fig. 1, the coverage calibration from Ref. (9), and Fig. 6.

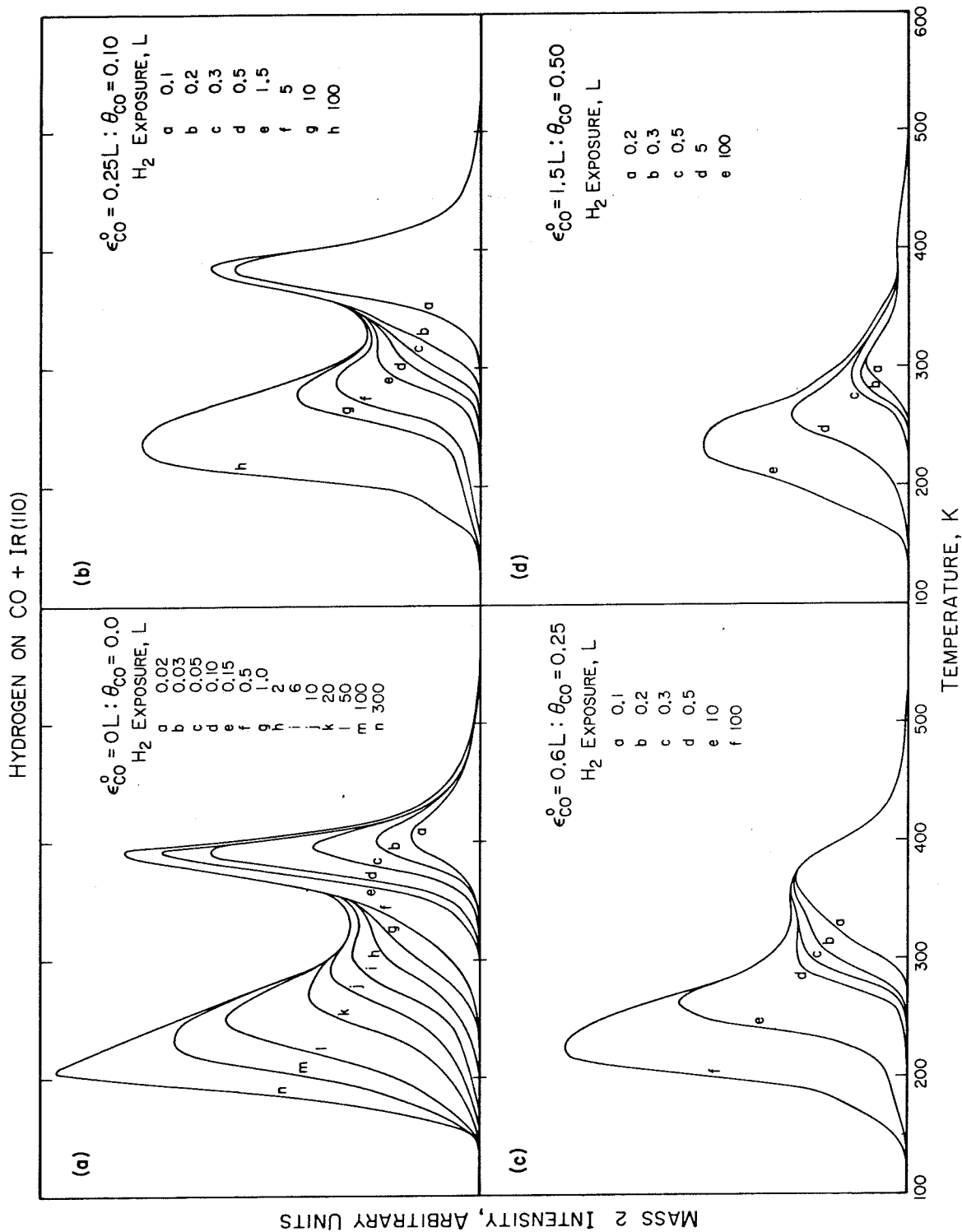


Figure 1

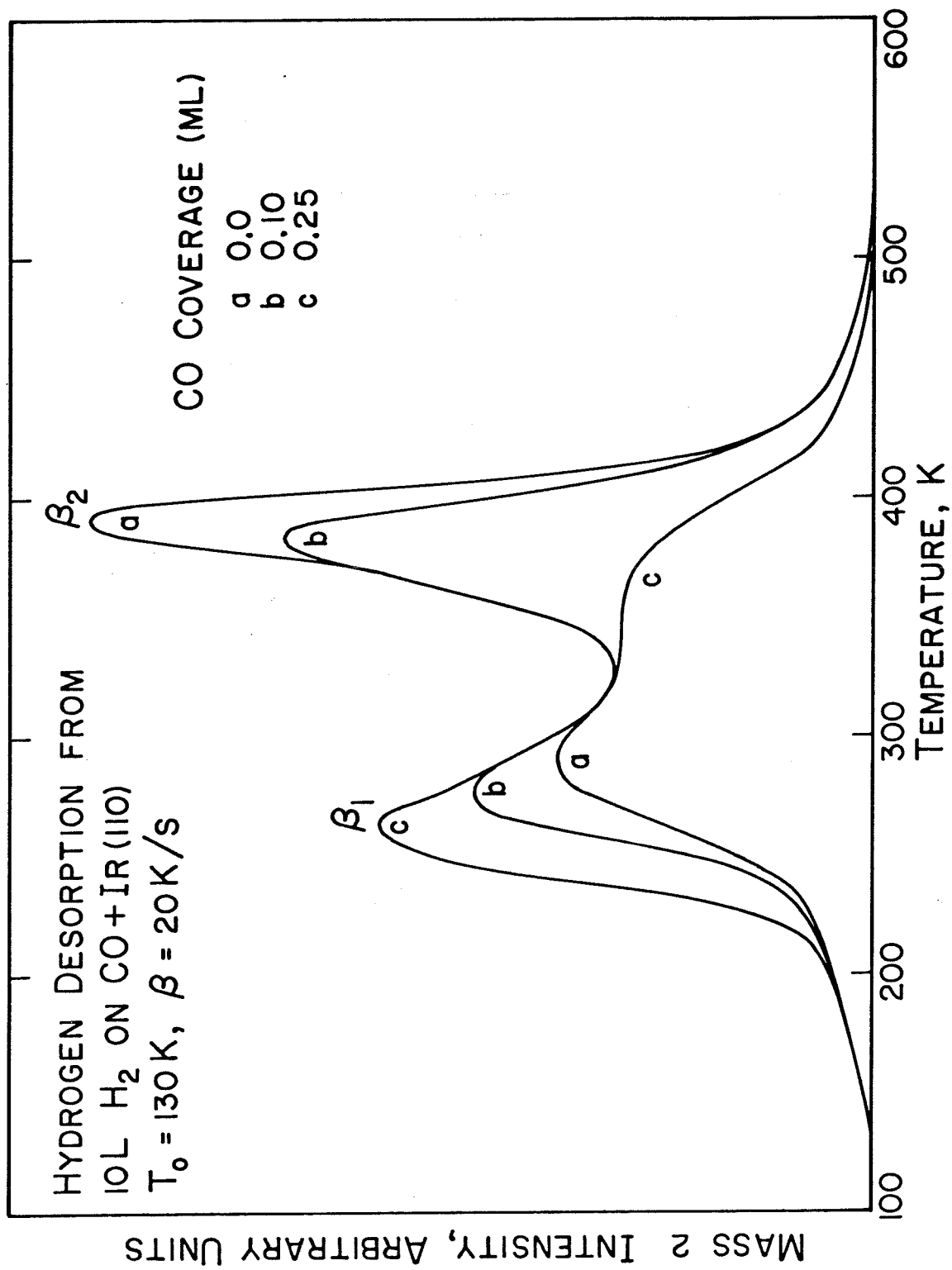


Figure 2

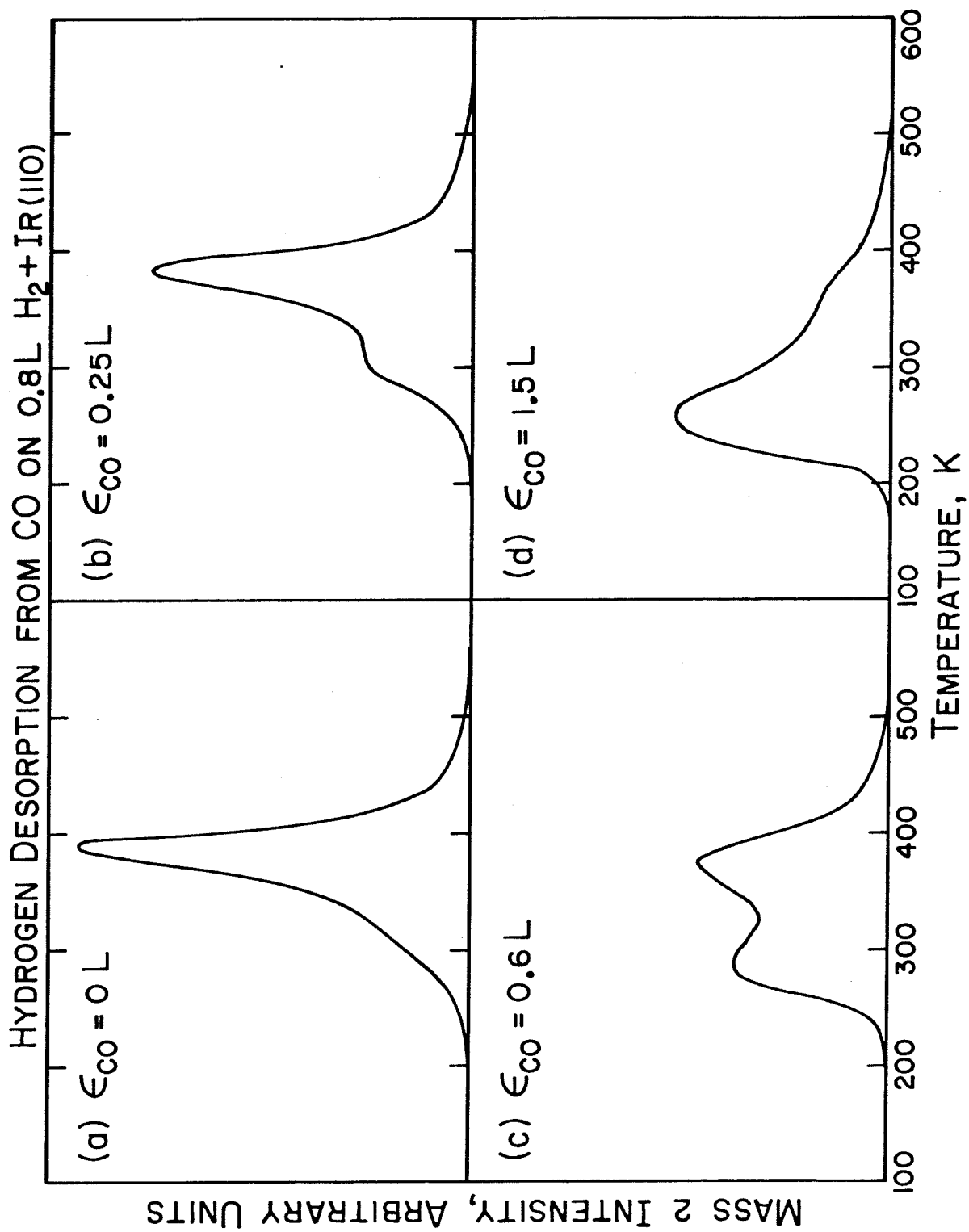


Figure 3

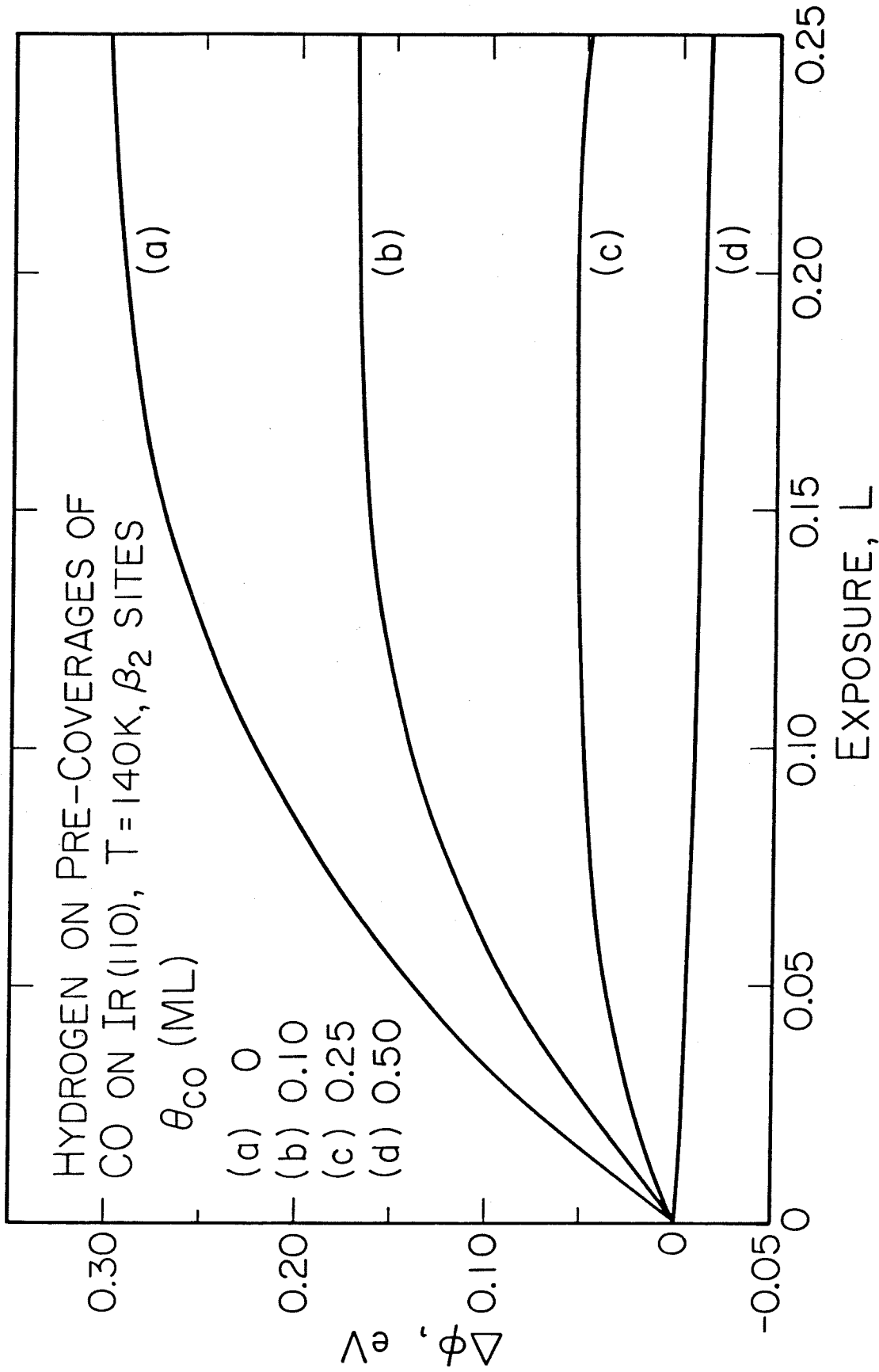


Figure 4

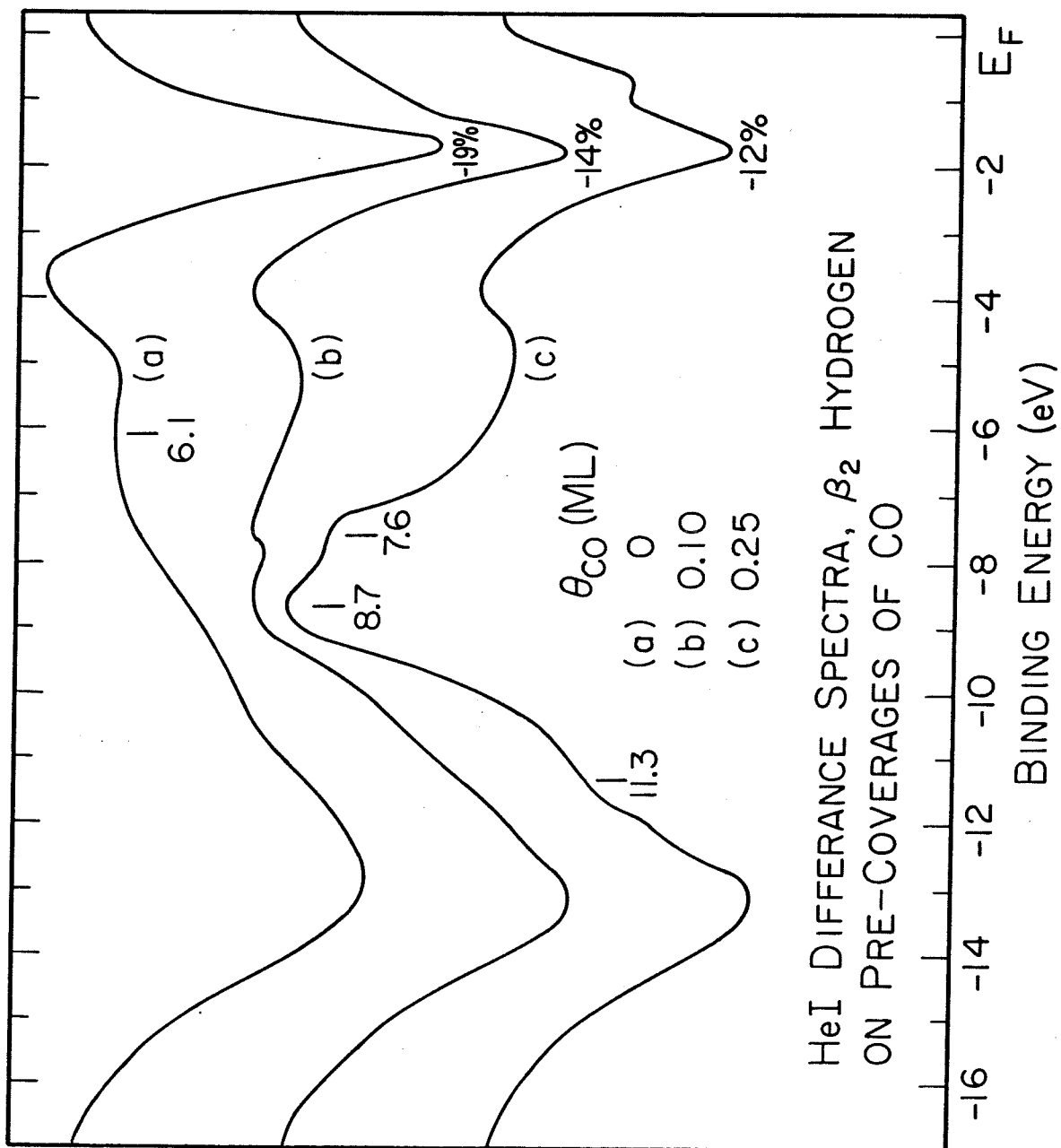


Figure 5

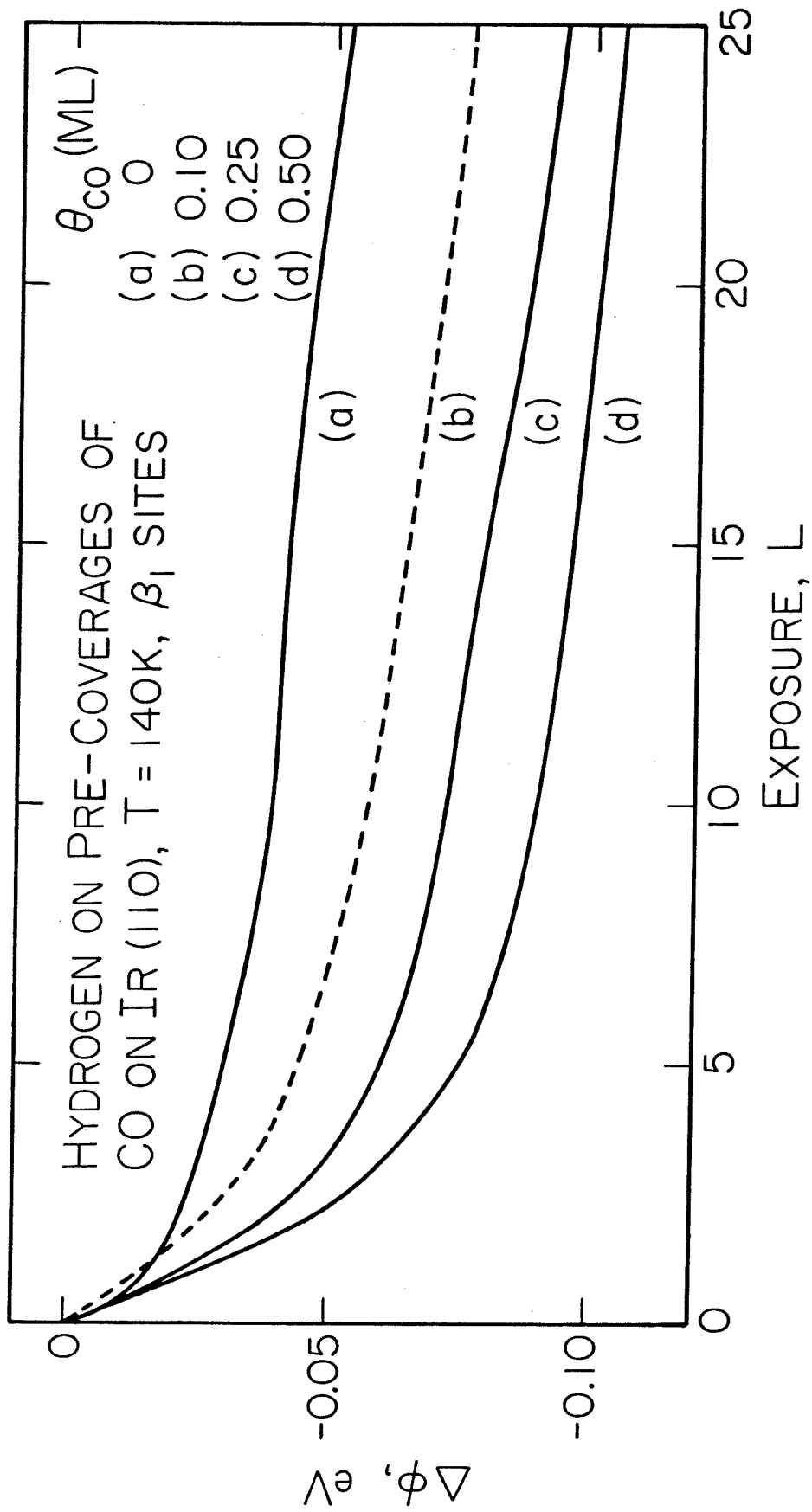


Figure 6

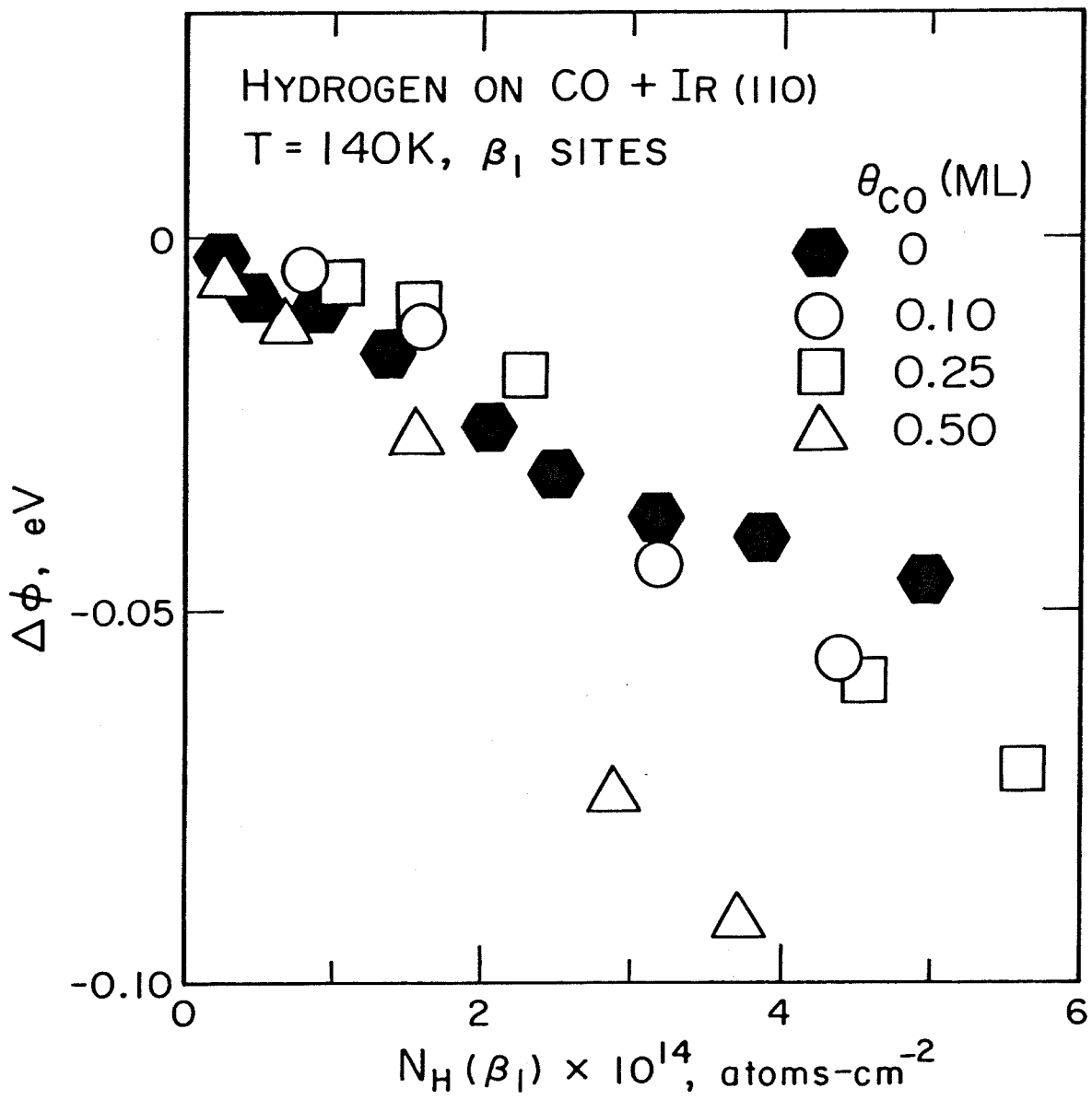


Figure 7

CHAPTER 4
THE CHEMISORPTION OF N₂ ON THE (110)
SURFACE OF IRIDIUM

(The text of Chapter 4 consists of an article coauthored with T. S. Wittrig and W. H. Weinberg that has been submitted to Surface Science.)

Abstract

The molecular chemisorption of N_2 on the reconstructed Ir(110)-(1x2) surface has been studied with thermal desorption mass spectrometry, XPS, UPS, AES, LEED and the co-adsorption of N_2 with hydrogen. Photoelectron spectroscopy shows molecular levels of N_2 at 8.0 ($5\sigma + 1\pi$) and 11.8 (4σ) eV in the valence band and at 399.2 eV with a satellite at 404.2 eV in the N(1s) region, where the binding energies are referenced to the Ir Fermi level. The kinetics of adsorption and desorption show that both precursor kinetics and interadsorbate interactions are important for this chemisorption system. Adsorption occurs with a constant probability of adsorption of unity up to saturation coverage ($4.8 \times 10^{14} \text{ cm}^{-2}$), and the thermal desorption spectra give rise to two peaks. The activation energy for desorption varies between 8.5 and 6.0 kcal-mole⁻¹ at low and high coverages, respectively. Results of the co-adsorption of N_2 and hydrogen indicate that adsorbed N_2 resides in the missing-row troughs on the reconstructed surface. Nitrogen is displaced by hydrogen, and the most tightly bound state of hydrogen blocks virtually all N_2 adsorption. A p1g1(2x2) LEED pattern is associated with a saturated overlayer of adsorbed N_2 on Ir(110)-(1x2).

1. Introduction

The chemisorption of molecular nitrogen [$N_2(ad)$] has been studied on Ir(110)-(1x2) at low temperatures with thermal desorption mass spectrometry (TDS), LEED, AES, XPS and UPS measurements. Also, the co-adsorption of hydrogen and molecular N_2 was investigated to clarify the type of sites occupied by N_2 and to observe the influence of hydrogen on the chemisorption properties of the molecularly adsorbed N_2 overlayer.

For all transition metals that have been studied previously, molecular adsorption of N_2 has been observed only at temperatures below 200 K. Molecular adsorption of N_2 occurs on Ni (1 - 4), Pd (3), Ru (5), Pt (6,7), Ir (8,9), Fe (10 - 12), and W (13,14), usually with a high probability of adsorption. Desorption of N_2 occurs between 130 and 200 K, exhibiting either one or two features in the thermal desorption spectrum, with activation energies ranging between 4 and 11 kcal-mole⁻¹. However, Fe (11,12) does not chemisorb molecular N_2 at surface temperatures above 140 K, but does below this temperature (10).

The X-ray photoelectron spectra reported for $N_2(ad)$ show two to three features in the N(1s) region. On Ni films (1,2), Fe films (10,11) and W(110) (13), the binding energies reported are (400.6, 405.7), (400.3, 405.3) and (399.1, 400.4, 405.5) eV, respectively. The transitions near 400 eV are normal values for a nitrogen containing molecular species, in this case N_2 . However, the transitions between 405 and 406 eV are too far removed (5 eV) to be attributed to another molecular species. Therefore, this transition is most likely a satellite due to an incomplete screening of the core hole, which is a consequence of

the relatively weak N_2 -metal bond (13). An earlier explanation of results obtained for $N_2(\text{ad})$ on $Fe(111)$ at 80 K was that the two widely separated features represented N_2 bonding perpendicular and parallel to the surface. Recent electron energy loss (EELS) experiments of $N_2(\text{ad})$ on $W(100)$ (14) showed that N_2 bonds through one nitrogen atom in analogy to CO. Hence, this is probably the case also on Fe.

Although the chemisorption bond of $N_2(\text{ad})$ is much weaker than CO on the transition metals, they are isoelectronic and should give somewhat similar UP spectra. On polycrystalline Ni (1), $N_2(\text{ad})$ yields levels at 8.0 and 11.8 eV below the Fermi level, E_F , by HeI UPS. Similarly, on $W(110)$ (13) levels are observed at 7.0 and 11.7 eV below E_F . The 5σ and 1π orbitals are assigned to the higher lying level and the 4σ orbital is assigned to the lower lying level on the respective surfaces, as for adsorbed CO. However, recent calculations, comparing CO and N_2 bonding to a Ni atom and UP spectra of CO and N_2 on $Ni(100)$, have concluded that the 4σ and 5σ orbitals of CO and N_2 behave differently (15,16), due to the greater degree of bonding interaction of the 4σ orbital in N_2 compared to CO. It was shown that the absolute separation between the 4σ and 5σ orbitals *increases* when N_2 is chemisorbed compared to free N_2 due to final state effects, opposite to the change in separation for CO (16). Alignment of ionization potentials for free N_2 and valence band emissions for adsorbed N_2 therefore should be with the nonbonding 1π orbital (15).

Finally, only two investigations have examined the influence of hydrogen adsorption on an $N_2(\text{ad})$ overlayer under UHV conditions. Hydrogen displaces $N_2(\text{ad})$ from a polycrystalline Fe surface (10). Also, adsorbed hydrogen on

W(100) tends to displace $N_2(ad)$ from a bridging site to an on-top site as shown by EELS results (14).

These previous results will provide a comparison for the present study of N_2 adsorbed molecularly on the reconstructed Ir(110) surface. In addition, LEED will be used to investigate the stability of the clean surface reconstruction to N_2 adsorption and to observe if $N_2(ad)$ forms an ordered superstructure. No ordered superstructures due to $N_2(ad)$ have been reported previously on the transition metals.

2. Experimental Methods

The experiments were conducted in an ion pumped stainless steel belljar that has been described previously (17,18). The base pressure for these experiments was below 2×10^{-10} torr of reactive contaminants. The Ir(110) crystal is the same as that used for the study of hydrogen chemisorption in this apparatus (17), and it shows the (1x2) reconstruction when clean, which is a surface with every other row of Ir atoms missing in the [001] direction. Since this previous work (17), the conduction path between the liquid nitrogen cooling reservoir and the crystal has been improved so that the lowest temperature routinely achieved is now 95 K compared to 130 K. The lower base temperature proved to be important for the study of nitrogen adsorbed molecularly on Ir(110)-(1x2).

3. XPS, UPS and AES of Adsorbed Nitrogen

This section presents results from electron spectroscopy measurements performed for low temperature adsorption of N_2 on Ir(110). The XPS, UPS and AES transitions observed when N_2 is exposed to the Ir(110) surface at 95 K are consistent with molecular adsorption, as seen by previous studies on other transition metals at low temperature.

Figure 1 shows XPS results for N_2 adsorbed on Ir(110) as a function of fractional coverage of N_2 . The coverages were measured from the relative areas under the N(1s) features in Fig. 1 and from thermal desorption spectra presented in the next section. Two transitions appear in the N(1s) region at binding energies of 399.2 and 404.2 eV. The ratio of the intensities of the two binding energies is equal to 1.37 at all coverages. The spectra shown here are similar to those measured for N_2 adsorption on polycrystalline Ni (1,2) and Fe (10,11) and W(110) (13) which has been attributed to molecular N_2 . The transition at 399.2 eV is reasonable for $N_2(ad)$, and the transition at 404.2 eV represents a satellite. The relatively high intensity of this satellite is due to the weak chemisorption bond, NN-Ir, which can cause incomplete screening of the core-hole as described previously for the case of N_2 on W(110) (13).

The HeI UPS presented in Fig. 2 verifies the molecular nature of N_2 adsorption on Ir(110) at low temperature. Spectra are shown in Fig. 2 for a surface saturated with N_2 (1.25 L) and a clean surface, and the corresponding difference spectrum. Two levels and a slight decrease in the d-band intensity near E_F are apparent in the difference spectrum. The level at 8.0 eV below E_F

may be assigned to a combination of the 5σ and 1π orbitals of $N_2(\text{ad})$ where the 5σ orbital has shifted toward the 1π level due to its (bonding) interaction with the surface. The 4σ orbital of $N_2(\text{ad})$ is less certain in its energy due to interference from secondary electrons at low kinetic energy, but it may be assigned at approximately $11.8 \pm .3$ eV below E_F . These levels are similar to those reported for molecular N_2 on polycrystalline Ni (1), Ni(100) (15) and W(110) (13), and orbital assignments are in analogy to CO.

The final electron spectrum of $N_2(\text{ad})$ on Ir(110) is the AE spectrum shown in Fig. 3. The Ir transitions at 355 and 380 eV in the clean surface spectrum have been subtracted. The features observed due to $N_2(\text{ad})$ are peaks at 362.0, 381.7 and 389.3 eV as well as a shoulder at 375.5 eV. The XAES result for N_2 on W(110) (13) is quite similar to Fig. 3, but both are different from the gas phase (19).

In Fig. 3, the labels A-J show calculated Auger transitions from a correlation of core and valence levels that have been presented above. The correlation (20) can be summarized by the following equation

$$E(kjl) = E(k) - E(j) - E(l) - (F_{jl} - R_{jl}), \quad (1)$$

where $E(kjl)$ is the normal Auger transition, $E(k)$ is the binding energy of state k , F_{jl} is the hole-hole repulsion energy in the final state, and R_{jl} is the excess relaxation energy in the final state. Here, $(F_{jl} - R_{jl})$ will be assumed to be zero when involving the N(1s) level at 399.2 eV. As indicated shortly, this term will be taken as -1.1 eV for transitions involving the N(1s) satellite at 404.2 eV. The binding energies used here are the N(1s), 5σ and 1π , 4σ , and 3σ levels for

$N_2(ad)$ on Ir(110). With the exception of the 3σ orbital, the other binding energies are measured directly as presented above. The binding energy of the 3σ orbital was estimated from gas phase data (19) as 30.5 eV with respect to E_F . Table 1 summarizes the calculated transitions that are shown as letters in Fig. 3. Good agreement between observed and calculated Auger transitions is achieved only if participation of the N(1s) satellite is included. Moreover, a value of -1.1 eV for the (F-R) contribution involving the N(1s) satellite aligns the calculated transitions D and F with the observed transitions at 389.3 and 381.7 eV in Fig. 3.

To summarize, XPS and UPS measurements indicate that adsorbed N_2 is molecular, and the spectra are similar to those reported for adsorption on other transition metals. Also, AES measurements of $N_2(ad)$ and calculated Auger transitions, derived from the difference in core level and valence level binding energies, agree quite well so long as the satellite level found in XPS is included.

4. Desorption and Adsorption Kinetics

When N_2 is exposed to Ir(110)-(1x2) at 95 K and then the surface is heated, N_2 is observed to desorb above 120 K, as shown in Fig. 4. Mass 14 was monitored to eliminate any interference due to CO in the measurement. No N_2 desorption occurs above 250 K where dissociatively chemisorbed nitrogen atoms would combine and desorb (21). The temperature range in which N_2 desorbs is further evidence of molecular adsorption. As the coverage of N_2 increases, the first peak that appears broadens and shifts to lower

temperatures. Near 0.8 L of N_2 , a second feature appears at lower temperature. It too shifts and broadens up to the saturation exposure, which is between 1.25 and 1.50 L. The fact that two peaks appear in the TD spectra may indicate two different sites are occupied on the Ir(110) surface. However, as will be seen later, the saturation coverage, adsorption kinetics, substrate structure and an overlayer LEED superstructure point to one site at saturation and to a compression of the adsorbed layer occurring as the coverage nears saturation. Therefore, the desorption characteristics seen in Fig. 4 indicate that precursor kinetics (see below) as well as intermolecular repulsive interactions influence desorption strongly for $N_2(ad)$ on Ir(110).

The adsorption kinetics of N_2 on Ir(110) were calculated from the areas under the TD spectra in Fig. 4, and the results are presented in Fig. 5. As seen in Fig. 5, the coverage of N_2 as a function of exposure is fit very well by a zero-order dependence of the probability of adsorption on coverage up to saturation, which corresponds to an exposure between 1.25 and 1.50 L N_2 . If one assumes an initial probability of adsorption, S_0 , of unity, the saturation coverage is equal to 4.8×10^{14} molecules-cm⁻². Moreover, a $p1g1(2 \times 2)$ LEED structure of adsorbed N_2 is observed at saturation (see Section 6), and this is consistent with the above coverage calculation.

Zero-order adsorption kinetics for N_2 on Ir(110) indicate the participation of a precursor state in the adsorption reaction. From microscopic reversibility, the same type of precursor should be involved also in desorption. Broadening and shifts of a thermal desorption peak with increasing coverage are predicted if a precursor is involved in desorption (22,23), which would explain

partially the desorption behavior of N_2 seen in Fig. 4. However, precursor kinetics alone cannot explain multiple peaks in the thermal desorption spectra. An additional complication (with the assumption of one type of site for adsorption) is embodied in the spectra if interadsorbate interactions become important at high coverage. An adsorbate-adsorbate interaction model, including repulsive interactions, predicts a shift in temperature with increasing coverage and multiple peaks (24). Since the adsorption kinetics strongly suggest that a precursor is involved and two peaks appear in the thermal desorption spectra, neither type of desorption model *alone* can explain the experimental data in a qualitative way. Multiple-site participation is not a valid argument from the LEED results presented in Section 6. Therefore, a combination of the precursor model and the interaction model for the N_2 -Ir(110) system is necessary to explain the adsorption and desorption kinetics.

To examine the desorption kinetics more closely, the rate parameters for desorption are needed: the activation energy, E_d , and the preexponential, ν_d , of the desorption rate coefficient. Since N_2 adsorption is molecular, the starting point for a desorption model is a first-order expression,

$$R_d = \nu(\theta) \theta \exp[-E_d(\theta)/kT], \quad (2)$$

where the terms in Eq. (2) have their usual significance. An analysis of precursor kinetics (22) indicates that a coverage dependence embodied in the preexponential factor would result from the presence of the precursor, even in the absence of additional interactions. If the activation energy for desorption can be measured as a function of coverage, independent of ν_d , then any variation of

E_d with coverage would be due to interactions between adsorbates.

An integral method of analysis by varying the heating rate (25) was used to measure E_d and ν_d at points of constant coverage. The method involves changing the heating rate over a wide range for each coverage. The slope of an Arrhenius plot, for a given coverage, is then proportional to E_d , and the intercept is proportional to $\ln \nu_d$. In these experiments, heating rates were varied from 5 to 120 K-s⁻¹, and the initial coverage was kept constant at 0.80 ML. Complicating factors of importance were desorption from the sample holder and changes in the pumping speed of the system with time. Consequently, the usable coverage range that could be analyzed in this way was between 0.05 and 0.60 ML. It was found that ν_d varied randomly in the Arrhenius plots, from 10⁸ to 10¹¹ s⁻¹ for coverages below 0.30 ML. Also, at low coverages, the calculated E_d was uncertain due to varying amounts of desorption from the sample holder. Therefore, it was deemed necessary to average the values of ν_d and then calculate the corresponding E_d from the desorption curves. Above 0.60 ML, ν_d was assumed to be constant near the average value $\bar{\nu}_d = 2 \times 10^9$ s⁻¹. With these uncertainties, the results for $E_d(\theta)$ shown in Fig. 6 are only semi-quantitative. At low coverage, E_d is 8.5 kcal-mole⁻¹, nearly that which is observed on Ni(110) (4) and Ru(10 $\bar{1}$ 0) (5), but lower than the estimated activation energy of desorption from the (110) orientation of an Ir FEM tip (8). However, N₂ was found to desorb in the same temperature range for the FEM tip (8) and in the present case, and thus the differences in the values of E_d are due solely to different choices of ν_d . In Fig. 6, a small linear decrease in E_d is observed below 0.75 ML and a larger linear decrease in E_d is observed for

$\theta > 0.75$ ML of N_2 . The uncertainties in the values of $E_d(\theta)$ and ν_d preclude a further analysis of the desorption kinetics beyond the qualitative arguments concerning the inclusion of both precursor and interadsorbate interaction contributions.

5. Co-adsorption of Nitrogen and Hydrogen

The co-adsorption of hydrogen and N_2 was examined in order to gain more insight concerning the type of site on the surface into which N_2 chemisorbs and what influence chemisorbed hydrogen has on pre- and post-adsorbed N_2 . Much is known concerning the interaction of hydrogen with Ir(110) (17), and this lends another approach to understanding the chemisorption of N_2 .

HeI difference spectra for three surface conditions of co-adsorbed hydrogen and N_2 are presented in Fig. 7 where the clean surface spectrum in Fig. 2 has been subtracted from each of the original spectra. For spectra (a) and (b) in Fig. 7, the initial fractional coverages of N_2 were 0.8 and 0.4, respectively. Both surfaces were exposed to sufficient hydrogen to obtain a coverage of hydrogen $\theta_H = 0.25$, where $\theta_H = 1$ corresponds to a saturation of the surface by hydrogen. It is apparent from (a) and (b) in Fig. 7 that $N_2(ad)$ maintains its molecular character, which was seen in Fig. 2. The difference between the spectra in Fig. 7 and Fig. 2 lies in the shape of the curves near the Fermi level. Spectra (a) and (b) in Fig. 7 show evidence of adsorbed hydrogen (17), although the H(1s) level cannot be detected at 6.1 eV below E_F .

Spectrum (c) in Fig. 7 shows the result of a 5 L N_2 exposure to a surface

with an initial precoverage of hydrogen of 0.33 ML. No observable evidence for N_2 adsorption is seen, but now the H(1s) level at -6.1 eV is clear. For $\Theta_H = 0.33$ on the clean Ir(110)-(1x2) surface, the high temperature β_2 -state is filled completely (17). The sites associated with β_2 -hydrogen are in the locations of the missing rows of Ir atoms for this reconstructed surface (17). This implies that N_2 prefers these sites as well, as discussed in Section 6.

A series of thermal desorption spectra measured for co-adsorbed overlayers of hydrogen and N_2 are shown in Figs. 8(A) H_2 and 8(B) (N_2). The labels in Fig. 8(B) correspond to those in Fig. 8(A), and in the latter figure () denotes the first exposure in the sequence for each overlayer. Considering the desorption of N_2 shown in Fig. 8(B), spectra (a) and (b) show the effect of two different exposures of H_2 to a saturated overlayer of N_2 . As the H_2 exposure increases from 5 to 10 L, the high temperature peak of N_2 decreases in intensity, and the low temperature peak increases in intensity. Moreover, the coverage of N_2 decreases to 0.77 ML in spectrum (a) and to 0.71 ML in spectrum (b). Hydrogen, on the other hand, increases in coverage in the same experiment as may be seen in spectra (a) and (b) in Fig. 8(A). As a comparison, spectrum (g) in Fig. 8(B) was reproduced from Fig. 4 for a 1.0 L N_2 exposure to the clean surface. Also, compare in Fig. 8(B) desorption spectra (c) and (g). In spectrum (c), 5 L H_2 was exposed to a surface preexposed to 1.0 L N_2 with the resulting loss of approximately 0.1 ML N_2 and the shift of some of the remaining N_2 to the low temperature peak. Although none of the $N_2(ad)$ was lost in spectrum (d) of Fig. 8(B) compared to spectrum (e) of Fig. 4, the same shift in desorption temperature is seen. For spectrum (e), the β_2 -state of hydrogen was filled (17),

and this caused almost no N_2 to adsorb, even after an exposure of 5 L N_2 . The small amount of N_2 desorption in (e) reflects mainly contributions from the sample holder.

With regard to the H_2 desorption shown in Fig. 8(A), the amount of H_2 increases as the precoverage of $N_2(ad)$ decreases for a given H_2 exposure, but appears to be always less than the coverage of β_2 -hydrogen at saturation on the clean surface. The rate of adsorption of hydrogen is lowered if N_2 is present on the surface, indicating at least a partial blockage by N_2 of adsites of hydrogen occurs. Another interesting aspect of the H_2 desorption spectra is that a small amount of H_2 desorbs at the same temperature of that of N_2 and has the same relative shape as that of N_2 . However, this was not investigated further considering the low intensities (coverages) involved.

The findings of the co-adsorption of N_2 and hydrogen may now be summarized. The β_2 -state of hydrogen, which bonds in the missing row troughs on the reconstructed Ir(110)-(1x2) surface, competes directly with $N_2(ad)$ for chemisorption sites. Moreover, hydrogen, in part, occupies these preferred sites when chemisorbed on a surface preexposed to N_2 and displaces a part of the N_2 from the surface. When the β_2 -state of hydrogen is filled on Ir(110), N_2 does not chemisorb appreciably. From HeI UPS, the $N_2(ad)$ molecular orbitals are not perturbed detectibly when N_2 is co-adsorbed with hydrogen. Therefore, the interaction of hydrogen and N_2 , when present together on the surface at low temperature, is largely a site competition and a compression of $N_2(ad)$ away from its preferred sites by hydrogen.

6. LEED Observations

The chemisorption of N_2 on Ir(110)-(1x2) was investigated at low temperature with LEED. As background information, an fcc (110)-(1x1) is a surface consisting of a series of rows and troughs. However, Ir(110) reconstructs from the bulk structure to form a surface with every other row of Ir atoms missing in the [001] direction (26). Moreover, the reconstruction is stable to the adsorption of hydrogen (17), CO (18), NO (21), with to oxygen (27) (< 700 K), water (28) and sulfur (29).

For exposures of N_2 below 0.6 L, the LEED pattern maintains a bright (1x2) structure of the reconstructed surface with little increase in the background intensity. Between 0.6 and 1.0 L N_2 , streaks appear between the rows of half-order substrate spots. For exposures of N_2 greater than 1.0 L up to saturation (≈ 1.5 L), the streaks begin to coalesce into spots and the background intensity increases uniformly. However, the pattern did not yield sharp spots, even at a temperature of 95 K or by maintaining a background pressure of N_2 . Careful annealing and cooling cycles failed to improve the order as well. The pattern observed is brightest at saturation coverage and is shown in Fig. 9(A). The photograph was taken at a beam energy of 137 eV and represents a "streaky" (2x2) pattern with extinguished beams at $(n+\frac{1}{2}, 0)$ on the (1x2) substrate.

The fact that the (1x2) substrate beams remain sharp and bright throughout the exposure sequence indicates the Ir(110) surface does not relax from its reconstructed state. The (2x2) pattern with missing beams then implies that a glide plane of symmetry is present on the surface. Consistent

with the saturation coverage of $4.8 \times 10^{14} \text{ cm}^{-2}$ (one N_2 molecule per reconstructed unit cell) and the fact that β_2 -hydrogen directly blocks N_2 adsorption, the overlayer structure is a $\text{p}1\text{g}1(2 \times 2)$ where the real space representation is shown in Fig. 9(B). The glide plane is parallel to the missing-row troughs, and the (2×2) unit cell is drawn in the figure. This superstructure for $\text{N}_2(\text{ad})$ at saturation coverage is identical to a possible structure found for sulfur adsorbed on the $\text{Ir}(110)-(1 \times 2)$ surface (29). Mobility of $\text{N}_2(\text{ad})$ might be expected even at 95 K due to the weak chemisorption bond, and this would cause disorder along the rows in the x-direction drawn in Fig. 9(B).

7. Summary

The results for the adsorption of N_2 on the $\text{Ir}(110)-(1 \times 2)$ surface may be summarized as follows:

1. XPS and UPS results show N_2 chemisorbs molecularly at low temperature. Two features appear for the $\text{N}(1s)$ binding energy at 399.2 and 404.2 eV, the former indicating a molecular species and the latter indicating a satellite. The degenerate 5σ and 1π , and the 4σ orbitals are seen at binding energies of 8.0 and (11.8 ± 0.3) eV.
2. The Auger electron spectrum of $\text{N}_2(\text{ad})$ on $\text{Ir}(110)$ shows transitions similar to that seen on $\text{W}(110)$ (13).

The peaks can be assigned to normal Auger transitions by a simple calculation (20). However, the $\text{N}(1s)$ satellite must be included in the calculation to account for all the Auger

features that are observed.

3. Thermal desorption of $N_2(ad)$ and the corresponding adsorption kinetics imply that precursor kinetics and repulsive adsorbate-adsorbate interactions are important in this chemisorption system. Adsorption occurs with an initial probability of adsorption of unity independent of coverage, and the surface coverage saturates at one molecule per reconstructed unit cell. However, thermal desorption measurements indicate that repulsive interactions become important at high coverages, as seen by the appearance of a second thermal desorption peak. At low coverage, the activation energy for desorption is approximately $8.5 \text{ kcal-mole}^{-1}$ and decreases to $6.0 \text{ kcal-mole}^{-1}$ at saturation.
4. The co-adsorption of hydrogen and N_2 was studied by UPS and TDS. The presence of hydrogen does not perturb the valence orbitals of N_2 detectibly. However, hydrogen does displace $N_2(ad)$ from the surface and, at least in part, takes up its preferred sites in the missing row troughs.
5. A $p1g1(2 \times 2)$ pattern forms for $N_2(ad)$ at saturation on $Ir(110)-(1 \times 2)$. The proposed structure is consistent both with the probable locations of N_2 in the missing-row troughs and the saturation coverage. This appears to be the first LEED superstructure reported for molecularly adsorbed nitrogen on a transition metal surface.

Acknowledgment

The authors are grateful to the National Science Foundation for support of this research (Grant No. CHE77-14976). The assistance of P. Szuromi in some of the experiments is appreciated.

References

1. C. R. Brundle and A. F. Carley, *Discussions Faraday Soc.* 60, 51 (1975).
2. C. R. Brundle, *J. Vacuum Sci. Technol.* 13, 301 (1976).
3. D. A. King, *Surface Sci.* 9, 375 (1968).
4. M. Grunze, R. K. Driscoll, G. N. Burland, J. C. L. Cornish and J. Pritchard, *Surface Sci.* 89, 381 (1979).
5. R. Klein and A. Shih, *Surface Sci.* 69, 403 (1977).
6. R. A. Shigeishi and D. A. King, *Surface Sci.* 62, 379 (1977).
7. M. Wilf and P. T. Dawson, *Surface Sci.* 60, 561 (1976).
8. B. E. Nieuwenhuys, D. Th. Meijer and W. M. H. Sachtler, *Surface Sci.* 40, 125 (1973).
9. J.-M. Derochette, *Phys. Stat. Sol. (a)* 45, 163 (1978).
10. D. W. Johnson and M. W. Roberts, *Surface Sci.* 87, L255 (1979).
11. K. Kishi and M. W. Roberts, *Surface Sci.* 62, 252 (1977).
12. F. Bozso, G. Ertl, M. Grunze and M. Weiss, *J. Catalysis* 49, 18 (1977).
13. J. C. Fuggle and D. Menzel, *Surface Sci.* 79, 1 (1979).
14. W. Ho, R. F. Willis and E. W. Plummer, *Surface Sci.* 95, 171 (1980).
15. P. S. Bagus, C. R. Brundle, K. Hermann and D. Menzel, *J. Electron Spectrosc. Relat. Phenom.* 20, 253 (1980).
16. K. Hermann, P. S. Bagus, C. R. Brundle and D. Menzel, to be published.

17. D. E. Ibbotson, T. S. Wittrig and W. H. Weinberg, *J. Chem. Phys.* 72, 4885 (1980).
18. J. L. Taylor, D. E. Ibbotson and W. H. Weinberg, *J. Chem. Phys.* 69, 4298 (1978).
19. W. E. Moddeman, T. A. Carlson, M. O. Krausse, B. P. Pullen, W. E. Bull and G. K. Schweitzer, *J. Chem. Phys.* 55, 2317 (1971).
20. G. G. Tibbetts and J. M. Burkstrand, *J. Vacuum Sci. Technol.* 15, 497 (1978).
21. D. E. Ibbotson, T. S. Wittrig and W. H. Weinberg, in preparation.
22. R. Gorte and L. D. Schmidt, *Surface Sci* 76, 559 (1978).
23. D. A. King, *Surface Sci.* 64, 43 (1977).
24. D. L. Adams, *Surface Sci.* 42, 12 (1974).
25. J. L. Taylor and W. H. Weinberg, *Surface Sci.* 78, 259 (1978).
26. C. M. Chan, M. A. Van Hove, W. H. Weinberg and E. D. Williams, *Solid State Commun.* 30, 47 (1979); *Surface Sci.* 91, 400 (1980).
27. J. L. Taylor, D. E. Ibbotson and W. H. Weinberg, *Surface Sci.* 79, 349 (1979).
28. T. S. Wittrig, D. E. Ibbotson and W. H. Weinberg, *Surface Sci.*, in press.
29. E. D. Williams, C. M. Chan and W. H. Weinberg, *Surface Sci.* 81, L309 (1979).

Table 1

Calculated Auger Transitions from Eq. (1).

Orbital (B.E., eV)

$$K = N(1s) = 399.2$$

$$K' = N'(1s) = 404.2 \text{ (satellite)}$$

$$I = 1\pi, 5\sigma = 8.0$$

$$II = 4\sigma = 11.8$$

$$III = 3\sigma \sim 30.5 \text{ [estimated from Ref. (17)]}$$

<i>Figure 3</i>	<i>Designation</i>	<i>E (kjl), eV</i>
A	KI I	383.2
B	KI II	379.4
C	KII II	375.6
D	K'I I	389.3*
E	K'I II	385.5*
F	K'II II	381.7*
G	KII III	356.9
H	KI III	360.7
I	K'II III	363.0*
J	K'I III	366.8*

* All K' transitions have been shifted by +1.1 eV in kinetic energy to align D and F with observed transitions in Fig. 3 at 389.3 and 381.7 eV, respectively.

Figure Captions

- Fig. 1. XPS of N_2 molecularly adsorbed on Ir(110) at 95 K as a function of $N_2(\text{ad})$ fractional coverage.
- Fig. 2. HeI UPS of $N_2(\text{ad})$ on Ir(110) at 95 K. (a) Saturated layer of N_2 . (b) Clean surface, and (c) Difference spectrum.
- Fig. 3. Nitrogen-KLL AES for $N_2(\text{ad})$ on Ir(110) at 95 K. The letters A-J denote calculated transitions for normal Auger processes. See Eq.(1) and Table 1 for assignments.
- Fig. 4. Thermal desorption spectra of $N_2(\text{ad})$ on Ir(110) at 95 K. Mass 14 was monitored at a heating rate of 22 K-s^{-1} .
- Fig. 5. Adsorption kinetics of N_2 on Ir(110) at 95 K. These were derived from the thermal desorption spectra in Fig. 4.
- Fig. 6. Activation energy for N_2 desorption from Ir(110). See the text for details.
- Fig. 7. HeI UP difference spectra of co-adsorbed $N_2(\text{ad})$ and hydrogen on Ir(110) at 95 K. (a) 5 L H_2 on 0.80 ML $N_2(\text{ad})$, (b) 1 L H_2 on 0.40 ML $N_2(\text{ad})$, and (c) 5 L N_2 on 0.33 ML $H_2(\text{ad})$.
- Fig. 8. Thermal desorption spectra of H_2 , (A), and N_2 , (B), from several overlayers of co-adsorbed hydrogen and N_2 on Ir(110) at 100 K. The heating rate for these spectra is 20 K-s^{-1} .

Fig. 9. (A) LEED pattern at 137 eV of a saturated N_2 overlayer on Ir(110) at 95 K. The substrate maintains its (1x2) reconstruction, and the overlayer forms a p1g1(2x2) superstructure. (B) Real space representation of the p1g1(2x2) pattern. The large circles are N_2 molecules and the small circles are Ir atoms, with diameters of 3.0 (Van der Waals Diameter) and 2.72 \AA , respectively.

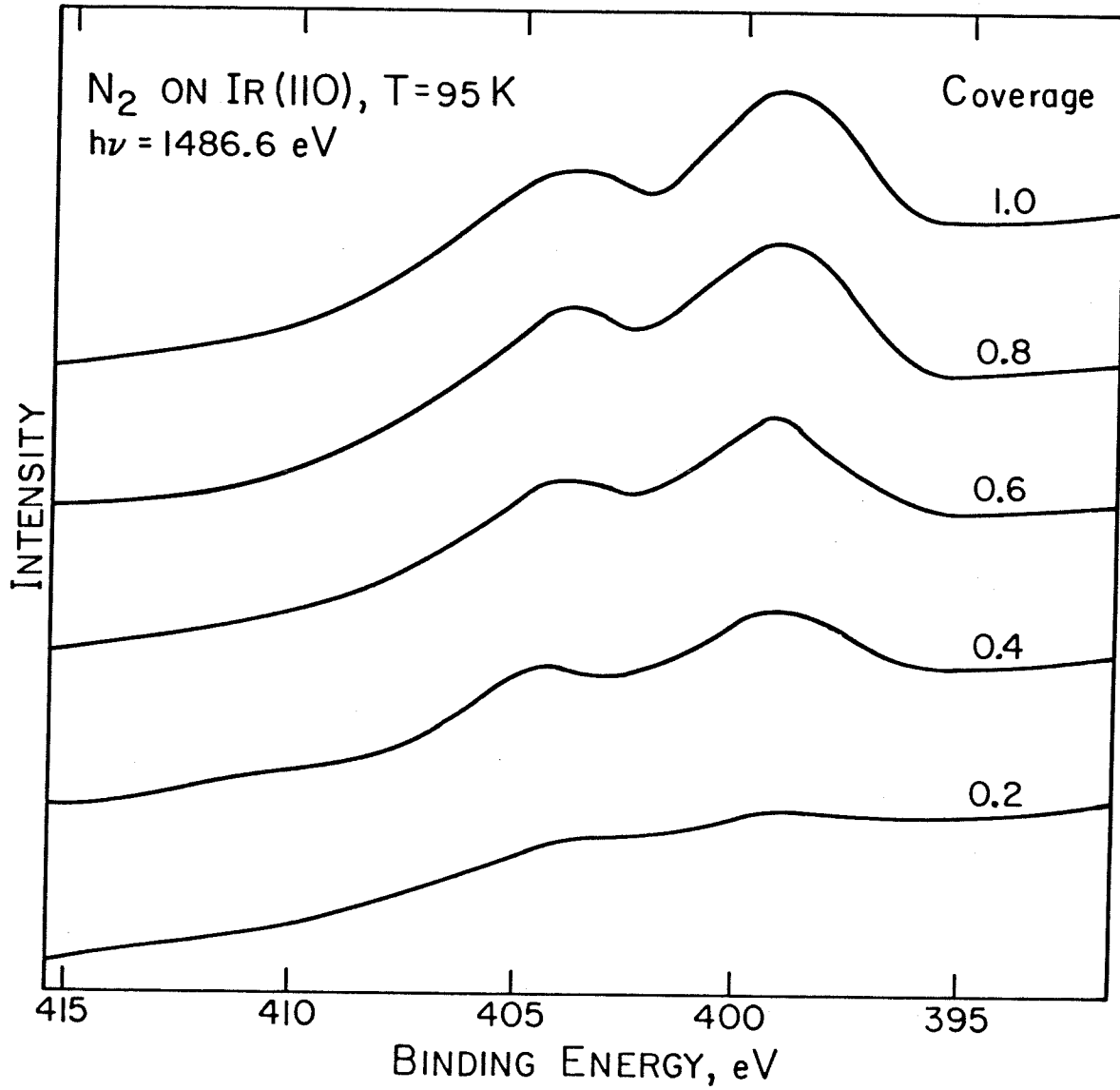


Figure 1

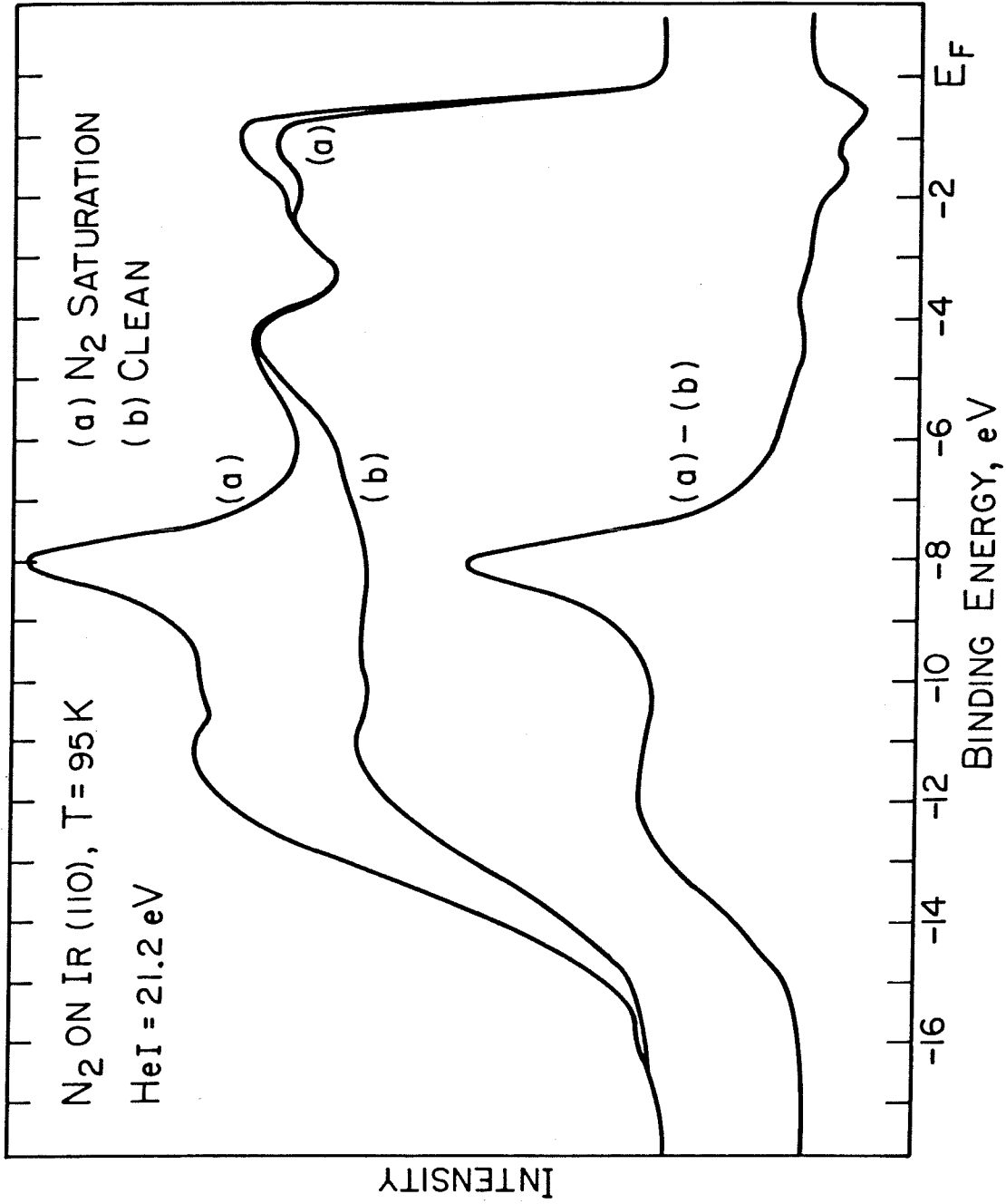


Figure 2

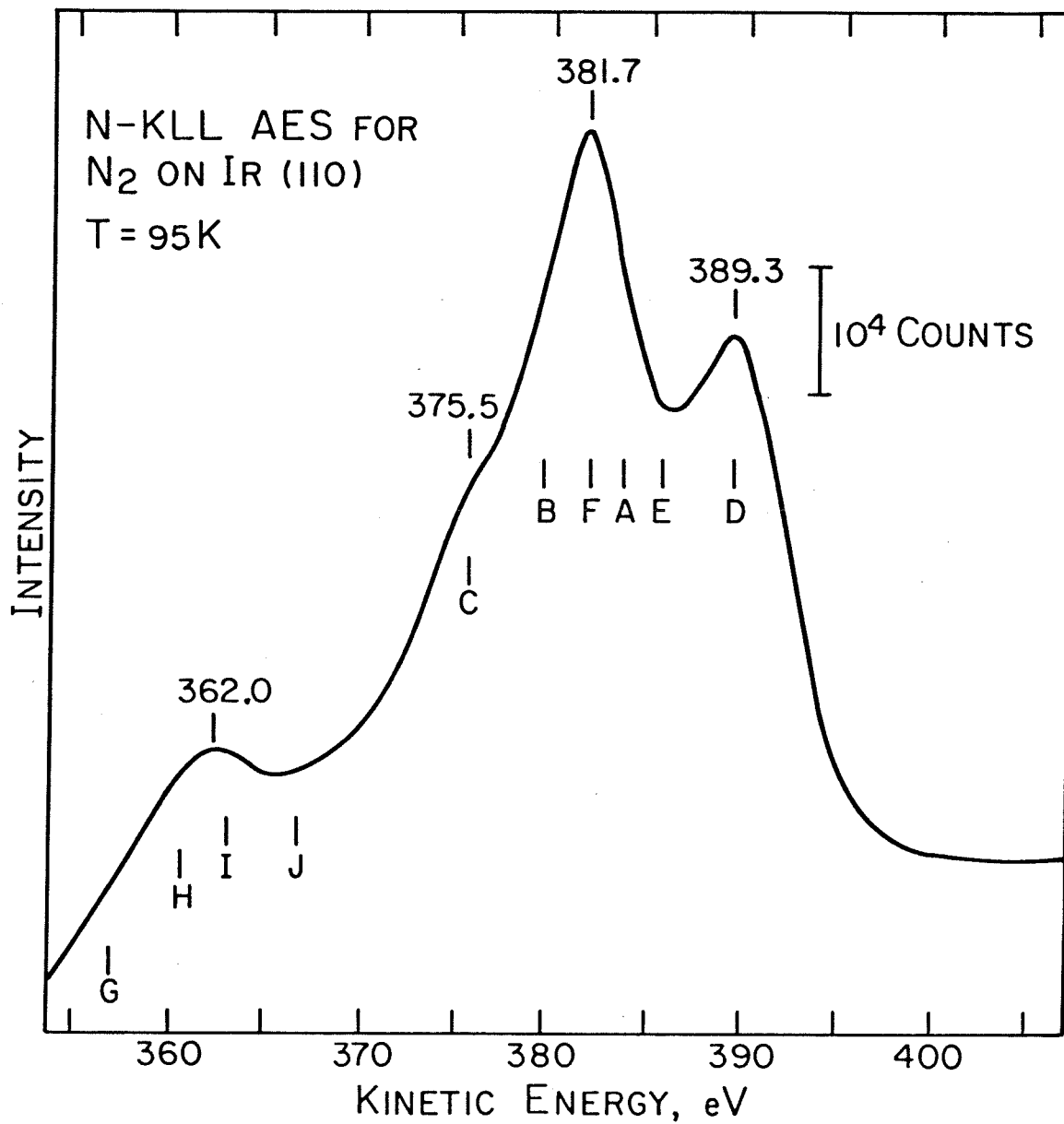


Figure 3

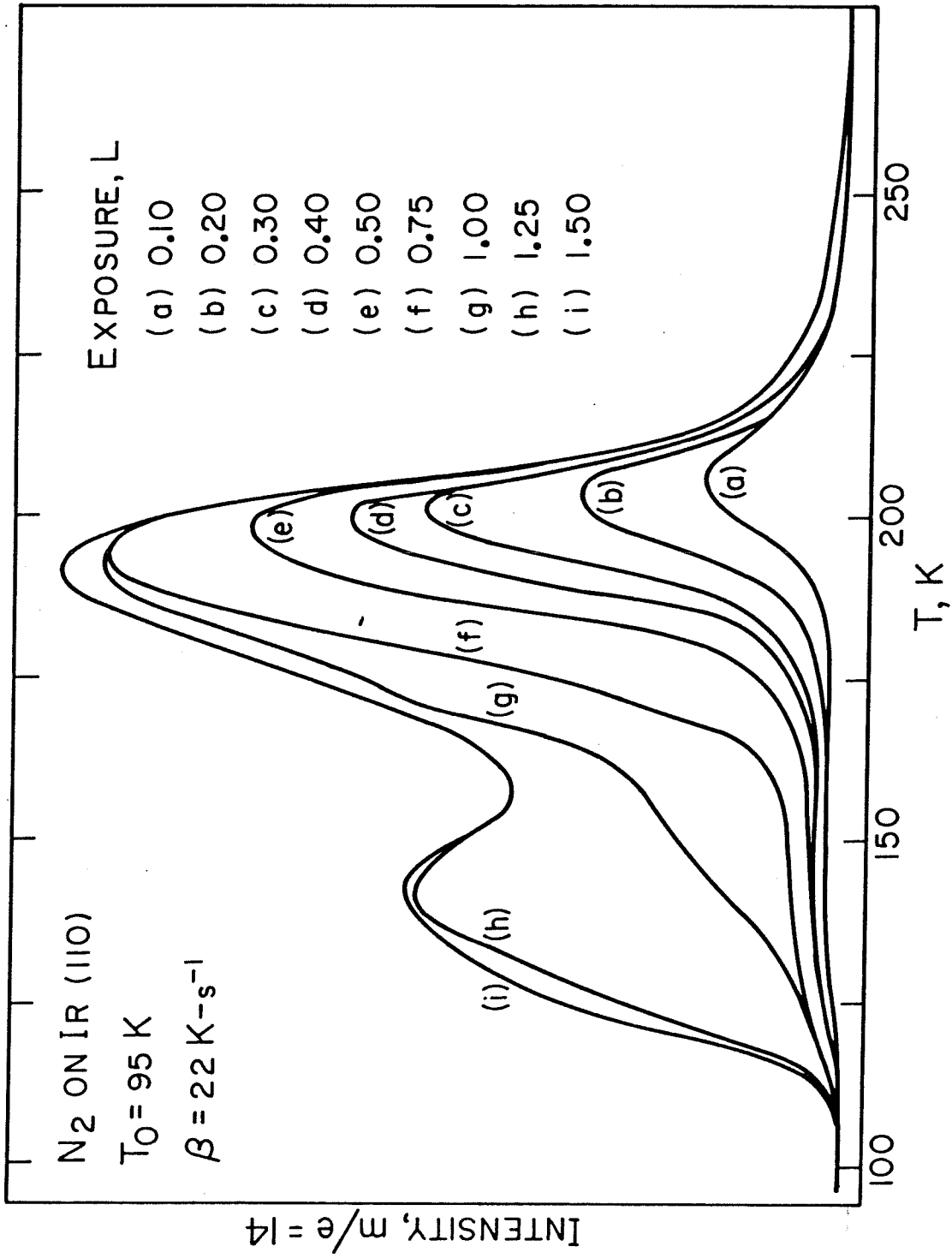


Figure 4

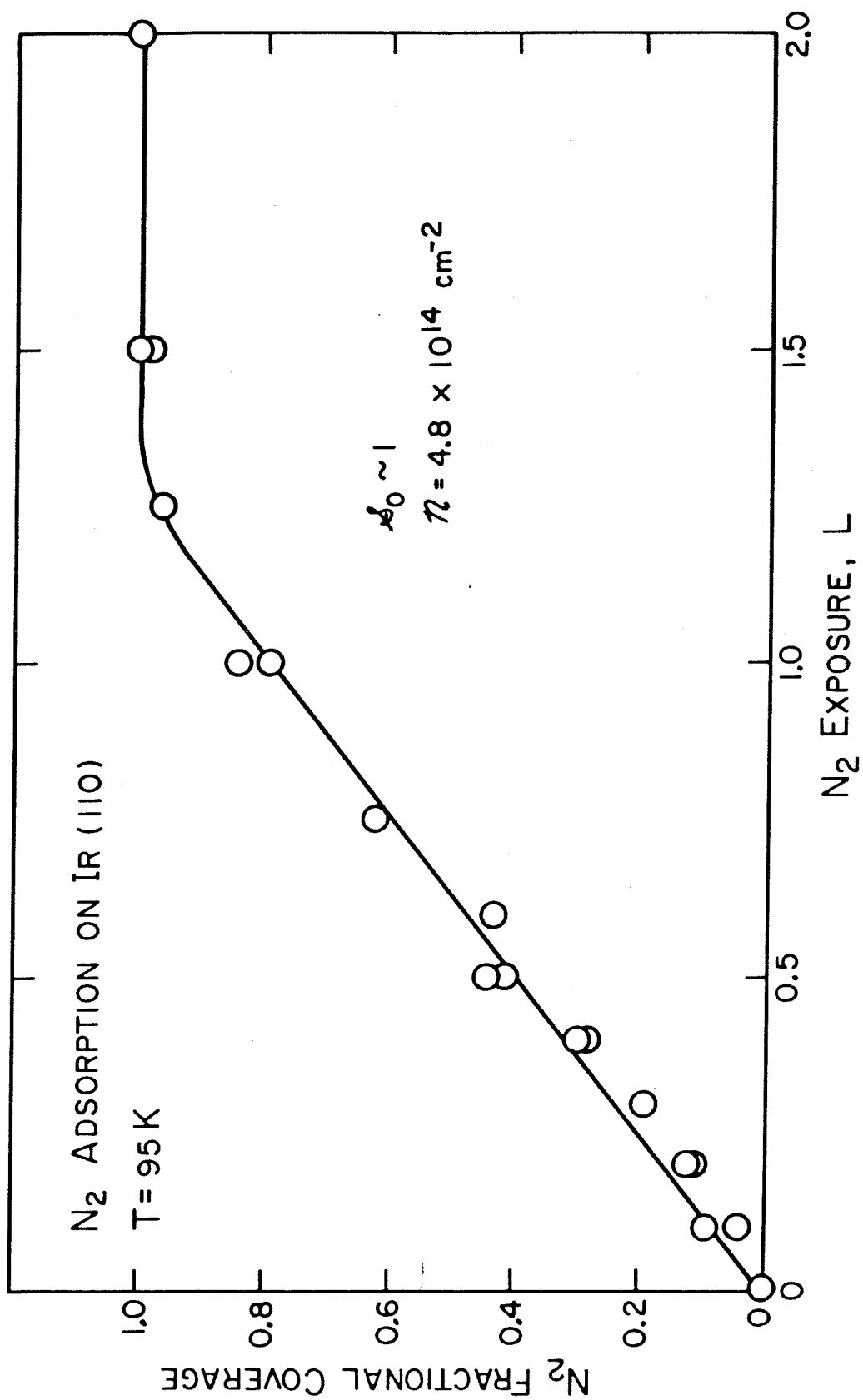


Figure 5

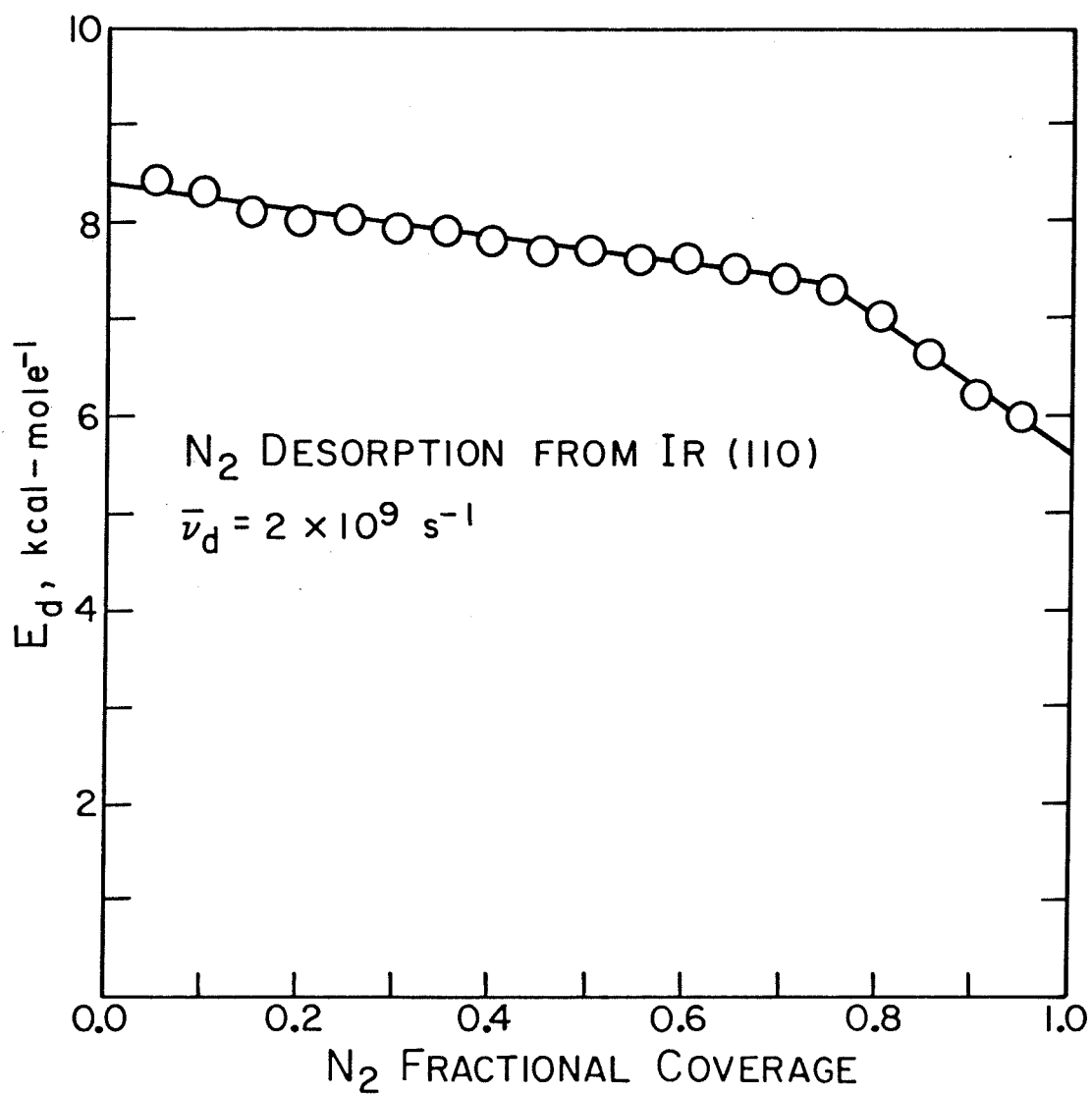


Figure 6

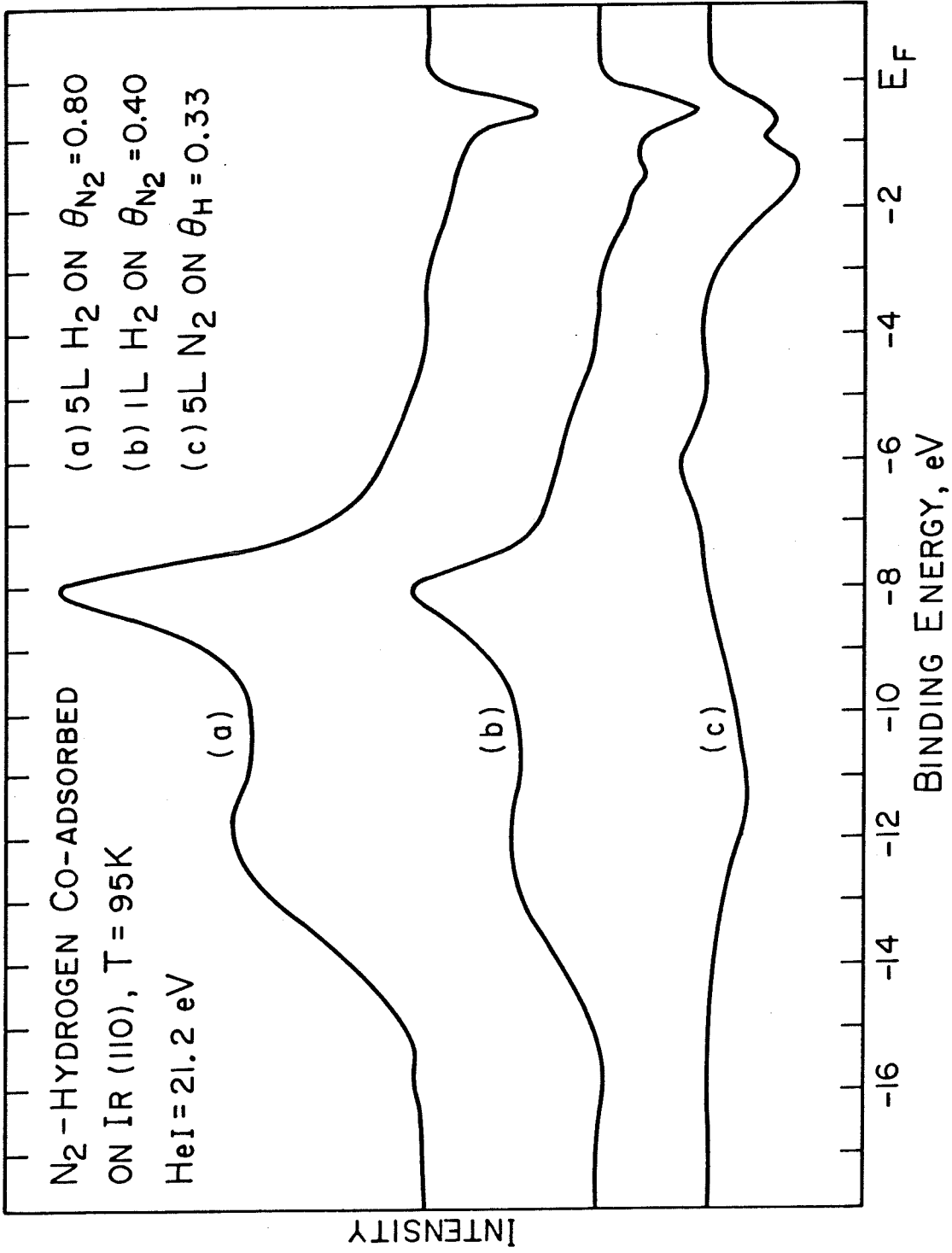


Figure 7

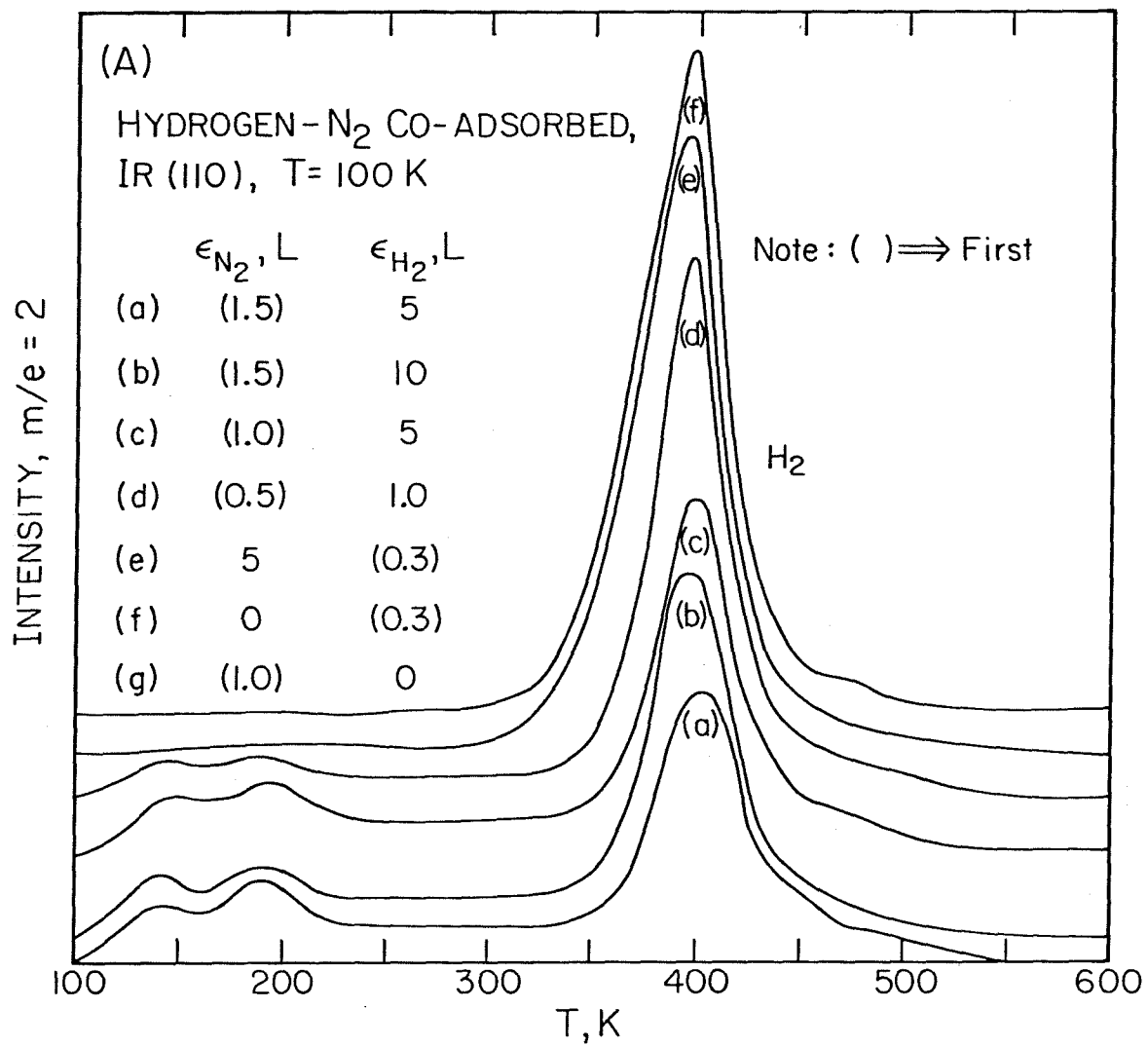


Figure 8 (a)

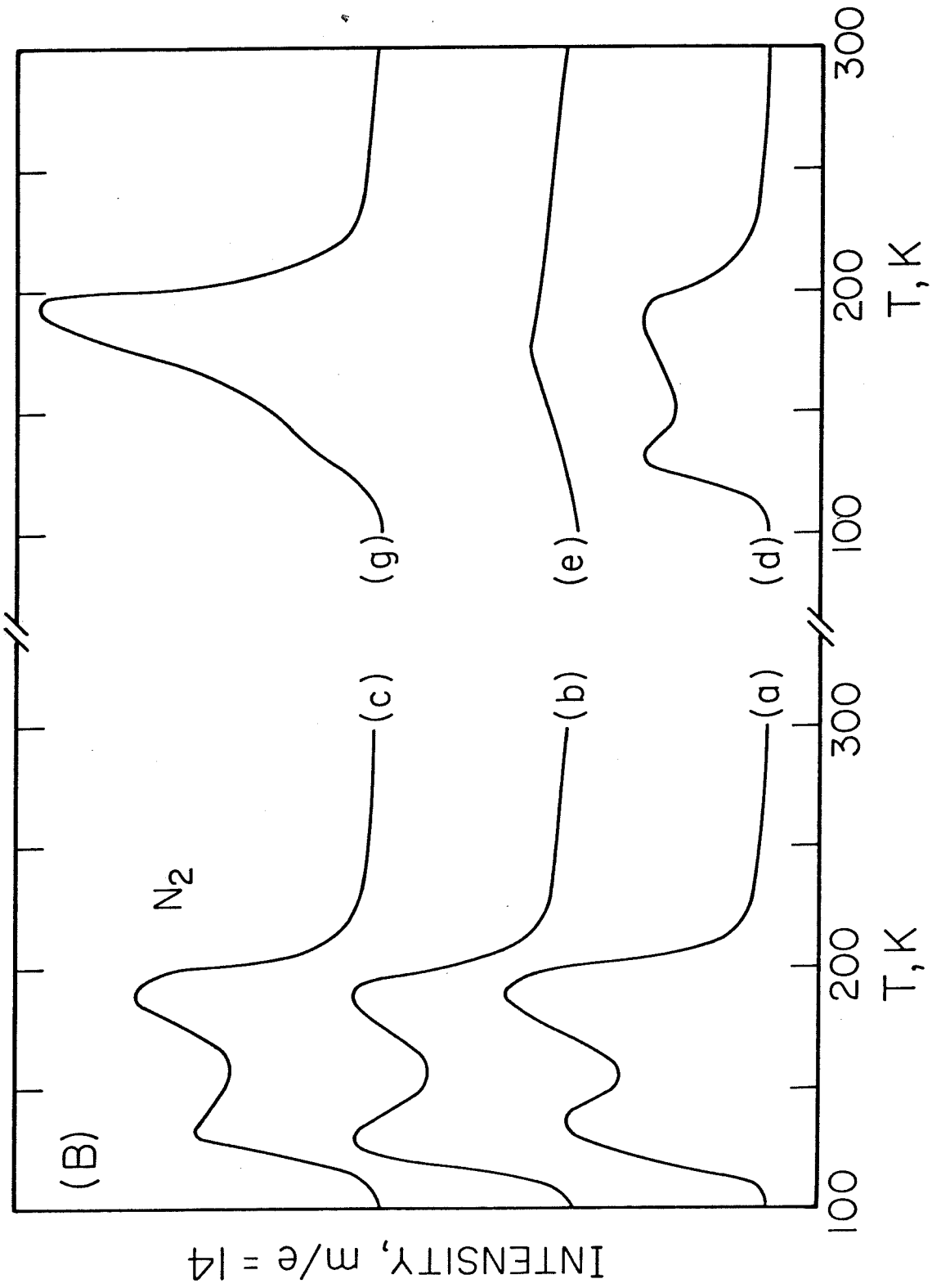
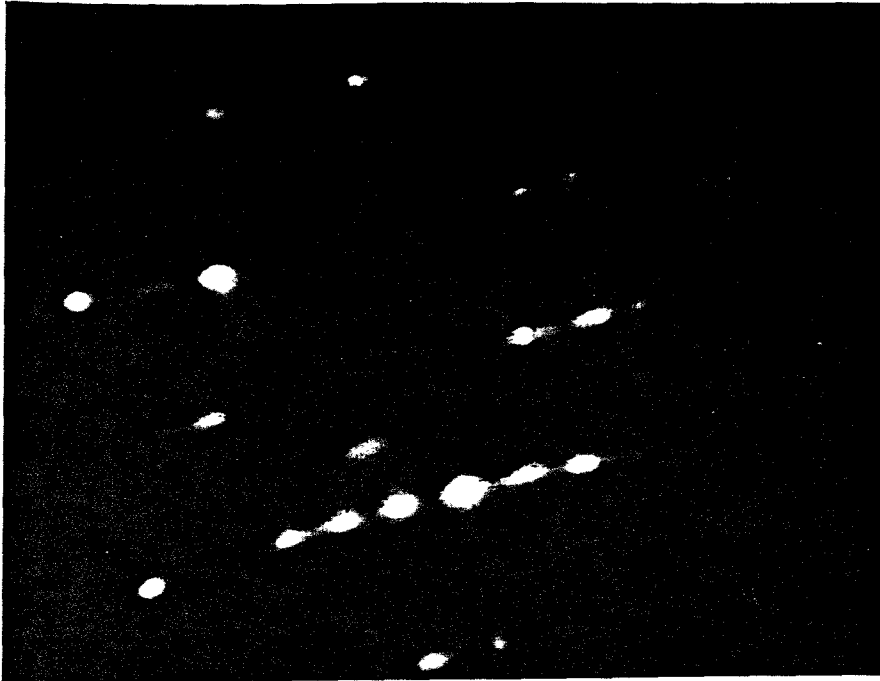


Figure 8(b)



N_2 - p1g1(2x2) ON Ir(110) - (1x2)

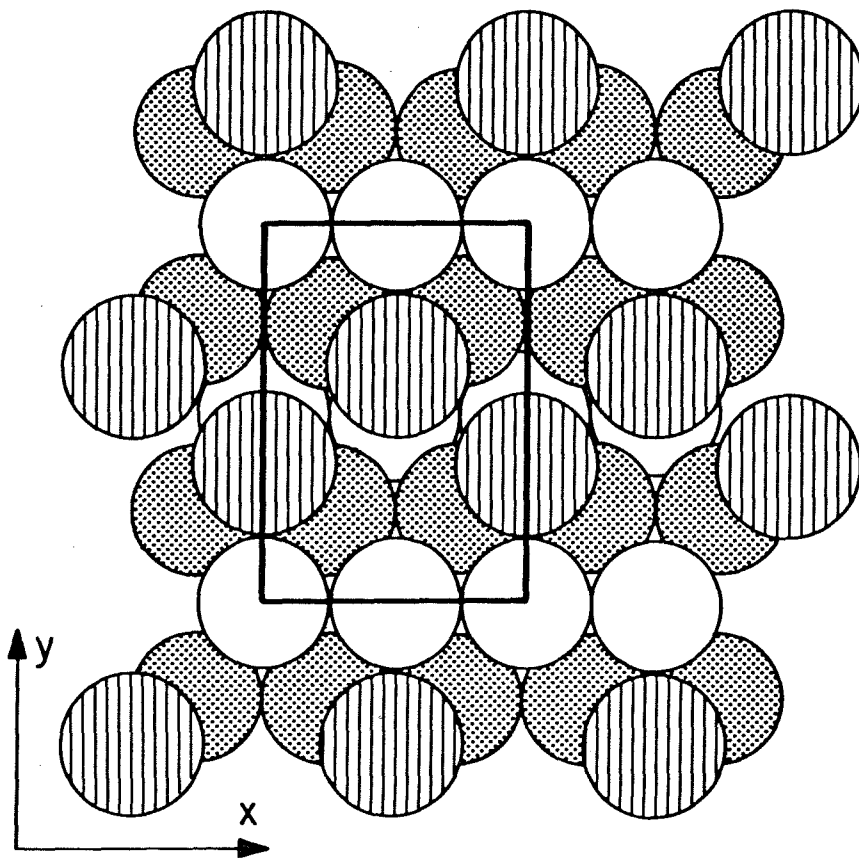


Figure 9

CHAPTER 5

THE CHEMISORPTION OF NO ON THE (110)

SURFACE OF IRIDIUM

(The text of Chapter 5 consists of an article coauthored with T. S. Wittrig and W. H. Weinberg that has been submitted to Surface Science.)

Abstract

The chemisorption of NO on Ir(110) has been studied with thermal desorption mass spectrometry (including isotopic exchange experiments), X-ray and UV-photoelectron spectroscopies, Auger electron spectroscopy, LEED and CPD measurements. Chemisorption of NO proceeds by precursor kinetics with the initial probability of adsorption equal to unity independent of surface temperature. Saturation coverage of molecular NO corresponds to $9.6 \times 10^{14} \text{ cm}^{-2}$ below 300 K. Approximately 35% of the saturated layer desorbs as NO in two well-separated features of equal integrated intensity in the thermal desorption spectra. The balance of the NO desorbs as N_2 and O_2 with desorption of N_2 beginning after the low-temperature peak of NO has desorbed almost completely. Molecular NO desorbs with activation energies of 23.4-28.9 and 32.5-40.1 kcal-mole⁻¹, assuming the preexponential factor for both processes is between 10^{13} - 10^{16} s^{-1} . At low coverages of NO, N_2 desorbs with an activation energy of 36-45 kcal-mole⁻¹, assuming the preexponential factor is between 10^{-2} and $10 \text{ cm}^2 \text{ s}^{-1}$. Levels at 13.5, 10.4 and 8.5 eV below the Fermi level are observed with HeI UPS, associated with 4σ , 5σ and 1π orbitals of NO, respectively. Core levels of NO appear at 531.5 eV [O(1s)] and 400.2 eV [N(1s)], and do not shift in the presence of oxygen. Oxygen overlayers tend to stabilize chemisorbed NO as reflected in thermal desorption spectra, a downshift in the 1π level to 9.5 eV and the CPD behavior of NO on the oxygen overlayers.

1. Introduction

The chemisorption of NO on the Ir(110)-(1x2) surface has been studied with thermal desorption mass spectrometry (TDS), X-ray and UV-photoelectron spectroscopies (XPS and UPS), Auger electron spectroscopy (AES), LEED and contact potential difference (CPD) measurements. The motivation for this investigation of NO on iridium is to gain insight into the various elementary chemical reactions that may be important in the dissociation and reduction of NO.

There have been many previous studies of NO on other transition metals, including Pd (1), Ru (2 - 5), Ni (9 - 11), Pt (8,12 - 17), Ir (18 - 21) and Rh (22). Adsorption behavior near 300 K ranges from completely dissociative for Ru, Rh and Ni and partially dissociative on Ir to molecular on Pd and Pt. Initial probabilities of adsorption tend to be greater than 0.5 and are usually close to unity. The kinetics of adsorption typically vary weakly with coverage, indicating that often a precursor species is involved.

However, with the exception of Pd (1), heating the surface causes the majority of nitrogen to desorb as N₂ rather than in NO. Near saturation coverage, NO desorbs molecularly on the transition metals. Therefore, the following reactions are generally observed with increasing surface temperature: desorption of NO, dissociation of NO, desorption of N₂ and finally desorption of O₂. The accumulation of oxygen during the first three reactions causes further complications that cannot be separated from the dissociation and desorption reactions. An additional mechanism, not mentioned above, is atom recombina-

tion $[N_{(a)} + O_{(a)} \rightarrow NO_{(g)}]$ which is thought to be important on Ir(100)-(1x1) (21). In summary, the successful separation of these competing reactions depends on their relative rates for a particular surface of a particular metal.

During adsorption, a c(4x2) LEED structure due to molecular NO is common to Pd(111) (1), Ru(100) (2,3) and Ni(111) (9). Also, a (2x2) structure is observed for NO on Pd(111) (1), Pt(111) (15,16) and Ir(111) (18). At saturation, a (2x1) forms on Ru(100) (2), and a (1x1) forms on Ni(100) (11). However, most of these superstructures are formed below room temperature due to the dissociative behavior of NO on the transition metals.

Generally, the valence region of chemisorbed NO exhibits three emission ranges which are near 2 eV, 7.3 - 10.5 eV and 13.9 - 15.2 eV relative to the Fermi level, E_F , of each metal. The first region falls in the metallic d-band, which makes the NO orbital less visible, but this is attributed to the singly-occupied 2π level of NO coupling to the metal. The second region from 7.3 to 10.5 eV contains the 1π and 5σ levels of NO. However, the separation and assignment of these levels are rather ambiguous. Using either HeI or HeII radiation, only one peak is observed on Pd(111) (1), Ru(100) (8), Pt(100) (8,12) and Ni(111) (9) near 9 eV. On Ru(001) (6), Ir(111) (18,20), Ir(100) (18) and Ni(100) (23) multiple features appear in the UP spectra. Different assignments have been made for the various metals. Multiple sites occupied by NO may give different emissions which is the case for Ru(001) (6) and is suggested by the data of one study on Ir(111) (20). Multiple features have been assigned also to separated 1π and 5σ orbitals on the (111) and (100) surfaces of Ir (18) and on Ni(100) (23). In this case, the ordering of the levels is subject to disagreement.

Angular-resolved photoemission results on Ni(100) show that the 1π orbital lies higher in energy than the 5σ orbital of NO (23). However, on Ir(111) and Ir(100), the assignment of these orbitals was reversed by assuming the same relative intensity variation of the two levels for adsorbed NO as for gas phase NO (18). Bent bonding was suggested in both cases (18,23) for NO on Ir and Ni, even though the two studies assign the 1π and 5σ orbitals differently. This issue will be discussed further with the present results for NO chemisorbed on Ir(110). Finally, the least ambiguous assignment is for the lowest lying emission which corresponds to the 4σ orbital of NO.

Bent bonding and multiple site adsorption may be inferred through XPS measurements as well. On Ru(001) (6) and Ir(111) (19,20), two peaks are observed in the O(1s) region near 531 eV and are attributed to multiple site occupation. For Ru(001), EELS (5) and TDS results (7) support this conclusion. The difference between O(1s) and N(1s) binding energies for NO chemisorbed on Pt(100) prompted the suggestion that NO bonds in a bent geometry, drawing on analogies to metal nitrosyls (12). Upon dissociation, the N(1s) and O(1s) core levels show peaks near 397 and 529 eV, respectively, on the transition metals.

Evidence that linear and bent bonding as well as multiple site participation occurs for NO indicates the complex adsorption behavior for NO. The desorption behavior is equally complex, considering the competition between desorption of N_2 and NO, dissociation of NO and the accumulation of oxygen. The present investigation of NO on Ir(110) will provide a comparative study to the previously mentioned results. In addition to examining the molecular

phase of NO, coadsorption studies of NO on oxygen overlayers will be presented. Since oxygen remains on the surface in appreciable concentrations as NO decomposes and N₂ desorbs, the adsorption of NO on oxygen overlayers will lend further insight into the reduction of NO by hydrogen performed on the Ir(110) surface (24).

2. Experimental Procedures

The experiments were performed in an ion pumped stainless steel belljar that has been described previously (25,26). The base pressure for these experiments was below 2×10^{-10} torr of reactive contaminants. The clean Ir(110) surface shows a (1x2) reconstruction, which is a surface with every other row of Ir atoms missing in the [001] direction (27). The surface may be visualized as alternate rows and troughs exposing (111) planes which are inclined to one another. Isotopic ¹⁵NO was used to separate ¹⁵N₂ desorption from any spurious effects due to CO ($m/e = 28$). Hereafter, ¹⁵NO and ¹⁵N₂ will be referred to only as NO and N₂, with the exception of the figure captions.

Exposures of the surface to NO were carried out both with a leak valve and with a directional beam doser that has not been described previously. With the exception of the LEED and contact potential difference (CPD) measurements, all the exposures were performed by the doser, once it was calibrated in Langmuirs. The doser consists of a baffled stainless steel tube capped with a glass capillary array. During dosing, the crystal is positioned approximately 3 mm from the doser face, which places the crystal in line-of-sight of the mass

spectrometer. The beam pressure to background pressure ratio is approximately 100:1. Gas is admitted to the dosing line by a capillary leak, the dosing line being pumped by a baffled, two-inch diffusion pump. Exposures by the beam doser are in torr-s where the pressure refers to the pressure in the storage bulb behind the capillary leak. Calibration of the exposure units (torr-s) of the beam doser to Langmuirs (L) was accomplished by comparison of the exposure needed to cause the appearance of a thermal desorption feature of NO (see Section 3) by the leak value and the doser. The result is that 7.2 ± 0.4 torr-s is equal to 1.0 L.

It is well known that NO interacts strongly with stainless steel. To insure that the stainless steel exposed in the belljar was as passive as possible, 1×10^{-7} torr NO was admitted after a bakeout, for one hour. Thereafter, only O₂ and NO were introduced into the system. During any leak valve exposure, less than 2% of the NO was converted to N₂ and the CO partial pressure increased by less than 5% over a period of a half hour. In all cases, doser exposures produced negligible amounts of background contamination.

3. Adsorption and Desorption Kinetics

When NO is exposed to Ir(110) at low temperature and the substrate is heated, both N₂ and NO are observed to desorb between 300 and 800 K, depending on the initial coverage of NO. Oxygen remaining on the surface, after all nitrogen species are removed, desorbs as O₂ above 900 K and shows the same shape as seen for oxygen desorption alone (28). No other desorption products,

such as N_2O or NO_2 were observed. Figures 1(A) and 1(B) present the thermal desorption spectra for N_2 and NO , respectively, at a heating rate of $27 \text{ K} \cdot \text{s}^{-1}$. Three exposure ranges of NO may be separated, as seen from the NO and N_2 desorption curves in Fig. 1: (1) $\epsilon < 0.33 \text{ L}$, (2) $0.33 < \epsilon < 1.7 \text{ L}$ and (3) $\epsilon > 1.7 \text{ L}$. These regimes will be discussed in turn.

At low exposures of NO only N_2 desorbs, as seen, for example, in Fig. 1(A), curve (a). The desorption maximum is near 850 K and the shape is symmetric, suggesting second-order kinetics for desorption. Furthermore, this shows that the NO has dissociated below 500 K at this exposure of NO (0.26 L) and this heating rate ($27 \text{ K} \cdot \text{s}^{-1}$). The next exposure, 0.33 L NO , shows a second peak appearing on the low temperature side of the original N_2 feature. By an exposure of 0.83 L , the shape of the N_2 thermal desorption trace has changed considerably. The onset in N_2 production becomes much more abrupt and asymmetric. The third N_2 feature that appears (at 520 K for an exposure of 0.83 L) becomes dominant, shifts to lower temperature and sharpens with increasing exposure. At an exposure of 0.83 L , some NO desorption is observed as shown in Fig. 1(B). Near an exposure of 1.7 L , a second feature appears in the NO thermal desorption spectra that increases in intensity as saturation coverage is approached. Estimates of the activation energies for the desorption of N_2 , the dissociation of NO and the desorption of NO may be calculated from the thermal desorption spectra. Due to the observed complexity of the desorption spectra apparent in Fig. 1, only peak temperatures and "normal" preexponential factors (ca. $10^{13} - 10^{16} \text{ s}^{-1}$) will be assumed in order to estimate bounds on the activation energies of these competing reactions.

For low exposures of NO, only N₂ desorbs. Assuming that spectrum (a) in Fig. 1(A) represents adatom-adatom recombination as the rate limiting step, the activation energy for N₂ desorption may be estimated to lie between 36 and 45 kcal-mole⁻¹ (for $10^{-2} \leq \nu \leq 10^1 \text{ cm}^2 - \text{s}^{-1}$). The desorption peak temperature, 650 K, is comparable to that observed for N₂ desorbing from dissociated NO on Pd(111) (1) and polycrystalline Rh (22). Higher exposures of NO causes the onset of N₂ desorption to become more abrupt and asymmetric, and this may well indicate that the rate of dissociation of NO is now rate limiting. The shift in peak temperature in Fig. 1(A) for the desorption of N₂ [spectra (c) - (h)] does not imply second-order kinetics; rather, it is related to the changing activation energy for the dissociation of NO, E_{dis}(NO) and is first order. Thus, the desorption peak temperature of N₂ is related to an *upper* bound for E_{dis}(NO). Correlating E_{dis}(NO) with the initial coverage of NO (see adsorption kinetics below) gives E_{dis}(NO) = (33.4 - 10.3 θ_{NO}) kcal-mole⁻¹ for 0.3 ≤ θ_{NO} ≤ 0.8 if ν_{dis} is equal to 10¹⁹ s⁻¹ and E_{dis}(NO) = (39.8 - 10.3 θ_{NO}) kcal-mole⁻¹ if ν_{dis} is equal to 10¹⁶ s⁻¹. Therefore, E_{dis}(NO) decreases with increasing θ_{NO} until the yield of N₂ saturates. The activation energy for the first order desorption kinetics of NO may be estimated from the thermal desorption spectra of Fig. 1(B). The low temperature peak near 400 K represents the desorption of NO from an oxygen-free surface, whereas the high temperature peak near 550 K represents desorption of NO from a surface containing significant concentrations of oxygen. The desorption energy for the former is between approximately 23.4 - 28.9 kcal-mole⁻¹ and for the latter approximately 32.5 - 40.1 kcal-mole⁻¹, for a preexponential factor for desorption between 10¹⁹ to 10¹⁶

s^{-1} . Comparing desorption and dissociation energies of NO estimated from Fig. 1 suggests that three regimes of desorption are important. At saturation coverage, some NO desorbs near 400 K (~17%) before appreciable dissociation occurs followed by N_2 desorption near 430 K. Finally, the desorption rates of N_2 and NO become comparable above 450 K.

Recently, it was concluded that recombination of nitrogen and oxygen adatoms becomes important for the high temperature desorption feature of NO on Ir(100) (21). Precoverages of ^{18}O exchanged with the high temperature feature of NO, whereas the lower temperature desorption was unperturbed. This is the case also on Ir(110). Enriched (23 at.%) ^{18}O was exposed to various precoverages of NO at 100 K. For low exposures of oxygen (< 5 L), the high temperature feature in Fig. 1(B) exchanges statistically. Therefore, the exchange experiment on Ir(110) is conclusive that the first peak is molecular in nature only and the second peak is at least partially due to the recombination process. In the N(1s) region of binding energy, no nitrogen atoms were detectable by XPS at a sensitivity level of approximately 0.1 ML if the desorption were terminated between 380 K and 500 K and the crystal cooled (see Section 4). Thus, although the high temperature peak of NO is at least partially due to nitrogen and oxygen adatom recombination, the concentration of nitrogen adatoms is always small. During desorption, preadsorbed oxygen inhibits the formation of N_2 and shifts the desorption population of NO to the higher temperature peak.

To obtain the adsorption kinetics of NO on Ir(110), integration of the thermal desorption spectra for NO and N_2 with respect to time is necessary. Also, a

calibration between the integrated intensities of NO and N₂ and the saturation coverage of NO are needed. Since at low exposures only N₂ and O₂ desorb, a convenient calibration for N₂ exists via a mass balance with oxygen, the coverage of which is known (28). This gives the initial coverage of NO and the initial probability of adsorption of NO, S₀. The relative mass spectrometer intensity to N₂ and NO is found by monitoring the saturation coverage of NO, which was measured by comparing O(1s) intensities of NO and oxygen by XPS. The saturation coverage measured for NO at 100 K is 9.6×10¹⁴ cm⁻² (± 5%). The adsorption kinetics of NO on Ir(110) at 100 K may be deduced from Fig. 2 where S₀ is unity. The kinetics are fit well by a first-order Kisliuk precursor model with the parameter K = 0.3, where K = 0 corresponds to Langmuir kinetics (zero lifetime of the precursor), and K = 1 corresponds to a constant probability of adsorption (infinite lifetime of the precursor) (29). A high value of S₀ and precursor kinetics for the adsorption of NO on the transition metals are common (1,3,4,9,10,13). The relative yields of N₂ and NO from thermal desorption are shown in Fig. 3. At saturation coverage of NO, 35% of the nitrogen on the surface desorbs as NO with approximately equal amounts in each feature [Fig. 1(B)], and 65% desorbs as N₂.

In summary, the desorption kinetics of N₂ and NO from an adlayer of NO depend strongly upon one another. The desorption kinetics of N₂ at medium to high coverages of NO reflect the rate of dissociation of NO. For the desorption of NO, two features develop fully at saturation coverage, one of which represents desorption from an oxygen-free surface and the other of which, a higher temperature feature, represents desorption from a surface partially

covered with oxygen. The adsorption kinetics follow a first-order precursor model at 100 K with an initial probability of adsorption of unity. At saturation coverage of NO, 65% desorbs as N_2 and 35% desorbs as NO. The adsorption kinetics of NO at higher temperatures will be discussed in Section 5.

4. UPS, XPS and AES Measurements of NO

Presented in Fig. 4 are HeI difference spectra of NO adsorbed at various coverages on Ir(110) at 100 K. Three levels are observed at 8.5, 10.4 and approximately 13.5 eV below the Fermi level, E_F . The lowest lying level at 13.5 eV may be assigned immediately as the 4σ orbital of molecularly chemisorbed NO. However, the levels at 8.5 and 10.4 eV are less straightforward in assignment. Gas phase ionization potentials for the 4σ , 5σ , 1π and 2π orbitals of NO are 21.7, 19.5, 15.7 and 9.3 eV, respectively. Assuming that the 4σ orbital for NO adsorbed on Ir(110) and gaseous NO are related by a static shift (8.2 eV), the orbitals of adsorbed NO would require the 5σ to destabilize by 0.9 eV and the 1π to stabilize by 1.0 eV with the premise that the 5σ and 1π levels maintain the same order in energy when NO is chemisorbed. If these levels cross, the 5σ level would destabilize to an even greater extent, and the 1π would stabilize correspondingly further upon chemisorption. It is thought that bonding of NO with the surface is through the 5σ orbital which is weighted toward the nitrogen end of the molecule. Furthermore, a backbonding interaction is assumed to occur through the singly-occupied 2π level, although this orbital is not observed in the spectra of Fig. 4. If NO bonds in a linear fashion to the

metal, the 5σ should stabilize. However, bent bonding has been suggested for NO on Pt(100) (12), Ir(111) (18), Ir(100) (18) and Ni(100) (23). Hence, rehybridization of valence orbitals may make a direct comparison between gaseous NO and adsorbed NO inappropriate.

Although bent bonding has been inferred for NO on Ir (18) and Ni (23), the 5σ and 1π orbital assignments disagree. For Ir(111) and Ir(100), the relative intensity variation with photon energy of 5σ and 1π orbitals in the gas phase was assumed to maintain for adsorbed NO, and it was concluded that the 5σ and 1π orbitals cross in energy when the NO is chemisorbed (18). For Ni(100), angular-resolved UPS and photon energy variation were employed to show that the 5σ and 1π levels do not cross, and the 1π orbital still lies higher in energy (23). The 1π orbital showed an increase in intensity as the photon energy decreased (23). Our present HeI results on Ir(110) compared to HeII results on the same surface (20) show the same trend. Moreover, an extensive investigation of $\text{Cr}(\text{NO})_4$ placed the 1π level higher than the 5σ one for this metal nitrosyl (30). Therefore, the most probable assignment of NO on Ir(110) is that the 5σ and 1π orbitals are at 10.4 and 8.5 eV, respectively. Data presented in Sections 3, 6 and below indicate that NO is stabilized by the presence of adsorbed oxygen. Results presented below show that the 1π level shifts from 8.5 to 9.5 eV when NO is coadsorbed with oxygen, an observation which is not understood at this time.

Annealing experiments were performed for low coverages of chemisorbed NO to determine above what temperature dissociation takes place. In Fig. 5 are shown UP difference spectra for two coverages of NO comparing annealed

and unannealed surfaces. Adsorption of 0.19 ML and 0.43 ML of NO on the clean surface at 100 K yields the spectra shown in Figs. 5(a) and 5(c), respectively. Annealing these two coverages of NO to 400 K yields the spectra shown in Figs. 5(b) and 5(d), respectively. It is apparent that for 0.19 ML coverage, dissociation has taken place by 400 K as judged by the disappearance of the molecular levels of NO and the appearance of a broad level near 5.7 eV which is due to emission from O(2p) and N(2p) orbitals. However, annealing 0.43 ML of NO does not cause complete dissociation since emission from the NO molecular orbitals is still observed. In fact, the peak intensities at 8.5 eV and 10.5 eV in Fig. 5(d) are equal to those in Fig. 5(c), although in Fig. 5(d) the 4σ orbital at 13.5 eV is not observed, and the intensity decrease near E_F is larger which is due to NO and oxygen coadsorbed. No desorption of either NO or N_2 occurs below 400 K for either initial coverage, so the changes in the UP spectra reflect a chemical reaction occurring *on the surface*. Therefore, depending on the initial coverage of NO, annealing to 400 K causes all or part of the overlayer of NO to dissociate.

UP difference spectra of coadsorbed NO and oxygen are shown in Fig. 6. The UP spectrum for the saturation coverage of NO on the initially clean surface is reproduced in Fig. 6(a) for comparison. Whether chemisorbed oxygen is converted to an oxide [curve (b)], or not [curve (c)], a shift in the highest lying (1π) level of NO is observed, from 8.5 eV on the clean surface to 9.1 eV in curve (b), and to 9.5 eV in curve (c). The other two levels at 10.5 eV and 13.5 eV do not shift, however. The substrate structure has a small effect since in curve (b) the substrate is (1x1) and in curve (c) it is (1x2). The presence of oxygen

Furthermore, in spectrum (b) the surface was saturated with NO after partial dissociation had occurred, which tends to displace nitrogen adatoms from the surface by the desorption of N₂. Thus, the XPS results verify the TDS results presented in Fig. 1 that oxygen accumulates on the surface when the overlayer of NO is heated slightly above 400 K.

Finally, O-KLL and N-KLL Auger transitions are presented in Fig. 8 for a saturated overlayer of NO at 95 K. The electron beam current density used was 10^{-8} amp - mm⁻² at an energy of 2 keV. Electron beam exposures to the surface were limited to 10 min. before a fresh surface was prepared in order to minimize beam induced dissociation. In Fig. 8 the peak positions are nearly identical to those found for X-ray induced Auger transitions observed of NO on Ru(001) (6), but they are somewhat different from gas phase spectra (31). The spectra of Fig. 8 point up very nicely the similarity of AES transitions for the same molecule adsorbed on different metals. An additional feature in the N-KLL region at 371 eV, not seen on Ru(001) (6), is attributed to nitrogen atoms formed by electron induced dissociation of NO. Nitrogen atoms formed during the steady state reaction between NO and H₂ (24) show an Auger transition here.

5. Isothermal Decomposition of NO

A series of mass spectrometric experiments at various constant surface temperatures was performed in order to measure the rate of NO adsorption and the rate of N₂ desorption on Ir(110). The calibration of the mass spec-

trometer intensity for NO (in absolute coverage units) and of the relative intensity of NO and N₂ allows the adsorption kinetics of NO to be measured at a given surface temperature (see Section 3).

The Ir crystal was exposed to NO by the beam doser at a constant beam pressure (approximately 9×10^{-8} torr). Since the doser and the crystal were positioned so that part of the molecules scattered from the crystal was in line-of-sight of the mass spectrometer, the intensities of NO and N₂ could be measured directly. Therefore, the decrease in the NO intensity is due to adsorption, and the increase in the N₂ intensity is due to desorption. Prior to each experiment, the crystal was cleaned by annealing above 1600 K and then was cooled to the appropriate surface temperature. The crystal was moved in front of the doser, and N₂ and NO intensities were monitored as a function of time until no further changes occurred.

Results of an experiment at 400 K, representative of other surface temperatures, are shown in Fig. 9. Shown in Fig. 9 are the adsorption rate of NO, the desorption rate of N₂ and the integrated intensities of NO and N₂ as a function of exposure (or equivalently time). The rate of adsorption of NO is inversely proportional to the measured gas phase partial pressure. It is clear from Fig. 9 that N₂ does not desorb immediately. However, for small exposures of NO, decomposition does occur at 400 K as seen, for example, from the UPS results in Fig. 5. Desorption of N₂ appears only after sufficient NO adsorbs, either associatively or dissociatively. Consequently, the activation energy for the desorption of N₂ decreases with surface coverage. Also, the initial adsorption rate of NO remains the same as that seen at 100 K (Fig. 2), so the initial

adsorption kinetics are independent of temperature and S_0 is unity. Interestingly, near the maximum in the rate of desorption of N_2 , a small, but reproducible change in the rate of adsorption of NO occurs, presumably due to the desorption of N_2 and the accumulation of oxygen:

The integrated mass spectrometric intensities, calibrated in absolute coverage units, represent the total amounts of NO that is adsorbed and of N_2 that is desorbed during the experiment. Subtraction of these curves gives directly the coverage of nitrogen (as NO or N) present on the surface at any point of exposure (time). The total coverage of N present on the surface as a function of exposure at various surface temperatures is shown in Fig. 10. Results from the TDS measurements for adsorption at 100 K are reproduced in Fig. 10(a) for comparison and are offset for clarity. For temperatures below 350 K, where desorption is negligible (cf. Fig. 1), the adsorption kinetics are identical. Although the initial rate of adsorption remains constant between 400 and 700 K, the shape of the curves in Fig. 10 changes due to desorption of N_2 and NO. A relative maximum occurs in the coverage of N as a function of exposure since N_2 desorption and NO adsorption are competitive reactions. As the temperature increases, the relative maximum in the coverage of N appears at lower exposures and decreases in magnitude. Above 600 K, no nitrogen species are present once the oxygen uptake is complete. Only NO is detected by XPS on the surface at the end of each experiment if any nitrogen species are still present, so nitrogen atoms (≥ 0.1 ML) are not favored once the surface is at steady state. Oxygen tends to stabilize the NO that remains on the surface with respect to dissociation.

The total yields of adsorbed NO and desorbed N₂ are shown in Table 1. The coverage of N left on the surface at steady state is the coverage of NO to a good approximation. By mass balance, the coverage of oxygen coadsorbed with the remaining NO is equal to the amount of N₂ desorbed since no other species desorbs. The maximum coverage of oxygen is near 0.5 ML, and this is associated with the formation of a c(2x2)-0 superstructure on the (1x1) Ir surface (see Section 7). This oxygen superstructure inhibits further dissociation of NO as it does for oxygen adsorption at these temperatures (28). Since the NO remaining on the surface is at steady state with the pressure of the beam doser, an estimate may be made for the activation energy of desorption of NO, $E_d(\text{NO})$, between 400 and 621 K. The flux of NO onto the surface is equated to the desorption flux of NO, and the preexponential is assumed to be $10^{18} - 10^{16} \text{ s}^{-1}$ as in Section 3. The results for $E_d(\text{NO})$ are shown in Table 1. As the coverage of NO decreases and the coverage of oxygen increases, $E_d(\text{NO})$ increases. These values are comparable to that calculated for the higher temperature peak in TDS, 32.5 - 40.1 kcal-mole⁻¹ [half of the NO that desorbs from a saturated layer of NO] associated with a surface on which oxygen adatoms are present.

To summarize, isothermal decomposition measurements of NO on Ir(110) provide complementary information concerning the adsorption of NO either on the clean surface (low temperature) or on a surface with oxygen adatoms present due to the dissociation of NO (high temperature). The initial probability of adsorption maintains near unity regardless of the surface temperature. Approximately 0.5 ML of NO may be decomposed above 500 K after which no

further dissociation can occur due to the high concentration of oxygen. Estimates for the activation energy for NO to desorb, $E_d(\text{NO})$, agree with the TDS estimate and show that $E_d(\text{NO})$ increases as NO decreases and oxygen increases in coverage.

8. CPD of NO and Coadsorbed NO and Oxygen

Although NO exhibits identical adsorption kinetics for temperatures below 350 K as seen previously, the contact potential difference of NO is different for adsorption at 100 K compared to near room temperature. The CPD of NO adsorbed at 100 K and 317 K are shown in Fig. 11 as a function of fractional surface coverage. At 100 K [curve (a)], the CPD decreases, attains a minimum at -0.085 eV at half a monolayer and increases to a final value of -0.04 eV at saturation. The increase between 0.75 and 0.85 ML is associated with the appearance of a streaked LEED pattern containing a mirror plane or glide plane of symmetry (see Section 7). This superstructure disorders above 0.85 ML, but the CPD does not change further. At 317 K the CPD decreases more strongly, reaches a minimum at higher coverage (-0.115 eV) and increases slightly, to a final value of -0.100 eV at saturation. The change in shape of the CPD with coverage, comparing the two adsorption temperatures, indicates that some dissociation has taken place at 317 K. Assuming the presence of oxygen causes the CPD of NO to be modified, a small precoverage of oxygen was adsorbed, and the CPD was measured for NO [curve (a) of Fig. 12] where $\theta_0 = 0.13$ ML. It is apparent that oxygen does influence the CPD of NO considerably

since the shape of the curve has changed and the magnitude of the decrease is much larger, -0.36 eV. If the change in the CPD is linear in oxygen coverage at low coverages of oxygen, then the amount of NO dissociated at 317 K is less than 5%. Therefore, the CPD of NO on Ir(110) is a sensitive indicator for the dissociation of NO.

Two different effects may occur to alter the CPD of NO when oxygen is present. First, NO may chemisorb on different sites due to the blockage of its preferred sites by oxygen adatoms. Second, a chemical interaction may occur between oxygen and NO on the surface. These two possibilities were investigated by preparing the surface in several different ways with preadsorbed oxygen and recording the CPD of NO as a function of exposure, as shown in Fig. 12. For curves (a), (b), (d), (e) and (g), the substrate is the reconstructed (110)-(1x2) surface with various initial coverages of chemisorbed oxygen. Curves (c) and (f) represent NO adsorbed on the unreconstructed (110)-(1x1) surface which is stabilized by a surface oxide (28) with two different coverages of preadsorbed oxygen present. Although the adsorption kinetics are not known so that the exposures of NO cannot be related to coverages on these oxygen overlayers, the trend in the CPD is quite useful to gain insight into the interaction between coadsorbed NO and oxygen. However, it is known that approximately one-half the amount of NO adsorbs on an oxygen-saturated surface as compared to the clean surface, measured by TDS.

Since the adsorption kinetics are not known for NO in these cases, except for curve (g) of Fig. 12 [clean (1x2) surface], the shapes of the CPD curves as a function of exposure are less instructive than the magnitude of the CPD of NO

when the surface is saturated. Noting that the zero of the CPD has been shifted by pairs for clarity in Fig. 12, the CPD of NO at saturation increases in magnitude, but is always negative, as the precoverage of oxygen increases, regardless of whether the substrate structure is (1x1) or (1x2). Moreover, the saturation CPD of NO relative to the *clean* surface [$\Delta\phi(O) - \Delta\phi(NO)$] is always between 0 and +0.25 eV when oxygen is preadsorbed. Therefore, the CPD of NO is approximately proportional to the amount of oxygen present and depends much less upon the structure of the substrate. Moreover, the CPD is rather insensitive to the binding site occupied by oxygen since oxygen changes its preferred sites from low coverage ($\theta < 0.25$) to high coverage, and from chemisorbed oxygen to the surface oxide (28). The interaction between NO and oxygen may be described best by through-metal interactions. Oxygen, which is quite electronegative, draws charge from the metal and causes the CPD to increase strongly. Adsorption of NO may then occur more readily near the electron deficient regions of the metal, which may cause the CPD relative to the *clean* surface to change only slightly, as observed. In effect, NO "titrates" the charge induced by oxygen. A similar CPD dependence for one state of NO coadsorbed with oxygen on Ru(001) has been reported (7). As was shown in Section 4, UPS of coadsorbed NO and oxygen indicates a strong interaction between the adsorbates as well.

7. LEED Observations

A clean, well-ordered Ir(110) surface gives a sharp (1x2) LEED pattern,

which is a surface with every other row of Ir atoms missing (27). At 100 K, fractional coverages of NO below 0.75 (exposures below 2 L) produce only a high background intensity which diminishes the intensity of the substrate beams uniformly. At fractional coverages between 0.75 and 0.85 (exposures between 2 and 2.5 L), very broad streaks appear between the rows containing half-order spots. In addition, little or no intensity is observed above and below the (00) beam. Although the streaks did not coalesce even with annealing cycles from 100 to 250 K, the absence of intensity where $(n \pm \frac{1}{2}, 0)$ beams would occur indicates that a mirror plane or glide plane of symmetry lies along the [001] direction, along the rows of Ir atoms. At fractional coverages above 0.85 (exposures above 2.5 L), the streaking diminished until only a disordered superstructure was present. Since no ordered superstructures were found with the exception of the one mentioned above, it is not possible to assign any surface structure to NO on the (1x2) substrate.

Annealing a saturated overlayer of NO above 400 K causes streaking reminiscent of chemisorbed oxygen adatoms (28). Furthermore, annealing a saturated overlayer to 750 K and cooling forms a sharp oxygen c(2x2) superstructure which occurs on the oxidized Ir(110)-(1x1) surface (28). A c(2x2) superstructure can be formed easily also by exposing NO to the surface above 700 K until the surface is saturated. Saturating the surface on which the c(2x2)-O superstructure is present at 300 K with NO forms a coadsorbed (1x2) superstructure having sharp integral order spots and large, diffuse half-order spots. It is not likely that this pattern is due to the oxidized (1x1) surface relaxing back to a (1x2) superstructure, since this does not occur for NO

adsorbed on the (1x1) oxide. Since the coverages of the two adsorbates are known, 0.5 ± 0.05 ML, a structure may be postulated. For oxygen, an analysis of the $c(2 \times 2)$ -O superstructure shows that it binds on top of the rows of Ir atoms in short-bridged sites (32). A possible structure for coadsorbed NO and oxygen on Ir(110)-(1x1) is one in which oxygen still occupies its preferred short-bridged sites, but half of the oxygen adatoms have shifted to yield a (1x2) superstructure. The NO molecules may then distribute randomly on the remaining open areas between the rows of oxygen adatoms. No superstructures could be found that contained both ordered NO and oxygen. However, the observed superstructure may certainly be due to other possible arrangements of the adsorbates on the surface.

8. Summary

The chemisorption and decomposition of NO on Ir(110) may be summarized as follows.

- (1) Molecular chemisorption of NO occurs below room temperature and saturates near $9.6 \times 10^{14} \text{ cm}^{-2}$. Adsorption occurs via precursor kinetics, and the initial probability of adsorption is equal to unity independent of surface temperature. Adsorption becomes competitive with NO dissociation and N_2 desorption above 400 K.
- (2) Above 300 K, desorption of NO and N_2 occurs in three phases. First, approximately 17% of the NO desorbs near 400 K. Second,

N_2 desorbs near 430 K as NO dissociates leaving an oxygen overlayer. Third, both NO and N_2 desorb where the NO desorption (18% of the adsorbed NO) is associated with oxygen present and at least in part is due to adatom-adatom recombination. Estimates of activation energies for the desorption of NO in the first and third steps are 23.4 - 28.9 and 32.5 - 40.1 kcal-mole⁻¹, respectively. The activation energy for the dissociation of NO was estimated from data involving the desorption of N_2 , and is equal to 25.2 - 30.7 kcal-mole⁻¹ for desorption from a saturated overlayer. The activation energy for N_2 to desorb in the low coverage limit of NO is approximately 36 - 45 kcal-mole⁻¹. The preexponential factor for each process is assumed to lie between $10^{19} - 10^{18} \text{ s}^{-1}$.

- (3) HeI UPS of NO shows levels at 13.5, 10.4 and 8.5 eV corresponding to the 4σ , 5σ and 1π orbitals, respectively. XPS of NO yields the O(1s) and N(1s) levels of NO at 531.5 and 400.2 eV, respectively, with or without oxygen present. The O(1s) level of chemisorbed oxygen at 528.8 eV is seen for surface temperatures above 400 K.
- (4) From TDS, oxygen overlayers tend to stabilize NO with respect to dissociation and to desorption. A strong interaction between NO and oxygen is seen by the shift of the 1π level to 9.5 eV and by the CPD behavior of NO on surfaces precovered with oxygen adatoms. Both phenomena may be due to charge transfer effects between NO and oxygen through the metal.

References

1. H. Conrad, G. Ertl, J. Kuppers and E. E. Latta, *Surface Sci.* 65, 235 (1977).
2. R. Ku, N.A. Gjostein and H. P. Bonzel, *Surface Sci.* 64, 65 (1977).
3. T. W. Orent and R. S. Hansen, *Surface Sci.* 67, 325 (1977).
4. P. D. Reed, C. M. Comrie and R. M. Lambert, *Surface Sci.* 72, 423 (1978).
5. P. A. Thiel, W. H. Weinberg and J. T. Yates, Jr., *Chem. Phys. Letters* 67, 403 (1979); G. E. Thomas and W. H. Weinberg, *Phys. Rev. Letters* 41, 1181 (1978).
6. E. Umbach, S. Kulkarni, P. Feulner and D. Menzel, *Surface Sci.* 88, 65 (1979).
7. P. Feulner, S. Kulkarni, E. Umbach and D. Menzel, to be published.
8. H. P. Bonzel and T. E. Fischer, *Surface Sci.* 51, 213 (1975).
9. H. Conrad, G. Ertl, J. Kuppers and E. E. Latta, *Surface Sci.* 50, 296 (1975).
10. G. L. Price, B. A. Sexton and B. G. Baker, *Surface Sci.* 60, 506 (1976).
11. G. L. Price and B. G. Baker, *Surface Sci.* 91, 571 (1980).
12. H. P. Bonzel and G. Pirug, *Surface Sci.* 62, 45 (1977).
13. H. P. Bonzel, G. Broden and G. Pirug, *J. Catalysis* 53, 96 (1978).
14. C. M. Comrie, W. H. Weinberg and R. M. Lambert, *Surface Sci.* 57, 619 (1976).

15. J. L. Gland and B. A. Sexton, *Surface Sci.* 94, 355 (1980).
16. H. Ibach and S. Lehwald, *Surface Sci.* 76, 1 (1978).
17. G. Pirug and H. P. Bonzel, *J. Catalysis* 50, 64 (1977).
18. J. Kanski and T. N. Rhodin, *Surface Sci.* 65, 63 (1977).
19. P. A. Zhdan, G. K. Boreskov, W. F. Egelhoff, Jr. and W. H. Weinberg, *J. Catalysis* 45, 281 (1976).
20. P. A. Zhdan, G. K. Boreskov, A. I. Boronin, A. P. Scheplin, W. F. Egelhoff, Jr. and W. H. Weinberg, *J. Catalysis* 60, 93 (1979).
21. J. Koppers and H. Michel, *Surface Sci.* 85, 201 (1979).
22. C. T. Campbell and J. M. White, *Appl. Surface Sci.* 1, 347 (1978).
23. G. Loubriel, E. W. Plummer, T. Gustafsson and C. L. Allyn, submitted to *Surface Science*.
24. D. E. Ibbotson, T. S. Wittrig and W. H. Weinberg, in preparation.
25. D. E. Ibbotson, T. S. Wittrig and W. H. Weinberg, *J. Chem. Phys.* 72, 4885 (1980).
26. J. L. Taylor, D. E. Ibbotson and W. H. Weinberg, *J. Chem. Phys.* 69, 4298 (1978).
27. C.-M. Chan, M. A. Van Hove, W. H. Weinberg and E. D. Williams, *Solid State Commun.* 30, 47 (1979); *Surface Sci.* 91, 400 (1980).
28. J. L. Taylor, D. E. Ibbotson and W. H. Weinberg, *Surface Sci.* 79, 349 (1979).
29. P. Kisliuk, *J. Phys. Chem. Solids* 3, 95 (1957).
30. G. Loubriel, E. W. Plummer, D. Rajora, M. Albert, L. Sneddon and

- W. R. Salaneck, *J. Electron Spectrosc. Relat. Phenom.* **19**, 35 (1980).
31. W. E. Moddeman, T. A. Carlson, M. O. Krausse, B. P. Pullen, W. E. Bull. and G. K. Schweitzer, *J. Chem. Phys.* **55**, 2317 (1971).
32. C.-M. Chan, K. L. Luke, M. A. Van Hove, W. H. Weinberg and S. P. Withrow, *Surface Sci.* **78**, 386 (1978).

Table 1

Yields of adsorbed NO and desorbed N₂ at various adsorption temperatures on Ir(110) from isothermal decomposition measurements. Estimates of the activation energy for desorption of NO at selected temperatures are also given.

T,K	$\Theta(\text{NO})$	$\Theta(\text{N}_2)$	$\Theta(\text{NO})$	$E_d(\text{NO})^*$
100	1.00	0	1.00	
312	1.00	0	1.00	
350	0.98	0.01	0.97	
400	0.85	0.23	0.62	
450	0.87	0.45	0.42	29.2-35.4
500	0.85	0.52	0.33	32.1-39.0
550	0.57	0.50	0.07	33.8-41.2
621	0.55	0.55	0	36.0-44.5
650	0.49	0.49	0	
680	0.47	0.47	0	
700	0.48	0.48	0	
720	0.49	0.49	0	

*Assuming 10^{13} to 10^{16} s⁻¹ for the preexponential factor of desorption.

Figure Captions

- Fig. 1. Thermal desorption spectra of (A) $^{15}\text{N}_2$ and (B) ^{15}NO as a function of exposure for ^{15}NO on Ir(110). Exposures were performed by a beam doser and have been converted to Langmuir units. The initial temperature was 100 K and the (linear) heating was $27 \text{ K} \cdot \text{s}^{-1}$.
- Fig. 2. The adsorption kinetics of ^{15}NO on Ir(110) as calculated from the TDS results in Fig. 1. The initial probability of adsorption is unity, and the saturation coverage as determined by XPS measurements is $9.6 \times 10^{14} \text{ cm}^{-2}$.
See the text for details.
- Fig. 3. Yields of $^{15}\text{N}_2$ and ^{15}NO from the TDS results in Fig. 1. The fractional coverage scale for $^{15}\text{N}_2$ has been normalized to provide a nitrogen atom balance. Desorption yields of $^{15}\text{N}_2$ and ^{15}NO saturate at 0.65 and 0.35 ML, respectively.
- Fig. 4. HeI UP difference spectra of ^{15}NO on Ir(110) as a function of the fractional coverage of ^{15}NO . The binding energy scale is referenced to the Fermi level, E_F .
- Fig. 5. HeI difference spectra of NO on Ir(110) showing the effects of annealing two coverages to 400 K and cooling. (a) 0.19. (b) 0.19 annealed to 400 K. (c) 0.43. (d) 0.43 annealed to 400 K.
- Fig. 6. HeI difference spectra of a saturated overlayer of ^{15}NO on various coverages of preadsorbed oxygen and substrate structures.

(a) Clean (1x2) substrate. (b) Surface oxide (0.25 ML) with (1x1) substrate. (c) 0.25 ML oxygen with (1x2) substrate and (d) 0.98 ML oxygen on (1x2) substrate.

Fig. 7. XPS of ^{15}NO adsorbed on Ir(110). Top: N(1s), Bottom: O(1s).

(a) 14.0 L ^{15}NO adsorbed and recorded at 95 K (saturation).

(b) 7.0 L exposed at 400 K and an additional 7.0 L exposed at 95 K. (c) Saturated ^{15}NO layer (95 K) annealed to 430 K and recorded at 95 K.

Fig. 8. Electron excited AES. (A) O-KLL and (B) N-KLL of NO on Ir(110) at 95 K for a saturated overlayer.

Fig. 9. Isothermal decomposition of ^{15}NO on Ir(100) at 400 K. The adsorption rate of ^{15}NO , the desorption rate of ^{15}NO , the desorption rate of $^{15}\text{N}_2$ and their respective coverages as a function of NO exposure are shown. These data were used to calculate curve (c) in Fig. 8.

Fig. 10. The total coverage of $\text{N}(^{15}\text{N}_{(a)} + ^{15}\text{NO}_{(a)})$ as a function of exposure to ^{15}NO on Ir(110).

Several different surface temperatures are shown.

Curve (a) is reproduced from Fig. 2. (b) ← 350 K, (c) 400 K,

(d) 450 K, (e) 500 K, (f) 550 K, (g) 621 K, (h) 650 K and

(i) 700 K. Curves (b) - (i) were calculated from beam doser experiments. See the text for details.

Fig. 11. CPD, $\Delta\phi$, of ^{15}NO as a function of fractional

coverage at (a) 100 K and (b) 317 K. The change in $\Delta\phi$

between the two temperatures is evidence for partial dissociation near room temperature.

Fig. 12. CPD of ^{15}NO exposed to various precoverages of oxygen on Ir(110). With the exceptions of (c) and (f) [(1x1)], the substrate maintains a (1x2) structure. The fractional coverages of oxygen are as follows: (a) 0.13, (b) 0.25, (c) 0.25 (oxide), (d) 0.41, (e) 0.46, (f) ~ 1.2 and (g) 0

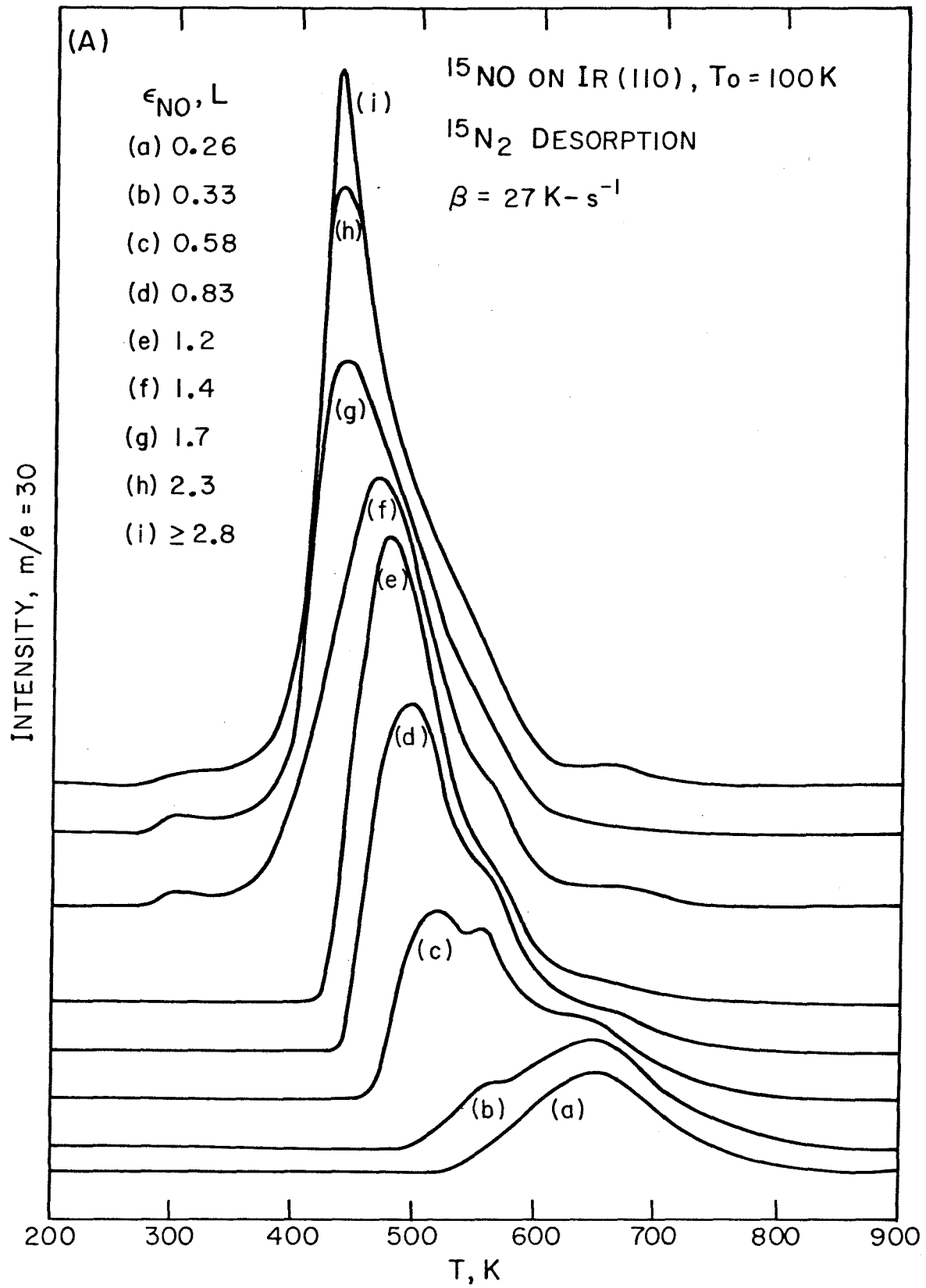


Figure 1(a)

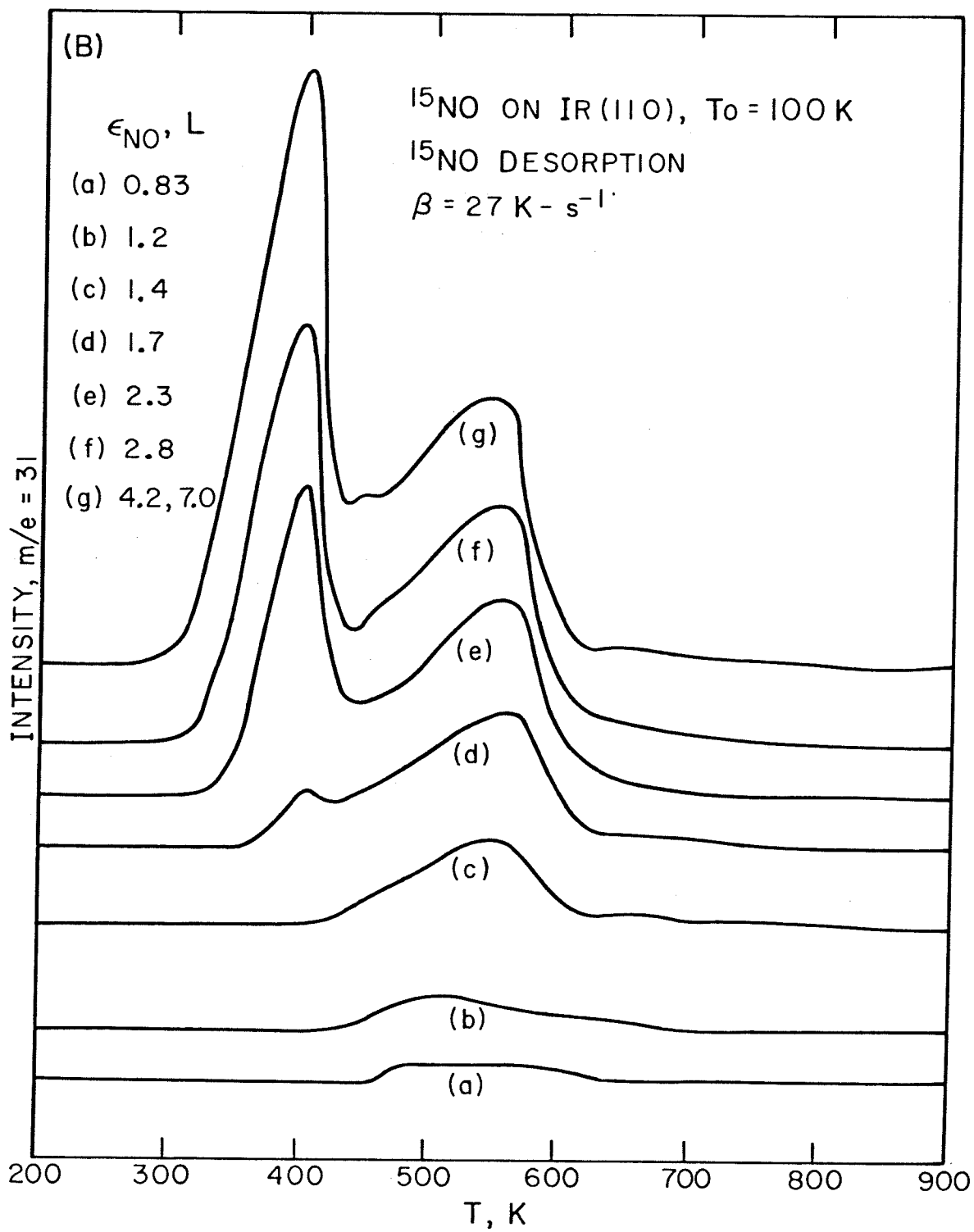


Figure 1(b)

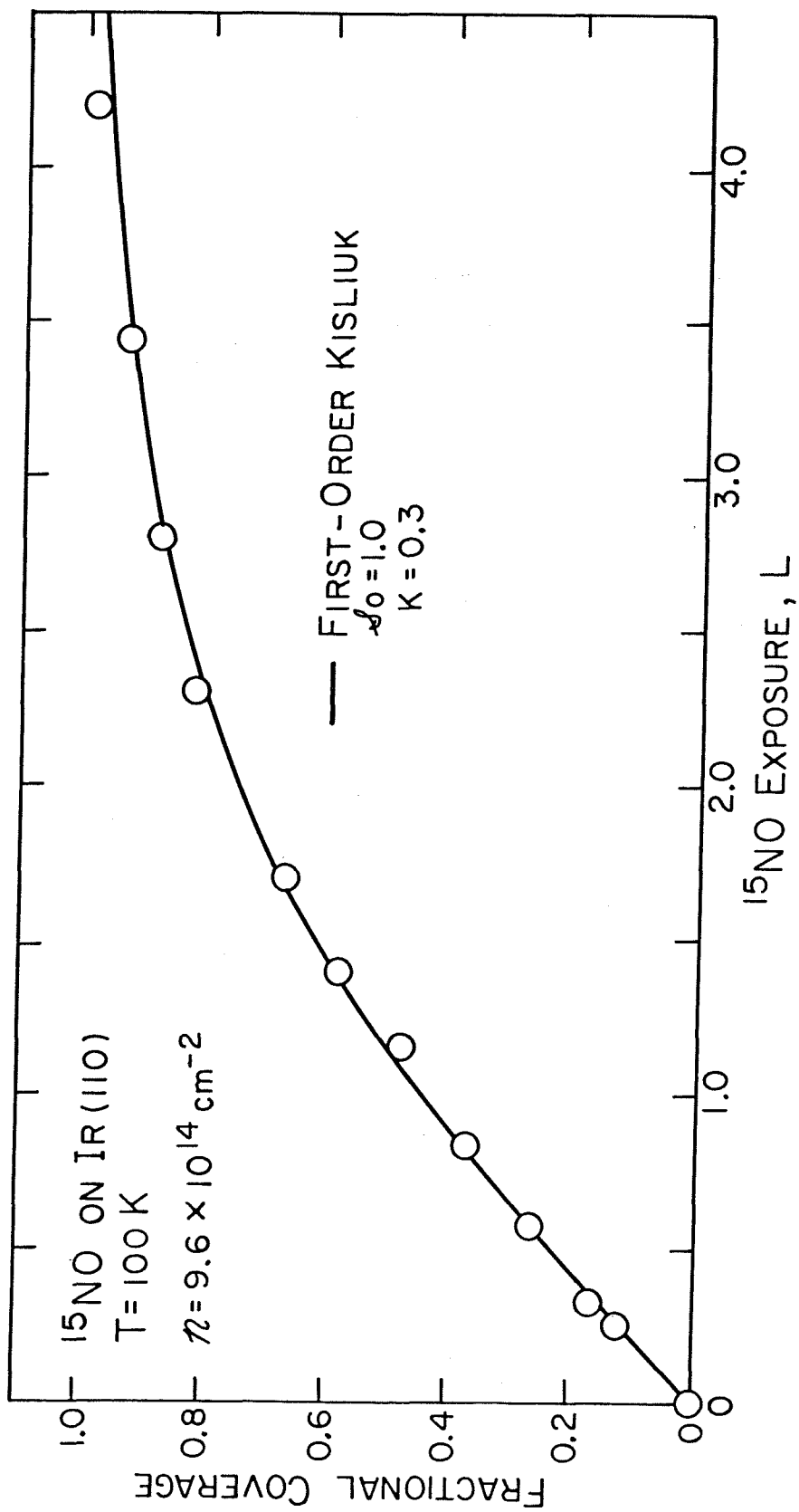


Figure 2

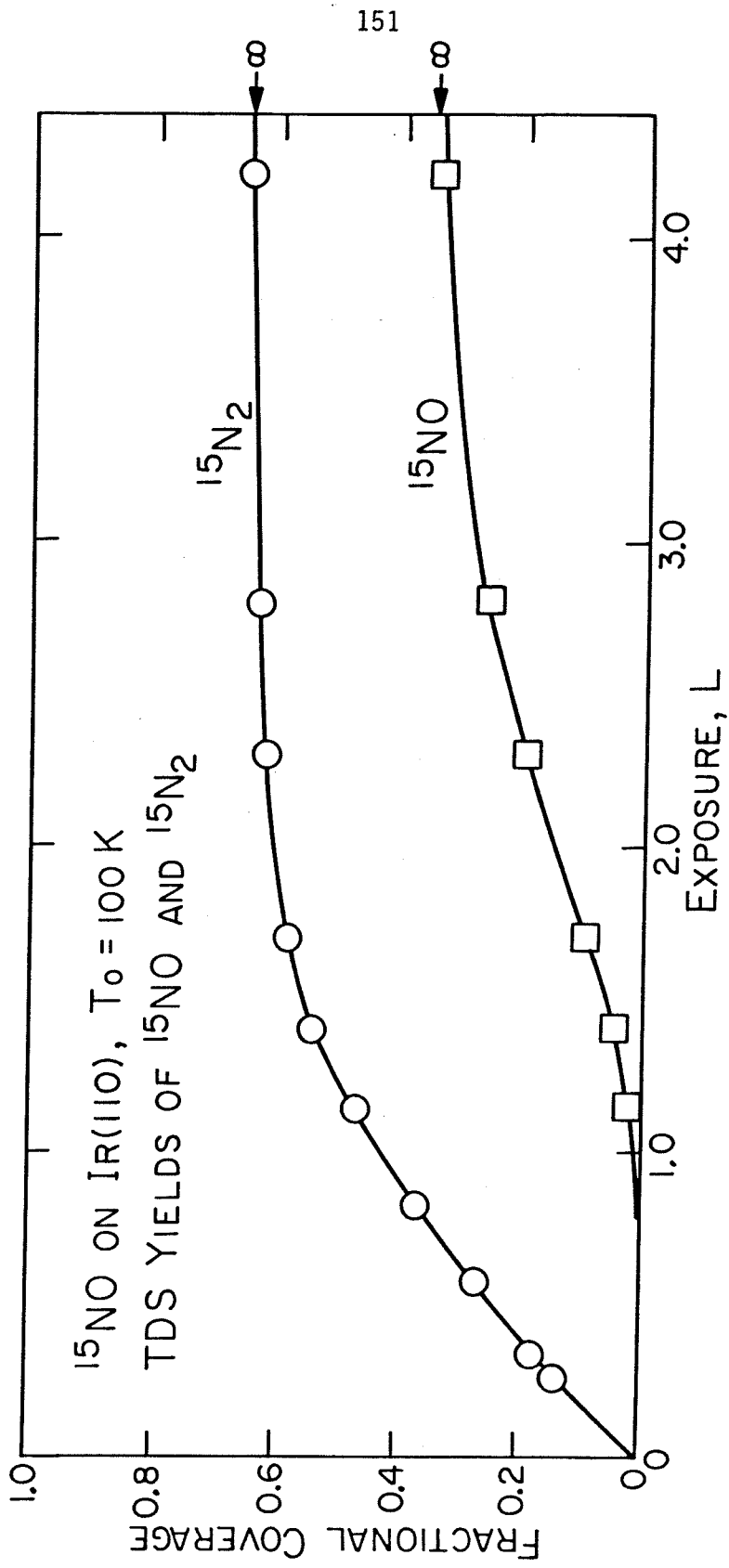


Figure 3

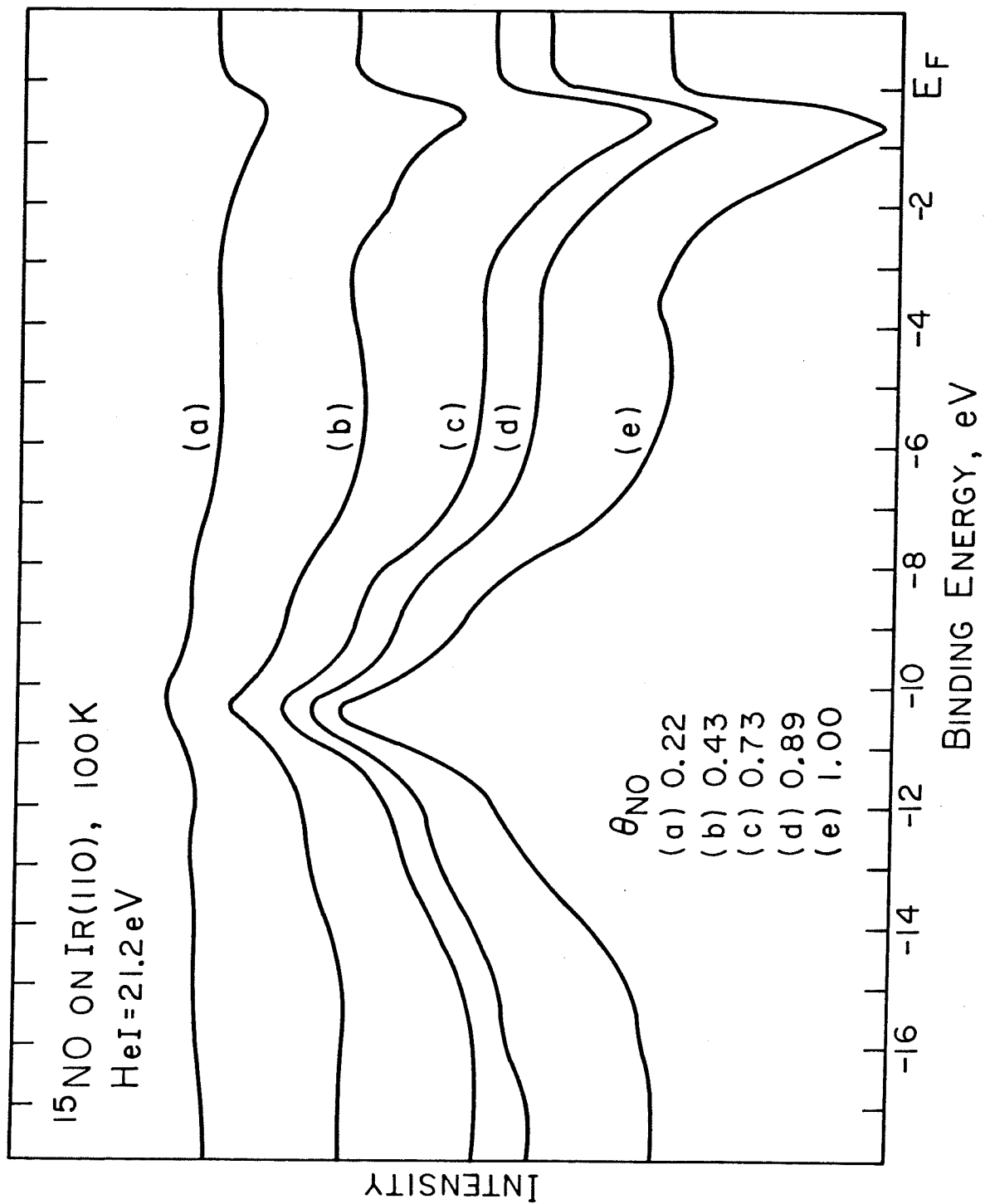


Figure 4

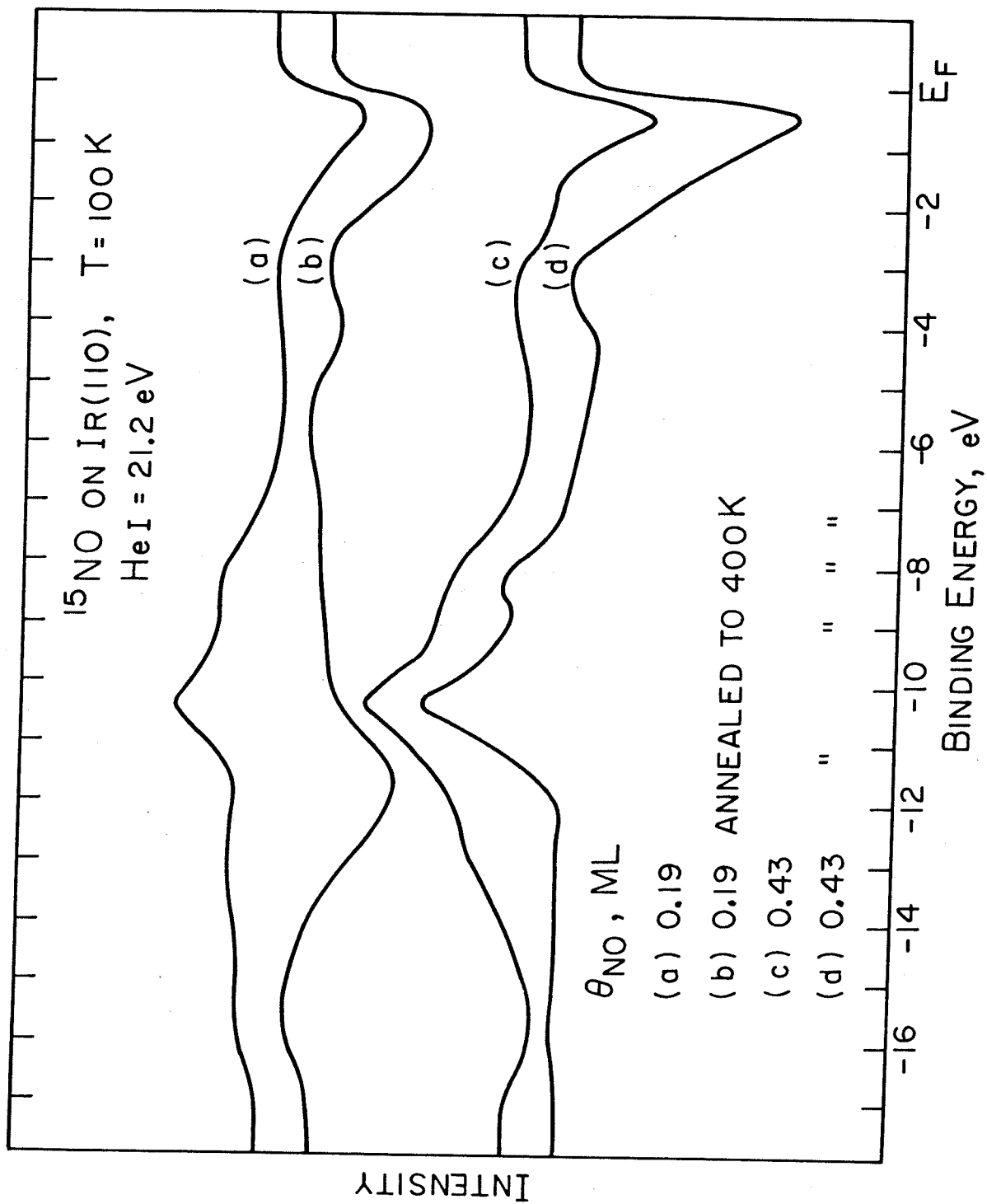


Figure 5

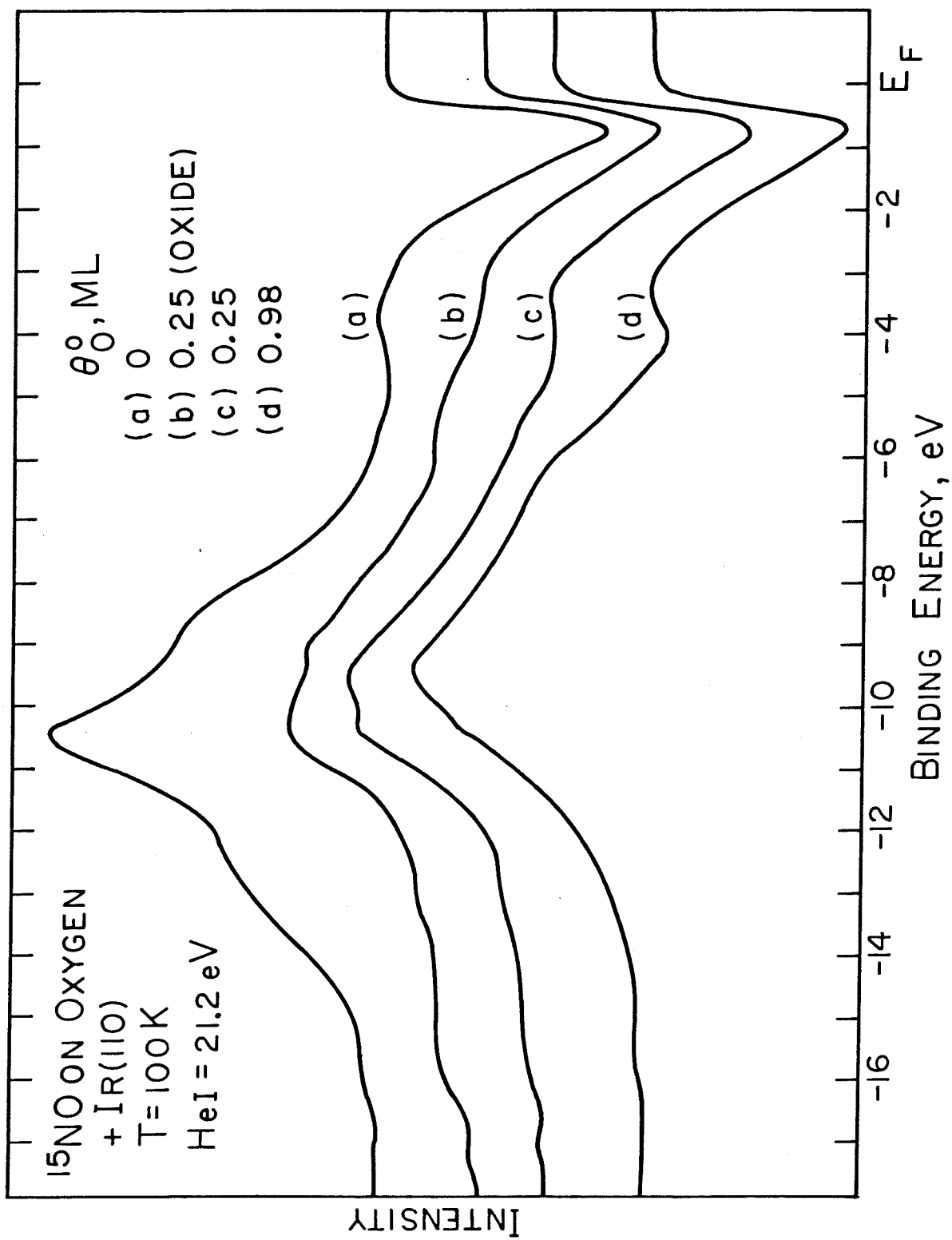


Figure 6

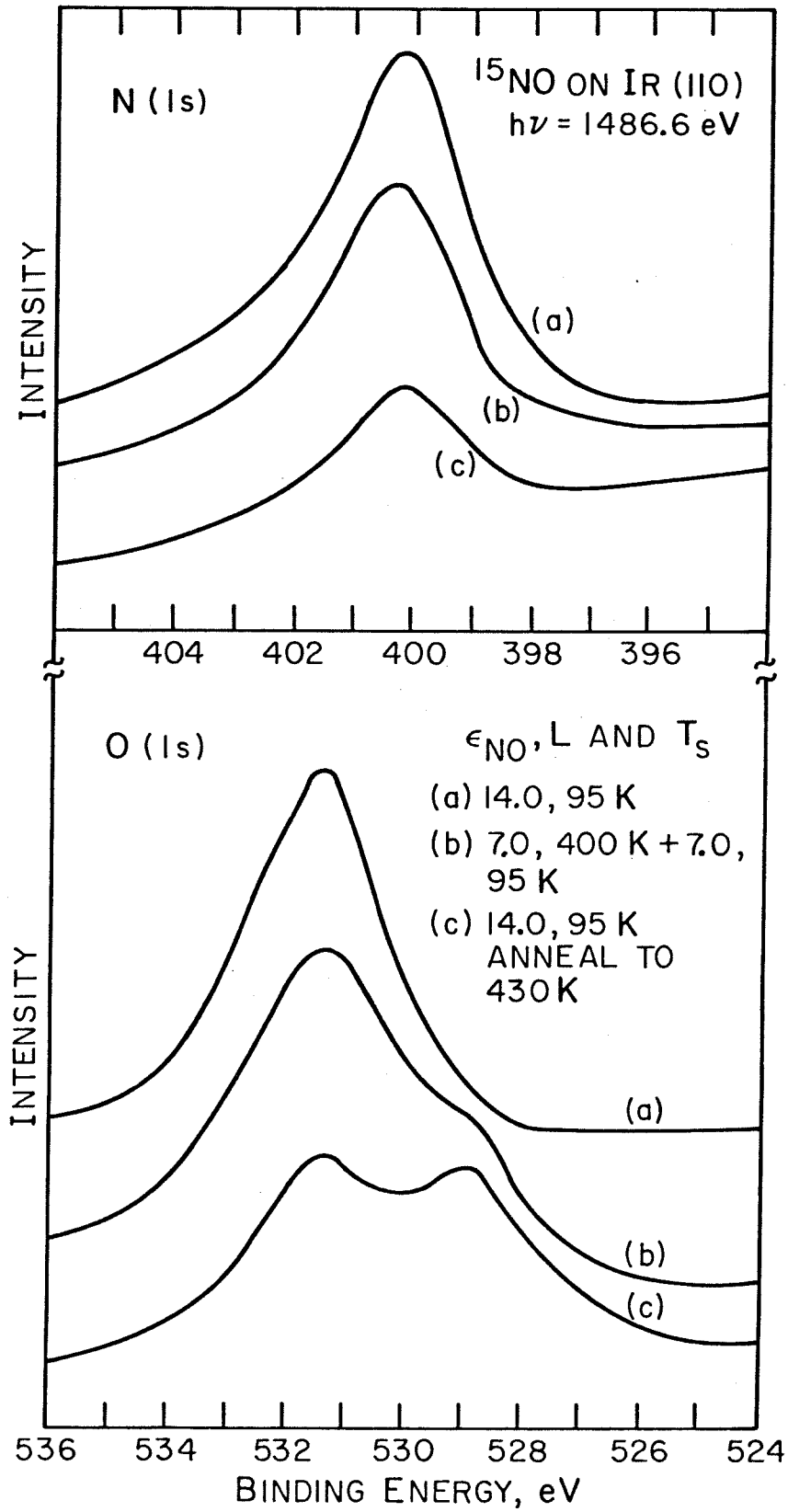


Figure 7

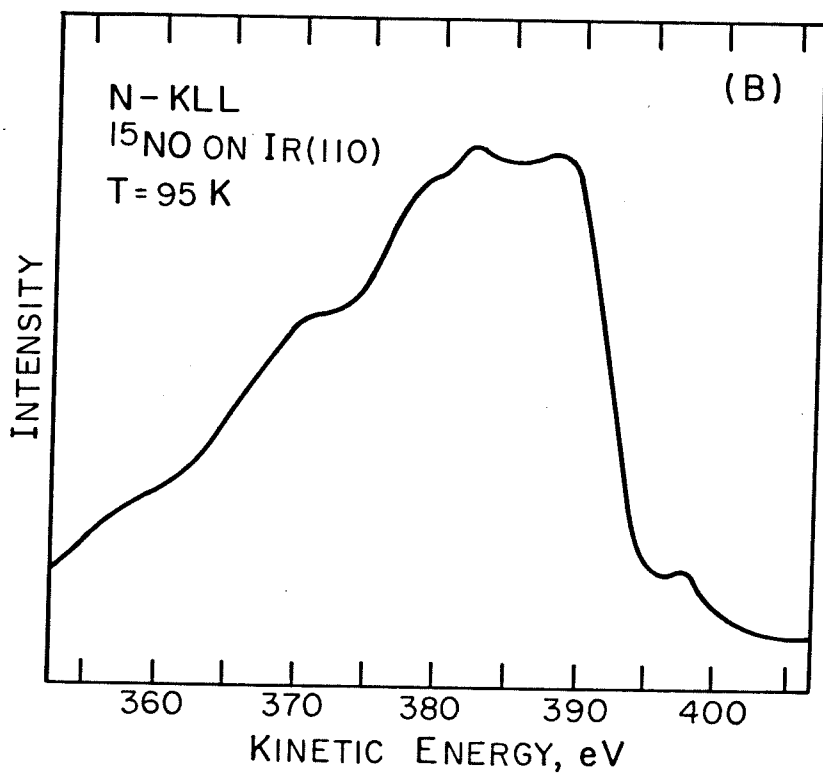
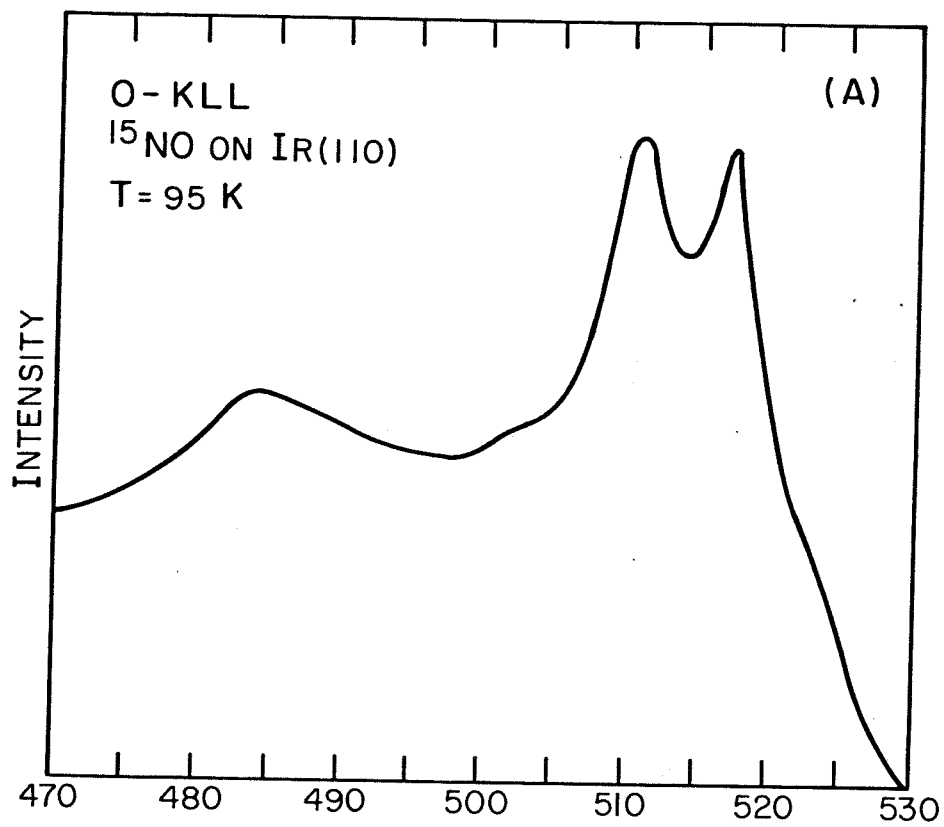


Figure 8

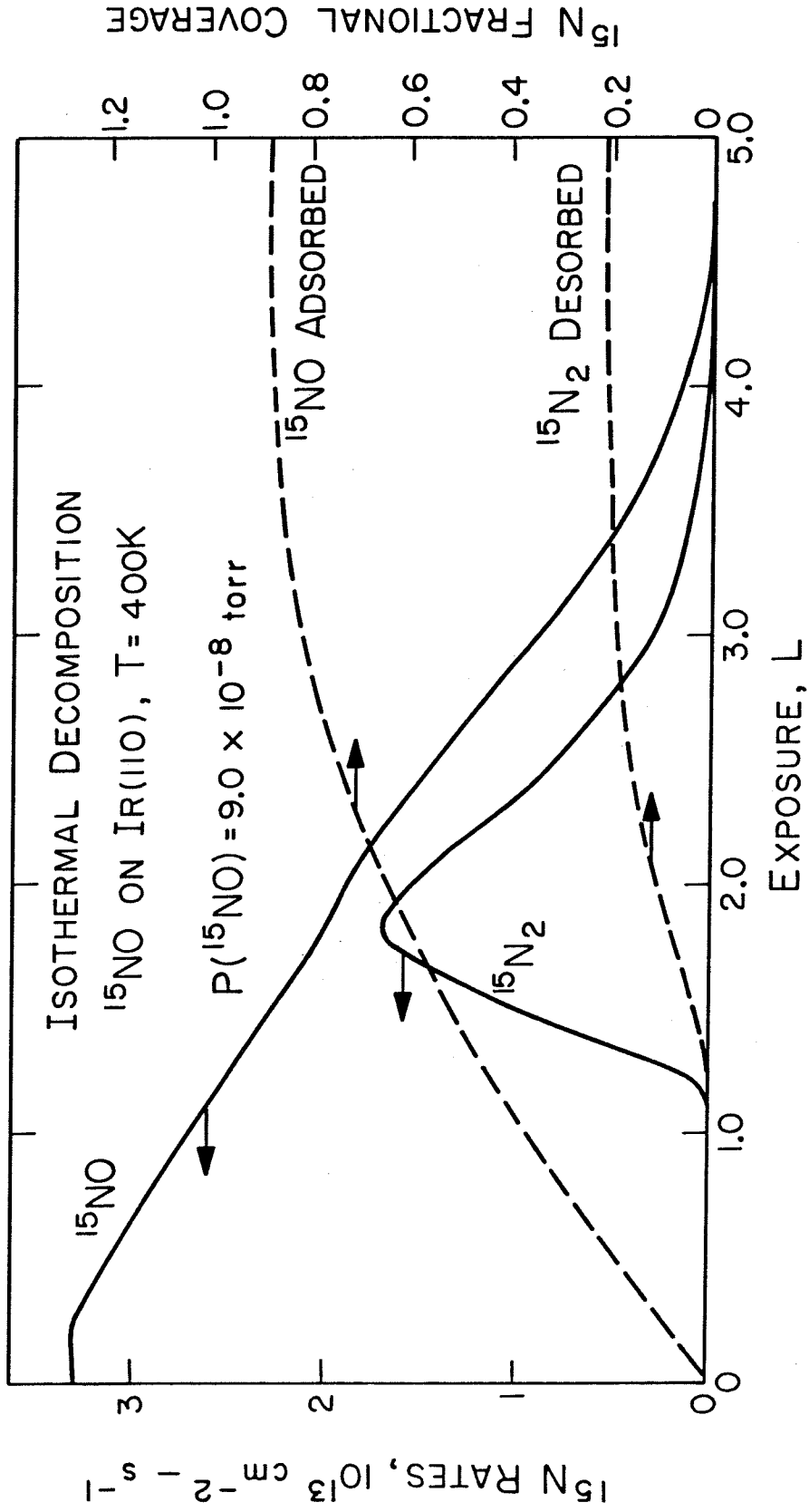


Figure 9

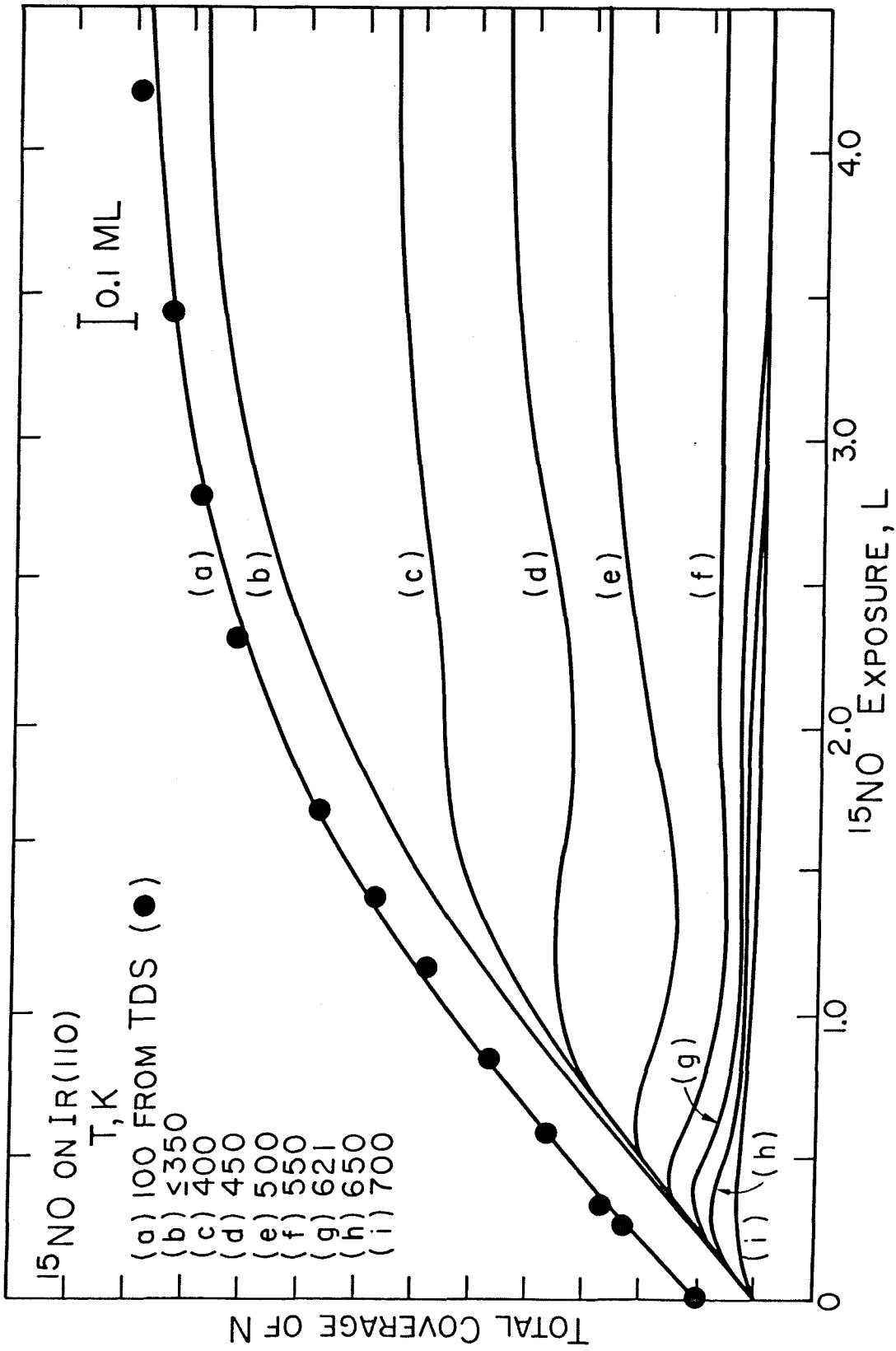


Figure 10

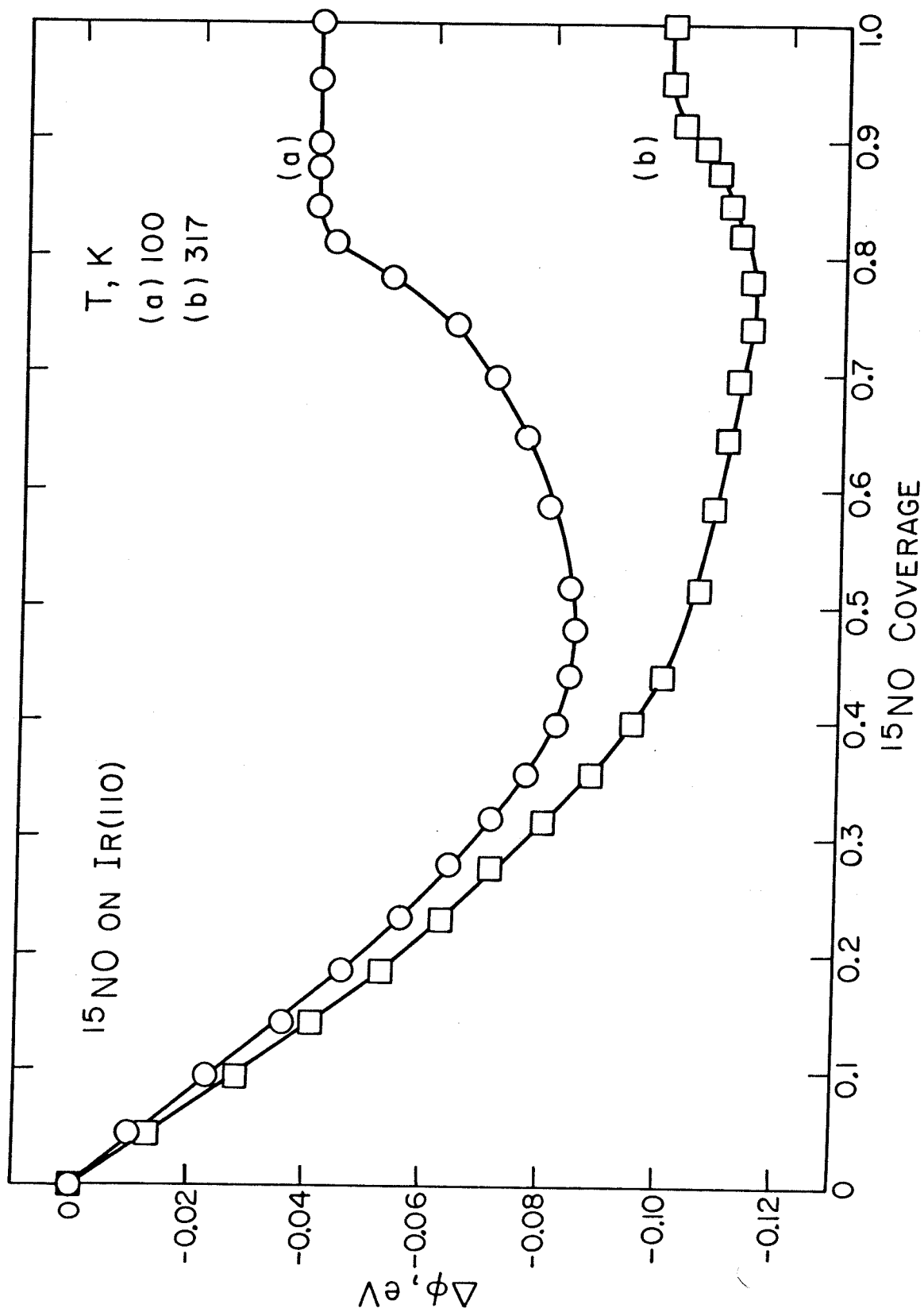


Figure 11

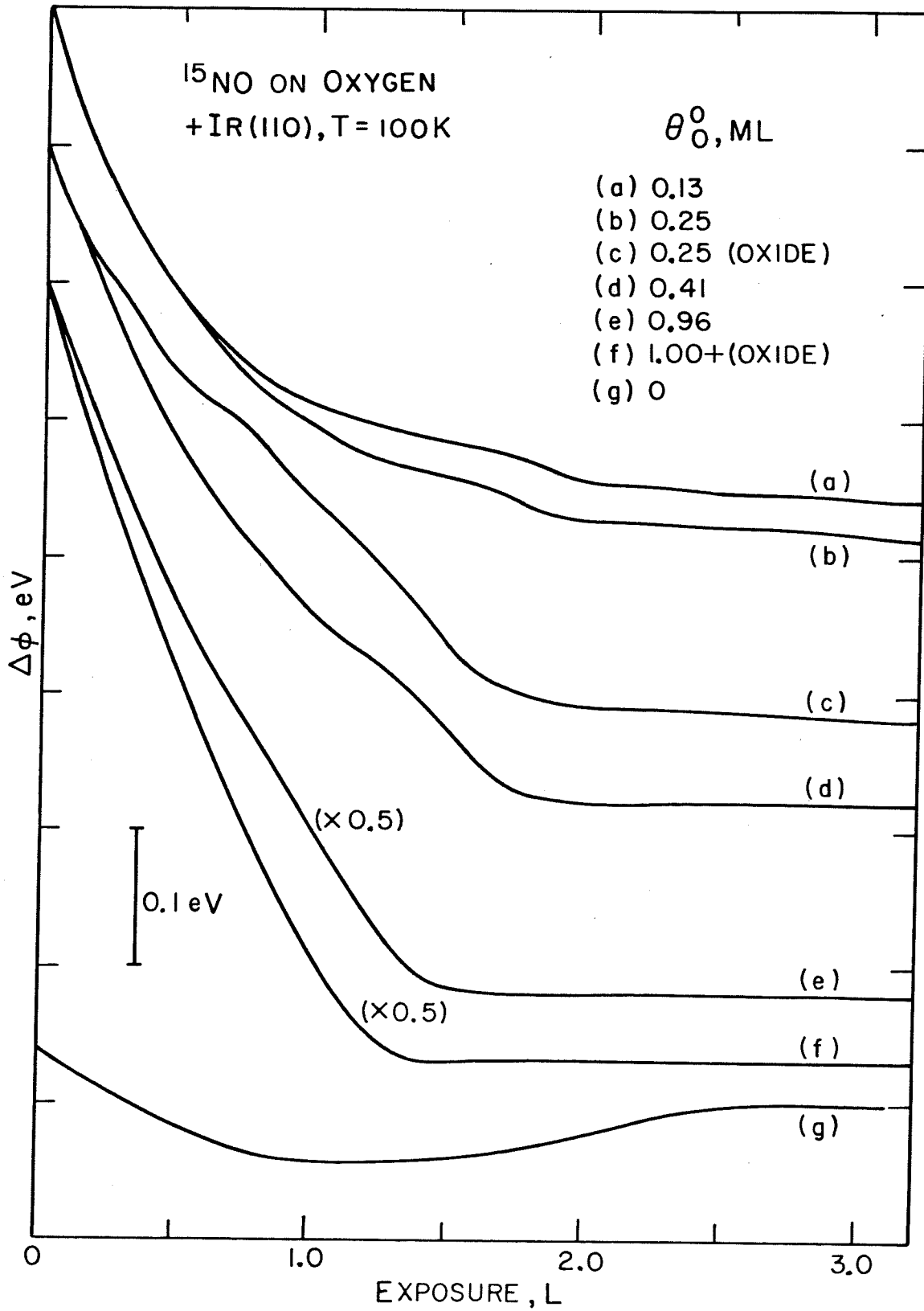


Figure 12

CHAPTER 6

THE REDUCTION OF NO WITH D₂ OVER IR(110)

(The text of Chapter 6 consists of an article coauthored with T. S. Wittrig and W. H. Weinberg that has been submitted to Surface Science.)

Abstract

The heterogeneously catalyzed reaction between NO and D₂ to produce N₂, ND₂ and D₂O over Ir(110) was investigated under ultra-high vacuum conditions for partial pressures of the reactants between 5 x 10⁻⁸ and 1 x 10⁻⁶ torr, total pressures between 10⁻⁷ and 10⁻⁶ torr, and surface temperatures between 300 and 1000 K. Mass spectrometry, LEED, UPS, XPS and AES measurements were used to study this reaction system. In addition, the competitive coadsorption of NO and deuterium was investigated via thermal desorption mass spectrometry and contact potential difference measurements to gain further insight into the observed steady state rates of reaction. Depending on the ratio of partial pressures ($R \equiv P_{D_2}/P_{NO}$), the rate of NO reduction to N₂ shows a pronounced enhancement when the surface is heated above a critical temperature. As the surface is cooled, the rate maintains a high value independent of temperature until a lower critical temperature is reached, where the rate drops uncontrollably. This hysteresis is due to a change in the structure and composition of the surface. For sufficiently large values of R and for an "activated" surface, N₂ and ND₂ are produced competitively between 470 and 630 K. Empirical models of the different regions of the steady state reaction are presented with interpretations of these models. Finally, the selectivity of Ir to form N₂ or ND₂ is discussed as compared to the other transition metals.

1. Introduction

The reduction of NO by deuterium has been studied on the Ir(110)-(1x2) surface under ultra-high vacuum conditions with thermal desorption mass spectrometry, LEED, X-ray and UV-photoelectron spectroscopies, Auger electron spectroscopy and contact potential difference measurements. Both transient and steady state conditions were investigated. The motivation for this study is to elucidate the mechanism of a heterogeneously catalyzed reduction reaction, using the NO/D₂ system as a model.

Although much has been reported concerning NO, hydrogen and CO chemisorbed on the transition metals, few studies are available for the heterogeneously catalyzed reduction of NO with either CO or hydrogen as the reducing agent. In ultra-high vacuum, the NO/H₂ system has been studied on polycrystalline Pt under steady state conditions (1), and the NO/CO system has been studied on the (111) and (110) surfaces of Pt (2) and polycrystalline Rh (3) under transient conditions via thermal desorption mass spectrometry. At atmospheric pressure the reduction of NO with CO or hydrogen under steady state conditions was conducted over supported Pt, Pd, Rh and Ru (4,5). It is more pertinent to discuss the results cited for the reduction of NO with hydrogen than with CO in the present context of the reaction between NO and D₂ on Ir(110).

Depending on the ratio of partial pressures of H₂ and NO ($R \equiv P_{H_2}/P_{NO}$) under steady state reaction conditions, the products were H₂O, N₂, NH₃ and N₂O on polycrystalline Pt for surface temperatures between 300 and 900 K and a total pressure of approximately 10⁻⁷ torr (1). It was suggested that the

limitation of the reduction reaction is related to the dissociation of NO (1). For $R = 1/2$, the major products are N_2 and H_2O with N_2O formed as a minor product. However, for $R = 5$ (excess hydrogen), NH_3 , N_2 and H_2O are observed. In this case, NH_3 competes strongly for nitrogen adatoms that are formed from the dissociation of NO. The reaction maximum at 495 K for the formation of NH_3 ($R = 5$) on polycrystalline Pt (1) agrees well with the reaction maximum at 500 K observed on supported Pt at atmospheric pressure (4). Good agreement is observed for the temperature at which 50% reduction of NO occurs for similar R values (1,4). Thus, a connection has been established in this case between these widely different pressures ranges.

The investigations of the NO/ H_2 system over the supported metals (4,5) reveal the selectivity of each catalyst with regard to the products formed. The overall reduction activity observed for NO/ H_2 ($R = 4$) is $Pd > Pt > Rh > Ru$ using the temperature at which 50% of the NO is reduced as the criterion. However, the major products formed are different among the metals. For Pd and Pt, NH_3 is formed preferentially; whereas for Rh and Ru, N_2 is the major product formed (4), more so for Ru. The relationship between the product distribution in the reduction reaction and the facility of the metal to dissociate NO may well be the factor that determines the behavior of each metal. The ease of dissociation of NO occurs in the following order: Pd (6,7) < Pt (1,2,8,9) < Rh (3) < Ru (9 - 11). The activity for NO dissociation on Ir (12 - 16) places this metal between Pt and Rh. Therefore, it would be expected that the product distribution for the NO/ H_2 system over Ir would be intermediate between Pt and Rh when the reduction reaction is performed under steady state condi-

tions. This postulate will be tested for the present case of NO/H₂ over Ir(110).

The steady state reaction of NO and deuterium over Ir(110) has been examined for the partial pressure of the reactants varying from 5×10^{-8} to 1×10^{-6} torr, the total pressures varying from 1×10^{-7} to 1×10^{-8} torr, the surface temperature varying from 300 to 1000 K, and ratios of the partial pressures of the reactants, $R(P_{D_2}/P_{NO})$, varying from 1/2 to 20. Both reactants and products were monitored with mass spectrometry during the steady state reaction. In order to assess the chemical composition of the overlayer under various conditions, XPS and UPS measurements were performed. The degree of order in the overlayer-substrate system was monitored using LEED.

In addition, the nonreactive coadsorption of NO and deuterium at low temperature has been investigated on Ir(110) as well as the rate of the transient reaction upon heating the surface on which these overlayers are present. Contact potential difference measurements of deuterium (NO) exposed to a surface partially covered with preadsorbed NO (deuterium) provide further insight into the competitive chemisorption of the two reactants. These data will supplement the previous studies of the chemisorption of NO (16) and deuterium (17) on Ir(110) and will aid in the interpretation of the steady state reduction reaction between NO and deuterium.

2. Experimental Details

The experiments were performed in an ion pumped stainless steel belljar that has been described previously (17,18). The base pressure was less than 2×10^{-10} torr of reactive contaminants. A clean Ir(110) surface shows a (1x2)

reconstruction, which is a surface with every other row of Ir atoms missing in the [001] direction (19). The surface may be visualized as alternate rows and troughs exposing (111) planes inclined to one another. Isotopic ^{15}NO and D_2 [which has identical adsorption properties as H_2 on Ir(110)] were used in both the transient and steady state experiments to separate the mass spectrometric intensities for each of the products and reactants. Monitored species are D_2 (4), D_2O (20), $^{15}\text{ND}_3$ (21), $^{15}\text{N}_2$ (30), ^{15}NO (31), $^{15}\text{N}_2\text{O}$ (46), and $^{15}\text{NO}_2$ (47). With the exception of the figure captions, the ^{15}N species will be referred to without the superscript hereafter.

For both the transient and the steady state experiments, NO was exposed to the surface using a directional beam doser, where the pressure of the beam has been calibrated with the pressure of the storage bulb that supplies the dosing gas (16). During the transient experiments involving coadsorbed overlayers of deuterium and NO, exposures of D_2 were performed via a leak valve. However, for the steady state reaction of D_2 and NO, both partial pressures of the reactants were exposed to the surface via the directional beam doser. A known partial pressure of each gas was admitted to the storage bulb of the doser. The partial pressures of the gases are calculated from the calibration for each gas, which is measured separately. For example, one torr of NO or D_2 in the storage bulb is approximately equal to 1.1×10^{-7} or 1.3×10^{-7} torr in the dosing beam, respectively. The calibration appropriate for the separate gases was the same as that when NO and D_2 were mixed in the bulb. The total pressure in the storage bulb was limited to 10 torr which is upper bound to the pressure that could be measured by the capacitance monometer (MKS Instru-

ments). Since the doser and the crystal were positioned so that part of the gases desorbing from the crystal are in line-of-sight of the mass spectrometer, the intensities of the reactants and products could be measured directly (although this is not crucial to the results). Also, the gas flux from the doser does not load the ion pumps causing pumping speed variations since the beam-to-background pressure ratio for NO is approximately 100:1. Another advantage of the beam method is that wall effects caused by backfilling the reactor are minimized.

The steady state reaction sequence is as follows. For a given pressure ratio R and a total pressure P_T , the surface was annealed in vacuum above 1600 K to remove any contaminants. The surface was allowed to cool to near room temperature before it was exposed to the beam of reactants for 10 minutes to saturate the adsorbed overlayer fully. Then, the surface was heated ($< 0.5 \text{ K} \cdot \text{s}^{-1}$), and the reactant and product intensities were measured with each sample every three seconds. Upon reaching the maximum temperature desired, the surface was cooled at approximately the same rate to near room temperature. In many temperature cycles, the temperature was held at various points for several minutes to ensure a steady state rate had been established. Under the chosen reaction conditions ($R \geq 1/2$), the intensity of D_2 did not vary measurably, and neither N_2O nor NO_2 were observed.

3. Coadsorption of NO and Deuterium

When NO is exposed to low precoverages of deuterium on Ir(110) at 100 K, the adsorption kinetics of NO are unchanged from NO adsorbed on a clean sur-

face (16), as evidenced by the combined thermal desorption yields of NO and N₂. Figure 1 presents thermal desorption spectra of NO, N₂, D₂O and D₂ from Ir(110). The surface was precovered first with 0.33 ML deuterium at 100 K, which saturates the most tightly bound state of deuterium (17), and subsequently various exposures of NO were applied. Heating the surface (20 K - s⁻¹) produces various amounts of the desorption products, depending on the initial exposure of NO. Although the saturation coverage of NO (9.6×10^{14} cm⁻²) is not affected by preadsorbed deuterium, the yields of NO and N₂ are different than that from the clean surface. Approximately 23% of the NO present initially desorbs as NO at saturation in Fig. 1, whereas 35% desorbs as NO from the clean surface (16). However, the fraction of NO desorbing from the high temperature feature is unchanged from the clean surface (18%) and represents desorption from a surface with oxygen present (16). The fraction of NO desorbing from the low temperature featured is decreased (at saturation) from 17% to 5% when deuterium is preadsorbed. This feature represents desorption of NO from a surface free of oxygen. The temperature and shape of the desorption features of NO and N₂ are unchanged in Fig. 1 from the clean surface. Therefore, low coverages of deuterium affect only the distribution of NO and N₂, i.e. the selectivity of the reaction for nitrogen desorption.

The desorption of D₂ in Fig. 1 is affected strongly by the presence of increasing coverages of NO as compared to the clean surface. The fractional coverages of D₂ calculated from the thermal desorption spectra among the five desorption curves of D₂ and D₂O was in the range 0.33 to 0.43 ML and varies by the coverage range since some background D₂ adsorbs on the surface during

the exposure to NO. Two peaks appear near 240 K and 490 K for the desorption of D_2 when the surface is saturated with NO compared to a single peak at 390 K when the surface is clean. The peak at 240 K is in the temperature region where D_2 desorbs from the low temperature state of deuterium (hydrogen) when present at higher coverages on the clean surface (17). Moreover, contact potential difference (CPD) measurements indicate that NO shifts deuterium from the high temperature state to the low temperature state as NO chemisorbs at 100 K, as presented later. After the desorption maximum of D_2 at 240 K is passed, a desorption peak for D_2O occurs when the deuterium layer is saturated with NO as seen in Fig. 1. Some dissociation of NO takes place below 300 K to cause D_2O to be formed, although the yield of D_2O is small since the curves are expanded by a factor of 25. Approximately 5% of the NO dissociates during adsorption near 300 K when deuterium is absent from the surface (16), and it may be approximately the same fraction that dissociates as the surface is heated in this case. The higher temperature peaks of D_2 (490 K) and D_2O (440 K) are of low intensity but are quite broad. These occur in the same temperature range where N_2 and NO desorb. In this region, the surface has large coverages of oxygen and NO and has low coverages of deuterium and nitrogen adatoms. As the temperature increases, the concentration of deuterium adatoms decreases causing the formation of D_2 to dominate over D_2O due to the larger mobility of deuterium compared to oxygen and due to diatomic recombination (D_2) being more likely than triatomic recombination (D_2O).

Thermal desorption spectra of reaction products from a surface prepared with a saturated layer of NO under three different conditions and then exposed

to 2 L D_2 are presented in Fig. 2. As in Fig. 1, the yield of D_2O is low compared to D_2 , but in Fig. 2 the yield of D_2 is lower than in Fig. 1. The desorption of D_2 at high temperature occurs as NO and N_2 desorb in Fig. 2, as in Fig. 1. Again, the temperature at which N_2 and NO desorb is not affected by exposures of D_2 if the overlayer of NO is saturated at 100 K. Also, the distribution of N_2 and NO is not affected and is the same as if no deuterium were adsorbed. However, the desorption results for the other two surface preparations are not so obvious. The concentration of deuterium that chemisorbs does not depend in a simple way upon the coverage of NO and the coverage of oxygen. Adsorbing NO at 450 K, cooling and exposing to 2 L D_2 at 100 K causes the surface composition to be 0.51, 0.31 and 0.20 fractional coverages of oxygen, NO and deuterium, respectively. Saturating the surface at 100 K with NO and then exposing to 2 L D_2 allows 0.33 fractional coverage of deuterium to chemisorb. Annealing the saturated overlayer of NO at 100 K to 400 K, cooling to 100 K and exposing to 2 L D_2 causes the surface composition to be 0.32, 0.51 and 0.23 fractional coverages of oxygen, NO and deuterium. Also, 2 L D_2 exposed to a saturated oxygen overlayer results in the adsorption of approximately 0.3 ML of deuterium. Thus, saturated overlayers of NO or oxygen (individually) do not block the adsorption of deuterium as does co-adsorbed NO and oxygen. Saturating the surface with oxygen and then saturating further with NO (< 0.5 ML) blocks deuterium adsorption completely. This observation will be pertinent to the steady state reaction of NO and D_2 presented in the following section. Finally in Fig. 2, the desorption temperature for D_2O and the yields of N_2 and NO depend on the relative initial surface coverages of NO and oxygen. Adsorbing NO at 450 K and adsorbing deuterium at low temperature allows deuterium to

react with oxygen to form D_2O more readily than the other two surface preparations in Fig. 2. Comparing the NO/N_2 desorption yields in this case and for the surface prepared by annealing a saturated overlayer of NO to 400 K shows that the presence of oxygen tends to cause increasing amounts of NO to desorb rather than N_2 , as observed when no deuterium is present (16).

As an additional technique to gain insight into the competitive adsorption of NO and deuterium (hydrogen), CPD measurements of NO (D_2) on deuterium (NO) overlayers were performed on Ir(110) at 100 K. The CPD of NO is presented in Fig. 3 as a function of fractional coverage for NO adsorbed on (a) a clean surface, and (b) a surface with 0.33 ML deuterium adsorbed initially [β_2 -state (17)]. The CPD of NO in Fig. 3(a) has been reported previously (16) but is reproduced here for comparison. Note that the CPD of NO decreases weakly with coverage, attains a minimum near 0.5 ML and increases slightly near 0.8 ML as the completion of a disordered overlayer superstructure is reached (16). However, the CPD of NO in Fig. 3(b) exposed to the β_2 -state of deuterium shows a much larger decrease and a different shape than Fig. 3(a). As seen in Fig. 1, the β_2 -state of deuterium is displaced by NO into the β_1 -state. Also, for the chemisorption of deuterium on Ir(110) (17), the CPD of deuterium increases by 0.30 eV for the β_2 -state and decreases weakly with coverage for the first adsorption sites sampled in the β_1 -state. Therefore, the change in the CPD behavior of NO in Fig. 3(b) [β_2 -state adsorbed] from Fig. 3(a) [clean] is due to the displacement of deuterium in the β_2 -state to the less tightly bound β_1 -state.

If this displacement reaction obeys a linear relationship with the coverage

of NO, then the difference between Figs. 3(a) and 3(b) would be a straight line, but this is not the case as can be visualized from the data in Fig. 3. The displacement of deuterium by NO from its preferred sites as measured by the CPD indicates that either the degree of displacement does not occur linearly with respect to the coverage of NO or that NO and deuterium do not maintain their clean surface dipole moments independent of one another. Both situations are plausible. If the difference between the CPD values in Figs. 3(a) and 3(b) are considered at the saturation coverage of NO, this may give the CPD change for converting deuterium from β_2 - to β_1 -sites. The value is equal to -0.33 eV and would be equal to -0.40 eV if NO and deuterium acted independently to compete for the β_2 -sites. Thus, it is more instructive to view these measurements only as showing that the conversion does occur, verifying the TDS results in Fig. 1.

The CPD of deuterium (or hydrogen) monitored as a function of exposure to a surface with different precoverages of NO provides complementary data to that of Fig. 3, and these results are shown in Fig. 4. In Fig. 4(A), the CPD of deuterium is presented over the exposure range required to saturate the β_2 -state, and in Fig. 4(B) the CPD of deuterium is shown over that part of the exposure range pertinent to the β_1 -state. Recalling that for the β_2 -state of deuterium the CPD increases by 0.30 eV on the clean surface, it is clear that the β_2 -adsorption sites are blocked strongly as the coverage of NO increases. For a saturation coverage of NO, the CPD of deuterium does not change [curve (c)] indicating that the β_2 -sites of deuterium are blocked completely. Since the adsorption kinetics of deuterium were not measured as a function of the pre-

coverage of NO, the relationship between the coverage of NO and the coverage of deuterium cannot be quantified further. Over the exposure range of the β_1 -state of deuterium in Fig. 4(B), NO (qualitatively) blocks these sites as well. Note that the zero in Fig. 4(B) has been shifted to the value of the CPD at 0.25 L D₂ in Fig. 4(A). For an initial coverage of NO equal to 0.23 ML, the CPD of deuterium as a function of exposure is the same as that of the clean surface. For higher coverages of preadsorbed NO, the CPD does not change as strongly with the exposure to deuterium, indicating a decreased probability for chemisorption.

In summary, the co-adsorption of deuterium and NO has been studied with TDS and CPD measurements to gain insight into the competition between the two adsorbates for adsites and to ascertain if the desorption properties of NO, N₂ and D₂ are different from the adsorption of NO and deuterium alone. Saturating a surface that is precovered with the β_2 -state of deuterium (0.33 ML) with NO gives the same saturation coverage of NO, but upon desorption more N₂ desorbs (from the dissociation of NO) than from a surface with no deuterium present. The desorption shapes and peak temperatures of NO and N₂ are not perturbed by the presence of deuterium, but the desorption of D₂ is changed strongly from the clean surface in the presence of NO. Saturating the surface with NO does not block the subsequent adsorption of deuterium completely. However, an overlayer saturated with NO and oxygen, a condition that occurs during the steady state reaction at low temperatures (see the following section), completely blocks deuterium from chemisorbing. On a surface free of oxygen, NO displaces deuterium from its preferred sites (β_2) in the missing row

trenches into the less tightly bound sites (β_1) along the (111) microfacets exposed on the Ir(110)-(1x2) surface (17).

4. Steady State Reaction between NO and Deuterium

The reduction of NO with deuterium over Ir(110), as measured by mass spectrometry under steady state conditions, is presented in this section. The procedure used to carry out the steady state experiments was described in Section 2. Under all conditions examined, i.e., partial pressure ratios between 1/2 and 20 ($R = P_{D_2}/P_{NO}$), temperatures between 300 and 1000 K and total pressures between 5×10^{-8} and 1×10^{-6} torr, the partial pressure of D_2 did not vary significantly ($< 10\%$), and no N_2O or NO_2 was observed. Typically, the time required to produce a reaction cycle was between 30 and 60 minutes, where a cycle refers to heating to the maximum temperature desired and cooling to near room temperature. During a reaction cycle, the pressure in the storage bulb (see Section 2) that supplies the reaction mixture to the Ir(110) catalyst decreased by less than 5% in any particular experiment, and this decrease could be accounted for as necessary since the decrease is approximately linear with respect to time. Finally, the gain of the mass spectrometer that was used to monitor the reactants and products during the steady state reaction was measured after each set of reaction cycles in order to compare relative reaction rates between several sets of data.

Reaction cycles corresponding to a set of four ratios of partial pressures ($R = 1, 2, 4, 8$) at $P_{NO} = 1 \times 10^{-7}$ torr are shown in Figs 5(A)-5(D), presenting the mass spectrometric intensities of NO, N_2 , D_2O and ND_3 [Fig. 5(D) only] as a

function of surface temperature. The intensity has been shifted between each specie for clarity. Arrows on each curve indicate whether the surface temperature is increasing or decreasing. The initial rise in N_2 production near 440 K is seen always in the first reaction cycle for all reaction conditions presented here, but never in succeeding reaction cycles if the surface is not cleaned of oxygen. This rise in N_2 production is not followed by a decrease in the NO intensity or by an increase in the D_2O intensity as required by mass balance. The N_2 peak is due to the surface initially containing a large coverage of NO near room temperature converting to a surface containing a large coverage of oxygen and NO. Thus, the surface conversion causes an *apparent* increase in the steady state rate of N_2 production. Rather, this initial desorption of N_2 is a *nonsteady state conversion* which depends only upon the rate at which the surface is heated. A second maximum in the rate of production of N_2 that occurs near 540 K is seen in most reaction cycles, and this is followed by a decrease in the intensity of NO and an increase in the intensity of D_2O . Consequently, this is due to a steady state reaction condition. However, part of this peak may be due to the surface conversion of some chemisorbed oxygen to a surface oxide which begins to form near this temperature (20), or it may be associated with a peak seen in thermal desorption spectra of NO and N_2 (16).

Returning to Fig. 5, as the surface temperature increases in Fig. 5(A), the N_2 and D_2O production increases with a concomitant decrease in the measured intensity of NO. The temperature was decreased after attaining a maximum value of 980 K, and a slight hysteresis occurred, i.e., a different rate of reaction is measured at the same temperature compared to when the surface is heated.

Below 600 K, the rate of N_2 production did not follow the upward reaction curve for the reason stated earlier concerning the "clean surface" conversion to one which contains a surface oxide as well as chemisorbed oxygen. Succeeding cycles for surfaces not cleaned by annealing to 1600 K follow closely the curve for decreasing temperature in the first cycle.

In contrast to the results for R equal to one in Fig. 5(A), the reaction for R equal to two and four in Figs. 5(B) and 5(C) is quite different at high temperatures. As the temperature increases, a plateau is reached in N_2 production that, once reached, persists at lower temperatures. An abrupt increase in D_2O production occurs at the onset of the N_2 plateau and thereafter maintains a constant value as well. As the temperature decreases further, the rate of N_2 production (NO reduction) decreases and eventually reaches the value observed as the surface temperature increased. Both the onset and the dropoff of the N_2 plateau depend upon the value of R as seen in Figs. 5(B) and 5(C). As P_{D_2} increases the temperature of the onset and the dropoff in the N_2 plateau both decrease. Moreover, the magnitude of the rate increases with P_{D_2} , noting that the reaction curves have been expanded differently. Although a constant rate of D_2O production is seen in Fig. 5(D) as the temperature is decreased, the rate of N_2 production does not remain constant. The decrease in N_2 production is due to the production of ND_3 that competes for nitrogen adatoms. The rate of production of ND_3 reaches a maximum near 560 K.

Doubling the pressure of NO (P_{NO}) for $R = 2$ inhibits the formation of an N_2 plateau in the rate, as seen in Fig. 6(A). These curves are similar to those in Fig. 5(A) in that both do not contain a plateau, but some hysteresis occurs at

high temperature. Thus, the existence of a plateau (high reduction rate) does not depend on R only, but depends also on the absolute value of P_{NO} . Doubling P_{D_2} [compare Figs. 6(B) and 6(A)] causes the N_2 plateau to appear near 840 K, and the curves are similar to those of Figs. 5(B) and 5(C).

The last set of reaction curves is presented in Fig. 7 where the production of ND_3 is maximized by the use of a low pressure of NO and large values of R . For $P_{NO} = 5 \times 10^{-8}$ torr and $R = 8$ [Fig. 7(A)], the plateau in the rate of N_2 production occurs near 700 K, accompanied by an abrupt increase in D_2O production, as seen before. As the temperature decreases, the N_2 intensity varies more strongly than was observed in Fig. 5(D) where ND_3 was first detected. In fact, a relative minimum and relative maximum occur in the N_2 curve which is directly associated with the maximum rate of production of ND_3 appearing near 540 K. Once the relative maximum in N_2 production is passed at 520 K, the rate of reaction falls uncontrollably, and the shape of the dropoff depends upon the rate of temperature decrease, i.e., the rate decreases in a smaller temperature range than shown here.

The final reaction cycle, presented in Fig. 7(B), represents the most favorable conditions to produce ND_3 examined on $Ir(110)$, namely, $P_{NO} = 5 \times 10^{-8}$ torr and $R = 20$. In Fig. 7(B), the onset of a high rate of reaction does not occur abruptly, as seen previously. Moreover, a small rate of ND_3 production occurs as the temperature increases. As the surface temperature decreases, the competition between N_2 and ND_3 production favors the formation of ND_3 which reaches a maximum near 530 K. This can be seen by a mass balance of ND_3 and N_2 with respect to NO . Again, the rate of N_2 production attains a relative

maximum as the ND_3 production falls to zero.

In summary, Figs. 5-7 provide representative data that may be used to gain insight into the competing processes which are important during the steady state reduction of NO with D_2 (or H_2). It is apparent that the formation of N_2 and ND_3 compete strongly for nitrogen adatoms, provided by the decomposition of NO , when a large excess of D_2 is present in the reaction mixture. Other factors depend strongly on the values of R as well, such as whether or not a plateau in N_2 production is formed, the magnitude of the reduction rate, and the temperature range over which the N_2 plateau is stable. Three reaction regimes are of interest: (1) The reduction reaction in the "unactivated" region regardless of whether or not a plateau exists in the reaction cycle, (2) The plateau in N_2 production, and (3) ND_3 production. Each of these reaction regimes will be examined with respect to the structure of the overlayer and substrate, composition of the adlayer, and the pressure dependences on the reactants for the rate of reduction.

Three N_2 production cycles are shown in Fig. 8 that were presented in the previous figures but are expanded to show clearly the changes caused by varying the partial pressures of the reactants. Increasing P_{NO} at a constant P_{D_2} [Figs. 8(b) and 8(c)] increases the temperature for the onset and dropoff of the N_2 plateau, increases the rate of N_2 production on the plateau, and decreases the rate of N_2 production before the plateau is reached. The latter two observations are for a constant temperature that allows the same reaction regime to be compared. Maintaining P_{NO} constant and increasing P_{D_2} [Figs. 8(a) and 8(b)] decreases the temperature for the onset and dropoff of the N_2 plateau

and increases the rate of N_2 production both on the plateau and before the plateau.

In order to gain insight into the reduction reaction when N_2 is the primary nitrogen-containing product, the dependence of the rate below and on the N_2 plateau and the dependence of the temperature for the onset and dropoff were fit empirically as a power law of the partial pressures of the reactants. For the rate of N_2 production at low rates (T increasing), in the presence or absence of a plateau, the rate may be expressed as

$$R_{N_2} = c P_{NO}^{-1/2} P_{D_2} \quad (1)$$

at a constant temperature. Also, on the N_2 plateau at temperatures where N_2 only is produced, the rate of N_2 production is described by

$$R_{N_2} = c' P_{NO} P_{D_2}^{1/2}. \quad (2)$$

Referring to Fig. 9, the temperature (T_h) and pressure dependences of the onset of the N_2 plateau obey the following relation

$$\ln[P_{NO}^{3/2} P_{D_2}^{-1}] = \frac{\Delta E_1}{k T_h} + \ln A_1 \quad (3)$$

where A_1 is a preexponential factor and ΔE_1 , equal to -11.2 kcal-mole $^{-1}$, is an energy difference between two competing processes. Finally, the empirical expression that fits the temperature dependence of the dropoff (T_l) in the N_2 plateau is

$$\ln[P_{NO}^{3/2} P_{D_2}^{-1/2}] = \frac{\Delta E_2}{k T_l} + \ln A_2$$

(4)

where A_2 is a preexponential factor and ΔE_2 , equal to $-8.3 \text{ kcal-mole}^{-1}$, is an energy difference between two competing activated processes. Each of these expressions will be discussed in Section 6.

For a given set of partial pressures of D_2 and NO , the rate of reaction of N_2 (below the plateau) as the surface temperature increases may be written as

$$R_{N_2} = \Gamma P_{D_2} P_{NO}^{-1/2} \exp[-E/kT], \quad (5)$$

using the empirical expression in Eq. (1), and writing out the term c in Eq. (1) as $\Gamma \exp[-E/kT]$. Plotting $\ln R_{N_2}$ as a function of T^{-1} should give a straight line if this expression holds, and three of these experimental plots are shown in Fig. 10 over the range of conditions observed. All three cases: (1) no N_2 plateau, (2) a N_2 plateau and (3) a N_2 plateau with ND_3 production, are included in Fig. 10. The slope of each straight line in Fig. 10 gives the effective activation energy, E , for the reaction to proceed. In Fig. 10, E varies from 10.3 to 12.6 kcal-mole^{-1} , and all other slopes that were calculated lie in this range. The intercepts of the lines in Fig. 10 are proportional to $\Gamma P_{D_2} P_{NO}^{-1/2}$. Once a calibration is obtained for R_{N_2} , the value of Γ may be calculated, and it was found to be equal to $1 \times 10^{19 \pm 1} \text{ molecules-cm}^{-2}\text{-s}^{-1}\text{-torr}^{-1/2}$. The error limits are estimates of the bounds due to the averaging of each experimental curve plotted.

Turning to the pressure dependence of ND_3 production at the ND_3 reaction maximum, the rate fits the following relation

$$R_{ND_3} = c'' P_{D_2}^2 P_{NO}^{-1} \quad (6)$$

including all experimental conditions that produce ND_3 . The interpretation of this expression, as for the other empirical rates, will be discussed in Section 6. Several experimental conditions that produce ND_3 in appreciable quantities are shown in Fig. 11. The rate of ND_3 production is shown only as a function of surface temperature for $P_{\text{NO}} = 5 \times 10^{-8}$ torr and R varying from 4 to 20. From Fig. 11, the rate of ND_3 production does not vary with respect to the temperature at which the maximum rate occurs (545 K), and it exhibits asymmetric behavior with a high temperature tail that broadens as R increases.

In summary, experimental reduction reaction cycles have been presented to show the widely different rates in the reduction of NO that occur on $\text{Ir}(110)$ as the surface temperature and the partial pressures of the reactants vary. Also, the reduction products containing nitrogen (N_2 and ND_3) are formed in different distributions that depend upon the partial pressures of the reactants and compete between one another strongly for nitrogen adatoms. The dependence of the reaction rate for N_2 and ND_3 on the partial pressures of the reactants has been derived empirically from the experimental curves. The results of this section will be combined with the results that will be presented in the following section, and they will be discussed together in Section 6.

5. XPS, UPS, AES and LEED Results

Several XPS and UPS measurements were performed to determine the chemical composition of the adlayer at various points during the steady state reaction. Also, LEED was used to monitor the order in the adlayer at similar points in the steady state reaction, lending another insight into the reaction.

During the steady state reaction under various conditions the reaction was terminated by suddenly cooling the Ir(110) surface and rotating it away from the reactant flow in the dosing beam. The surface was then analyzed in the N(1s) and O(1s) regions of binding energy by XPS and in the valence region by HeI UPS. In Fig. 12 (XPS) and in Fig. 13 (UPS), three points in the steady state reaction are shown for $P_{\text{NO}} = 5 \times 10^{-8}$ torr: (a) $R = 10$, quenched at ND_3 reaction maximum (540 K); (b) $R = 10$, completion of a reaction cycle; and (c) $R = 1$, completion of a reaction cycle. The N(1s) region in Fig. 12 shows one feature centered at 396.7 eV, which is due to nitrogen adatoms, when the reaction is terminated at the ND_3 reaction maximum. Under the same conditions, the O(1s) shows one low intensity feature centered near 530.5 eV. The corresponding result with UPS [Fig. 13(a)] yields an emission of low intensity between 5 and 6 eV below the Fermi level, E_F , which is due to mainly the nitrogen (2p) orbital. The emission in the O(1s) region of binding energy at 530.5 eV may be caused by hydroxyl groups which exhibit this binding energy on Ir(110) (21). However, no UPS features are observed corresponding to this water fragment, which occur at 11.1 and 7.8 eV on Pt(111) (22). Thus, the assignment of the O(1s) peak in Fig. 12(a) is subject to question, but it is of rather low intensity.

Performing the steady state reaction for $R = 10$ through a complete reaction cycle and then recording the XP and UP spectra yield the results shown in Figs. 12(b) and 13(b). The N(1s) binding energy region has a single peak with a large high binding energy tail at 400.1 eV which is due to adsorbed NO (16). Also, the O(1s) region has a peak due to adsorbed NO at a binding energy of

531.5 eV. In addition, adsorbed oxygen is present as evidenced by the peak near 528.8 eV. Adsorbed NO is seen as well in Fig. 13(b) for the valence region at 8.5 and 10.4 eV which are emissions from the 1π and 5σ orbitals of molecular NO (16). The emission near 12.8 eV is due to the 4σ orbital but has shifted from its value on the clean surface at low temperature, 13.5 eV. Similar to Fig. 13(a), emission is seen also near 6 eV in Fig. 13(b) which, in this instance, is due to the oxygen (2p) orbital.

The reaction cycle for $R = 1$, represented in Figs. 12(c) and 13(c) by the XPS and UPS measurements, indicates only one nitrogen-containing species, NO, is present here as for the case of $R = 10$. However, the concentration of NO is smaller and the concentration of chemisorbed oxygen is larger, as seen in Figs. 12(c) compared to Figs. 12(b). In agreement with this, the valence orbitals (UPS) in Fig. 13(c) are of lower intensity for adsorbed NO, and the O(2p) emission near 6 eV is larger. The orbitals of NO are not perturbed greatly in the reaction cycles compared to the clean surface (16).

The last electron spectroscopy measurement was to record the Auger N-KLL transitions of nitrogen adatoms after terminating the reaction at the ND_2 rate maximum. Two features are seen in Fig. 14 at kinetic energies of 385.7 and 372.5 eV for the N-KLL region. Two features were observed also for nitrogen adatoms on polycrystalline Pd (23) at similar kinetic energies. The transition at 385.7 eV involves the N(2p) levels in the Auger process and the transition at 372.5 eV involves both the (2p) and (2s) orbitals of the nitrogen adatoms, as calculated from a simple approximation for the Auger transitions (24).

Finally, LEED observations were made after the reaction was terminated, and the order of the overlayer and substrate was monitored. For low values of R which do not cause a plateau in N_2 production, an imperfect oxygen-c(2x2) overlayer structure is observed as the rate of N_2 production increases with surface temperature and this represents oxygen chemisorbed on the *unreconstructed* (1x1) surface that is stabilized by a surface oxide (20). The degree of order of this LEED superstructure depends upon the reaction conditions. After the termination of the reaction, if the temperature were lower or if R were larger the order in the overlayer was always (qualitatively) less. After the reaction cycle was completed for low values of R and the surface cooled to near room temperature, a (1x2) LEED superstructure was observed with sharp integral order spots and large, diffuse half-order spots. This superstructure does not represent the reconstructed substrate (1x2) pattern since the half-order substrate spots never were large and diffuse, but were streaked in the [001] direction, if the substrate was disordered somewhat. Rather, this overlayer contains approximately 0.5 ± 0.05 ML of both NO and oxygen. It was observed also if an oxygen-c(2x2) superstructure was formed, and then the overlayer was saturated with NO at 300 K (16). Thus, the (1x2) pattern is a superstructure of NO and oxygen co-adsorbed on the Ir(110)-(1x1) surface.

If the value of R is sufficiently large to achieve a plateau in N_2 production, the LEED superstructure is a sharp (1x2) which is a clean and reconstructed substrate pattern. The coverages of NO and oxygen are less than 2% as measured by thermal desorption mass spectrometry. As the surface temperature decreases (with sufficiently large R) and the maximum rate in ND_3 production

is reached, the LEED pattern shows streaks between the substrate spots in the [001] direction with some modulation of intensity, if the reaction is terminated and the surface is cooled to room temperature. From the XPS, UPS and AES results only nitrogen adatoms are present, and this pattern is probably a poorly ordered $p(2 \times 2)$ superstructure on Ir(110)-(1x2). Near the drop-off in N_2 production at low temperature, LEED shows a (1x2) structure with streaking along and between the substrate spots and a higher background than before the dropoff. The streaking along the substrate spots is reminiscent of chemisorbed oxygen (20), and the streaking between the rows is due to both oxygen and nitrogen adatoms. Once the reaction cycle is complete (for large R , > 4), the (1x2) substrate is still observed at room temperature, but the background is quite high as it appears when the surface is saturated with NO at 300 K or below (16).

In the following section, the results of this section and Section 4 will be discussed in terms of understanding microscopically the various stages of the reaction between NO and D_2 over Ir(110). Modelling of the elementary steps will be limited to building qualitatively a conceptual model due to the rather complex competing processes occurring as the reaction proceeds.

6. Discussion

As seen from the data presented in the previous sections, the reduction of NO with D_2 (or H_2) over Ir(110) is quite complex. Depending on the surface temperature and the partial pressure of the reactants the rate of reduction and the product distribution vary considerably. Moreover, the history of the surface (whether the surface is clean or oxidized) during a reaction cycle

influences the rate of reaction. In this section general observations concerning the relative activity of Ir(110) compared to the other transition metals will be discussed. The majority of this section will be devoted to interpreting the observed reaction phenomena for $\text{NO} + \text{D}_2$ over Ir(110).

Although hysteresis in the rate of reduction of NO with H_2 over polycrystalline Pt (1) was not reported, the distribution of the major products containing nitrogen (N_2 and NH_3) did change in the same way as seen here for Ir(110). Under similar conditions, the maximum rate of ammonia production is near 540 K on Ir(110) compared to 495 K on polycrystalline Pt (1). The temperature at which 50% of the NO is reduced varies for Ir(110), as seen previously, but it is always higher than 445 K which was reported for polycrystalline Pt (1). Also, the ratio of partial pressures (D_2/NO) required to achieve approximately the same fraction of NO converted to ND_3 is (qualitatively) higher for Ir(110) than Pt (1). Thus, the postulate put forth in Section 1 is verified, namely the activity of the Ir catalyst to produce ammonia is lower than that of Pt, and may be related to the observation that NO dissociates more readily on Ir than Pt. Since the reduction reaction has not been studied on Rh under ultra-high vacuum conditions, it cannot be verified further that the activity of Ir is intermediate between Pt and Rh as suggested by the trend in the activity to dissociate NO. From the investigations of the NO/H_2 system on supported metals at atmospheric pressure the trend would at least place the activity of Ir to produce ammonia as less than that of Ru (4,5). This would concur also with the ease of dissociation of NO on Ir (12-16) compared to Ru (9-11).

Three regions of interest may be considered separately as suggested by

the steady state reaction cycles. The first region is where N_2 is produced at a lower rate prior to the formation of a plateau (if there is) and after the rate has passed through a second relative maximum above 500 K as T increases. At this point, the conversion of the surface from one which is relatively free of oxygen to one which is partially covered with oxide and chemisorbed oxygen and NO is completed. The second region is the plateau in N_2 production (and D_2O production by mass balance) which is insensitive to the surface temperature but is dependent upon the partial pressures of the reactants. The third region is the temperature and pressure range under which ammonia production competes strongly with the N_2 production for nitrogen adatoms, i.e., for $R > 4$ and $470 < T < 630$ K, after the surface achieves a high rate of NO reduction. In addition to these three regions, the transitions between the high and low rates of NO reduction will be discussed.

Region 1. Low Rate of N_2 Production

As seen in Figs. 5-7, the rate of production of N_2 is inhibited strongly in the region where the rate is not on a plateau as the temperature increases. The results in Section 2 concerning the adsorption of deuterium on a saturated overlayer of co-adsorbed NO and oxygen showed that deuterium is blocked almost completely from chemisorbing, whereas NO or oxygen alone did not block deuterium completely. In this region, the surface contains approximately a half ML of oxygen, at least a part of which is a surface oxide since the surface has reverted to the (1x1) unreconstructed structure from the (1x2) structure. Also, the surface has a partial coverage of NO which varies as the temperature varies due to the competition between desorption and adsorption

of NO under steady state conditons. As the surface temperature increases, the rate of N_2 production increases. However, N_2 cannot be produced unless the surface is cleaned of oxygen by D_2 . The empirical pressure dependence of the rate on the reactants, given by Eq. (1) at a constant temperature, indicates that NO acts as a poison unlike D_2 .

The dependence of the rate on P_{D_2} may be visualized by considering the elementary steps involved in producing D_2O ,



where S_{D_2} is the probability of adsorption of deuterium, and the various k_i are the rate coefficients of each elementary reaction. Applying the steady state approximation to adsorbed deuterium implies that

$$2S_{D_2}F_{D_2} - k_2\theta_D^2 - 2k_3\theta_O\theta_D = 0
 \tag{10}$$

where F_{D_2} is the impingement flux of D_2 (proportional to P_{D_2}) in the reactant beam, and the fractional coverage of OD, θ_{OD} , is considered small. Under the conditions in this region, $2S_{D_2}F_{D_2}/k_2$ in Eq. (10) is small compared to

$(k_3\theta_0/k_2)^2$ and θ_D is given approximately by

$$\theta_D = \frac{S_{D_2}F_{D_2}}{k_3\theta_0} \quad (11)$$

Substituting Eq. (11) into the expression for the rate of production of D_2O yields

$$R_{D_2O} = S_{D_2}F_{D_2} \quad (12)$$

i.e., the proper dependence of P_{D_2} on the rate of production of N_2 .

However, understanding the dependence of the rate on NO , $P_{NO}^{-1/2}$, is not so straightforward. It is appealing to think of NO as a poison since oxygen depleted by deuterium is supplied by the dissociation of NO . Moreover, NO will desorb, rather than dissociate, if the coverage of oxygen is sufficiently large. The competition between the removal rate of oxygen (R_{D_2O}), the accumulation rate of oxygen via the dissociation of NO , and the desorption rate of NO govern the rate of N_2 production.

Lastly, Arrhenius plots in Fig. 10 give the effective activation energy (E) for the steady state reaction and it lies between 10.3 and 12.6 kcal-mole⁻¹ under all conditions. It may be that this value represents the difference in activation energies for the desorption and the dissociation of NO . This would not be unreasonable since estimates of this difference in energy, in the absence of deuterium, place it near 8 kcal-mole⁻¹ (16). However, other elementary reactions are important, so that additional activation energy differences may be embodied in E .

Region 2. Plateau in N_2 Production

For sufficiently large values of P_{D_2} compared to P_{NO} and sufficiently large temperatures, the low rate of N_2 production in Region 1 becomes unstable, and a high rate occurs that does not depend sensitively on temperature, over some temperature range. In this second region, only conditions that produce the N_2 plateau and do not form ND_3 will be considered. As observed by both TDS and LEED, when the reaction is terminated during the steady state reaction on the N_2 plateau, the surface is a clean (1x2) substrate with small coverages of nitrogen and oxygen adatoms unlike the surface condition in Region 1. Although the oxygen adatoms present on the surface above 700 K are probably in an oxide form (20), they are in low concentration and still react readily with deuterium (26).

As seen in Fig. 8 and quantified by the empirical expression in Eq. (2), both NO and D_2 accelerate the rate in the plateau region. The linear dependence on P_{NO} in Eq. (2) indicates that within the pressure range studied for NO, 5×10^{-8} to 4×10^{-7} torr, the reaction for form N_2 (for a given P_{D_2}) is limited by the rate of dissociation of NO, so long as P_{D_2} is sufficiently large to maintain the plateau behavior. Also, the dependence on P_{D_2} is easily understood in the plateau region by examining the limit in Eq. (10) for $2S_{D_2}F_{D_2}/k_2$ large compared to $(k_3\theta_0/k_2)^2$ in order to approximate θ_D in Eq. (11). Substituting this result into the expression for R_{D_2O} gives

$$R_{D_2O} = k_3 \left[\frac{2S_{D_2}F_{D_2}}{k_2} \right]^{1/2} \theta_0. \quad (13)$$

where k_2 and k_3 appear in Eqs. (7) and (8) for the desorption of D_2 and the reaction between deuterium and oxygen to form OD, respectively.

Over the pressure range of D_2 that is accessible (5×10^{-8} to 1×10^{-6} torr), the rate of N_2 formation depends on $P_{D_2}^{1/2}$. However, if larger pressures of D_2 were studied, the rate should reach a limiting value for a give P_{NO} . This rate should be limited by the flux of NO to the surface since the initial probability of adsorption is unity independent of temperature (16). The $P_{D_2}^{1/2}$ dependence in Region 2 indicates that small coverages of oxygen influence the rate of dissociation compared to the rate of desorption of NO.

The two points of instability mentioned in Section 4, termed the "onset" and "dropoff", may be conveniently discussed with Region 2 since they occur at the temperature extremes of the N_2 plateau. Although the onset becomes less sharp in temperature when ammonia is produced (at large R), these data as well as the corresponding data concerning the dropoff may be included since these points occur outside of the temperature range where ND_3 appears.

The onset in the plateau may be defined by a temperature (T_h) at which the plateau occurs and is accompanied often by a spike in D_2O production [e.g. Figs. 5(B), 5(C) and 7(A)]. Moreover, the onset is truly unstable since near T_h the rates of N_2 and D_2O production increase irreversibly to their values at the plateau. The surface reverts from a (1x1) oxide to a (1x2) clean at this point as well. It was shown in Eq. (3) that the onset depends upon $P_{NO}^{3/2} P_{D_2}^{-1}$ as a function of T_h^{-1} . If T_h is at the intersection of the asymptotic rates in Regions 1 and 2, modelled by Eqs. (1) and (2), then the dependence would be $P_{NO}^{3/2} P_{D_2}^{-1/2}$. The

$P_{\text{NO}}^{3/2}$ term is correct but the $P_{\text{D}_2}^{-1}$ dependence is more like Region 1. This is reasonable since Region 1 dictates *where* in temperature the onset occurs. The energy associated with an Arrhenius plot of Eq. (3) [Fig. 9(a)] is equal to 11.2 kcal-mole⁻¹ which is in the same range found for the effective activation energy to produce N₂ in Region 1. It is not apparent, however, that these energies can be compared meaningfully.

As the temperature decreases toward the point at which the rate of NO reduction decreases, oxygen adatoms and NO admolecules begin to accumulate on the surface, seen by TDS and XPS. At some point in coverage, deuterium does not adsorb further to sustain the reaction and the dropoff occurs. At the dropoff, the nitrogen adatoms remaining on the surface are desorbed due to an increasing coverage of NO (16). Once the production of N₂ is inhibited completely below the dropoff, NO and oxygen, only, remain on the surface, as determined by XPS and UPS results. In order to achieve the N₂ plateau again, the temperature must be increased to the onset found previously.

The dropoff in the high rate of NO reduction, whether the products are ND₃ and N₂ or N₂ only, was modelled empirically by Eq. (4). This expression gives the correct dependence, $P_{\text{NO}}^{3/2}P_{\text{D}_2}^{-1/2}$, on the temperature of the dropoff (T_l) if the asymptotic rates of Eqs. (1) and (2) are considered, as before for T_h . Figure 9(b) shows that $P_{\text{NO}}^{3/2}P_{\text{D}_2}^{-1/2}$ as a function of T_l^{-1} fits a straight line with $E = 8.3$ kcal-mole⁻¹, but again it is not clear what significance this value of the energy has in relation to the observed phenomena.

Region 3. Ammonia Production

Ammonia is formed on Ir(110) between 470 and 630 K for values of R greater than four depending also on the partial pressure of NO. It was found from XPS, UPS and LEED results that the surface is a (1x2) substrate with a partially ordered nitrogen-p(2x2) superstructure near the ND_3 reaction maximum. Since ND_x ($x = 1,2$) groups are not observed with either XPS or UPS if the reaction is terminated where ND_3 is produced, the rate limiting step to form ND_3 is $\text{N} + \text{D} \rightarrow \text{ND}$. The desorption of ND_3 is rapid in the reaction region. This is verified by thermal desorption results for NH_3 on Ir(111) where NH_3 desorbs molecularly near 300 K (27).

Under conditions that produce ND_3 in competition with N_2 , the empirical dependence of the rate of ND_3 production on the partial pressures of the reactants is given by $P_{\text{D}_2}^2 P_{\text{NO}}^{-1}$ [see Eq. (6)]. As in Region 1 where N_2 is produced at a low rate, NO acts as a poison by supplying oxygen that consumes deuterium which would otherwise react with nitrogen to form ND_3 . A squared dependence on P_{D_2} may suggest that diffusion of deuterium adatoms in pairs is important, which was inferred near the rate maximum for CO oxidation on Ir(110), for the squared dependence on the pressure of oxygen (25). Also, the stoichiometry of the reaction between NO and D_2 to form ND_3 and D_2O requires five deuterium adatoms for every NO admolecule and would cause the rate to depend more on P_{D_2} than on P_{NO} , although $\text{N} + \text{D} \rightarrow \text{ND}$ and $\text{O} + \text{D} \rightarrow \text{OD}$ are the rate limiting steps as deduced from the data. It should be noted also that a high temperature thermal desorption feature of D_2 appears between 460 and 650 K when NO and deuterium are co-adsorbed (see Figs. 1 and 2). This desorption of D_2

brackets the range where ND_3 is produced (470 - 630 K) and may play a role in the reaction rate for ND_3 production. However, these are postulates only, since the microscopic events occurring on the surface are too complex, with the available data, to predict a priori the observed pressure dependence of the rate of N_2 production on the partial pressure of D_2 .

7. Summary

The reaction between NO and D_2 over $\text{Ir}(110)$ has been studied under ultra-high vacuum conditions by means of measurements of the steady state rate of NO reduction as a function of the partial pressures of the reactants (5×10^{-8} to 1×10^{-6} torr) and the surface temperature (300 to 1000 K). In addition, co-adsorption studies of NO and deuterium at low temperature were performed to gain insight into the competitive nature of the chemisorption process and to observe the desorption characteristics of the co-adsorbed overlayers as the surface is heated. The results of this investigation may be summarized as follows.

(1) Small precoverages of deuterium do not affect the kinetics of adsorption of NO but do affect the distribution of N_2 and NO that thermally desorbs from the surface. More N_2 desorbs when deuterium is present than in its absence due to the reaction between oxygen (from the dissociation of NO) and deuterium to form D_2O .

(2) The adsorption of deuterium is decreased, relative to the clean surface, when the latter is saturated with NO . However, D_2 is inhibited strongly from adsorbing when the surface is saturated with oxygen and NO , a condition that occurs under some steady state reaction conditions.

(3) Depending on the value of R , under steady state conditions a marked hysteresis occurs in the rate of NO reduction. For certain values of R and T , a plateau in the rate appears that persists as the temperature is decreased. At some temperature, depending upon P_{NO} and P_{D_2} , the rate falls uncontrollably to a new steady state where the reduction reaction is slow.

(4) For large values of R (> 4), ND_3 is produced between 470 and 630 K and competes strongly for nitrogen adatoms with N_2 production.

(5) Three regimes of the steady state reaction were examined separately:

(a) Low rates producing N_2 and D_2O only with an inhibition by NO; (b) High rates with a plateau in the rate producing N_2 and D_2O only; and (c) High rates where N_2 and ND_3 are produced competitively. Tentative explanations of the empirically observed rates were discussed in light of XPS, UPS, TDS and LEED results.

Acknowledgment

The authors are grateful to the National Science Foundation for support of this work (Grant No. CHE77-14976).

References

1. G. Pirug and H. P. Bonzel, *J. Catalysis* 50,64(1977).
2. R. M. Lambert and C. M. Comrie, *Surface Sci.* 46, 61(1974).
3. C. T. Campbell and J. M. White, *Appl. Surface Sci.* 1, 347(1978).
4. T. P. Kobylinski and B. W. Taylor, *J. Catalysis* 33, 376(1974).
5. K. C. Taylor and R. L. Klimisch, *J. Catalysis* 30, 478(1973).
6. H. Conrad, G. Ertl, J. Koppers and E. E. Latta, *Faraday Discuss. Chem. Soc.* 58, 116(1974).
7. H. Conrad, G. Ertl, J. Koppers and E. E. Latta, *Surface Sci.* 65, 235(1977).
8. H. P. Bonzel and G. Pirug, *Surface Sci.* 62, 45(1977).
9. P. A. Thiel, W. H. Weinberg and J. T. Yates, Jr., *Chem. Phys. Letters* 67, 403(1979).
10. G. E. Thomas and W. H. Weinberg, *Phys. Rev. Letters* 41, 1181(1978).
11. E. Umbach, S. Kulkarni, P. Feulner and D. Menzel, *Surface Sci.* 88, 65(1979).
12. J. Kanski and T. N. Rhodin, *Surface Sci.* 65, 63(1977).
13. P. A. Zhdan, G. K. Boreskov, W. F. Egelhoff, Jr. and W. H. Weinberg, *J. Catalysis* 45, 281(1976).
14. P. A. Zhdan, G. K. Boreskov, A. I. Boronin, A. P. Scheplin, W. F. Egelhoff, Jr. and W. H. Weinberg, *J. Catalysis* 60, 93(1979).
15. J. Koppers and H. Michel, *Surface Sci.* 85, 201(1979).
16. D. E. Ibbotson, T. S. Wittrig and W. H. Weinberg, *Surface Sci.* (submitted).

17. D. E. Ibbotson, T. S. Wittrig and W. H. Weinberg, *J. Chem. Phys.* 72, 4885(1980).
18. J. L. Taylor, D. E. Ibbotson and W. H. Weinberg, *J. Chem. Phys.* 69, 4298(1978).
19. C. M. Chan, M. A. Van Hove, W. H. Weinberg and E. D. Williams, *Solid State Commun.* 30, 47(1979); *Surface Sci.* 91, 400(1980).
20. J. L. Taylor, D. E. Ibbotson and W. H. Weinberg, *Surface Sci.* 79, 349(1979).
21. T. S. Wittrig, D. E. Ibbotson and W. H. Weinberg, *Surface Sci.*(in press).
22. G. B. Fisher and B. A. Sexton, *Phys. Rev. Letters*(submitted).
23. K. Kunimori, T. Kawai, T. Kondow, T. Onishi and K. Tamaru, *Surface Sci.* 59, 302(1976).
24. G. G. Tibbetts and J. M. Burkstrand, *J. Vacuum Sci. Technol.* 15, 497(1978).
25. J. L. Taylor, D. E. Ibbotson and W. H. Weinberg, *J. Catalysis* 62, 1(1980).
26. D. E. Ibbotson, Ph. D. Thesis, California Institute of Technology, 1981.
27. R. J. Purtell, R. P. Merrill, C. W. Seabury and T. N Rhodin, *Phys. Rev. Letters* 44, 1279(1980).

Figure Captions

Fig. 1 Thermal desorption spectra from NO adsorbed on the β_2 state of deuterium (0.33 ML) preadsorbed on Ir(110) at 100 K. The desorption products monitored are NO, N₂, D₂ and D₂O with a heating rate of 20 K-s⁻¹. Under these conditions deuterium was not displaced from the surface as NO was adsorbed. For comparison, the desorption of the β_2 state of deuterium is shown ($\times 0.5$) in the absence of adsorbed NO.

Fig. 2 Thermal desorption spectra of NO, N₂, D₂ and D₂O from 2 L D₂ adsorbed on various surfaces of Ir(110) at 100 K prepared with saturation exposures of NO. ----- Saturated layer of NO adsorbed at 100 K; - - - - Saturated layer of NO adsorbed at 450 K and cooled to 100 K; and Saturated layer of NO adsorbed at 100 K and annealed briefly to 400 K. The heating rate is 20 K-s⁻¹.

Fig. 3 The CPD of NO adsorbed at 100 K on Ir(110) as a function of the fractional coverage of NO. (a) Clean surface; and (b) preadsorbed β_2 state of deuterium (or hydrogen) (0.33 ML).

Fig. 4 The CPD of H₂(or D₂) adsorbed on fractional coverages of NO on Ir(110) at 100 K: (a) 0.23; (b) 0.44; and (c) 1.00. In (A) the exposure of H₂ is sufficient to saturate the β_2 state, and in (B) the exposure of H₂ includes part of the β_1 state (see text).

The zero in (B) for the CPD is equal to the "saturation" value (at 0.25 L H₂) in (A).

Fig. 5 Steady state reaction for NO + D₂ over Ir(110).

$P_{\text{NO}} = 1 \times 10^{-7}$ torr, and $R (= P_{\text{D}_2} / P_{\text{NO}})$

equal to: (A) 1; (B) 2; (C) 4; and (D) 8.

The intensities monitored in the gas phase are NO, N₂, ND₃, D₂ and D₂O.

For all values of R, the intensity of D₂ did not vary appreciably in a reaction cycle, and it is not shown here or in following figures.

Arrows pointing to the right (left) indicate the surface temperature is increasing (decreasing).

Ammonia (ND₃) production occurs in (D) only.

Fig. 6 Steady state reaction for NO + D₂ over Ir(110).

$P_{\text{NO}} = 2 \times 10^{-7}$ torr, and R equal to: (A) 2; and

(B) 4. No ND₃ is produced under these conditions.

Fig. 7 Steady state reaction for NO + D₂ over Ir(110) under conditions that favor the production of ND₃.

$P_{\text{NO}} = 5 \times 10^{-8}$ torr, and R is equal to: (A) 8;

and (B) 20.

Note that ND₃ and N₂ compete strongly for nitrogen adatoms.

Fig. 8 Steady state rates of N₂ production from Figs. 5 and 6. (a)

$P_{\text{NO}} = 1 \times 10^{-7}$ torr and R = 4; (b) $P_{\text{NO}} = 1 \times 10^{-7}$

torr and R = 8; and (c) $P_{\text{NO}} = 2 \times 10^{-7}$ torr and R = 4.

The intensity of N_2 has been expanded by 0.5 in (c).

Note that in (b) some ND_3 is produced near the dropoff in N_2 production, as the temperature is decreased.

Fig. 9 The empirical pressure dependence of (a) the onset, $\ln(P_{NO}^{3/2}P_{D_2}^{-1})$ and (b) the dropoff, $\ln(P_{NO}^{3/2}P_{D_2}^{-1/2})$ of the plateau in N_2 production as a function of T^{-1} , inverse of the surface temperature at which they occur.

Fig. 10 The temperature dependence of the rate of N_2 production as the temperature increases but before a plateau is reached (if it is present).

Three different reaction conditions are presented, as noted in the figure, for $\ln R_{N_2}$ as a function of T^{-1} .

The slope of each curve is proportional to the effective activation energy for the reaction, which is presented as well.

Fig. 11 Steady state rate of ND_3 production for $P_{NO}=5 \times 10^{-8}$ torr and R equal to: (a) 4.0; (b) 6.0; (c) 8.0; (d) 10.0; (e) 12.6; (f) 16.0; and (g) 20.0.

Fig. 12 XPS ($h\nu = 1486.6$ eV) for the N(1s) and the O(1s) regions of binding energy, relative to the Fermi level, at three points in the steady state reaction.

$P_{NO}=5 \times 10^{-8}$ and (a) $R = 10$ at the ND_3 reaction maximum; (b) $R = 10$ after a reaction cycle; and (c) $R = 1$ after a reaction cycle.

For each spectrum, the reaction was terminated by simultaneously

removing the Ir(110) surface from the reactant gas beam and cooling to near room temperature.

Fig. 13 HeI UPS ($h\nu = 21.2$ eV) of Ir(110) near room

temperature for three points in the steady state reaction.

The corresponding conditions for (a) - (c) are given in Fig. 12.

Fig. 14 Auger electron spectrum of the N-KLL region of energy.

The steady state reaction was terminated for this spectrum

at the ND_3 reaction maximum proceeding under the same

conditions as in Figs. 12(a) and 13(a).

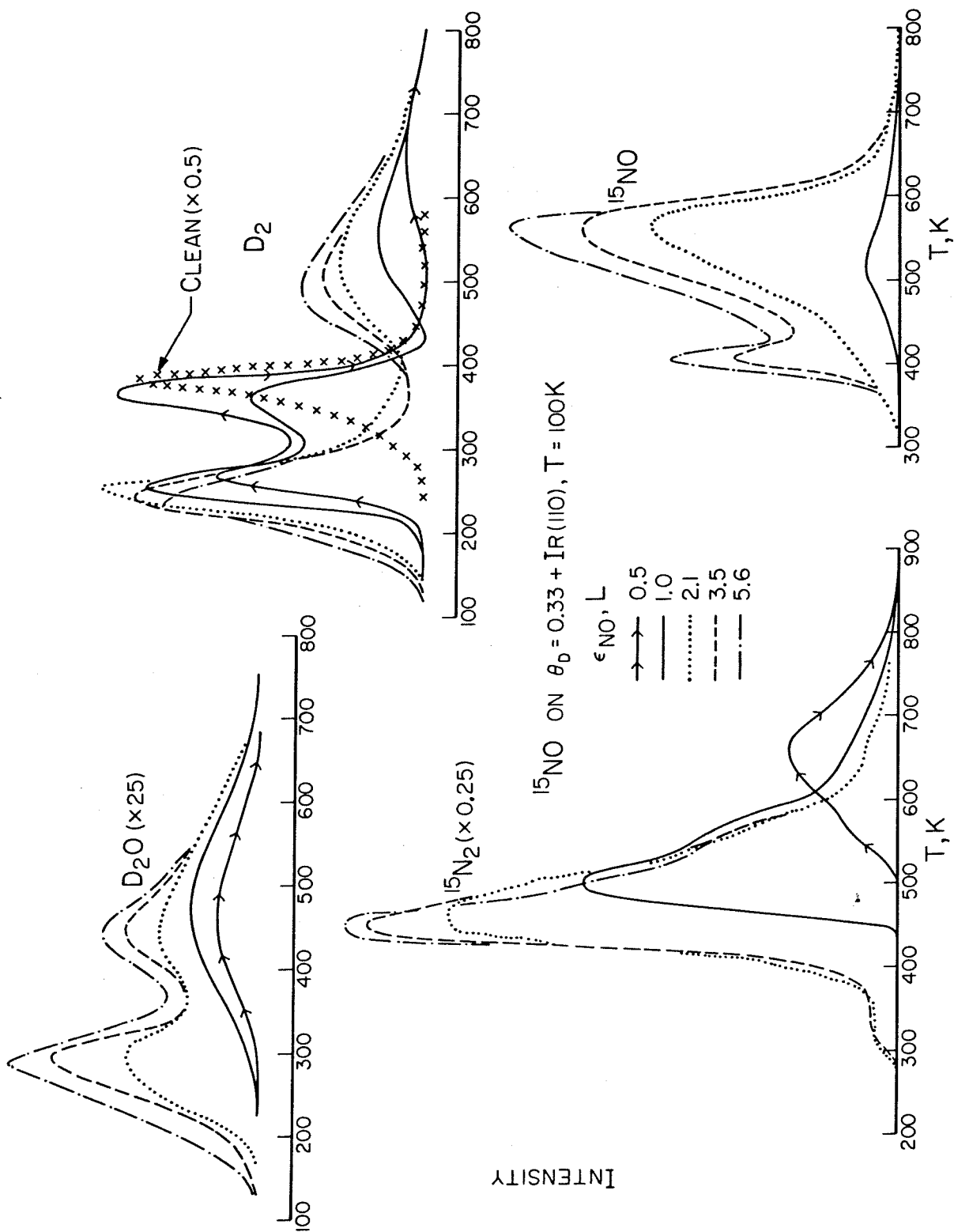


Figure 1

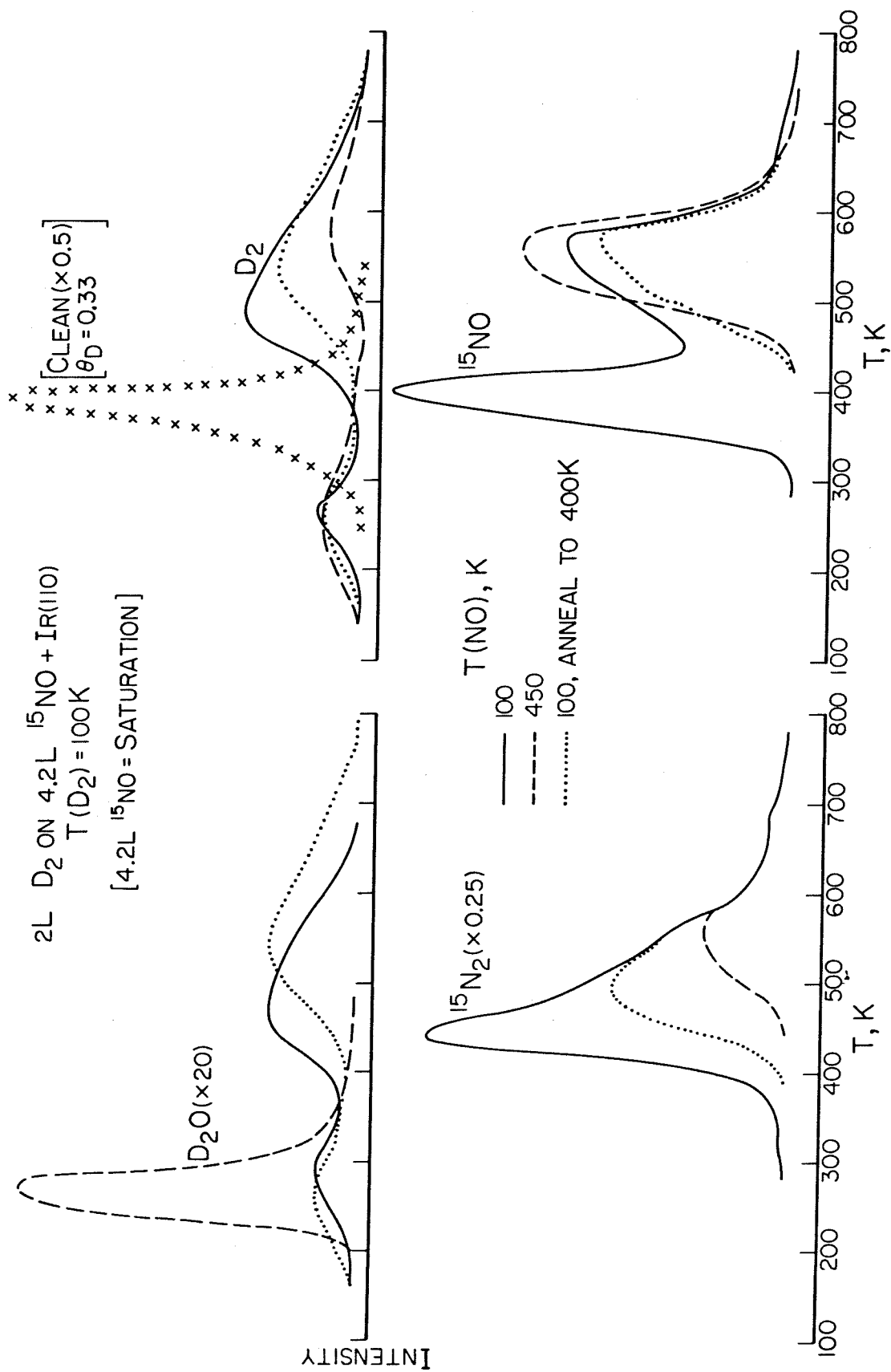


Figure 2

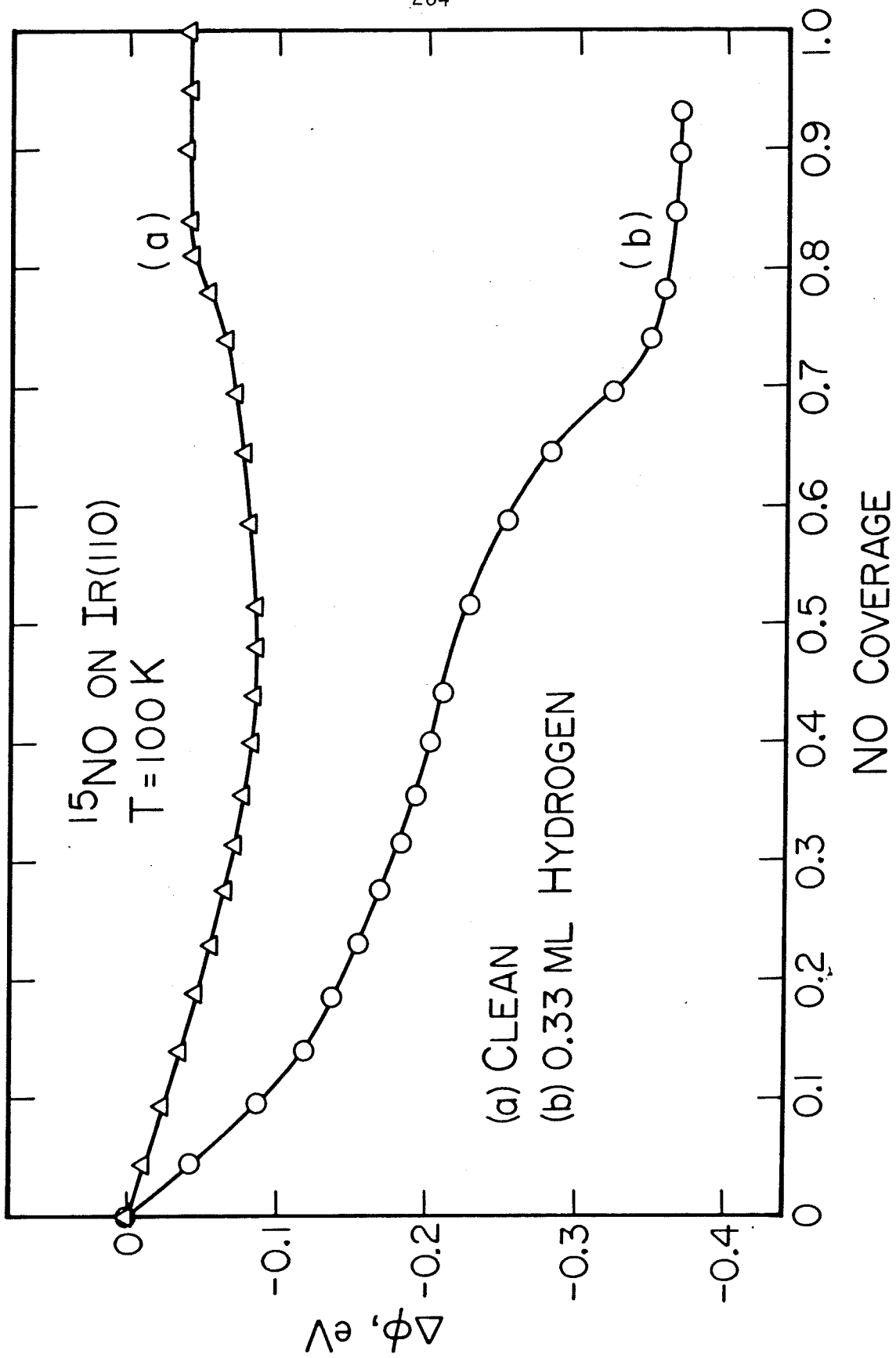


Figure 3

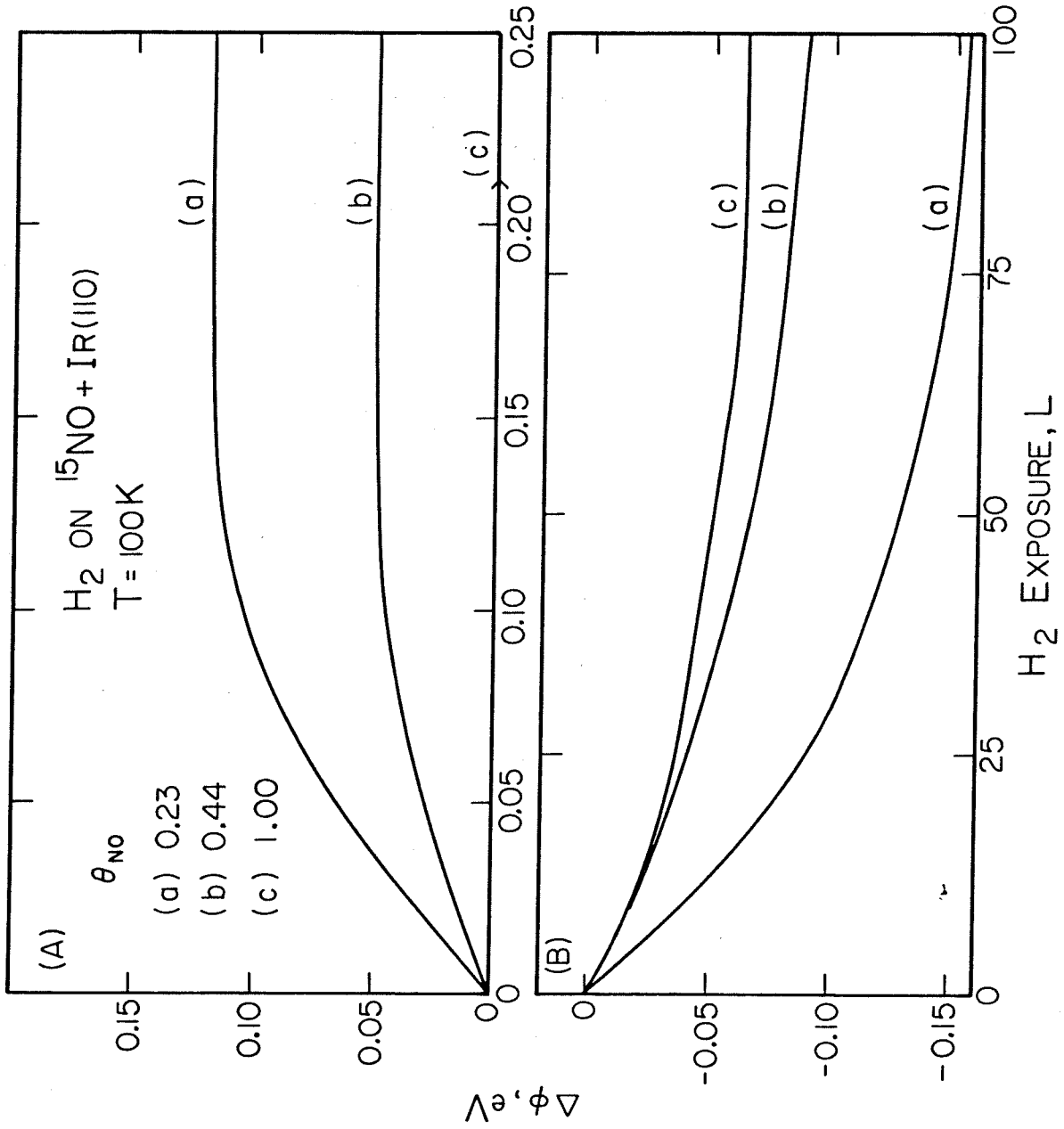


Figure 4

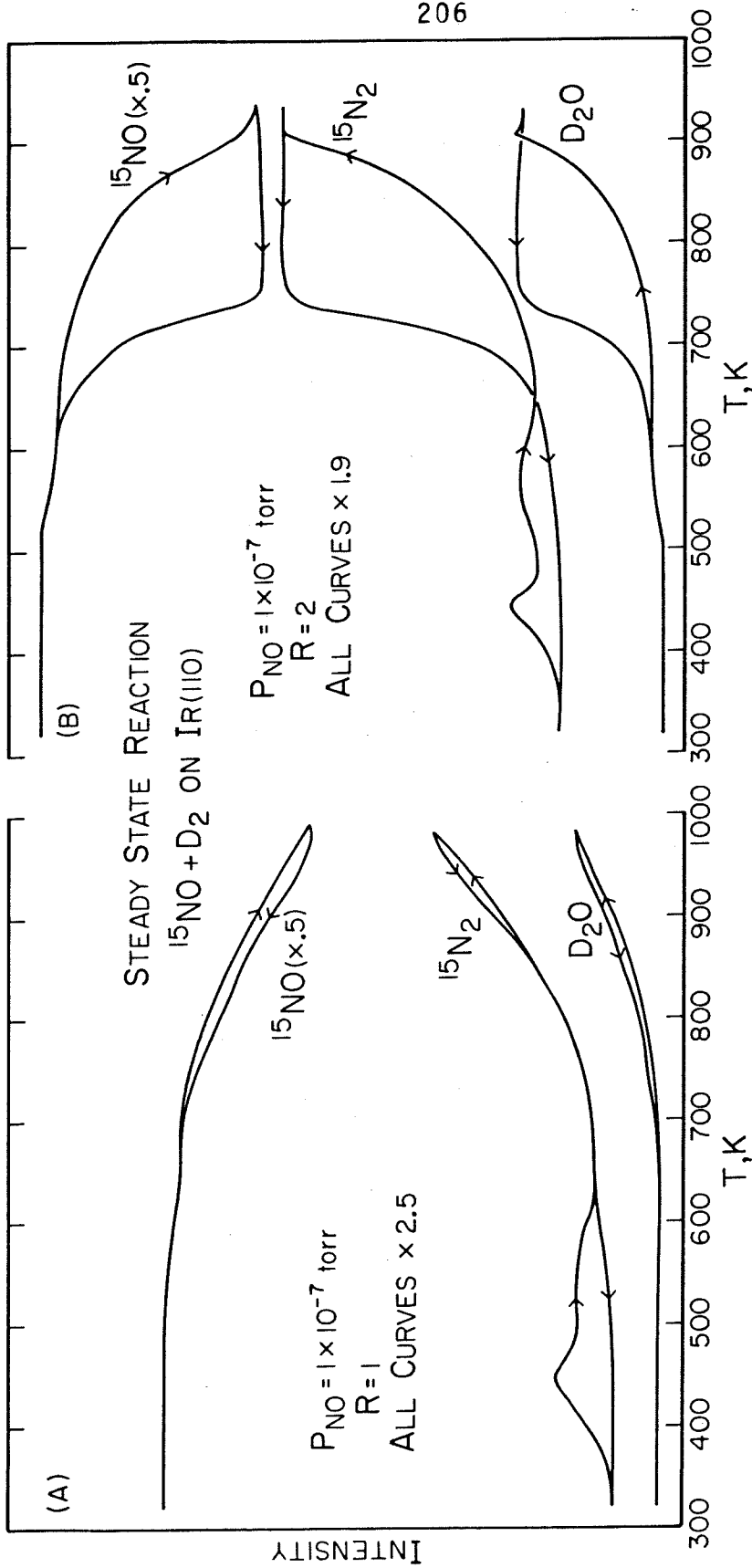


Figure 5-1

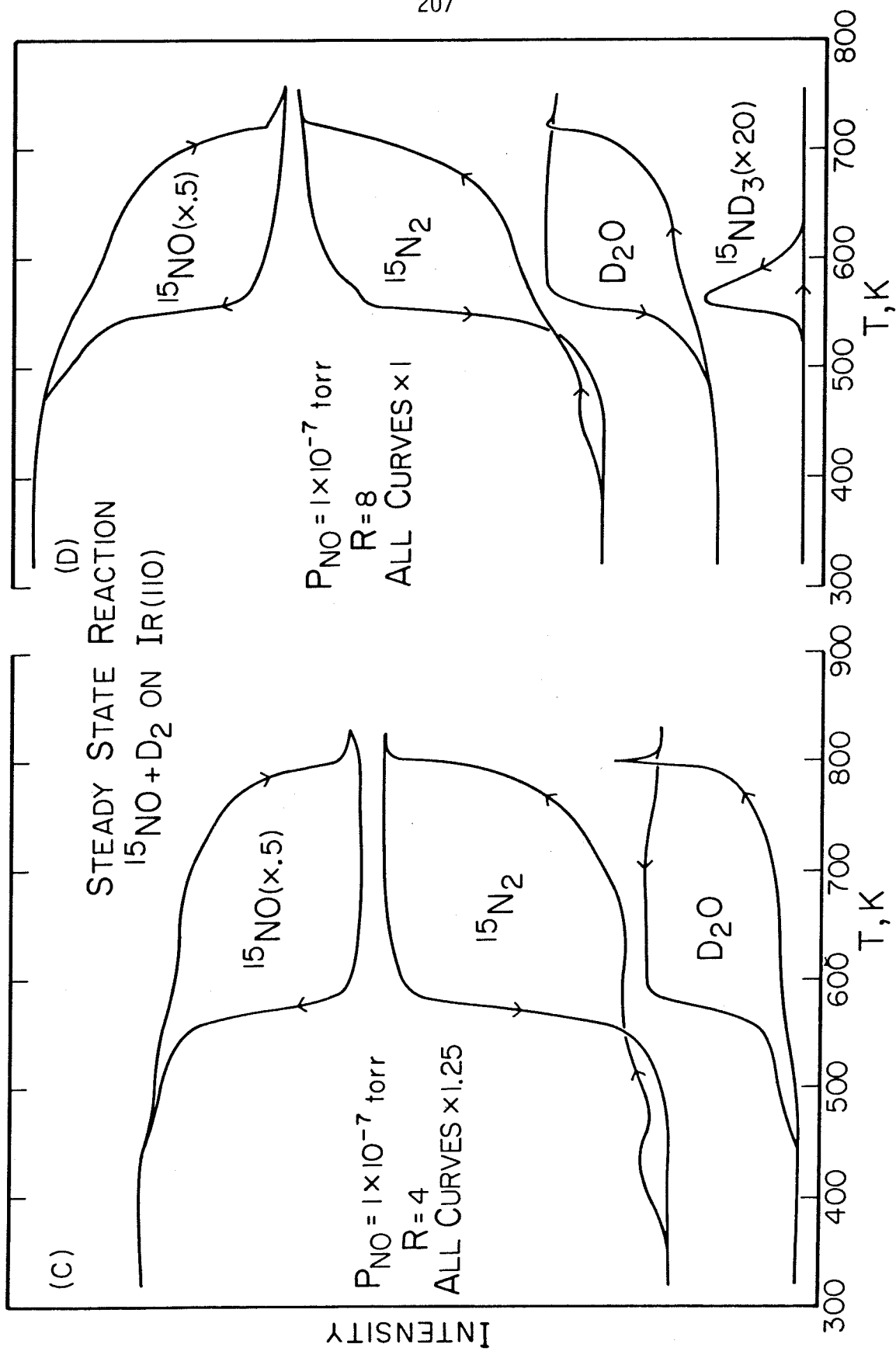


Figure 5-II

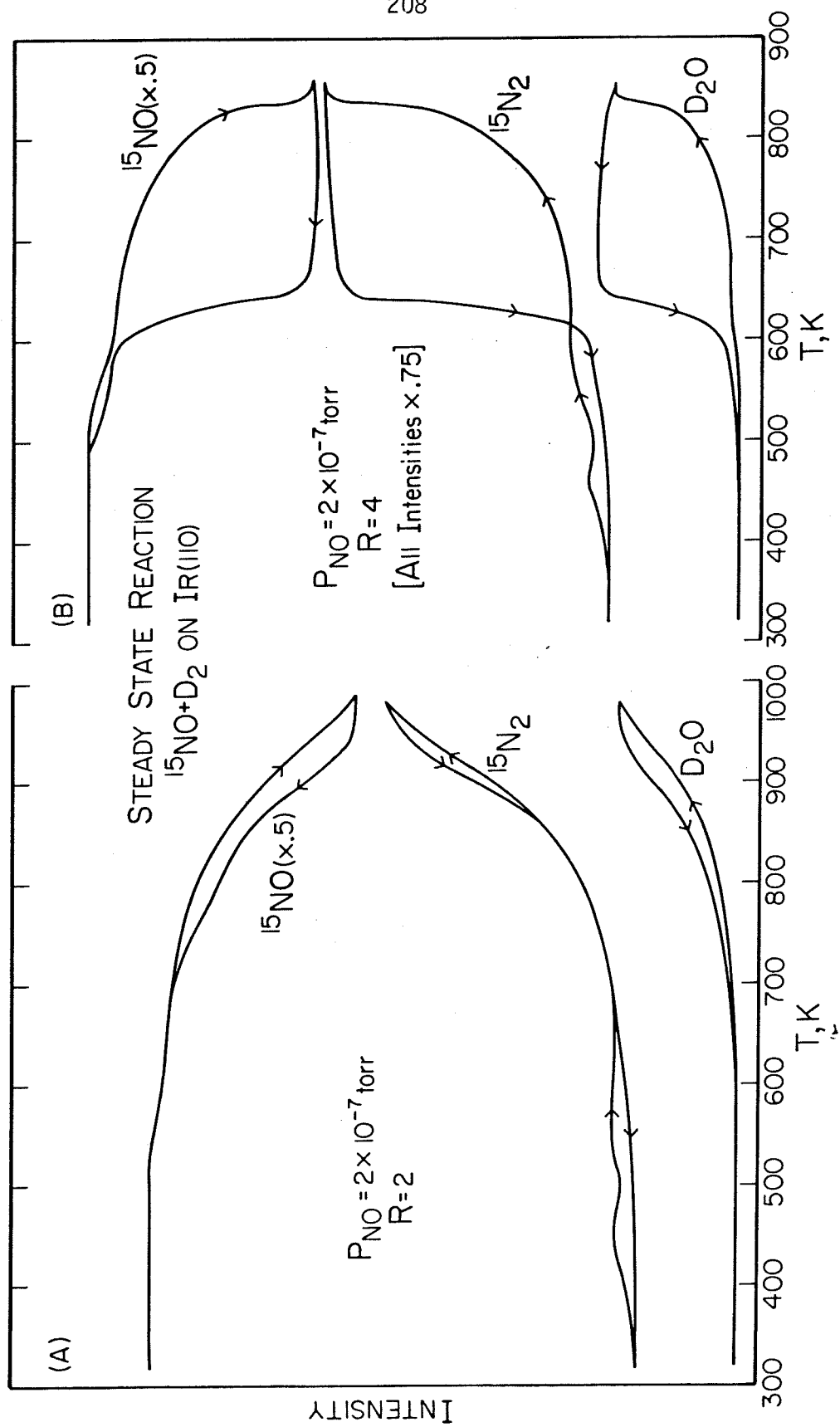


Figure 6

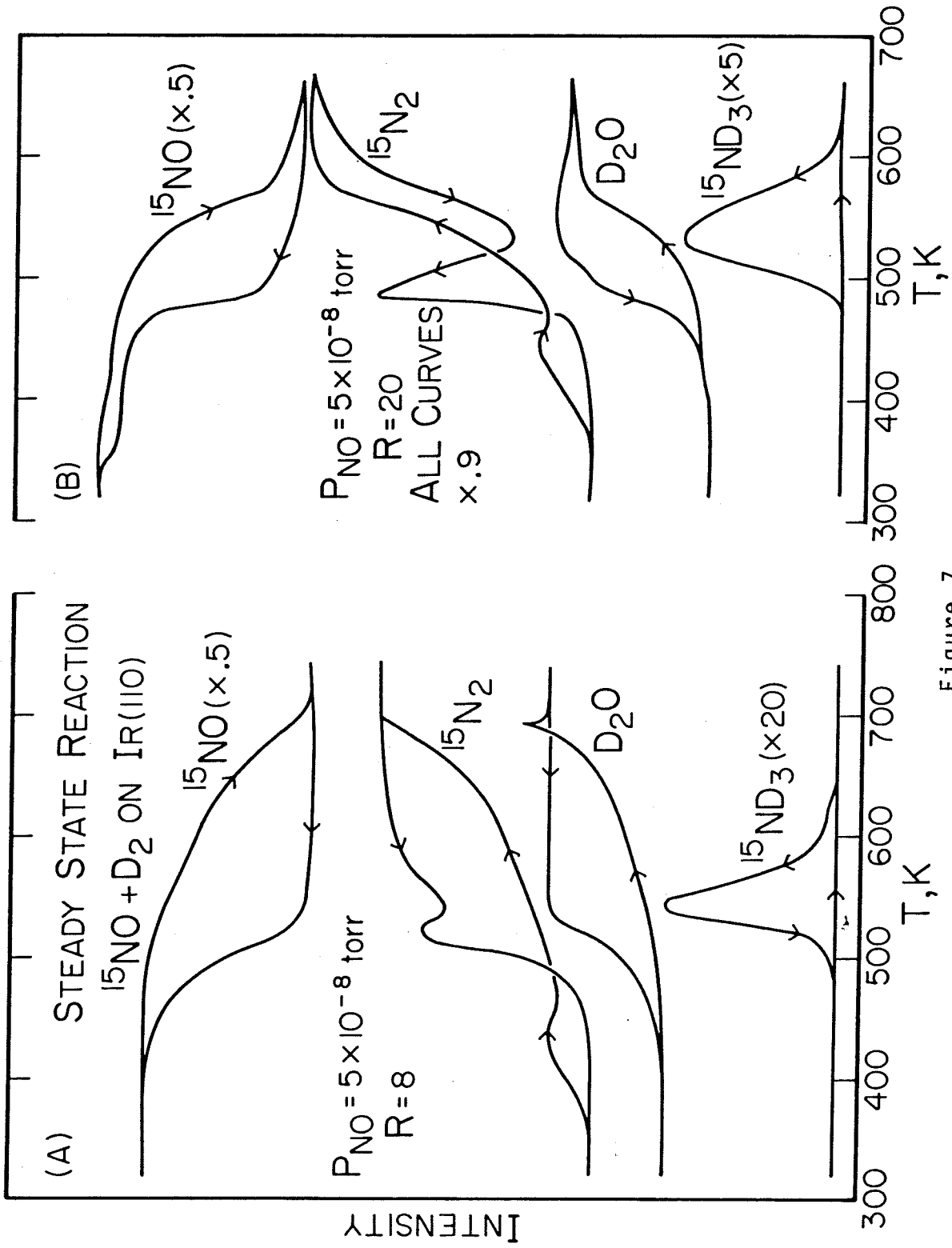


Figure 7

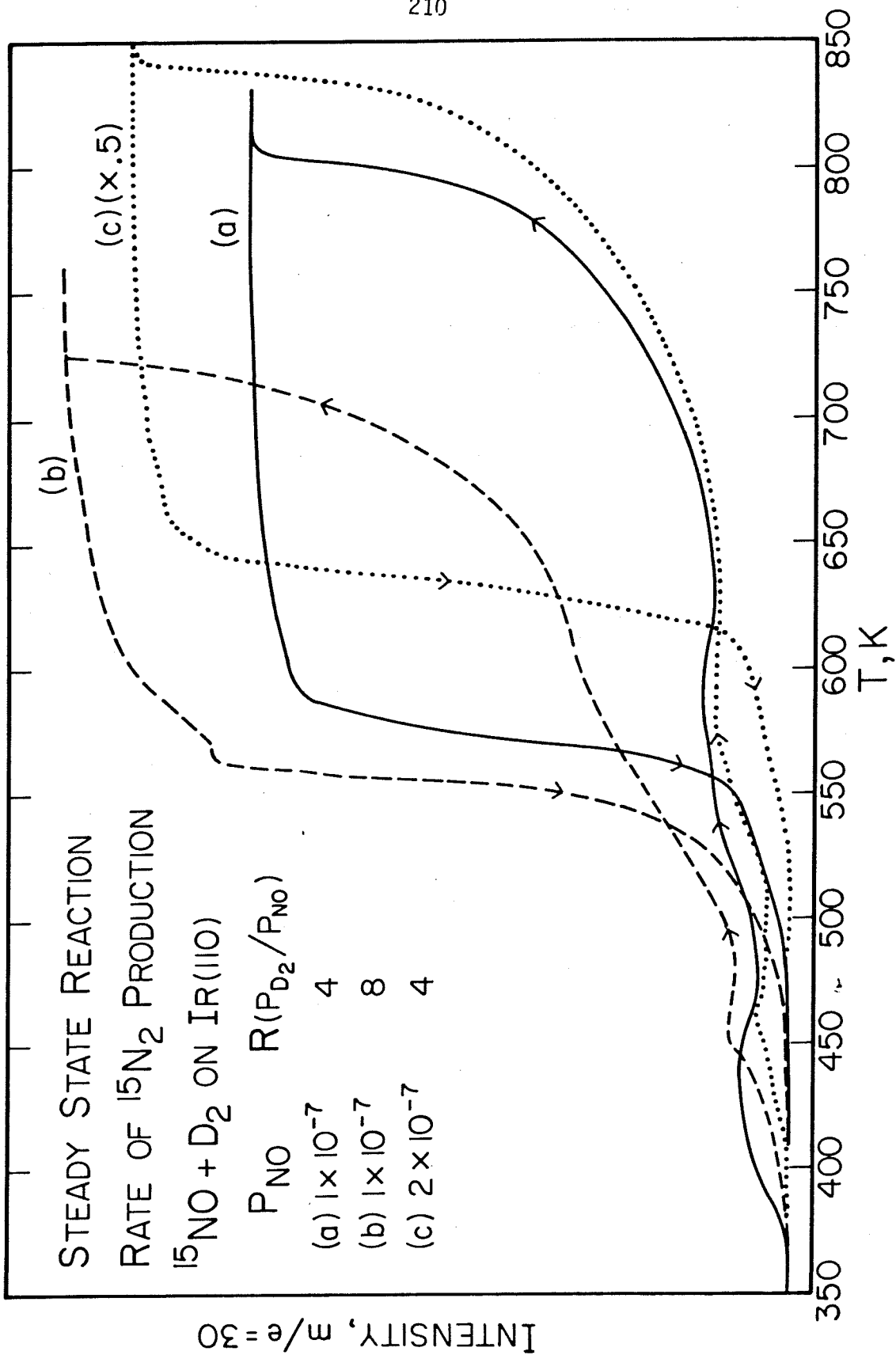


Figure 8

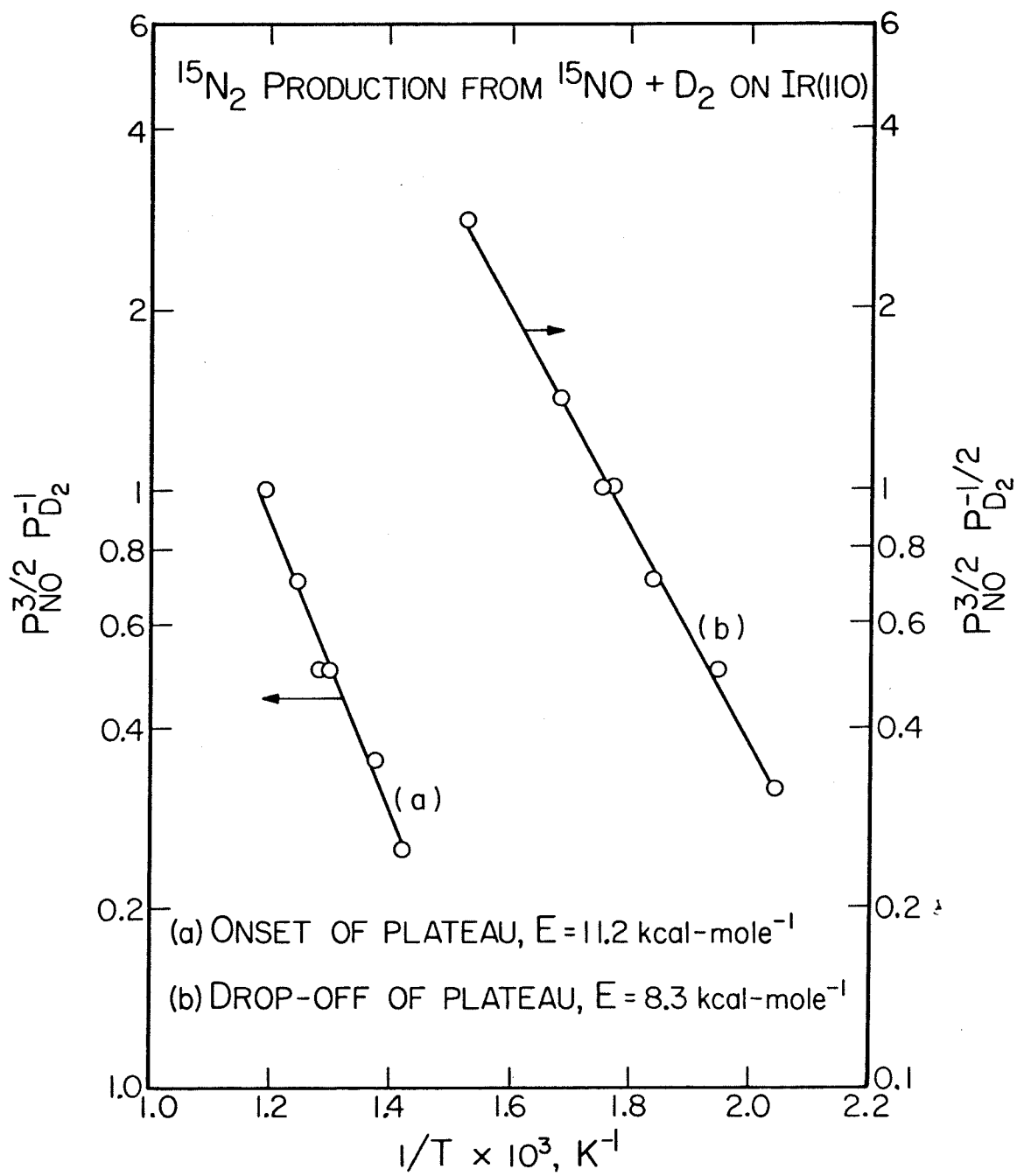


Figure 9

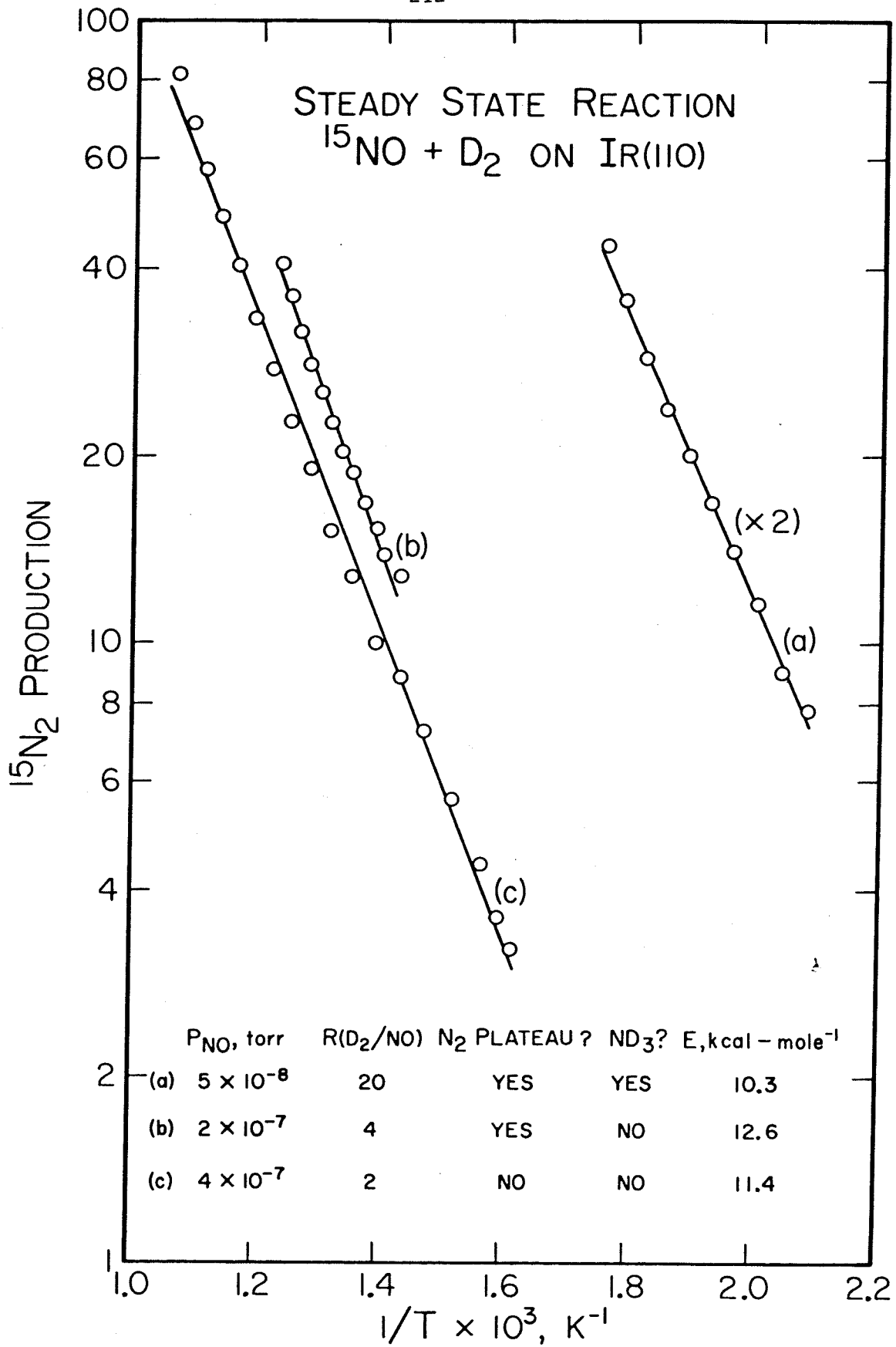


Figure 10

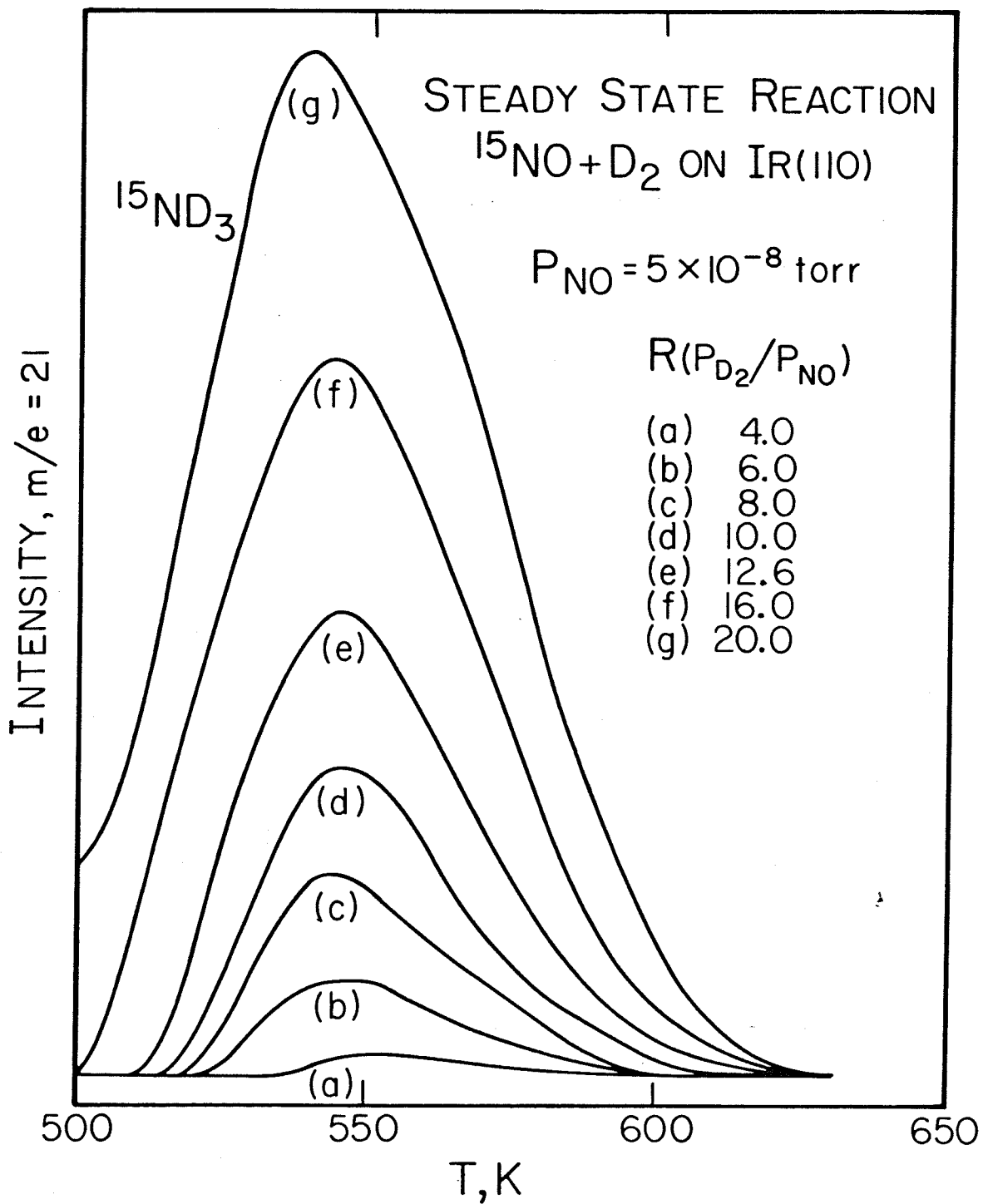


Figure 11

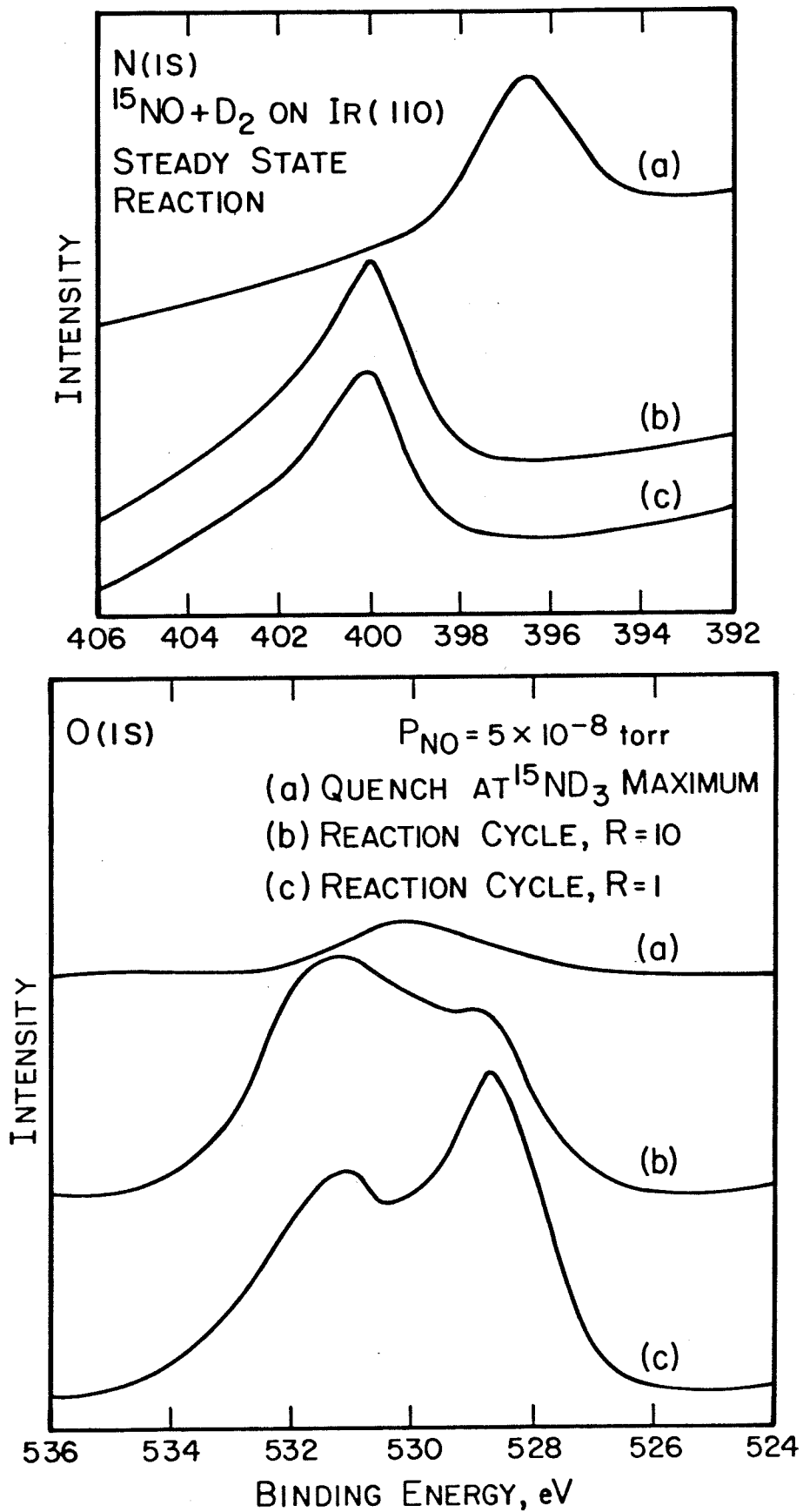


Figure 12

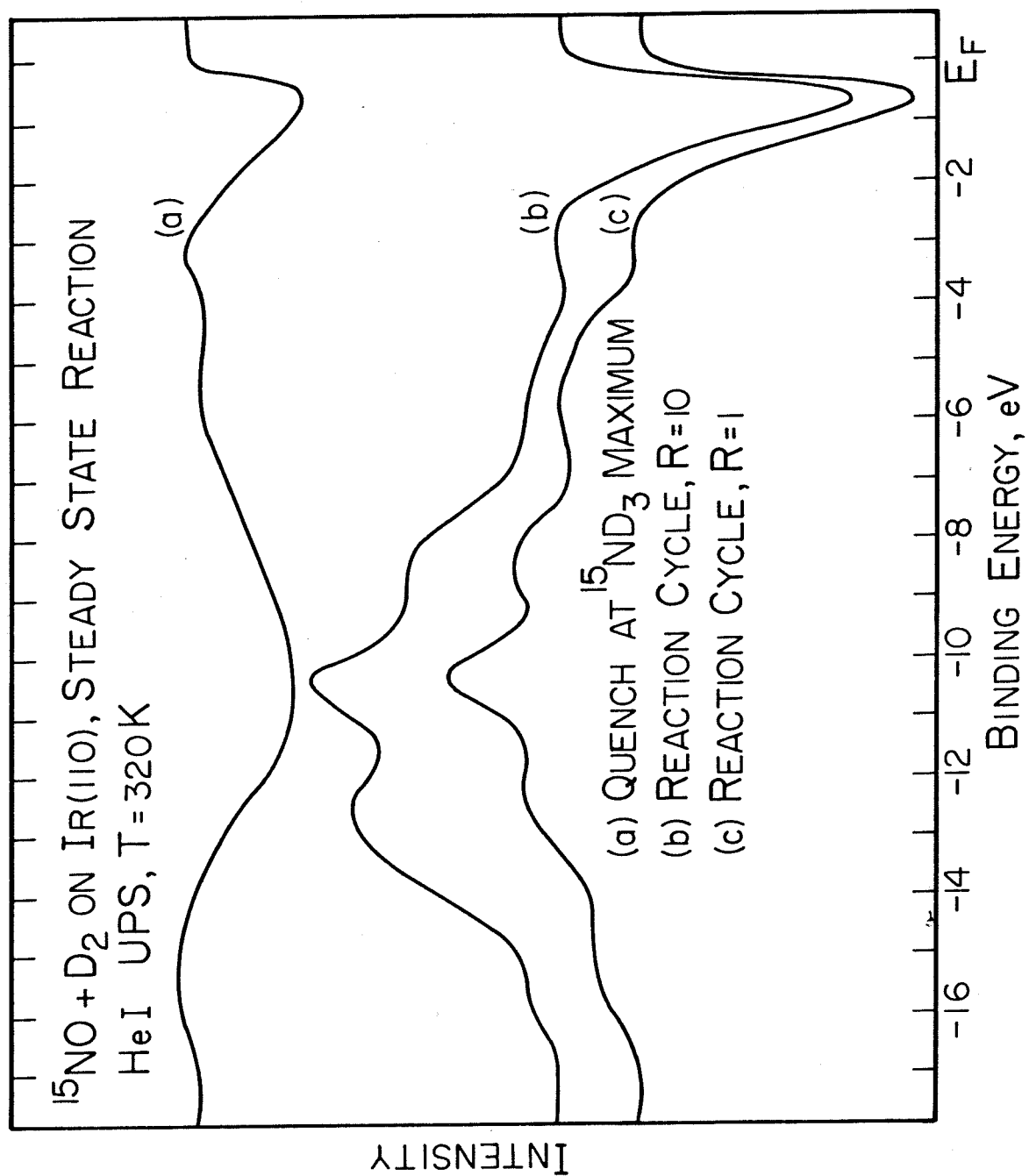


Figure 13

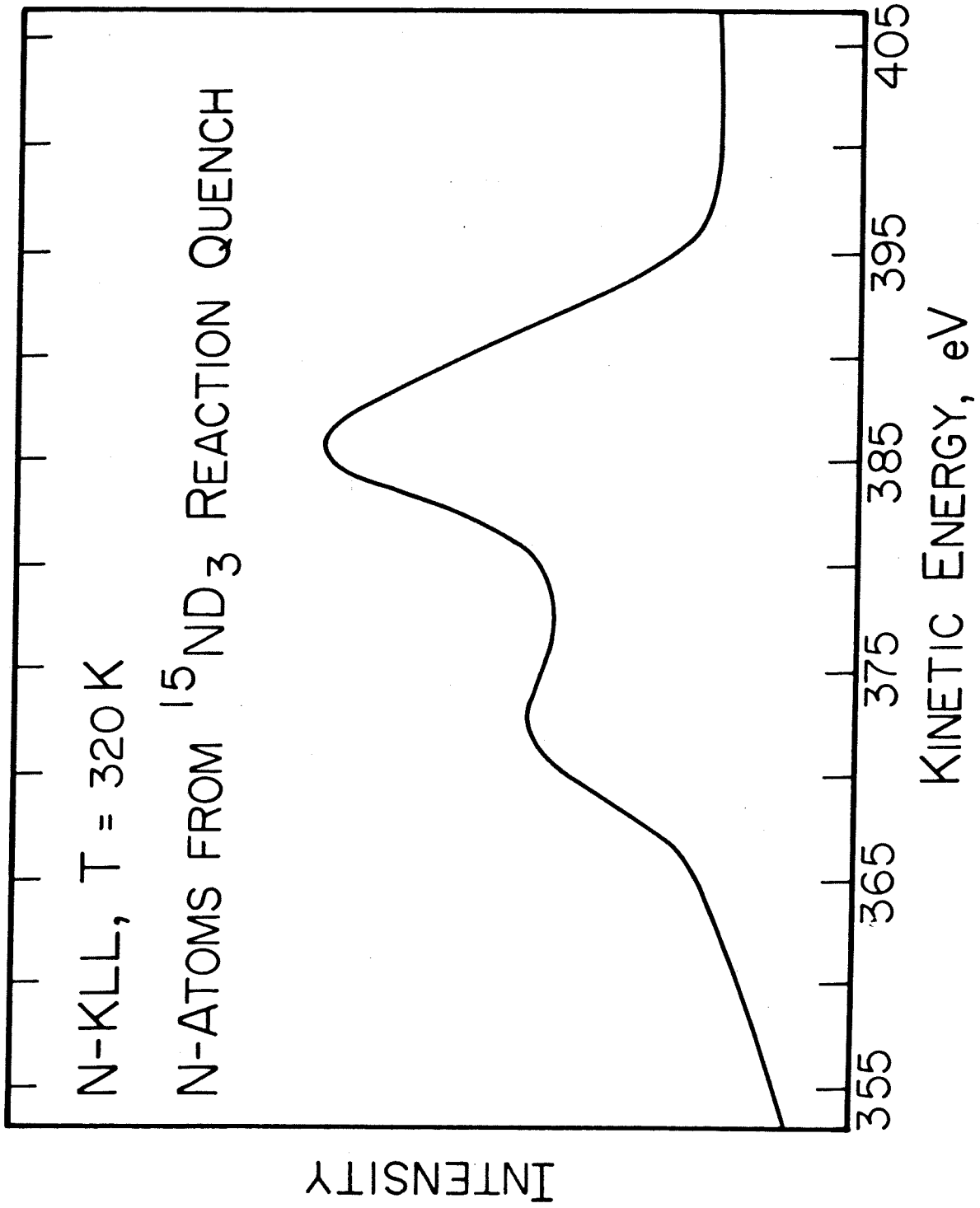


Figure 14

CHAPTER 7

SUMMARY

The heterogeneously catalyzed reduction of NO with hydrogen over Ir(110) has been studied at low pressures ($<10^{-5}$ torr). The experiments were performed with several surface sensitive probes-- thermal desorption mass spectrometry(TDS), contact potential difference(CPD) measurements, LEED, X-ray and UV photoelectron spectroscopies(XPS and UPS) and Auger electron spectroscopy.

The following summarizes the chemisorption of hydrogen on Ir(110).

(1) Hydrogen adsorbs dissociatively on Ir(110) and saturates the surface at 130 K with a density of $(2.2 \pm 0.2) \times 10^{15}$ atoms-cm⁻². Two states β_1 and β_2 of hydrogen desorb with relative intensities of 2 and 1, respectively, and exhibit marked differences in their adsorption and desorption kinetics.

(2) The rate parameters for hydrogen desorption were measured as a function of surface coverage. Hydrogen in the β_2 state shows a sympathetic increase in the rate parameters up to at least half of its saturation coverage where E_d and ν_d assume values of 23 kcal-mole⁻¹ and 1.5×10^{-2} cm²-s⁻¹, respectively. The increase may be due to a strong H-H interaction. The value of E_d for the β_1 state decreases linearly with increasing coverage ($E_d = 17 - 10\theta$ for θ between 0.4 and 0.7) and ν_d is approximately equal to 2×10^{-7} cm²-s⁻¹. Desorption was modeled best for all coverages as second order.

(3) The adsorption kinetics of the β_2 state of hydrogen follows a first order Langmuir model with S_0 equal to unity. For the β_1 state S_0 is 7×10^{-3} and obeys second order Langmuir kinetics. The CPD of the β_2 state increases to 0.30 eV at saturation, and the CPD of the β_1 state decreases to below the clean surface contact potential at saturation.

Two linear regions with very different slopes ($d\Delta\phi/d\theta$) were observed for the β_1 state which implies more than one site is participating.

(4) The absolute coverage, CPD and UPS measurements infer probable binding sites for hydrogen on Ir(110). The β_2 state of hydrogen binds between the rows of Ir atoms in the locations of the missing Ir rows on this reconstructed surface. The β_1 state of hydrogen may bind to two types of sites (twofold or threefold) exposed on (111) microfacets of the reconstructed surface.

The following summarizes the co-adsorption of CO and hydrogen on Ir(110).

(1) The adsorption and desorption properties of hydrogen are affected strongly by the presence of small amounts of CO. For small coverages of CO preadsorbed, a continuous decrease in the desorption of the β_2 state of hydrogen is observed with increasing CO coverages. A concomitant increase occurs for the high coverage β_1 state of hydrogen which is due to a continuous conversion of hydrogen from β_2 sites to β_1 sites as a consequence of the partial mobility of CO. At high CO coverages, the surface is poisoned to hydrogen adsorption.

(2) The adsorption of CO on preadsorbed hydrogen shows the same trends for H_2 as for the reverse case. The binding energy decreases as the CO coverage increases. The desorption of H_2 at 130 K is seen for large CO exposures.

(3) The CPD of hydrogen in the presence of CO preadsorbed is affected strongly also. However, the induced dipole of hydrogen in the β_2 state is unaffected if the number of sites blocked by CO (1.5) is taken into account. For the β_1 state, the induced dipole of hydrogen is unaffected

in the presence of less than 0.25 ML of CO. For 0.50 ML of CO some of the β_1 sites sampled by hydrogen first are blocked due to a H-CO repulsive interaction.

The following summarizes the chemisorption of N_2 and the co-adsorption of N_2 and hydrogen on Ir(110).

(1) XPS and UPS results show N_2 chemisorbs molecularly at low temperature. The N(1s) region of binding energy shows peaks at 399.2 and 404.2 (satellite) eV. The degenerate 5σ and 1π , and the 4σ orbitals are seen at 8.0 and (11.8 ± 0.3) eV binding energy.

(2) The Auger electron transitions of N_2 on Ir(110) may be assigned to normal Auger processes by a simple calculation using XPS and UPS results. However, the N(1s) satellite must be included to account for all of the Auger features observed.

(3) The adsorption and desorption kinetics for N_2 imply that precursor kinetics and repulsive adsorbate-adsorbate interactions are important. Adsorption occurs with S equal to unity independent of coverage and saturates at a coverage of one molecule per reconstructed unit cell ($4.8 \times 10^{14} \text{ cm}^{-2}$). However, thermal desorption measurements indicate that repulsive interactions become important at high coverages, as seen by the appearance of a second desorption peak. The values of E_d at low and high coverages are approximately 8.5 and 6.0 kcal-mole⁻¹, respectively.

(4) A $p1g1(2 \times 2)$ superstructure forms for N_2 at saturation on Ir(110)-(1x2). The proposed structure is consistent with the location of N_2 in the missing row troughs and the saturation coverage.

(5) The co-adsorption of N_2 and hydrogen was studied via UPS and TDS. Hydrogen does not perturb the valence orbitals of N_2 detectibly. However, hydrogen does displace N_2 from the surface, and at least in part, takes up its preferred sites in the missing row troughs.

The following summarizes the chemisorption of NO on Ir(110).

(1) Molecular chemisorption of NO occurs below room temperature and saturates near $9.6 \times 10^{14} \text{ cm}^{-2}$. Adsorption implies precursor kinetics may be involved and S_0 is equal to unity independent of surface temperature. Above 400 K, NO dissociation and N_2 desorption compete with NO adsorption.

(2) The desorption of NO and N_2 occurs in three phases for a saturated overlayer. First, NO desorbs near 400 K and accounts for 17% adsorbed. Second, N_2 desorbs near 430 K as NO dissociates and the coverage of oxygen increases. Third, NO and N_2 desorb where NO (18% adsorbed) desorbing here is associated, in part, with the recombination of nitrogen and oxygen adatoms. Estimates of activation energies for the desorption of NO in the first and third phases are 23.4 and 32.5 kcal-mole⁻¹, respectively. For a saturated layer of NO initially, the activation energy for the dissociation of NO is equal to 25.2 kcal-mole⁻¹. The desorption of N_2 in the low coverage limit of NO has an activation energy equal to 36 kcal-mole⁻¹. The above estimates assume the preexponential factor in each reaction is equal to 10^{13} s^{-1} for a first order reaction or the equivalent $10^{-2} \text{ cm}^2\text{-s}^{-1}$ for a second order reaction.

(3) Oxygen overlayers tend to stabilize NO to dissociation and to desorption. A strong interaction between NO and oxygen is seen by a shift in the 1π level (UPS) and by the CPD behavior of NO on oxygen

precoverages. Both interactions may be due to charge transfer effects between NO and oxygen through the metal.

The following summarizes the reduction of NO with D₂ over Ir(110) under transient and steady state conditions.

(1) Small precoverages of deuterium do not affect the adsorption kinetics of NO but do cause more N₂ to desorb relative to NO at saturation on the clean surface. Deuterium will adsorb on a saturated overlayer of NO. However, deuterium will not adsorb on Ir(110) if it is saturated with NO and oxygen, a situation that occurs under some steady state reaction conditions.

(2) Under steady state conditions and depending on the ratio of partial pressures $R(P_{D_2}/P_{NO})$, a marked hysteresis occurs in the rate of NO reduction as the surface temperature is cycled. At some temperature T a plateau in the rate may appear that persists as T decreases. At a lower T the rate falls uncontrollably to a lower value, and depends upon P_{D_2} and P_{NO} where this occurs.

(3) For R large (>4) ND₃ is produced between 470-630 K and competes strongly with N₂ production. Under most conditions, the reaction products are N₂ and D₂O.

(4) Three regions of the steady state reaction were examined separately: (a) low rate producing N₂ and D₂O only that is inhibited by NO, (b) high rate on plateau producing N₂ and D₂O only and (c) high rate where N₂ and ND₃ are produced competitively. Tentative explanations of the empirical rate expressions derived from the data were discussed in light of XPS, UPS, TDS and LEED results that were presented as well.

However, the conceptual models are limited due to the complexity of the competing elementary reactions and the diffusion of adatoms in the overlayer.

APPENDIX A

THE ADSORPTION OF WATER ON THE RECONSTRUCTED

IR(110)-(1x2) SURFACE

(The text of Appendix A consists of an article coauthored with T. S. Wittrig and W. H. Weinberg that has been accepted for publication in Surface Science.)

Abstract

The interaction of water with the reconstructed Ir(110)-(1x2) surface has been studied with LEED, CPD, XPS and thermal desorption mass spectrometry. It is shown that at most, 6% of the adsorbed water dissociates upon adsorption at a temperature of 130 K. Water does dissociate to OH groups when adsorbed on an Ir(110)-(1x2) surface with preadsorbed oxygen. Water exhibits a constant sticking coefficient for all submonolayer coverages. There exist four distinct thermal desorption states of water on the clean Ir(110)-(1x2) surface. A qualitative model is put forth to rationalize the complex thermal desorption behavior.

1. Introduction

Recently, several ultrahigh vacuum studies of the interaction of water with transition metal surfaces have been carried out (1-5). There are several reasons for this attention. From a fundamental viewpoint, water is a complex and interesting adsorbate, due partly to strong inter-adsorbate interactions caused by hydrogen bonding. Also at issue are the questions of whether water dissociates on metal surfaces, and what role the oxygen lone pair plays in the bonding. From a more practical standpoint, detailed knowledge of the interaction of water with metal surfaces has obvious practical applications in such diverse areas as corrosion, effects on catalytic reactions (either as a reactant or modifier) and the microstructure of electrode surfaces.

This study is the first ultrahigh vacuum investigation of water on iridium. The reconstructed Ir(110)-(1x2) surface was chosen for this study because it is an "open" surface (not geometrically smooth) with many possible "active" sites. It therefore presents the possibility of observing new, geometry-induced effects.

2. Experimental Procedures

The experiments were performed in an ion-pumped stainless steel bell jar with a base pressure below 2×10^{-10} torr. Several surface sensitive probes — a quadrupole mass spectrometer, LEED optics, a CPD apparatus, AES and XPS — are contained in the experimental chamber. The XPS and AES are performed in the pulse counting mode with a double pass cylindrical mirror electron energy analyzer. Continuous work function measurements

were performed by a retarding potential method described elsewhere (6). All probes are interfaced to a PDP 11/10 minicomputer (7). In addition, the system contains a directional beam doser that can be used for introducing adsorbates onto the crystal without backfilling the bell jar. The use of this directional doser allows the creation of an effective pressure at the crystal face that is approximately 100 times greater than the background pressure in the system.

The substrate was cut from a single crystal boule of Ir and was polished on both sides to within 1° of the (110) orientation using standard techniques (8). Carbon was cleaned from both sides of the crystal through a series of oxidation and reduction cycles. Annealing above 1600 K removed oxygen, calcium and potassium impurities. Details of the cleaning procedure are described elsewhere (9). The substrate was heated resistively by two 10 mil Ta support wires, and it was cooled conductively by liquid nitrogen. Temperatures were measured with a W/5%Re-W/26%Re thermocouple spotwelded to a 1 mm^2 Ta foil on the back of the Ir crystal. The thermocouple was referenced to an icepoint junction, and temperatures are accurate within ± 5 K. The base pressure of water in the UHV system was below 5×10^{-11} torr. The water was doubly distilled and checked mass spectrometrically for purity. In particular, no O_2 was observed with the mass spectrometer.

3. Low-Energy Electron Diffraction

If a simple termination of the bulk structure is considered, the Ir(110) surface is a series of rows and troughs. However, a clean surface is reconstructed to form a (1x2) LEED pattern (10). Recently, the structure of reconstructed Ir(110) has been determined to be a surface with every other row of surface atoms in the [001] direction missing (11). The

surface may be thought of as (111) microfacets inclined to one another to form a series of troughs that are two layers deep.

Low-energy electron diffraction was performed for water adsorption on this surface at 130 K and room temperature for water coverages up to several monolayers. For this range of conditions, the surface reconstruction was stable. In addition, no additional LEED spots were observed due to scattering by ordered superstructures of the adsorbed water molecules.

4. Thermal Desorption Mass Spectrometry

The thermal desorption mass spectrometry (TDMS) of water on the clean surface was performed using two different methods of exposure. For submonolayer exposures, the adsorbate was introduced into the bell jar through a leak valve. This method allows accurate exposures to be made and exposes the front and the back of the crystal to equal fluxes of adsorbate. However, the use of this technique with water is limited to low exposures due to adsorption on the crystal supports and saturation of the walls of the bell jar which causes subsequently a high partial pressure of water in the system. Therefore, the TDMS of high exposures of water was performed by introducing the adsorbate through the beam doser in the system. This method introduces very little water onto the system walls and minimizes the adsorption of water on the crystal support. The disadvantages of this method for TDMS are that the flux of adsorbate molecules to the front face of the crystal is higher than to the back face, and the exposure is not related in a linear manner to the time of exposure. This

latter problem is due to the fact that the flux of water molecules rises gradually over a long period of time from the time the valve is opened. Despite these problems, the TDM spectra obtained by this method give a good qualitative understanding of the thermal desorption characteristics of high coverages of water.

The results of the low coverage TDMS are shown in Fig. 1. Three distinct thermal desorption states appear after a one Langmuir exposure. As shown in the figure, these states will be referred to as the β , γ_1 and γ_2 states in order of increasing peak temperature.

At exposures below 0.5 L, the only states to appear are the γ states. As shown in Fig. 2, both of the γ states are present even at 0.05 L, which was the lowest exposure that was studied. The two states develop with increasing exposure at approximately the same rate. Though uncertainty about the background makes an accurate determination of the relative populations impractical, it appears that the two γ states have approximately equal populations at a saturation exposure of 0.5 L.

Determination of Arrhenius desorption parameters by peak shape analysis was rendered impossible by the unknown shape of the background. However, with the assumption that the Arrhenius preexponential factor, ν_d , falls in the range from 10^{12} s^{-1} to 10^{14} s^{-1} , an analysis following Redhead (12) yields a value for the energy of desorption, E_d , of the γ_1 state of $15.8 \pm 1.2 \text{ kcal/mole}^{-1}$ and an E_d of $17.5 \pm 1.3 \text{ kcal/mole}^{-1}$ for the γ_2 state.

At exposures of greater than 0.5 L, the β state begins to populate near 200 K. The β state reaches saturation near one L exposure, and, at

saturation, its population is approximately the same as that of the combined γ states. Saturation of the β and γ states will be referred to hereafter as one monolayer (ML) coverage. Making use of the assumptions employed above, E_d of the β state is found to be 11.6 ± 0.9 kcal/mole⁻¹.

The relationship between surface coverage and exposure derived from Fig. 1 is shown in Fig. 3. It reveals that the sticking coefficient for water on Ir(110)-(1x2) is constant for all submonolayer coverages. It will be assumed that this sticking coefficient is unity for the following two reasons. First, it is difficult to envision circumstances in which only a certain constant fraction of water molecules impinging on the surface would adsorb irreversibly and additionally that this fraction would show no dependence on surface coverage or conditions. Secondly, with the assumption of a unity sticking coefficient and an impingement flux of 4.5×10^{14} molecules/cm² per L (corrected for ion gauge sensitivity), a one L saturation exposure corresponds to each molecule occupying one reconstructed unit cell on the surface.

Beginning at 1 L exposure, the multilayer thermal desorption state begins to emerge. This will be referred to as the α state. The development of this state, which apparently grows without limit, was followed by performing doser exposures in conjunction with the TDMS. The results of this experiment are shown in Fig. 4. The exposure units shown in the figure are the product of the pressure in the doser storage bulb in torr and the time that the crystal was exposed to the beam. These units are not related in any simple manner to Langmuirs, and they are unique to the geometry of the system. The shape of the desorption from the α state indicates zeroth order desorption. The leading edge is exponential when

plotted as a function of $1/T$ and does not depend on initial coverage. In addition, the high temperature edge of the peak indicates a very sharp drop. From an Arrhenius plot of the leading edge of this peak, an E_d of $10 \pm 1 \text{ kcal/mole}^{-1}$ was calculated. No assumption of the magnitude of ν_d is needed to obtain this value. This value agrees well with that observed previously for multilayers of water on transition metal surfaces (2,3).

Figure 4 also contains two qualitative features worthy of mention. First, the β state is definitely distinct from the multilayer α state and therefore represents water molecules that are interacting with the metal surface as opposed to those exclusively in an ice matrix. Second, the presence of the β and γ states in the doser TDMS indicates clearly that they are not artifacts due to desorption from the manipulator and crystal supports.

A series of experiments was also performed to check for residual oxygen left after water had been desorbed thermally from the surface. These experiments were performed to provide information concerning the possible dissociation of water on the surface. The results are presented in Fig. 5. A calibration was carried out first by adsorbing 2.5×10^{14} atoms/cm² of oxygen on the surface and performing an oxygen TDMS. For an initial coverage of approximately 1 ML of water, a small amount of O₂ desorption was detected. This amount corresponded to the oxygen contained in 3% of a ML of H₂O. It is possible that if the water did dissociate on the surface, some of it might recombine during the thermal desorption. In a separate set of experiments, when deuterium and oxygen were adsorbed on the surface in amounts corresponding to 0.5 ML of water, it was found that only 40% of the reactants left the surface as water, while the remainder

desorbed as D_2 and O_2 . If it is assumed that all the O_2 in the water adsorption experiment of Fig. 5 came from water that dissociated on the surface and also that approximately half of it recombined, then approximately 6% of the water dissociated on the surface. However, this small amount of oxygen could have come from another source (e.g., water dissociating elsewhere and providing oxygen to the surface).

5. Contact Potential Difference Measurements

The work function change ($\Delta\phi$) of the surface plotted as a function of H_2O exposure at 140 K is shown in Fig. 6. Since surface coverage is linearly related to exposure, this is equivalent to a $\Delta\phi - \theta$ relationship. The work function decreases in an approximately linear manner throughout the submonolayer coverages from the work function of ice. The plateau in the multilayer region above 1.0 Langmuir continues up to three Langmuirs which was the highest exposure studied. The incremental dipole moment in the submonolayer regime is 0.4 ± 0.1 D per water molecule.

This experiment shows very clearly that only the first Langmuir of water interacts directly with the surface, as has already been indicated by the thermal desorption measurements. It also provides further evidence that little, if any, water dissociates on the surface at 140 K, since the adsorbed dissociation products would almost certainly have different dipole moments than the adsorbed water species. If the first monolayer were totally dissociated, this would also be consistent with the observed work function change, but it would not be consistent with the XPS results presented in the next section or with the TDMS results.

6. X-Ray Photoelectron Spectroscopy

The XPS of the oxygen 1s region of water adsorbed on Ir(110) is shown in Fig. 7. The coverages shown in the figure are derived from thermal desorption mass spectra performed immediately following the XPS. Since the exposures were carried out with the doser, the coverages are subject to a 20% error. The dominant feature in these spectra has a binding energy of 532.1 ± 0.2 eV for all coverages from 0.25 ML to 1.5 ML. This agrees well with the oxygen 1s binding energy of 532.2 ± 0.3 eV observed for nondissociatively adsorbed water on Pt(111) by Fisher and Gland (3). Since this peak shows no shift or splitting well into the multilayer region, it almost certainly represents nondissociatively adsorbed water. At low coverages, there exists also a small asymmetric broadening to the low binding energy side of the peak. This may represent a small amount of dissociatively adsorbed water on the surface.

Figure 8 shows the results of adsorbing water on a surface pre-exposed to oxygen. An amount of water corresponding to one-half monolayer (i.e., 2.5×10^{14} molecules/cm²) was adsorbed on the surface with an equal concentration of oxygen atoms. The oxygen 1s photoelectron spectrum of the oxygen-covered surface was subtracted from the resulting photoelectron spectrum for clarity. The spectrum exhibits one species with a binding energy of 530.5 ± 0.2 eV. Fisher and Gland have reported a photoelectron spectrum of water on an oxygen-covered Pt(111) surface in which a peak at 530.5 eV was observed (3). This species has since been shown to be an adsorbed OH species (13). The oxygen 1s XPS of adsorbed oxygen on Ir(110) is shown in Fig. 9 for comparison. The binding energy of this species is 528.8 eV.

7. Discussion

The combined data from XPS, CPD and TDMS indicate that little, if any, water dissociates on the clean surface at an adsorption temperature of 130 K. The XPS of the oxygen 1s binding energy region show mainly a one-peak structure at 532.1 eV throughout the coverage range from 0.25 ML to 1.5 ML, and this peak is associated with nondissociated water molecules. The slight broadening of the peak to low binding energy at low coverages may indicate that a small amount of water does dissociate on the surface. The $\Delta\phi - \theta$ behavior at a temperature of 140 K displays a relatively constant slope throughout the submonolayer region, which implies that there do not exist separate regimes of adsorption at this temperature as would be the case if some appreciable fraction of the water molecules were dissociating. The dissociation of 6% of a monolayer of water, indicated by the experimental data of Fig. 4 is small but significant. It could either come from a small amount of water dissociated on the surface or, as mentioned previously, from water dissociating elsewhere in the system and depositing oxygen on the surface.

In the interpretation of electron energy loss spectra of water on reconstructed Pt(100) (1), Ibach and Lehwald have proposed a model for water adsorption that may shed some light on the complex thermal desorption behavior observed in this work. At coverages below 0.5 monolayer, they suggest that water polymers form on the surface through hydrogen-bonding. Due to the constraints of the hydrogen bonds, this would introduce inequivalent types of water molecules on the surface. Above 0.5 ML, they observe a structural change which they attribute to a coalescence of these

separate polymers into an ice-like monolayer. Clustering of water molecules at low coverages is also implied by a recent EELS and LEED study of water on Ru(001) (4).

The ideas above suggest a qualitative picture of what may be occurring on the Ir(110)-(1x2) surface. At coverages below 0.5 monolayer, both of the γ states are present in approximately equal concentrations at all coverages. Furthermore, the peak temperatures shift only slightly with coverage. This would be the expected thermal desorption behavior if water formed small noninteracting clusters on the surface with two inequivalent types of water in the clusters. At coverages above 0.5 monolayer, the β state would then represent the water molecules that could not participate in the more stable cluster configuration due to steric factors.

It is worthy of mention that thermal desorption states equivalent to the γ states have not previously been observed on transition metal surfaces (2-5). This is true even of the studies from which the ideas for this model were adopted (1,4). It may be that the γ states are resolvable here due to the unusually open geometry of this surface.

8. Conclusions

Our conclusions may be summarized as follows:

1. The amount of water that dissociates upon the adsorption of a monolayer of water on Ir(110)-(1x2) at a temperature of 130 K is at most 6% of a monolayer.
2. When water is adsorbed on an oxygen-covered Ir(110)-(1x2) surface, OH groups are formed on the surface.

3. Water adsorbs on an Ir(110)-(1x2) surface at a temperature of 130 K with a constant sticking coefficient throughout the submonolayer regime. This sticking coefficient is assumed to be unity.
4. Water exhibits four distinct thermal desorption states from the Ir(110)-(1x2) surface. The low coverage γ states develop simultaneously up to 0.5 L exposure. The β state evolves for exposures between 0.5 L and 1.0 L. The α state is the multi-layer ice state and grows without bound for exposures greater than 1.0 L.
5. A tentative model has been put forth as a plausible explanation of the complex thermal desorption behavior of this system. The γ_1 and γ_2 states in this model represent two differently bound states of water which exist in small clusters of water molecules that are stabilized by hydrogen-bonding. The β state represents water molecules that interact with the surface, but are excluded sterically from joining into the more stable cluster structures.

References

1. H. Ibach and S. Lehwald, Surface Sci. 91 (1980) 187.
2. T. E. Madey and J. T. Yates, Jr., Chem. Phys. Letters 51 (1977) 77.
3. G. B. Fisher and J. L. Gland, Surface Sci. (submitted).
4. P. A. Thiel, F. M. Hoffmann and W. H. Weinberg, Proc. Fourth International Conf. Solid Surfaces, Cannes, September 1980.
5. J. J. Zinck and W. H. Weinberg, J. Vacuum Sci. Technol. 17 (1980) 188.
6. J. L. Taylor and W. H. Weinberg, J. Vacuum Sci. Technol. 15 (1978) 1811.
7. J. L. Taylor, Ph.D. Thesis, California Institute of Technology, 1978.
8. C. M. Comrie and W. H. Weinberg, J. Chem. Phys. 64 (1976) 250.
9. J. L. Taylor, D. E. Ibbotson and W. H. Weinberg, J. Chem. Phys. 69 (1978) 4298.
10. K. Christmann and G. Ertl, Z. Naturforsch. 28a (1973) 1144.
11. C.-M. Chan, M. A. Van Hove, W. H. Weinberg and E. D. Williams, Solid State Commun. 30 (1979) 47; Surface Sci. 91 (1980) 440.
12. P. A. Redhead, Vacuum 12 (1962) 203.
13. G. B. Fisher and B. A. Sexton, Phys. Rev. Letters 44 (1980) 683.

Figure Captions

- Figure 1: Thermal desorption mass spectra of submonolayer coverages of water on Ir(110).
- Figure 2: Thermal desorption mass spectrum of 0.05 L exposure of water on Ir(110).
- Figure 3: Water coverage on Ir(110) as a function of exposure.
- Figure 4: Thermal desorption mass spectra of high coverages of water on Ir(110).
- Figure 5: Oxygen thermal desorption from (a) O_2 adsorbed on Ir(110), and (b) 1 ML H_2O adsorbed on Ir(110).
- Figure 6: Work function changes as a function of H_2O exposure on Ir(110).
- Figure 7: Oxygen 1s XPS for H_2O on clean Ir(110).
- Figure 8: Oxygen 1s XPS for H_2O on oxygen-covered Ir(110).
- Figure 9: Oxygen 1s XPS for 3L O_2 on Ir(110).

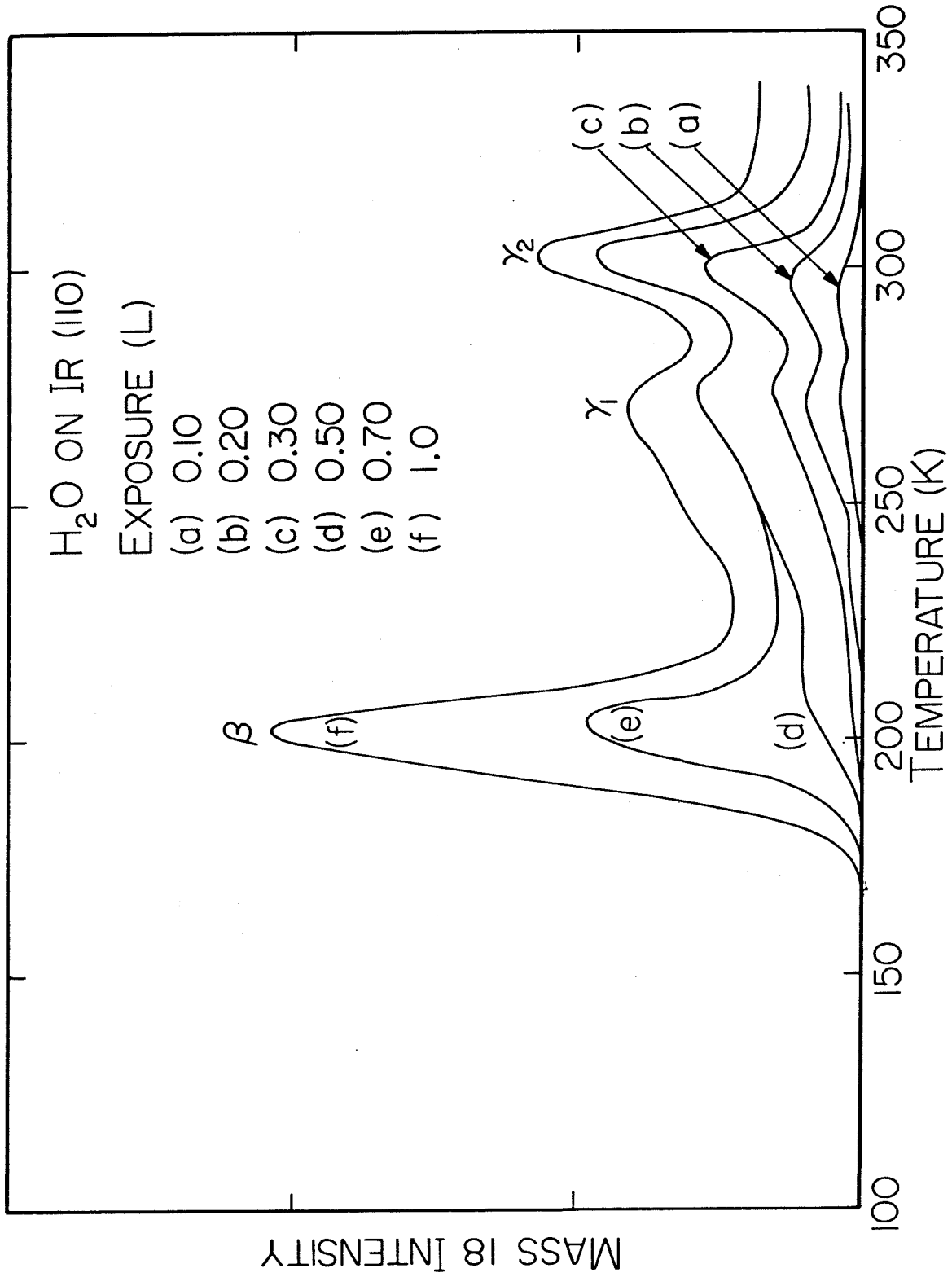


Figure 1

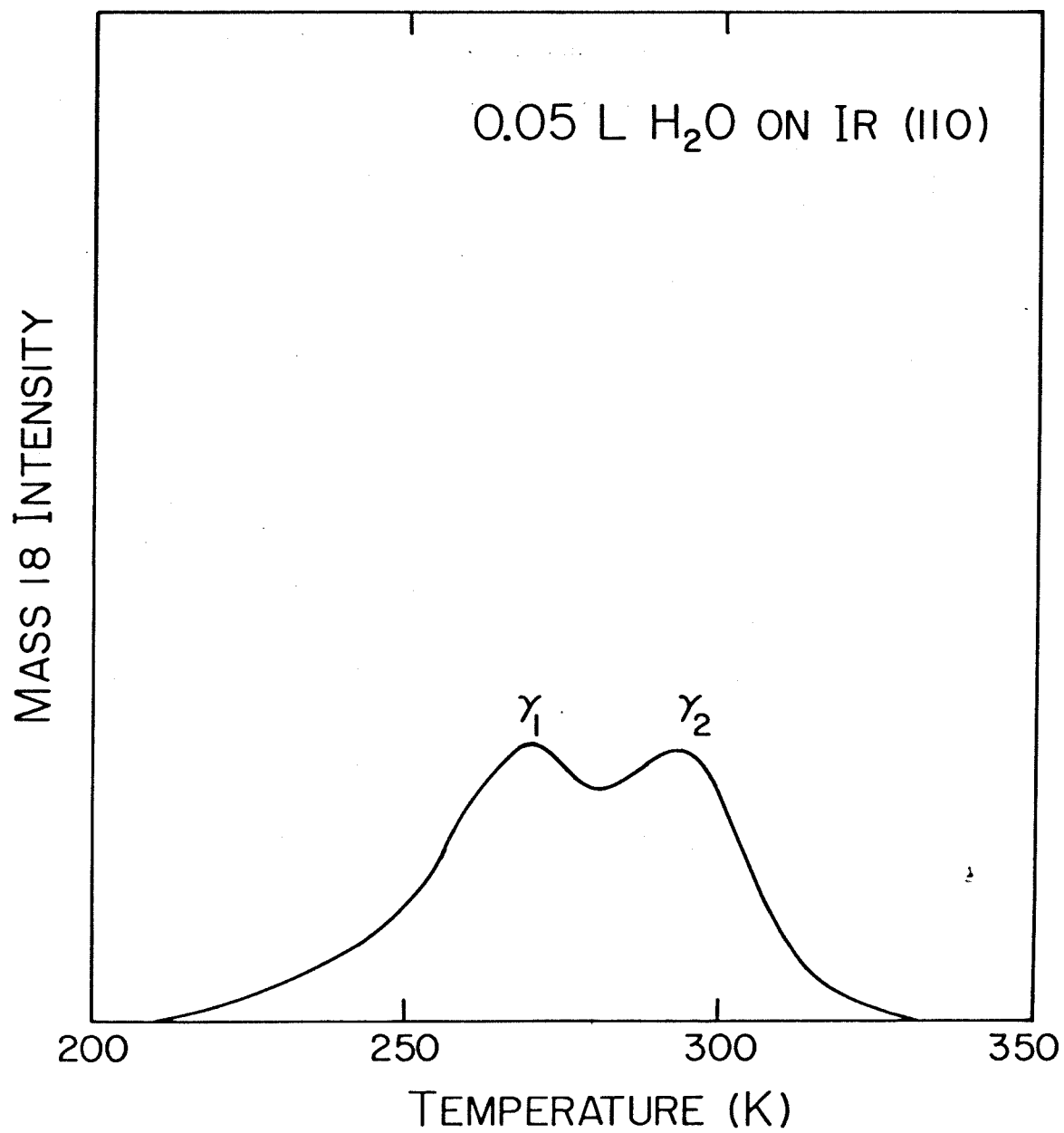


Figure 2

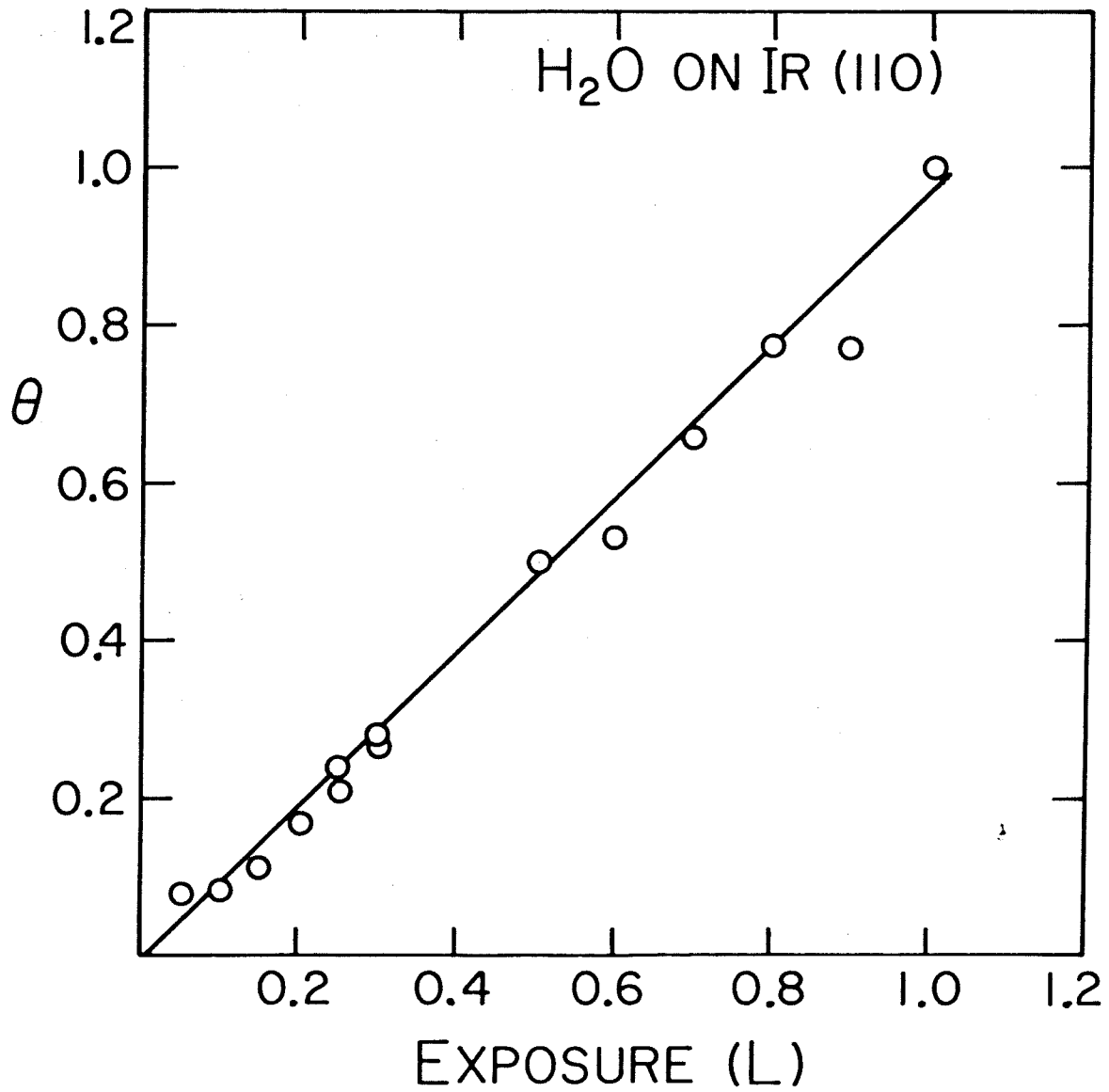


Figure 3

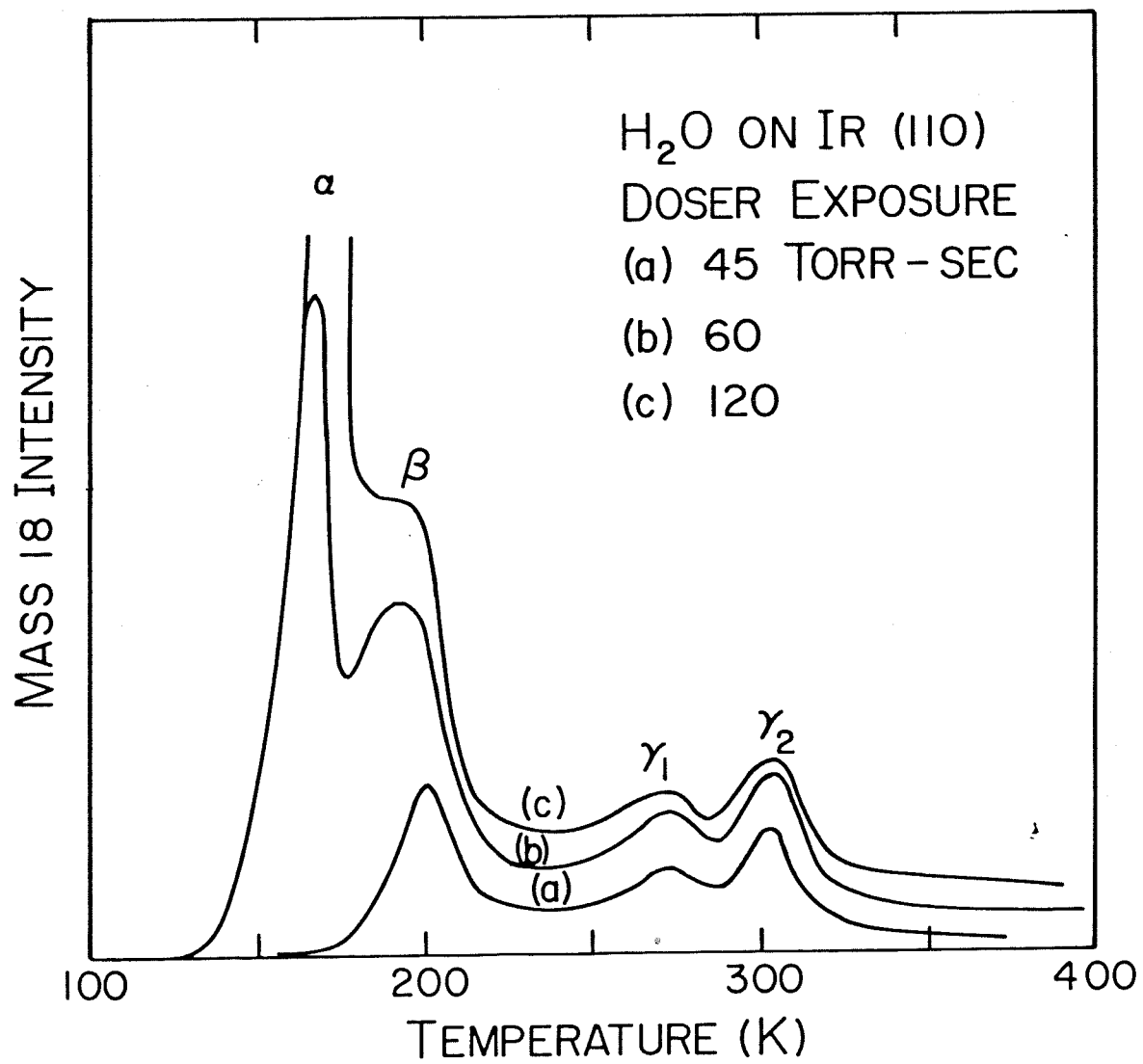


Figure 4

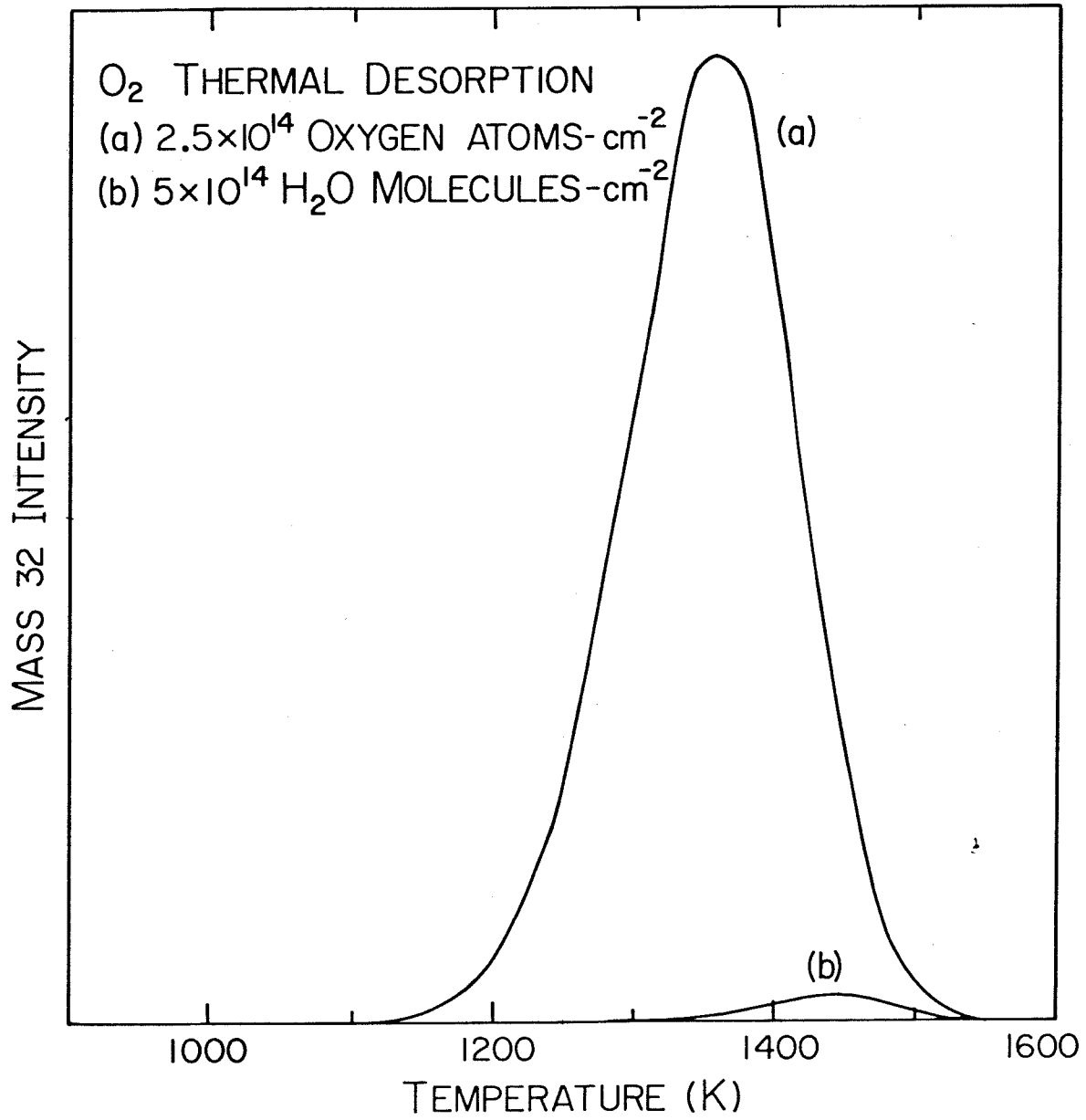


Figure 5

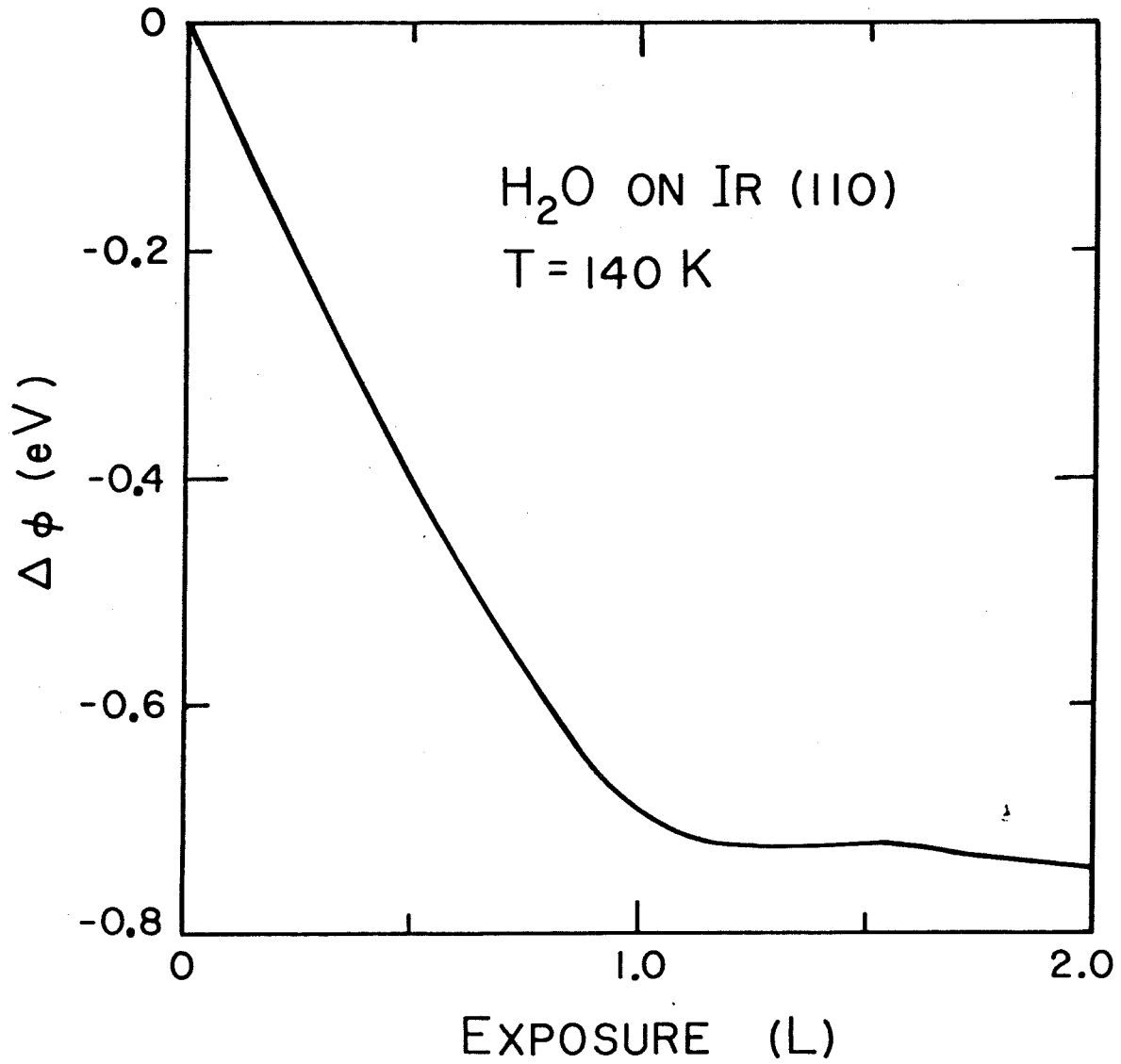


Figure 6

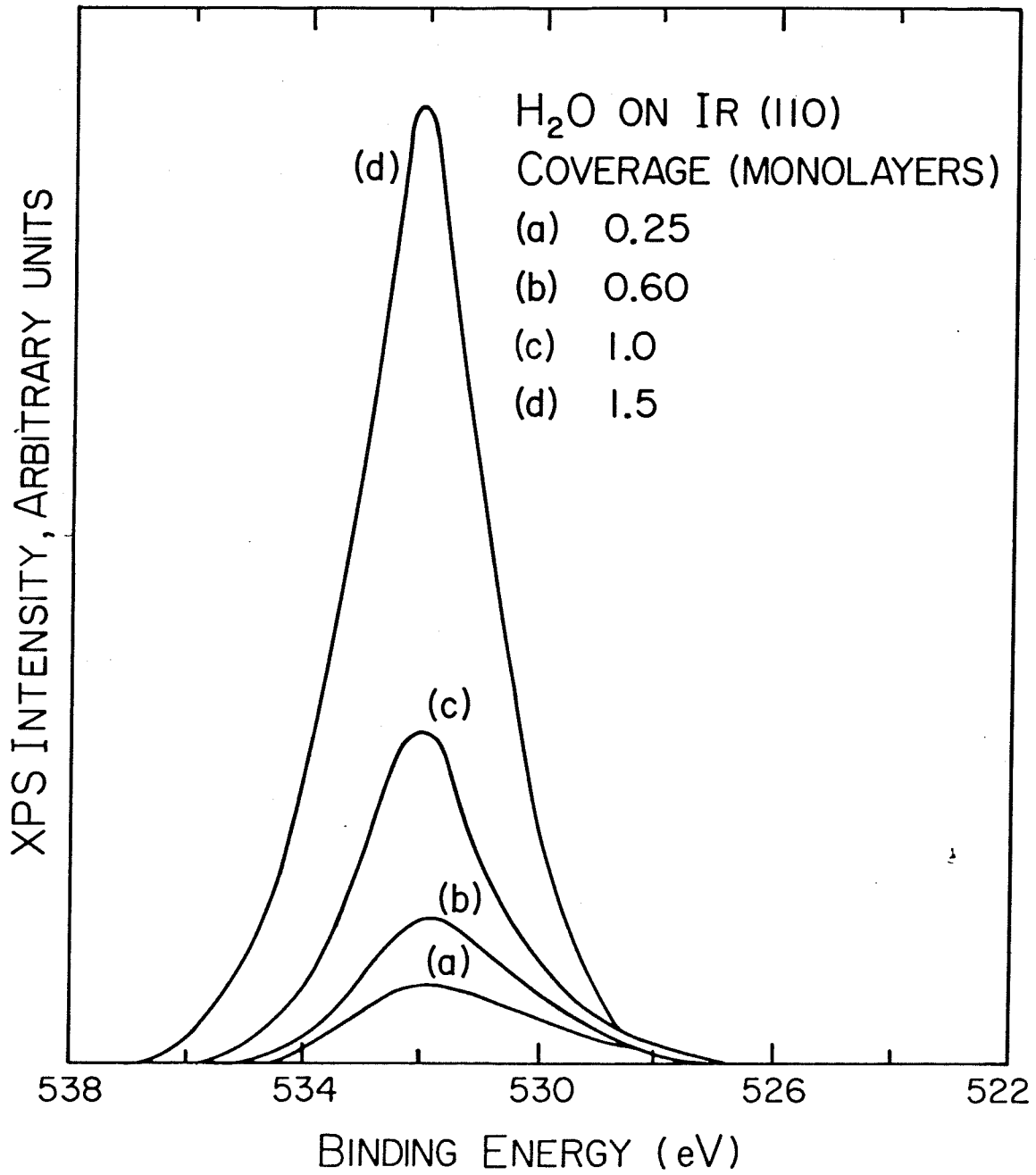


Figure 7

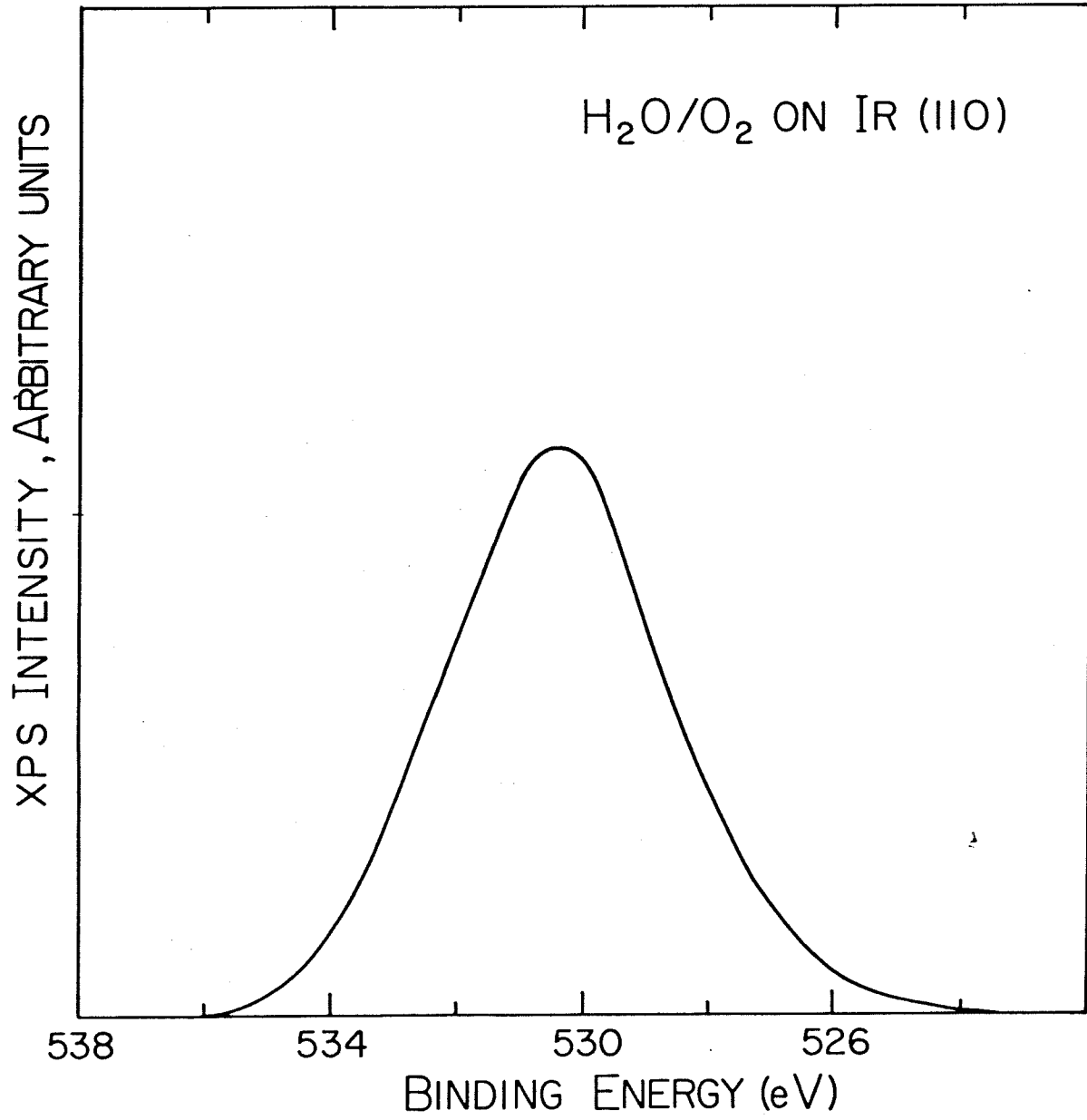


Figure 8

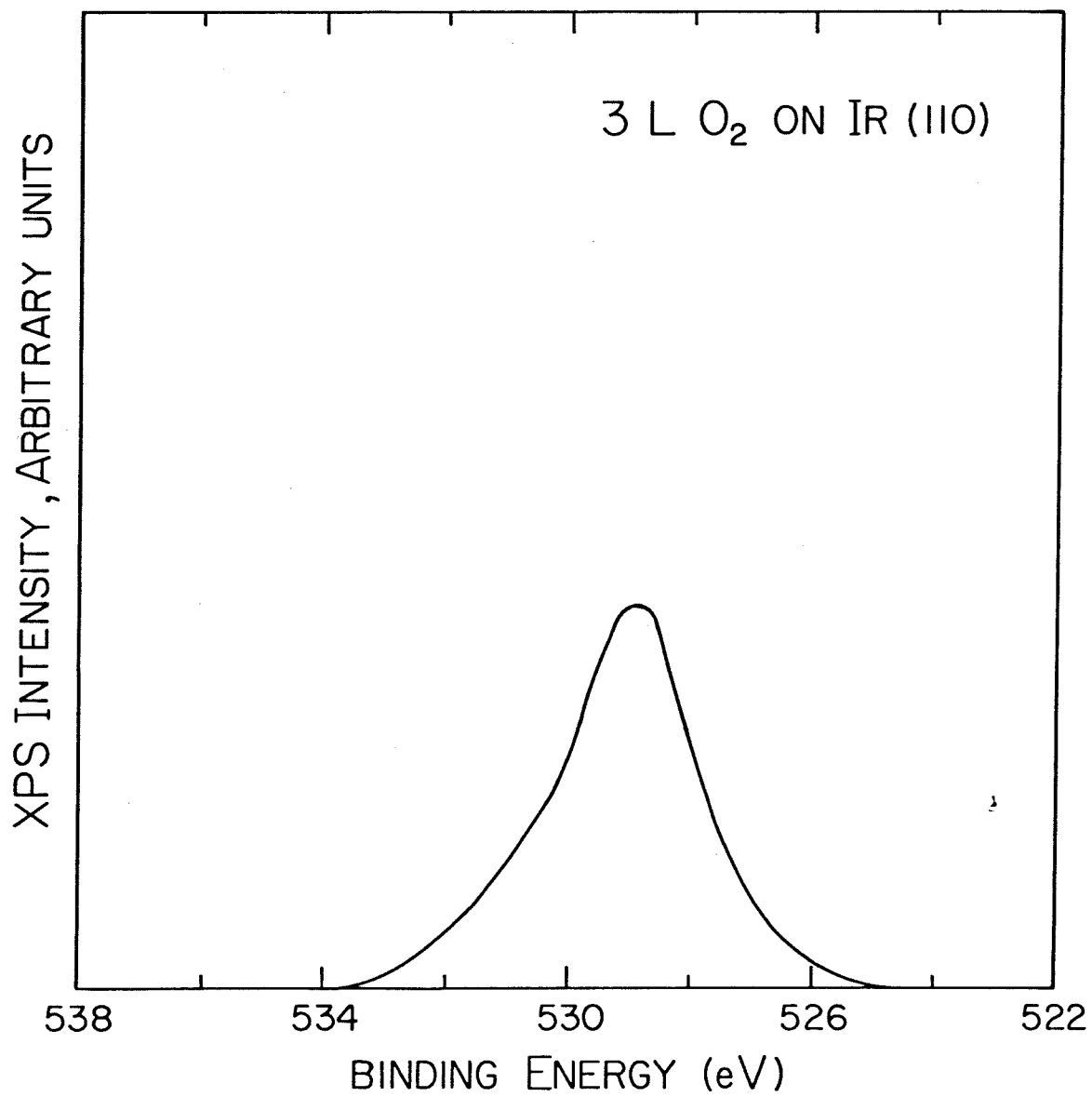


Figure 9

APPENDIX B

A TRANSIENT STUDY OF THE CO-ADSORPTION AND REACTION
OF DEUTERIUM AND OXYGEN ON IR(110)

A brief study was performed of the thermal desorption characteristics of co-adsorbed deuterium and oxygen on the (110) surface of iridium. The first step in all of these experiments was either to adsorb 0.25 ML of oxygen onto the surface or to make the surface oxide(0.25 ML) of Ir(110)(1). Various amounts of deuterium were exposed thereafter to the oxygen covered surfaces at 130 K and the thermal desorption mass spectra of D_2 and D_2O were recorded with a heating rate of approximately 20 K-s^{-1} .

The results of this study are shown in Figs. 1 and 2 for 0.25 ML chemisorbed oxygen and oxide adsorbed initially, respectively. This reaction system is complicated due to several factors. First, even for single adsorbate systems there are various adsorption sites for both oxygen(1) and deuterium(2) on Ir(110). This will lead to several different mechanisms of reaction that will depend on adsorption sites of the reactants as well as temperature (e.g., mobility of reactants and partitioning of the reactants between sites available). Other complicating factors inherent in the nature of the experiment were the changing coverages of the reactants throughout each experiment and the dependence of the peak shapes (and product distributions) on the heating rate. These difficulties made comparison between experiments with different initial coverages ambiguous. Thus, detailed modelling of the kinetics of this system were rendered impractical.

However, it was found in the course of this study that it is possible to remove all of the oxygen from the surface as D_2O if the initial exposure of deuterium is large enough (200 L). This can easily be confirmed by monitoring the oxygen thermal desorption trace. This fact makes it possible to obtain an absolute coverage calibration for D_2 (or H_2) by making use of the known coverage calibration for oxygen on Ir(110)(1).

The calibration consists of three thermal desorption experiments. A schematic of these three steps is shown in Fig. 3. The first step is to expose the surface to a known amount of D_2 (in this case 0.5 L) and record the resulting thermal desorption mass spectrum of D_2 . This gives rise to a peak of area A'_{D_2} . Step 2 consists of quantitatively reacting off 0.25 ML (2.4×10^{14} atoms-cm $^{-2}$) of oxygen in the form of D_2O . This results in a D_2O peak with an area A'_{D_2O} corresponding to a D_2O coverage of 2.4×10^{14} atoms-cm $^{-2}$. This gives an absolute coverage calibration for water. Step 3 consists of adsorbing 0.5 L D_2 and subsequently adsorbing 0.25 L O_2 and recording the thermal desorption traces of D_2 and D_2O . The resulting curves define peak areas of A''_{D_2} and A''_{D_2O} , respectively. The amount of deuterium represented by A''_{D_2O} is known from step 2. Since the amount of deuterium originally on the surface is the same for both step 1 and step 3, the difference ($A'_{D_2} - A''_{D_2}$) also corresponds exactly to the amount of deuterium represented by A''_{D_2O} . The result

of this experiment is that 300 L of deuterium exposed to Ir(110) at 130 K yields a coverage of $(2.2 \pm 0.2) \times 10^{15}$ atoms-cm⁻².

References

1. J. L. Taylor, D. E. Ibbotson and W. H. Weinberg, *Surface Sci.* 79, 349(1979).
2. D. E. Ibbotson, T. S. Wittrig and W. H. Weinberg, *J. Chem. Phys.* 72, 4885(1980).

Figure Captions

- Fig. 1: Desorption of D₂O(A) and D₂(B) from co-adsorbed overlayers of deuterium and oxygen on Ir(110). Oxygen was preadsorbed(0.25 ML) and subsequently D₂ was exposed to the surface at 130 K.
- Fig. 2: Desorption of D₂O(A) and D₂(B) from D₂ adsorbed at 130 K on an oxidized Ir(110) surface(0.25 ML).
- Fig. 3: Schematic of the absolute coverage calibration for deuterium on Ir(110) using the reactive co-adsorption of deuterium and oxygen. Step 1: Desorption of D₂ from Ir(110) as a relative coverage measurement. Step 2: Desorption of 0.25 ML oxygen as D₂O, which gives a coverage calibration for D₂O. Step 3: Desorption of D₂ and D₂O from a layer of deuterium and oxygen where the relative coverage of deuterium is known initially.

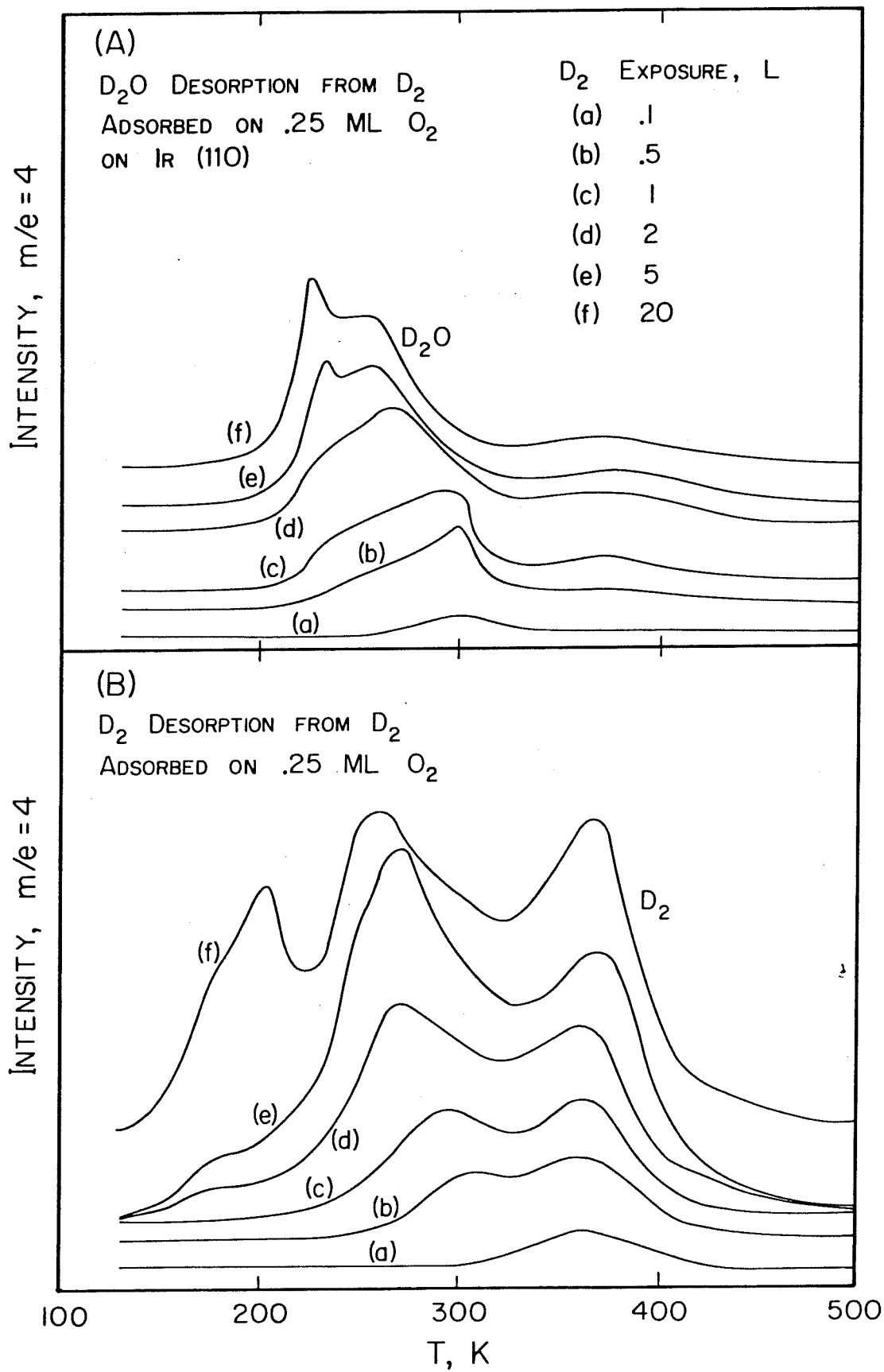


Figure 1

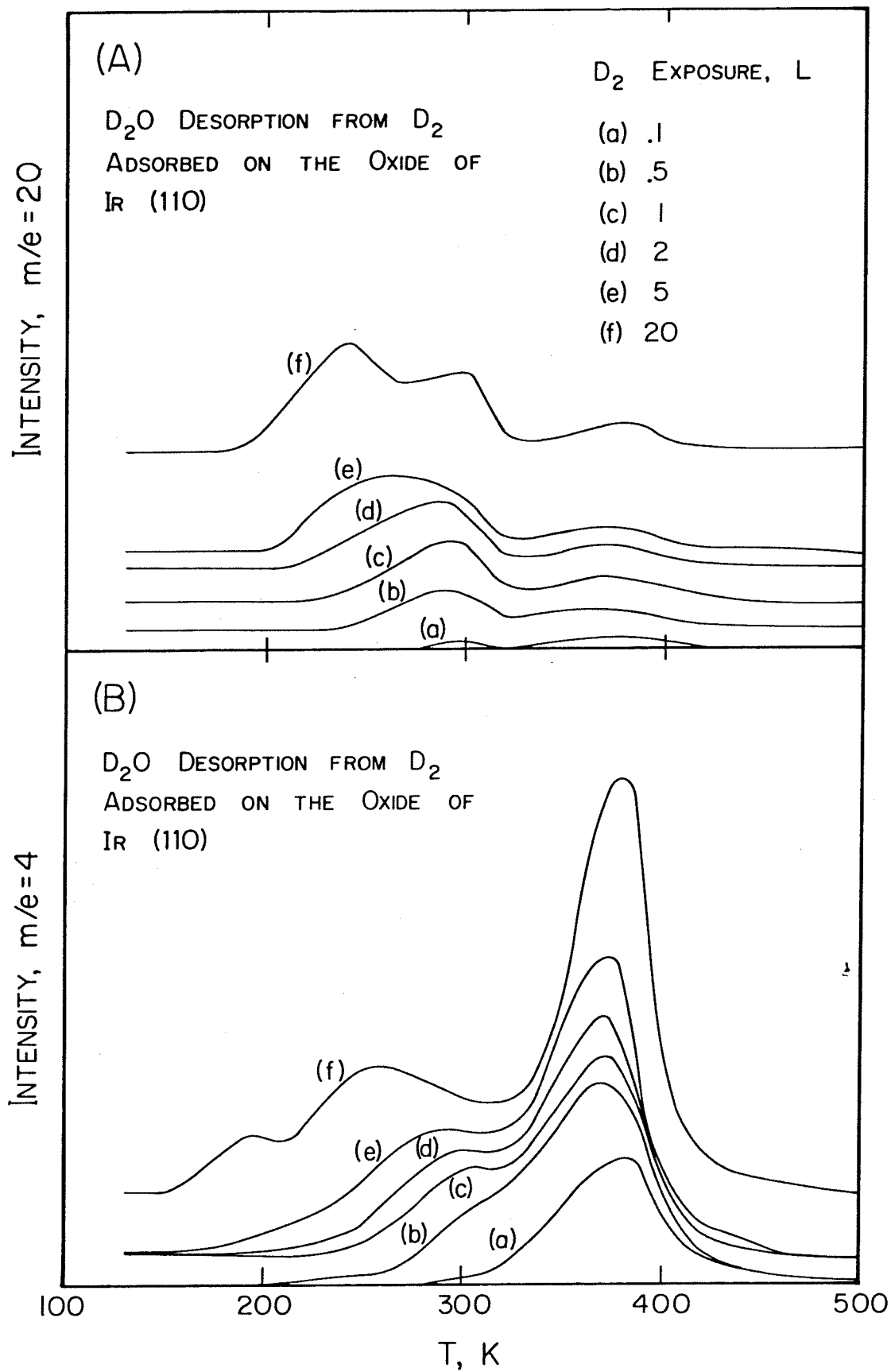


Figure 2

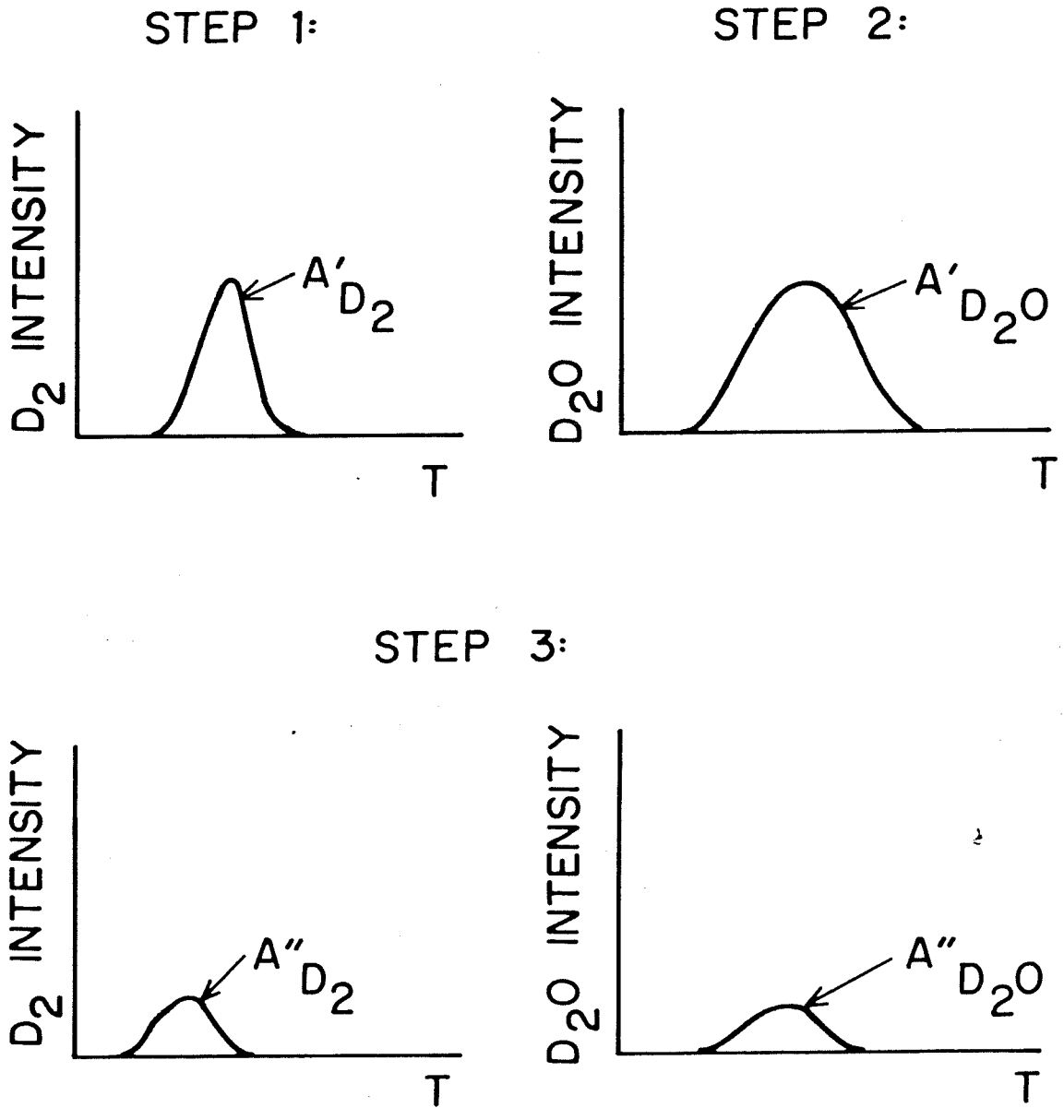


Figure 3

APPENDIX C

"ORDER PLOTS" IN THERMAL DESORPTION

MASS SPECTROMETRY

(The text of Appendix C consists of an article coauthored with T. S. Wittrig and W. H. Weinberg that has appeared in Applications of Surface Science 4, 234(1980).)

Applications of Surface Science 4 (1980) 234–237
 © North-Holland Publishing Company

“ORDER PLOTS” IN THERMAL DESORPTION MASS SPECTROMETRY ★

T.S. WITTRIG ‡, D.E. IBBOTSON and W.H. WEINBERG ‡

*Division of Chemistry and Chemical Engineering, California Institute of Technology,
 Pasadena, California 91125, USA*

Received 11 June 1979

Revised manuscript received 6 August 1979

A common method to determine the rate law for desorption of a gas from a solid surface is to construct order plots derived from thermal desorption experiments. The purpose of this letter is to show that the assumptions on which order plots are based can lead to serious errors in the determined order, and to show how proper corrections can be made.

The starting point of the derivation involves the following expression for the desorption rate,

$$R_d = \nu_d(\theta)\theta^n \exp[-E_d(\theta)/kT]. \quad (1)$$

The order n is assumed to be a constant integer representing the elementary desorption reaction. Logarithmic differentiation of eq. (1) with respect to the fractional surface coverage θ at constant T yields

$$\left(\frac{\partial \ln R_d}{\partial \ln \theta}\right)_T = n + \left(\frac{\partial \ln \nu_d(\theta)}{\partial \ln \theta}\right)_T - \frac{1}{kT} \left(\frac{\partial E_d(\theta)}{\partial \ln \theta}\right)_T. \quad (2)$$

Usually, it is assumed that the last two terms in eq. (2) are zero, and n is equal to the slope for a plot of $\ln R_d$ as function of $\ln \theta$ at constant temperature. However, recent experimental evidence has shown that both rate parameters, E_d and ν_d , can vary strongly with coverage [1, 2]. If the terms $(\partial \ln \nu_d / \partial \ln \theta)_T$ and $(\partial E_d / \partial \ln \theta)_T$ are large, the slope of an order plot may not represent the true order of the desorption reaction, n . Furthermore, if the derivatives vary rapidly with coverage, the order plot is not necessarily linear.

To illustrate these effects, recent thermal desorption data of hydrogen on Ir(110) will be considered [3]. Fig. 1 shows the coverage dependence of E_d and ν_d . Saturation coverage ($\theta = 1$) is defined in this case as the coverage resulting from a 300 L

★ Supported by the National Science Foundation (Grant Number DMR77-14976).

‡ Fannie and John Hertz Foundation Predoctoral Fellow.

* Camille and Henry Dreyfus Foundation Teacher-Scholar.

T.S. Wittrig et al. / "Order plots"

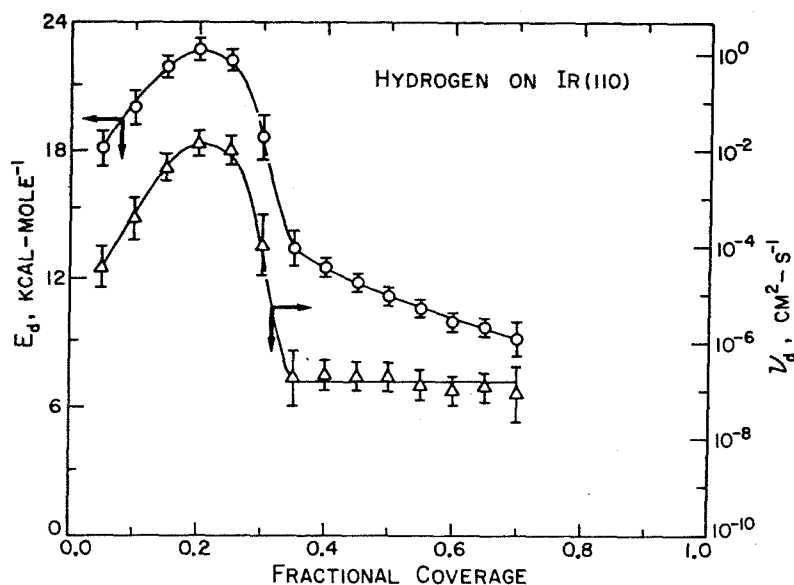


Fig. 1. Activation energy (E_d) and pre-exponential factor (ν_d) for hydrogen desorption from Ir(110) as a function of fractional surface coverage.

exposure of hydrogen to an Ir(110) surface at 130 K. At this coverage, the probability of adsorption of hydrogen is less than 10^{-5} , and higher exposures introduce problems of CO contamination. The values of the parameters were determined by an integral method using variable heating rates [4]. The heating rates were varied from 3 K/s to 110 K/s. This set of experiments was performed twice to enhance the reliability of the results. Further experimental details will be provided in a forthcoming publication [3].

An increase in E_d and ν_d is observed up to a fractional coverage of 0.20. The rapid variation in the rate parameters between coverages of 0.25 and 0.35 is associated with the completion of the low coverage state of hydrogen [3]. At higher coverages, E_d varies approximately linearly with coverage and ν_d varies only weakly with coverage. Fig. 2 illustrates representative order plots for this system. As shown in fig. 2, $(\partial \ln R_d / \partial \ln \theta)_T$ varies strongly with temperature. It is approximately equal to two for $T \geq 380$ K, but it is unreasonably large at lower temperatures.

Table 1 compares the slopes of two representative order plots with values calculated using eq. (2) and fig. 1. The coverage was chosen as the logarithmic mean of the coverage extremes in the experimental order plots, although any reasonable coverage choice will give qualitatively similar results. The order n was chosen as two for all coverages since hydrogen adsorbs dissociatively [3].

For $T \geq 380$ K both the experimental and calculated values for $(\partial \ln R_d / \partial \ln \theta)_T$ are equal to two, as would be expected from a traditional order plot for dissociative

T.S. Wittrig et al. / "Order plots"

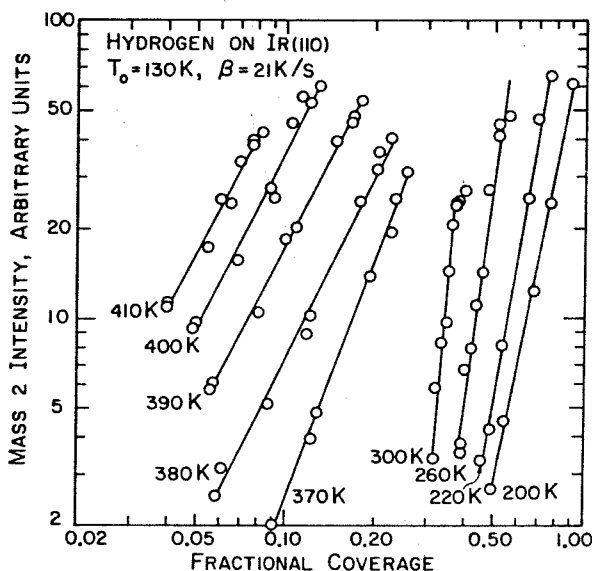


Fig. 2. Traditional order plots for hydrogen desorption from Ir(110) constructed from data in ref. [3].

adsorption. However, the terms $-kT^{-1}(\partial E_d/\partial \ln \theta)_T$ and $(\partial \ln \nu_d/\partial \ln \theta)_T$ in eq. (2), as shown in table 1, are not small but rather cancel one another. This low coverage result may be a general consequence of the so-called compensation effect mentioned in the literature [5, 6]. The low temperature result (220 K) in table 1 provides an example of the large error in the measured order from a traditional order plot, where the apparent order $[(\partial \ln R_d/\partial \ln \theta)_T]$ is equal to 6.1. Assuming that $n = 2$, the calculated order using eq. (2), 10 ± 5 , agrees with the experimental value. The error limits are large for the calculated $(\partial \ln R_d/\partial \ln \theta)_T$ due to the uncertainty in measuring derivatives in fig. 1. It should be noted in the low temperature case that the deviation of the traditional order plot from yielding an order of two is caused primarily by the observation that $dE_d/d\theta = -10 \text{ kcal-mole}^{-1}\text{-monolayer}^{-1}$

Table 1
Parameters of order plot for H₂ desorption from Ir(110)

T, K	θ	$-\frac{1}{kT} \left(\frac{\partial E_d}{\partial \ln \theta} \right)_T$	$\left(\frac{\partial \ln \nu_d}{\partial \ln \theta} \right)_T$	$\left(\frac{\partial \ln R_d}{\partial \ln \theta} \right)_{T, \text{calc}}$	$\left(\frac{\partial \ln R_d}{\partial \ln \theta} \right)_{T, \text{expt}}$
220	0.58	10.5 ± 4	-2.5 ± 2	10 ± 5	6.1 ± 0.3
390	0.10	-4.6 ± 1.0	4.8 ± 1.0	2.2 ± 1.5	2.0 ± 0.1

T.S. Wittrig et al. / "Order plots"

for fractional coverages between 0.4 and 0.7. *This value is not unusual when compared to other adsorption systems in the literature [1,2,7,8].*

In conclusion, it has been shown that traditional order plots may lead to errors in the true order of the desorption reaction of the rate parameters for desorption vary with coverage. However, a procedure for correcting the traditional order plots has been developed. A specific example of hydrogen desorption from Ir(110) was discussed for illustration purposes.

References

- [1] H. Pfnür, P. Feulner, H.A. Engelhardt and D. Menzel, Chem. Phys. Letters 59 (1978) 481.
- [2] J.L. Taylor, D.E. Ibbotson and W.H. Weinberg, J. Chem. Phys. 69 (1978) 4298.
- [3] D.E. Ibbotson, T.S. Wittrig and W.H. Weinberg, in preparation.
- [4] J.L. Taylor and W.H. Weinberg, Surface Sci. 78 (1978) 259.
- [5] G.C. Bond, Catalysis by Metals (Academic Press, New York, 1962).
- [6] E. Bauer, F. Bonczek, H. Poppa and G. Todd, Surface Sci. 52 (1975) 237.
- [7] K. Christmann, O. Schober, G. Ertl and M. Neumann, J. Chem. Phys. 60 (1974) 4528.
- [8] P.A. Thiel, E.D. Williams, J.T. Yates, Jr. and W.H. Weinberg, Surface Sci. 84 (1979) 54.

APPENDIX D
THE CHEMISORPTION OF CO ON CLEAN
AND OXIDIZED IR(110)

(The text of Appendix D consists of an article coauthored with J. L. Taylor and W. H. Weinberg that has appeared in Journal of Chemical Physics 69, 4298(1978).)

Abstract

The chemisorption of CO on clean and oxidized Ir(110) has been investigated under ultra-high vacuum conditions with thermal desorption mass spectrometry, contact potential difference measurements, Auger electron spectroscopy, and LEED. On both surfaces, adsorption is non-dissociative under all conditions examined, i.e., temperatures between 90 and 1300 K and pressures below 10^{-6} torr. Two LEED patterns, a $p(2 \times 2)$ and a (4×2) disordered in the [001] direction, form on the clean surface. A $(2 \times 1)_{p1g1}$ structure forms on the oxidized surface. Thermal desorption spectra from the clean and oxidized surfaces exhibit three and two features. The desorption energy and pre-exponential factor in the Arrhenius equation describing the desorption kinetics have been measured as functions of surface coverage. The compensation effect occurs on both surfaces. In the limit of zero coverage, the desorption energies are 37 and 31 kcal/mole for clean and oxidized Ir(110). The adsorption kinetics are identical for both surfaces. At 90 K, the sticking probability is unity until the surface coverage nears saturation. At 300 K, the adsorption kinetics display second-order behavior with an initial sticking probability of unity. The saturation coverage is about 10^{15} molecules/cm² for both surfaces at 90 and 300 K. Upon adsorption, the work function increases for both surfaces, but is larger for the clean surface and at lower temperatures. A model developed to fit the change in work function with coverage and temperature indicates that binding sites between the topmost rows of surface atoms are preferred energetically.

I. Introduction

This investigation of CO chemisorption was undertaken to give insight into the catalytic behavior of the CO oxidation reaction on Ir(110). Surface sensitive techniques—thermal desorption mass spectrometry (TDS), contact potential difference (CPD) measurements, Auger electron spectroscopy (AES), and LEED—were used to examine various aspects of CO chemisorption on Ir(110) under ultra-high vacuum conditions. These aspects include the spectroscopic characterization of the overlayer, overlayer structures, desorption kinetics, adsorption kinetics, and charge transfer in the overlayer. Each aspect is developed as a separate topic in this article. Inferences drawn from the various results are presented in the discussion that parallels each topic.

Although CO chemisorption has been studied extensively on several surfaces of the platinum metals, including the (110) surfaces of Ni (1, 2), Rh (3), Pd (4, 5), Pt (6, 7), and Ir (8), the different behavior among the various metals justifies this new study. Moreover, many aspects of CO chemisorption have not been treated thoroughly for Ir(110). Examples of different behavior are numerous. CO adsorbs either molecularly or dissociatively depending on the surface and the surface temperature. Although a CO-(2x1)p1g1 LEED pattern appears on all (110) faces of the platinum metals, c(2x2) structures have been observed on Ni, Rh, and Pd; and (4x2) structures on Ni and Pd. First-order adsorption kinetics with an initial sticking probability near unity have been reported in most studies of CO chemisorption, but second-order kinetics have been observed on Ir(111) (9). CPD measurements are understandably

different for CO adsorption on the various metals. However, values varying by several hundred meV have been reported for saturation coverages on surfaces of the same metal and orientation (10).

One explanation for the different observations is that an impurity, a surface oxide, alters the CPD for CO. Often oxygen is used to clean carbon from the surfaces of platinum metals. As this work demonstrates, residual oxides are difficult to detect with AES. Surface oxides, distinct from chemisorbed oxygen, have been observed on Ni (11), Pd (12), Pt (7), and Ir (13) surfaces. A stable, well characterized surface oxide forms on Ir(110) (14). Understanding the chemisorption of CO on this oxidized surface is crucial in this study because the CO oxidation reaction is rapid at temperatures where the oxide forms (15). Therefore, all aspects of CO chemisorption mentioned above are considered for both clean and oxidized Ir(110).

One additional goal of this work is modeling certain facets of CO chemisorption. Specifically, models are developed for describing the influence of inter-adsorbate repulsion upon adsorption kinetics and for explaining the coverage and temperature dependences of CPD measurements.

II. Experimental

The experiments were performed in a stainless steel belljar equipped with ion and Ti sublimation pumps. The base pressure of the vacuum system was 2×10^{-10} torr. The belljar contained several probes for surface analysis, including a quadrupole mass spectrometer (UTI-100C), LEED

optics (Varian), AES (PHI) and XPS (PHI). A double-pass cylindrical mirror analyzer (PHI) performed the energy analysis for the various electron spectroscopies. CPD measurements were recorded by a continuous retarding potential technique (16). The Ir(110) crystal was spot welded to two 10 mil Ta wires, which were mounted on a precision manipulator. The crystal could be cooled to 90 K with liquid nitrogen or could be heated conductively by passing a current through the Ta wires. The surface temperature in the range from 200 - 1800 K was measured with a Pt-Pt10%Rh thermocouple that was spot welded to the crystal. Lower temperatures were measured through the change in the resistance of the Ta wires supporting the crystal.

A computer was interfaced to all probes (17). The pass energy of the analyzer and the filter of the mass spectrometer were controlled by the computer. The intensity of the mass spectrometer, pulse counts from the analyzer, the thermocouple EMF, and CPD measurements were recorded by the computer. A variety of programs analyzed and displayed the data. Although most data were recorded digitally by the computer, smooth curves have been drawn through the data to facilitate the presentation.

The Ir sample was cut from a single crystal (Materials Research Corp.) and was aligned within 1° of the (110) orientation through standard preparation and polishing techniques (18). All data have been reproduced after the sample was repolished, which was done several times during this investigation. Because Ar ion bombardment was inefficient in removing carbon from the crystal in situ, the surface was cleaned chemically through a series of oxidation and reduction cycles. The sample

was heated to 900 K in an atmosphere of 10^{-7} torr of O_2 for several minutes, the belljar was evacuated, and the sample was annealed above 1600 K to remove surface oxygen and to drive carbon from the bulk to the surface. Annealing above 1600 K was absolutely necessary for decomposing surface oxides. During the oxidation cycles, the surface temperature and oxygen pressure were optimized to remove carbon rapidly and to inhibit the formation of oxides. The oxygen used for cleaning the crystal, as well as the carbon monoxide for the chemisorption studies, were research grade (99.99% pure).

All experiments of CO chemisorption were performed on both clean and oxidized Ir(110). The clean surface was free from impurities within the detection limits of Auger spectroscopy (~ 0.01 ML where $1 \text{ ML} = 10^{15}$ atoms/cm²). However, the oxide, which is distinct from chemisorbed oxygen, is relatively insensitive to Auger detection and is characterized as follows (14). At 700 K, the oxide layer forms rapidly until the layer saturates at a coverage of 0.25 ± 0.05 ML. Upon annealing an oxygen covered surface to 1200 K, a $p(1 \times 4)$ LEED pattern slowly appears. Oxygen that does not incorporate into the oxide layer desorbs. Above 1600 K, the oxide desorbs as oxygen molecules; no iridium oxides appear as desorption products. An oxidized surface with reproducible physical properties is formed routinely by adsorbing $0.8 \text{ L } O_2$ ($1 \text{ L} = 10^{-6}$ torr - sec) on the clean surface at 300 K. This exposure corresponds to a surface coverage of 0.25 ML. To transform the chemisorbed oxygen into an oxide layer, the surface is annealed at 1100 K for one minute.

III. Spectroscopic Characterization of the Overlayer

Contrary to previous studies (8), evidence from Auger spectroscopy indicates that CO adsorbs non-dissociatively on both clean and oxidized Ir(110) at temperatures between 90 and 1300 K. X-ray photoelectron spectroscopy (XPS) is not useful for characterizing the adsorbate because the carbon 1s transition is coincident in energy with the Ir $4d_{5/2}$ line. Moreover, the oxygen transitions of CO, chemisorbed oxygen, and the oxide layer differ neither in shape nor in energy within the resolution of the energy analyzer (0.5 eV).

Fig. 1a shows the oxygen KLL Auger transitions of chemisorbed CO and oxygen at 300 K. For all spectra reported here, the electron gun current was approximately 10 nA at 2000 V. Several spectra were summed to obtain the necessary resolution. To accentuate the Auger features, a linear background was subtracted from each spectrum. The oxygen KLL transition of CO resembles that of gaseous CO in shape but is shifted in energy. Because these spectra are similar in shape, but are quite different from the transition of chemisorbed oxygen, which chemisorbs dissociatively at 300 K, CO adsorption must be at least partially molecular. This comparison was suggested first for CO on Ru by Fuggle *et. al.* (19), who assigned hole states to the oxygen peaks for CO. Even though the CO and oxygen are adsorbed on different metals, their spectra are nearly identical in shape and energy to those in Fig. 1a.

The carbon KLL transitions of chemisorbed CO and carbon on clean Ir(110) at 300 K are shown in Fig. 1b. Because the carbon KLL transition

lies near the $\text{Ir N}_4\text{O}_3\text{O}_3$ line, each transition has been accentuated by subtracting the Auger spectrum of the clean surface from the spectrum of the chemisorbed system. The transitions are not altered if the surface is oxidized. The spectrum of chemisorbed CO is quite similar to a derivative spectra reported for CO on polycrystalline Ir (20). By comparison to a gas phase spectrum (21), peaks in the CO spectra have been associated with final hole states as noted in Fig. 1b. The peak intensity associated with the 5σ orbital is reduced with respect to the gas phase spectrum because the surface bond is made largely through this orbital.

The CO transition appears to be superimposed on the carbon transition so that adsorption might be partially dissociative. If the surface is annealed to 800 K after the spectrum is recorded, CO and CO_2 desorb. Carbon is the only species remaining so some surface carbon must have been co-adsorbed with molecular CO. However, dissociation is induced by the electron beam, not through a thermally activated process. Auger spectroscopy has been used to prove this statement. If an Ir(110) surface is heated to 1400 K for 10 min. in 10^{-6} torr of CO, less than 0.02 ML of carbon is detected on the surface following evacuation. The coverage is determined by assuming that the area under an Auger transition is proportional to coverage and that the Auger sensitivities of CO and carbon are equal. When the experiment is repeated in vacuum, only slightly less carbon is detected. No carbon is detected when either experiment is repeated at lower temperatures. Therefore, chemisorbed CO does not dissociate detectably through a thermally activated process below 1400 K.

Instead, carbon appears on the surface either by electron stimulated dissociation of CO or by diffusion of carbon from the bulk.

The cross section for electron stimulated dissociation of CO is estimated as follows. When an electron beam of 0.5 μA , 50 V, and approximately 1 mm diameter impinges on an Ir(110) surface saturated with CO at 300 K, 0.05 ML of surface carbon is formed in 5 min. A background pressure of 10^{-7} torr of CO is maintained to replace CO removed by electron stimulated desorption. The electron flux (J) is $8 \times 10^{14} \text{ cm}^{-2} \text{ sec}^{-1}$. The rate of formation of surface carbon is related to the cross section for electron stimulated dissociation (Q) by (22)

$$d\theta_c/dt = JQ\theta \quad (1)$$

where θ_c is the coverage of carbon and θ is the coverage of CO, which is assumed to be 1 ML. The cross section is $2 \times 10^{-19} \pm 1 \text{ cm}^2$, which is the same as that for CO dissociation on Pt(111) under similar conditions (22). This cross section should not vary substantially for higher electron impact energies (22). Although the cross section appears to vary with surface temperature, this subject was not pursued.

IV. Overlayer Structures

Under the conditions examined, below 1000 K, the clean Ir(110) surface reconstructs to give a (1x2) LEED pattern. Some possible surface structures for Pt(110), which also reconstructs to a (1x2) structure, are described elsewhere (6). Formation of an oxide layer diminishes the intensity of the half-

order LEED beams so that the surface appears to relax to the (1x1) structure, and streaks appear between the spots in the [001] azimuth (14). An earlier study of chemisorption on Ir(110) associated the (1x1) pattern, but not the streaks, with surface oxygen (8).

The carbon patterns, which should not be confused with CO patterns, form on both clean and oxidized Ir(110), and also appear on Ni(110) (23). Schematic representations as well as photographs of the p(2x1) and the (4x5) patterns of carbon are shown in Fig. 2. The p(2x1) pattern forms by electron stimulated dissociation of chemisorbed CO. If CO and the oxygen formed from electron beam dissociation are removed from the surface by annealing to 700 K (oxygen reacts with CO to form CO₂, but does not desorb), the pattern sharpens. The p(2x1) pattern transforms into the (4x5) pattern by annealing the surface to 1200 K. As determined by AES, both patterns form above coverages of 0.05 ML. When the crystal is heated to 900 K in an oxygen atmosphere, these carbon patterns vanish rapidly, and CO and CO₂ are formed. An earlier study of Ir(110) associated a c(2x2) pattern with carbon (8). In the present study, this structure is associated with oxygen only (14). The pattern disappears and CO₂ forms when the surface is heated to 600 K in the presence of CO. Moreover, this pattern is never observed if oxygen is absent from the surface.

Different LEED patterns for CO appear on clean and oxidized Ir(110). On the clean surface, two patterns, a p(2x2) and a (4x2) appear near 90 K, but are poorly ordered at room temperature. The (4x2) pattern is disordered somewhat in the [001] azimuth, perhaps as a result

of surface reconstruction in that direction. Both patterns are disordered rapidly by the electron beam and could not be photographed. Drawings of these patterns are shown in Fig. 3. As determined by TDS, the $p(2 \times 2)$ and (4×2) patterns are sharpest at $1/4$ and $3/4$ of saturation coverage. The overlayer compresses continuously since, as coverage increases, the $p(2 \times 2)$ pattern streaks in the $[001]$ azimuth and broadens in the $[110]$ azimuth. Then the broad streak coalesces to form the elongated spots of the (4×2) pattern. The (4×2) pattern appears on the (110) surfaces of Ni (1, 2) and Pd (4, 5), but the $p(2 \times 2)$ pattern has not been reported previously. Since the saturation coverage of CO on Ir(110) is one molecule per unit cell (1 ML), as will be shown, surface structures for these patterns may be postulated and are shown in Fig. 3. Although theories of CO chemisorption on transition metals suggest that binding sites between the topmost row of surface atoms are energetically favorable (24), additional experimental evidence is needed to fix the registry of the overlayer with respect to the surface. CPD measurements (q.v.) indicate that CO indeed binds preferentially between the topmost rows of surface atoms.

A $(2 \times 1)p1g1$ pattern forms on the oxidized surface, and appears from 100 - 500 K and between 5 - 100% of saturation coverage. This pattern has been observed on the (110) face of all platinum metals (1 - 8), including Ir (8). Fig. 4 contains a photograph and a drawing of the $(2 \times 1)p1g1$ pattern. Since certain spots, represented by dotted circles, are missing, this structure is distinct from the carbon $p(2 \times 1)$ pattern. The missing spots indicate that $p1g1$ symmetry exists in the overlayer. Lambert (25) proposed the structure in Fig. 4 that is consistent with

this symmetry condition. Because the $(2 \times 1)_{p1q1}$ pattern is intense at low coverages, CO molecules coalesce to form islands on the oxidized surface. If the oxide layer is partially formed, i.e., the oxide coverage is less than 0.25 ML, the $(2 \times 1)_{p1q1}$ pattern forms, but streaks in the $[001]$ azimuth. Hence, the oxide layer is crucial in ordering this CO pattern on Ir. Also the overlayer appears to influence the structure of the oxidized surface. When CO adsorbs on an amorphous or an ordered oxidized surface with a (1×1) or a (1×4) structure, respectively, the substrate rapidly displays a sharp (1×2) pattern. Similar observations have been reported for CO chemisorption on Pt(110) (6) and Ir(110) (8), suggesting that those studies were conducted on oxidized surfaces.

V. Desorption Kinetics

Several thermal desorption spectra of CO from clean and oxidized Ir(110) were collected as a function of CO exposure at 300 K. These data are useful for investigating both the desorption and the adsorption kinetics of CO on Ir(110). The latter subject will be treated in the next section. The desorption spectra for both surfaces show no evidence for dissociative adsorption since neither a CO nor a CO₂ feature appears near 900 K where the reaction between chemisorbed carbon and oxygen is rapid (as was shown previously).

Fig. 5a shows representative curves of 40 desorption spectra for CO from clean Ir(110). The average heating rate (β) for each spectrum is 36 K/sec. Three features appear with relative intensities of 1:2:1 for saturation coverage. The completion of the first and second structures

is associated with 1/4 and 3/4 of saturation coverage. Since LEED patterns appearing at these relative coverages may be associated with absolute coverages of 1/4 and 3/4 ML, saturation coverage is 1 ML or 9.6×10^{14} molecules/cm². Moreover, this determination coincides with results obtained from adsorption kinetics (q.v.).

Assuming a pre-exponential factor of 10^{13} sec⁻¹, desorption energies of 23, 29 and 35 kcal/mole are associated with the three features, but this approximation is both unnecessary and incorrect (26). These data may be analyzed to yield the coverage dependences of the pre-exponential factor [$\nu_d(\theta)$] and the desorption energy [$E_d(\theta)$] in the Arrhenius expression for desorption

$$R_d = -C_s \frac{d\theta}{dt} \\ = \nu_d(\theta) C_s \theta \exp [-E_d(\theta)/kT] \quad (2)$$

where R_d , C_s , k , t , and T are the desorption rate, the concentration of CO sites (9.6×10^{14} /cm²), the Boltzmann constant, time and surface temperature. The order of the desorption is assumed to be one since CO adsorption is non-dissociative. Because the experimental chamber is pumped rapidly, the desorption rate is proportional to the intensity of the mass spectrometer signal (I) so that

$$- \frac{d\theta}{dt} = \eta I \quad (3)$$

where η is the proportionality constant. The coverage for any point in

a desorption spectrum is determined by integrating Eq. (3),

$$\theta_0 - \theta(t) = \eta \int_0^t I dt \quad (4)$$

No special form for the heating schedule need be assumed in performing this integration if the intensity and temperature are monitored as independent functions of time. If the initial coverage (θ_0) is known, the constant (η) may be determined by integrating Eq. (4) over the entire spectrum. Since the desorption rate and temperature for a particular coverage vary with the initial coverage, an Arrhenius plot of $\ln R_d$ versus $1/T$ for a particular coverage gives the desorption energy from the slope [$-E_d(\theta)/k$] and the pre-exponential factor from the intercept $\ln [v_d(\theta) C_s \theta / \eta]$. However, the resulting values are highly inaccurate because the desorption rate and temperature do not vary strongly with coverage if the pre-exponential factor is large ($\sim 10^{13} \text{ sec}^{-1}$).

Excellent accuracy is obtained if the heating schedule, rather than the initial coverage, is altered to vary the desorption rate and temperature for a particular coverage. Ten desorption spectra of CO from clean Ir(110) were collected by varying the heating rate from 4.5 to 212 K/sec (27). By exposing the surface to 10.0 L of CO at 300 K, the initial surface coverage was fixed at 0.82 ML for each run. Arrhenius plots constructed from these data are shown in Fig. 6a. This procedure could be inaccurate since three features appear in the desorption spectra, implying that desorption may occur from multiple distinct sites at any particular coverage. However, the peaks in the spectra are separated in energy sufficiently that desorption from multiple sites is a second order

effect since the difference in the desorption energies of the peaks is greater than 10% of the desorption energy of the highest temperature peak (26). Moreover, LEED data (q.v.) indicate the overlayer compresses continuously so that the three peaks in the thermal desorption spectra appear as a result of interadsorbate interactions, rather than desorption from multiple sites.

In Fig. 7a, the desorption energy and pre-exponential factor from the Arrhenius plots are shown as a function of surface coverage. Substantial decreases in the desorption energy near 0.25 and 0.75 ML are associated with the completion of peaks in the desorption spectra and with the formation of LEED structures. Because CO adsorption on the platinum metals is not believed to be activated (28), the desorption energy is nearly equal to isosteric heats measured for CO chemisorption on the (110) faces of other platinum metals. In the low coverage limit, the desorption energy 37 kcal/mole, does not differ appreciably from isosteric heats of 30, 31, 40, 31 and 37 kcal/mole measured for Ni (2), Rh (3), Pd (5), Pt (6) and Ir (8). Although the isosteric heats for Ir, Ni (2) and Pd (5) decrease continuously with coverage, substantial decreases in the isosteric heats occur at different coverages. As shown in Fig. 7a, the desorption energy of chemisorbed CO on Ir varies almost linearly with coverage. Some models for chemisorption indicate that a linear decrease in the isosteric heat is associated with intermolecular repulsion (29), but the large decrease for Ir, 16 kcal/mole-ML, cannot be attributed solely to nearest-neighbor repulsive interactions. A model for the adsorption kinetics (q.v.) indicates that these interactions reduce the isosteric heat by about 2 kcal/mole-ML. The additional decrease may be attributed to other phenomena, such as changes in CO binding sites with coverage or longer-range inter-adsorbate interactions. The former conjecture is unlikely since it contradicts the results from

CPD measurements and from the continuous compression seen with LEED (q.v.).

The compensation effect (28) occurs for CO desorption from Ir; that is, the desorption energy and the pre-exponential factor vary in sympathy. As discussed elsewhere (30), this effect should be common to most desorption systems. To describe the compensation effect in desorption kinetics, Bauer and coworkers (31) developed a modified form of the Arrhenius expression,

$$R_d = v_0 C_s \theta^n \exp \left[-\frac{E_d(\theta)}{k} \left(\frac{1}{T} - \frac{1}{T_s} \right) \right] \quad (5)$$

where n , v_0 and T_s are constants, and are equal to 1, $7 \times 10^5 \pm 1 \text{ sec}^{-1}$ and $1240 \pm 50 \text{ K}$, respectively, for CO desorption from clean Ir(110).

Activated complex theory (28) is useful for rationalizing the substantial decrease in the pre-exponential factor with coverage. In this theory, the pre-exponential factor is related to the entropies of the activated and chemisorbed phases, $S_*(\theta)$ and $S_s(\theta)$,

$$\ln v_d(\theta) = [S_*(\theta) - S_s(\theta)]/k \quad (6)$$

The activated phase may be thought of as a precursor state to desorption. Since the pre-exponential factor decreases with coverage, either the entropy in the activated phase decreases, or the entropy in the adsorbed phase increases. Both conjectures are reasonable. Since the number of molecules in the activated phase is approximately proportional to the number in the adsorbed phase, the population in the activated phase

increases, but the entropy decreases as the number increases (32). If the overlayer becomes more mobile as coverage increases, and the mobility of the activated complex does not change, the entropy of the adsorbed phase increases. This conjecture is substantiated by theories of CO chemisorption on the platinum metals, which indicate that CO binds less deeply in the potential wells of the surface as coverage increases (24). The precursor model for desorption developed by King (33) is not appropriate for describing the change in the pre-exponential factor with coverage. This theory would predict that the pre-exponential factor increases with coverage, but the opposite trend is observed.

Desorption spectra of CO from oxidized Ir(110) are different from those obtained on a clean surface. Representative spectra from the oxidized surface with a heating rate (β) of 40 K/sec are shown in Fig. 5b. CO reacts with the oxide layer to produce both CO and CO₂ as desorption products. Since some CO is created when CO₂ is ionized by the mass spectrometer, this CO signal, which is deduced from the cracking pattern for CO₂ and from the CO₂ spectrum, has been subtracted from each CO spectrum. To account for the different sensitivities of CO and CO₂ in the mass spectrometer, the CO₂ spectra have been multiplied by a weighing factor also. From comparing the area under the CO spectrum for clean Ir(110) to the sum of the CO and CO₂ areas for the oxidized surface, saturation coverage on oxidized Ir(110) is 1 ML. This result is also in agreement with the observed (2x1)p1g1 LEED structure. A maximum of 65% of the oxide layer reacts with CO at 4 L exposure. This fraction decreases slightly for higher exposures. The oxide is distinct from chemisorbed oxygen because all chemisorbed oxygen reacts with CO under similar conditions. Further details of the CO oxidation reaction

involving the two forms of surface oxygen are discussed elsewhere (15).

Two peaks with relative intensities of 1:1 at saturation coverage appear in the CO desorption spectra from the oxidized surface. McCabe and Schmidt (7) observed similar two-peak spectra for CO desorption from an oxidized Pt(110) surface, but reported different spectra for a clean surface. If the pre-exponential factor is assumed to be 10^{13} sec^{-1} , desorption energies of 29 and 36 kcal/mole are associated with the two peaks for oxidized Ir(110). The coverage dependences of the desorption energy and pre-exponential factor are calculated from Arrhenius plots constructed from the desorption spectra and are shown in Fig. 6b. Suitable accuracy is obtained because the pre-exponential factor is relatively small ($\lesssim 10^{11} \text{ sec}^{-1}$) (30). The CO coverage is determined from the weighted sum of the integrals [Eq. (4)] of the CO and CO₂ spectra. Although the CO and oxide coverages should be held constant in an Arrhenius plot, the oxide coverage varies for each plot shown in Fig. 6b. Thus, the calculated rate parameters may be somewhat inaccurate.

The coverage dependences of the desorption energy and the pre-exponential factor for the oxidized surface are shown in Fig. 7b. Although the shapes of these curves are nearly identical to those obtained for the clean surface, both the desorption energy and the pre-exponential factor for any coverage are substantially lower on oxidized Ir(110). In the limit of low coverage, these rate parameters assume values of 31 kcal/mole and 10^{11} sec^{-1} . The desorption features from the oxidized surface appear at higher temperatures than those from the clean surface, not because the desorption energy is larger on the oxidized surface, but because the pre-exponential factor is smaller. The desorption energy is

again a strong function of coverage, varying by 16 kcal/mole over 0.5 ML, and the compensation effect occurs once more. The parameters ν_0 and T_S in Eq. (5) assume values of $4 \times 10^{\pm 1} \text{ sec}^{-1}$ and $650 \pm 10 \text{ K}$, which differ substantially from those for the clean surface. As Bauer and coworkers have suggested (31), these parameters are quite sensitive to the condition of the surface. Since the desorption kinetics of CO differ markedly for the clean and oxidized surfaces, the two surfaces might be expected to display different catalytic behavior for the CO oxidation reaction. This is indeed the case (15).

VI. Adsorption Kinetics

By integrating Eq. (4) over an entire desorption spectrum, an initial coverage is associated with a gas exposure. In this way, the adsorption kinetics of CO on clean and oxidized Ir(110) at 300 K have been deduced from the spectra in the previous section and are shown in Fig. 8. An absolute coverage may be associated with each exposure since, as shown previously, the saturation coverage on either surface at 300 K is 1 ML ($9.6 \times 10^{14} \text{ molecules/cm}^2$). The adsorption kinetics for CO exposures below 10 L are identical for the two surfaces within experimental error. Above 10 L exposure, the coverage of CO increases slowly until the surface saturates at several hundred Langmuirs. This trend is definitely not an artifact resulting from drift in the gain of the mass spectrometer and has been observed previously on Ir(111) (18). Near saturation coverage, the overlayer desorbs slowly at a rate of about 10^{-4} ML/sec at 300 K. This behavior is predicted from the

measurements of desorption kinetics (q.v.) by extrapolating the rate parameters to saturation coverage.

The probability of adsorption (S), or the sticking probability, is the ratio of the number of gaseous CO molecules that chemisorb to the number that impinge on the surface (9),

$$S = (2\pi M_{\text{CO}} kT_g)^{\frac{1}{2}} C_s \frac{d\theta}{d\varepsilon} \quad (7)$$

where M_{CO} , T_g , and ε are the molecular weight, temperature, and exposure of the gaseous CO. After the exposures are adjusted for the CO sensitivity of the ion gauge that monitored the exposures, an initial sticking probability (S_0) of 1.04 ± 0.05 is calculated for CO adsorption on either surface. This result agrees closely with other values reported for CO adsorption on the platinum metals (9). Regardless of the metal or the orientation of the surface, the initial sticking probability is nearly one.

Different models for adsorption kinetics fit the data, depending on the coverage range. The Langmuir model (35) is appropriate below 0.4 ML, a first-order precursor model (36) is appropriate below 0.7 ML, but the best overall fit is obtained with a second-order precursor model developed by King and Wells(37). This model has two noteworthy features. A molecule in the precursor state may not chemisorb unless it is above an empty adsorption site having one or more empty nearest neighbors. Second,

the overlayer is ordering and disordering continually because of repulsive or attractive interactions between adsorbates, and thermal randomization of the adlayers. This model is apposite for the non-dissociative adsorption of CO if the probability of chemisorption is zero above an empty site with no empty nearest neighbor and is constant otherwise. This hypothesis does not imply that an adsorbed molecule cannot be surrounded completely by other adsorbates, but does mean that chemisorption must occur in one site in a pair of empty and adjacent sites.

In the second-order precursor model (37), the sticking probability (S) is related to the initial sticking probability (S_0), a constant (κ) that is inversely proportional to the lifetime of the precursor state, and the fraction of empty sites with an empty nearest neighbor (θ_{00}),

$$\frac{S}{S_0} = [(1 - \kappa) + \kappa/\theta_{00}]^{-1} \quad (8)$$

The value of θ_{00} depends on the fractional coverage and a constant B ,

$$\theta_{00} = (1 - \theta) - \frac{2\theta(1 - \theta)}{(1 - 4B\theta(1 - \theta))^{\frac{1}{2}} + 1} \quad (9)$$

but is insensitive to whether the adlayer is twofold, fourfold, or sixfold symmetric (34). The constant B is related to the attractive or repulsive energy between nearest neighbors,

$$\psi = -kT \ln(1 - B) \quad (10)$$

where a negative value for ψ is associated with an attractive interaction. For CO adsorption on both clean and oxidized Ir(110) at 300 K, the second-order model with $S_0 = 1.0$, $\kappa = 0.2$, and $B = 0.96$ fits the kinetic data well. This model in the integrated form, obtained from Eqs. (7)-(9), is shown as a solid line in Fig. 8.

The repulsive energy determined from this model, $\psi = 2$ kcal/mole, may be compared to that from a Lennard-Jones potential between two adsorbates (38),

$$\psi(r) = 4kT_{\sigma} \left[\left(\frac{\sigma}{r} \right)^{12} - \left(\frac{\sigma}{r} \right)^6 \right] \quad (11)$$

Values of $\sigma = 3.76 \text{ \AA}$ and $T_{\sigma} = 100 \text{ K}$ for gaseous CO approximate the values for chemisorbed CO. The distance between the centers of adsorbates (r) may be estimated as 3.3 \AA , which is the largest distance consistent with $(2 \times 1) \text{ p}1\text{g}1$ symmetry of the overlayer on the oxide (see LEED results (25)). Hence, the value for ψ from the Lennard-Jones potential, 2 kcal/mole, equals the value from the kinetic model. If the overlayer has $\text{p}1\text{g}1$ symmetry, each adsorbate has two nearest neighbors so that intermolecular repulsion reduces the heat of adsorption by about 2 kcal/mole-ML. The decrease in the heat of adsorption with coverage, 16 kcal/mole-ML, results only in part from intermolecular repulsion.

Second-order behavior for CO adsorption kinetics on the platinum metals is not unique to Ir(110) and has been reported on Ir(111) (9). Moreover, two independent groups have reported the coverage dependence of the sticking probability of CO on Pt(111) (39), which shows second-order behavior. This kinetic behavior might be observed for other

surfaces of the platinum metals if higher exposure regimes (>10 L) are investigated.

The adsorption kinetics of CO on Ir(110) at 90 K are inferred from CPD measurements (q.v.). The sticking probability is uniformly one up to 0.8 ML and decreases somewhat at higher coverages. The saturation coverage at 90 K is 1 ML. For this reason and since the CPD is not altered after annealing the overlayer to 300 K, CO does not appear to adsorb physically at 90 K. At first glance, the measurements of a uniformly large sticking probability at 90 K might appear to be inconsistent with the second-order kinetics observed at 300 K. If thermal randomization of the overlayer is negligible at 90 K, the parameter B would approach one so that the saturation coverage at 90 K would be 0.5 ML (37). However, since 90 K is near the sublimation point of CO, the lifetime of the precursor state is protracted, and the parameter κ approaches zero. Therefore, the extended lifetime of the precursor state compensates for the poor thermal randomization of the overlayer so that the kinetic behavior at 90 K is consistent with the second-order behavior at 300 K.

VII. Charge Transfer to the Overlayer

The contact potential differences (CPD) for clean and oxidized Ir(110) at 90 and 300 K were measured as a function of CO exposure and are shown in Fig. 9. In all cases, the CPD is positive, i.e., the work function of the surface increased with CO coverage. For saturation coverage on the clean surface, the CPDs were 0.28 and 0.23 ± 0.01 eV at 90 and 300 K; on

the oxidized surface, 0.17 and 0.13 ± 0.01 eV at 90 and 300 K. For any temperature, and coverage, the CPD is markedly different on the two surfaces. Previously reported variations in the CPD on identical surfaces under the same conditions, which are as large as 0.2 eV for CO on some platinum metals (10), may result from inadvertent measurements on oxidized surfaces.

The sensitivity of the CPD to the surface oxide is estimated readily. If 1 ML of CO is adsorbed on the oxidized surface and is flashed off at 800 K, a subsequent measurement of CPD versus CO exposure lies between the curves for clean and oxidized Ir(110). The curve for the clean surface is obtained after this cycle is repeated five times. As stated previously, about 65% of the complete oxide layer reacts with 1 ML of CO during a flash. If 65% of the remaining oxide is removed with each additional cycle, then 0.005 ML of oxide remains after five cycles. Hence, the CPD is sensitive to oxide concentrations of less than 1%, which exceeds the detection limit of AES.

MacDonald and Barlow (40) have related the CPD to the apparent polarizability (α) and the apparent dipole moment (μ) for the adsorbate near zero coverage. Because of the image charge in metals, the apparent dipole moment is twice the component of the true dipole moment of the adsorbate that is normal to the surface and must be divided by two before it is compared to gas phase values. The apparent polarizability is the normal component of the true dipole moment divided by the normal component of the effective field at the surface (41). This field equals the average surface field that occurs at a binding site in the absence

of induced charge (E_n) plus the field that is induced by the dipole moment (E_d). Since the induced field produces the image charge of the dipole, the apparent polarizability is the ratio of the apparent dipole moment (μ) to the average field normal to the surface (E_n). These conventions for μ and α , which are used throughout this article and others (40), are convenient because the induced field may be ignored completely if the apparent dipole moment (μ) is used in place of the true dipole moment ($\mu/2$). If the sign of μ is positive, negative charge is transferred from the surface to the adlayer.

The model of MacDonald and Barlow (40), a modified form of the Topping model, accounts for the depolarization of the overlayer resulting from dipole-dipole interactions. For a fixed surface temperature, the ratio of the coverage (θ) to the CPD at that coverage ($\Delta\phi$) is plotted versus coverage. The slope of the resulting line is $(\alpha\Lambda C_s^{1/2}/4\pi\mu)$, and the intercept is $(1/4\pi C_s\mu)$, where Λ is a structural parameter for the overlayer and is equal to 9.46 if the overlayer has the periodicity of the (110) surface (14). This model, one of two developed by MacDonald and Barlow, is appropriate for adsorption at specific sites, rather than on an amorphous surface.

For CO adsorption at 300 K, Topping plots of $\theta/\Delta\phi$ versus θ are constructed by relating a coverage from adsorption kinetics to a CPD through points of constant exposure. At 90 K, the plots are produced by assuming that the initial sticking probability is one, and the plot gives a single straight line. The adsorption kinetics at 90 K were deduced from these plots. The initial sticking probability is one because CO adsorption is not activated. Since the plots at

300 K give a single line, the plots at 90 K presumably behave similarly. Moreover, this construction gives a value of 1 ML for saturation coverage of CO on both clean and oxidized Ir(110) at 90 K. However, Topping plots do not produce a single line always, but sometimes give two or more linear portions, as for oxygen adsorption on Ir(110) (14). Plots for CO adsorption on clean and oxidized Ir(110) at 90 and 300 K are shown in Fig. 10. The calculated values for the normal components of the polarizability and dipole moment for CO, shown in Fig. 10, are temperature dependent.

Two models, involving the thermal randomization of the rotational and the translation motions of the adsorbate, will be developed to describe the temperature dependences of the polarizability and the dipole moment. Although population in a vibrational mode that is normal to the surface varies with temperature, the CPD does not because the mean displacement of the adsorbate from the surface, which is proportional to the dipole moment, is constant (41).

The CPD for any coverage may change as a result of the thermal randomization of a rotational motion (42). The Auger spectra of CO on Ir(110) (q.v.) indicates that CO is attached to the surface through a carbon-metal bond. Assuming that the substrate is flat, the adsorbate may precess about this bond at angles of up to 90° with respect to the surface normal. The field at the surface (\underline{E}) tends to orient the

apparent permanent dipole moment of the adsorbate ($\underline{\mu}_0$) either normal or parallel to the surface, depending on whether the signs of the field and the dipole are either aligned or juxtaposed. The potential energy (U) for orientation is (41)

$$U = \mp \underline{\mu}_0 \cdot \underline{E} = \mp \mu_0 E_n \cos \theta \quad (12)$$

where θ is the angle between the dipole and the surface normal. That is, the average field (\underline{E}) for a flat metal surface equals the normal component (E_n). The sign of U is minus (plus) if the field and the dipole are aligned (juxtaposed).

The apparent polarizability [$\alpha(T)$] of the overlayer equals the normal component of the apparent dipole moment [$\underline{\mu} = \mu_0 \langle \cos \theta \rangle$] divided by the magnitude of the field (E_n) (41)

$$\alpha(T) = \mu_0 \langle \cos \theta \rangle / E_n \quad (13)$$

Here $\langle \cos \theta \rangle$ is the thermal average value of $\cos \theta$,

$$\begin{aligned} \langle \cos \theta \rangle &= \frac{\int_{\Omega} e^{-U/kT} \cos \theta d\Omega}{\int_{\Omega} e^{-U/kT} d\Omega} \\ &= -\frac{1}{x} \pm \frac{e^x}{e^x - 1} \end{aligned} \quad (14)$$

where $d\Omega$ is an element of solid angle in the half sphere in which the

adsorbate may precess, and $x = \mu_0 E_n / kT$. Because μ_0 , E_n and T are typically $1D (=10^{-18} \text{ esu} \cdot \text{cm})$, 10^6 V/cm , and 100 K ; x is on the order of 0.1. Hence, Eq. (14) may be expanded in a Taylor series about $x = 0$. To first order, $\langle \cos\theta \rangle = \frac{1}{2} \pm \frac{x}{12}$, and

$$\alpha(T) = \frac{1}{2} \alpha_e \pm \frac{\mu_0^2}{12kT} \quad (15)$$

where the electronic polarizability (α_e) is defined as μ_0/E_n . If the signs of the field and the dipole are aligned (juxtaposed), the sign of the second term is plus (minus).

Except for the numerical coefficients on the two terms, Eq. (15) is identical to the Langevin relation (41), which describes the temperature dependence of the polarizability of a homogeneous dielectric field (41). The mathematical formulation of the two models is identical except for the limits of integration in Eq. (14). If the true dipole moment replaces the apparent value, Eq. (15) reduces to the Langevin relation. However, the Langevin relation in terms of the apparent dipole moment has been applied erroneously to metal surfaces (40). In both cases for a surface, the limiting value of $\langle \cos\theta \rangle$ with increasing temperature is 0.5, which explains why the term $\frac{1}{2} \alpha_e$ rather than α_e appears in Eq. (15).

Since the polarizabilities for CO on Ir(110) decrease with increasing temperature, the signs of the field at the Ir(110) surface and the permanent dipole moment of CO are aligned and a plus sign is associated with the second term in Eq. (15). The term x for these data is of order one so that μ_0 and α_e must be determined from Eqs. (13) and (14).

Electronic polarizabilities of 20 and 60 Å³ and apparent permanent dipole moments of 0.55 and 0.8 D are obtained for CO on clean and oxidized Ir(110), respectively. At any temperature, $\langle \cos\theta \rangle$ is $\mu(T)/\mu_0$ so, in three of the four cases, $\langle \cos\theta \rangle$ is significantly less than 0.5. Because Eq. (14) dictates that $\langle \cos\theta \rangle$ is no less than 0.5 if the signs of the field and the dipole are aligned, this model does not describe the temperature dependences of the CPD for these data consistently. This model might be appropriate if CO binds on the ridges in the (001) azimuth where $\langle \cos\theta \rangle$ could be less than 0.5. However, the diameter of a chemisorbed CO molecule, 3.3 Å (as shown in the last section) is comparable to the distance between the troughs, 3.8 Å, so the surface should appear flat to chemisorbed CO. Therefore, this rotational model does not describe the temperature dependence of the CPD adequately for these data.

In the second model, which is similar to one developed by Ertl et al. (39), the CPD for any coverage changes with temperature, because the adsorbed molecules are energetically partitioned between two states of different electronic polarizabilities and permanent dipole moments. Since the LEED patterns of CO disorder only in the [001] azimuth as the surface temperature increases, thermal randomization must be significant in the [001] azimuth, but may be ignored for the [110] azimuth. The potential variation for chemisorption in the [001] azimuth may be approximated by a periodic square well of height U . The magnitude of the permanent dipole moment is μ_1 for the minima and μ_2 for the maxima. The electronic polarizability varies similarly (43). Hence, by Boltzmann statistics (32), the temperature dependence of the apparent dipole moment is

$$\mu(T) = \frac{\mu_1 e^{U/kT}}{1 + e^{U/kT}} + \frac{\mu_2}{1 + e^{U/kT}} \quad (16)$$

where the rotational motion will be ignored for the time being. This expression may be simplified in the limit of small U/kT ,

$$\mu(T) = \bar{\mu} + \frac{\Delta\mu}{4} \frac{U}{kT} \quad (17)$$

where $\bar{\mu} = \frac{\mu_1 + \mu_2}{2}$ and $\Delta\mu = \mu_2 - \mu_1$. The same expression in $\bar{\alpha}$ and $\Delta\alpha$ is obtained for the temperature dependence of the apparent polarizability $[\alpha(T)]$. If the electric fields at both types of sites are equal, the ratio of the dipole moment to the polarizability for any temperature is independent of temperature and equals the field, but this need not be the case.

This ratio is independent of temperature for CO on either clean or oxidized Ir(110), and this result is not surprising. The diameter of chemisorbed CO ($d_{CO} = 3.3 \text{ \AA}$) is large compared to the depth of the troughs on the surface, which are about one-half the diameter of a Ir atom ($d_{Ir} = 2.7 \text{ \AA}$). Furthermore, the area occupied by chemisorbed CO ($\frac{\pi}{4} d_{CO}^2 = 9 \text{ \AA}^2$) is comparable to the area of a unit cell ($\sqrt{2} d_{Ir}^2 = 10 \text{ \AA}^2$). Hence, the field acting on CO is averaged over a relatively large volume on the surface and is independent of the binding site. This is not the case for oxygen on Ir(110) where the dimensions of the adsorbate are much smaller than the dimensions of a unit cell (14). The average surface fields for CO on clean and oxidized Ir(110) are approximately 10^7 and 3×10^6 V/cm. As an aside, the electronic polarizability depends on the total field normal to the

surface. In field emission microscopy (44), the applied field ($\sim 10^7$ V/cm) is comparable to the naturally occurring field at the surface so the measured CPD is understandably different from values obtained by other methods, which perturb the surface minutely.

Since this translational model has three parameters, but only two dipole moments are available from the data, values for α_1 , α_2 , μ_1 , μ_2 and U may be estimated only. Based upon the electronegativities for C, O, and Ir atoms (45), the dipole of CO is not expected to have a large negative sign; that is, a large transfer of charge toward the carbon atom and the surface is not anticipated. A minimum value of $-1D$ may be postulated for the dipole moment of CO. This requires that the potential (U) be 0.1 - 1 kcal/mole, which is close to the potential between sites for CO on Pt(111), 0.5 kcal/mole (39). Since the potential is on the order of tenths of kcal/mole, $\alpha_1 \gtrsim \alpha(90\text{ K})$, $\alpha_2 \lesssim 0$, $1D \gtrsim \mu_1 \gtrsim \mu(90\text{ K})$ and $-1D \lesssim \mu_2 \lesssim 0$ for CO on either clean or oxidized Ir(110). The dipole moments on the oxidized surface are understandably smaller than those on the clean surface, for the oxide layer is expected to localize charge closer to the surface.

Because the dipole moment of CO on clean or oxidized Ir(110) is between -1 and $1D$, the overlayer is rotationally randomized above 300 K. In this temperature range, the thermal average angle between CO and the surface normal is 60° , the calculated values of μ_1 and μ_2 are directly comparable to gas phase values, and the apparent polarizability equals the true dipole moment ($\mu/2$) divided by the average surface field (E_n). These results appear to contradict those of an angular resolved UPS study of CO on Ni(100) (46), which indicate that the angle between CO and the

surface normal is no greater than 20° at 300 K. However, the dipole moment and polarizability of CO on Ni(100) are expected to be very different from the values for Ir(110) because the CPD for an equivalent coverage is markedly different (10).

The dipole moments from the translational model are close to the gas phase value, -0.12 D, where the minus sign indicates that the net flow of charge is toward the C atom (47). Although the bonding electrons move toward the O atom, the non-bonding electrons move toward the C atom. Similar chemical arguments are used to determine whether sites on top of the rows of surface atoms or sites in the troughs are favored energetically. The flow of charge in the C-Ir bond will be ignored because the electronegativities of these atoms are nearly identical (45). From the Pauli exclusion principle, the movement of the non-bonding electrons from CO toward the surface is more likely for sites on the rows than in the troughs where the average density of metal electrons is greater (24). Only sites on the rows are expected to have a vanishing or negative dipole moment. Therefore, trough sites are energetically favored since the dipole moment in the energetically disfavored sites on Ir(110) is no greater than zero. This reasoning agrees with several theoretical studies of CO chemisorption on the platinum metals (24), but contradicts arguments based on the vibrational spectroscopy of CO on these metals (48). However, these arguments have been questioned elsewhere (39), and the experimental results are controversial (49).

Both experiments and theory demonstrate clearly that the CPD for any coverage may vary with temperature. By assuming this variation is

insignificant, isosteric heats of adsorption often are measured for points of constant CPD (50). A method for estimating the error in these measurements will be developed.

If the partial molar volume of the adsorbed phase is small compared to that in the gas phase (v_G), and if the surface area (a) does not vary upon chemisorption, the chemical potential in the adsorbed phase (μ_s) is approximated by (51)

$$d\mu_s = - \bar{s}_s dT + \left(\frac{\partial \mu_s}{\partial \theta} \right)_{T,P,a} d\theta \quad (18)$$

where \bar{s}_s is the partial molar entropy of the adsorbate. The chemical potential for an ideal gas (μ_G) is

$$d\mu_G = - s_G dT + kT d \ln P \quad (19)$$

where s_G and P are the molar entropy and the pressure in the gas phase. (The symbol μ with a subscript of s or G denotes a chemical potential, not a dipole moment.) Since the chemical potentials for the two phases are equal at equilibrium, and since the isosteric heat q_{st} is approximated closely by $(s_G - \bar{s}_s)T$, the Clausius-Clapeyron relation for points of constant CPD is

$$- \left[\frac{\partial \ln P}{\partial (1/T)} \right]_{\Delta \phi} = \frac{q_{st}}{k} + \frac{T}{k} \left(\frac{\partial \mu_s}{\partial \theta} \right)_{T,P,a} \left(\frac{\partial \theta}{\partial T} \right)_{\Delta \phi} \quad (20)$$

Eq. (20) is simply the usual Clausius-Clapeyron relation (51) with an

extra term, which equals the error (ϵ/k) introduced by ignoring the temperature variation of the CPD.

The term $\left(\frac{\partial\theta}{\partial T}\right)_{\Delta\phi}$ is evaluated by assuming that the Topping equation relates the coverage and CPD at any temperature

$$\left(\frac{\partial\theta}{\partial T}\right)_{\Delta\phi} = -\theta^2 \left(\frac{4\pi C_s}{\Delta\phi} \frac{\partial\mu}{\partial T} - \Lambda C_s^{3/2} \frac{\partial\alpha}{\partial T} \right) \quad (21)$$

In the translational model, both the polarizability and the dipole moment of the adsorbate vary with temperature according to Eq. (17).

Once again, the Topping equation gives $\Delta\phi$ so Eq. (21) reduces to

$$\left(\frac{\partial\theta}{\partial T}\right)_{\Delta\phi} = \frac{\theta}{T^2} \left(\frac{U}{4k} \right) \left[\frac{\Delta\mu}{\mu_R} + \theta \Lambda C_s^{3/2} \left(\frac{\Delta\mu}{\mu_R} \alpha_R - \Delta\alpha \right) \right] \quad (22)$$

where θ , μ_R , and α_R are the coverage, dipole moment, and polarizability associated with the CPD ($\Delta\phi$) at a fixed reference temperature. At this temperature, the coverage-CPD relation is established to give the coverage dependence of the isosteric heat. The error (ϵ in kcal/mole) depends upon the choice of reference temperature (usually 300 K),³ as well as the coverage and the temperature at which the Clausius-Clapeyron expression is evaluated. Because the average surface field for Ir(110) is the same for the two types of binding sites, the second term in brackets vanishes. As argued previously, this uniformity should occur generally on metals if the dimensions of chemisorbed CO are comparable or larger than the dimensions of a unit cell. Assuming that the potential variation between sites (U) is 0.5 kcal/mole, which has been shown to be

a reasonable value, and that the reference temperature is 300 K, $\mu_R = 0.17 D$ and $\Delta\mu = 0.70 D$ (from Eq. 16). Because the potential energy for rotation is small for this case ($\mu_0 E_n \langle \cos\theta \rangle \sim 0.1$ kcal/mole), the adlayer is rotationally randomized above 90 K. Little error is introduced by entirely ignoring this motion. For CO on clean Ir(110), Eq. (22) is approximated closely by

$$\left(\frac{\partial\theta}{\partial T}\right)_{\Delta\phi} = \frac{\theta U}{T^2 k} \quad (23)$$

Intuitively, the term $\left(\frac{\partial\mu}{\partial\theta}\right)_{T,P,a}$ in Eq. (20) is approximately

$$-\left(\frac{\partial E_d}{\partial\theta}\right) = 16 \text{ kcal/mole-ML, but may be estimated more precisely. The}$$

enthalpy in the adsorbed phase (H_s) is related to the entropy (S_s), the surface pressure (ϕ), and the chemical potential (μ_s) by (51)

$$H_s = TS_s - \phi a + \mu_s n_s \quad (24)$$

where n_s is the number of adsorbed molecules. By differentiating with respect to n_s with T , P , and a constant, Eq. (24) becomes

$$\bar{h}_s = T\bar{s}_s - \left(\frac{\partial\phi}{\partial n_s}\right)_{T,P,a} a + \mu_s + \left(\frac{\partial\mu_s}{\partial n_s}\right)_{T,P,a} n_s \quad (25)$$

where $\bar{h}_s = \left(\frac{\partial H_s}{\partial n_s}\right)_{T,P,a}$ and $\bar{s}_s = \left(\frac{\partial S_s}{\partial n_s}\right)_{T,P,a}$ are partial molar

quantities. Because $\bar{h}_s - T\bar{s}_s = \mu_s$, $n_s/aC_s = \theta$, and $\phi = kT \int_0^P (n_s/a) d \ln P$, which is a good approximation of the Gibbs equation for surfaces (51),

$$\left(\frac{\partial \mu_s}{\partial \theta}\right)_{T,P,a} = \frac{kT}{\theta} \frac{\partial}{\partial \theta} \left[\int_0^P \theta d \ln P \right]_{T,P,a} \quad (26)$$

Eq. (26) is evaluated directly from thermodynamic data.

When no such data are available, Eq. (26) may be evaluated from kinetic data. At equilibrium, the product of the flux of molecules to the surface and the sticking probability [from Eq. (7)] equals the desorption rate [Eq. (5)]

$$\frac{PS(\theta, T)}{(2\pi M_{CO} kT_g)^{1/2}} = v_0 C_s \theta \exp \left[- \frac{E_d(\theta)}{k} \left(\frac{1}{T} - \frac{1}{T_s} \right) \right] \quad (27)$$

Substituting Eq. (27) into Eq. (26),

$$\begin{aligned} \left(\frac{\partial \mu_s}{\partial \theta}\right)_{T,P,a} &= \frac{kT}{\theta} - \frac{kT}{\theta} \left[\frac{\partial}{\partial \theta} \int_0^\theta \theta \left(\frac{\partial \ln S(\theta, T)}{\partial \theta} \right)_T d\theta \right] \\ &\quad - \left(\frac{1}{\theta} - \frac{T}{T_s} \right) \frac{\partial}{\partial \theta} \left[\int_0^\theta \theta \left(\frac{\partial E_d(\theta)}{\partial \theta} \right) d\theta \right] \end{aligned} \quad (28)$$

Eq. (28) is evaluated at the temperature and coverage at which the error in the isosteric heat is to be calculated. For CO on Ir(110), the adsorption kinetics are second order, $S = S_0(1 - \theta)^2$, and the desorption energy varies linearly, or piecewise linearly, with coverage, $\left(\frac{\partial E_d}{\partial \theta}\right) =$

- E_δ . Hence, Eq. (28) reduces to

$$\left(\frac{\partial \mu_s}{\partial \theta}\right)_{T,P,a} = kT \left[\frac{1+\theta}{\theta(1-\theta)} \right] + E_\delta \left(1 - \frac{T}{T_s}\right) \quad (29)$$

If the first term is ignored and T is much less than T_s , $\left(\frac{\partial \mu_s}{\partial \theta}\right)_{T,P,a}$ equals $-(\partial E_d/\partial \theta)$ as stipulated earlier.

From Eqs. (20), (23) and (29), the total error in the Clausius-Clapeyron equation evaluated for points of constant CPD and for a reference temperature of 300 K is

$$\epsilon = U \frac{(1+\theta)}{(1-\theta)} + \frac{UE_\delta \theta}{k} \left(\frac{1}{T} - \frac{1}{T_s}\right) \quad (30)$$

where $U = 0.5$ kcal/mole and $T_s = 1240$ K. The coverage variation of the energy of desorption, which nearly equals the isosteric heat of adsorption (52), may be approximated by a piecewise linear fit and is shown as a dashed line in Fig. 11. The error in the isosteric heat at 500 K, given by Eq. (30), is superimposed on the isosteric heat and is represented by a dotted line. At 500 K, the adsorption and desorption rates of CO on Ir(110) are approximately 0.5 ML/sec at 10^{-6} torr, which is a typical pressure for evaluating the isosteric heat under UHV conditions. If the temperature is varied by ± 100 K, the error (ϵ) is not altered significantly, but the $1/T$ term in ϵ introduces some skewness in the Clausius-Clapeyron plots [Eq. (20)]. This skewness is negligible to first order. The solid line in Fig. 11 represents the isosteric heat measured for points of constant

CPD if the discontinuities in the piecewise linear fit are smoothed.

Several artifacts arise if the isosteric heat is evaluated for points of constant CPD. Since the measured heats are too large, pre-exponential factors deduced from these heats are also too large because this factor offsets the overestimation of the isosteric heat. The compensation effect in the desorption kinetics may be masked entirely. The error in the isosteric heat is particularly great at high coverages. Moreover, the error is accentuated near coverages at which $\left(\frac{\partial \mu}{\partial \theta}\right)_{T,P,a}$ is large (for example, near coverages at which the overlayer structure changes).

VIII. Conclusions

The chemisorption of CO on a clean surface and a well characterized oxidized surface of Ir(110) has been studied to give insight into the CO oxidation reaction on Ir(110). CO adsorbs non-dissociatively on both surfaces at temperatures between 90 and 1300 K. The saturation coverage on both surfaces at 90 and 300 K is 1 ML (9.6×10^{14} molecules/cm²). Different LEED patterns form on each surface. On the clean surface, a p(2x2) pattern and a (4x2) pattern disordered in the [001] azimuth, form near 0.25 and 0.75 ML. Between these coverages, the overlayer appears to compress continuously. A (2x1)p1g1 pattern forms on the oxidized surface between 0.05 and 1.0 ML, indicating that the overlayer coalesces into islands.

The thermal desorption spectra of CO from the two surfaces differ also. Three peaks with relative intensities of 1:2:1 appear in the spectra from the clean surface; two peaks with relative intensities of 1:1 appear in the spectra from the oxidized surface. Up to 65% of the oxide layer reacts with CO to form CO₂. The desorption energy and the pre-exponential factor in the Arrhenius expression describing the desorption kinetics have been measured as functions of coverage for both surfaces. The compensation effect occurs for both cases, and the shape of the desorption energy versus coverage relations are similar. The desorption energy decreases continuously with increasing coverage up to 0.25 ML, drops off sharply there, and levels off up to 0.6 ML. In the limit of zero coverage, the desorption energy and the pre-exponential factors are 37 kcal/mole and 10^{13} sec^{-1} for the clean surface, and are 31 kcal/mole and 10^{11} sec^{-1} for the oxidized surface. Although the desorption kinetics for the two surfaces differ, the adsorption kinetics are the same. At 90 K, the sticking probability is one up to 0.8 ML, and CO does not appear to adsorb physically. At 300 K, the adsorption kinetics display a second-order behavior with an initial sticking probability of one. This behavior does not result from dissociative adsorption, but from intermolecular repulsion.

The contact potential difference (CPD) increases with CO coverage on both surfaces at 90 and 300 K. The CPD is greater on the clean surface and at lower temperatures. A Topping model, which relates the coverage to the CPD for a fixed temperature, was used to determine the normal components of the dipole moment and the polarizability of CO. The dipole

moment is larger on the clean surface although the polarizability is greater on the oxidized surface. On both surfaces, these quantities decrease with temperature. Two models, involving the thermal randomization of the rotational and the translational motions of CO, were developed to explain the temperature dependence of the CPD. The second model, which is appropriate for CO on both surfaces, suggests that binding sites between the topmost rows of surface atoms are preferred energetically. A method was presented to estimate the error in the isosteric heat of adsorption caused by evaluating the Clausius-Clapeyron equation at points of constant CPD, rather than constant coverage.

Acknowledgment

The authors are grateful for helpful correspondence with Dr. R. M. Lambert and discussions with Professor W. A. Goddard. This research was supported by the National Science Foundation.

References

1. T. N. Taylor and P. J. Estrup, *J. Vacuum Sci. Technol.* 10, 26(1973).
2. H. H. Madden, J. Küppers and G. Ertl, *J. Chem. Phys.* 58, 3401(1973).
3. R. A. Marbrow and R. M. Lambert, *Surface Sci.* 67, 489(1977).
4. G. Ertl and P. Rau, *Surface Sci.* 15, 443(1969).
5. H. Conrad, G. Ertl, J. Koch and E. E. Latta, *Surface Sci.* 43, 462(1974).
6. C. M. Comrie and R. M. Lambert, *JCS Faraday I* 72, 1659(1976).
7. R. W. McCabe and L. D. Schmidt, *Surface Sci.* 60, 85(1976).
8. K. Christmann and G. Ertl, *Z. Naturforsch.* 28a, 1144(1973).
9. W. H. Weinberg, C. M. Comrie and R. M. Lambert, *J. Catalysis* 41, 489(1976).
10. S. Andersson, *Solid State Commun.* 21, 75(1977).
11. S. W. Johnson and R. J. Madix, *Surface Sci.* 66, 189(1977).
12. C. T. Campbell, D. C. Foyt and J. M. White, *J. Phys. Chem.* 81, 491(1977).
13. V. P. Ivanov, G. K. Boreskov, V. I. Savchenko, W. F. Egelhoff, Jr. and W. H. Weinberg, *J. Catalysis* 48, 269 (1977).
14. J. L. Taylor, D. E. Ibbotson and W. H. Weinberg, *Surface Sci.* 79, 349(1979).
15. J. L. Taylor, D. E. Ibbotson and W. H. Weinberg, *J. Catalysis* 62, 1(1980).

16. J. L. Taylor, Ph. D. Thesis, California Institute of Technology, 1978.
17. J. L. Taylor and W. H. Weinberg, Surface Sci. 78, 259(1978).
18. C. M. Comrie and W. H. Weinberg, J. Chem. Phys. 64, 250 (1976).
19. J. C. Fuggle, E. Umbach and D. Menzel, Solid State Commun. 20, 89(1972).
20. M. P. Hooker and J. T. Grant, Surface Sci. 62, 21(1977).
21. W. E. Moddeman, T. A. Carlson, M. O. Krause, B. P. Pullen W. E. Bull and G. K. Schweitzer, J. Chem. Phys. 55, 2317 (1971).
22. R. M. Lambert and C. M. Comrie, Surface Sci. 38, 197(1973).
23. N. M. Abbas and R. J. Madix, Surface Sci. 62, 739(1977).
24. G. Doyen and G. Ertl, Surface Sci. 43, 197(1974).
25. R. M. Lambert, Surface Sci. 49, 325(1975).
26. The methods presented in the next two paragraphs are reviewed thoroughly in: J. L. Taylor and W. H. Weinberg, Surface Sci. 78, 259(1978).
27. No artifacts were introduced by using these large heating rates. See Ref. 26.
28. G. C. Bond, Catalysis by Metals, Academic Press, New York, 1962.
29. D. H. Everett, Proc. Chem. Soc. 38, 38(1957).
30. The details are discussed in Ref 26.
31. E. Bauer, F. Bonczek, H. Poppa and G. Todd, Surface Sci. 53, 87(1975).

32. R. H. Fowler and E. A. Guggenheim, Statistical Thermodynamics, Macmillan, New York, 1939.
33. D. A. King, Surface Sci. 64, 43(1977).
34. This statement is proved by calculating Θ_{00} for twofold and sixfold symmetries according to Ref. 37.
35. J. B. Taylor and I. Langmuir, Phys. Rev. 44, 423(1933).
36. P. Kisliuk, J. Phys. Chem. Solids 3, 95(1957).
37. D. A. King and M. G. Wells, Proc. R. Soc. A339, 245(1974).
38. J. O. Hirschfelder, C. F. Curtis and R. B. Bird, The Molecular Theory of Gases and Liquids, Wiley, New York, 1954.
39. G. Ertl, M. Neumann and K. M. Streit, Surface Sci. 64, 393(1977).
40. J. R. MacDonald and C. A. Barlow, J. Chem Phys. 39, 412 (1963).
41. J. D. Jackson, Classical Electrodynamics, Wiley, New York, 1962, Chapter 4.
42. The motion described in this paragraph is a vibration, rather than a true rotation. It is called a rotation because the motion is formulated analogously to a rotation in the gas phase.
43. This model is not rigorously correct for describing the polarizability. Because the order in the adlayer changes with temperature, the structural parameter must be temperature dependent. Ignoring this introduces little error in the analysis. This is discussed in Ref. 14.

44. G. Ertl and J. Küppers, Low Energy Electrons and Surface Chemistry, Verlag Chemie, Weinheim, 1974.
45. C. L. Allyn, T. Gustafsson and E. W. Plummer, Chem. Phys. Letters 47, 127(1977).
46. R. M. Stevens and M. Karplus, J. Chem. Phys. 49, 1094 (1968).
47. L. Pauling, Nature of the Chemical Bond, Cornell University Press, Ithaca, 1960.
48. H. Froitzheim, H. Hopster, H. Ibach and S. Lehwald, Appl. Phys. 13, 147(1977).
49. R. A. Shigeishi and D. A. King, Surface Sci. 58, 379(1976).
50. J. C. Tracy and P. W. Palmberg, J. Chem. Phys. 51, 4852 (1969).
51. T. L. Hill, J. Chem. Phys. 18, 246(1950).
52. P. Kisliuk, J. Chem. Phys. 30, 174(1959).

Figure Captions

- Figure 1: Auger KLL transitions for CO, oxygen and carbon chemisorbed on clean Ir(110), (a) oxygen transitions, (b) carbon transitions.
- Figure 2: LEED patterns of carbon on clean or oxidized Ir(110), (a) $p(2 \times 1)$ pattern at 60 eV, (b) (4×5) pattern at 60 eV.
- Figure 3: LEED patterns and proposed structures for CO on clean Ir(110), (a) $p(2 \times 2)$ pattern and structure, (b) (4×2) pattern and structure.
- Figure 4: $(2 \times 1)_{p1g1}$ LEED pattern at 102 eV and proposed structure for CO on oxidized Ir(110). The spots represented by dashed circles are missing for all voltages.
- Figure 5: Thermal desorption spectra of CO on Ir(110), (a) clean surface, (b) oxidized surface. Both CO and CO₂ appear as desorption products from the oxidized surface.
- Figure 6: Arrhenius plots for CO desorption from Ir(110) for various coverages, (a) clean surface, (b) oxidized surface.
- Figure 7: Variations in the desorption energy and the pre-exponential factor with surface coverage for CO on Ir(110), (a) clean surface, (b) oxidized surface.
- Figure 8: Adsorption kinetics of CO on clean and oxidized Ir(110) at 300 K.
- Figure 9: CPD as a function of CO exposure on Ir(110) at 90 and 300 K, (a) clean surface, (b) oxidized surface.
- Figure 10: Topping plots for CO on Ir(110) at 90 and 300 K, (a) clean surface, (b) oxidized surface.
- Figure 11: The coverage dependence of the isosteric heat, for CO on clean Ir(110), (---) true value, (···) value obtained from the piecewise linear approximation (see text), (—) value obtained by evaluating the Clausius-Clapeyron equation at points of constant CPD.

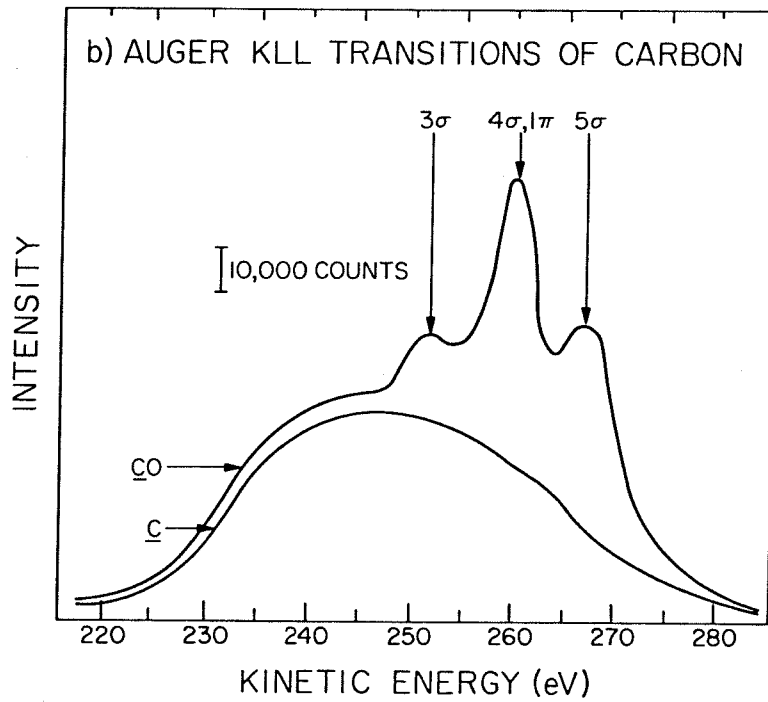
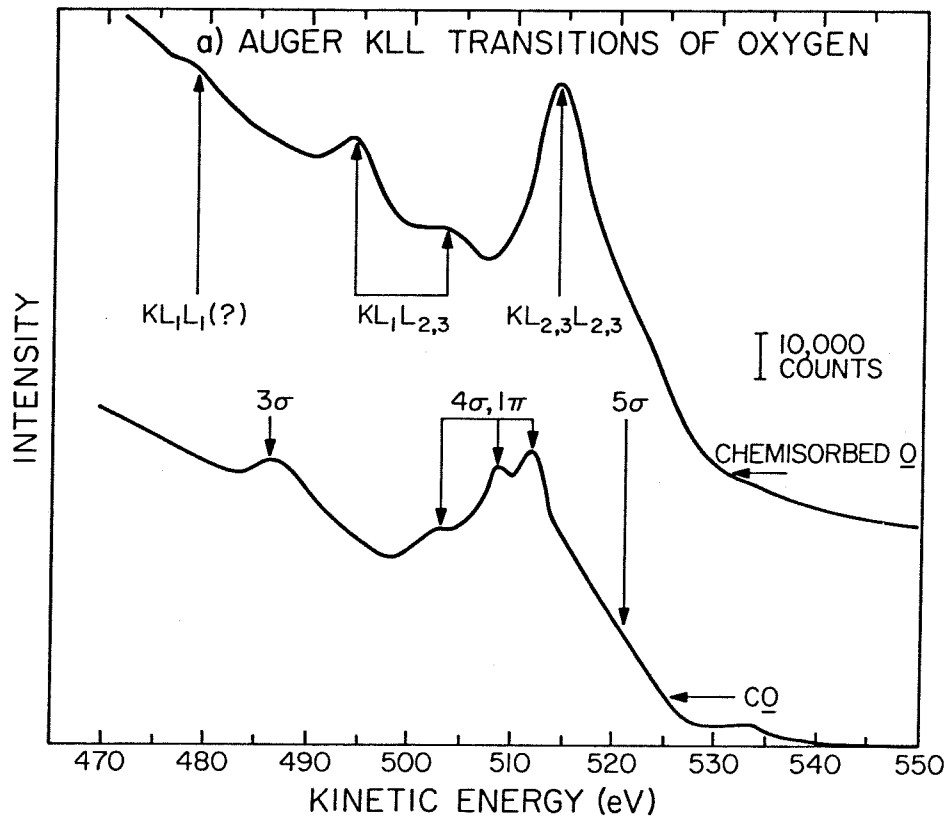


Fig. 1

a) C-(2x1) ON IR(110)

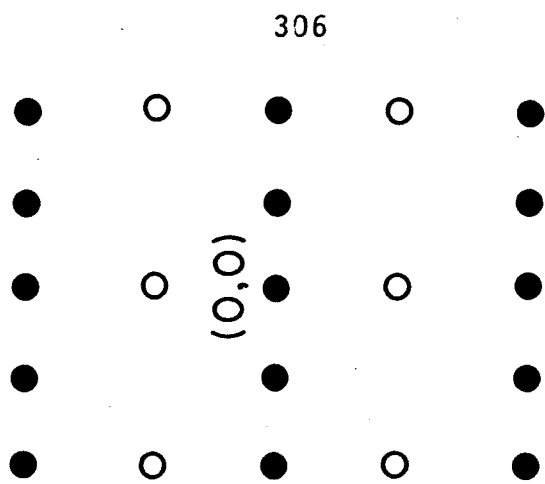
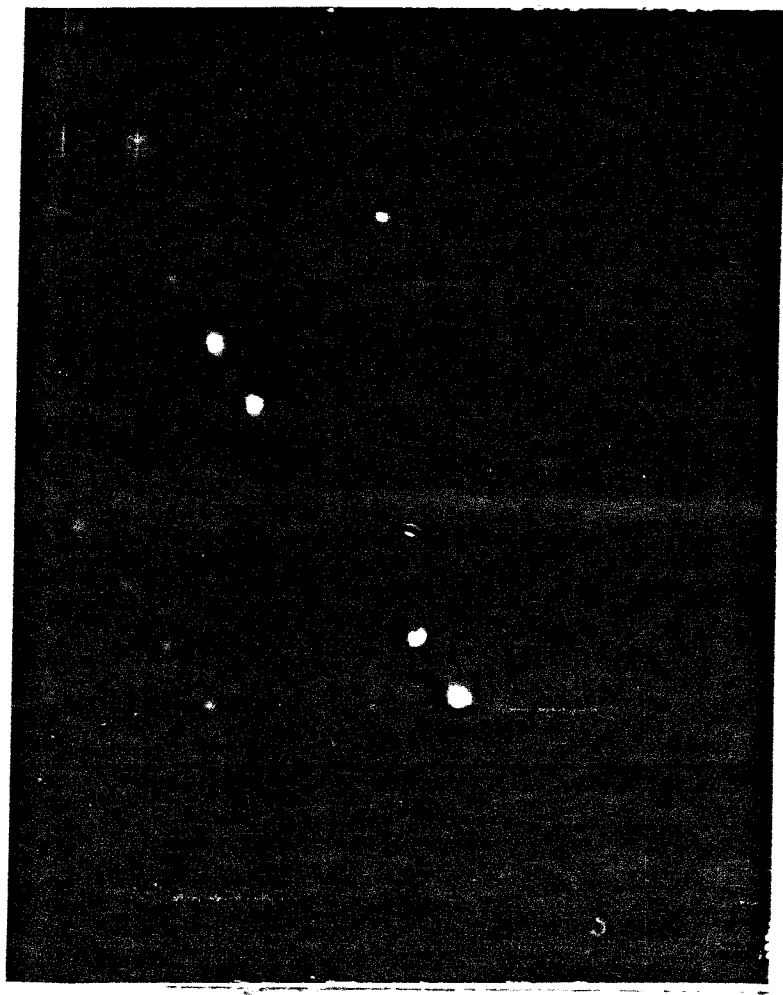


Fig. 2a

b) C-(4x5) ON IR(110)

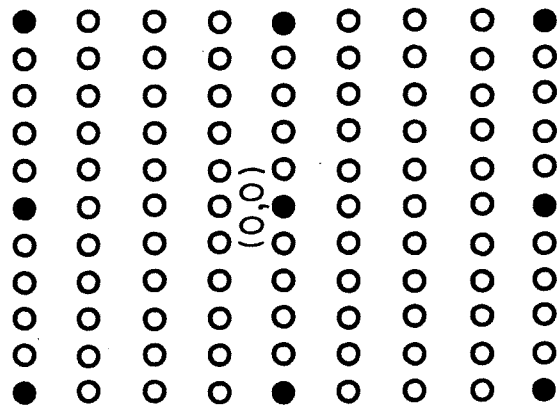
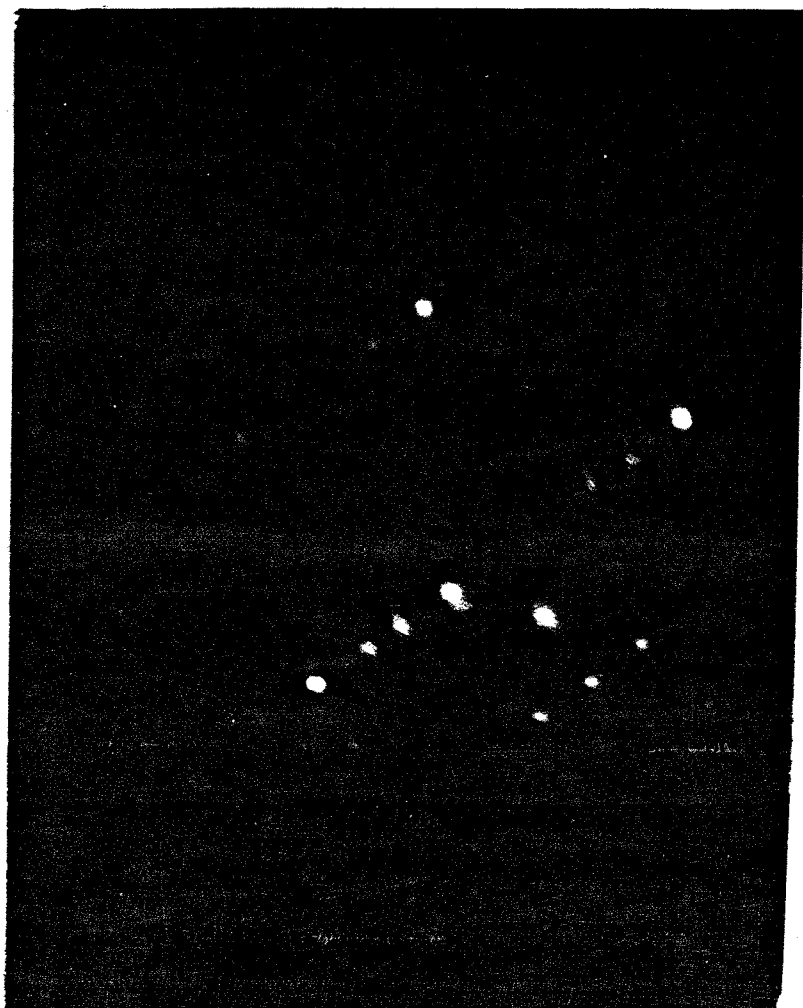
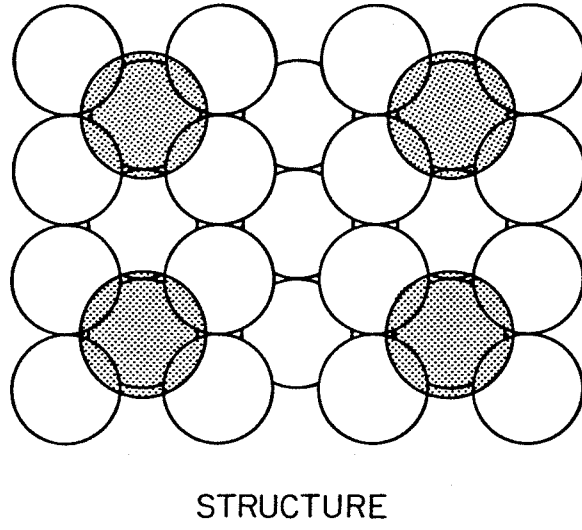
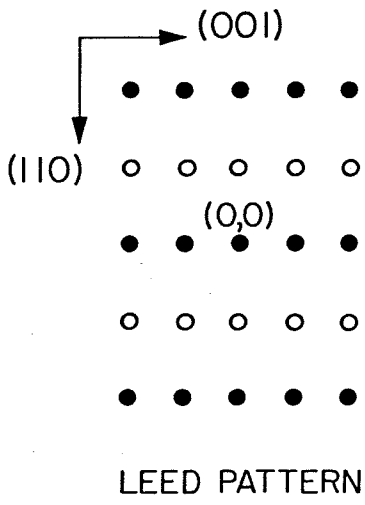


Fig. 2b

308
a) CO-p (2x2) ON IR(110)



b) CO-(4x2) ON IR(110)

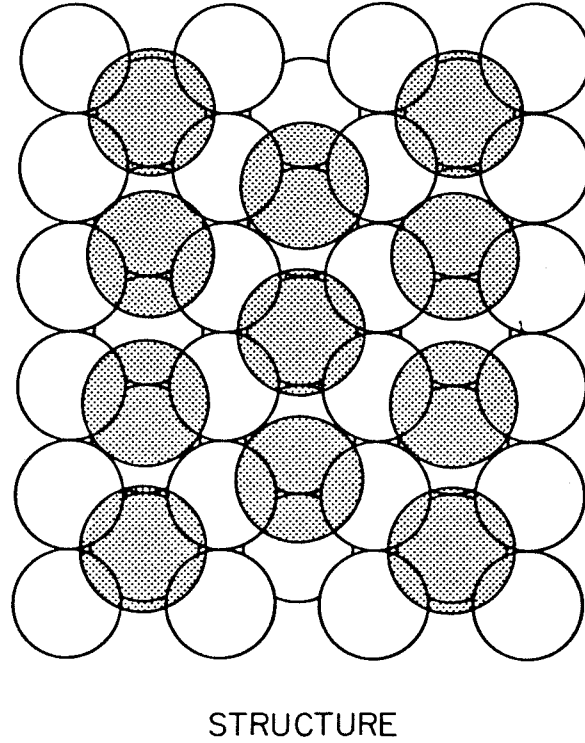
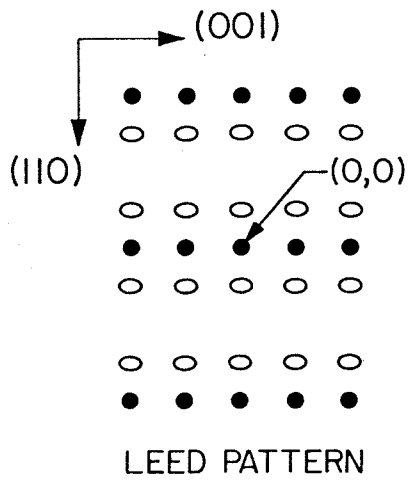
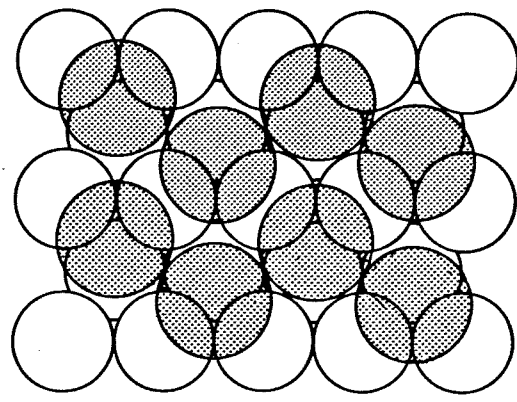
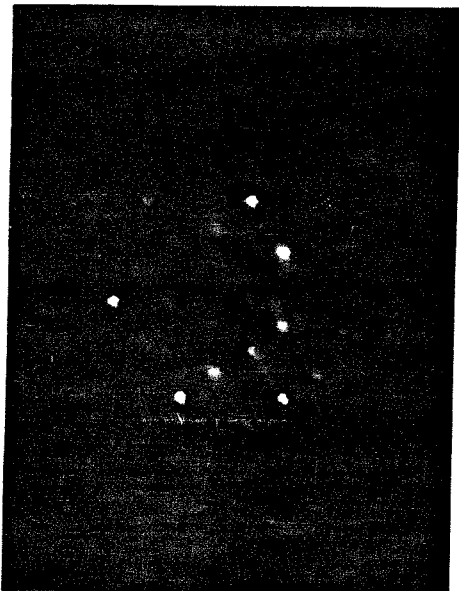
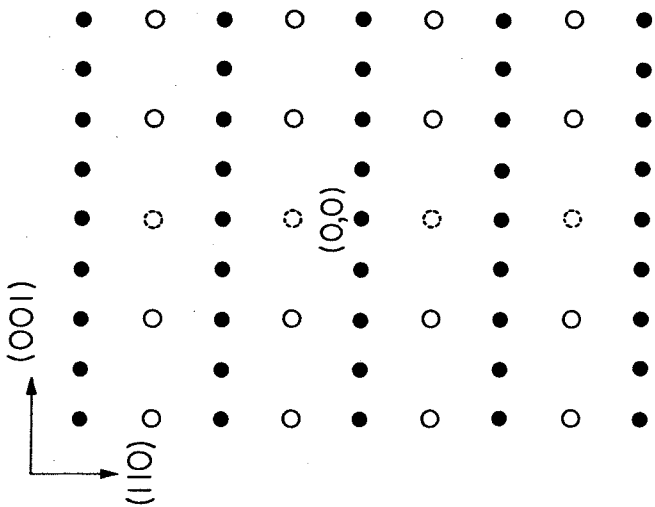


Fig. 3

CO-p(1) ON IR(110) OXIDE



LEED PATTERN

STRUCTURE

Fig. 4

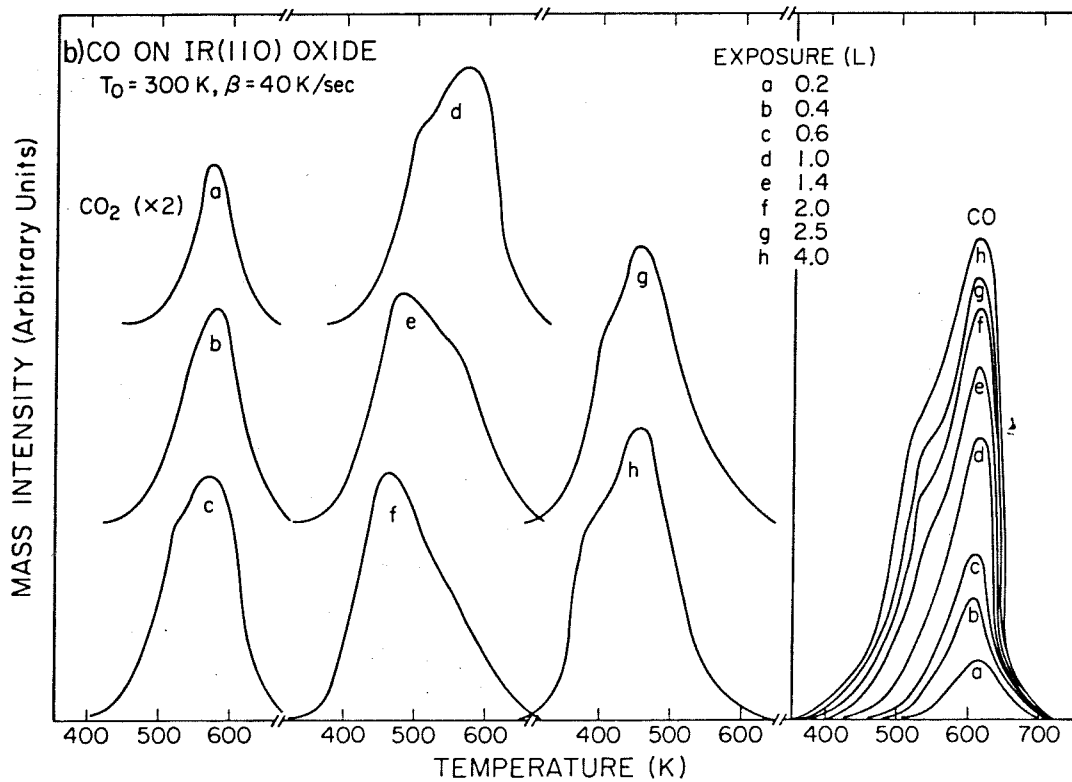
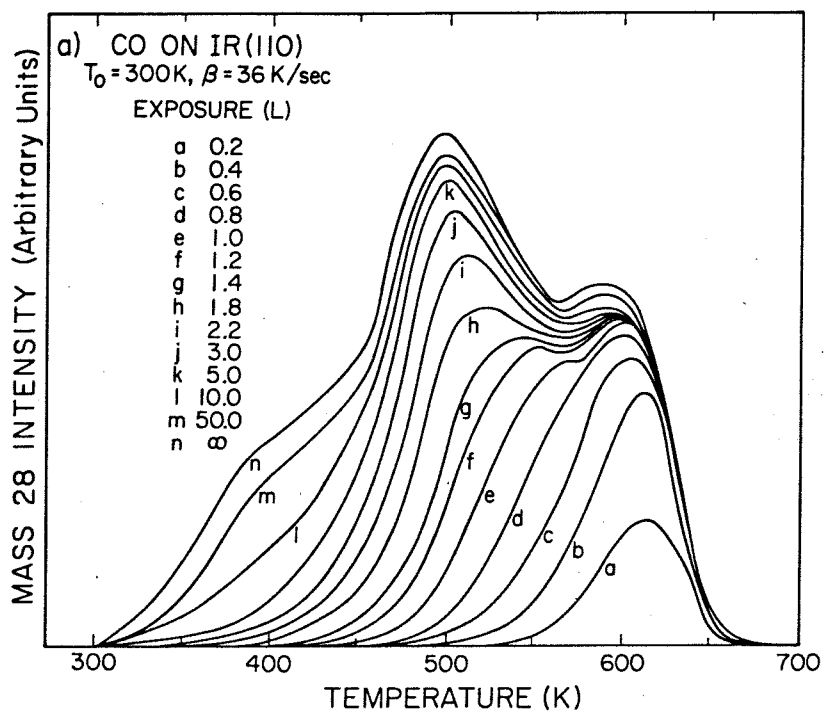


Fig. 5

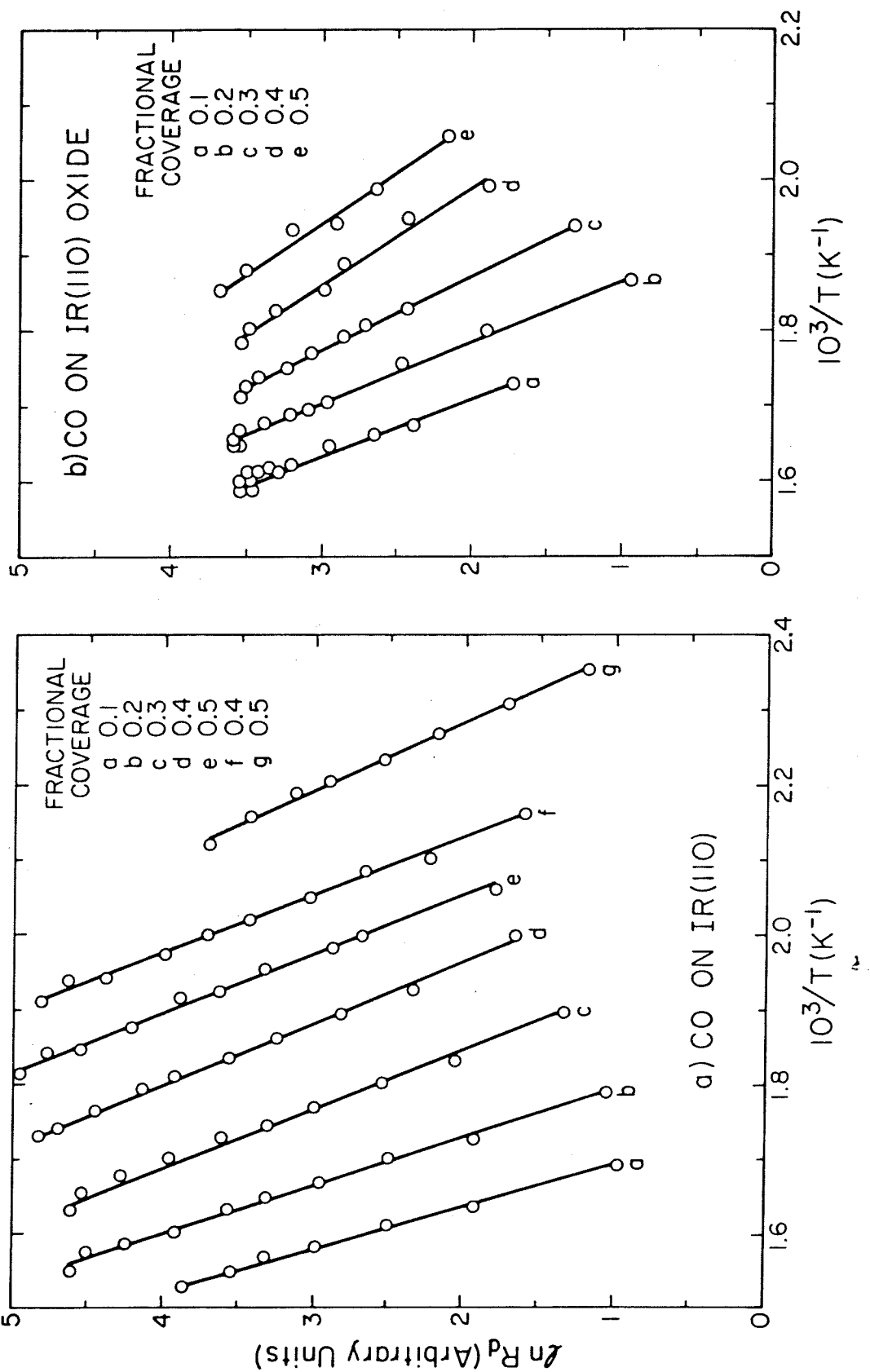


Fig. 6

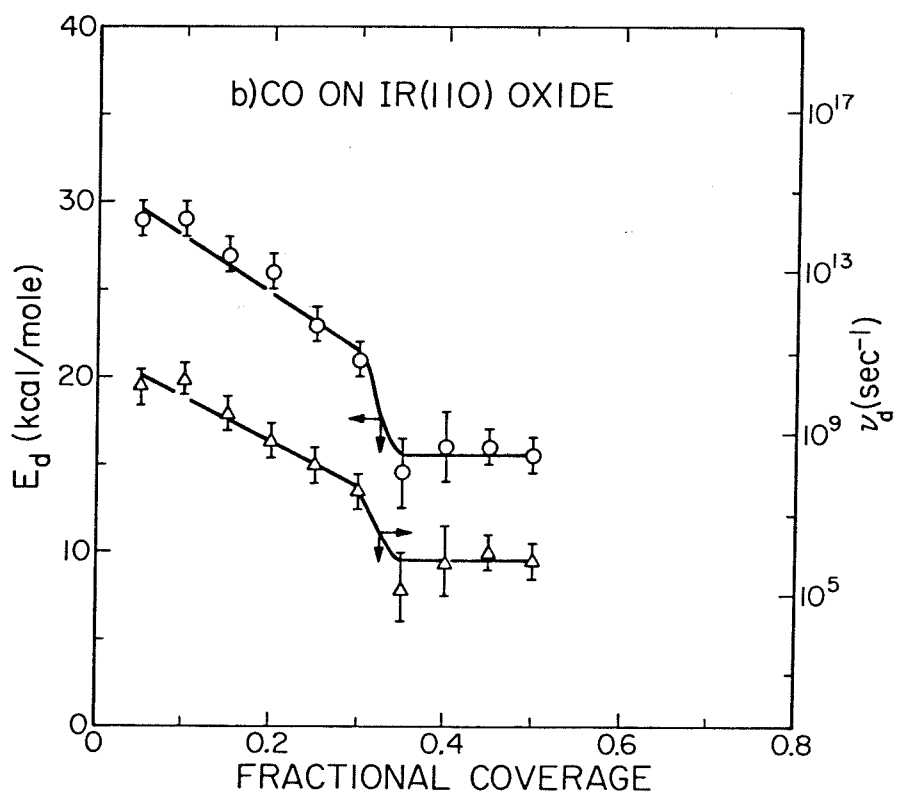
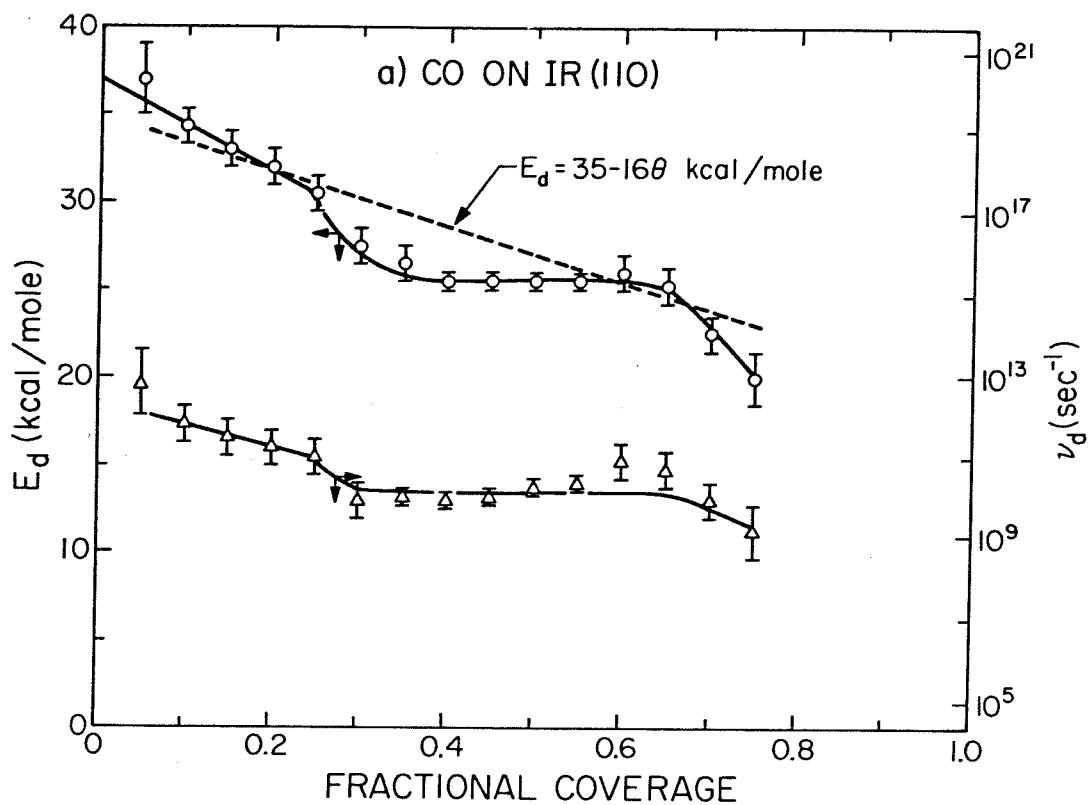


Fig. 7

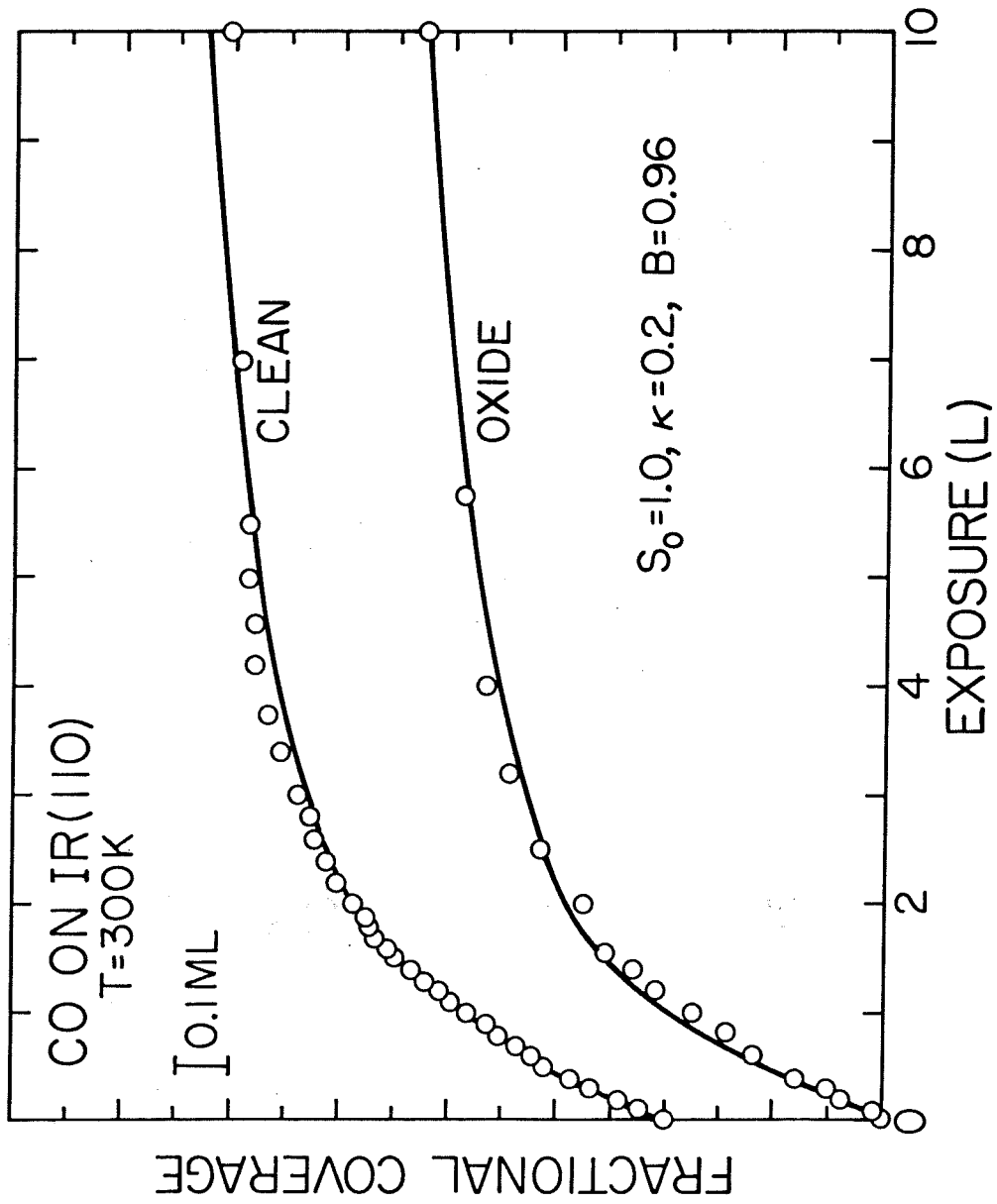


Fig. 8

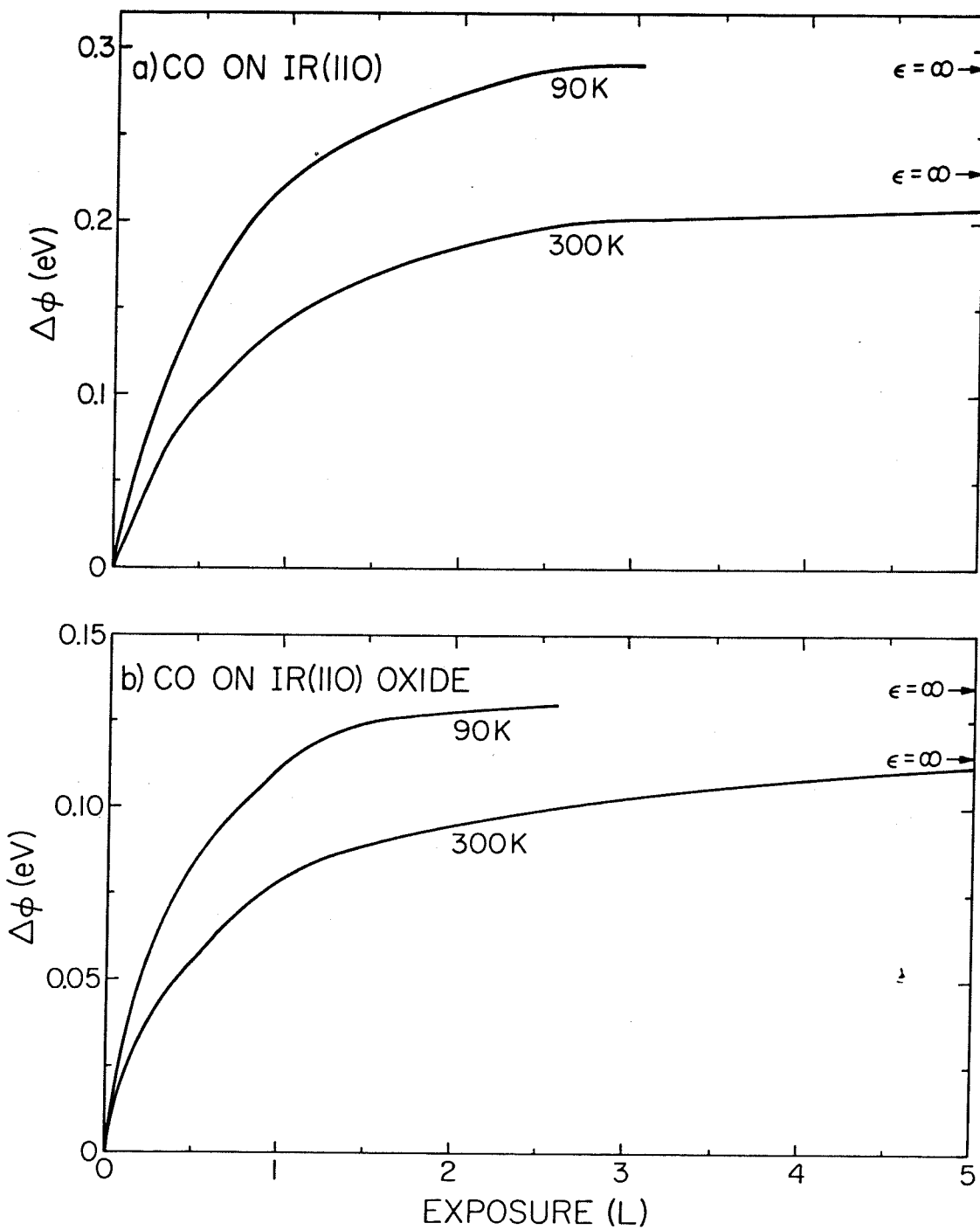


Fig. 9

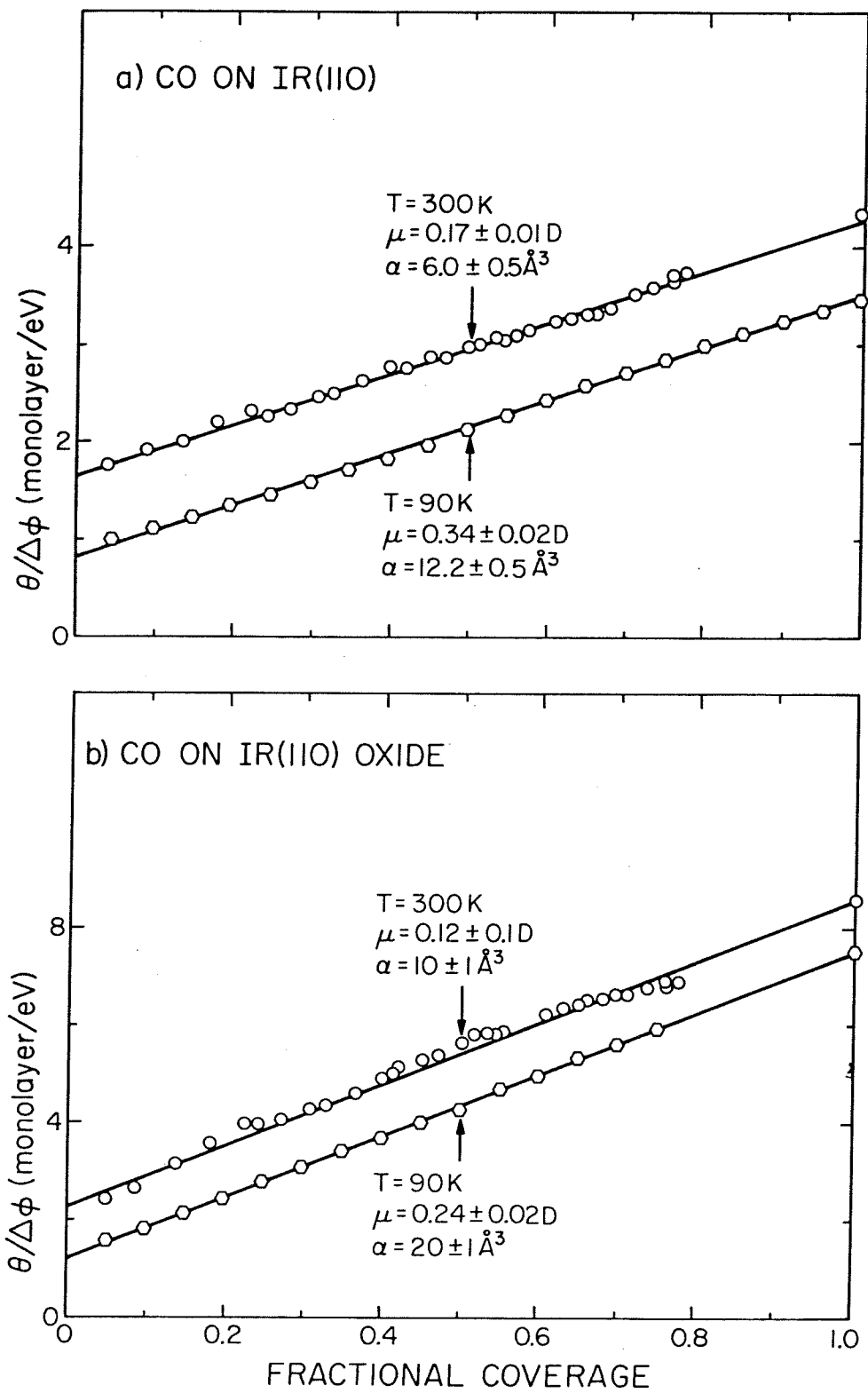


Fig. 10

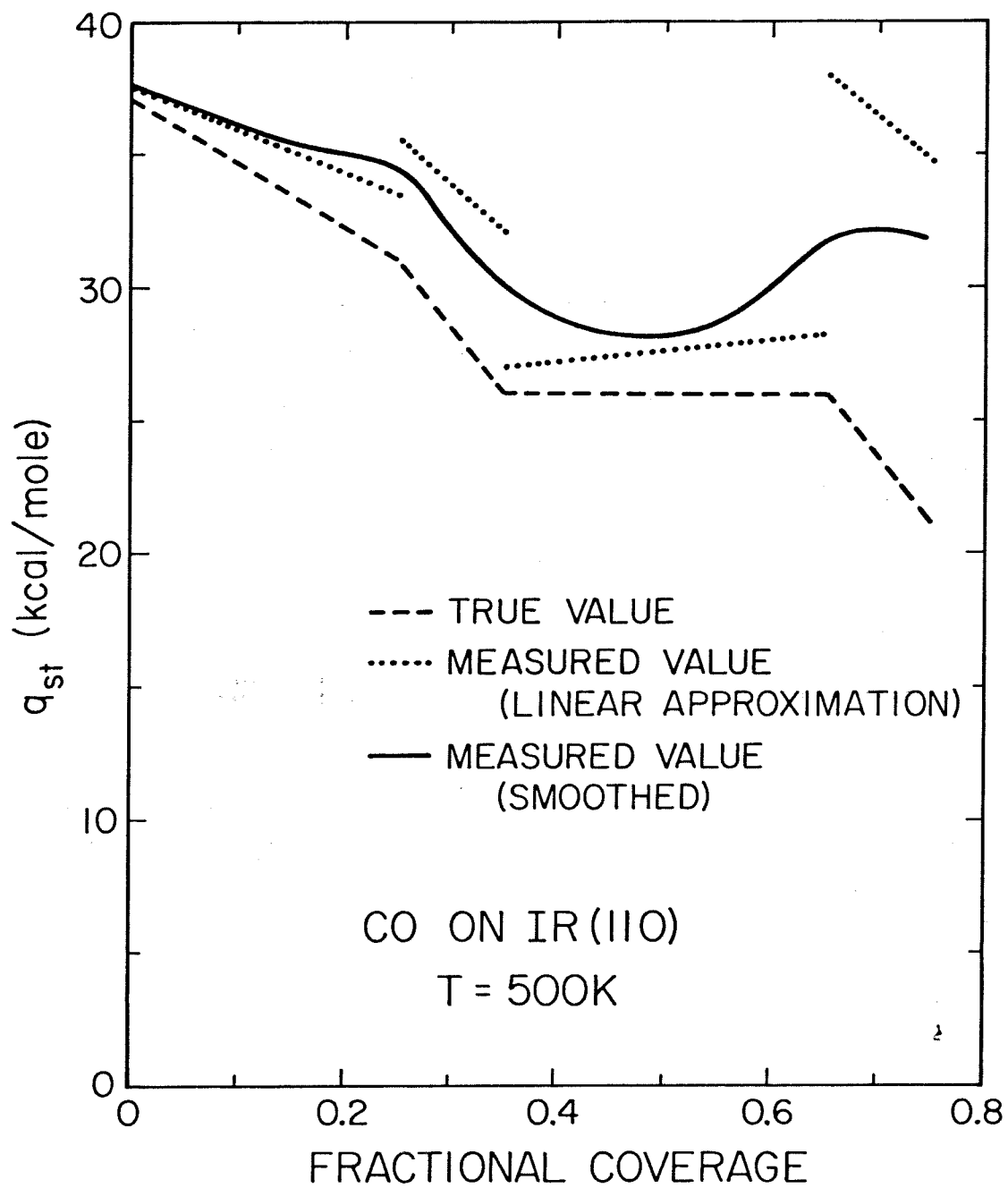


Fig. 11

APPENDIX E
THE CHEMISORPTION OF OXYGEN ON THE
(110) SURFACE OF IRIDIUM

(The text of Appendix E consists of an article coauthored with J. L. Taylor and W. H. Weinberg that has appeared in Surface Science 79, 349(1979).)

Surface Science 79 (1979) 349–384
© North-Holland Publishing Company

THE CHEMISORPTION OF OXYGEN ON THE (110) SURFACE OF IRIDIUM *

J.L. TAYLOR **, D.E. IBBOTSON and W.H. WEINBERG ***

Division of Chemistry and Chemical Engineering, California Institute of Technology, Pasadena, California 91125, USA

Received 26 May 1978; manuscript received in final form 5 September 1978

The chemisorption of oxygen on Ir(110) has been investigated under ultra-high vacuum conditions with thermal desorption mass spectrometry, contact potential difference measurements, Auger electron spectroscopy, and LEED. Oxygen may adsorb in three distinct chemical states: a molecularly chemisorbed species that is stable below 100 K, a dissociatively chemisorbed species, and a surface oxide that forms rapidly above 700 K. The oxide layer saturates at a coverage of 0.25 ML (1 ML = 9.6×10^{14} atoms/cm²) and orders to form a (1 × 4) LEED pattern. Different LEED patterns of dissociatively chemisorbed oxygen are observed on clean and oxidized Ir(110). A p(2 × 2) pattern forms on the clean surface near 0.25 ML coverage whereas a c(2 × 2) pattern forms on the oxidized surface near 0.5 ML coverage. Oxygen desorbs molecularly from Ir(110) with an activation energy of 45–70 kcal/mole, decreasing continuously with increasing coverage. The adsorption kinetics are described by a second-order precursor model for surface temperatures between 300–700 K. Oxygen chemisorption is not activated since the initial sticking probabilities on the clean and the oxidized Ir(110) surfaces are equal to 0.28 and 0.4, irrespective of the surface temperature. The dipole moment and polarizability of dissociatively chemisorbed oxygen change at 0.25 ML coverage on the clean surface and at 0.5 ML coverage on the oxidized surface. Although the dipole moment for any coverage is independent of temperature, the polarizability is inversely proportional to temperature. The activation energy for the dissociation of molecularly chemisorbed oxygen is 8 kcal/mole.

1. Introduction

This study of oxygen chemisorption was undertaken to give insight into the catalytic behavior of the CO oxidation reaction on Ir(110). Surface sensitive probes — thermal desorption mass spectrometry (TDS), contact potential difference (CPD) measurements, LEED, Auger electron spectroscopy (AES) and X-ray photoelectron spectroscopy (XPS) — were used for studying oxygen chemisorption under ultra-high vacuum (UHV) conditions. Since the understanding of catalytic phenomena

* Supported by the National Science Foundation under Grant Number DMR 77-14976.

** National Science Foundation Predoctoral Fellow.

*** Camille and Henry Dreyfus Foundation Teacher–Scholar, and Alfred P. Sloan Foundation Fellow.

was the impetus for this study, the characterization of the kinetic properties and the chemical states of adsorbed oxygen was emphasized. This study reveals that oxygen may adsorb in three distinct chemical states on Ir(110): a dissociatively chemisorbed species, a surface oxide and a molecularly chemisorbed species. The latter two species are described in separate sections of this article; the dissociatively chemisorbed species is described in four sections, which focus on overlayer structures, desorption kinetics, adsorption kinetics and charge transfer in the overlayer. In each section, a discussion parallels the presentation of experimental results.

A surface oxide, which modifies several aspects of oxygen chemisorption, forms on Ir(110). Oxide formation on the platinum metals, i.e., the incorporation of oxygen into the surface lattice, was reported first for Rh(110) [1] and subsequently has been observed on other platinum metals [2–8]. However, some ambiguity exists in the definition of a surface oxide. A surface oxide is defined here as a second dissociatively chemisorbed state of oxygen, which forms irreversibly through thermal activation and has different physical properties than the first state of dissociatively chemisorbed oxygen. Moreover, the formation of the oxide layer may cause the total saturation coverage of oxygen to increase [4,5,7]. The oxygen atoms of the surface oxide presumably bind in the subsurface region, but this region is difficult to define for rough surface orientations, such as the (110) face of the fcc metals. Since the oxide may be incorporated into the surface lattice, oxides are not necessarily inert to reaction with other adsorbates. For example, oxides formed on the (111) surfaces of Ni [3], Pd [7] and Ir [5] are inert to reduction by CO for pressures below 10^{-6} Torr and surface temperatures below 1000 K, whereas oxides formed on Rh(110) [1] and polycrystalline Pt [8] are reactive. Previous studies of oxide formation on Ni [3], Rh [1], Pd [7], Pt [2,4,6,8] and Ir [5,9] have focused on characterizing the oxide layer, but few studies have described how the oxide layer modifies oxygen chemisorption with respect to the clean surface. Both subjects are treated in this work.

Several aspects of oxygen chemisorption are similar among the platinum metals. Oxygen generally chemisorbs dissociatively for surface temperatures above 300 K, but adsorbs molecularly on polycrystalline Pt near 100 K [10]. Oxygen contamination on the (110) surfaces of Ni [11], Rh [1], Pd [12], Pt [13] and Ir [14] introduces streaks between the substrate spots in the [001] azimuth of the LEED pattern. If the contamination is sufficiently large, the streaks coalesce upon annealing to form (1 × 2) patterns on Rh [1] and Pd [12], and (1 × 3) patterns on Rh [1], Pd [12] and Pt [4]. Several overlayer structures of dissociatively chemisorbed oxygen – including the c(2 × 2) pattern on Rh [1], Pt [4] and Ir [14], and the c(2 × 4) pattern on Rh [1] and Pd [12] – are common among the (110) surfaces of the platinum metals. Depending on the metal, the surface orientation and the coverage, the activation energy for oxygen desorption from the platinum metals is between 36–80 kcal/mole [12,13]. The initial sticking probability of oxygen is reported generally to be between 0.1 and 1.0 [3–5,7,8,13,15,16]. The adsorption kinetics usually are described by a dissociative Langmuir model or a second-order

precursor model, and are independent of the surface temperature below 700 K [3, 4,7,8,13,15,16]. Although the CPD has not been reported widely for oxygen chemisorption on the platinum metals, a curious phenomenon is observed on Ni(100) and Ni(111) [3]. The CPD changes sign at a coverage associated with the completion of a LEED pattern. Although the results of this study are generally in concurrence with those described previously, several new findings are reported.

To avoid confusion, each of the three chemical states of adsorbed oxygen will be denoted differently in this work. The molecularly chemisorbed species will be termed molecular oxygen. Chemisorbed oxygen will refer to the dissociatively chemisorbed species, and the oxide phase will be designated as the oxide or the oxide layer. Oxidized Ir(110) will denote an Ir(110) surface covered with a saturated oxide layer. Irrespective of the chemical state of oxygen, all coverages will be reported on an atomic basis where 1 ML is equal to 9.6×10^{14} atoms/cm².

2. Experimental

The experiments were performed in a stainless steel belljar with a base pressure below 2×10^{-10} Torr. Several surface sensitive probes – a quadrupole mass spectrometer, LEED optics, a CPD apparatus and Auger electron and X-ray photoelectron spectrometers – were contained in the experimental chamber. CPD measurements were obtained by a continuous retarding potential method [17]. A double-pass cylindrical mirror analyzer (CMA) performed the energy analysis for the electron spectroscopies. All probes were interfaced to a PDP 11/10 computer [17]. Although all data reported here, except the LEED data, were obtained in digital form, the data are shown in analog form to facilitate the presentation. A more detailed description of the experimental system is reported elsewhere [18].

The substrate was cut from a single crystal of Ir and was polished within 1° of the (110) orientation using standard polishing techniques. During the course of this investigation, the substrate was repolished several times, and the results of many experiments were reproduced after repolishing. Carbon was cleaned from the substrate through a series of oxidation and reduction cycles. Annealing above 1600 K was necessary to remove O, Ca and K impurities from the substrate. Prior to each experiment, the surface was free from impurities within 0.01 ML as determined by Auger spectroscopy and CPD measurements. The substrate was heated conductively by passing current through two 10 mil Ta wires, on which the crystal was mounted. Temperatures in the range between 200 and 1800 K were measured with a Pt–Pt 10% Rh thermocouple that was spot-welded to the Ir crystal. Lower temperatures were measured by noting the change in the resistance of the Ta wires. All surface temperatures reported in this work are accurate to ± 5 K, except when noted otherwise.

When thermal desorption was monitored with the surface in a line-of-sight of the mass spectrometer, no iridium oxides – IrO, IrO₂ or IrO₃ – appeared as desorption

products. Also, from a line-of-sight experiment, oxygen desorption was determined to be molecular. The ratio of the mass 16 to mass 32 signals for any surface temperature was 0.12, which is equal exactly to the measured ratio for gaseous oxygen. Moreover, atomic desorption is not expected on a thermodynamic basis [19]. Following the completion of a thermal desorption spectrum, no oxygen was detected on the surface by Auger spectroscopy or CPD measurements.

The measured heating schedule during desorption was exponential, rather than linear, since the sample was heated conductively by passing a constant current through the Ta support wires that held the Ir(110) surface [20]. In the temperature regime where oxygen desorbed, the heating rate (β) varied between 80 and 300 K/sec. Since the intensity of the mass 32 signal and the surface temperatures were measured as independent functions of time, this variation introduced no artifacts when the data were analyzed. Moreover, the pumping speed was sufficiently large that these high heating rates did not distort the spectra [21]. When the substrate received large exposures to oxygen, the gain of the electron multiplier in the mass spectrometer, which was quite sensitive to oxygen contamination, drifted by as much as a factor of four. The gain was calibrated repeatedly by comparing the total intensities for spectra obtained under the same conditions but at different times.

Absolute coverages of adsorbed oxygen were determined by comparing the mass 28 and 32 signals of the thermal desorption spectra of CO and oxygen for saturation coverages. Since oxygen desorbs molecularly, the mass 16 signal for oxygen was not monitored. The absolute sensitivity of the mass spectrometer to CO was determined from the CO spectrum for saturation coverage, which is 9.6×10^{14} molecules/cm² on Ir(110) [18]. The relative sensitivities for CO and O₂ were determined by calibrating the mass spectrometer intensities against an ion gauge where the ionization efficiencies for the two species were known. The experimental chamber contained a poppet valve, which was closed sufficiently that the ratio of the pumping speeds for O₂ and CO was equal to the square root of the ratio of their molecular weights [22,23]. Then absolute coverages of oxygen were determined from twice the product of the absolute sensitivity of the mass spectrometer to CO, the ratio of the relative sensitivities for CO and O₂, the ratio of the pumping speeds for O₂ and CO, and the ratio of the pressure-time integrals for the O₂ and CO spectra. The factor of two is included above since the coverage of CO is given in molecules/cm², whereas the coverage of O₂ is given in atoms/cm².

3. The oxide layer

At 300 K, the saturation coverage of chemisorbed oxygen on clean Ir(110) was measured as 1.0 ± 0.1 ML by TDS; but the total coverage of adsorbed oxygen could be increased to 1.25 ± 0.1 ML as follows. First, a surface covered with more than 0.25 ML of oxygen was annealed between 700 and 1200 K in an oxygen atmosphere. When the surface was placed in an oxygen atmosphere again, the saturation

coverage was 1.25 ML at 300 K. The saturation coverage was increased by no more than 0.25 ML if the surface temperature and the oxygen pressure were maintained below 1200 K and 10^{-6} Torr. The additional 0.25 ML of oxygen coverage, which is obtained through thermal activation, is associated with the oxide layer. The formation of this surface oxide is particularly important in studying the CO oxidation reaction since the rates of CO_2 production are different for clean and oxidized Ir(110) [22]. The saturation coverage of oxygen on Rh(110) has been reported as 1.25 ML [1]. Although annealing in an oxygen atmosphere to 600 K was necessary to obtain this coverage, it was not associated with an oxide layer.

A clean Ir(110) surface is reconstructed into a (1×2) structure [14]; extended annealing of the oxide layer reconstructs the surface further to a (1×4) structure. When CO or oxygen is chemisorbed on the oxidized surface, the (1×4) pattern, shown in fig. 1, is transformed into a (1×2) pattern. Hence, the (1×4) pattern is not associated with a coincidence lattice of oxygen, but with a composite structure involving both oxygen and Ir. The (1×4) pattern was observed after a surface covered with more than 0.25 ML of oxygen was annealed at 1200 K in vacuum for several minutes. Alternatively, a clean surface was annealed to 1200 K in an oxygen atmosphere for several minutes, and the oxygen was evacuated prior to cooling. When the (1×4) pattern was formed in either of these ways, the coverage of adsorbed oxygen was 0.25 ML, as determined by TDS. If the initial oxygen coverage exceeded 0.25 ML, the excess oxygen desorbed during annealing. The (1×4) pattern did not form for coverages below 0.20 ML. Since both the oxide layer and the (1×4) pattern correspond to coverages of 0.25 ML and are formed through thermal activation, the (1×4) structure is associated with the oxide layer.

One possible structure for the (1×4) pattern, which is consistent with an oxide coverage of 0.25 ML, is shown in fig. 1 where the oxygen atoms are shaded. If the rows of surface atoms move in the directions indicated by the arrows, further oxi-

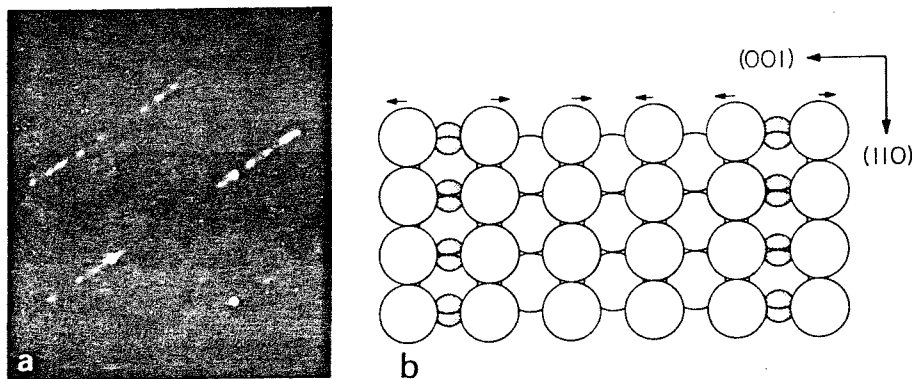


Fig. 1. (a) (1×4) LEED pattern at 56 eV and (b) proposed structure for an oxidized Ir(110) surface.

dation beyond 0.25 ML coverage may be inhibited by the pairwise approach of the surface atoms. Moreover, this movement coincides with the notion that the (1×4) pattern is formed through a reconstruction of the surface. The (1×4) pattern orders at elevated temperatures like the (1×2) patterns of oxygen on the (110) surfaces of Rh [1] and Pd [12], and the (1×3) patterns on Rh [1], Pd [12] and Pt [4]. Hence, these structures may be associated with oxide layers also. When Pd(110) is oxidized, a similar pairwise approach of the rows of surface atoms may occur. At elevated temperatures, no oxygen dissolves into the bulk of Pd(110) whereas dissolution is rapid on Pd(111) [7].

The oxide layer may be either ordered or partially ordered. Both forms have identical chemical properties. The partially ordered oxide was observed when a surface covered with 0.25 ML of chemisorbed oxygen was annealed rapidly between 800 and 1200 K. Upon cooling, the LEED pattern had streaks between the substrate beams in the [001] azimuth. Also, the half-order beams of the substrate were reduced in intensity and were quite diffuse. Similar streaks, associated with oxygen contamination have been observed on the (110) surfaces of Ni [11], Rh [1], Pd [12], Pt [4] and Ir [14].

The activation energy for forming the oxide layer was estimated from a coadsorption experiment involving CO. First, a clean surface at 300 K was exposed to 2.7 L (1 L = 10^{-6} Torr sec) of oxygen, which corresponds to an oxygen coverage of 0.5 ML (see section 6). After the surface was annealed at fixed temperatures between 300 and 1200 K for one minute, the surface was exposed to 0.6 L CO at 300 K, which corresponds to a CO coverage of 0.25 ML [22]. No LEED patterns were observed which could be related to coadsorbed CO and oxygen on the surface. The thermal desorption spectra for CO and CO₂ were obtained with an average heating rate (β) of 40 K/sec.

In fig. 2, the CO₂ spectra are shown as a function of the annealing temperature. For temperatures above 800 K, the spectra are identical to the spectrum for 800 K. The CO spectra give a single peak near 600 K; only the intensity of the peak changes with the annealing temperature. A second state in the CO₂ spectrum near 600 K, which is associated with the growth of the oxide layer, appears for annealing temperatures above 600 K. When the second state appears, the amount of CO₂ produced decreases substantially. For annealing temperatures near 700 K, the oxide layer forms almost completely, as evidenced by the CO₂ spectra, and grows at a rate of approximately 0.25 ML/min. Assuming the formation kinetics are described by a first-order Arrhenius expression with a pre-exponential factor of 10^{13} sec⁻¹, the energy of formation for the oxide layer is 45 kcal/mole based upon an oxide concentration of 0.05 ML. The energies of formation for the oxide layers on polycrystalline Pt [8] and Ir(111) [5] are similar since these oxides form rapidly near 700 K.

In contrast to the oxide layer on the (111) surfaces of Ni [3], Pd [7] and Ir [5], the oxide formed on Ir(110) can be reduced by CO. Oxides formed on Rh(110) [1] and polycrystalline Pt [8] can be reduced also. A second type of oxide, which is un-

J.L. Taylor et al. / Chemisorption of oxygen on iridium

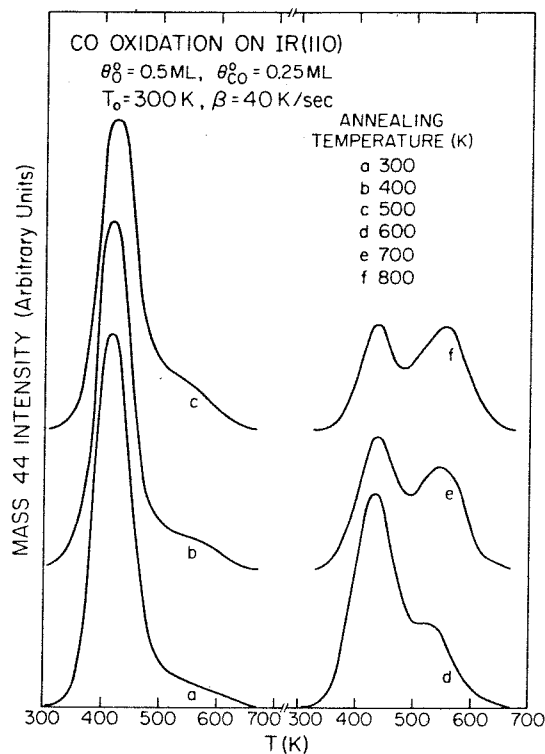


Fig. 2. Thermal desorption spectra of CO_2 formed from the reaction of adsorbed oxygen and CO on Ir(110). Oxygen was adsorbed on the surface, and then the substrate was annealed to one of the temperatures shown. The CO_2 spectrum was measured after CO was adsorbed on the surface at 300 K.

reactive to CO reduction, may form on Ir(110). This is reasonable, for two types of oxide layers have been observed on Ir(111) [9]. On Ir(110), the unreactive oxide was formed by annealing the surface above 1400 K in an oxygen atmosphere and was desorbed by heating the surface to 1800 K in vacuum for extended times. Since this oxide does not form in the temperature regime from 400 to 900 K where the CO oxidation reaction is rapid [22], it was not characterized more extensively. Since the LEED data show no evidence of a rutile structure, neither type of oxide on Ir(110) is associated with the most stable Ir oxide, IrO_2 .

The Auger KLL transitions are different for chemisorbed oxygen and the oxide, indicating that these two forms of surface oxygen represent different chemical states. XPS was not useful for characterizing the different states since the 1s transitions for each species differed neither in shape nor in energy. Similar behavior for chemisorbed oxygen and the oxide was observed in the X-ray spectra for Ni(110), but not Ni(111) or Ni(100) [6]. The Auger KLL spectra of chemisorbed oxygen and the oxide layer on Ir(110), shown in fig. 3, were recorded for 0.25 ML

J.L. Taylor et al. / Chemisorption of oxygen on iridium

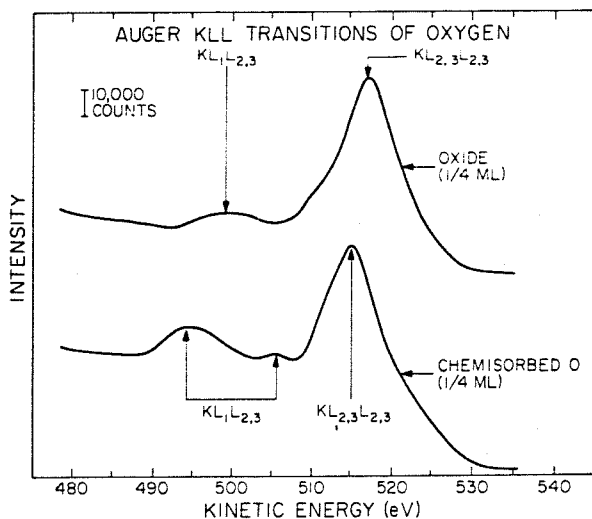


Fig. 3. Auger KLL transitions of an oxide layer and dissociatively chemisorbed oxygen on Ir(110) at 300 K. The coverage in each spectrum is 0.25 ML.

coverage at 300 K. The oxide layer was formed when a surface covered with 0.25 ML of chemisorbed oxygen was annealed between 700 and 1200 K. When a surface covered with chemisorbed oxygen was annealed between 300 and 500 K, the Auger spectrum was not changed. For the spectra in fig. 3, the incident current density was 10^{-6} A/cm² at 2 kV. In obtaining each spectrum, several individual spectra were summed to attain the desired resolution and to minimize the effects of background contaminants. A linear background has been subtracted from each spectrum to accentuate the oxygen transitions.

The spectrum of oxygen chemisorbed on Ir(110) at 300 K is typical of dissociatively chemisorbed oxygen [24]. As noted in fig. 3, Fuggle et al. [24] have associated transitions to peaks in that spectrum. The spectrum of the oxide layer and chemisorbed oxygen differ in three respects: (1) the slope of the inelastic background, which has been subtracted from the spectra in fig. 3, is larger for the oxide; (2) the peaks are broader in the oxide spectrum by approximately 1 eV; (3) the $KL_{2,3}L_{2,3}$ peak for the oxide is shifted by more than 2 eV with respect to chemisorbed oxygen. The shift is much larger than the resolution of the analyzer, 0.5 eV, and cannot be attributed solely to differences in the CPD for the two overlayers (see section 7). The first two observations indicate that the oxide atoms bind more deeply in the Ir lattice than chemisorbed oxygen. For a more deeply bound species, inelastic electron scattering should be more pronounced, and the peaks should be more band-like and broadened [3,6]. Hence, the atomic positions in fig. 1, are reasonable. Derivative spectra for chemisorbed oxygen and an oxide layer on polycrystalline Pt [8] are similar in shape but shifted in energy relative to those in fig. 3.

Since the oxide layer on Ir(110) is a second state of dissociatively chemisorbed oxygen that is formed irreversibly by thermal activation, it is truly a surface oxide according to the definition given in section 1. In the following sections, the term oxide or oxidized surface will refer to an Ir(110) surface with a saturated oxide layer (0.25 ML coverage). Furthermore, the distinction between an ordered oxide, which gives a (1×4) LEED pattern, and a partially ordered oxide, which gives a (1×2) LEED pattern with streaks in the $[001]$ azimuth, is unnecessary since both forms have identical chemical properties otherwise. In this work, the oxide layer was made routinely by adsorbing 0.25 ML of oxygen on clean Ir(110) and then annealing the surface to 1100 K for 1 min.

4. Overlayer structures

Different overlayer structures of oxygen were observed on clean and oxidized Ir(110). The $p(2 \times 2)$ pattern, reported previously for Ir(110) [14], but no other platinum metals, appeared sharpest for 0.25 ML coverage on clean Ir(110). The coverage was determined by TDS (see section 2). A photograph of the $p(2 \times 2)$ pattern is shown in fig. 4. The overlayer beams were sharpened by slowly cooling the substrate below 300 K. When clean Ir(110) at 300 K was exposed to oxygen initially, the overlayer structure was disordered in the $[001]$ azimuth. The disorder disappeared after a few minutes, indicating that a substantial activation barrier to diffusion exists in the $[001]$ azimuth. A similar slow ordering of the oxygen (2×2) pattern on Ir(111) has been observed near room temperature [5]. In that work, an

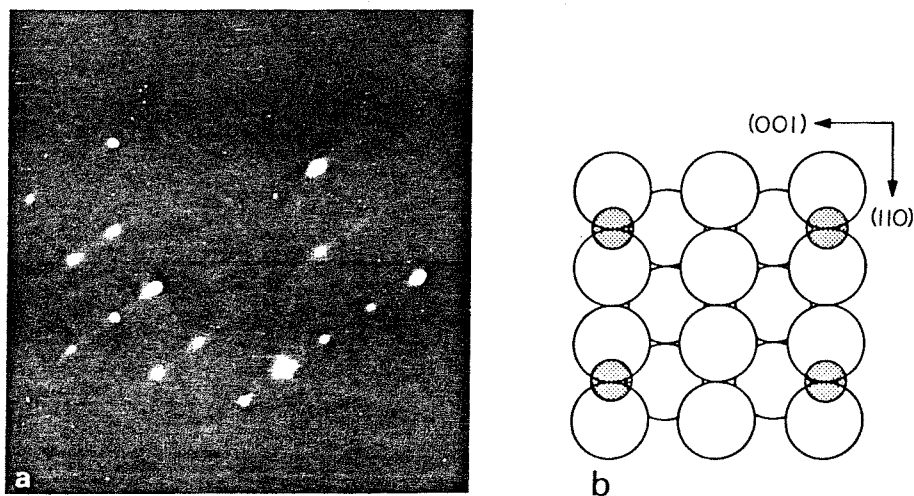


Fig. 4. (a) $p(2 \times 2)$ LEED pattern at 55 eV and (b) proposed structure for oxygen chemisorbed on clean Ir(110).

activation energy for diffusion of 17 ± 2 kcal/mole was calculated by assuming that the kinetics for diffusion could be described by a zero-order Arrhenius expression with a pre-exponential factor of 10^{13} sec^{-1} . Subsequently, a value of 10^{12} sec^{-1} for the pre-exponential factor has been measured directly for oxygen diffusion on Rh(111) [25]. Using this pre-exponential factor and a half-life of 1 min for ordering the overlayer at 300 K, an activation energy of 20 kcal/mole is estimated for diffusion in the [001] azimuth of clean Ir(110). A possible structure for the $p(2 \times 2)$ pattern, which is consistent with 0.25 ML coverage, is shown in fig. 4. As CPD measurements indicate (see section 7), oxygen binds above the topmost rows of surface atoms at this coverage so that the registry of the overlayer that is shown in fig. 4 is reasonable.

Two oxygen patterns, a $c(2 \times 2)$ and a (3×2) disordered in the [001] azimuth, were observed on oxidized Ir(110). These patterns are shown in fig. 5. When oxy-

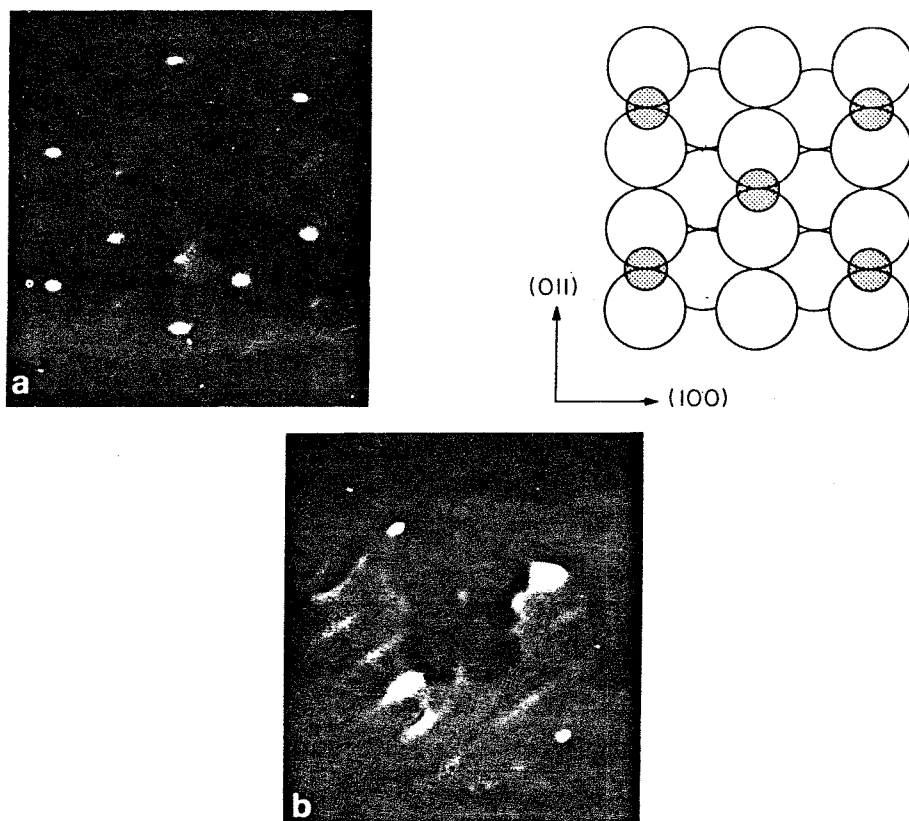


Fig. 5. LEED patterns of oxygen chemisorbed on oxidized Ir(110): (a) $c(2 \times 2)$ pattern at 90 eV, and proposed structure; (b) (3×2) pattern at 40 eV.

gen was chemisorbed on an ordered oxide layer, the quarter order beams of the substrate disappeared entirely. Similarly, when oxygen was chemisorbed on a partially ordered oxide layer, the streaks between the substrate beams in the [001] azimuth vanished. Hence, the chemisorbed layer reorders the substrate.

For chemisorbed oxygen coverages between 0.2 and 0.6 ML at 300 K, a streak appeared in the [001] azimuth between the substrate spots. After the overlayer was annealed to 700 K for a few minutes, the streak coalesced to form the $c(2 \times 2)$ pattern. The activation energy for the diffusion of oxygen in the [001] azimuth may be calculated as was done for the clean surface. Assuming a pre-exponential factor of 10^{12} sec^{-1} and a half-life of one min for ordering the overlayer at 700 K, the diffusion energy is 47 kcal/mole on the oxidized surface. The oxygen $c(2 \times 2)$ structure has been reported previously on the (110) surfaces on Rh [1], Pt [4] and Ir [14]. In all cases, annealing between 700 and 800 K necessary for ordering this structure so the $c(2 \times 2)$ pattern may be associated with chemisorbed oxygen on oxidized surfaces of these metals. The $c(2 \times 2)$ pattern on Ir(110) appeared sharpest near 0.5 ML coverage of chemisorbed oxygen. A possible structure for this pattern, consistent with this coverage, is shown in fig. 5. Once again, CPD measurements (q.v.) indicate that chemisorbed oxygen binds above the topmost rows of surface atoms at this coverage.

The partially disordered (3×2) pattern was observed on oxidized Ir(110) after a clean or oxidized surface was annealed near 1000 K in an oxygen atmosphere. The pattern appeared sharper for lower surface temperatures. Certain overlayer beams, indexed $(\frac{1}{3}h, 0)$ where h is an integer, are missing from the LEED pattern, indicating that the overlayer is symmetric about a glide line running parallel to the [110] azimuth. Because of the disorder in the [001] azimuth, any structure suggested for this pattern is subject to question, but a structure for a (3×2) pattern with glide symmetry has been proposed elsewhere [1]. Except for the (3×1) pattern on Ni [11], no oxygen patterns resembling the (3×2) have been observed on the (110) surfaces of other platinum metals.

5. Desorption kinetics

To study the desorption and adsorption kinetics of chemisorbed oxygen, thermal desorption spectra were collected as a function of oxygen exposure on clean and oxidized Ir(110) at 300 K. The adsorption kinetics will be treated in the next section. The heating schedule was exponential in the temperature region where oxygen desorbed and varied between 80 and 300 K/sec. Since the intensity of the mass 32 signal and the surface temperature were measured as independent functions of time, this variation introduced no artifacts when the data were analyzed. Representative spectra are shown in fig. 6. The spectrum for the oxidized surface gives a finite intensity for zero exposure because the oxide layer, which is associated with an oxygen coverage of 0.25 ML, contributes intensity in addition to that of the

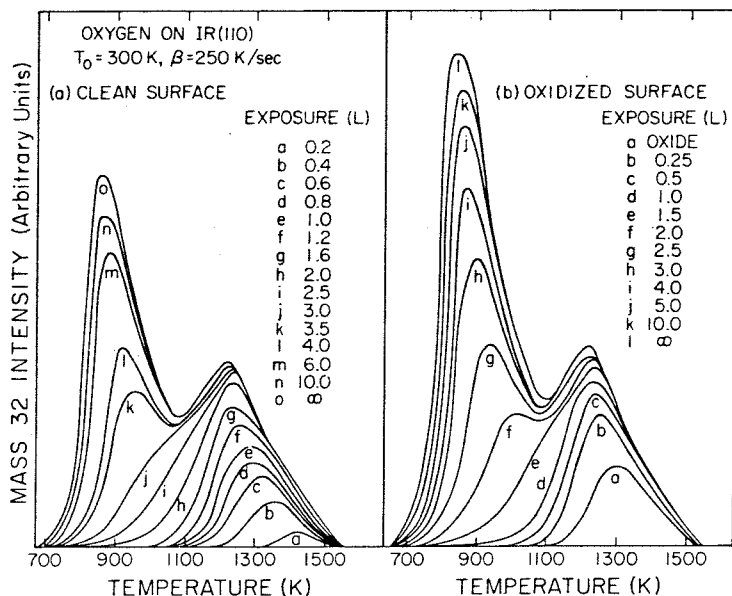


Fig. 6. Thermal desorption spectra of adsorbed oxygen on Ir(110): (a) clean surface; (b) oxidized surface.

chemisorbed oxygen. Since the oxide forms rapidly at temperatures where oxygen begins to desorb, the spectra for the clean and oxidized surfaces are not markedly different in shape.

Three peaks, two associated with chemisorbed oxygen and one high temperature peak associated with the surface oxide, appear in the desorption spectra of oxygen from clean and oxidized Ir(110). For saturation coverage, the intensity of the low temperature peak is increased for the oxidized surface since the total oxygen coverage at saturation is 1.25 ML on the oxidized surface, but it is 1.0 ML on the clean surface (see section 3). The ratios of the intensities of the three peaks are 1 : 2 : 1 and 2 : 2 : 1 for saturation coverage on clean and oxidized Ir(110), respectively. These ratios were not obtained directly from the spectra in fig. 6 since the two higher temperature peaks, associated with chemisorbed oxygen and the surface oxide, are not well separated. To separate the two peaks, a slow heating rate was used in the temperature region above 1100 K. Nearly all of the chemisorbed oxygen desorbed before the oxide phase decomposed and desorbed. This allowed the above ratios to be determined. The total coverages upon completion of the higher temperature peaks are 0.25 and 0.75 ML, which are associated with the (1×4) LEED pattern of the oxide and the $c(2 \times 2)$ LEED pattern on the oxidized surface, respectively.

The desorption rate (R_d in atoms/cm² · sec) may be modeled by the Arrhenius

expression

$$R_d = -C_s \frac{d\theta}{dt} = \nu_d(\theta) C_s^n \theta^n \exp[-E_d(\theta)/kT], \quad (1)$$

where C_s , θ , t , T , n , k , $\nu_d(\theta)$ and $E_d(\theta)$ are the concentration of adsites ($9.6 \times 10^{14}/\text{cm}^2$ for chemisorbed oxygen), total fractional coverage of oxygen, time, surface temperature, order of the desorption process, Boltzmann constant, pre-exponential factor and desorption energy, respectively. However, eq. (1) is applicable to oxygen desorption only if the oxide atoms enter the chemisorbed phase before desorbing. This must be the case on Ir(110) since oxygen desorbs molecularly (see section 2).

If the rate parameters, $\nu_d(\theta)$ and $E_d(\theta)$, vary weakly with coverage, the order of the desorption process (n) is given by the slope of a plot of $\ln R_d$ as a function of $\ln \theta$ at points of constant temperature [26]. Since the pumping speed in these experiments was rapid [21], the desorption rate (R_d) is proportional to the intensity of the mass 32 signal (I) at any instant. Substituting this relation into eq. (1), and integrating, the coverage for any temperature in the desorption spectrum [$\theta(T)$] is given by [21]

$$\theta_0 - \theta(T) = \eta \int_0^{t'} I dt, \quad (2)$$

where t' is the time when the sample reaches the temperature T , and θ_0 is the initial coverage of oxygen. Since the saturation coverage of oxygen on clean Ir(110) is known to be 1 ML at 300 K, the proportionality constant η is the ratio of 1 ML to the total intensity-time integral for saturation coverage.

Order plots of $\ln R_d$ as a function of $\ln \theta$, constructed from the spectra in fig. 6, are shown in fig. 7. For total coverages below 0.1 ML where all oxygen is in the oxide phase, the desorption order is one. Before two oxygen atoms may combine to desorb as a molecule, atoms in the oxide layer must enter the chemisorbed phase. This first-order process is presumably rate limiting below 0.1 ML coverage. Between 0.1 and 0.2 ML coverage, the order is two, which is expected for the chemisorbed atoms, which desorb as molecules. Above 0.2 ML coverage, the order appears to exceed two since the desorption energy is a strong function of coverage.

Plots of $\ln I$ as a function of T^{-1} for points of constant coverage were constructed from the desorption spectra to determine the coverage dependences of the desorption energy [$E_d(\theta)$] and the pre-exponential factor [$\nu_d(\theta)$] [21]. From eq. (1), such plots should give lines with slope [$-E_d(\theta)/R$] and intercept $\ln[\nu(\theta)C_s^{n-1}\theta^n/\eta]$. For oxygen desorption from Ir(110), n is one for coverages below 0.1 ML, but is two otherwise. No artifacts associated with desorption from multiple states should appear at any coverage since the peaks in fig. 6 are separated sufficiently in energy [27]. Due to a problem of accuracy in this analysis [21], this procedure gave reliable values of the rate parameters between 0.3 and 0.4 ML coverage only. In this range, the desorption energy [$E_d(\theta)$] and the pre-exponential fac-

J.L. Taylor et al. / Chemisorption of oxygen on iridium

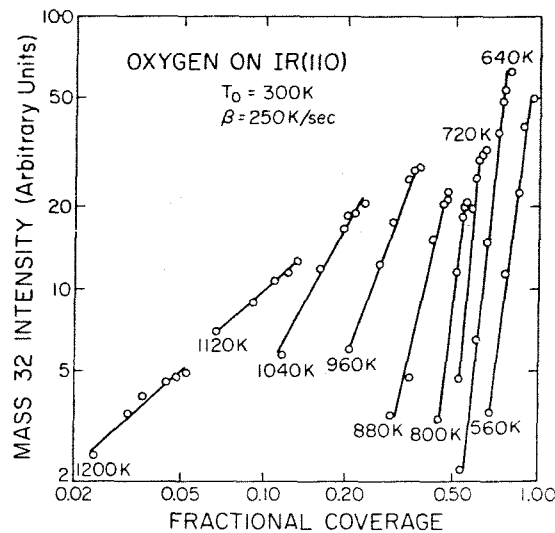


Fig. 7. Order plots for oxygen desorption from Ir(110).

for $[\nu_d(\theta)]$ are 64 ± 2 kcal/mole and $3.5 \times 10^{-4} \pm 3$ cm²/sec.

If the pre-exponential factor varies weakly with coverage, the desorption energy $[E_d(\theta)]$ is given by $kT \ln(I\eta/\nu_d C_s^{n-1} \theta^n)$, which may be averaged over several spectra at points of constant coverage. Using this method and $\nu_d = 3.5 \times 10^{-4}$ cm²/sec, the variation in desorption energy with total coverage of oxygen, was calculated, and the result is shown in fig. 8. For coverages between 1.00 and 1.25 ML on the oxidized surface, the desorption energy is equal to 45 ± 3 kcal/mole. The desorption energies of 45–70 kcal/mole measured for oxygen on Ir(110) do not differ appreciably from the energies of 48–80 and 36–59 kcal/mole measured on Pd(110) [12] and polycrystalline Pt [8], respectively.

Ignoring the coverage dependence of the pre-exponential factor probably introduces a substantial error in the calculated desorption energies, for the compensation effect, a sympathetic variation in the desorption energy and the pre-exponential factor with coverage, has been observed in other desorption systems [21]. For such systems, the desorption kinetics are described by a modified Arrhenius equation [28]

$$R_d = \nu_0 C_s^n \theta^n \exp \left[-\frac{E_d}{k} \left(\frac{1}{T} - \frac{1}{T_s} \right) \right], \quad (3)$$

where ν_0 and T_s are constants, and could not be obtained directly from the data in fig. 6. If T_s is large compared to the temperature range where desorption is observed, little error is introduced by neglecting the coverage dependence of the pre-exponential factor. However, if T_s is assumed to be 2100 K, which approximates the value for oxygen desorption from W(110) [28], the calculated desorption

J.L. Taylor et al. / Chemisorption of oxygen on iridium

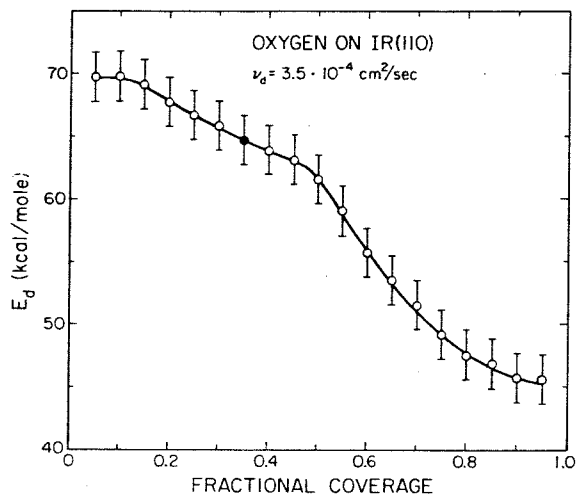


Fig. 8. The coverage dependence of the activation energy of desorption of oxygen from Ir(110). The pre-exponential factor is fixed at $3.5 \times 10^{-4} \text{ cm}^2/\text{sec}$ for all coverages.

energies for Ir(110) are substantially in error, particularly at the extremes of coverage. At 0.05 ML, the energy is underestimated by 10 kcal/mole; at 0.95 ML, the energy is overestimated by 10 kcal/mole.

6. Adsorption kinetics

By integrating eq. (2) over the entire desorption spectrum, the absolute coverage of chemisorbed oxygen was fixed for a given gas exposure since the saturation coverage of oxygen on clean or oxidized Ir(110) at 300 K was determined to be 1 ML ($= 9.6 \times 10^{14} \text{ atoms/cm}^2$). The adsorption kinetics for oxygen were derived in this way. Although the reaction of chemisorbed oxygen with the background impurities H_2 and CO may introduce errors in coverages measured in this way [15], these artifacts are insignificant in this work. Even if the reaction probability is unity for each CO and H_2 molecule impinging on the surface, the calculated coverages are in error by no more than $\pm 0.05 \text{ ML}$. The coverage exposure relations for oxygen on clean and oxidized Ir(110) at 300 K, obtained from the spectra in fig. 6, are shown in fig. 9. In determining the coverage of chemisorbed oxygen on the oxidized surface, the coverage of the oxide layer (0.25 ML) was subtracted from the total coverage.

The adsorption kinetics of oxygen on clean and oxidized Ir(110) are somewhat different. By evaluating the zero-coverage limit of the sticking probability (S) [29],

$$S = \frac{1}{2} C_s (2\pi M k T_g)^{1/2} d\theta/d\epsilon, \quad (4)$$

J.L. Taylor et al. / Chemisorption of oxygen on iridium

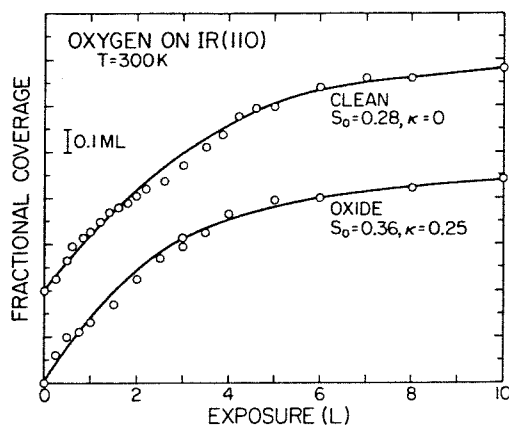


Fig. 9. Adsorption kinetics of oxygen on clean and oxidized Ir(110) at 300 K.

where M , T_g and ϵ are the molecular weight, the temperature and the exposure (the pressure–time product) of gaseous oxygen, initial sticking probabilities (S_0) of 0.28 ± 0.02 and 0.36 ± 0.09 were calculated for oxygen chemisorption on the clean and oxidized surfaces at 300 K. The factor of $\frac{1}{2}$ appears in eq. (4) since each adsorbed molecule occupies two sites. In calculating S_0 , the exposures in fig. 9 were multiplied by 1.22, which is the relative sensitivity of oxygen for the ion gauge that monitored the pressure.

For larger exposures, the data in fig. 9 were fit by a second-order precursor model developed by Kisliuk [30]. In this model, the sticking probability depends on the initial sticking probability, the coverage and a parameter κ that is inversely proportional to the lifetime of the precursor state,

$$\frac{S}{S_0} = \frac{(1 - \theta)^2}{1 - (1 + S_0 - \kappa)\theta + S_0\theta^2}, \quad (5)$$

or in integrated form,

$$\frac{2S_0\epsilon}{C_s(2\pi MkT_g)^{1/2}} = S_0\theta + \frac{\kappa\theta}{1 - \theta} - (1 - S_0 - \kappa) \ln(1 - \theta). \quad (6)$$

The value of κ is different for clean and oxidized Ir(110). Values of zero and 0.25 ± 0.07 for the respective surfaces were obtained from a least squares fit of the data above 3.0 L exposure. The kinetic models for the two surfaces, given by eq. (6), are shown as solid lines in fig. 9.

A more complex second-order model [31], which includes an additional parameter to account for the ordering of the adlayer by interadsorbate repulsion or attraction between nearest neighbours, is not needed to describe the data in fig. 9. Repulsion between nearest neighbours is not expected to be significant for these data because the hard-sphere diameter of a chemisorbed oxygen atom, $d_0 = 1.5 \text{ \AA}$

[32], is small compared to the size of an adsorption site, $C_s^{-1/2} \sim 3 \text{ \AA}$. On the other hand, a simpler model, such as a Langmuir model, does not fit the adsorption kinetics at room temperature where diffusion is slow. Moreover, the Langmuir model cannot describe the temperature dependence of the adsorption kinetics seen below.

The dependence of the adsorption kinetics of oxygen upon the surface temperature of clean Ir(110) was measured to determine the activation energy for oxygen chemisorption and to assess the validity of the precursor model. The kinetic behavior for oxygen chemisorption on the platinum metals is not well established since, in studies of oxygen chemisorption on polycrystalline Pd [16] and Pt [8], and Pt(111) [13], the kinetics appeared to vary randomly with surface temperature. In the present work, the coverage-exposure relations for surface temperatures between 293 and 723 K were derived from TDS, as was done for the data in fig. 9. These relations are shown in fig. 10. Surface temperatures for these data are accurate to $\pm 5 \text{ K}$. The coverages for any surface temperature depended on the oxygen exposure only, but not the total pressure. Since the gain of the electron multiplier in the mass spectrometer drifted markedly for larger oxygen exposures, the gain was calibrated frequently by comparing the total intensities for spectra obtained for the

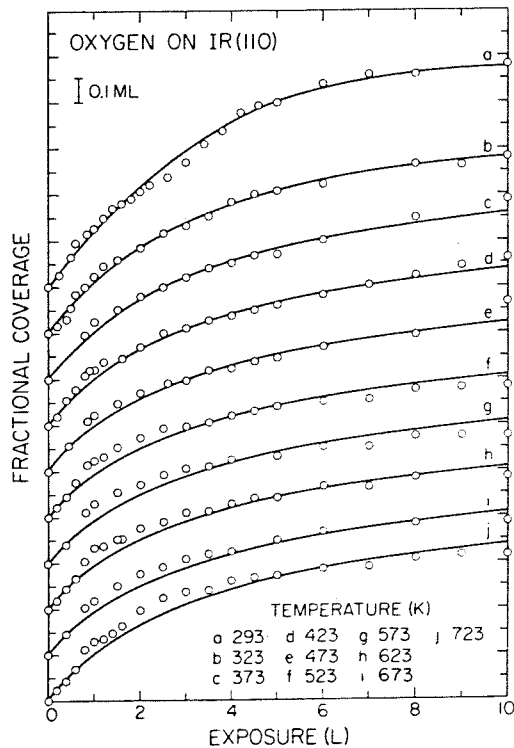


Fig. 10. Adsorption kinetics of oxygen on clean Ir(110) at various temperatures.

same exposures at 300 K, but at different times. This calibration procedure was crucial for obtaining reproducible results and was also necessary for determining absolute surface coverages. Oxygen chemisorption is irreversible for the temperature and exposure ranges in fig. 10. That is, desorption of the chemisorbed layer was negligible for these data, as evidenced by the desorption energies calculated in the previous section.

The initial sticking probability was calculated to be 0.28 ± 0.04 , irrespective of the surface temperature. Therefore, oxygen chemisorption on clean Ir(110) is not activated for gaseous molecules that impinge with a temperature of 300 K. Kinetic models, calculated from eq. (6) with $S_0 = 0.28$ for each surface temperature, are shown as solid lines in fig. 10. The parameter κ for any temperature was determined by a least-square fit to the kinetic data above 3.0 L exposure. The temperature dependence of κ is shown in fig. 11.

Since the initial sticking probability for oxygen chemisorption is constant with temperature, $\ln \kappa$ should be inversely proportional to temperature [30]. The proportionality constant is E_p/k , where E_p is the difference between the activation energies for the desorption and diffusion of the precursor [33]. The plot of $\ln \kappa$ as a function of T^{-1} in fig. 11 gives a line between 323 and 573 K with $E_p = 2.1$ kcal/mole. This value for oxygen chemisorption on Ir(110) is close to the value of 1.4 kcal/mole measured for oxygen on Pt field emission tips [2]. The value of $\kappa = 0$ calculated from the kinetic data at 293 K does not fall on the line since diffusion in the chemisorbed layer is slow at this temperature, but is rapid at slightly higher temperatures (see section 4). Diffusion and the subsequent ordering or disordering of the chemisorbed layer influences the adsorption kinetics markedly [30,31].

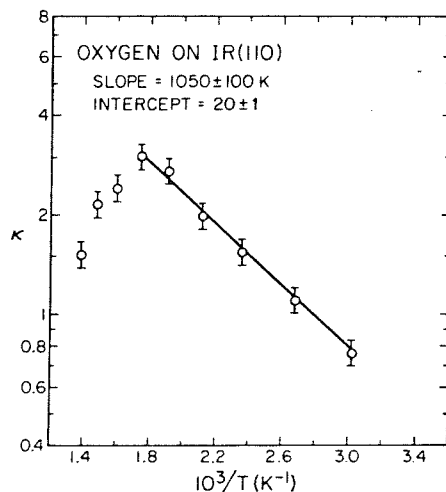


Fig. 11. The temperature dependence of the parameter κ calculated from the data in fig. 10. Here κ is inversely proportional to the lifetime of the precursor state.

Oxide formation, which has been shown to modify the kinetics of oxygen chemisorption on Ir(110), occurs above 573 K. Hence, values of κ for surface temperatures above 573 K also deviate from the line in fig. 11. Despite these deviations, the second-order precursor model given by eq. (6) describes the kinetics of oxygen chemisorption consistently.

The kinetic behavior observed in the present work is quite similar to the behavior reported for oxygen chemisorption on other surfaces of the platinum metals. At 300 K, oxygen adsorbs dissociatively with a saturation coverage near 10^{15} atoms/cm² [4,5,7,15]. Generally, the adsorption kinetics are described accurately by a second-order Langmuir model or a second-order precursor model [3,4,6–8,13,15, 16]. For surface temperatures near 300 K, the initial sticking probability for oxygen decreases with increasing molecular weight of the metal and on smoother surface orientations. The initial sticking probability is approximately equal to unity on Ni(111), Ni(110), Ni(100) [3,6] and polycrystalline Pd [16]; 0.3 on Pd(111) [7], Pt(110) [4] and polycrystalline Pt [8]; and 0.1 or less on Pt(111) [15] and Ir(111) [5]. The formation of an oxide layer on Ni surfaces [3,6], polycrystalline Pt [8] and Pt(110) [4] alters the adsorption kinetics of oxygen perceptibly. Moreover, oxidation of these surfaces increases the total coverage of oxygen.

7. Charge transfer to the overlayer

The contact potential differences (CPD) on clean and oxidized Ir(110) at 90 and 300 K were measured as a function of oxygen exposure. In fig. 12, the data are shown as curves I and III for the respective temperatures. The CDP, ($\Delta\phi$), or equivalently, the work function, increased monotonically with oxygen coverage. For all CPD measurements reported in this work, the CPD for any surface temperature varied with the oxygen exposure only, but not the partial pressure of oxygen. When the substrate was annealed from 90 to 300 K, the CPD for an overlayer chemisorbed at 90 K changed irreversibly. This suggests that another state of chemisorbed oxygen, presumably molecularly chemisorbed oxygen, is stable at low temperatures. The data for adsorption at 90 K will be treated in the next section.

To obtain accurate coverages at 90 K for the chemisorbed phase that is entered irreversibly upon annealing from 90 to 300 K, the substrate was exposed to oxygen at 300 K. Then the CPD was calculated from the difference between the surface potentials for the chemisorbed layer and the clean or oxidized surface at 90 K. The corresponding data points are shown as circles in fig. 12; curves IIa and IIb approximate the data. The coverages for these data may be somewhat inaccurate since the surface temperature varied by ± 10 K during the exposures. As shown in the last section, the adsorption kinetics, especially for larger exposures, are quite sensitive to the surface temperature near 300 K.

When the coverages obtained from the adsorption kinetics are related to CPD measurements at points of constant exposure, the apparent dipole moment at infi-

J.L. Taylor et al. / Chemisorption of oxygen on iridium

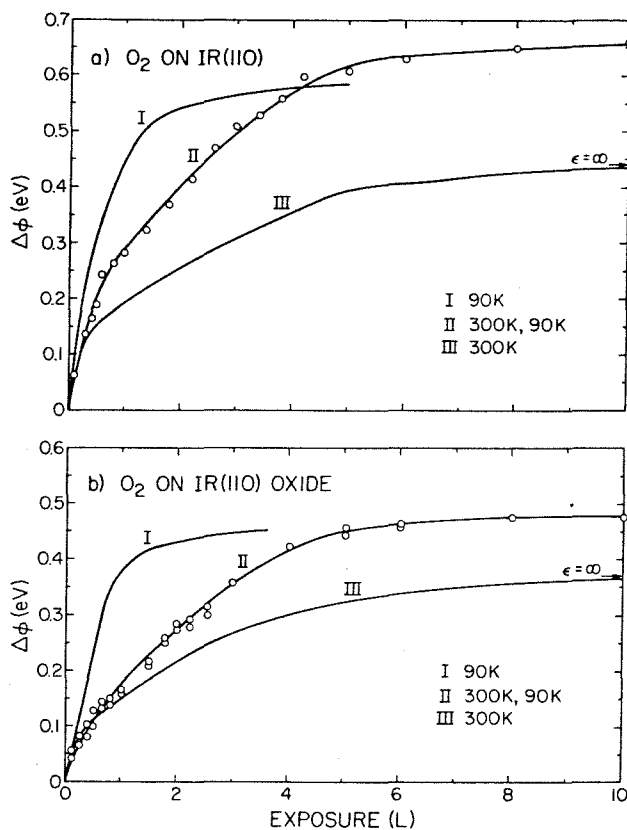


Fig. 12. CPD as a function of oxygen exposure on Ir(110): (a) clean surface; (b) oxidized surface. The exposures and CPD measurements were performed at 90 K for curves I; at 300 and 90 K for curves II (see text); and at 300 K for curves III.

nite dilution (μ) and the apparent polarizability (α) of the adsorbate may be calculated from a modified Topping model [34]. This model accounts for the depolarization of the overlayer resulting from dipole-dipole interactions. For any surface temperature, the ratio of the coverage to the CPD at that coverage ($\theta/\Delta\phi$) is plotted as a function of coverage (θ). The slope and intercept of the resulting line are $(\Lambda\alpha C_s^{1/2}/4\pi\mu)$ and $(4\pi\mu C_s)^{-1}$. Here Λ is a structural parameter for the overlayer and is equal to 9.46 for an overlayer with periodicity of the Ir(110) surface. This value was obtained from a lattice sum over a (101×101) matrix according to a procedure described elsewhere [34]. The modified Topping model is appropriate for adsorption at specific sites, rather than on an amorphous surface [34]. For the latter case, the ratio ($\theta/\Delta\phi$) is plotted versus $\theta^{3/2}$, but the slope and intercept assume the same values as for adsorption at specific sites.

Since the apparent dipole moment is the sum of the normal components of the

true dipole moment of the adsorbate and the image dipole of the adsorbate in the surface, the apparent dipole moment at infinite dilution (μ) is equal to twice the component of the true dipole moment that is normal to the surface. Similarly, the apparent polarizability of the adsorbate (α) is equal to the apparent dipole moment divided by the normal component of the average field at the surface (E_n), which orients the apparent dipole moment in the absence of induced charge. The image dipole of the adsorbate accounts for the field resulting from the induced charge [18].

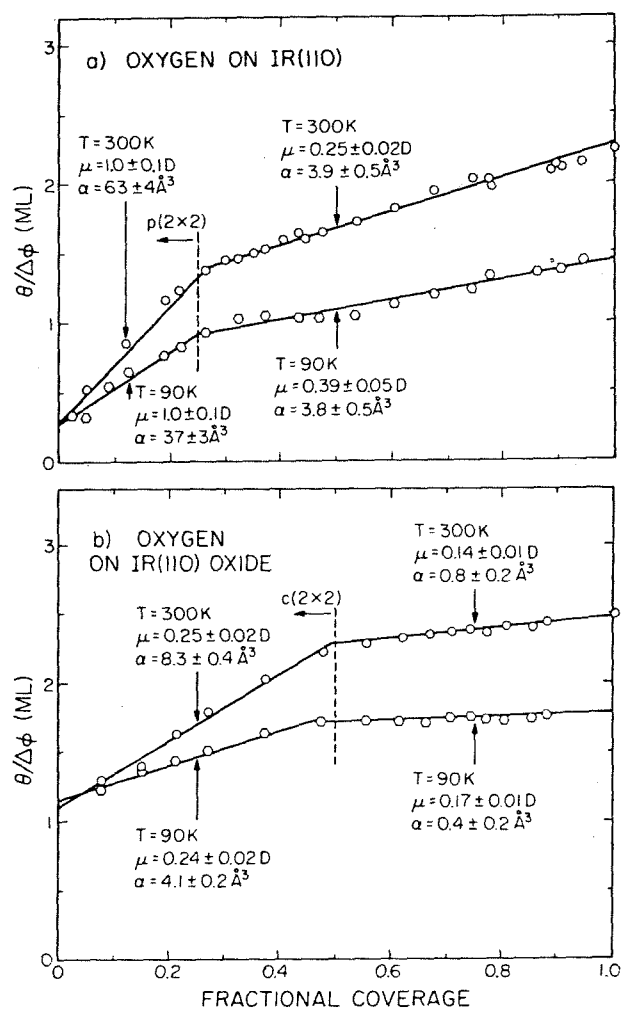


Fig. 13. Topping plots for dissociatively chemisorbed oxygen on Ir(110) at 90 and 300 K: (a) clean surface; (b) oxidized surface.

Topping plots for the CPD measurements in curves II and III of fig. 12 were constructed using the coverage—exposure relations for oxygen chemisorption on clean and oxidized Ir(110) at 300 K, shown in fig. 9. The plots, as well as the apparent dipole moments and polarizabilities, deduced from the intercepts and slopes, are shown in fig. 13. The dipole moments of oxygen on the oxidized surface are smaller than those on the clean surface since the oxide layer draws charge toward the surface. The Topping plots for the clean surface have discontinuities at 0.25 ML coverage where the $p(2 \times 2)$ LEED pattern is formed completely. Similarly, the plots for the oxidized surface have discontinuities at 0.50 ML coverage where the $c(2 \times 2)$ pattern is formed completely. In all cases, the apparent dipole moments and polarizabilities decrease for coverages exceeding the point of discontinuity. A pronounced change in the CPD, or equivalently, the dipole moments with coverage has been observed for oxygen chemisorption on Ni(100) [3] and Ru(001) [19] also. For these systems, the CPD also changes discontinuously for coverages where an ordered overlayer structure appears with maxima intensity.

The binding sites for oxygen on either clean or oxidized Ir(110) may be inferred from the pronounced change in the dipole moment with coverage. On either surface, the dipole moment for the low coverage state is substantially larger. If the binding sites of oxygen are above the topmost row of surface atoms, the apparent dipole moment, i.e., the normal component of the true dipole moment of the adsorbate, is expected to be larger than the dipole moment for sites between the rows. That is, for sites above the rows, the movement of the bonding electrons would be more nearly normal to the surface. Therefore, the low coverage states on clean and oxidized Ir(110) are associated with binding sites above the topmost rows of surface atoms, whereas the high coverage states are associated with binding sites between the rows. Since the $p(2 \times 2)$ pattern on clean Ir(110) and the $c(2 \times 2)$ pattern on oxidized Ir(110) correspond to the low coverage states of oxygen, the binding sites of oxygen in figs. 4 and 5 were fixed above the topmost rows of surface atoms [35]. Although chemisorbed oxygen may bind in different states at low and high coverages, no differences in the Auger or X-ray photoemission spectra of oxygen could be resolved for the two states when the spectra were normalized to the same intensity.

The data in fig. 12 show that the CPD for oxygen chemisorption is a function of temperature as well as coverage. The temperature dependence of the CPD was investigated more thoroughly by measuring the CPD as a function of oxygen exposure on clean Ir(110) for temperatures between 300 and 723 K. The data are shown in fig. 14. When the surface temperature was maintained between 300–673 K, the CPD changed reversibly, within experimental error (± 0.01 eV) upon rapidly annealing or cooling the sample. The CPD is altered irreversibly upon annealing above 673 K since the oxide layer forms rapidly at these temperatures. Topping plots, shown in fig. 15, were constructed from the coverage—exposure relations in fig. 11 and the CPD measurements in fig. 14.

The Topping plots for surface temperatures below 673 K give a discontinuity

J.L. Taylor et al. / Chemisorption of oxygen on iridium

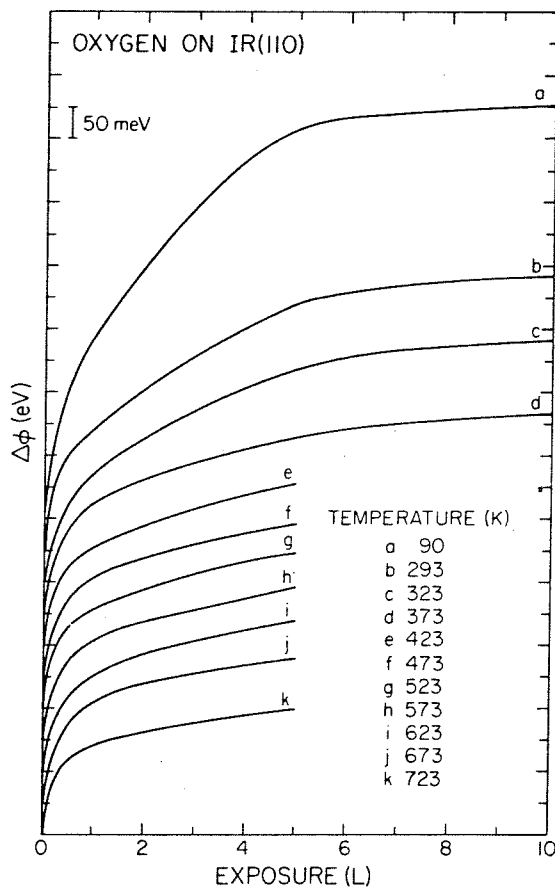


Fig. 14. CPD as a function of oxygen exposure on clean Ir(110) at various surface temperatures.

near 0.25 ML coverage, where the $p(2 \times 2)$ LEED pattern of the overlayer appears with maximum intensity on the clean surface. At 723 K, the discontinuity vanishes since the oxide layer forms rapidly and changes the dipole moment and polarizability of oxygen. In this case, these quantities are 0.43 ± 0.04 D ($1 \text{ D} \equiv 10^{-18}$ esu cm) and $25 \pm 2 \text{ \AA}^3$, respectively. For temperatures below 673 K, where the oxide forms slowly, the apparent dipole moments for the low coverage (≤ 0.25 ML) and the high coverage (> 0.25 ML) states are 1.0 ± 0.1 D and 0.25 ± 0.02 D as calculated from a least squares fit to the data. Moreover, the dipole moment for either state is independent of temperature. One exception to this generality occurs for the dipole moment of the high coverage state at 90 K, which is 0.39 ± 0.05 D. However, this value may be inaccurate since, as noted previously, some error was introduced in determining the coverage for this particular case.

Although the dipole moments for oxygen in either coverage state are indepen-

J.L. Taylor et al. / Chemisorption of oxygen on iridium

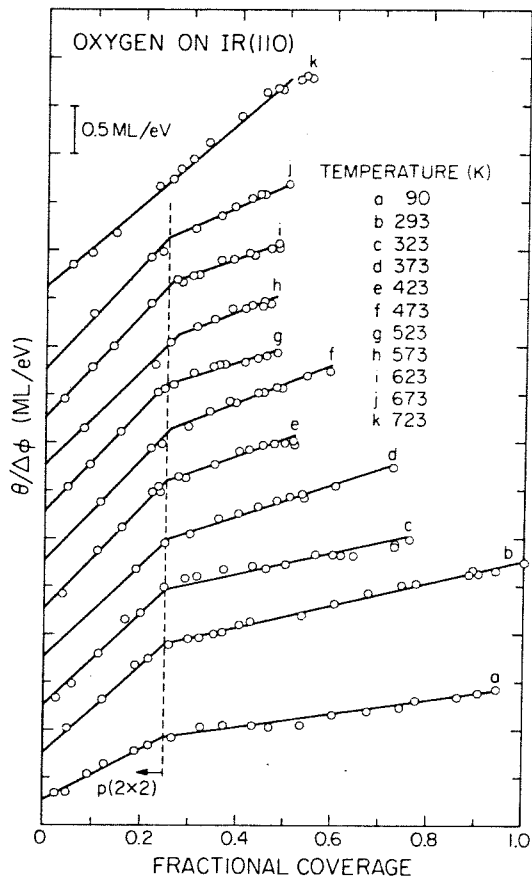


Fig. 15. Topping plots for dissociatively chemisorbed oxygen on clean Ir(110) at various temperatures.

dent of temperature, the polarizabilities are not. The polarizability for either state is inversely proportional to temperature, as shown in fig. 16. A model will be developed now to explain this temperature dependence. The polarizability may change with temperature as a result of the thermal randomization of the chemisorbed species among different electronic, vibrational or translational modes. Since the dipole moment for either coverage state is independent of temperature, only the energy of chemisorbed oxygen and the average surface field ($E_n = \mu/\alpha$) vary among the modes. Since the thermal energy required to populate low-lying electronic levels is usually quite large [35], the temperature dependence of the polarizability cannot be explained in this way. When the first vibrational mode is entered, the equilibrium separation of nuclei typically changes by $\sim 0.1 \text{ \AA}$ [35], which is small compared to the diameter of a chemisorbed oxygen atom ($d_o = 1.5 \text{ \AA}$) [32]. Since the vol-

J.L. Taylor et al. / Chemisorption of oxygen on iridium

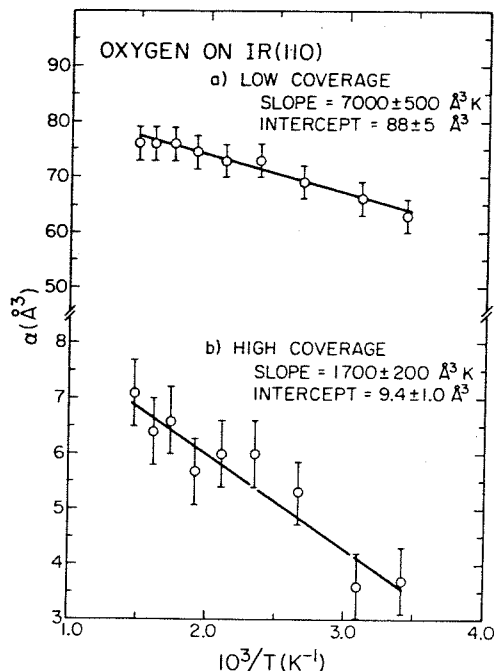


Fig. 16. The temperature dependences of the polarizabilities of oxygen chemisorbed on clean Ir(110), calculated from the data in fig. 15: (a) low coverage state ($\theta < 0.25$ ML); (b) high coverage state ($\theta > 0.25$ ML).

ume, over which the surface field is averaged, does not vary appreciably for the various vibrational modes, the temperature dependence of the polarizability cannot be explained by this motion either. Therefore, this phenomenon can be attributed only to the thermal randomization of the translational motion. The translational motion for the two coverage states will be treated separately.

Motion in the [001] azimuth may be ignored since the barrier for diffusion in this direction is relatively large, as will be shown. The potential variation for chemisorption in the [110] azimuth will be approximated by a periodic square well of height U . Although the dipole moment does not vary for the sites at the top and bottom of the well, the polarizability does change since the average surface field (E_n) is different for the two sites. The field is expected to vary between the sites since the field acting on an oxygen atom is averaged over a relatively small volume, $\pi d_0^3/6 \approx 2 \text{ \AA}^3$, compared to the volume of a unit cell, $C_s^{-3/2} \approx 30 \text{ \AA}^3$. However, the field acting on chemisorbed CO on Ir(110) does not change among the binding sites [18], for the volume of the CO molecule is comparable to the size of a unit cell. The apparent polarizabilities (μ/E_n) for sites in the bottom and on the top of the well are denoted α_1 and α_2 .

The apparent polarizability of chemisorbed oxygen [$\alpha(T)$] is a thermal average

between the polarizabilities for the two types of sites, i.e.,

$$\alpha(T) = \alpha_1 \left[\frac{\exp(U/kT)}{1 + \exp(U/kT)} \right] + \alpha_2 \left[\frac{1}{1 + \exp(U/kT)} \right], \quad (7)$$

where the terms in brackets are the Boltzmann weighting factors for the two sites [36,37]. Although this model will be used to describe the temperature dependence of the polarizability for the two coverage states of oxygen, the values of α_1 , α_2 and U are expected to be different for the two states since the dipole moments are different. Eq. (7) may be simplified by a Taylor series expansion about any temperature T_α

$$\alpha(T) = i + s/T, \quad (8)$$

$$i = \alpha_1 + (\alpha_2 - \alpha_1)(1 + U/kT_\alpha) \exp(-U/kT_\alpha),$$

$$s = (U/k)(\alpha_2 - \alpha_1) \exp(-U/kT_\alpha),$$

where s and i are the slope and intercept in a plot of $\alpha(T)$ as a function of T^{-1} , as in fig. 16. This analysis is not rigorously valid, for the structural parameter Λ was assumed to be constant when the polarizability in fig. 16 were calculated. The value of Λ is expected to vary with temperature since the order in the adlayer is changed. However, as is shown in Appendix I, ignoring the temperature dependence of Λ introduces a negligible error in this analysis.

The polarizability (α_1) for the energetically favored sites of oxygen on clean Ir(110) may be approximated as the apparent polarizability at 90 K, which is 37 \AA^3 for the low coverage state and 3.8 \AA^3 for the high coverage state. The potential variation between the sites (U) is

$$k \left[\left(\frac{i - \alpha_1}{s} \right) \frac{1}{T_\alpha} \right]^{-1}.$$

If this expression is evaluated at 400 K, which corresponds to the mean value of T^{-1} in fig. 16, the potential variations for the high and low coverage states are 0.42 and 2.5 kcal/mole. As stated previously, the potential variation in the [110] azimuth, approximately 1 kcal/mole, is small compared to the variation in the [001] azimuth, approximately 20 kcal/mole (see section 4), so diffusion in the [001] azimuth may be ignored. By evaluating eq. (8) at 400 K, the polarizabilities (α_2) for the energetically disfavored sites are 94 and 35 \AA^3 for the low and high coverage states. These calculated values of α_1 , α_2 and U for chemisorbed oxygen on clean Ir(110) are accurate to $\pm 20\%$.

The dipole moments for the low and high coverage states of oxygen on oxidized Ir(110), which are equal to 0.24 ± 0.03 and 0.15 ± 0.03 D from fig. 13, also appear to be independent of temperature. Hence, this translational model may be used to describe the temperature dependence of the polarizability in this system. If the potential variations (U) for the low and high coverage states on oxidized Ir(110) are approximated by the variations on the clean surface, values of $\alpha_1 = 4$ and

J.L. Taylor et al. / Chemisorption of oxygen on iridium

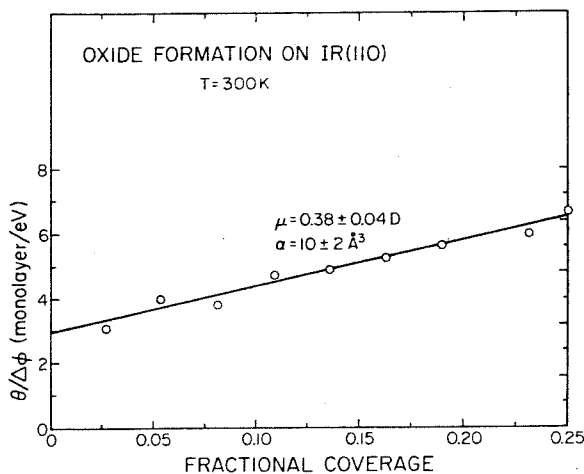


Fig. 17. Topping plot for the oxide layer on Ir(110) at 300 K.

0.4 \AA^3 , and $\alpha_2 = 17$ and 27 \AA^3 are calculated for the respective states. For any site on either surface, the field ($E_n = \mu/\alpha$) that orients the dipole moment of chemisorbed oxygen is on the order of 10^7 V/cm , which is comparable to the field acting on chemisorbed CO on Ir(110) [18].

The dipole moment and polarizability for the oxide atoms also were determined from CPD measurements. To fix the coverage in the oxide layer, a clean surface at 300 K was exposed to oxygen. Then the oxide layer was formed by annealing the overlayer to 1100 K for 1 min. The CPD for the oxide layer ($\Delta\phi$) was calculated from the difference in the surface potentials for the annealed layer and the clean surface at 300 K. Data obtained from this experiment are shown in the Topping plot in fig. 17. The concentration of sites in the oxide layer is $2.4 \times 10^{14} \text{ cm}^{-2}$ (0.25 ML), so the dipole moment and the polarizability for an oxide atom at 300 K are $0.38 \pm 0.04 \text{ D}$ and $8 \pm 4 \text{ \AA}^3$. Since these values for the oxide are much different from those obtained for chemisorbed oxygen at the same coverage and temperature, the chemical states of the two forms of oxygen must be different.

8. Molecularly chemisorbed oxygen

The irreversible change in the CPD, which occurs when an oxygen overlayer that is chemisorbed at 90 K is annealed to 300 K, must result from a change in the chemical state of oxygen. A similar change is observed when chemisorbed atoms enter the oxide phase. The irreversibility at low temperatures cannot be associated with the ordering of the overlayer by diffusion since the irreversibility is observed at high coverages where the ordering of the adlayer is expected to produce a negligible change in the CPD [38]. In the remainder of this section, evidence will be presented

to show that oxygen chemisorbs molecularly, rather than dissociatively, on clean or oxidized Ir(110) at 90 K. The existence of this third chemisorbed state of oxygen not only explains the irreversible change in the CPD, but also relates other experimental data consistently. A molecularly chemisorbed state of oxygen has not been reported previously on the platinum metals, except on polycrystalline Pt [10]. The TDS spectrum of oxygen adsorbed on polycrystalline Pt at 100 K shows a feature near 200 K, which has been attributed to molecularly chemisorbed oxygen.

Several TDS spectra of oxygen adsorbed on clean and oxidized Ir(110) at 90 K were measured in the present study. Below room temperature, less than 0.1 ML of oxygen was desorbed. Because the yield of desorbed oxygen fluctuated randomly with the exposure of oxygen and the heating rate, the low temperature feature was associated with desorption from the manipulator, rather than from the Ir(110) surface. Hence, the desorption of molecular oxygen on Ir(110) occurs at a negligibly slow rate compared to the dissociation of this species.

Because artifacts appeared in the desorption spectra at low temperatures, these spectra could not be used for measuring the adsorption kinetics of oxygen on Ir(110) at 90 K. However, the initial sticking probability of molecularly chemisorbed oxygen could be determined from CPD measurements. The surface was exposed to oxygen at 90 K and then was annealed to 300 K. Using the Topping plots for dissociatively chemisorbed oxygen at 90 K, which are shown in fig. 13, the coverage for each exposure was determined from the difference in the surface potentials for the annealed overlayer and the clean or oxidized surface at 90 K. This technique was not used for larger exposures (>2 L) since the coverages associated with these exposures are somewhat inaccurate, as shown in the last section. From these CPD measurements, the initial sticking probabilities for oxygen chemisorption on clean and oxidized Ir(110) at 90 K are 0.28 ± 0.03 and 0.54 ± 0.10 . These data are further evidence that oxygen chemisorption on either surface is not activated. The discrepancy in the initial sticking probabilities on the oxidized surface at 90 and 300 K may be accounted for entirely by experimental errors. Moreover, since the initial sticking probability on the oxidized surface appears to decrease with temperature, an activation barrier cannot exist, for the opposite trend should be observed.

Using the initial sticking probabilities derived above, Topping plots for oxygen chemisorption on clean and oxidized Ir(110) at 90 K were constructed from the CPD-exposure relations of curves Ia and Ib in fig. 12. The plots, as well as values for the dipole moments and polarizabilities (per atom) of molecular oxygen, are shown in fig. 18. The concentration of adsorption sites was assumed to be $9.6 \times 10^{14} \text{ cm}^{-2}$ in determining these values. Although the Topping plots were fit to a single line, no discontinuities in the plots were detected experimentally when the coverage for any CPD was measured with the method described previously.

At 90 K, the dipole moments (per atom) of molecular oxygen on clean and oxidized Ir(110) are nearly equal to those of dissociatively chemisorbed oxygen in the respective low coverage states. This suggests that molecular oxygen binds above

J.L. Taylor et al. / Chemisorption of oxygen on iridium

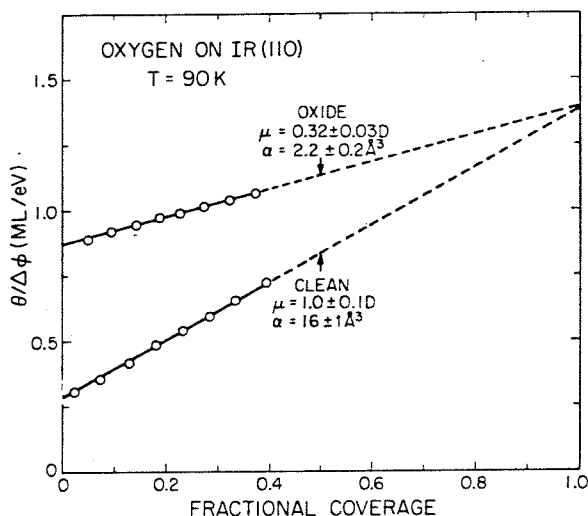


Fig. 18. Topping plots for molecularly chemisorbed oxygen on clean and oxidized Ir(110) at 90 K. Dipole moments and polarizabilities shown here were calculated on a per atom basis.

the topmost rows of surface atoms, like dissociatively chemisorbed oxygen in the low coverage states, and fills two adjacent adsorption sites. Moreover, the interatomic axis of molecular oxygen is parallel, rather than normal to the surface. This assignment of a parallel orientation is supported by XPS data since the 1s line for molecular oxygen on clean or oxidized Ir(110) is not split into two peaks. Although the dipole moments (per atom) do not differ for molecularly and dissociatively chemisorbed oxygen at 90 K, the polarizabilities do differ. This, as well as the absence of discontinuities in Topping plots in fig. 18, is further evidence that oxygen may chemisorb into two distinct chemical states, depending on the surface temperature.

The adsorption kinetics of molecular oxygen on clean and oxidized Ir(110) at 90 K were deduced from the Topping plots in fig. 18 and the CPD-exposure relations in fig. 12. The coverage-exposure relations are shown in fig. 19. A second-order precursor model, which accounts for the ordering of a mobile overlayer by intermolecular repulsion [31], describes the kinetics data for either surface accurately. If the adsorbates fill two adjacent sites, as is the case for molecular oxygen on Ir(110), this model is appropriate for describing non-dissociative adsorption. In this model [31], the sticking probability at any coverage, S , is related to the initial sticking probability; a parameter, κ , that is identical to the parameter κ in eq. (5) (q.v.); and a parameter, B , that is related to the repulsive energy between nearest neighbors [$-kT \ln(1 - B)$].

$$S/S_0 = [(1 - \kappa) + \kappa/\theta_{00}]^{-1}, \quad (9)$$

J.L. Taylor et al. / Chemisorption of oxygen on iridium

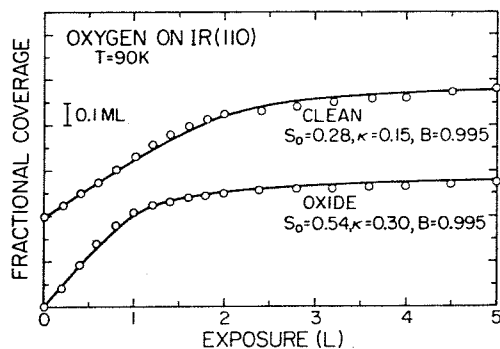


Fig. 19. Adsorption kinetics of oxygen on clean and oxidized Ir(110) at 90 K.

where

$$\theta_{00} = (1 - \theta) - \frac{2\theta(1 - \theta)}{[1 - 4B\theta(1 - \theta)]^{1/2} + 1} \quad (10)$$

For clean Ir(110), this second-order model with $S_0 = 0.28$, $\kappa = 0.15$ and $B = 0.995$ fits the kinetic data well; for oxidized Ir(110), $S_0 = 0.54$, $\kappa = 0.30$ and $B = 0.995$. The integrated forms of models with these parameters from eqs. (4), (9) and (10) are shown as solid lines in fig. 19. The repulsive energy between nearest-neighbors is equal to 1 kcal/mole on either surface. This intermolecular repulsion reduces the sticking probabilities for higher coverages so that the adsorption kinetics at 90 K for higher coverages are slow compared to the rate at 300 K, where the repulsion is negligible.

The activation energy for the dissociation of molecular oxygen on Ir(110) also was determined from CPD measurements. When molecular oxygen was chemisorbed on clean or oxidized Ir(110) at 90 K, the CPD of the overlayer decayed exponentially to the value obtained by annealing the sample to 300 K. The half-life for the decay was independent of coverage and was calculated to be about 20 min, as extrapolated from experimental data. In this experiment, care was exercised to insure that the adsorption of background impurities did not affect the CPD. If the rate of dissociation is described by a first-order Arrhenius expression with a pre-exponential factor of 10^{13} sec^{-1} , the activation energy for dissociation is approximately 8 kcal/mole. This activation energy cannot be associated with diffusion. In the previous sections, the activation energies for diffusion in the [001] and [110] azimuths were determined to be approximately 20 and 1 kcal/mole. Moreover, slow dissociation did not influence the CPD measurements shown in fig. 12 since these experiments were completed after 100 sec.

Oxygen chemisorption above 200 K is effectively dissociative since the rate of dissociation may be estimated as 10^5 ML/sec at 200 K. Although the activation energy for the dissociation of molecular oxygen is substantial, chemisorption need not be activated. The maximum in the barrier between the molecularly and dissoci-

J.L. Taylor et al. / Chemisorption of oxygen on iridium

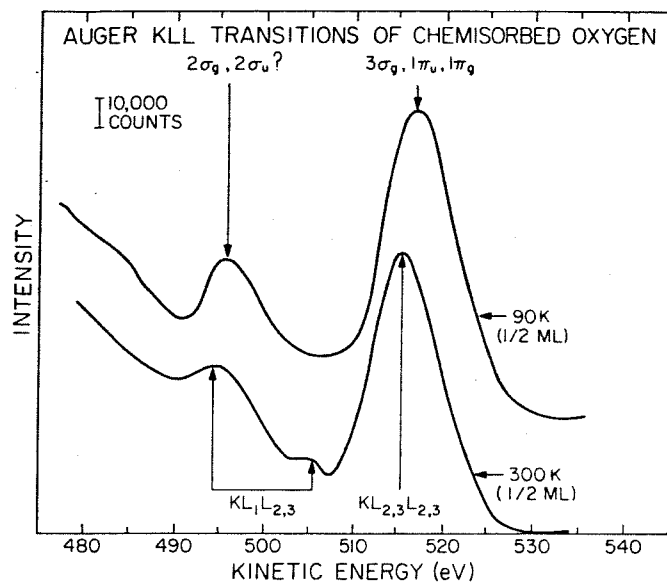


Fig. 20. Auger KLL transitions of molecularly and dissociatively chemisorbed oxygen on clean Ir(110). The spectra for the respective overlayers were measured following oxygen exposures at 90 and 300 K. The coverage in each spectrum is 0.5 ML.

atively chemisorbed states must be substantially below the vacuum potential since little, if any, molecular oxygen desorbs from the surface below room temperature. Hence, this barrier does not influence the adsorption kinetics of oxygen on Ir(110). Assuming that no more than 0.1 ML desorbs upon annealing the surface from 90 to 300 K, the activation energy for desorption must be at least 10 kcal/mole.

The Auger KLL transitions for molecularly and dissociatively chemisorbed oxygen on clean Ir(110) are different in shape and energy. The spectra for the respective chemical states, shown in fig. 20, were recorded upon chemisorption at 90 and 300 K. When an oxygen overlayer was chemisorbed at 90 K and then was annealed to 300 K, the spectrum observed at 90 K was identical to the spectrum for dissociatively chemisorbed oxygen, as expected. The spectra in fig. 20 were obtained under conditions similar to those for the spectra in fig. 3 (q.v.). The coverages for the two chemical states were nearly the same value, 0.5 ML. To inhibit electron beam dissociation, the spectrum for molecular oxygen was obtained by summing fifty individual spectra of 120 sec duration each. By comparison to a gas phase spectrum [39], peaks in the spectrum of molecular oxygen have been associated with final hole states as noted in fig. 20. The intensity of the peak near 495 eV is increased substantially for molecular oxygen. This increase may result from a shift in the energy of the $2\sigma_u$ orbital toward the $2\sigma_g$ orbital, as compared to the gas phase energies. However, further evidence from UPS experiments is needed to verify this conjecture.

9. Conclusions

The chemisorption of oxygen on Ir(110) has been studied to give insight into the CO oxidation reaction on Ir(110). Oxygen may adsorb into three distinct chemical states: (1) a molecularly chemisorbed species that is stable below 100 K, (2) a dissociatively chemisorbed species, and (3) a surface oxide that forms rapidly above 700 K. The oxide layer saturates at 0.25 ML (1 ML = 9.6×10^{14} atoms/cm²) coverage and forms with an activation energy of 45 kcal/mole. The oxide, compared to dissociatively chemisorbed oxygen, is less reactive to reduction by CO. Although the oxide layer may be either well ordered, giving a (1 × 4) LEED pattern, or partially ordered, giving a (1 × 1) LEED pattern with streaks between the beams in the [001] azimuth, the chemical properties for these two forms of oxide are otherwise identical.

The saturation coverage of oxygen on clean or oxidized Ir(110) at 300 K is 1 ML. Different LEED patterns are observed on the two surfaces. A p(2 × 2) pattern forms near 0.25 ML coverage on the clean surface; a c(2 × 2) pattern forms near 0.5 ML coverage on the oxidized surface. In both cases, the overlayer must be annealed to order the pattern in the [001] azimuth. The activation energy for diffusion of dissociatively chemisorbed oxygen on either surface is approximately 20 kcal/mole in the [001] azimuth and 1 kcal/mole in the [110] azimuth.

Oxygen desorbs molecularly from Ir(110) with an activation energy of 45–70 kcal/mole, decreasing continuously with coverage. The pre-exponential factor for the desorption rate coefficient is 3.5×10^{-4} cm²/sec near 0.35 ML coverage. The oxide forms rapidly while chemisorbed oxygen desorbs. The desorption kinetics are second-order above 0.1 ML coverage, but are first-order at lower coverages since the decomposition of the oxide, rather than the recombination of chemisorbed atoms, is rate limiting.

For surface temperatures between 300 and 700 K, the adsorption kinetics are described by a second-order precursor model. The difference in the activation energies for the desorption and the diffusion of the precursor is 2.1 kcal/mole on clean Ir(110). Oxygen chemisorption is not activated on clean or oxidized Ir(110). That is, the initial sticking probability is independent of the surface temperature, and is equal to 0.28 and 0.4 on the respective surfaces.

The CPD on Ir(110) always increases with oxygen coverage, regardless of the chemical state. The dipole moment and polarizability of dissociatively chemisorbed oxygen on clean and oxidized Ir(110) change at coverages of 0.25 and 0.50 ML, respectively. For lower coverages, the dipole moment and polarizability for either surface are larger, indicating that oxygen adsorbs above the topmost rows of surface atoms at lower coverages and between the rows at higher coverage. Although the dipole moment for any coverage of dissociatively chemisorbed oxygen on either surface is independent of temperature, the polarizability is not. The polarizability changes since, as the surface temperature increases, oxygen diffuses in the [110] azimuth and occupies sites with different energies and polarizabilities.

J.L. Taylor et al. / Chemisorption of oxygen on iridium

If an overlayer of oxygen that is chemisorbed at 90 K is annealed to 300 K, the CPD changes irreversibly indicating that oxygen chemisorbs molecularly at 90 K. The activation energy for the dissociation of molecular oxygen is 8 kcal/mole whereas the desorption energy is at least 10 kcal/mole. On clean and oxidized Ir(110), the dipole moment (per atom) of molecular oxygen is equal to that of dissociatively chemisorbed oxygen in the low coverage state on the respective surfaces. This suggests that molecular oxygen chemisorbs with the molecular axis parallel to the surface and occupies two adjacent sites above the topmost row of surface atoms. The adsorption kinetics of molecular oxygen are described by a second-order precursor model, which accounts for intermolecular repulsion in the overlayer.

Acknowledgment

This research was supported by the National Science Foundation under Grant Number DMR 77-14976.

Appendix I

The translational model in section 7, which describes the temperature dependence of the polarizabilities in fig. 16, is not rigorously correct. These polarizabilities were calculated for a fixed value of the structural parameter, Λ_1 , where Λ_1 is the structural parameter for an overlayer with the same periodicity as the (110) surface of an fcc metal. In the translational model, the order in the adlayer changes with temperature and, consequently, the structural parameter $[\Lambda(T)]$, as well as the polarizability, vary with temperature. Therefore, the polarizabilities in fig. 16 (α_0) are rigorously equal to

$$\alpha_0 = \alpha(T) \Lambda(T) / \Lambda_1, \quad (11)$$

where $\alpha(T)$ is given by eq. (7).

The structural parameter $[\Lambda(T)]$ for oxygen on Ir(110) is estimated as follows. Motion in the [001] direction is ignored as was done in section 7. At low temperatures, the overlayer is assumed to have the periodicity of the Ir(110) surface. The position of an adsorbate in the [110] direction is δr in any unit cell. The value of δ varies between $-1/2$ and $1/2$, and r , which is equal to 2.7 Å for Ir(110), is the distance between the centers of nearest unit cells in the [110] direction. Step changes in the square-well potential occur for $hr/2$ where h is an integer. When the adsorbate is in an energetically favored site, δ lies between 0 and $+1/2$; for an energetically disfavored site, δ lies between $-1/2$ and 0. Since the hard sphere diameter of oxygen (1.5 Å) [32] is approximately equal to $r/2$, intermolecular repulsion is accounted for by constraining the motion of the center of an adsorbate between $-1/4 < \delta < +1/4$. The mean positions of the adsorbate in energetically favored and

disfavored sites are $\delta = +1/8$ and $\delta = -1/8$. To simplify the calculation of lattice parameters, the adsorbate will be constrained to these two positions. This may introduce some error in the calculation, but intermolecular repulsion, which correlates the motion of adsorbates, is treated approximately also.

The dipole-dipole interaction between any two adsorbates is described by one of three situations: (1) Both adsorbates are in energetically favored sites with $\delta = 1/8$. The probability of this case occurring is p_1^2 where p_1 is the Boltzmann weighting factor for the energetically favored sites, $[1 + \exp(-U/kT)]^{-1}$. (2) Both adsorbates are in energetically disfavored sites with $\delta = -1/8$. The probability for this situation is p_2^2 , where p_2 is the Boltzmann weighting factor for the energetically disfavored sites, $[1 + \exp(U/kT)]^{-1}$. (3) One adsorbate is in an energetically favored site, and one is in an energetically disfavored site. Since this case has a degeneracy of two, the probability is $2p_1p_2$. The structural parameter is Λ for cases (1) and (2), but is Λ_2 for case (3) where Λ_2 is calculated from a lattice sum around one adsorbate at $\delta = -1/8$, but with all other adsorbates at $\delta = +1/8$ [34,40]. Then the structural parameter $[\Lambda(T)]$ is a weighted sum of the structural parameters for the three cases

$$\Lambda(T) = p_1^2 \Lambda_1 + p_2^2 \Lambda_1 + 2p_1p_2 \Lambda_2 \quad (12)$$

Upon substituting eq. (12) and $\alpha(T) = \alpha_1 p_1 + \alpha_2 p_2$, eq. (11) becomes

$$\alpha_0 = (\alpha_1 p_1 + \alpha_2 p_2)(p_1^2 + p_2^2 + 2p_1p_2 \Lambda_2 / \Lambda_1) \quad (13)$$

If the Boltzmann weighting factors in eq. (13) are expanded in a Taylor series about T_α , eq. (13) is approximated by

$$\alpha_0 = i' + s'/T, \quad (14)$$

$$i' = \alpha_1 + (\alpha_2 - \alpha_1 \Delta)(1 + U/kT_\alpha) \exp(-U/kT_\alpha),$$

$$s' = (U/k)(\alpha_2 - \alpha_1 \Delta) \exp(-U/kT_\alpha),$$

where $\Delta = (3 - 2\Lambda_2/\Lambda_1)$. Here s' and i' remain the slope and intercept from the plots in fig. 16, but eq. (14) accounts for the temperature dependence of the structural parameter, whereas eq. (8) does not. By evaluating lattice sums over a (101 × 101) overlayer matrix [34,40], Λ_1 is equal to 9.46 and Λ_2 is equal to 11.00. If α_1 , α_2 and U are evaluated with eq. (14), as was done with eq. (8) in section 7, the values for α_1 and U are not altered from those in section 7, whereas the values for α_2 are lower by 10%. Imperfections in the surface may distort α_1 , α_2 and U by a larger amount. Therefore, the temperature dependence of the structural parameter Λ is negligible for oxygen adsorption on Ir(110).

References

- [1] C.W. Tucker, Jr., J. Appl. Phys. 37 (1966) 4147; 38 (1967) 2696.
- [2] R. Lewis and R. Gomer, Surface Sci. 12 (1968) 157.

J.L. Taylor et al. / Chemisorption of oxygen on iridium

- [3] P.H. Holloway and J.B. Hudson, *Surface Sci.* 43 (1974) 123; 43 (1974) 141.
- [4] R. Ducros and R.P. Merrill, *Surface Sci.* 55 (1976) 227.
- [5] V.P. Ivanov, G.K. Boreskov, V.I. Savchenko, W.F. Egelhoff, Jr. and W.H. Weinberg, *Surface Sci.* 61 (1976) 207.
- [6] P.R. Norton, R.L. Tapping and J.W. Goodale, *Surface Sci.* 65 (1977) 13.
- [7] H. Conrad, G. Ertl, J. Küppers and E.E. Latta, *Surface Sci.* 65 (1977) 245.
- [8] T. Matsushima, D.B. Almy and J.M. White, *Surface Sci.* 67 (1977) 89.
- [9] H. Conrad, J. Küppers, F. Nitschké and A. Plagge, *Surface Sci.* 69 (1977) 668.
- [10] R.P. Norton, *Surface Sci.* 47 (1975) 98.
- [11] L.H. Germer, J.W. May and R.J. Szostak, *Surface Sci.* 8 (1967) 430.
- [12] G. Ertl and P. Rau, *Surface Sci.* 15 (1969) 443.
- [13] H.P. Bonzel and R. Ku, *Surface Sci.* 33 (1972) 91.
- [14] K. Christmann and G. Ertl, *Z. Naturforsch.* 28a (1973) 1144.
- [15] H.P. Bonzel and R. Ku, *Surface Sci.* 40 (1973) 85.
- [16] T. Matsushima and J.M. White, *Surface Sci.* 67 (1977) 122.
- [17] J.L. Taylor, Ph.D Thesis, California Institute of Technology (1978).
- [18] J.L. Taylor, D.E. Ibbotson and W.H. Weinberg, *J. Chem. Phys.*, in press.
- [19] T.E. Madey, H.A. Engelhardt and D. Menzel, *Surface Sci.* 48 (1975) 304.
- [20] G. Ehrlich, *J. Appl. Phys.* 32 (1961) 4.
- [21] J.L. Taylor and W.H. Weinberg, *Surface Sci.* 78 (1978) 259.
- [22] J.L. Taylor, D.E. Ibbotson and W.H. Weinberg, *J. Catalysis*, submitted.
- [23] Pumping by the walls was negligible since these surfaces, as well as the substrate, received saturation coverages of the adsorbates during exposure.
- [24] J.C. Fuggle, E. Umbach and D. Menzel, *Solid State Commun.* 20 (1972) 89.
- [25] P.A. Thiel, J.T. Yates, Jr. and W.H. Weinberg, *Surface Sci.*, in press.
- [26] J.L. Falconer and R.J. Madix, *J. Catalysis* 48 (1977) 262.
- [27] From ref. [21], two peaks are separated sufficiently in energy if the difference in the energies at the peaks is greater than 10% of the larger energy.
- [28] T. Engel, T. von dem Hagen and E. Bauer, *Surface Sci.* 62 (1977) 361.
- [29] W.H. Weinberg, C.M. Comrie and R.M. Lambert, *J. Catalysis* 41 (1976) 489.
- [30] P. Kisliuk, *J. Phys. Chem. Solids* 5 (1958) 78.
- [31] D.A. King and M.G. Wells, *Proc. Roy. Soc. (London)* A339 (1974) 245.
- [32] P.M. Marcus, J.E. Demuth and D.W. Jepsen, *Surface Sci.* 53 (1975) 501.
- [33] More precisely, $\ln \kappa$ is equal to $a - \ln[1 + b \exp(E_p/kT)]$, where a and b are constants if chemisorption is not activated. For $E_p = 2.1$ kcal/mole, $\ln \kappa$ is proportional to T^{-1} between 300 and 600 K. Also E_p is defined rigorously as the difference in the activation energies for desorption and diffusion of the precursor when the precursor is above a site occupied by an adsorbate. See ref. [30].
- [34] J.R. MacDonald and C.A. Barlow, *J. Chem. Phys.* 39 (1963) 412.
- [35] A LEED study of the $c(2 \times 2)$ pattern, which followed this work, has shown that oxygen binds above the topmost rows of surface atoms and between adjacent Ir atoms, as shown in fig. 5; C.-M. Chan, S.L. Cunningham, K.L. Luke, W.H. Weinberg and S.P. Withrow, *Surface Sci.* 78 (1978) 15.
- [36] R.H. Fowler and E.A. Guggenheim, *Statistical Thermodynamics* (MacMillan, New York, 1939).
- [37] A similar expression has been used to model the temperature dependence of the dipole moment in: G. Ertl, M. Neumann and K.M. Streit, *Surface Sci.* 64 (1977) 393.
- [38] At lower coverages, the order affects the term Λ in the modified Topping model since the number and position of nearest neighbors for each adsorbate depends on the order. However, the registry of the overlayer, rather than the order, fixes these quantities at higher coverages so that Λ , i.e., the CPD, is not influenced by the order at higher coverages. Also see ref. [34].

J.L. Taylor et al. / Chemisorption of oxygen on iridium

- [39] W.E. Moddeman, T.A. Carlson, M.O. Krause, B.P. Pullen, W.E. Bull and G.K. Schweitzer, *J. Chem. Phys.* 55 (1971) 2317.
- [40] Rigorously, $\Lambda_1 = 2^{3/4} \sum_{ij} [i^2 + 2j^2]^{-3/2}$, where i and j are integers, but the term $i = j = 0$ is excluded from the sum. Also, $\Lambda_2 = 2^{3/4} \sum_{ij} [(i + 1/4)^2 + 2j^2]^{-3/2}$, where i and j assume the same limits as before. Imperfections in the surface distort the values of Λ_1 and Λ_2 . Also see ref. [34].

APPENDIX F

A TRANSIENT STUDY OF THE CO-ADSORPTION
AND REACTION OF CO AND OXYGEN ON IR(110)

(The text of Appendix F consists of an article coauthored with J. L. Taylor and W. H. Weinberg that has appeared in Surface Science 90, 37(1979).)

Surface Science 90 (1979) 37–56
©North-Holland Publishing Company

A TRANSIENT STUDY OF THE CO-ADSORPTION AND REACTION OF CO AND OXYGEN ON Ir(110)[†]

J.L. TAYLOR *, D.E. IBBOTSON and W.H. WEINBERG **

Division of Chemistry and Chemical Engineering, California Institute of Technology, Pasadena, California 91125, USA

Received 12 January 1979; accepted for publication 7 August 1979

The heterogeneously catalyzed reaction of CO and O₂ to form CO₂ over Ir(110) has been studied through measurements of the transient kinetics of the various elementary reactions that may limit the steady state rate. Rate expressions for these elementary reactions – the desorption of CO, the oxidation of CO via the Langmuir–Hinshelwood mechanism, the adsorption of CO and the adsorption of oxygen – were developed using thermal desorption mass spectrometry. Several phenomena were observed: (1) the activation energies for CO desorption and CO oxidation depend markedly upon the composition of the adlayer; (2) diffusion in the adlayer may limit the rates of CO desorption and CO oxidation; (3) the formation of a surface oxide modifies these four rate processes; and (4) chemisorbed CO blocks sites for oxygen adsorption, but chemisorbed oxygen does not block sites for CO adsorption.

1. Introduction

The nonreactive co-adsorption and subsequent reaction of CO and oxygen under transient conditions have been studied on Ir(110) to give insight into the catalytic behavior of the steady state rate of CO oxidation. The relative simplicity of this reaction allows one to isolate individual elementary reactions in the chemical mechanism for CO oxidation and to describe the influence of surface phenomena on the reaction rate. Molecular beam studies [1,2] have shown that CO oxidation on Pd(111) occurs through the Langmuir–Hinshelwood (LH) mechanism (reaction between chemisorbed CO and chemisorbed oxygen) for surface temperatures below 600 K. Hence, the adsorption of oxygen and CO, the desorption of CO, and the LH reaction to form CO₂ are the four elementary reactions that may limit the rate of CO oxidation over the platinum metal catalysts. For surface temperatures between 300 and 1000 K, where the steady state rate is greatest at low pressures, the Eley–Rideal (ER) mechanism (reaction between physically adsorbed CO and chemi-

[†] Supported by the National Science Foundation under Grant No. DMR 77-14976.

* National Science Foundation Predoctoral Fellow.

** Alfred P. Sloan Foundation Fellow, and Camille and Henry Dreyfus Foundation Teacher-Scholar.

J.L. Taylor et al. / Transient study of CO and oxygen on Ir(110)

sorbed atomic oxygen) and the desorption of CO_2 are thought to affect the rate only slightly [1,3].

Several surface phenomena complicate the interpretation of the steady state rate data for CO oxidation. Although the overall oxidation rate on Pd is insensitive to the geometric arrangement of the metal atoms on the surface of the catalyst, LEED studies indicate that the structure of the chemisorbed layer influences the rate [1,4,5]. Hence, the rate may be limited by surface diffusion of CO molecules between islands of oxygen atoms. Oxidation of the surface of the catalyst changes the steady state rate markedly with respect to the clean surface [1,5-7]. Moreover, the activation energies for the LH reaction and CO desorption are quite sensitive to the composition of the adlayer and may vary by a factor of two on Pd(111) [1]. Hence, the variation in the rate of oxidation resulting from the coverage dependence of an activation energy may overshadow completely the coverage variation resulting from the leading coefficients in rate expressions that enter as concentrations of adspecies to integral exponents.

The objective of this present study, which supplements those of earlier investigations, is to determine how the coverages of various adsorbed species influence the rate of individual elementary reactions that may limit the steady state rate of CO_2 production on the platinum metals with particular application to Ir. The kinetics of the elementary reactions were measured using thermal desorption mass spectrometry under ultra-high vacuum conditions. To determine how ordering phenomena influence the oxidation rate, the structure of the chemisorbed layer was investigated with LEED. A second objective, to model the dependence of the steady state rate upon these elementary reactions under various conditions, will be presented with the experimental results of steady state rates of CO_2 production over Ir(110) in a separate paper [8]. The results of this study of CO oxidation over Ir(110) focus on the following: (1) the dependence of the rate expressions for CO desorption and CO oxidation upon the composition of the adlayer; and (2) the competitive adsorption of CO and oxygen.

2. Experimental procedures

The experiments were conducted in a stainless steel belljar with a base pressure below 2×10^{-10} Torr. Thermal desorption mass spectra were measured with a quadrupole mass spectrometer (UTI 100-C). The order in the overlayer under static conditions was determined by LEED. The substrate, which was attached to a precision manipulator by two 10 mil Ta wires, could be cooled with liquid nitrogen or heated resistively. Typical heating rates used in these experiments were near 40 K/sec, although the total range of heating rates was from 4 to 200 K/sec. The temperature of the substrate was measured with a Pt-Pt 10% Rh thermocouple. The mass spectrometer intensity and the thermocouple EMF were read by a PDP-11/10

computer [9]. Although these data were recorded digitally, they are presented in analog form for convenience.

The catalyst was cut from a single crystal of Ir and was polished within 1° of the (110) orientation. Carbon was cleaned from the surface through a series of oxidation and reduction cycles, whereas oxygen was removed by annealing above 1600 K. Prior to each experiment, the surface was free from impurities within 0.01 ML (where $1 \text{ ML} \equiv 10^{15} \text{ cm}^{-2}$), as determined by Auger electron spectroscopy. The gases used in this study, CO and O₂, were research grade (99.99% purity).

Although CO does not dissociate at low pressure on Ir(110) below 1300 K [10], the measurement of steady state oxidation rates [8] was complicated by the formation of a surface oxide at temperatures where the reaction rate is rapid [8,11]. The oxide, which is distinct chemically from chemisorbed oxygen, is less reactive to reduction by CO. When a surface that is saturated with chemisorbed oxygen is heated to 700 K, the oxide forms irreversibly with a saturation coverage of $0.25 \pm 0.05 \text{ ML}$. Neither atomic oxygen nor iridium oxides desorb from Ir(110) [11]. By annealing a saturated oxide layer at 1200 K, the oxide orders to give a $p(1 \times 4)$ LEED pattern. The Auger line shape and the adsorption and reaction kinetics of CO are the same for the ordered and partially ordered oxide layer. In this study, the oxide layer was formed routinely by annealing a surface with 0.25 ML of chemisorbed oxygen present to 1100 K. This coverage was obtained after a clean surface of Ir(110) at 300 K was exposed to 0.8 L ($1 \text{ L} \equiv 10^{-6} \text{ Torr sec}$) of oxygen. The oxide decomposed by annealing the surface above 1600 K. Since the presence of the oxide layer is known to affect the chemisorption of CO [10] and oxygen [11] on Ir(110), experiments were performed with both clean and oxidized surfaces of Ir(110). Hereafter, oxidized Ir(110) will refer to a surface on which a saturated oxide layer is present, whereas clean Ir(110) will refer to a surface having no oxide layer.

Several thermal desorption spectra of CO, O₂ and CO₂ were obtained by flashing co-adsorbed layers of CO and oxygen from clean and oxidized Ir(110) at a constant heating rate. Activation energies for CO desorption and CO oxidation were determined from an analysis of the desorption spectra by varying the initial coverage of one reactant as discussed in the next section. The co-adsorbed layers were formed by first exposing the surface to either O₂ or CO and by subsequently exposing the surface to the other gas. During the exposures, the surface temperature was 300 K, where the oxidation reaction is negligibly slow. Hence, the adsorption kinetics of oxygen (CO) on a surface partially covered with CO (oxygen) could be measured, since the coverage of the second component in the exposure sequence could be determined from the thermal desorption spectra. The coverage of the first component in the exposure sequence was known from separate measurements of the adsorption kinetics of CO [10] and oxygen [11] on clean and oxidized Ir(110). The spectrum for each desorption product in any sequence of exposures was obtained in a separate flash. This introduced no problems in analyzing the data since the heating schedule for any set of flashes was nearly invariant, approximately

J.L. Taylor et al. / Transient study of CO and oxygen on Ir(110)

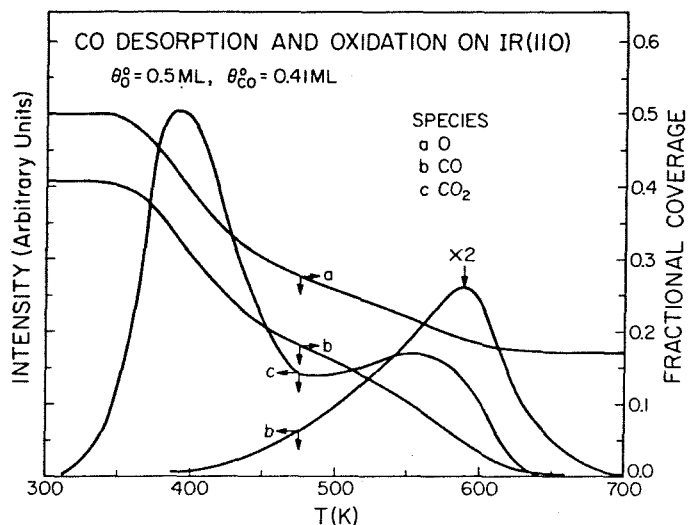


Fig. 1. A typical thermal desorption spectrum of co-adsorbed CO and oxygen from Ir(110). The spectra for CO and CO₂, as well as the temporal variations in the coverages of CO and oxygen, are shown here. The spectrum of O₂ appears above 1000 K.

± 0.5 K/sec for a typical heating rate of 40 K/sec. Hence, the spectra for each exposure sequence could be analyzed accurately by aligning the spectra at points of constant temperature.

To summarize the method of analysis, a specific example will be considered. A clean Ir(110) surface at 300 K was exposed first to 2.7 L of O₂, which corresponds to a coverage of 0.50 ML [11], and then to 2 L of CO. The desorption spectra of the individual products – CO, O₂ and CO₂ – were obtained in separate flashes. The spectra of CO and CO₂ are shown in fig. 1; the O₂ spectrum, which appears above 1000 K, is not shown. To account for the fraction of CO₂ that ionized to CO⁺ (which is determined experimentally), 12% of the intensity of the CO₂ spectrum has been subtracted from the CO spectrum at points of constant time, or equivalently, temperature. Also, the CO₂ spectrum has been multiplied by 1.3 so that the CO and CO₂ spectra are directly comparable. These two manipulations have been performed on all CO and CO₂ spectra shown subsequently. The initial coverage of CO was found to be equal to 0.41 ML. The temporal variation in the coverages of CO and oxygen, used for determining the activation energies for CO desorption and CO oxidation, are shown also in fig. 1.

3. Rate expressions for CO desorption and CO oxidation

Representative thermal desorption spectra of CO and CO₂, obtained by flashing co-adsorbed layers of CO and oxygen from Ir(110), are shown in fig. 2. The desorp-

J.L. Taylor et al. / Transient study of CO and oxygen on Ir(110)

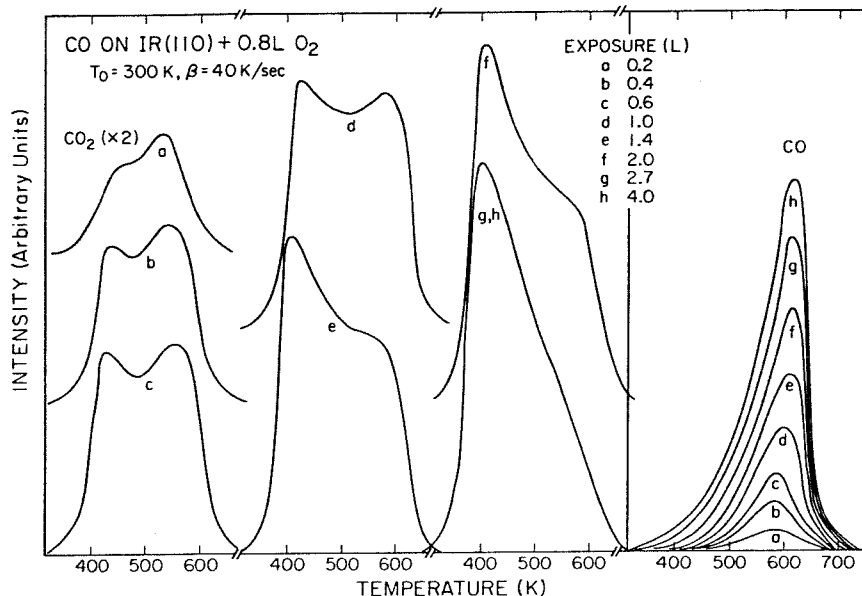


Fig. 2. Representative thermal desorption spectra of CO and CO₂ from Ir(110). A clean Ir(110) surface at 300 K initially was exposed to 0.8 L of oxygen, which corresponds to a coverage of 0.25 ML, and then received varying exposures of CO as noted. The average heating rate for these spectra was 40 K/sec.

tion of O₂ appears above 1000 K and is identical to flashing chemisorbed oxygen layers alone [11]. For the data shown in fig. 2, 0.25 ML of oxygen was first adsorbed at 300 K, and then varying amounts of CO were exposed to the surface, as noted in the figure. Regardless of whether the surface is clean or oxidized prior to the exposure sequence, and regardless of the order of exposure, the spectra are similar to those shown in fig. 2. The spectra of CO give a single peak near 600 K, whereas the spectra of CO₂ give two peaks near 400 and 550 K. The desorption rate for CO is correlated with the oxidation rate near 500 K. The desorption of CO from Ir(110) oxide (with no additional oxide present) occurs at higher temperatures than for the surface with no oxide present [10]. Similar behavior has been observed for CO both on Pt(110) [12] and Pt(111) [13] and qualitatively on Ir(110) [14]. However, on Ir(110) it was shown that both rate parameters for CO desorption decrease on the oxidized surface causing the desorption to occur at higher temperatures [10].

The CO desorption spectra in fig. 2 appear to vary as zero-order in the coverage of CO. The maximum of the peak shifts to higher temperatures with increasing CO exposure, and the intensity rises exponentially with temperature [15]. For small CO coverages, the order of the desorption reaction (n) is given by the slope of a plot of $\ln I_{28}^*$ as a function of $\ln \theta_{CO}$ at points of constant temperature [16], where I_{28}^* is the mass 28 intensity with the CO₂ cracking fraction subtracted, and θ_{CO} is the coverage of CO (in ML). An order plot, constructed from the spectra in fig. 2

J.L. Taylor et al. / Transient study of CO and oxygen on Ir(110)

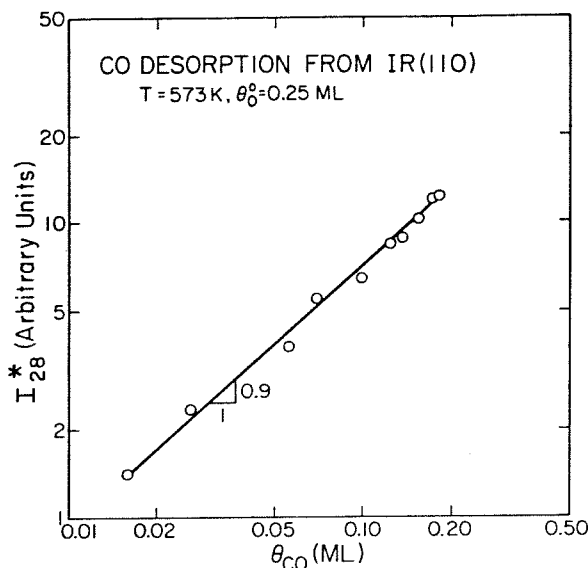


Fig. 3. An order plot for CO desorption at 573 K. The slope of the line gives the order of the desorption process in the coverage of CO. The plot was derived from the data in fig. 2.

for a temperature of 573 K, is shown in fig. 3. The slope in fig. 3 is 0.9 ± 0.1 , so the order of the desorption reaction in the coverage of CO is, in fact, unity. This is expected since CO chemisorbs molecularly on Ir(110), and the shift in the thermal desorption peak maxima to higher temperature with increasing coverage is a consequence of a strong variation of the desorption rate coefficient (both the activation energy and the pre-exponential factor) with surface coverage, a point which is discussed in detail below.

For Ir(110) covered with co-adsorbed oxygen and CO, the desorption rate of CO (R_d in molecules/cm² · sec) is modeled best with the first-order Arrhenius expression [17]

$$R_d = -\nu_d(\theta_{CO}, \theta_O) C_s \theta_{CO} \exp[-E_d(\theta_{CO}, \theta_O)/kT], \quad (1)$$

where θ_O is the coverage of oxygen at any instant in a spectrum, the concentration of adsites (C_s) is 10^{15} cm⁻² for either CO or oxygen, k is the Boltzmann constant and T is the surface temperature. Also, the rate parameters, $\nu_d(\theta_{CO}, \theta_O)$ and $E_d(\theta_{CO}, \theta_O)$, depend on the coverage of both oxygen and CO. Arrhenius plots of $\ln I_{28}^*$ as a function of T^{-1} at points of constant CO and oxygen coverages should give straight lines with slope $-E_d(\theta_{CO}, \theta_O)/k$ and intercept $\ln[\nu_d(\theta_{CO}, \theta_O)\theta_{CO}]$. In constructing each plot, a large number of spectra would be required to obtain sufficiently accurate rate parameters. Hence, only the coverage of CO is held constant for the Arrhenius plots presented here. The dependence of the rate parameters upon the coverage of oxygen was investigated by varying the initial coverage of

J.L. Taylor et al. / Transient study of CO and oxygen on Ir(110)

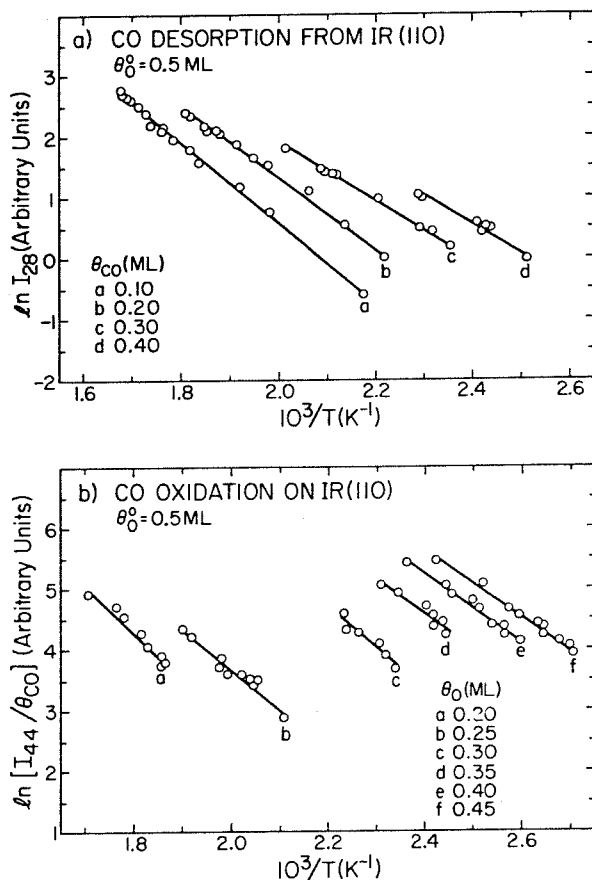


Fig. 4. Arrhenius plots for: (a) CO desorption, and (b) CO oxidation over Ir(110). The surface initially was covered with 0.5 ML of oxygen and then was covered with varying amounts of CO. The plots for CO desorption were derived by evaluating the CO desorption spectra at points of constant CO coverage. The plots for CO oxidation were derived by evaluating the CO₂ desorption spectra at points of constant oxygen coverage.

oxygen from one set of desorption spectra to the next. Although some error is introduced by this procedure, the coverage of oxygen varies typically by less than a factor of two in Arrhenius plots presented here. Fig. 4a shows Arrhenius plots for CO desorption from a clean Ir(110) surface initially covered with 0.5 ML of oxygen. These plots are evaluated at points of constant coverage. Each data point represents a separate flash where the initial coverage of CO was varied, keeping the heating rate constant. Fewer data were available at points of higher CO coverage due to the competition between desorption and oxidation of CO in the temperature region from 400 to 500 K. Nevertheless, at least a 30 K temperature range (typically 40 to 50 K) is spanned for any coverage and any set of data in the Arrhenius

plots. Moreover, plots with few points still yield consistent rate parameters within a given data set.

The rate parameters for CO oxidation may be obtained as those for CO desorption. For CO oxidation from co-adsorbed layers of oxygen and CO, the rate (R_r in molecules/cm² · sec) is given by the LH expression [3],

$$R_r = -\nu_r(\theta_{CO}, \theta_O) C_s^2 \theta_{CO} \theta_O \exp[-E_r(\theta_{CO}, \theta_O)/kT], \quad (2)$$

where $E_r(\theta_{CO}, \theta_O)$ and $\nu_r(\theta_{CO}, \theta_O)$ are the activation energy and pre-exponential factor of the rate coefficient for CO oxidation. The rate is truly first-order in the coverages of CO and oxygen since order plots of $\ln I_{44}$ as a function of $\ln(\theta_{CO}\theta_O)$ at 423 and 573 K for the data in fig. 2 give a straight line with a slope of unity for small coverages ($\theta_{CO}\theta_O < 0.01$). The *apparent* order decreases to zero for larger coverages ($\theta_{CO}\theta_O > 0.04$), indicating that the rate parameters for CO oxidation depend on the composition of the overlayer. Arrhenius plots for CO oxidation, $\ln[I_{44}/\theta_{CO}]$ as a function of T^{-1} at points of constant oxygen coverage, are shown in fig. 4b. As in fig. 4a, the surface contained initially 0.5 ML of oxygen, and the CO exposure was varied keeping the heating rate constant. The slopes of the lines in fig. 4b give $-E_r(\theta_O)/k$, whereas the intercepts give $\ln[\nu_r(\theta_O)C_s\theta_O]$. As before, this construction is only approximately since the concentration of CO is not constant in each plot. Moreover, Arrhenius plots of $\ln(I_{44}/\theta_O)$ as a function of T^{-1} at points of constant CO coverage do not yield straight lines. Intensities from the two CO₂ peaks in the desorption spectra must be plotted in separate Arrhenius constructions; otherwise, linearity is not obtained. This indicates that a thermally activated process other than CO oxidation, such as the diffusion of CO or oxygen on the surface [1], may limit the oxidation rate for some range of temperature. Although some coverages of oxygen in the Arrhenius plots have few points in fig. 4b because they fall between the two CO₂ peaks, the calculated rate parameters are consistent as evidenced by fig. 6. For most of these plots evaluated at constant oxygen coverage, the temperature range was 25 to 35 K, even with the complication of two features in the desorption spectra.

The dependence of the rate parameters for CO desorption from clean Ir(110) upon the coverage of CO and the initial coverage of oxygen is shown in fig. 5a. The rate parameters were derived from Arrhenius plots using the technique described previously, with the exception of the rate parameters for CO from a surface having no adsorbed oxygen initially. These rate parameters were obtained by a detailed analysis employing a variation in heating rates keeping the initial coverage of CO constant [17]. Oxygen was adsorbed first for these data, and the initial coverage is denoted by θ_O^0 . If the surface first is covered with 0.25 ML CO and then exposed to oxygen, the activation energy for CO desorption is 16 ± 1 kcal/mole for CO coverages between 0.05 and 0.20 ML. The data in fig. 5a show that the desorption energy decreases as the coverage of CO or oxygen is increased. For any initial coverage of oxygen, the desorption energy varies almost linearly in the coverage of CO; that is, $E_d(\theta_{CO}) = E_0 - E_\delta\theta_{CO}$. Regardless of the initial coverage of oxygen, E_δ is

J.L. Taylor et al. / Transient study of CO and oxygen on Ir(110)

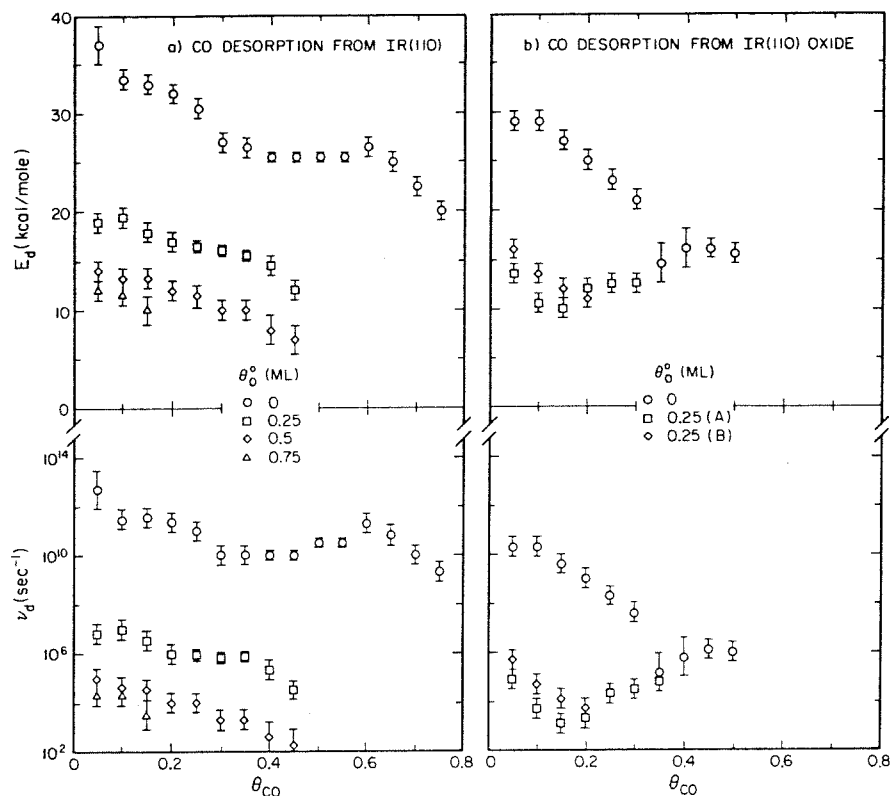


Fig. 5. The variation in the activation energy and pre-exponential factor for CO desorption with the CO coverage on: (a) clean Ir(110), and (b) oxidized Ir(110).

equal to $15 \text{ kcal} \cdot \text{mole}^{-1} \cdot \text{ML}^{-1}$, but E_0 is 35, 21, 16 and 15 kcal/mole for initial oxygen coverages of 0, 0.25, 0.50 and 0.75 ML, respectively. If the Ir(110) surface is partially covered with oxygen, the observed desorption energies for CO are rather small for a thermal desorption peak near 600 K [18], and indicate that another thermally activated process, such as the diffusion of CO, may be rate limiting for CO desorption [1].

The dependence of the rate parameters for CO desorption from oxidized Ir(110) upon the composition of the overlayer is shown in fig. 5(b). Prior to the exposure sequence, the surface was oxidized according to the procedure described in section 2. Then, oxygen was exposed to the surface first. For the rate parameters labeled *A*, the chemisorbed layer of oxygen was annealed to 1000 K before CO was exposed to the surface; for the rate parameters labeled *B*, no annealing occurred. These experiments were undertaken to determine if ordering of the chemisorbed layer of oxygen influences the transient rates of CO desorption and oxidation. A $c(2 \times 2)$ structure of chemisorbed oxygen on oxidized Ir(110) does not order until

J.L. Taylor et al. / Transient study of CO and oxygen on Ir(110)

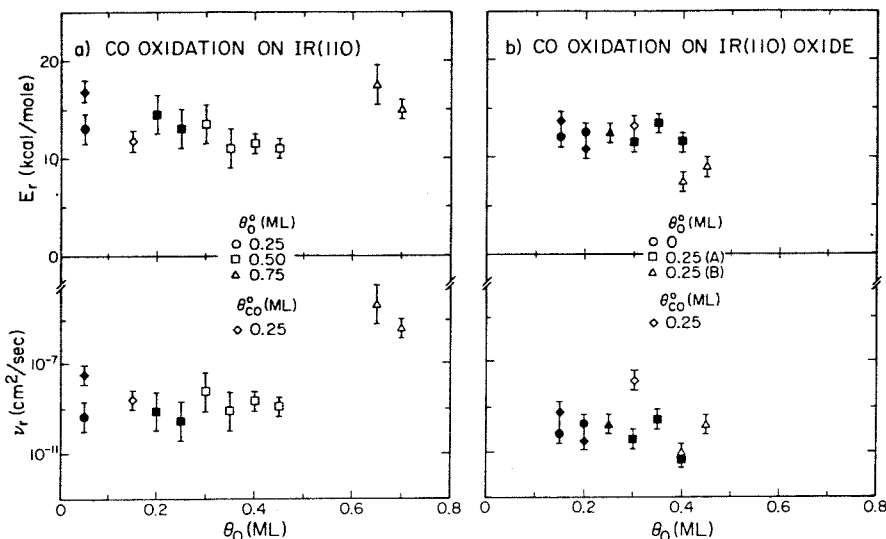


Fig. 6. The variation in the activation energy and pre-exponential factor for CO oxidation with the oxygen coverage on: (a) clean Ir(110), and (b) oxidized Ir(110). Rate parameters that pertain to the peak at lower temperature in the CO₂ spectra are hollow, whereas parameters that pertain to the peak at higher temperature are solid. The parameters are appropriate for describing CO oxidation via the Langmuir–Hinshelwood mechanism only.

the surface is annealed to greater than 700 K [11,19]. From the rate parameters shown in fig. 5b, the structure in the oxygen overlayer has little effect on the desorption rate for CO. However, the fraction of CO that desorbs, compared to the fraction that reacts to form CO₂ is slightly larger for a surface with an ordered oxygen adlayer. *Major* differences in the mechanism of the oxidation of hydrogen on Rh(111) by either ordered or disordered oxygen have been documented recently by Yates, et al. [20].

For any coverage of CO and any initial coverage of oxygen, the rate parameters E_d and ν_d are smaller for oxidized Ir(110). Since the desorption kinetics of CO affect the steady state rate of CO oxidation [3], the rates are expected to be different on clean and oxidized Ir(110). This is indeed the case as will be shown in a separate paper [8]. Again, the desorption energy of CO from oxidized Ir(110) changes markedly with the composition of the adlayer, but an average desorption energy associated with steady state rates of CO oxidation may be estimated. Using the extremes in the coverages for CO and oxygen and averaging these values for E_d , an average desorption energy of 14 kcal/mole is estimated for the oxidized surface. Using this same procedure, an average desorption energy on the clean surface of 17 kcal/mole results.

The pre-exponential factors and activation energies for CO desorption vary in sympathy; that is, the compensation effect occurs. A modified Arrhenius expres-

sion may be used to describe this effect [21]. The appropriate rate expression for CO desorption is

$$R_d = -\nu_{0d}C_s\theta_{CO} \exp\left[-\frac{E_d(\theta_{CO}, \theta_O)}{k} \left(\frac{1}{T} - \frac{1}{T_{sd}}\right)\right], \quad (3)$$

where ν_{0d} and T_{sd} are constants, and only E_d depends on the composition of the adlayer. If the overlayer contains no oxygen, ν_{0d} and T_{sd} are approximately 10^6 sec^{-1} and 1240 K, respectively; if the surface is covered initially with only the oxide layer or with only 0.25 ML of chemisorbed oxygen, ν_{0d} and T_{sd} are 3 sec^{-1} and 650 K; for all other cases, ν_{0d} and T_{sd} are 0.3 sec^{-1} and 540 K. These values of ν_{0d} and T_{sd} were obtained by a least squares fit of the rate parameters, shown in fig. 5, and they are accurate within a factor of three and ± 30 K, respectively. Regardless of whether ν_{0d} and T_{sd} are chosen as 3 sec^{-1} and 650 K or 0.3 sec^{-1} and 540 K, the pre-exponential factor associated with the average desorption energy for the clean surface, 17 kcal/mole, is 10^6 sec^{-1} . Similarly, the pre-exponential factor associated with the average desorption energy for the oxidized surface, 14 kcal/mole, is 10^5 sec^{-1} . These average values of the rate parameters for CO desorption will be used for modeling the steady state rate of CO oxidation, which will be presented in a separate paper [8].

The pre-exponential factor and activation energy for CO desorption from both clean and oxidized Ir(110) decreases continuously with increasing coverage of CO, but assumes different initial values, depending on the initial coverage of oxygen. The clean surface values for no initial oxygen adsorbed may be compared to the values obtained for Ru(001) [22]. In this case, large pre-exponential factors (up to approximately 10^{19} sec^{-1}) were observed using four independent methods, where both the energy of desorption and pre-exponential factor increased from the low coverage values up to the completion of a $(\sqrt{3} \times \sqrt{3})R30^\circ$ overlayer structure which persists even to the onset of desorption. In the present study, an equally rigorous analysis [17] used for CO desorption from clean Ir(110) indicates different behavior from Ru(001), as shown in fig. 5a. The less rigorous analysis for CO desorption when oxygen is present also shows the same general trend in the rate parameters as a function of the coverage of CO. This may be rationalized by the fact that CO and oxygen do not compete for adsorption sites, as shown in the next section. Also, the adsorption kinetics of CO on clean Ir(110) and Ir(110) oxide are identical, so that the rate parameters for CO desorption would be expected to scale similarly with CO coverage, although the energy of desorption and pre-exponential factor are lower for the oxide surface.

As shown in fig. 6, the rate parameters for CO oxidation, E_r and ν_r , vary weakly with the total coverage of oxygen, θ_O . For the abscissae of these data only, θ_O is the sum of the coverages in the chemisorbed and oxide layers. The parameters for CO oxidation on clean and oxidized Ir(110) are shown in figs. 6a and 6b, respectively, and they are appropriate for describing oxidation by the LH mechanism only. Rate parameters calculated from the low and high temperature peaks in the

J.L. Taylor et al. / Transient study of CO and oxygen on Ir(110)

CO₂ spectra are shown as empty and filled symbols, respectively. Both oxygen and CO were introduced first in the exposure sequences for these data; for the respective cases, the initial coverages are denoted by θ_{O}^0 and θ_{CO}^0 in fig. 6. The rate parameters do not depend upon the exposure sequence or upon the order in the chemisorbed layer of oxygen. The points labeled A and B in fig. 6b are the parallel rates of CO₂ production for the points labeled A and B in fig. 5b for CO desorption. In general, the activation energy for CO oxidation via the LH mechanism does not depend strongly on the composition of the chemisorbed layer, or whether the surface is clean or oxidized. In most instances, the activation energy may be estimated as 12 kcal/mole.

The compensation effect occurs for CO oxidation, as well as for CO desorption. The rate equation that describes the sympathetic variation in the activation energy and the pre-exponential factor for CO oxidation is [18]

$$R_r = -\nu_{\text{or}} C_s^2 \theta_{\text{CO}} \theta_{\text{O}} \exp \left[-\frac{E_r(\theta_{\text{CO}}, \theta_{\text{O}})}{k} \left(\frac{1}{T} - \frac{1}{T_{\text{sr}}} \right) \right], \quad (4)$$

where ν_{or} and T_{sr} are constants, and E_r varies with the composition of the adlayer. Although E_r does not depend strongly on any physical parameters, ν_{or} and T_{sr} differ for the two peaks in the CO₂ desorption spectrum. From a least squares fit of the rate parameters in fig. 6, ν_{or} and T_{sr} are $7 \times 10^{-16 \pm 1}$ cm²/sec and 390 ± 30 K for the peak at lower temperatures, and they are $8 \times 10^{-17 \pm 1}$ cm²/sec and 430 ± 30 K for the peak at higher temperatures. Using 12 kcal/mole as an average activation energy for CO oxidation, the average pre-exponential factors (ν_r) are 3×10^{-9} cm²/sec and 3×10^{-10} cm²/sec for the respective peaks. Relatively low values of the rate parameters, like those determined here, are reported frequently for CO oxidation via the LH mechanism on the platinum metals, and they are associated with the diffusion kinetics of chemisorbed CO onto islands of oxygen atoms [1,4,5]. On Pt(110) [23], Pd(111) [1,24] and Ir(111) [5,25], the activation energy is about 10 kcal/mole, and the pre-exponential factor is near 10^{-10} cm²/sec.

When oxygen is the first component introduced in the exposure sequence, the coverage of CO that desorbs as CO₂ (θ_{CO_2}) depends predictably upon the initial coverage of CO (θ_{CO}^0). This dependence for various initial coverages of oxygen (θ_{O}^0) on clean and oxidized Ir(110) is shown in fig. 7. If the coverage of chemisorbed oxygen exceeds that of CO prior to the flash, 85% of the CO desorbs as CO₂. The same trend is observed for the reaction of *chemisorbed* oxygen on the oxidized surface. However, if the chemisorbed layer is ordered, as for points labeled A in fig. 7b, rather than random as for the points labeled B, slightly less CO₂ is formed. Also, the oxide layer is less reactive than chemisorbed oxygen to CO reduction. If the oxide coverage exceeds the initial coverage, no more than 50% of the CO is oxidized. In a single flash, no more than 70% of the oxide will be reduced by CO, whereas all chemisorbed oxygen, for an equivalent coverage, will be reduced if sufficient CO is available. Similar trends are observed when CO is introduced first in the exposure sequence. Therefore, the product distribution in these transient

J.L. Taylor et al. / Transient study of CO and oxygen on Ir(110)

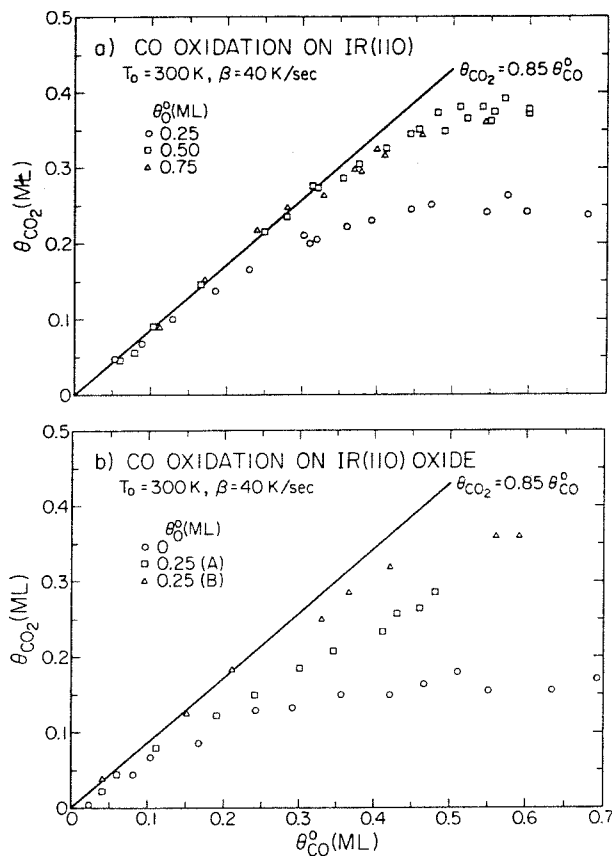


Fig. 7. The total amount of CO_2 produced in the thermal desorption spectra for various co-adsorbed adlayers of oxygen and CO from: (a) clean Ir(110), and (b) oxidized Ir(110). The initial coverages of CO and oxygen are as shown. The oxide layer is composed of 0.25 ML of oxygen, which may be reduced also.

experiments depends on the composition of the overlayer, but not on the exposure sequence.

Several conclusions may be drawn from the data for CO desorption and oxidation from co-adsorbed layers of CO and oxygen on clean and oxidized Ir(110). The desorption order is unity for CO. The energy of desorption varies strongly with both the coverage of CO and the initial coverage of oxygen. Also, the energy of desorption and the pre-exponential factor vary in sympathy, i.e., the compensation effect occurs for this process. The low values for the pre-exponential factor may indicate diffusion of CO on the surface limits the desorption rate. This effect is more pronounced on the oxidized surface where both the desorption energy and the pre-exponential factor are smaller than for the clean surface. The rate param-

eters for the oxidation of CO via the LH mechanism vary only weakly with the coverages of CO and oxygen on both clean and oxidized Ir(110) and with the order of the oxygen overlayer. Average values for the activation energy and pre-exponential factor for CO oxidation are 12 kcal/mole and 10^{-9} or 10^{-10} cm²/sec, depending on the surface temperature, where the low pre-exponential factor indicates that surface diffusion of the reactants may limit the reaction. Finally, the surface oxide is less reactive to CO than chemisorbed oxygen. These results will be used to model the steady state rates of CO₂ production presented elsewhere [8].

4. The co-adsorption kinetics of CO and oxygen

The adsorption kinetics of CO on oxygen overlayers and the adsorption kinetics of oxygen on CO overlayers, for the Ir(110) surface at 300 K, were measured using thermal desorption mass spectrometry. For each exposure sequence, the thermal desorption spectra of CO, O₂ and CO₂ were monitored to determine the initial coverages of CO and oxygen. The results and a parallel discussion will be presented first for CO adsorption on clean and oxidized Ir(110) partially covered with oxygen; and, second, for oxygen adsorption on the two surfaces partially covered with CO.

The adsorption kinetics of CO on Ir(110) surfaces that were partially covered with chemisorbed oxygen are shown in fig. 8a. Since the initial sticking probability of CO is unity, regardless of the initial coverage of oxygen, oxygen does not block sites for CO adsorption. Similar behavior for CO chemisorption has been observed on Pd(111) [1] and polycrystalline Pt [26]. At higher coverages, the kinetic data for Ir(110) may be fit by a second-order precursor model that accounts for ordering of the adlayer by intermolecular forces [27]. This model depends on two assumptions: (1) the overlayer of adsorbing species orders continually due to nearest-neighbor intermolecular forces, but it also disorders due to thermal randomization; and (2) a molecule in the precursor state may chemisorb only if two empty and adjacent sites for chemisorption are available. This model may pertain to non-dissociative adsorption [10], as is the case for CO, as well as dissociative adsorption [27]. In this second-order precursor model [27], the ratio of the sticking probability (S) to the initial sticking probability (S_0) depends on the fraction of empty sites with empty nearest-neighbors (θ_{00}) and a parameter κ that is inversely proportional to the lifetime of the precursor state,

$$S/S_0 = [(1 - \kappa) + \kappa/\theta_{00}]^{-1} . \quad (5)$$

The sticking probability is related to coverage (θ) and the exposure (ϵ) of the adsorbing species by [28]

$$S = (2\pi M_g k T_g)^{1/2} C_s d\theta/d\epsilon , \quad (6)$$

where M_g and T_g are the molecular weight and temperature of the adsorbing gas. The initial sticking probability is calculated by evaluating eq. (6) in the limit of

J.L. Taylor et al. / Transient study of CO and oxygen on Ir(110)

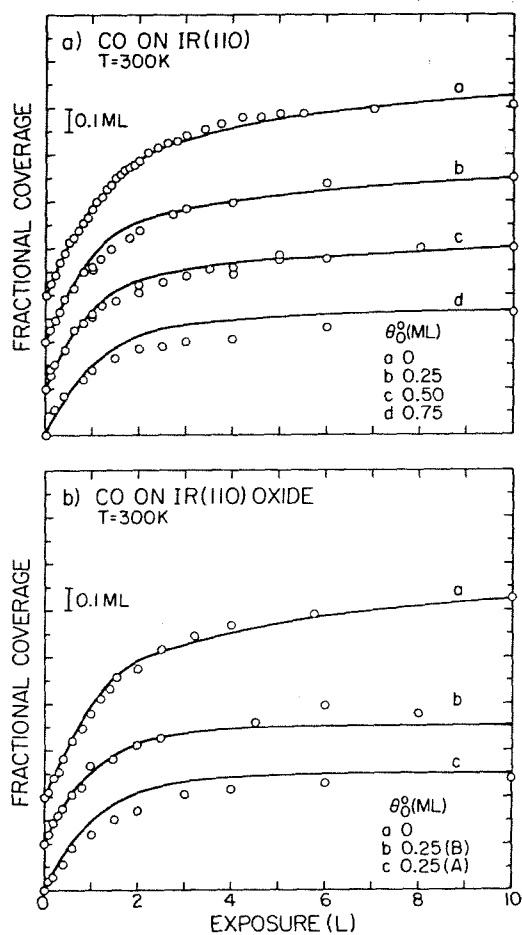


Fig. 8. The adsorption kinetics of CO on: (a) clean Ir(110), and (b) oxidized Ir(110) surfaces that initially were covered with varying amounts of oxygen. Curves derived from the second-order precursor model are shown as solid lines. The ordinate has been shifted between each data set for convenience.

small coverage. For a CO overlayer on the Ir(110) surface, the expression for θ_{00} is [10]

$$\theta_{00} = (1 - \theta) - \frac{2\theta(1 - \theta)}{[1 - 4B\theta(1 - \theta)]^{1/2} + 1} \quad (7)$$

The intermolecular force between nearest-neighbors (ψ) is related to the parameter B by [27]

$$\psi = -kT \ln(1 - B), \quad (8)$$

J.L. Taylor et al. / Transient study of CO and oxygen on Ir(110)

where a positive value of ψ is associated with a repulsive interaction.

Chemisorbed oxygen does not block sites for CO chemisorption so that the pertinent coverage in eq. (7) is the CO coverage, rather than the sum of the coverages of CO and oxygen. However, the repulsive interaction between chemisorbed CO molecules increases, and the lifetime of the CO precursor decreases as the initial coverage of oxygen increases. The parameters B and κ , which are related to these respective phenomena, vary with the initial oxygen coverage according to the expressions

$$-kT \ln(1 - B) = 2 + 0.4\theta_{\text{O}}^0, \quad (9)$$

and

$$\kappa = \exp[1.6(\theta_{\text{O}}^0 - 1)] \quad (10)$$

that were derived empirically from the data in fig. 8a, where the kinetic models are shown as solid lines. At 300 K, the lifetime of a CO precursor on Ir(110) decreases as θ_{O} increases; at temperatures where the steady state reaction is rapid, the lifetime decreases even further. Regardless of the value of B , the adsorption kinetics for lower CO coverages (<0.5 ML) approach the simple limit $S(\text{CO})/S_0(\text{CO}) = (1 - \theta_{\text{CO}})^2$ as the precursor lifetime becomes small [27]. As will be shown, CO blocks oxygen chemisorption almost completely for larger CO coverages, so the oxidation reaction is inhibited. Hence, from eq. (6), the adsorption rate of CO (in molecules/cm² · sec) may be approximated by

$$C_s \, d\theta_{\text{CO}}/dt = P_{\text{CO}}(1 - \theta_{\text{CO}})^2 / (2\pi M_{\text{CO}} k T_g)^{1/2}, \quad (11)$$

regardless of the coverage of chemisorbed oxygen. Here, the partial pressure of CO is P_{CO} , and the initial sticking probability for CO is taken to be unity. This result will be used to model the steady state oxidation data [8].

As shown in fig. 8b, the adsorption kinetics of CO on oxidized Ir(110) at 300 K also exhibit second-order behavior when oxygen is chemisorbed on the surface. The initial sticking probability for CO is unity, so oxygen does not block sites on the oxidized surface, regardless of the coverage of oxygen. In the absence of chemisorbed oxygen, the values of B and κ are identical for clean and oxidized Ir(110). When 0.25 ML of oxygen is chemisorbed on the oxidized surface, both B and κ assume values of unity. Kinetic models with these parameters are shown as solid lines in fig. 8b. Hence, the second-order behavior is even more pronounced for CO chemisorption on the oxidized surface. Moreover, ordering in the chemisorbed layer of oxygen, into a $c(2 \times 2)$ structure, as in curve c in fig. 8b, changes the adsorption kinetics only slightly with respect to a disordered layer, as in curve b. Therefore, eq. (11) may be used to describe the adsorption kinetics of CO on oxidized Ir(110) when the oxidation reaction proceeds under steady state conditions. The second-order behavior is not unique to Ir(110) and has been observed in other studies of CO oxidation [1,26], including the early work of Langmuir [3].

Although chemisorbed oxygen does not block sites for CO adsorption, chemi-

J.L. Taylor et al. / Transient study of CO and oxygen on Ir(110)

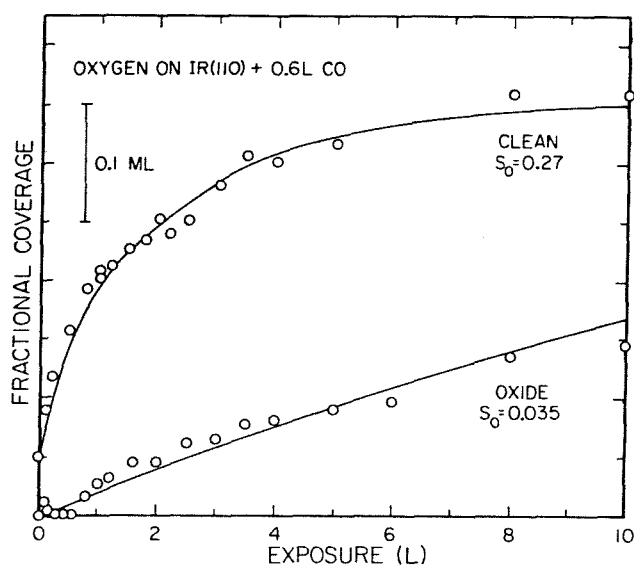


Fig. 9. The adsorption kinetics of oxygen on clean and oxidized Ir(110) at 300 K. The surfaces initially were exposed to 0.6 L of CO, which corresponds to a coverage of 0.25 ML. Curves derived from second-order Langmuir models are shown as solid lines. The ordinate has been shifted for the clean surface data for clarity.

sorbed CO blocks sites for oxygen adsorption. For a clean surface initially covered with 0.75 ML of CO, no detectable amount of oxygen is chemisorbed following an oxygen exposure of 10 L. When the experiment was repeated with an initial CO coverage of 0.5 ML, only 0.1 ML of oxygen chemisorbs, whereas the oxygen coverage would be near saturation if the CO were absent [11]. Fig. 9 shows the kinetic data for oxygen chemisorption on clean and oxidized Ir(110) surfaces that were initially covered with 0.25 ML of CO. The coverage of oxygen associated with each exposure was determined from thermal desorption spectra. Although the data for the clean surface are not fit well by the second-order Langmuir model,

$$S(\text{O}_2)/S_0(\text{O}_2) = (1 - \theta_{\text{O}} - \theta_{\text{CO}})^2, \quad (12)$$

the data for the oxidized surface are, as shown by the solid line in fig. 9. In this case, the initial sticking probability of oxygen [$S_0(\text{O}_2)$] is 0.035, which is an order of magnitude smaller than the value obtained when CO is absent from the surface.

The kinetic data for oxygen chemisorption on clean Ir(110) may be modeled by a second-order Langmuir model if the CO overlayer orders into a $p(2 \times 2)$, rather than a random configuration. The $p(2 \times 2)$ LEED pattern of CO, which forms near 0.25 ML coverage on clean Ir(110) only, is ordered at 90 K, but is disordered somewhat at 300 K [10]. In developing this model for oxygen adsorption, a random number generator was used to select the pair of adsorption sites. The surface consisted of a (20×20) array of adsorption sites, upon which the $p(2 \times 2)$ array of CO

J.L. Taylor et al. / Transient study of CO and oxygen on Ir(110)

was superposed and filled 25% of the adsorption sites. If a gaseous oxygen molecule struck a pair of empty sites, it would chemisorb with probability $S_0(\text{O}_2)$ and would occupy the two sites. Otherwise, it was reflected from the surface. For an initial sticking probability [$S_0(\text{O}_2)$] of 0.27, which is nearly equal to the value obtained when CO is absent [11], this model accurately fits the data for the clean surface in fig. 9. The model is shown as a solid line in this figure.

Since the $p(2 \times 2)$ structure of CO disorders as the surface temperature increases [10], the adsorption kinetics of oxygen on clean Ir(110) are expected to follow eq. (12) for temperatures where the steady state rate of CO oxidation is large. Under these conditions, the rate of oxygen adsorption on either clean or oxidized Ir(110) may be approximated further by

$$S(\text{O}_2)/S_0(\text{O}_2) = (1 - \theta_{\text{O}})^2(1 - \theta_{\text{CO}})^2,$$

or

$$C_s \frac{d\theta_{\text{O}}}{dt} = \frac{2S_0(\text{O}_2) P_{\text{O}_2} (1 - \theta_{\text{O}})^2 (1 - \theta_{\text{CO}})^2}{(2\pi M_{\text{O}_2} k T_g)^{1/2}}. \quad (13)$$

Moreover, this approximation for eq. (12) may be necessary since the sum of the coverages of chemisorbed oxygen and CO may exceed unity, as in fig. 8, but either coverage alone cannot exceed unity [10,11]. The factor of two appears in eq. (13) since oxygen adsorbs dissociatively.

Since chemisorbed oxygen does not block sites for CO adsorption, but chemisorbed CO blocks sites for oxygen adsorption, oxygen and CO do not compete for adsorption sites on Ir(110). In previous studies on other platinum metals [7,29], the ER reaction was thought to be rate-limiting for the rapid reduction of an oxygen overlayer by gaseous CO, but the LH reaction was thought to be rate-limiting for the slow oxidation of a CO overlayer by gaseous O_2 . Both processes may be described in terms of the LH mechanism if the adsorption kinetics of CO and oxygen are modeled like the kinetics of Ir(110). That is, CO oxidation via the LH reaction is rate-limiting in the first case, whereas oxygen adsorption is rate-limiting in the second case. Also, other studies [30] have indicated that CO oxidation may occur through the reaction of chemisorbed oxygen with a reactive form of chemisorbed CO which is present only when the coverage of CO is small. This phenomenon might be explained better by the fact that adsorbed CO strongly blocks oxygen adsorption to limit the CO oxidation reaction.

The measured kinetics for oxygen adsorption on oxidized Ir(110) partially covered with CO are modeled accurately by Langmuir kinetics [eq. (12)] for a disordered CO overlayer. This is surprising since chemisorbed CO orders into a $(2 \times 1)p1g1$ structure on oxidized Ir(110) below 500 K and above 0.05 ML coverage. When oxygen is adsorbed on either the CO- $p(2 \times 2)$ structure on clean Ir(110) or the CO- $(2 \times 1)p1g1$ structure on oxidized Ir(110) [10], the order in the overlayer is not changed although the background intensity of the LEED pattern increases. Similarly, when CO is adsorbed on either the O- $p(2 \times 2)$ structure on clean Ir(110)

J.L. Taylor et al. / Transient study of CO and oxygen on Ir(110)

or the $O\text{-c}(2 \times 2)$ structure on oxidized Ir(110) [11], the order is not affected. The LEED patterns for these four co-adsorbed systems sharpen when cooled to 90 K, but vanish when annealed to 400 K. Upon annealing, the overlayer is lost through the CO oxidation reaction. No LEED patterns that are unique to co-adsorbed systems were detected in this study, even though these structures were sought extensively.

5. Summary

The transient kinetics of elementary reactions that may limit the steady state rate of CO_2 production over Ir(110) by gaseous CO and O_2 have been studied. The results of this investigation form a basis to model the data for the steady state rates presented elsewhere [8]. Both clean and oxidized Ir(110) surfaces were used as the catalysts.

The kinetics of CO desorption and CO oxidation via the LH mechanism may be modeled accurately by Arrhenius expressions. However, the dependence of the rates upon leading coefficients that vary as coverages to integral exponents may be overshadowed completely by the variation in the pre-exponential factors and activation energies with the composition of the adlayer. The activation energy for CO desorption, which depends on the coverages of *both* CO and oxygen, may vary from 10 to 36 kcal/mole, but maintains near 16 kcal/mole where the steady state rate of CO oxidation is rapid [8]. The pre-exponential factor associated with this activation energy is 10^6 sec^{-1} . The activation energy for CO oxidation via the LH mechanism is relatively insensitive to the composition of the adlayer and is equal to approximately 12 kcal/mole. The pre-exponential factor for the oxidation reaction is 3×10^{-9} or $3 \times 10^{-10} \text{ cm}^2/\text{sec}$, depending on the surface temperature. This variation, as well as the small value of the pre-exponential factor (and other evidence), indicates that diffusion of the reactants on the surface, rather than the adatom-admolecule reaction, may limit the oxidation rate on the surface.

Since the initial sticking probability of CO on clean or oxidized Ir(110) at 300 K is unity, regardless of the coverage of chemisorbed oxygen, oxygen does not block sites for CO chemisorption. However, if a sufficient concentration of oxygen is chemisorbed on the surface, the adsorption kinetics of CO are of Langmuir type and are second-order in the coverage of CO. Both chemisorbed oxygen and CO block sites for oxygen chemisorption so that the adsorption kinetics of oxygen are of the Langmuir type, vary as second-order in the sum of the coverages of CO and oxygen, but also depend on the structure of the chemisorbed layer. If the sites occupied by CO are accounted for, the initial sticking probability for oxygen adsorption at a surface temperature of 300 K is 0.27 on the clean surface, which is close to the value obtained in the absence of CO; but it is 0.035 on the oxidized surface, which is an order of magnitude lower than the value obtained in the absence of CO.

Acknowledgment

The authors are grateful for the support of the National Science Foundation under Grant No. DMR77-14976.

References

- [1] T. Engel and G. Ertl, *J. Chem. Phys.* 69 (1978) 1267.
- [2] R.L. Palmer and J.N. Smith, Jr., *J. Chem. Phys.* 60 (1973) 1453. In this reference the authors first reported that, when a modulated molecular beam of CO impinges on polycrystalline Pt, the phase lag for CO₂ production decreases with increasing surface temperature and O₂ pressure in the background. However, they did not associate this trend with the residence time of chemisorbed CO. This was done in ref. [1] to prove conclusively that CO oxidation on Pd(111) occurs via the Langmuir–Hinshelwood mechanism.
- [3] I. Langmuir, *Trans. Faraday Soc.* 17 (1922) 621.
- [4] G. Ertl and P. Rau, *Surface Sci.* 15 (1969) 443.
- [5] V.P. Ivanov, G.K. Boreskov, V.I. Savchenko, W.F. Egelhoff, Jr. and W.H. Weinberg, *J. Catalysis* 48 (1977) 269.
- [6] J.S. Close and J.M. White, *J. Catalysis* 36 (1975) 185.
- [7] T. Matsushima and J.M. White, *J. Catalysis* 39 (1975) 265.
- [8] J.L. Taylor, D.E. Ibbotson and W.H. Weinberg, *J. Catalysis*, in press.
- [9] J.L. Taylor, Ph.D. Thesis, California Inst. of Technology (1978).
- [10] J.L. Taylor, D.E. Ibbotson and W.H. Weinberg, *J. Chem. Phys.* 69 (1978) 4298.
- [11] J.L. Taylor, D.E. Ibbotson and W.H. Weinberg, *Surface Sci.* 79 (1979) 349.
- [12] R.W. McCabe and L.D. Schmidt, *Surface Sci.* 60 (1976) 85.
- [13] R.W. McCabe and L.D. Schmidt, *Surface Sci.* 65 (1977) 189.
- [14] B.E. Nieuwenhuys and G.A. Somorjai, *Surface Sci.* 72 (1978) 8.
- [15] G. Ehrlich, *J. Appl. Phys.* 32 (1961) 4.
- [16] J.L. Falconer and R.J. Madix, *J. Catalysis* 48 (1977) 262.
- [17] J.L. Taylor and W.H. Weinberg, *Surface Sci.* 78 (1978) 259.
- [18] P.A. Redhead, *Vacuum* 12 (1962) 203.
- [19] C.-M. Chan, K.L. Luke, M.A. Van Hove, W.H. Weinberg and S.P. Withrow, *Surface Sci.* 78 (1978) 386.
- [20] J.T. Yates, Jr., P.A. Thiel and W.H. Weinberg, *Surface Sci.* 82 (1979) 45.
- [21] T. Engel, T. van dem Hagen and E. Bauer, *Surface Sci.* 62 (1977) 361.
- [22] H. Pfnür, P. Feulner, H.A. Engelhardt and D. Menzel, *Chem. Phys. Letters* 59 (1978) 481.
- [23] H.P. Bonzel and J.J. Burton, *Surface Sci.* 52 (1975) 223.
- [24] G. Ertl and M. Neumann, *Z. Physik. Chem. NF* 90 (1974) 127.
- [25] J. Küppers and A. Plagge, *Z. Naturforsch.* 34a (1979) 81.
- [26] N. Pacia, A. Cassuto, A. Pentenero and B. Weber, *J. Catalysis* 41 (1976) 455.
- [27] D.A. King and M.G. Wells, *Proc. Roy. Soc. (London)* A339 (1974) 245.
- [28] W.H. Weinberg, C.M. Comrie and R.M. Lambert, *J. Catalysis* 41 (1976) 489.
- [29] H.P. Bonzel and R. Ku, *Surface Sci.* 33 (1972) 91.
- [30] W.L. Winterbottom, *Surface Sci.* 36 (1973) 205.

APPENDIX G

THE OXIDATION OF CARBON MONOXIDE OVER THE
(110) SURFACE OF IRIDIUM

(The text of Appendix G consists of an article coauthored with J. L. Taylor and W. H. Weinberg that has appeared in Journal of Catalysis 62, 1(1980).)

The Oxidation of Carbon Monoxide over the (110) Surface of Iridium¹J. L. TAYLOR,² D. E. IBBOTSON, AND W. H. WEINBERG³*Division of Chemistry and Chemical Engineering, California Institute of Technology, Pasadena, California 91125*

Received June 28, 1978; revised June 18, 1979

The heterogeneously catalyzed reaction of gaseous CO and O₂ to form CO₂ over Ir(110) has been studied, through measurements of the steady-state rate of CO₂ production, by mass spectrometry for surface temperatures between 300 and 1000 K, and for partial pressures of the reactants between 10⁻⁸ and 3 × 10⁻⁶ Torr. The rate expressions developed from a previous analysis of transient reactions were combined into a model that both qualitatively and quantitatively predicts trends in the steady-state measurements. However, the following four phenomena limit the applicability of this model: (1) The activation energies for CO desorption and CO oxidation depend markedly upon the composition of the adlayer on the surface. (2) Diffusion in the adlayer may limit the rates of CO desorption and CO oxidation, but this effect can be included empirically in the rate expression. (3) The catalyst surface is oxidized at temperatures where the steady-state rate of CO oxidation is rapid, i.e., a second species of atomically adsorbed oxygen forms irreversibly near 700 K. (4) Hysteresis in the rate of production of CO₂ with temperature occurs in the steady-state reaction.

INTRODUCTION

Steady-state rates of CO₂ production at low pressures (<10⁻⁵ Torr) have been measured as a function of surface temperature for several platinum metal catalysts (1-7). The rate of production is observed to increase rapidly with temperature until a maximum is reached near 600 K and then to decrease slowly at higher temperatures. In the regime where the rate increases with temperature, the desorption of chemisorbed CO and the subsequent competitive adsorption of oxygen and CO have been thought to be the rate-limiting steps since Langmuir first described this reaction (1). However, the elementary reaction that depicts the combination of oxygen and CO to form CO₂ has been a subject of controversy until recently (6). Although other mechanisms have been suggested (8, 9), the reaction of chemisorbed oxygen atoms with either chemisorbed or physically adsorbed CO

molecules is thought to be the most probable path for CO oxidation (1). In the first case, termed the Langmuir-Hinshelwood (L-H) reaction, the rate of oxidation is proportional to the concentration of chemisorbed CO molecules; in the second case, termed the Eley-Rideal (E-R) reaction, the rate is proportional to the partial pressure of CO. In either instance, the rate is proportional to the coverage of chemisorbed oxygen atoms. At first, the dominant path for CO oxidation was thought to be the E-R reaction (1). The decrease in the steady-state rate of CO₂ production with increasing surface temperature was attributed to a decrease in the coverage of oxygen (2-4). Early studies with modulated molecular beams (10, 11) demonstrated that the decrease in the rate with temperature above 600 K could be explained only by the L-H reaction, for the coverage of CO, rather than oxygen, decreased with increasing temperature. A subsequent study with molecular beams (6) showed that CO oxidation on Pd(111) occurs through the L-H mechanism for surface temperatures below 600 K. Moreover, the oxidation of CO obeys the L-H reaction on Ir(111) (12, 13). Hence, the adsorption of

¹ Supported by the National Science Foundation under Grant DMR77-14976.

² Present address: Proctor and Gamble Company, Miami Valley Laboratories, Cincinnati, Ohio 45247.

³ Camille and Henry Dreyfus Foundation Teacher-Scholar.

oxygen and CO, the desorption of CO, and the L-H reaction to form CO₂ are the four elementary reactions that may limit the rate of CO oxidation over the platinum metal catalysts. For surface temperatures between 300 and 1000 K, where the steady-state rate is greatest at low pressures, the E-R reaction and the desorption of oxygen and CO₂ are thought to affect the rate to second order at most (1, 6).

The present study of CO oxidation over Ir(110) was undertaken to supplement those of earlier investigations and to model the dependence of the steady-state rate of CO₂ production under various conditions. Much of the preliminary modeling of the steady-state rates of CO oxidation has utilized transient studies as presented in a previous paper (14). These transient studies by thermal desorption mass spectrometry focused on the following: (1) the dependence of the rate expressions for CO desorption and CO oxidation upon the composition of the adlayer; and (2) the competitive adsorption of CO and oxygen (14). The present work used a mass spectrometer to monitor the steady-state rate of CO₂ production. In these studies, the partial pressures of the reactants, CO and O₂, were varied between 10⁻⁸ and 3 × 10⁻⁶ Torr, and the temperature of the single-crystal catalyst was varied between 300 and 1000 K. To determine how ordering phenomena influence the oxidation rate, the structure of the chemisorbed layer was investigated with LEED. An interpretation of steady-state oxidation rates will be presented based on the kinetic expressions which were developed earlier (14).

2. EXPERIMENTAL DETAILS

The experiments were conducted in a stainless-steel bell jar with a base pressure below 2 × 10⁻¹⁰ Torr. Partial pressures in the steady-state reactions were measured with a quadrupole mass spectrometer. The order of the overlayer during steady-state reactions was assessed by LEED. The substrate, which was held on a precision manipulator by two 10-mil Ta wires, could be

cooled with liquid nitrogen or heated resistively. The temperature of the substrate was measured with a Pt-Pt/10% Rh thermocouple. The intensity from the mass spectrometer and the EMF from the thermocouple were recorded digitally by a PDP-11/10 computer (15), but they are presented in analog form for convenience.

The catalyst was cut from a single crystal of Ir and was polished within 1° of the (110) orientation. Carbon was removed from the surface through a series of oxidation and reduction cycles, whereas oxygen was removed by annealing the substrate above 1600 K. Prior to each experiment, the surface was free from impurities with 0.01 ml (where 1 ml = 10¹⁵ cm⁻²), as judged by Auger spectroscopy.

Although CO does not dissociate on Ir(110) at low pressures below 1300 K (16), the measurement of steady-state oxidation rates was complicated by the formation of a surface oxide at temperatures where the rate of oxidation is rapid (17). The oxide is distinct chemically from chemisorbed oxygen, and it is less reactive to reduction by CO (14). When a surface that is covered with chemisorbed oxygen is heated to 700 K, the oxide forms irreversibly with a saturation coverage of 0.25 ± 0.05 ml, but decomposes by annealing the surface above 1600 K. Since the presence of the surface oxide is known to affect the chemisorption of CO (16) and oxygen (17) on Ir(110), experiments were performed with both clean and oxidized surfaces of Ir(110) for the transient experiments mentioned (14) and the present steady-state experiments.

The mass spectrometer was used to monitor steady-state rates of CO₂ production as a function of surface temperature and of the composition of the reactant gas. The total pressure of the reactants was varied between 10⁻⁷ and 3 × 10⁻⁶ Torr, whereas the partial pressure of each reactant was varied between 10⁻⁸ and 3 × 10⁻⁶ Torr. The steady-state rates of CO₂ production were measured in the following way. A clean Ir(110) crystal at 300 K was exposed first to

OXIDATION OF CO OVER Ir(110)

CO. Oxygen was not admitted into the reactor until the surface had been exposed to 100 liters of CO. Following this exposure, the surface is covered with CO, which is typically the situation at steady state as is shown in the following section. After the partial pressures of CO, O₂, and CO₂ had equilibrated, the partial pressure of each gas was measured. To obtain reaction rates, the partial pressure of CO₂ was measured as the temperature of the surface was varied at a rate of 80 K min⁻¹. The measured oxidation rate at any temperature did not vary for slower heating rates. The temperature first was increased to 1000 K and then was returned to 300 K. As the temperature of the surface changed, the partial pressures of the reactants, CO and O₂, were not monitored

since these could be determined directly from the change in the partial pressure of CO₂. Moreover, the extents of reaction were small, less than 20%, so that these partial pressures did not change significantly.

3. STEADY-STATE RATES OF CO₂ PRODUCTION

The steady-state rate of CO₂ production (R_r , molecules cm⁻² s⁻¹) was measured as a function of the surface temperature (T) and the partial pressures (P_{CO} and P_{O_2}) of the reactants, CO and O₂. Representative data for total pressures (P_T) of 3.0×10^{-7} and 3.0×10^{-6} Torr are shown in Fig. 1. Oxidation rates were measured for total pressures of 1.0×10^{-7} and 1.0×10^{-6} Torr also. For each total pressure, the ratio of the CO partial pressure to the O₂ partial pressure ($Q \equiv$

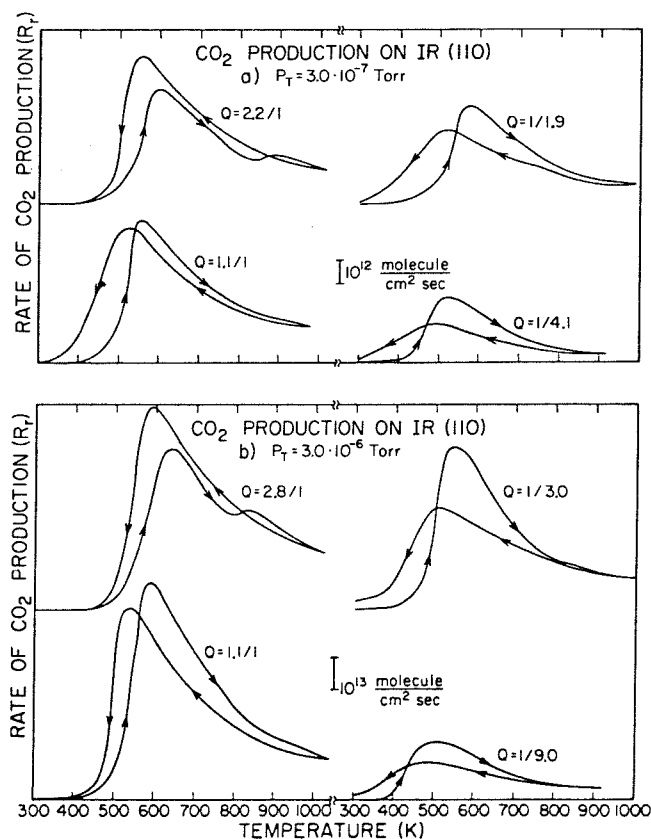


FIG. 1. Steady-state rates of CO₂ production as a function of the surface temperature with the ratio of the partial pressures of the reactants ($Q = P_{CO}/P_{O_2}$) as a parameter. Data are shown for total pressures of: (a) 3.0×10^{-7} , and (b) 3.0×10^{-6} Torr. The arrows on the curves point to the right if the temperature is increasing and to the left if the temperature is decreasing.

TAYLOR, IBBOTSON, AND WEINBERG

$P_{\text{CO}}/P_{\text{O}_2}$) was varied between 0.1 and 10 in separate experiments, which will be referred to as cycles. The arrows shown in Figs. 1 and 2 for each cycle point to the right if the surface temperature is increasing and to the left if the temperature is decreasing. Since typically less than 10% of either reactant gas was converted to CO_2 in these experiments, the ratio Q did not vary significantly with surface temperature. The values of Q shown in Fig. 1 were fixed at 300 K.

Several qualitative features are common among the cycles shown in Fig. 1. The variation in the steady-state rate with the surface temperature for any cycle is similar to that reported for CO oxidation over other surfaces of the platinum metals (1-7). A maximum in the rate appears near 600 K. At this temperature, CO begins to desorb rapidly from the platinum metals, suggesting that CO desorption limits the oxidation rate at lower temperatures (1). On Ir(110), the temperature associated with the maximum rate is independent of the total pressure in the gas phase (at least below approximately 10^{-5} Torr), but it is shifted to higher temperatures as Q is increased. From the transient studies of CO and oxygen on Ir(110), regardless of the coverage of oxygen, the rate of CO adsorption during the steady-state reaction is approximated by (14)

$$C_s \frac{d\theta_{\text{CO}}}{dt} = \frac{P_{\text{CO}}(1 - \theta_{\text{CO}})^2}{(2\pi M_{\text{CO}} k T_g)^{1/2}}, \quad (1)$$

where C_s , θ_{CO} , M_{CO} , k , and T_g are the concentration of adsites (10^{15} cm^{-2}), the fractional coverage of CO, the molecular weight of CO, Boltzmann's constant, and the gas-phase temperature (taken as 300 K.), respectively. Since the rate of CO adsorption [Eq. (1)] increases with Q , this shift is further indication that the desorption of CO limits the rate below 600 K. Two features, which generally are not reported for CO oxidation, appear in the cycles in Fig. 1: (i) A second local maximum in the oxidation rate occurs near 800 K for larger values of

Q ; and (ii) the oxidation rates exhibit hysteresis as the catalyst temperature is varied. Moreover, a change in the maximum rate of CO_2 production is associated with this hysteresis.

The hysteresis might result from the oxidation of the surface since the rates of several elementary reactions in the overall oxidation differ for clean and oxidized Ir(110) (14). To test this hypothesis, the maximum temperature of the catalyst, rather than Q , was varied among cycles. Several cycles for values of Q of 2.7/1 and 1/4.4 are shown in Fig. 2. In these experiments, the surface was cleaned *before the first cycle only*. The total pressure was 1.0×10^{-6} Torr. In the absence of CO, the surface is oxidized near 700 K (17), but, in the presence of CO, the surface may be oxidized at higher temperatures since the processes of CO oxidation and oxide formation may compete for chemisorbed oxygen.

For a value of Q of 2.7, the maximum rate of oxidation did not change if the maximum surface temperature in the first cycle was maintained below 750 K. However, hysteresis still occurred, as is shown in Fig. 2a. This hysteresis appears not to be time dependent; the oxidation rates at the two maxima were stable over 30 min, which was the longest time that the stability was tested. If after the surface temperature had returned to 300 K and the reactant gases were evacuated, CO was the only desorption product observed when the surface was heated to 1800 K. During the second cycle, the second local maximum in the steady-state rate appeared when the surface temperature first exceeded 850 K but did not occur subsequently. As the temperature was returned to 300 K, the maximum rate of CO_2 production increased. Moreover, the increase was irreversible since the rate at the maxima did not change in succeeding cycles so long as the sample was not cleaned. When the reactants were evacuated following the second or succeeding cycles, a $(2 \times 1) p 1g 1$ LEED pattern, characteristic of CO chemisorption on

OXIDATION OF CO OVER Ir(110)

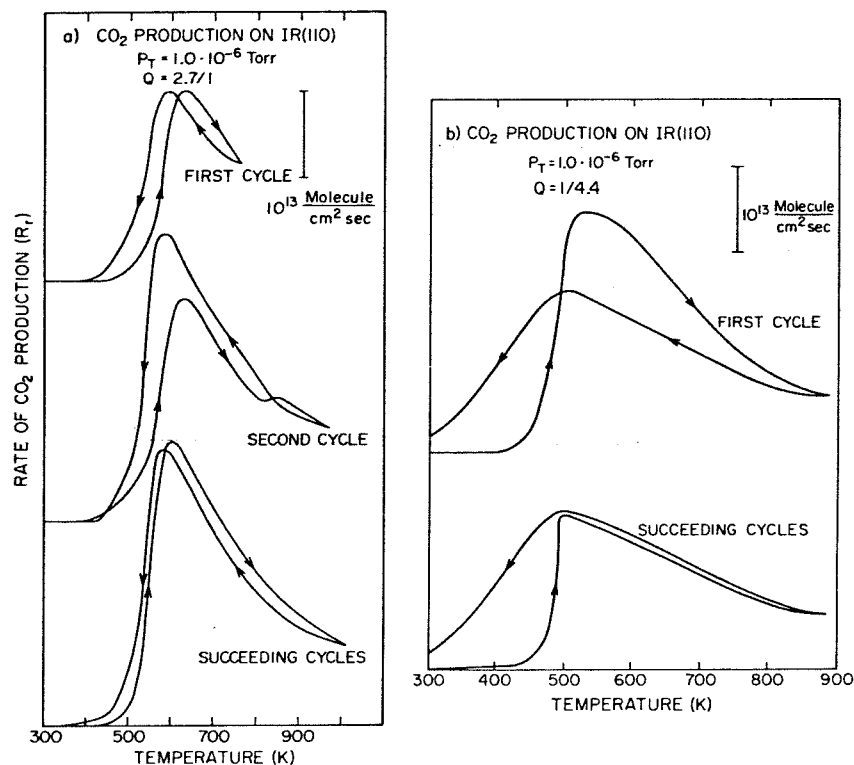


FIG. 2. Steady-state rates of CO_2 production as a function of surface temperature with the surface history as a parameter. Data are shown for a total pressure of 1.0×10^{-6} Torr and for ratios of the partial pressures of the reactants ($Q = P_{\text{CO}}/P_{\text{O}_2}$) of: (a) 2.7/1 and (b) 1/4.4. The arrows on the curves point to the right if the temperature is increasing and to the left if the temperature is decreasing.

oxidized Ir(110) only (16), was observed on the surface. Upon flashing the surface to 1800 K, CO, O_2 , and CO_2 were desorbed so that the catalyst was oxidized during the second cycle, but not during the first cycle. Therefore, although the hysteresis cannot be attributed solely to oxide formation on the catalyst, the second local maximum in the steady-state rate with increasing temperature and the change in the maximum steady-state rate of CO_2 production are associated with oxide formation on the catalyst. Moreover, although the oxide layer may be reduced by CO (14, 16), at least a fraction of the oxide is stable between 300 and 1000 K while CO_2 is produced under steady-state conditions. For values of Q greater than 2, the hysteresis is less pronounced following the oxidation of the surface. Also, the maximum steady-

state rate of CO_2 production is *increased* following the formation of the oxide. Both trends are evident in Fig. 2a.

Data for the experiment described above are shown in Fig. 2b, but here $Q (= P_{\text{CO}}/P_{\text{O}_2})$ is 1/4.4. After the catalyst temperature first exceeded 700 K, oxidation of the surface occurred, and it had to be cooled below 300 K to quench the production of CO_2 . As before, the oxidation of the catalyst was verified both by LEED and by thermal desorption. As Q decreased, the oxide layer generally formed at lower temperatures. As shown in the curve for the first cycle, the maximum steady-state rate of CO_2 production was larger before the surface was oxidized. For values of Q less than 1, the maximum steady-state rate decreased after the surface was oxidized. Moreover, significant hysteresis was not observed for

temperatures above the maximum but was quite pronounced at lower temperatures. Again, hysteresis cannot be attributed solely to differences in the catalytic behavior on the clean and oxidized surfaces. Hysteresis is observed in cycles for which the surface is always clean, i.e., unoxidized, as in the first cycle in Fig. 2a, or always oxidized, as in succeeding cycles in Fig. 2b.

Hysteresis would appear in the CO oxidation rate if the kinetics of the elementary reactions that limit the steady-state rate vary nonlinearly in the coverage of either CO or oxygen. Hence, two or more minima in the total Gibbs energy, each associated with different coverages of reactants, may exist at any surface temperature. Although the Gibbs energy for one minimum may be substantially smaller than the energy for all others, a large activation energy may prevent the system from attaining the lowest possible Gibbs energy. The minimum that is entered as the temperature changes depends upon the composition of the adlayer prior to the change and, therefore, depends upon the rate and the sign of the change. The "steady-state" rates shown in Figs. 1 and 2 did not vary with heating rate as long as it was maintained below 4 K s^{-1} , but they did vary considerably with the sign of the heating rate. Although the two different rates at the same temperature were stable, the rates for larger values of Q tended to become unstable and fall rapidly for temperatures below 600 K as the surface was cooled. In this and other respects, the hysteresis reported for CO oxidation over polycrystalline Pt (7) is similar to that observed in this study.

LEED was not only useful for indicating that the surface was oxidized but was also useful for showing that chemisorbed oxygen clusters into islands when the steady-state rate of CO oxidation is large. On clean Ir(110), a $p(2 \times 2)$ pattern, which appears for oxygen coverages near 0.25 ml in the absence of CO, is formed for temperatures near the maximum in the steady-state rate. On oxidized Ir(110), a $c(2 \times 2)$ pattern,

which appears for oxygen coverages between 0.2 and 0.6 ml in the absence of CO, formed for temperatures near the maximum also.

To obtain apparent activation energies for CO oxidation under steady-state conditions, the logarithm of the steady-state rate of production of CO_2 was plotted as a function of the reciprocal of the surface temperature for each cycle, as in Fig. 3. For all cycles shown, the surface was clean initially, but it was oxidized as the temperature was decreased (i.e., for curves with arrows pointing to the right). The slope of the linear part of each plot gives an apparent activation energy divided by the Boltzmann constant (E_a/k), whereas the intercept gives the logarithm of the apparent preexponential factor ($\ln \nu_a$), recognizing that the rate of production of CO_2 may be written as $R_r = \nu_a \exp(-E_a/RT)$, where T is the surface temperature.

In the region where the rate increases with temperature of the clean surface, the apparent activation energy (E_1) is between 13 and 16 kcal mole $^{-1}$, regardless of the total pressure and the value of Q . In the same region for the oxidized surface, the activation energy is between 5 and 20 kcal mole $^{-1}$, and tends to increase with Q . In the region where the oxidation rate decreases with temperature of clean or oxidized Ir(110), the apparent activation energy (E_2) is between -6 and -3 kcal mole $^{-1}$, regardless of the total pressure and the value of Q .

The apparent preexponential factors for the oxidation reaction may be related empirically to the reactant partial pressures (P_{CO} and P_{O_2}) by

$$\nu_a = \nu_i P_{\text{CO}}^m P_{\text{O}_2}^n \quad (2)$$

where ν_i , m , and n are constants. In the region where the rate increases with temperature on the clean surface, the apparent preexponential factor is proportional to $P_{\text{O}_2}^2/P_{\text{CO}}$ ($=P_{\text{O}_2}/Q$), as shown in Fig. 4. For this region, the oxidation rate (R_r in molecules $\text{cm}^{-2} \text{ s}^{-1}$) is given by

OXIDATION OF CO OVER Ir(110)

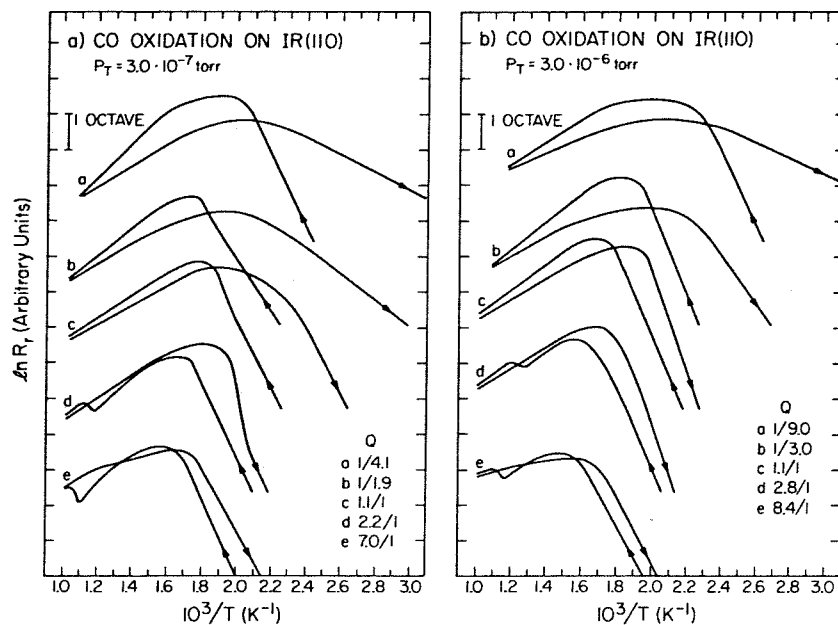


FIG. 3. Arrhenius plots for the variation in the steady-state rates of CO_2 production with surface temperature. Data are shown for various ratios of the partial pressures (Q) and for total pressures of: (a) 3.0×10^{-7} , and (b) 3.0×10^{-6} Torr. The arrows on the curves point to the left if the temperature is increasing and to the right if the temperature is decreasing.

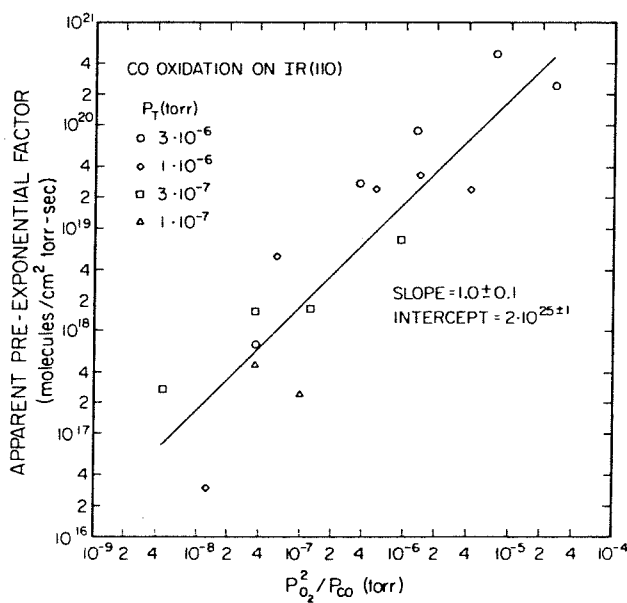


FIG. 4. The variation in the apparent preexponential factor with the ratio of the square of the oxygen pressure to the CO pressure. The apparent preexponential factors were derived from plots similar to those in Fig. 3 and pertain to the region where the apparent activation energy is positive. Only points associated with an increasing surface temperature are shown.

TAYLOR, IBBOTSON, AND WEINBERG

$$R_{r1} = \nu_1(P_{O_2}^2/P_{CO})\exp[-E_1/RT], \quad (3)$$

where E_1 is between 13 and 16 kcal mole⁻¹, and ν_1 , from the intercept of Fig. 4, is $2 \times 10^{25 \pm 1}$ molecules cm⁻² Torr⁻¹ s⁻¹. The scatter in the data of Fig. 4 is not surprising since an error of 2 kcal mole⁻¹ in E_1 causes a tenfold variation in ν_1 . The apparent preexponential factors were proportional to $P_T Q$ and $P_{O_2}^{3/2}$ also, but these correlations fit poorly at the extremes in the abscissa. In the region where the rate increased with temperature on the oxidized surface, no correlation could be found since the apparent activation energy varied markedly with the partial pressures of the reactants.

In the region where the rate decreases with the temperature of the clean or oxidized Ir(110) surface, the apparent preexponential factor is proportional to P_{CO} , as shown in Fig. 5. There, the factors for the clean surface are shown as empty symbols, whereas the factors for the oxidized surface are shown as filled symbols. No other correlation in the form of Eq. (2) that fits the data could be found. For this tem-

perature regime, the oxidation rate (R_{r2}) is given by

$$R_{r2} = \nu_2 P_{CO} \exp[-E_2/kT], \quad (4)$$

where E_2 is between -6 and -3 kcal mole⁻¹, and ν_2 , from the intercept of Fig. 5, is $2 \times 10^{19 \pm 1}$ molecules cm⁻² Torr⁻¹ s⁻¹.

As is clear from Fig. 3, Eqs. (3) and (4) intersect at temperatures near the maximum in the steady-state oxidation rate. If the intersection coincides exactly with the maximum, the temperature at the maximum (T_{max}) would be a function of $Q (= P_{CO}/P_{O_2})$ only, and it would be given implicitly by

$$Q^2 = \nu_3 \exp[-E_3/kT_{max}], \quad (5)$$

where ν_3 is equal to ν_1/ν_2 or approximately $10^{6 \pm 2}$, and E_3 is equal to $(E_1 - E_2)$, approximately 19 ± 3 kcal mole⁻¹. This equation does not predict T_{max} correctly since T_{max} is to the left of the intersection for values of Q less than 2 and is to the right of the intersection for values of Q greater than 2. However, as shown in Fig. 6, a plot of $\ln Q$ as a function of T_{max}^{-1} gives approximately lines

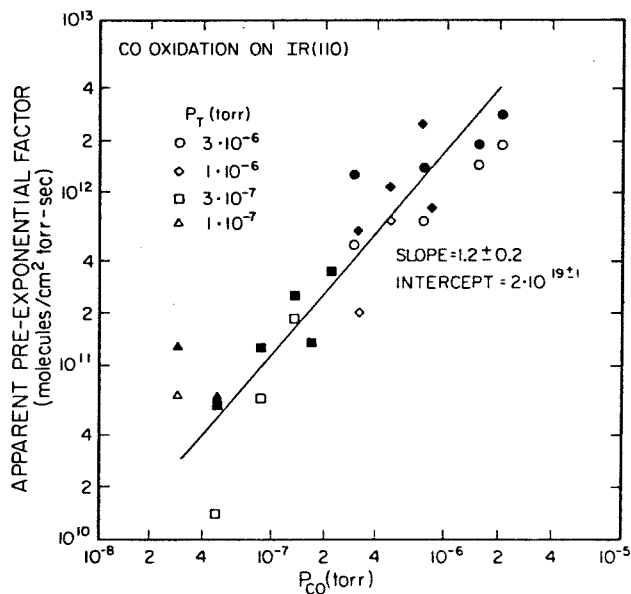


FIG. 5. The variation in the apparent preexponential factor with the partial pressure of CO. The apparent preexponential factors were derived from plots similar to those in Fig. 3 and pertain to the region where the apparent activation energy is negative. Points associated with an increasing surface temperature are hollow whereas points associated with a decreasing surface temperature are solid.

OXIDATION OF CO OVER Ir(110)

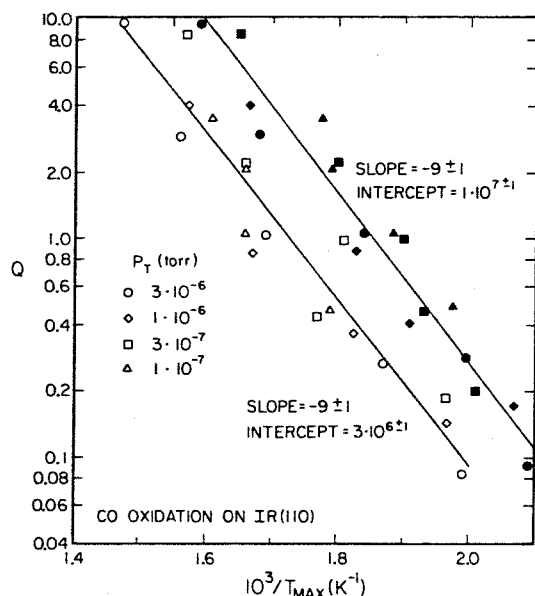


FIG. 6. The variation in the partial pressure ratio $Q (= P_{CO}/P_{O_2})$ with the reciprocal of the temperature associated with the maximum steady-state rate of CO_2 production. Points pertaining to clean Ir(110) are hollow whereas points pertaining to oxidized Ir(110) are solid.

for both clean and oxidized Ir(110). There, points for the respective surfaces are empty and filled. In either case, the slope is -9000 ± 1000 K, which is nearly equal to E_3/k . Also, the intercepts, 3×10^6 for the clean surface and 1×10^7 for the oxidized surface, are nearly equal to ν_3 . Hence, the temperature at the maximum in the steady-state rate is approximated by Eq. (5) if the exponent of Q is changed from 2 to 1. Moreover, the rate at the maximum is generally within a factor of 2 lower than the rate given by the intersection of Eqs. (3) and (4).

4. KINETIC MODEL OF STEADY-STATE OXIDATION RATES

A kinetic model will be developed to interpret the steady-state oxidation rates in light also of the transient studies presented elsewhere (14). The rates of three elementary reactions—the desorption of CO_2 , the desorption of oxygen, and the oxidation of CO via the E-R mechanism—are not in-

cluded in this model. In the temperature range where the steady-state rates were measured, the rate of CO_2 desorption is extremely rapid and the rate of oxygen desorption is extremely slow, so that both processes do not affect the overall oxidation rate. Studies with modulated molecular beams (6, 10, 11) have shown that CO oxidation over the platinum metals between 300 and 1000 K occurs predominantly through the L-H mechanism, whereas the oxidation rate via the E-R mechanism is undetectable. Moreover, the decrease in the oxidation rate observed above 600 K on Ir(110) cannot be attributed to a decrease in the coverage of oxygen and can be explained only if oxidation occurs by the L-H mechanism.

Four processes—the desorption of CO, the oxidation of CO via the L-H mechanism, the adsorption of CO, and the adsorption of oxygen—may limit the steady-state rate of CO_2 production. The rate expressions for the respective processes, determined from transient experiments (14), are given by Eqs. (6), (7), (1), and (8).

$$R_d = -\nu_d(\theta_{CO}, \theta_O) C_s \theta_{CO} \exp[-E_d(\theta_{CO}, \theta_O)/kT], \quad (6)$$

$$R_r = -\nu_r(\theta_{CO}, \theta_O) C_s^2 \theta_{CO} \theta_O \exp[-E_r(\theta_{CO}, \theta_O)/kT], \quad (7)$$

$$C_s \frac{d\theta_O}{dt} = \frac{2S_O(O_2)P_{O_2}(1-\theta_O)^2(1-\theta_{CO})^2}{(2\pi M_{O_2}kT_g)^{1/2}}. \quad (8)$$

Here, $S_O(O_2)$, θ_O , and M_{O_2} are the initial sticking probability of oxygen, the fractional coverage of oxygen, and the molecular weight of oxygen, respectively. The diffusion of oxygen and CO on the surface also may influence the steady-state rate, but these effects are included empirically in Eqs. (6) and (7). When CO oxidation is proceeding under steady-state conditions, the time derivatives of the oxygen and CO coverages are each zero. That is, the rate of CO oxidation is equal to the rate of oxygen ad-

TAYLOR, IBBOTSON, AND WEINBERG

sorption, and the sum of the rates of CO oxidation and CO desorption is equal to the rate of CO adsorption. Hence, Eqs. (6), (7), (1), and (8) may be reduced to three equations

$$R_r + k_2\theta_{\text{CO}} = k_1P_{\text{CO}}(1 - \theta_{\text{CO}})^2, \quad (9)$$

$$R_r = k_3P_{\text{O}_2}(1 - \theta_{\text{CO}})^2(1 - \theta_{\text{O}})^2, \quad (10)$$

$$R_r = k_4\theta_{\text{O}}\theta_{\text{CO}} \quad (11)$$

in three unknowns— θ_{CO} , θ_{O} , and R_r . Here,

$$k_1 = (2\pi M_{\text{CO}}kT_g)^{-1/2},$$

$$k_2 = \nu_d C_s [\exp -E_d/kT],$$

$$k_3 = 2S_{\text{O}}(\text{O}_2)[2\pi M_{\text{O}_2}kT_g]^{-1/2},$$

$$k_4 = \nu_r C_s^2 \exp[-E_r/kT].$$

The temperature in the gas phase for the steady-state data is 300 K, $S_{\text{O}}(\text{O}_2)$ is approximately equal to 0.25 (17), and C_s is 10^{15} cm⁻². Hence, the values of k_1 and k_3 are approximately 4×10^{20} and 2×10^{20} molecules cm⁻² Torr⁻¹ s⁻¹, respectively. Average values of ν_d , E_d , ν_r , and E_r that are pertinent for the steady-state data are $10^{5.5 \pm 0.5}$ s⁻¹, 14–17 kcal mole⁻¹, 3×10^{-10} cm² s⁻¹, and 12 kcal mole⁻¹ (14). Although Eqs. (9)–(11) may be solved exactly for the steady-state rate under any conditions, the data are analyzed best by using these equations to describe the asymptotic rates above and below the maximum.

In the region where the steady-state oxidation rate increases with the surface temperature, the reaction rate is limited by the desorption of CO and the competitive adsorption of oxygen and CO (1–3, 6, 10–13). In this region, the coverage of oxygen is small and may be ignored in Eq. (10) since chemisorbed CO is present to block sites for oxygen chemisorption. Also, the flux of CO molecules to the surface always exceeds the measured oxidation rate by one or two orders of magnitude. Thus, the desorption rate must be large compared to the oxidation rate. (From the average values of the rate parameters for CO oxidation and desorption, the predicted ratio of the rates is nearly unity between 500 and 1000 K. How-

ever, an error of 2 kcal mole⁻¹ in either of the activation energies would change the ratio by tenfold, so the experimentally determined rates are more appropriate for interpreting the steady-state data.) If the coverage of oxygen is small, and if the desorption rate of CO substantially exceeds the oxidation rate, Eqs. (9) and (10) reduce to

$$R_r = (k_3\nu_d C_s/k_1)Q^{-1} \exp[-E_d/kT]. \quad (12)$$

In deriving Eq. (12), the coverage of CO was assumed to vary negligibly in temperature and to be near one. These assumptions are appropriate since, as was shown previously (14), the variation in the rate resulting from the change in the activation energy with coverage may overshadow completely the variation resulting from coefficients that depend on coverages to integral exponents. Moreover, the coverage of CO is near unity for the onset of the steady-state reaction. Equation (12) is identical to the expression derived by Langmuir (1) to describe the oxidation rate on Pt in the same temperature regime. Although the adsorption kinetics given by Eqs. (1) and (8) differ from the expressions used by Langmuir, the same expression describes the steady-state rate in either case since the desorption of CO is rate limiting in both models.

For clean Ir(110), the empirical activation energy from Eq. (3), 13–16 kcal mole⁻¹, agrees closely with the predicted value from Eq. (12), 17 kcal mole⁻¹, which was estimated from transient experiments, described elsewhere (14). However, the predicted and empirical dependences of the rate upon the reactant partial pressures are different. The rate is proportional to the pressure of oxygen in the model expression, but varies as the pressure of oxygen squared in the empirical expression. This squared dependence, which is observed also for CO oxidation over Pd(111) for similar temperatures (6), may be related to the diffusion of chemisorbed oxygen. Oxygen diffusion on Ir(110) becomes rapid at temperatures where the oxidation rate becomes

OXIDATION OF CO OVER Ir(110)

rapid (17). Moreover, chemisorbed oxygen must diffuse since the O- p (2×2) and the O- c (2×2) LEED patterns are observed during the steady-state reaction. Oxygen atoms may diffuse in pairs so that the diffusion rate depends upon the square of the coverage (18). In the regime where oxygen competes with CO for adsorption sites, the coverage of oxygen is proportional to the pressure of oxygen as indicated by Eqs. (10) and (12). Hence, if the diffusion of oxygen limits the overall oxidation rate, the rate would vary as the square of the partial pressure of oxygen. (This variation in the rate cannot be explained by the reaction being limited to the edges of islands of chemisorbed oxygen atoms, for the rate would then vary as the square root of the oxygen pressure.) Information concerning the kinetics of oxygen diffusion is needed to relate the empirical preexponential factor in Eq. (3) to a predicted value, like that in Eq. (12).

For oxidized Ir(110), no empirical expression for the overall oxidation, similar to Eq. (12), could be found. The data for the oxidized surface were obtained in the part of the hysteresis cycles where the surface temperature is decreasing, rather than increasing, so that the model presented in the previous two paragraphs may not be appropriate for this region. Moreover, the oxide, which is reactive to reduction by CO, may be decomposed partially as the temperature is decreased, but this conjecture was not tested.

In the region where the steady-state rate is decreasing with the surface temperature, the empirical expression for the rate over clean and oxidized Ir(110) [Eq. (4)] may be derived from Eqs. (9)–(11). As determined from desorption rates of CO calculated elsewhere (14), the coverage of CO is small for this temperature regime. As shown previously, the desorption rate of CO is much larger than the oxidation rate. Hence, Eq. (9) is approximated closely by $\theta_{CO}k_2 = k_1P_{CO}$. Using this expression to give the coverage of CO, Eq. (11) becomes

$$R_r = (k_1C_s\theta_0\nu_r/\nu_d)P_{CO} \exp[(E_d - E_r)/kT]. \quad (13)$$

Both the activation energy (6) and the pressure dependence (5–7, 19–21) for the oxidation rate in this expression have been derived previously for other platinum metal catalysts. The coverage of CO is too small to inhibit the adsorption of oxygen, and, as determined from the data in Fig. 1, the oxidation rate is not limited by the flux of oxygen to the surface. Thus, the coverage of oxygen in this temperature regime approaches the saturation value, 0.5 ml. Using the average values for ν_d and ν_r that were given previously, the predicted value of the preexponential factor from Eq. (13), $k_1C_s\theta_0\nu_r/\nu_d = 2 \times 10^{20 \pm 1}$ molecules $\text{cm}^{-2} \text{Torr}^{-1} \text{s}^{-1}$, is quite close to the empirical value from Eq. (4), $2 \times 10^{19 \pm 1}$ molecules $\text{cm}^{-2} \text{Torr}^{-1} \text{s}^{-1}$. Moreover, the pressure dependences of the two expressions are identical, and the predicted value for the activation energy, -5 to -2 kcal mole^{-1} , is quite close to the observed value, -6 to -3 kcal mole^{-1} .

CONCLUSIONS

The heterogeneously catalyzed reaction of gaseous CO and O₂ to form CO₂ over Ir(110) has been studied through measurements of the steady-state rate of CO₂ production and of the transient kinetics of elementary reactions that may limit the steady-state rate (14). Both clean and oxidized Ir(110) were used as catalysts. The surface oxide, which is distinct chemically from chemisorbed oxygen, forms irreversibly at temperatures where the steady-state rate of CO oxidation is rapid. The desorption of CO, the oxidation of CO via the Langmuir–Hinshelwood mechanism, the adsorption of CO, and the adsorption of oxygen may limit the steady-state rate of CO oxidation, whereas the desorption of oxygen, the desorption of CO₂, and the oxidation of CO via the Eley–Rideal mechanism do not affect the rate significantly for catalyst temperatures between 300 and 1000

TAYLOR, IBBOTSON, AND WEINBERG

K. The rates of the four elementary reactions that may limit the steady-state rate depend complexly on the composition of the adlayer. Moreover, the steady-state rate may depend critically upon the diffusion rates of chemisorbed oxygen and CO, which were not measured directly in this study.

Models for the steady-state oxidation rate, based on the rate expressions developed from the transient experiments (14), give a consistent interpretation of the rate data for surface temperatures from 300 to 1000 K and for partial pressures of the reactants between 1×10^{-8} and 3×10^{-6} Torr. Below 600 K, where the oxidation rate increases with the surface temperature, the rate is inversely proportional to the partial pressure of CO, but is proportional to the square of the partial pressure of oxygen. The unusual variation in the rate with the oxygen pressure may be associated with the diffusion of chemisorbed oxygen on the surface. If the steady-state rate is measured as the surface temperature is increased below 600 K, the apparent activation energy and preexponential factor for the steady-state rate on clean Ir(110) are 14 ± 2 kcal mole⁻¹ and $2 \times 10^{25 \pm 1}$ molecules cm⁻² Torr⁻¹ s⁻¹. However, if the rate is measured as the temperature is decreased, the apparent activation energy and preexponential factor vary considerably due to hysteresis in the rate of CO₂ production. Since the rates of the elementary reactions that limit the steady-state rate are nonlinear functions of the coverages of CO and oxygen, the Gibbs energy for any surface temperature may have several local minima so that hysteresis may occur. Above 600 K, where the steady-state rate decreases with the surface temperature, the oxidation rate is proportional to the partial pressure of CO, but is independent of the partial pressure of oxygen. Regardless of whether the surface is clean or oxidized, and whether the surface temperature is being increased or de-

creased, the apparent activation energy and preexponential factor for the overall rate coefficient are -4 ± 2 kcal mole⁻¹ and $2 \times 10^{19 \pm 1}$ molecules cm⁻² Torr⁻¹ s⁻¹. The temperature associated with the maximum oxidation rate at steady state occurs near the intersections of the asymptotic curves above and below 600 K, and it is inversely proportional to the logarithm of the ratio of the CO partial pressure to the oxygen partial pressure.

REFERENCES

1. Langmuir, I., *Trans. Faraday Soc.* 17, 621 (1922).
2. Ertl, G., and Rau, P., *Surface Sci.* 15, 443 (1969).
3. Bonzel, H. P., and Ku, R., *J. Vac. Sci. Technol.* 9, 663 (1971).
4. Christmann, K., and Ertl, G., *Z. Naturforsch. A* 28a, 1144 (1973).
5. Close, J. S., and White, J. M., *J. Catal.* 36, 185 (1975).
6. Engel, T., and Ertl, G., *J. Chem. Phys.* 69, 1267 (1978).
7. Golchet, A., and White, J. M., *J. Catal.* 53, 266 (1978).
8. Heyne, H., and Tompkins, F. C., *Proc. Royal Soc. A* 292, 460 (1966).
9. Winterbottom, W. L., *Surface Sci.* 36, 205 (1973).
10. Palmer, R. L., and Smith, J. N., Jr., *J. Chem. Phys.* 60, 1453 (1973).
11. Pacia, N., Cassuto, A., Pentenero, A., and Weber, B., *J. Catal.* 41, 455 (1976).
12. Zhdan, P. A., Borekov, G. K., Egelhoff, W. F., Jr., and Weinberg, W. H., *Surface Sci.* 61, 377 (1976).
13. Ivanov, V. P., Borekov, G. K., Savchenko, V. I., Egelhoff, W. F., Jr. and Weinberg, W. H., *J. Catal.* 48, 269 (1977).
14. Taylor, J. L., Ibbotson, D. E., and Weinberg, W. H., Submitted.
15. Taylor, J. L., Ph.D. thesis, California Institute of Technology, 1978.
16. Taylor, J. L., Ibbotson, D. E., and Weinberg, W. H., *J. Chem. Phys.* 69, 4298 (1978).
17. Taylor, J. L., Ibbotson, D. E., and Weinberg, W. H., *Surface Sci.* 79, 349 (1979).
18. Thiel, P. A., Yates, J. T., Jr., and Weinberg, *Surface Sci.* 82, 22 (1979).
19. Matsushima, T., and White, J. M., *J. Catal.* 39, 265 (1975).
20. Matsushima, T., Almy, D. B., and White, J. M., *Surface Sci.* 67, 89 (1977).
21. Matsushima, T., and White, J. M., *Surface Sci.* 67, 122 (1977).

APPENDIX H
ADDITIONS TO THE POL OPERATING SYSTEM

Two additions to the Peripheral Oriented Language (POL) operating system, used for the experiments described in this thesis, were implemented that are worthy of mention. The first described is a new command added to the existing software(1) and the second is the description of an additional digital-to-analog converter (DAC) wired to the POL system.

(A) SHI(FT) n, n = 1-10

SHI(FT) is the 69th command for the POL program. It is used as an immediate command to shift data contained in a file by n data slots. Useful applications of this data analysis command are: (1) to align the elastic beam energy of several EELS files at a constant channel number (zero of energy) and (2) to align XPS or UPS files that are offset from one another by an integral multiple of the energy increment used in an experiment. SHI(FT) operates on the file that is last referenced in the immediate mode. Data are always shifted to lower slot numbers, where the first n slots are lost and the last n slots are duplicated. The label is not altered by the command, so the user must be aware of this fact when analyzing data.

To implement this command entries were appended to various Fixed Reserve Addresses as delimited below.

Fixed Reserve Table- COMADD COMNAM LIMIT1 LIMIT2 COMFL1 COMFL2
 (Entry) SSHIFT 26063 0 10 4 201

The command subroutine, SSHIFT, was added to the source file, POLNUM.MAC, and is given below.

```
SSHIFT:   JSR     PC,NUMONE
          MOV     R5,R2
1$:       ADD     #4,R5
          DEC     R3
          DEC     R1
          BGT     1$

2$:       MOV     (R5)+,(R2)+ (one slot = two words)
          MOV     (R5)+,(R2)+
          DEC     R3
          BGT     2$
          JMP     NEWCOM
```

Reference

1. J. L. Taylor, Ph. D. Thesis, California Institute of Technology, 1978.

(B)

A 16-bit digital-to-analog converter (DAC) was added to the POL system to control the mass filter of the UTI 100C mass spectrometer and the electron energy sampled by the PHI double-pass cylindrical mirror analyzer. The motivation behind this addition was to improve the stability and resolution available for measuring several mass peaks in one experiment (such as in thermal desorption mass spectrometry) and for setting a constant electron energy that is desired (such as in XPS), respectively, over a period of several hours. Resolutions available using 16 bits are 0.0046 amu and 0.061 eV, respectively, corresponding to (0 - 10 V) a least significant bit resolution of 153 μ V. In order to maintain this resolution, it was necessary to eliminate any possible ground loops by tying the grounds of the unit controlled and the DAC at a single point. Furthermore, the experimental system and the POL operating system must have isolated grounds from one another as well. With these considerations the schematic for the DAC unit is shown in Fig. 1.

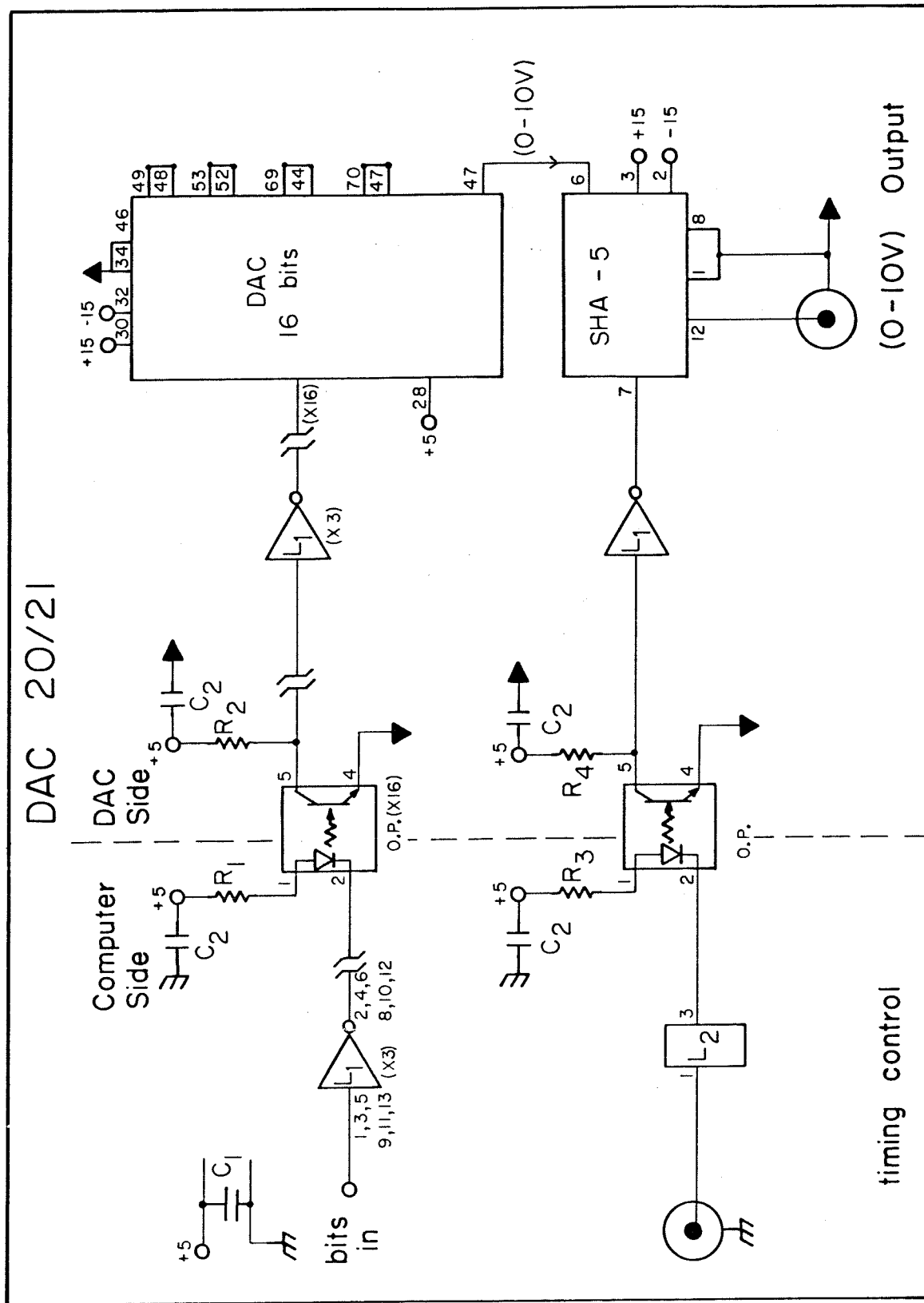


Figure1

C_1 200 μ F/25 V Ta
 C_2 1 μ F/35 V Ta
 R_1 470 Ω
 R_2 5 k Ω
 R_3 270 Ω
 R_4 200 Ω
 L_1 7414 Hex Inverter
O.P. 4N32 Optical Isolator, Darlington Pair
 L_2 8838 Line Driver
DAC 1136J Analog Devices
SHA-5 Sample-Hold Amplifier, Analog Devices
All resistors are $\frac{1}{4}$ W/1%.